NEW METHODS FOR RED BLOOD CELL RESEARCH AND DIAGNOSIS

EDITED BY: Richard Van Wijk and Paola Bianchi
PUBLISHED IN: Frontiers in Physiology and Frontiers in Medicine

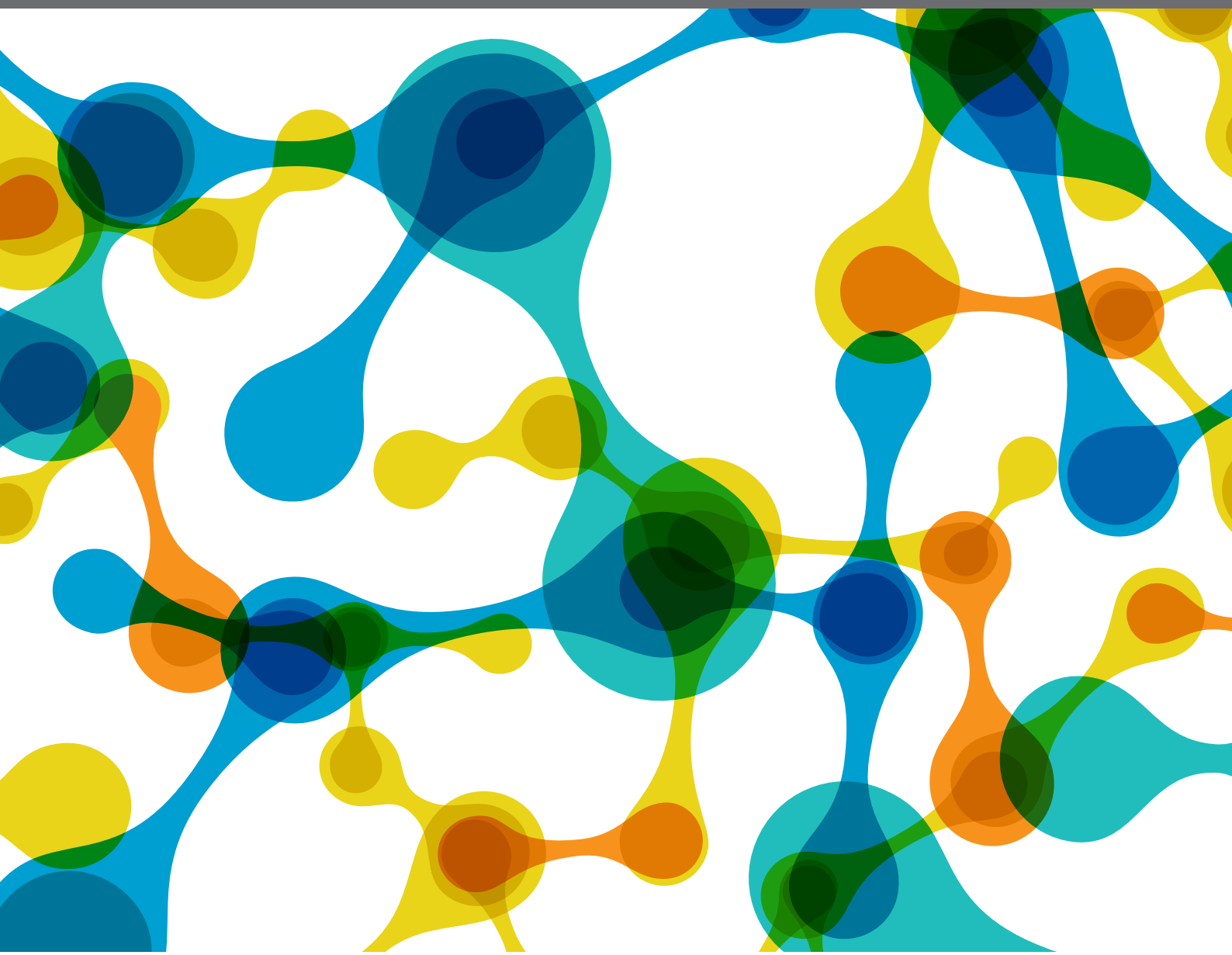

frontiers Research Topics

frontiers

ISSN 1664-8714
ISBN 978-2-88971-699-9
DOI 10.3389/978-2-88971-699-9

About Frontiers

Frontiers is more than just an open-access publisher of scholarly articles: it is a pioneering approach to the world of academia, radically improving the way scholarly research is managed. The grand vision of Frontiers is a world where all people have an equal opportunity to seek, share and generate knowledge. Frontiers provides immediate and permanent online open access to all its publications, but this alone is not enough to realize our grand goals.

Frontiers Journal Series

The Frontiers Journal Series is a multi-tier and interdisciplinary set of open-access, online journals, promising a paradigm shift from the current review, selection and dissemination processes in academic publishing. All Frontiers journals are driven by researchers for researchers; therefore, they constitute a service to the scholarly community. At the same time, the Frontiers Journal Series operates on a revolutionary invention, the tiered publishing system, initially addressing specific communities of scholars, and gradually climbing up to broader public understanding, thus serving the interests of the lay society, too.

Dedication to Quality

Each Frontiers article is a landmark of the highest quality, thanks to genuinely collaborative interactions between authors and review editors, who include some of the world's best academicians. Research must be certified by peers before entering a stream of knowledge that may eventually reach the public - and shape society; therefore, Frontiers only applies the most rigorous and unbiased reviews.
Frontiers revolutionizes research publishing by freely delivering the most outstanding research, evaluated with no bias from both the academic and social point of view. By applying the most advanced information technologies, Frontiers is catapulting scholarly publishing into a new generation.

What are Frontiers Research Topics?

Frontiers Research Topics are very popular trademarks of the Frontiers Journals Series: they are collections of at least ten articles, all centered on a particular subject. With their unique mix of varied contributions from Original Research to Review Articles, Frontiers Research Topics unify the most influential researchers, the latest key findings and historical advances in a hot research area! Find out more on how to host your own Frontiers Research Topic or contribute to one as an author by contacting the Frontiers Editorial Office: frontiersin.org/about/contact

NEW METHODS FOR RED BLOOD CELL RESEARCH AND DIAGNOSIS

Topic Editors:
Richard Van Wijk, Utrecht University, Netherlands
Paola Bianchi, IRCCS Ca 'Granda Foundation Maggiore Policlinico Hospital, Italy

Topic Editors Dr. Paola Bianchi and Dr. Richard Van Wijk provide consultancy to Agios Pharmaceuticals. Dr. Richard Van Wijk has research support from RR Mechatronics and Agios Pharmaceuticals.

Citation: Van Wijk, R., Bianchi, P., eds. (2021). New Methods for Red Blood Cell Research and Diagnosis. Lausanne: Frontiers Media SA.
doi: 10.3389/978-2-88971-699-9

Table of Contents

frontiers in Physiology

EDITORIAL
published: 29 September 2021
doi: 10.3389/fphys.2021.755664

Editorial: New Methods for Red Blood Cell Research and Diagnosis

Paola Bianchi[1] *and Richard van Wijk*[2*]

[1] *Hematology Unit, Pathophysiology of Anemias Unit, Foundation IRCCS Ca' Granda Ospedale Maggiore of Milan, Milan, Italy,* [2] *Central Diagnostic Laboratory-Research, University Medical Center Utrecht, Utrecht University, Utrecht, Netherlands*

Keywords: red blood cell, anemia, diagnostics, ektacytometry, next generation sequencing, metabolomics (OMICS), sickle cell disease, RBC membrane defects

Editorial on the Research Topic

New Methods for Red Blood Cell Research and Diagnosis

The last few years have been a challenging and exciting period for the study of RBC pathophysiology and related defects associated with hemolytic anemia. In fact, these disorders, regarded as hematological niche disorders, have today aroused greater interest thanks to the availability of new technological and therapeutical approaches, such as gene therapy for sickle cell disease (SCD) (Orkin and Bauer, 2019) and thalassemia (Boulad et al., 2018) or more recently small molecule activator therapy for pyruvate kinase deficiency (Grace et al., 2019). In this context, the need of a more precise diagnosis becomes crucial, accelerating the improvement of diagnostic procedures and differential diagnosis by developing new methodologies to investigate RBC properties in normal and pathological conditions.

This Research Topic has been specifically designed to give rooms to new experimental and diagnostic approaches for the study of red blood cells. The success of this Research Topic, with 15 articles accepted for publications and ranging from topics that address basic science, diagnosis and therapy as well confirms the growing interest of the scientific community on these themes.

In an extensive review by Russo et al., advantages and disadvantages of Next Generation Sequencing (NGS) are critically reviewed, focusing on diagnosis and basic research of rare hemolytic anemias and considering the future perspectives in this era of precision medicine. There are several approaches to this molecular testing, including custom-designed targeting panels (t-NGS), whole-exome sequencing (WES), or wide genome sequencing (WGS), the choice of which depends on phenotyping, genetic heterogeneity, and gene size. For patients who show complete phenotyping, single-gene testing remains recommended. The use of NGS, also allows the identification of new causative genes, and of polygenic conditions and genetic factors that modify disease severity of hereditary anemias. As a consequence, NGS has been adopted by many expert centers for hemolytic anemias as part of the diagnostic work-up. In a monocentric study, the 3 years' experience with targeted-NGS platform (consisting of 43 genes) used in the diagnosis of congenital hemolytic anemias has been critically evaluated by Fermo et al. One hundred and twenty two patients were investigated, and the results compared with that of a conventional laboratory diagnostic workup. The method was able to establish the diagnosis in 74% of patients with a diagnostic workup based on laboratory testing, and in an additional 35% of patients that were undiagnosed after extensive hematologic investigations. This indicates that rare and ultra-rare RBC diseases definitely benefits of t-NGS approaches. This is for example the case for a new variant of *ALAS2* gene associated with sideroblastic anemia described by Lira Zidanes et al. Iron loading anemias are characterized by ineffective erythropoiesis and iron overload and in the presented case iron parameters were discussed in light of the atypical clinical presentation and genotype. Finally, a combined t-NGS and WES approach has been used to characterize a series of five patients

OPEN ACCESS

Edited and reviewed by:
Lars Kaestner,
Saarland University, Germany

***Correspondence:**
Richard van Wijk
r.vanWijk@umcutrecht.nl

Specialty section:
This article was submitted to Red Blood Cell Physiology, a section of the journal Frontiers in Physiology

Received: *09 August 2021*
Accepted: *20 August 2021*
Published: *29 September 2021*

Citation:
Bianchi P and van Wijk R (2021) Editorial: New Methods for Red Blood Cell Research and Diagnosis. Front. Physiol. 12:755664. doi: 10.3389/fphys.2021.755664

with unstable hemoglobinopathies, as reported by Rizzuto et al. Also this group of rare disorders represents a diagnostic challenge due to its rarity, the dominant pattern of inheritance and the occurrence of *de novo* variants. The inclusion of α and β-globin genes in routine NGS approaches for rare anemia disorders has to be considered to improve the diagnostic efficiency of rare anemias.

The recent developments in high-throughput omics approaches paved the way to perform proteomic and metabolomic analys of RBCs, focusing on differences between normal and pathological conditions. RBCs offer in fact an interesting model to study cellular metabolism. Moreover metabolomics may be used to better understand the changes that occur during storage of blood for transfusion purposes. Zoomics is a new branch of metabolomics that is uses to investigate the blood metabolome across species. Bertelone et al. provide the here first comparative metabolomics analysis of fresh and stored human, baboon, and macaque RBCs. The results indicated similarities and differences across species, which ultimately resulted in a differential propensity to undergo morphological alterations and lysis as a function of the duration of refrigerated storage.

The pathophysiological basis of RBC membrane channel defects has only recently been described, establishing the molecular basis that underlies hereditary dehydrated (*PIEZO1*) and overhydrated (*RhAg*) forms of hereditary stomatocytosis, and some other rarer forms (*KCNN4*, *GLUT1*, *ABCB6*, and *ABCB5*). Most of the causative mutations encode gain of function variants and a very tight interplay among specific and non-selective channels has been described. Recent studies also confirm that hereditary stomatocytosis is often associated with a certain degree of dyserythropoiesis. *PIEZO1* expression for example is not limited to RBC but its expression levels are significantly higher in erythroid precursors. In a study by Aglioro et al. it was observed that integrin α4β1 and α5β1 present on erythroblasts facilitate *PIEZO1* interactions in erythroblastic islands. Chemical activation of *PIEZO1* leads to increased adhesion to VCAM1 and fibronectin in flowing conditions, suggesting an inside-out activation of integrin on erythroblasts. This phenomenon seems to be facilitated by calcium-dependent activation of Ca^{2+}-dependent protein kinase C and Calpain. This study suggests a novel involvement of Ca^{2+} signaling during erythropoiesis. From a diagnostic point of view, Gardos channelopathies are often difficult to be diagnosed due to the absence of specific laboratory markers of the disease. A novel and quick approach to differentiate between *KCNN4* and *PIEZO1* variants, allowing to rapidly target these patients for gene analysis, has been proposed by Picard et al. For this they used automated reticulocytes parameters obtained from an ADVIA 2120 (Siemens®) analyzer, in particular the reticulocyte mean corpuscular volume (rMCV) and mean corpuscular hemoglobin concentration (rMCHC). rMCV was found to be significatively smaller than MCV and rMCHC higher than MCHC in 15 *KCNN4* mutated patients vs. 79 *PIEZO1* cases. Cut-off values were proposed to obtain a 100% sensitivity and specificity, regardless of age, mutation or splenectomy status.

Ektacytometry is a technique that is more and more commonly applied in diagnostic approaches for red blood cell disorders. In particular osmotic gradient ektacytometry is now considered the gold standard for the diagnosis of red blood cell membrane disorders, such as hereditary spherocytosis (HS), and hydration disorders such as *PIEZO1*-defective hereditary xerocytosis. Very recently a new form of ektacytometry, oxygen gradient ektacytometry, was developed that especially holds promise for patients with SCD. This technique measures red blood cell deformability under deoxygenation and reoxygenation, thereby capturing the dynamic process of red blood cell sickling. In this issue, Sadaf et al. evaluate the correlation between oxygen gradient ektacytometry-derived parameters and "classical" biomarkers in the field of SCD such as levels of fetal hemoglobin and the percentage of dense RBCs. They convincingly show that individual parameters correlate with known biomarkers of SCD severity. In addition, they demonstrate that oxygen gradient ektacytometry assesses the cumulative effect of known biomarkers and, likely, additional factors that contribute to sickling. Therefore, their findings further establish this technique as a novel useful biomarker for clinical severity and treatment efficacy in the field of SCD. Berrevoets et al. explore another, relatively unknown, form of ektacytometry. This cell membrane stability test (CMST) was used in combination with osmotic gradient ektacytometry to study the longitudinal effects of splenectomy on RBC characteristics in a small cohort of HS patients. They show that before splenectomy the composition of the RBC population is more heterogeneous, with RBC that are more rigid and have increased intracellular viscosity and reduced deformability. Splenectomy improves cellular hydration status and allows cells to regain the ability to shed membrane. The latter was assessed using the CMST and the authors postulate that this yet-undescribed RBC feature reflects RBC membrane health, and as such the CMST holds promise as a novel biomarker for clinical severity and phenotypic expression in HS.

Eosin-5-maleimide binding to extracellular proteins of the RBC membrane is a very specific test for the diagnosis of HS. In an attempt to further optimize this commonly used test Glenthøj et al. circumvent the need for blood samples from healthy control individuals by using commercially available fluorescent beads in performing this test. By analyzing a large cohort of HS patients, using osmotic gradient ektacytometry as a gold standard, they found that the EMA binding test results were not compromised by this modification of the EMA test and an accuracy of 90.3% was obtained (vs. 88.6% for the "classical" version of the test). Since fluorescent beads are more stable and better standardized, this modification represents an attractive alternative of the EMA binding test, also allowing for interlaboratory comparisons and quality control programs.

Porro et al. extend the use of ektacytometry into the field of cardiovascular diseases by investigating the association between RBC morphodynamic features, i.e., aggregability and deformability, in patients with different grades of coronary stenosis. They calculated a global RBC morphodynamic score and a related risk chart, which was associated with the extent of high-risk plaque features. In a cohort of nonobstructive

coronary artery disease patients positive correlations were found between RBC rigidity, osmotic fragility or aggregability and high-risk plaque features. This led them to conclude that RBC morphodynamic features may be used in the identification of high-risk patients in this specific patient category.

The disadvantage of osmotic gradient ektacytometry is that the technique assesses RBC deformability of the entire RBC population, not individual RBCs. Therefore, the development of new diagnostic tools able to analyze a statistically relevant number of single cells would provide important complementary information. Faivre et al. have addressed this issue by evaluating the mechanical response of artificially altered RBCs and RBCs from HS and SCD patients flowing through a microfluidic constriction. Comparison of the differences in extension at the exit and the shape recovery time between healthy and chemically altered RBCs provide a direct signature of the RBC membrane composition and architecture. Further analysis of HS and SCD RBCs demonstrate a first proof-of-principle that a passive microfluidic approach could be used to discriminate between the two diseases, thereby warranting further study of this technique for diagnostic and prognostic purposes.

Another example of single cell analysis is Raman spectroscopy. Jacob et al. used this technique to analyze the toxic effects of bilirubin on RBC. Regardless of the underlying cause, a common feature of hemolytic anemia is increased levels of bilirubin, the breakdown product of hemoglobin. Using minimal-invasive sample handling procedures and using a home-built micro-Raman spectroscopy system coupled with laser-tweezers the authors obtained specific fingerprints from RBC obtained from healthy volunteers and patients with jaundice, indicating biochemical alterations resulting from increased bilirubin levels. Their study paves the way for further investigations using this technique in understanding fundamental RBC behavior in different RBC diseases.

Analysis of single RBCs as well as the whole population of RBCs was done in a study by Cloos et al. They used a vast number of techniques for a comprehensive analysis of the acantocytes present in a patient with hypobetalipoproteinemia due to a pathogenic mutation in *APOB*. In particular they wondered how, and to what extent hypobetalipoproteinemia could affect RBC functionality. The major findings led them to conclude that the RBCs in this patient, who was hematologically normal, had altered cytoskeletal and membrane lipid lateral asymmetry while deformability was only mildly impaired. Their case report study is a nice example of the potential use of membrane biophysics and lipid vital imaging as new methods in the study of RBC disorders.

Currently, many new forms of therapy are being developed for the treatment of hemoglobinopathies, in particular SCD and beta-thalassemia. Among them are therapies that aim to increase the level of fetal hemoglobin. Manchinu et al. now further explore an alternative strategy that aims to increase the levels of HbA2. They report on considerably increased levels of δ-globin mRNA in a deoxyribonuclease II-α knock out mouse model in which interferon β (IFNb) is activated. At the same time IFNb activation in the fetal liver reduces β-globin mRNA levels. They translated their findings to a cohort of patients with multiple sclerosis on IFNb treatment, in whom they detected a small but significant increase in HbA2 levels. Therefore, their study represents a first proof of principle that elevating the levels of HbA2 could be explored as a novel therapeutic option for treating β-hemoglobinopathies.

The considerable technological progress reported in this Research Topic will contribute to increasing our knowledge on RBC pathophysiology, and a better understanding of RBC disorders. In turn, this may enhance the development of new diagnostic procedures and targeted therapies for these rare disorders. Because of its success, the second volume of this Research Topic has recently been launched and is now open for submission.

AUTHOR CONTRIBUTIONS

PB and RvW wrote the manuscript and approved the final version. Both authors contributed to the article and approved the submitted version.

REFERENCES

Boulad, F., Mansilla-Soto, J., Cabriolu, A., Rivière, I., and Sadelain, M. (2018). Gene therapy and genome editing. *Hematol. Oncol. Clin. North Am.* 32, 329–342. doi: 10.1016/j.hoc.2017.11.007

Grace, R.F., Rose, C., Layton, D. M., Galactéros, F., Barcellini, W., Morton, D. H. et al. (2019). Safety and efficacy of mitapivat in pyruvate kinase deficiency. *N. Engl. J. Med*. 381, 933–944. doi: 10.1056/NEJMoa1902678

Orkin, S. H., and Bauer, D. E (2019). Emerging genetic therapy for sickle cell disease. *Annu. Rev. Med*. 70, 257–271. doi: 10.1146/annurev-med-041817-125507

Conflict of Interest: The authors declare that the research was conducted in the absence of any commercial or financial relationships that could be construed as a potential conflict of interest.

The handling editor declared a past co-authorship with the authors.

frontiers in Medicine

BRIEF RESEARCH REPORT
published: 22 May 2020
doi: 10.3389/fmed.2020.00163

Delta-Globin Gene Expression Is Enhanced *in vivo* by Interferon Type I

Maria Francesca Manchinu[1], Michela Simbula[1], Cristian Antonio Caria[1], Ester Musu[1], Lucia Perseu[1], Susanna Porcu[1], Maristella Steri[1], Daniela Poddie[1], Jessica Frau[2], Eleonora Cocco[2], Laura Manunza[3], Susanna Barella[3] and Maria Serafina Ristaldi[1]†*

[1] Istituto Di Ricerca Genetica e Biomedica Del Consiglio Nazionale Delle Ricerche, Monserrato, Italy, [2] Department of Medical Science and Public Health, Centro Sclerosi Multipla, University of Cagliari, Cagliari, Italy, [3] Ospedale Microcitemico "A. Cao" - A.O. "G. Brotzu", Cagliari, Italy

Beta hemoglobinopathies are widely spread monogenic lethal diseases. *Delta-globin* gene activation has been proposed as a possible approach for curing these pathologies. The therapeutic potential of delta-globin, the non-alpha component of Hemoglobin A_2 ($\alpha 2\delta 2$; HbA2), has been demonstrated in a mouse model of beta thalassemia, while its anti-sickling effect, comparable to that of gamma globin, was established some time ago. Here we show that the *delta-globin* mRNA level is considerably increased in a *Deoxyribonuclease II-alpha* knockout mouse model in which type 1 interferon (interferon beta, IFNb) is activated. IFNb activation in the fetal liver improves the *delta-globin* mRNA level, while the *beta-globin* mRNA level is significantly reduced. In addition, we show that HbA2 is significantly increased in patients with multiple sclerosis under type 1 interferon treatment. Our results represent a proof of principle that delta-globin expression can be enhanced through the use of molecules. This observation is potentially interesting in view of a pharmacological approach able to increase the HbA2 level.

Keywords: erythropoiesis, δ-*globin* gene, interferon type 1, beta thalassemia, sickle cell anemia

OPEN ACCESS

Edited by:
Richard Van Wijk, Utrecht University, Netherlands

Reviewed by:
Cornelis Harteveld, Leiden University Medical Center, Netherlands
Emile Van Den Akker, Sanquin Diagnostic Services, Netherlands

***Correspondence:**
Maria Serafina Ristaldi
ristaldi@irgb.cnr.it

†*Maria Serafina Ristaldi*
orcid.org/0000-0002-5472-9871

Specialty section:
This article was submitted to Hematology, a section of the journal Frontiers in Medicine

Received: *28 January 2020*
Accepted: *09 April 2020*
Published: *22 May 2020*

Citation:
Manchinu MF, Simbula M, Caria CA, Musu E, Perseu L, Porcu S, Steri M, Poddie D, Frau J, Cocco E, Manunza L, Barella S and Ristaldi MS (2020) Delta-Globin Gene Expression Is Enhanced in vivo by Interferon Type I. Front. Med. 7:163. doi: 10.3389/fmed.2020.00163

INTRODUCTION

Modulations of Fetal-hemoglobin (HbF) and possibly hemoglobin-A2 (HbA2) are of interest given their potential roles in ameliorating beta thalassemia (beta thal) and sickle cell anemia phenotypes (1–4).

Recently, through genome-wide association studies (GWASs) in the SardiNIA cohort, Danjou et al. identified new variants associated with levels of HbF, HbA1 (Hemoglobin A1), and HbA2 (5). In the regional association plots, at the loci associated with HbF reported by the authors (5), we noticed some suggestive, although not genome wide significant, signals covering a region on chromosome 19 were two genes related to erythropoiesis are present: *Krüppel-like factor 1 (Klf1)* and *Deoxyribonuclease II-alpha (DNase2a)*. The effect of Klf1 on HbF, HbA1, and HbA2 expression has been largely elucidated (6–9), while a possible effect of DNase2a on hemoglobins expression has not yet been investigated (10, 11).

DNase2a is expressed in the central macrophage of erythroblastic islands (CMEI), where it is involved in the digestion of extruded nuclei of developing erythrocytes (10, 12). *DNase2a* knockout (KO) mice die at around embryonic day 17 (E17) of lethal anemia, which is caused by IFNb production by macrophages (12). Undigested DNA directly stimulates CMEIs to express IFNb and, therefore, Interferon-responsive genes (12). *Ifnar1* KO rescues the impaired erythropoiesis of the *DNase2a* KO phenotype (12).

To investigate a possible effect of DNase2a on the expression of beta-like (*gamma*, *delta*, and *beta*) globin genes, we intercrossed *DNase2a* KO mice with a transgenic mouse line (ln72) containing the full human *beta-globin* gene cluster (13). Expression of *globin* genes and erythropoiesis have been analyzed in fetal liver. Here we show that type I interferon activation led to a significant increase in the *delta-globin* mRNA level offset by a decrease in the *beta-globin* mRNA level and to a different pattern of erythroid differentiation compared to the control mice. No significant increase in the *gamma-globin* mRNA level was observed.

With the aim of verifying whether the use of type I interferon was able to modify the expression of HbA2 in humans, we conducted a study in patients with multiple sclerosis (MS) who underwent therapy with IFNb. Our results show a significant increase in HbA2 level in patients.

Beta hemoglobinopathies affect the health of countless people worldwide (14). At present, bone marrow transplantation provides the only definitive cure for these diseases. Alternative therapies such as gene therapy (15, 16) will be difficult to apply on a large-scale basis and in developing countries. Therefore, the development of a pharmacological approach for these pathologies would make care accessible in countries where these diseases are more widespread and mortality is very high (17–19).

Recently, we have validated the therapeutic potential of the *delta-globin* gene in a mouse model of beta thal (4). It is also well-known that HbA2 can inhibit Sickle hemoglobin (HbS) polymerization as efficiently as HbF (3).

Our results show, just as proof of principle, that HbA2 can be increased pharmacologically, and this observation could be a starting point for future studies aimed at increasing HbA2 levels through the use of molecules.

MATERIALS AND METHODS

Mice

All experimental protocols were approved by the Cagliari University Institutional Animal Care and Use Ethical Committee (OPBA, Approval number: 22/2016). All methods were performed in accordance with relevant guidelines/regulations.

The original ln72 (provided by Dr. Frank Grosveld's laboratory) and the *DNase2a/Ifnar1* KO (bought from RIKEN BioResource Center, Japan) mouse lines were maintained on a hybrid C57BL/6 background.

Genotyping

Genotypes were determined from genomic DNA by PCR.

Transgenic mouse line ln 72, an established single copy transgene that contains the full human beta-globin cluster (12), was genotyped using the primers listed in **Supplemental Table 1**.

WT and *Ifnar1* KO were detected with a wild-type-specific primer or mutant-specific reverse primer and a common forward primer.

WT and *DNase2a* KO were detected with a wild-type-specific or mutant-specific primer and an antisense primer. All primers are listed in **Supplemental Table 1**.

Real-Time Quantitative PCR (RT-qPCR)

Total RNA was extracted from E12.5, E14.5, and E 16.5 fetal livers, or human tissue culture cells, using the RNeasy Mini Kit (Qiagen) as described by the manufacturer's protocol. The cDNA was made from total RNA using Superscript III reverse transcriptase (Invitrogen). RT-qPCRs were performed using SYBR Green chemistry (Applied Biosystems) with an ABI PRISM 7900 thermocycler (Applied Biosystems, Foster City, CA).

RT-qPCR was performed to measure the *gamma*, *beta,* and *delta globin* gene mRNA expression, and samples were normalized with respect to alpha mouse levels or HPRT human levels.

All primers are listed in **Supplemental Table 1**.

The reactions were performed on at least three different samples in triplicate for mice fetal liver and three times for two separate samples of human tissue culture cells. The analysis of RT-qPCR data was done using the $\Delta\Delta$CT method.

Flow Cytometry Analysis

Fetal liver cells were collected, from a minimum of three embryos per genotype, at 14.5 and 16.5 days post coitum (dpc). Cell suspensions were obtained, and isolated cells (1×10^6 per sample) were stained with anti-mouse Ter119 FITC and anti-mouse CD71 PE antibodies (BD-Bioscience) at a final concentration 1:100. Cells were incubated for 20 min at 4°C, washed with PBS (5% BSA), and re-suspended in FACS buffer. A FACSCANTO (BD-Bioscience) flow cytometer was used to collect data and analyzed with FACSDiva software Version 6.1.3 (BD Biosciences) and FlowJo V7.6.5.

Primary Human Erythroid Cultures

Human erythroid progenitor cells from peripheral blood were obtained from healthy individuals.

Donors cells were cultured using the two-phase liquid culture described by Fibach et al. (20) and Pope et al. (21) in the presence of 0, 10, or 100 UI IFNb 1a.

Written, informed consent was provided by the study participants.

Patient Selection and Blood Sample Analysis

All experimental protocols were approved by the Ethics Committee ATS Sardegna (approval number 85/2018/CE). All methods were carried out in accordance with relevant guidelines and regulations. Written informed consent was obtained from all subjects.

A total of 81 Multiple Sclerosis patients were enrolled in the study from the Multiple Sclerosis Center (Binaghi Hospital, ATS Sardegna, Department of Medical Sciences and Public Health, University of Cagliari). Blood samples were collected from all patients in tubes containing EDTA anticoagulant for hemoglobin electrophoresis. Hemochrome was carried out by standard techniques. HbA2 levels were measured with high-performance chromatography.

Globin chain analyses were performed on a VARIANT II high-performance liquid chromatography system (Bio-Rad, Segrate MI, Italy). Two-level calibration of the instrument and

sample analysis were carried out according to the manufacturer's recommendations. Types of interferon administrated during the study are listed in **Supplemental Table 2**.

Statistics

In order to avoid problems related to non-normal distribution of values when applying statistical parametric tests (i.e., the *t*-test) to blood sample measurements, the inter-group difference was assessed with the non-parametric Wilcoxon signed-rank test (one-sided). In particular, differences in HbA2 levels between groups were assessed using the unpaired two-samples Wilcoxon test while, when comparing HbA2 levels before and after treatment, the paired samples Wilcoxon test was applied (**Supplemental Table 3**). Statistical power was calculated with a Wilcoxon-Mann-Whitney test for two groups at a significance of 0.05, one-sided.

Otherwise, statistical differences were calculated using the unpaired Student's *t*-test.

P-value$<$ 0.05 was considered statistically significant, and a Bonferroni correction for multiple testing was applied when appropriate.

The statistical analyses were performed using R (http://www.Rproject.org) and G*Power Version 3.1.9.2.

RESULTS

Human *Delta-Globin* Gene Expression Is Increased in *DNase2a*-Deficient Mouse Fetal Liver

In this study, we aimed to evaluate the possible effect of *DNase2a* deficiency on human *beta-like globin* gene expression *in vivo*. To this end, we crossed a transgenic line containing the entire human *beta-globin* gene locus (ln72) (13) with the *DNase2a* KO mouse model (12).

Since mice deficient in *DNase2a* die around E17, we evaluated *beta-like globin* mRNA levels in fetal liver at 12.5, 14.5, and 16.5 dpc.

No effect on the *gamma-globin* mRNA level was detected (**Figure 1A**).

The *beta-* and *delta-globin* mRNA levels at 12.5 dpc were comparable in WT and *DNase2a*-deficient mouse fetal livers (**Figures 1B,C**).

At 14.5 dpc, the *beta-globin* mRNA level was diminished in *DNase2a* KO with respect to WT fetal liver (0.48 $\pm$ 0.07, $p = 8.93 \times 10^{-5}$). The decreased level of *beta-globin* mRNA was also observed at 16.5 dpc (0.37 $\pm$ 0.06, $p = 5.57 \times 10^{-5}$) (**Figure 1B**).

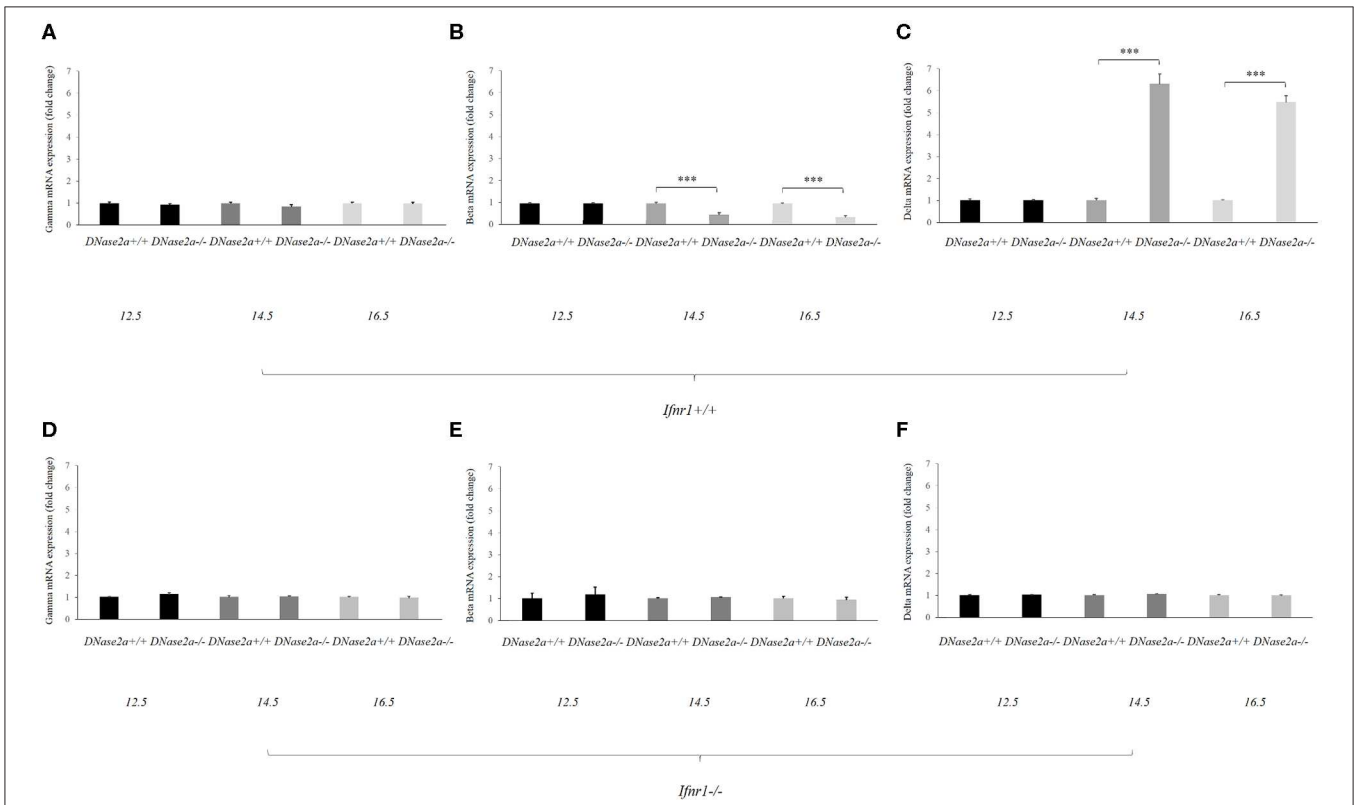

FIGURE 1 | Human delta-globin gene expression is increased in *DNase2a*-deficient mouse fetal liver. **(A–C)** represent the mRNA expression level of the human *gamma, beta*, and *delta globin* genes, respectively, in *DNase2a* $^{+/+}$ *Ifnar1*$^{+/+}$ ($n = 4$ for each time point) and *DNase2a* $^{-/-}$ *Ifnar1*$^{+/+}$ ($n = 4$ for each time point) fetal liver at 12.5, 14.5, and 16.5 dpc. **(D–F)** represent the expression levels of the human *gamma, beta*, and *delta globin* genes, respectively, in *DNase2a* $^{+/+}$ *Ifnar1*$^{-/-}$ ($n = 4$ for each time point) and *DNase2a*$^{-/-}$ *Ifnar1*$^{-/-}$ ($n = 4$ for each time point) fetal liver at 12.5, 14.5, and 16.5 dpc. Levels of significance, calculated by Student's *t*-test, are indicated. ***$p < 0.001$.

At the same time the *delta-globin* mRNA level was increased in *DNase2a* KO embryos with respect to WT embryos at 14.5 dpc (6.15 ± 0.4, $p = 2.30 \times 10^{-4}$) and 16.5 dpc (5.34 ± 0.2, $p = 1.09 \times 10^{-5}$) (**Figure 1C**).

As a control, we crossed ln72 mice to *DNase2a/Ifnar1* double KO mice. Embryos with a double deficiency for *DNase2a* and *Ifnar1* do not show differences in the expression of the human globin genes with respect to WT (**Figures 1D–F**).

These results indicated that IFNb affects the levels of *beta-* and *delta-globin* mRNAs. Starting from day 14, when definitive erythropoiesis definitely takes place, the *delta-globin* mRNA level is increased (6.15- and 5.34-folds at 14.5 and 16.5 dpc, respectively) while the *beta-globin* mRNA level is significantly reduced (0.48- and 0.37-fold at 14.5 and 16.5 dpc, respectively).

The mouse alpha-globin mRNA level is not affected by DNase2a deprivation (**Supplemental Figure 1**).

Fetal Liver Erythropoiesis in *DNase2a*-Deficient Mouse

In *DNase2a*-deficient mice, definitive erythropoiesis is impaired due to IFNb activation (12). However, fetal liver erythropoiesis in *DNase2a* KO mice has never been analyzed by flow cytometry before. To evaluate whether the observed increase in *delta-globin* gene expression could be somewhat correlated to a modification of the normal erythropoietic kinetics (22), we analyzed, through flow cytometry, fetal liver definitive erythropoiesis. Analysis was conducted on WT, *DNase2a* KO, and *DNase2a/Ifnar1* double KO freshly isolated fetal liver cells from 14.5 and 16.5 dpc mice embryos according to levels of expression of TER119 and CD71 (23) (**Figure 2A**). We excluded from the analysis all events that expressed neither TER119 nor CD71, since only cells in the erythroid lineage were considered. Four different states of maturation were analyzed: Pop. I (TER119 low or absent/CD71 low or absent), Pop. II (TER119 low or absent/CD71 high), Pop. III (TER119 high/CD71high), and Pop. IV (TER119 high/CD71 low or absent). No significant differences were observed in the frequency, morphology, and levels of expression of Ter119 and CD71 in maturing erythroid cells between WT and *DNase2a/Ifnar1* double KO mice fetal livers at 14.5 dpc or at 16.5 dpc (**Figure 2B**). On the other hand, analysis of mice lacking *DNase2a* gene displayed different frequencies of the maturing cells (**Figure 2B**). Analysis showed a significant increase in Pop I in 16.5 dpc (WT: $15.6\% \pm 1.44$; *DNase2a KO*: $34.5\% \pm 3.4$ in 16.5 dpc, $P = 1.79 \times 10^{-5}$). No significant difference in the percentage of Pop. II was detected, while a significant reduction of Pop. III was observed (WT: $76.82\% \pm 2.37$; *DNase2a KO*: $49.53\% \pm 13.31$ in 14.5 dpc, $P = 0.0032$, WT: $74.45\% \pm 2.86$; *DNase2a KO*: $30.98\% \pm 6.22$ in 16.5 dpc, $P = 4.13 \times 10^{-6}$). A significant contemporary increase in Pop. IV was registered in the *DNase2a* KO genotype in comparison to WT (WT: $4.21\% \pm 1.09$; *DNase2a* KO: $21.5\% \pm 7.63$ in 14.5 dpc, $P = 0.001$, and WT: $5.64\% \pm 2.22$; *DNase2a* KO: $23.98\% \pm 6.03$ in 16.5 dpc, $P = 7.3 \times 10^{-4}$).

Taken together, our data show a variation in the erythropoietic pattern of differentiation in mice lacking *DNase2a* gene, with a decreased frequency of Pop. III and an increased frequency of later populations (Pop. IV).

An increased frequency of Pop I, containing the earliest erythroid progenitors (21), is observed in the 16.5 dpc *DNase2a* KO. This increase, which is not observed in the 14.5 dpc KO mice, is most likely explained by the anemia that becomes progressively more and more severe starting from the establishment of definitive erythropoiesis in the fetal liver of *DNase2a* KO mice (12). The observed varied pattern of erythroid differentiation in *DNase2* KO fetal liver is, however, distinct from that observed in the ineffective erythropoiesis seen, for example, in beta thal, which is characterized by a decrease in the number of the later population (Pop IV) and an increased number of earlier populations (Pop I, II, and III) (24, 25).

Hemoglobin A2 Levels Increase After IFNb Treatments in Multiple Sclerosis Patients

In this study, we have shown that the *delta-globin* mRNA level is increased in *DNase2a* null fetal liver at 14.5 and 16.5 dpc. We have also shown that higher *delta-globin* mRNA is the consequence of type 1 interferon (IFN1) activation.

To evaluate the effect IFNb on the *delta-globin* mRNA level in human erythroid cells, we carried out human erythroid progenitor liquid culture (20, 21) from two healthy donors. The relative normalized mRNA level of the human *delta* vs. *beta-globin* genes at 12 and 14 days after stimulation with 0, 10, or 100 UI of IFNb 1a was evaluated. The results did not show statistical differences in the expression of the *delta-globin* gene in either of the two independent cultures analyzed (**Supplemental Figure 2**).

It has been reported that multiple sclerosis patients treated with IFNb have higher levels of HbA2 in comparison to those treated with other drugs (26). For the purpose of verifying whether therapy with IFNb was the cause of the increase in HbA2 *in vivo*, we performed a study in MS patients.

First, a transversal study was carried out on 47 MS patients undergoing IFNb therapy for at least 1 year; HbA2 average did not show any difference compared to the control population ($2.70\% \pm 0.26$ vs. $2.71\% \pm 0.32$). Since a compensatory mechanism could occur in the erythropoiesis of patients treated for a long period, we carried out a longitudinal study ($n = 25$) analyzing HbA2 levels at the diagnosis of the disease (T0) and after 3 months of drug treatment (T1). HbA2 average in MS patients before IFNb treatment (T0) was $2.75\% \pm 0.71$, while after treatment, it was $2.87\% \pm 0.80$. Blood counts were within normal limits for all patients, and no significant differences were detected between at T0 and T1 (**Supplemental Table 4**).

Interestingly, in a beta thal carrier patient, the effect of interferon therapy was found to be the highest in all of the studied samples, from 5.9% (T0) to 6.4% (T1) g/dl.

The box plot in **Figure 3A** shows HbA2 before and after treatment, and the Wilcoxon test revealed a significant difference in HbA2 levels ($p = 1.6 \times 10^{-3}$, one-sided). Stratification of the sample according to the type of IFNb administrated (IFNb 1a or IFNb 1b, see **Supplemental Table 2**) revealed that this difference is mainly due to IFNb 1a (IFNb 1a + IFNb 1a peg) treatment. HbA2 in patients before treatment with IFNb 1a was $2.8\% \pm$

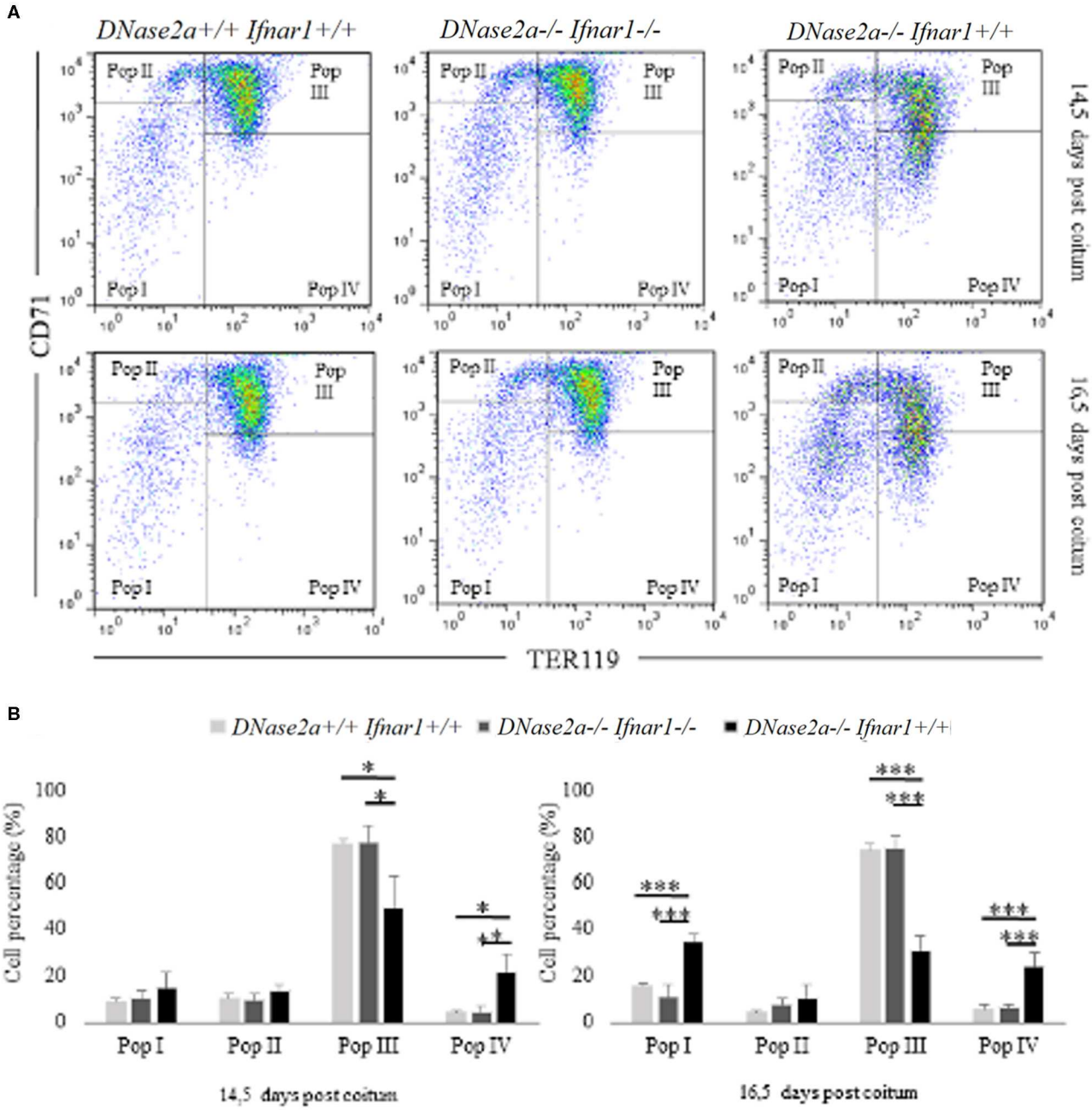

FIGURE 2 | Flow cytometry analysis of fetal liver cells from 14.5 and 16.5 dpc embryos. In panel **(A)**, Pop. I, Pop. II, Pop III, and Pop IV were gated (according to levels of expression CD71 and TER119) and analyzed for each genotype studied at 14.5 dpc (upper panel) and at 16.5 dpc (bottom panel) in fetal liver cells. **(B)**: Bar plots showing flow cytometry analysis from 14.5 dpc ($n = 4$; left panel) and 16.5 dpc ($n = 4$; right panel) fetal liver cells. Levels of significance, calculated by Student's *t*-test, are indicated. $^{*}p < 0.05$; $^{**}p < 0.01$; $^{***}p < 0.001$.

0.8, while after treatment, it was 3.02% ± 0.9 ($p = 1.8 \times 10^{-3}$, one-sided), as shown in **Figure 3B**.

A significant number ($n = 9$) of beta thal carriers were represented in our transversal study, so we analyzed them separately. Average HbA2 in beta thal carriers/MS patients was 6.24% ± 0.42 compared to 5.84% ± 0.53 in beta thal carriers.

The box plot in **Figure 3C** shows the HbA2 levels in the two different carrier groups; the Wilcoxon test revealed a significant difference in HbA2 levels ($p = 0.01$ one-sided). Stratification of the sample revealed, as before, that this difference is mainly due to IFNb 1a treatment. The HbA2 value in carriers of beta thal treated with IFNb 1a was 6.55% ± 0.1, while that of those treated

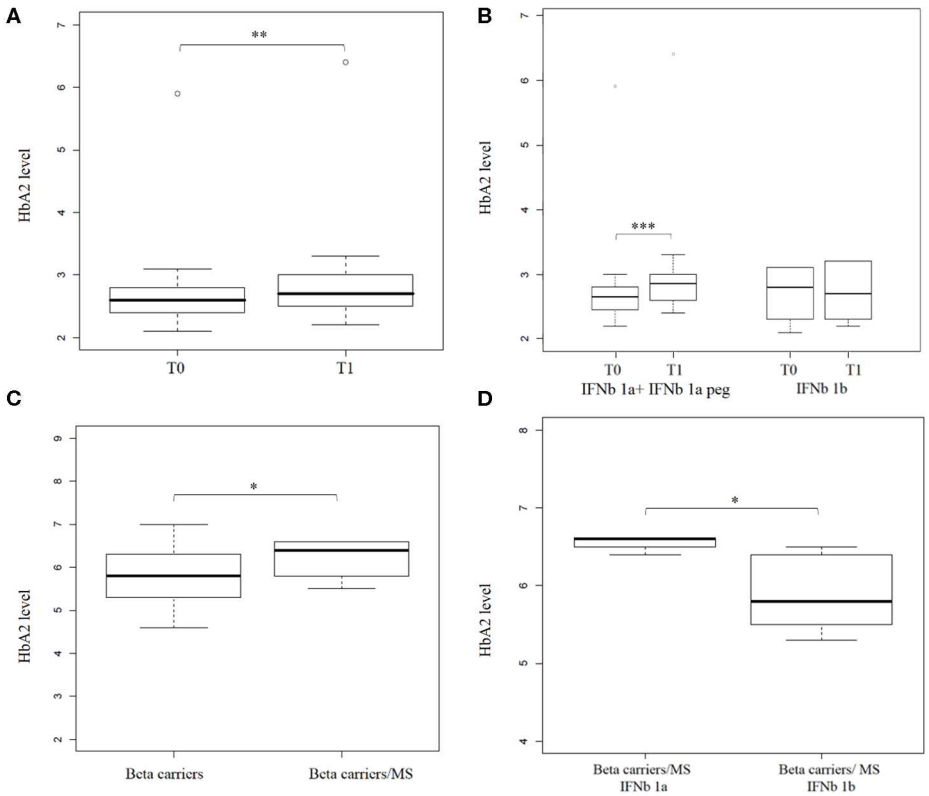

FIGURE 3 | Hemoglobin A2 levels increase after interferon beta (IFNb) treatment in Multiple Sclerosis (MS) patients. **(A)** shows a box plot of HbA2 levels in ($n = 25$) MS patients before (T0) and after (T1) IFNb treatment. **(B)** shows a box plot of HbA2 level in ($n = 22$) MS patients before (T0) and after (T1) IFNb treatment stratified by IFNb type (16 and 6 patients under IFNb 1a + IFNb 1a peg and IFNb 1b treatment, respectively). **(C)** shows a box plot of HbA2 levels in beta thal carriers ($n = 643$) and in beta thal carriers/MS patients under IFNb treatment ($n = 9$). **(D)** shows a box plot of HbA2 levels determined in beta thal carriers/MS patients stratified by IFNb type (4 and 5 patients under IFNb 1a and IFNb 1b treatment, respectively). Levels of significance, calculated by Wilcoxon test, are indicated. *$p < 0.05$; **$p < 0.01$; ***$p < 0.001$.

with IFNb 1b was 5.9%± 0.5 ($p = 0.023$, one-sided), as shown in **Figure 3D**.

Our results suggest that IFNb induced a significant increase in Hemoglobin A2 levels in patients with MS. Moreover, this effect seems to be more relevant and persistent in beta thal carriers/MS.

DISCUSSION

In this study, we have investigated the effect of DNase2a deprivation on globin gene expression and erythropoiesis *in vivo*. In *DNase2a* null fetal liver, the *delta-globin* mRNA level is increased while the *beta-globin* mRNA level is significantly reduced. Erythropoiesis is altered with an increased frequency of the Ter 119 high/CD71 low or absent cell population (Population IV) (23).

In definitive terminal erythropoiesis, in humans, the peak of *delta-globin* expression appears in earlier stages compared to that of *beta-globin*, and it tends to drop in enucleated circulating reticulocytes and RBCs (3). A similar effect occurs with regards to earlier *delta-globin* expression in the beta-locus transgenic mice used in the present study (**Supplemental Figure 3**). Since reticulocytes have little *delta-globin* mRNA, it can be deduced that the observed increase is likely due to the increased proportion of Pop. IV, which is mainly composed of orthochromatic erythroblasts (23).

The asynchronous synthesis of beta and delta chains during erythroid maturation is most probably due to a mechanism linked to the activation of the promoter based on the proximity to the LCR for which the closest promoter is activated earlier, or more frequently, and then stabilized at the *beta-globin* gene promoter (22, 27). Another contributing factor is the different stability of the *beta-* and *delta-globin* mRNAs (28). The combination of these mechanisms would explain the higher level of *delta* mRNA in earlier populations.

The observed altered pattern of erythroid differentiation and increase in *delta-globin* mRNA level is due to type I interferon activation in the fetal liver, as demonstrated by the fact that erythropoiesis and globin gene expression are rescued to those of WT in *DNase2a/Ifnar1* double KO mice. In support of this notion, there is also the observation that there is a small but significant increase of HbA2 in patients affected by MS and undergoing IFNb therapy. The increase appears to be more consistent and durable in beta thal carrier MS patients. The effect is primarily due to the increase in HbA2 levels in patients subjected to therapy with interferon-beta1a (IFNb 1a, produced by mammalian cells), whereas interferon-beta1b (IFNb

1b, produced by genetically modified E. coli) does not seem to have an effect, at least with the doses used for MS. This difference may be due to the difference in biological activity between the two drugs, with IFNb 1a being ten times more active than IFNb 1b (29), as well as to the difference in dose and frequency of administration of the two types of interferon (30). Despite the low number of MS patients affected by beta thal (9 subjects) with respect to non-MS beta thal patients [data derived from Danjou et al. (5)] available for this study, the difference we observed was supported by a moderate statistical power (52%). Even stronger was the power to observe a significant difference in HbA2 levels between beta thal MS patients treated with INFb 1a and 1b (67%), further supporting the robustness of our results. However, it would be interesting to assess the effect on HbA2 levels of IFNb 1a in carriers of beta thal not affected by MS, though this would require a dedicated clinical study.

In humans, only three patients homozygous for a *DNase2a* null mutation have been described in the literature (31). In these patients, type one interferon is activated. An effect on erythropoiesis with mild anemia, especially at birth, has been described (28). We had the chance to test mRNA levels for *delta-globin* in one of these patients before and after treatment, which strongly ameliorated patient condition (31). A significantly different level of *delta-globin* mRNA was detected, with a 30% (±4.15%) higher *delta-globin* mRNA level before treatment than after treatment ($p = 0.031$, technical triplicate). These data, although limited to a single patient, suggest that in humans, the activation of type 1 interferon affects erythropoiesis (31), with effects on the *delta-globin* mRNA level.

The increase in *delta-globin* represents an alternative experimental approach for the treatment of beta thal and sickle cell anemia (3, 4). A therapeutic strategy for beta thal and sickle cell anemia based on the increase in *delta-globin* may have the advantage over reactivating *gamma-globin* that the expression of the *delta-globin* gene is pan-cellular, while that of the *gamma-globin* gene is heterocellular (3). Moreover, the oxygen affinity of HbA2 is more similar to that of HbA1 than is HbF. In this work, we also observed that, as a consequence of interferon activation, the increased *delta-globin* mRNA level corresponds to a decrease in the *beta-globin* mRNA level. In sickle cell anemia, this may represent a further advantage.

Several drugs are under investigation as HbF-inducing agents. However, up to today, only Hydroxyurea is utilized in the clinic, with many limitations (32). Other strategies for the reactivation of the *gamma-globin* gene have been based on interventions aimed at modifying hemoglobin switching through genomic modification (1, 2). Similar approaches have been proposed for the *delta-globin* gene (4, 33). These strategies, however, are in their infancy, and several issues concerning safety and efficacy have to be addressed before translating these approaches to the clinic.

It is difficult to predict what increase in HbA2 could be achievable with a targeted pharmacological approach. In the case of sickle cell anemia, HbA2 above 10% (about 4 times the normal level) of total hemoglobin would be beneficial. Levels above 30% (about 12 times the normal level) should be curative (34, 35). These predictions are based on the anti-sickling properties of HbA2, which are similar to those of HbF (3). On the other hand, higher increases would be needed for an improvement in beta thal major. However, even if the achievable increase was not enough to cure the diseases in combination with other globin therapies, this may be a contributing factor to improve patient condition.

The precise molecular pathway by which IFNb causes a perturbation of terminal erythroid maturation, with an increase in Pop IV, and of *delta-globin* mRNA is not fully elucidated and needs further investigation. Most likely, however, the observed change in erythroid maturation kinetics is in part due to the perturbation of the apoptotic program, necessary to terminal erythroid differentiation (36, 37), caused by IFNb (38).

We are aware that repositioning of IFNb for beta hemoglobinopathies is unlikely, since type 1 interferon has been universally known as a lethal inhibitor of erythropoiesis (39, 40). Other pathways that may affect the erythropoietic cell cycle kinetics should be investigated. In this regard, it is interesting to note that CCND3, a D-type cyclin that coordinates the cell cycle during erythroid differentiation (41), was found to be associated with increased HbA2 levels in a recent study (5). *CCND3* gene product cyclin D3 plays a critical role in regulating the number of cell divisions that erythroid precursors undergo during terminal differentiation (41). CCND3 null mice are viable and fertile and do not show important signs of anemia (41). These observations suggest that there could be a viable pathway to alter the cell cycle during terminal erythroid differentiation, as happens in CCND3 KO mice, through the use of molecules and without serious pathological consequences. The molecular mechanism through which CCND3 affects *delta-globin* gene expression remains, however, to be more clearly determined.

In summary, our study represents "a proof of principle" that elevation of delta-globin could be an interesting target for a pharmacological approach aimed at the therapy of beta hemoglobinopathies.

DATA AVAILABILITY STATEMENT

All datasets generated for this study are included in the article/**Supplementary Material**.

ETHICS STATEMENT

The studies involving human participants were reviewed and approved by Ethics Committee ATS Sardegna (approval number 85/2018/CE). The patients/participants provided their written informed consent to participate in this study. The animal study was reviewed and approved by Cagliari University Institutional Animal Care and Use Ethical Committee (OPBA, Approval number: 22/2016).

AUTHOR CONTRIBUTIONS

MM, MSi, CC, EM, LP, MSt, and DP performed the experiments and contributed to the interpretation of the results. EC and

JF supervised the collection of samples and clinical data from patients. SB performed hematological evaluation of patients. LM carried out human erythroid progenitor liquid culture. MM, MSi, CC, and SP contributed to the writing of the manuscript and prepared the figures. MR and MM designed the study. MR designed the study, supervised the research, and wrote the manuscript. All authors contributed to the discussion and approved the final manuscript.

FUNDING

This research was supported, in part, by the Telethon grants GGP14065 to MR.

ACKNOWLEDGMENTS

We thank Emilio Melis for technical assistance and animal care. We thank Doctor Alberto Tommasini and Doctor Alessandra Tesser for providing cDNA samples of a patient homozygous for a *DNase2a* null mutation. We thank Doctor Maria Franca Marongiu for assistance with Flow Cytometry.

SUPPLEMENTARY MATERIAL

The Supplementary Material for this article can be found online at: https://www.frontiersin.org/articles/10.3389/fmed.2020.00163/full#supplementary-material

REFERENCES

1. Vinjamur DS, Bauer DE, Orkin SH. Recent progress in understanding and manipulating haemoglobin switching for theopathies. *Br J Haematol.* (2018) 180:630–43. doi: 10.1111/bjh.15038
2. Wienert B, Martyn GE, Funnell APW, Quinlan KGR, Crossley M. Wake-up sleepy gene: reactivating fetal globin for β-hemoglobinopathies. *Trends Genet.* (2018) 34:927–40. doi: 10.1016/j.tig.2018.09.004
3. Steinberg MH, Rodgers, GP. HbA2: biology, clinical relevance and a possible target for ameliorating sickle cell disease. *Br J Haematol.* (2015) 170:781–7. doi: 10.1111/bjh.13570
4. Manchinu MF, Marongiu MF, Poddie D, Casu C, Latini V, Simbula M, et al. *In vivo* activation of the human δ-globin gene: the therapeutic potential in β-thalassemic mice. *Haematologica.* (2014) 99:76–84. doi: 10.3324/haematol.2012.082768
5. Danjou F, Zoledziewska M, Sidore C, Steri M, Busonero F, Maschio A, et al. Genome-wide association analyses based on whole-genome sequencing in Sardinia provide insights into regulation of hemoglobin levels. *Nat Genet.* (2015) 47:1264–71. doi: 10.1038/ng.3307
6. Borg J, Papadopoulos P, Georgitsi M, Gutiérrez L, Grech G, Fanis P, et al. Haploinsufficiency for the erythroid transcription factor KLF1 causes hereditary persistence of fetal hemoglobin. *Nat Genet.* (2010) 42:801–5. doi: 10.1038/ng.630
7. Tallack MR, Perkins AC. Three fingers on the switch: krüppel-like factor 1 regulation of γ-globin to β-globin gene switching. *Curr Opin Hematol.* (2013) 20:193–200. doi: 10.1097/MOH.0b013e32835f59ba
8. Wienert B, Martyn GE, Kurita R, Nakamura Y, Quinlan KGR, Crossley M. KLF1 drives the expression of fetal hemoglobin in British HPFH. *Blood.* (2017) 130:803–7. doi: 10.1182/blood-2017-02-767400
9. Perseu L, Satta S, Moi P, Demartis FR, Manunza L, Sollaino MC, et al. KLF1 gene mutations cause borderline HbA(2). *Blood.* (2011) 118:4454–8. doi: 10.1182/blood-2011-04-345736
10. Porcu S, Manchinu MF, Marongiu MF, Sogos V, Poddie D, Asunis I, et al. Klf1 affects DNase II-alpha expression in the central macrophage of a fetal liver erythroblastic island: a non-cell-autonomous role in definitive erythropoiesis. *Mol Cell Biol.* (2011) 31:4144–54. doi: 10.1128/MCB.05532-11
11. Keyel, PA. Dnases in health and disease. *Dev Biol.* (2017) 429:1–11. doi: 10.1016/j.ydbio.2017.06.028
12. Yoshida H, Okabe Y, Kawane K, Fukuyama H, Nagata S. Lethal anemia caused by interferon-beta produced in mouse embryos carrying undigested DNA. *Nat Immunol.* (2005) 6:49–56.
13. Strouboulis J, Dillon N, Grosveld F. Developmental regulation of a complete 70-kb human beta-globin locus in transgenic mice. *Genes Dev.* (1992) 6:1857–64. doi: 10.1101/gad.6.10.1857
14. Weatherall DJ. The inherited diseases of hemoglobin are an emerging global health burden. *Blood.* (2010) 115:4331–6. doi: 10.1182/blood-2010-01-251348
15. Thompson AA, Walters MC, Kwiatkowski J, Rasko JEJ, Ribeil JA, Hongeng S, et al. Gene therapy in patients with transfusion-dependent β-thalassemia. *N Engl J Med.* (2018) 378:1479–93. doi: 10.1056/NEJMoa1705342
16. Cavazzana M, Mavilio F. Gene therapy for hemoglobinopathies. *Hum Gene Ther.* (2018) 29:1106–13. doi: 10.1089/hum.2018.122
17. Modell B, Darlison M. Global epidemiology of haemoglobin disorders and derived services indicators. *Bull World Health Organ.* (2008) 86:480–7. doi: 10.2471/blt.06.036673
18. Piel FB, Hay SI, Gupta S, Weatherall DJ, Williams TN. Global burden of sickle cell anaemia in children under five, 2010-2050: modelling based on demographics, excess mortality, and interventions. *PLoS Med.* (2013) 10:e1001484. doi: 10.1371/journal.pmed.1001484
19. Origa R. β-Thalassemia. *Genet Med.* (2017) 19:609–19. doi: 10.1038/gim.2016.173
20. Fibach E, Manor D, Oppenheim A, Rachmilewitz EA. Proliferation and maturation of human erythroid progenitors in liquid culture. *Blood.* (1989) 73:100–3.
21. Pope SH, Fibach E, Sun J, Chin K, Rodgers GP. Two-phase liquid culture system models normal human adult erythropoiesis at the molecular level. *Eur J Haematol.* (2000) 64:292–303. doi: 10.1034/j.16000609.2000.90032.x
22. Menzel S, Garner C, Rooks H, Spector TD, Thein SL. HbA2 Levels in normal adults are influenced by two distinct mechanisms. *Br J Haematol.* (2013) 160:101–5. doi: 10.1111/bjh.12084
23. Socolovsky M, Murrell M, Liu Y, Pop R, Porpiglia E, Levchenko A. Negative autoregulation by FAS mediates robust fetal erythropoiesis. *PLoS Biol.* (2007) 5:e252. doi: 10.1371/journal.pbio.0050252
24. Ribeil JA, Arlet JB, Dussiot M, Moura IC, Courtois G, Hermine O. Ineffective erythropoiesis in β-thalassemia. *Sci World J.* (2013) 2013:394295. doi: 10.1155/2013/394295
25. Gupta R, Musallam KM, Taher AT, Rivella, S. Ineffective erythropoiesis: anemia and iron overload. *Hematol Oncol Clin North Am.* (2018) 32:213–21. doi: 10.1016/j.hoc.2017.11.009
26. Ozcan ME, Ince B, Karadeli HH, Gedikbasi A, Asil T, Altinoz MA. Higher minor hemoglobin A2 levels in multiple sclerosis patients correlate with lesser disease severity. *Neuropsychiatr Dis Treat.* (2016) 16;12:2033–8. doi: 10.2147/NDT.S109954
27. Palstra RJ, de Laat, W, Grosveld F. Beta-globin regulation and long-range interactions. *Adv Genet.* (2008) 61:107–42. doi: 10.1016/S0065-2660(07)00004-1
28. Ross J, Pizarro A. Human beta and delta globin messenger rnas turn over at different rates. *J Mol Biol.* (1983) 167:607–17.
29. Runkel L, Meier W, Pepinsky RB, Karpusas M, Whitty A, Kimball K, et al. Structural and functional differences between glycosylated and non-glycosylated forms of human interferon-beta (IFN-beta). *Pharm Res.* (1998) 15:641–9.
30. Durelli L, Verdun E, Barbero P, Bergui M, Versino E, Ghezzi A, et al. Every-other-day interferon beta-1b versus once-weekly interferon beta-1a for multiple sclerosis: results of a 2-year prospective randomised multicentre study (INCOMIN). *Lancet.* (2002) 359:1453–60. doi: 10.1016/s0140-6736(02)08430-1

31. Rodero MP, Tesser A, Bartok E, Rice GI, Della Mina E, Depp M, et al. Type I interferon-mediated autoinflammation due to DNase II deficiency. *Nat Commun.* (2017) 8:2176. doi: 10.1038/s41467-017-01932-3
32. Paikari A, Sheehan VA. Fetal haemoglobin induction in sickle cell disease. *Br J Haematol.* (2018) 180:189–200. doi: 10.1111/bjh.15021
33. Ristaldi MS, Casula S, Porcu S, Marongiu MF, Pirastu M, Cao A. Activation of the delta-globin gene by the beta-globin gene CACCC motif. *Blood Cells Mol Dis.* (1999) 25:193–209.
34. Powars DR, Weiss JN, Chan LS, Schroeder WA. Is there a threshold level of fetal hemoglobin that ameliorates morbidity in sickle cell anemia?. *Blood.* (1984) 63:921–6.
35. Estepp JH, Smeltzer MP, Kang G, Mstats CL, Wang WC, Abrams C, et al. A clinically meaningful fetal hemoglobin threshold for children with sickle cell anemia during hydroxyurea therapy. *Am J Hematol.* (2017) 92:1333–9. doi: 10.1002/ajh.24906
36. Testa U. Apoptotic mechanisms in the control of erythropoiesis. *Leukemia.* (2004) 18:1176-99. doi: 10.1038/sj.leu.2403383
37. Sarvothaman S, Undi RB, Pasupuleti SR, Gutti U, Gutti RK. Apoptosis: role in myeloid cell development. *Blood Res.* (2015) 50:73–9. doi: 10.5045/br.2015.50.2.73
38. Manchinu MF, Brancia C, Caria CA, Musu E, Porcu S, Simbula M, et al. Deficiency in interferon type 1 receptor improves definitive erythropoiesis in Klf1 null mice. *Cell Death Differ.* (2018) 25:589–99. doi: 10.1038/s41418-017-0003-5
39. Means RT Jr, Krantz SB. Inhibition of human erythroid colony-forming units by tumor necrosis factor requires beta interferon. *J Clin Invest.* (1993) 91:416–9.
40. Means RT Jr, Krantz SB. Inhibition of human erythroid colony-forming units by interferons alpha and beta: differing mechanisms despite shared receptor. *Exp Hematol.* (1996) 24:204–8.
41. Sankaran VG, Ludwig LS, Sicinska E, Xu J, Bauer DE, Eng JC, et al. Cyclin D3 coordinates the cell cycle during differentiation to regulate erythrocyte size and number. *Genes Dev.* (2012) 26:2075–87. doi: 10.1101/gad.197020

Conflict of Interest: The authors declare that the research was conducted in the absence of any commercial or financial relationships that could be construed as a potential conflict of interest.

frontiers in Physiology

ORIGINAL RESEARCH
published: 12 June 2020
doi: 10.3389/fphys.2020.00576

Mechanical Signature of Red Blood Cells Flowing Out of a Microfluidic Constriction Is Impacted by Membrane Elasticity, Cell Surface-to-Volume Ratio and Diseases

Magalie Faivre[1], Céline Renoux[2,3,4], Amel Bessaa[2,3], Lydie Da Costa[3,5,6,7], Philippe Joly[2,3,4], Alexandra Gauthier[2,3,8] and Philippe Connes[2,3,9]*

[1] Université de Lyon, Institut des Nanotechnologies de Lyon INL-UMR 5270 CNRS, Université Lyon 1, Villeurbanne, France, [2] Laboratoire Interuniversitaire de Biologie de la Motricité (LIBM) EA7424, Equipe "Biologie Vasculaire et du Globule Rouge", UCBL1, Villeurbanne, France, [3] Laboratoire d'Excellence (Labex) GR-Ex, Paris, France, [4] Biochimie des Pathologies Érythrocytaires, Centre de Biologie et de Pathologie Est, HCL, Bron, France, [5] AP-HP, Service d'Hématologie Biologique, Hôpital Robert-Debré, Paris, France, [6] Université Paris Diderot, Université Sorbonne, Paris Cité, Paris, France, [7] INSERM U1149, CRI, Faculté de Médecine Bichat-Claude Bernard, Paris, France, [8] Institut d'Hématologie et d'Oncologie Pédiatrique (IHOP), Hospices Civils de Lyon, Lyon, France, [9] Institut Universitaire de France, Paris, France

OPEN ACCESS

Edited by:
Richard Van Wijk, Utrecht University, Netherlands

Reviewed by:
Giovanna Tomaiuolo, University of Naples Federico II, Italy
Michael J. Simmonds, Griffith University, Australia

***Correspondence:**
Magalie Faivre
magalie.faivre@univ-lyon1.fr

Specialty section:
This article was submitted to Red Blood Cell Physiology, a section of the journal Frontiers in Physiology

Received: *12 February 2020*
Accepted: *07 May 2020*
Published: *12 June 2020*

Citation:
Faivre M, Renoux C, Bessaa A, Da Costa L, Joly P, Gauthier A and Connes P (2020) Mechanical Signature of Red Blood Cells Flowing Out of a Microfluidic Constriction Is Impacted by Membrane Elasticity, Cell Surface-to-Volume Ratio and Diseases. Front. Physiol. 11:576. doi: 10.3389/fphys.2020.00576

Despite the fact that Red Blood Cells (RBCs) have been intensively studied in the past 50 years to characterize mechanical phenotypes associated with both healthy and pathological states, only ektacytometry (i.e., laser diffractometry) is currently used by hematologists to screen for RBC membrane disorders. Therefore, the development of new diagnostic tools able to perform analysis at the scale of a single cell, over a statistically relevant population, would provide important complementary information. But these new diagnostic tools would have to be able to discriminate between different disorders causing a change in RBCs mechanical properties. We evaluated the mechanical response of artificially rigidified RBCs flowing through a microfluidic constriction. The geometry consists in a 50 μm wide channel with a succession of 14 tooth-like patterns, each composed of a 5 μm wide and 10 μm long constriction, associated with a 25 μm wide and 10 μm long enlargement. RBCs deformability was altered using two chemical treatments, known to affect RBCs membrane surface area and membrane deformability, lysolecithine (LPC) and diamide, respectively. Differences between samples were highlighted by the representation of the inverse of the shape recovery time ($1/\tau_r$), versus the extension at the exit of the constriction, D_{out}. The results demonstrate that our approach is able to provide a direct signature of RBCs membrane composition and architecture, as it allows discriminating the effect of changes in RBCs membrane surface area from changes in RBCs membrane deformability. Finally, in order to evaluate the potential of our microsystem to detect pathological cells, we have performed preliminary experiments on patients with Hereditary Spherocytosis (HS) or Sickle Cell Anemia (SCA).

Keywords: mechanical phenotype, microfluidics, red blood cells, pathologies, chemical treatment

INTRODUCTION

Red Blood Cells (RBCs) membrane possesses a unique structure responsible for their remarkable ability to deform to flow through the small capillaries of the microcirculation. RBCs have an elastic 2D mesh-like spectrin cytoskeleton anchored to the internal side of a lipid bilayer (Mohandas and Evans, 1994). The membrane of RBCs encloses a cytoplasm made of hemoglobin which viscosity is 10 mPa.s at 25°C. The membrane and the absence of nucleus in the internal media, plays a key role in the regulation of RBCs deformability.

Under normal conditions, the membrane deforms at constant surface area and exhibits a viscoelastic behavior. Once the cell surface area excess has been unfolded, further extension of the membrane is governed by the lipid bilayer, which tends to resist area expansion. The shear resistance of the membrane is directly related to the density of spectrin and thus, to the cytoskeleton molecular structure (Waught and Agre, 1988). RBCs have been extensively studied in the past 50 years in order to characterize mechanical phenotypes associated with both healthy and pathological states.

Various diseases such as malaria (Shelby et al., 2003; Suresh et al., 2005; Mauritz et al., 2010) diabetes (Buys et al., 2003) Sickle Cell Anemia (Ballas and Mohandas, 2004; Maciaszek and Lykotrafitis, 2011; Iragorri et al., 2018) (SCA) or Hereditary Spherocytosis (Waught and Agre, 1988) (HS) are associated with variation of RBCs deformability. Although conventional techniques allowing the quantification of cellular mechanical properties, (Suresh, 2007) such as atomic force microscopy (AFM), micropipette aspiration and optical tweezers are well-established, they present throughput too low (of the order of several tens of cells per day) to be envisaged as routine diagnostic tools. Currently only osmotic gradient ektacytometry (osmoscan), which consists in following the behavior of a suspension of RBCs sheared into a Couette system across an osmotic gradient, is used by hematologists to screen for RBC membrane disorders (Mohandas et al., 1980; Da Costa et al., 2013, 2016). However, up to now, they cannot provide any quantitative information such as parasitemia for malaria or distribution of cell populations which would provide valuable insights for SCA or HS (Dondorp et al., 1997).

Due to a match between cell sizes and typical dimensions accessible by microfabrication methods, microfluidic technologies propose attractive solutions for the study of cellular mechanics at the single cell level, while being compatible with high throughput (Antia et al., 2008; Hauck et al., 2010). Previous studies have demonstrated the use of various microfluidic geometries (Tomaiuolo, 2014) to detect alteration of RBCs deformability. Very different readouts have been used, such as deformation index, cell flowing velocity, transit time, relaxation time, etc. For example, Tsukada et al. (2001) have shown that the shape of cells flowing in micro-capillaries according to their velocity can be used to discriminate diabetic from healthy RBCs. Shelby et al. (2003) have shown that the ability of malaria infected RBCs to flow through microfluidic constrictions could be related to the stage of maturation of the parasite inside the host cells. Zheng et al. (2013) combined the flow of RBCs in a geometric constriction and impedance measurement to differentiate adult from neonatal RBCs. Guo et al. (2012) have measured the cortical tension associated with healthy, and *Plasmodium falciparum* infected RBCs, using funnel channels. Differences in velocities of RBCs flowing through geometrical constrictions have been used to discriminate healthy and diamide treated RBCs (Vilas Boas et al., 2018) or healthy and malaria infected RBCs (Bow et al., 2011). Faustino et al. (2014) took advantage of the strong extensional flow associated with a microchannel implementing a hyperbolic constriction, to differentiate RBCs from RBCs in contact with tumoral cells and healthy RBCs from RBCs of End-Stage Kidney Disease (ESKD) patients (Faustino et al., 2019). Tomaiuolo et al. (2011) have used the behavior of RBCs flowing through converging constrictions in order to evaluate cell membrane viscoelastic properties. Several papers have focused on the measurement of RBCs relaxation time (Tomaiuolo and Guido, 2011; Braunmüller et al., 2012; Prado et al., 2015) in microfluidics – i.e., the time necessary for the cell to recover its discocyte-like shape after cessation of the flow.

Although many research teams have demonstrated the ability to detect modification of molecular structure, (Forsyth et al., 2010; Hansen et al., 2011; Guo et al., 2012) to the best of our knowledge, none of them have tried to evaluate the specificity of their measurement by demonstrating their ability to discriminate between several diseases inducing an overall stiffening of the cells.

While many researches focused on the flow of RBCs through a microfluidic geometric constriction, we explored for the first time the maximum deformation of the cells being stretched by the sudden extension of the channel, in relation to its shape recovery time. We report the effect of two chemical treatments known to affect RBCs membrane surface area or membrane deformability on the dynamical behavior of RBCs flowing out a microfluidic constriction. We evaluated whether the response of the cells at the exit of the constriction was sensitive enough to discriminate between both effects (i.e., excess surface area and membrane elasticity). Finally, preliminary results highlighting the mechanical responses of RBCs in few patients with HS and SCA are discussed, thus addressing the specificity of our approach for potential diagnosis applications.

MATERIALS AND METHODS

Blood Samples

Healthy Samples

Healthy blood samples were collected in EDTA tubes. Mechanically impaired RBCs were obtained by treating healthy RBCs with one of the following molecules: lysolecithin (LPC) or diamide (Clark et al., 1983). Before and after treatment, RBCs were washed twice with phosphate buffered saline (PBS) 1X (Biosolve chemicals BV, Netherlands) and then re-suspended at a concentration of 19×10^6 RBCs/mL – corresponding to a hematocrit (Ht) of 0.17% – in PBS 1X. This dilution was necessary in order to avoid the flow of several cells simultaneously in the microchannel. Finally, after centrifugation,

RBCs were re-suspended in dextran solutions (Sigma-Aldrich, Saint-Louis, MO, United States) (Dextran from *Leuconostoc* spp., $M_w = 2 \times 10^6$ g/mol was used) at 0.9 mg/mL of PBS 1X, to avoid RBCs sedimentation in the reservoir and guaranty the injection of a homogeneous concentration of cells during the time of an experiment while maintaining the low Ht condition. Dextran solutions were always filtered at 0.2 μm on the day of use. The use of dextran solutions also increased the hydrodynamic stress undergone by the cells in the channel. Viscosity, pH and osmolarity of the solutions were verified to be 31.5 mPa.s, 7.4 and 300 mOsmol, respectively.

Cell Surface and *S/V* Reduction (LPC Treatment)

Washed RBCs were incubated for 5 min at room temperature with LPC (Sigma-Aldrich, Saint-Louis, MO, United States) (LPC from egg yolk with M_w = 505 g/mol was used) at final concentrations ranging from 0 to 1.0 μmol/mL of cells, according to the protocol reported by Clark et al. (1983) LPC changes discocyte RBCs to type III echinocytes, induces membrane vesiculation and loss of membrane, resulting in a reduction of the surface to volume ratio (noted *S/V*).

Membrane Deformability Reduction (Diamide Treatment)

As previously described,30,31 washed RBCs were incubated with diamide (Sigma-Aldrich, Saint-Louis, MO, United-States) at final concentrations ranging from 0 to 1.0 mmol/L for 1 h at 37°C. Diamide induces the formation of disulfide bonds between spectrin proteins and increases the shear modulus of RBCs (Fischer et al., 1978; Safeukui et al., 2012).

Pathological Samples

Blood samples from 3 healthy individuals, 3 patients with HS and 2 SCA patients were collected in EDTA tubes. The protocol was approved by the "Hospices Civils de Lyon – CPP Est" Ethics Committee (L14-127).

Device Fabrication

Microfluidic channels in polydimethylsiloxane Sylgard 184 (PDMS) were manufactured using standard soft photolithographic techniques (Duffy et al., 2004) and sealed on glass via oxygen plasma treatment (Harrick Plasma, Ithaca, NY, United States). The geometry consisted in a 50 μm wide and 10 μm high channel, in which a succession of 15 tooth-like patterns have been implemented as illustrated in **Figure 1**. Each teeth-like pattern was composed of a 5 μm wide and 10 μm long constriction, associated with a 25 μm wide and 10 μm long enlargement. This width oscillation has been repeated over 290 μm and was chosen for its ability to significantly center the RBCs at the exit of the last constriction.

Video-Microscopy

Polyethylene (PE 20) tubes (Harvard Apparatus, Holliston, MA, United States) connected the blood reservoirs to the inlet hole in the device and the outlet hole to the trash reservoir. RBC suspensions were injected in the microsystems by the flow control system MFCS^{TM}-EZ (Fluigent, Paris, France) at a pressure of 200 mbar. Video-microscopic recordings of the cell behavior were performed with an inverted phase contrast microscope (Leica DMI 4000B, Germany) with a 40× magnification and a high speed camera (Mikrotron EoSens MC1362, Germany). The microscope was equipped with an environmental chamber (Ibidi, Martinsried, Germany) thus allowing the experiments to be done at 37°C.

Image Analysis

Post processing of the movies was performed using a self-edited Matlab code to study cell dynamics and deformation. Briefly, on each image, after background subtraction, allowing to get rid of the microchannel walls, RBCs were automatically detected and cells contour was fitted with an elliptical shape. The position of the ellipse center of mass, the length of both axes along (*x*-direction) and perpendicular to (*y*-direction) the flow direction (2*a* and 2*b*, respectively, see inset **Figure 1**), were measured, allowing the calculation of the deformation index *D* defined as $D = (2a-2b)/(2a + 2b)$. Currently, the routine takes a couple of minutes (2–5 min) per cell on a regular computer, because the process is not fully automatized yet, which account for the quite low number of cells investigated (∼60 cells/sample). However, this step could be optimized in the future to reach nearly real-time analysis as reported by Deng and Chung (2016) on similar analysis with a throughput of 2000 cells/s.

For each condition, roughly 50 cells were analyzed. Results are presented as box-and-whisker plots. A non-parametric ANOVA test for independent measurements was used to compare the different readouts before and after chemical treatments. *Post hoc* comparisons were performed using Fisher's Least Squares Difference method. A Multivariate Analysis of Variance (MANOVA) test was used to compare the different pathological samples (HS, SCA, and control samples). The significance level was defined as $p < 0.05$.

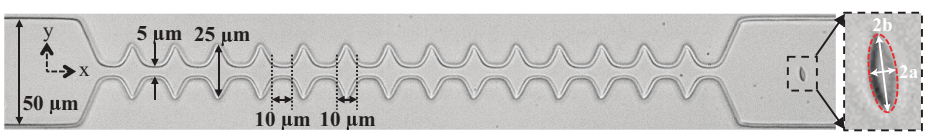

FIGURE 1 | The geometry consists in a 50 μm wide channel implementing 14 tooth-like patterns. The height of the device is 10 μm. The different dimensions are reported on the pictures. The inset shows a close-up of a RBC which contour is fitted by an ellipse (dashed red line). The two axes of the ellipse along (2a) and perpendicular (2b) to the flow direction allows the calculation of a deformation index such as *D* = (2a–2b)/(2a + 2b).

Ektacytometry

Osmoscan experiments have also been performed on the LoRRca MaxSis® device (RR Mechatronics, Hoorn, Netherlands) to confirm the effects of the different molecules tested on RBCs, as well as to verity the presence of the specific osmoscan signatures already described in HS and SCA patients. Osmoscan consisted in the measurements of a RBC deformability or elongation index (*EI*) under a defined shear stress (30 Pa), at increasing osmolality from 90 to 600 mOsm/kg and at 37°C, as recommended (Nemeth et al., 2015; Da Costa et al., 2016; Zaninoni et al., 2018). Buffer viscosity was 30.4 mPa.s. Several parameters were determined: O_{min} (i.e., the osmolality at which RBC deformability value reaches a minimum in the hypotonic region of the curve), EI_{max} (i.e., the highest RBC deformability) and O_{hyper} (also called *O'*), which corresponds to the osmolality at half of the EI_{max} on the hypertonic region of the curve (Zheng et al., 2013). O_{min} reflects the osmotic fragility and the surface-to-volume ratio, EI_{max} depends on the membrane deformability and RBC surface area, and O_{hyper} reflects Mean Cellular Hemoglobin Concentration (MCHC) and Mean Cell Volume (MCV) and is therefore highly dependent on the hydration status of the cells (Clark et al., 1983; Da Costa et al., 2013).

RESULTS AND DISCUSSION

Typical Behavior of Healthy RBCs

Video-microscopic recordings of RBCs flowing in the microfluidic channel allowed the visualization of the cell deformation – quantified using the deformation index D – as it travels through the device. **Figure 2** presents the typical behavior of a RBC flowing in the geometry of interest. The sequence of deformation associated with the flow of a healthy RBC in the geometry is reported in **Figure 2a** and the associated deformation index D is presented in **Figure 2b**. The cell flowing in the 50 μm wide channel presents a slipper-like shape, typical of RBC in confined flow ($D \approx -0.2$). As it approached the first constriction, the cells got compressed which is traduced by its elongation along the flow direction (x-axis). Indeed, D rose until reaching a maximum value around $x = 0$. Then, it underwent a stretching along the y-axis (i.e., perpendicular to the flow direction) when entering in the enlargement, before being compressed again by the next constriction. Accordingly, D dropped until reaching a local minimum (for $x = 10$ μm), before increasing again at $x = 20$ μm. This cycle of compressing/stretching is repeated due to the tooth-like patterns as illustrated by the oscillations of D versus x. The cyclic deformation of the cell within the geometry can be characterized through the measurement of the amplitude of deformation ΔD defined as $\Delta D = D_{max} - D_{min}$, where D_{max} and D_{min} are the mean of D in the constrictions and the enlargements, respectively, as illustrated in **Figure 2b**. Finally, as it exited the last narrowing, around $x = 290$ μm, RBC got strongly stretched perpendicular to the flow direction, which is traduced by the sudden drop of D. After reaching a minimum value noted D_{out} around $x = 310$ μm, D returns slowly to its initial value and reaches a plateau corresponding to the steady slipper-like shape.

The variation of D between the last deformed state at the exit, D_{out}, and the final steady shape, corresponding to the plateau value, is represented versus time in **Figure 2c**. The experimental data were fitted using an exponential growth, hence allowing the extraction of the shape recovery time τ_r defined as the time necessary for the cell to return to a stationary shape after exiting the last constriction, while being still under hydrodynamic stress. We have measured the shape recovery time of healthy RBCs while varying different viscous stress applied, i.e., hydrodynamic parameters such as buffer viscosity and cell speed (**Supplementary Figure SI.2B**). Because RBC steady shape is reached under hydrodynamic stress rather than at rest, the recovery time of RBCs does not directly correspond to their relaxation time. Indeed the relaxation time is defined as the time necessary for the cell to adopt the resting « discocyte-like » shape after total cessation of any stress. As already reported in the literature, the relaxation time τ depends only on the intrinsic mechanical properties of the RBC membrane, i.e., $\tau = \eta_m/\mu$, where η_m is the 2D membrane viscosity and μ the membrane shear modulus. According to the literature, τ has been measured using different techniques to be in the range 100–300 ms (Hochmuth et al., 1979; Mohandas et al., 1980; Braunmüller et al., 2012). Indeed, in specific experimental conditions, recovery times were measured at $\tau_r = 129$ ms for $\eta_{out} = 1.3$ mPa.s and $V_{cell} = 170$ μm/s, which is in good agreement with values previously reported in the literature for the relaxation time (Hochmuth et al., 1979; Mohandas et al., 1980; Evans, 1989; Tomaiuolo and Guido, 2011; Braunmüller et al., 2012). But they can also reach values as low as $\tau_r = 4$ ms for $\eta_{out} = 20.3$ mPa.s and $V_{cell} = 1500$ μm/s (Amirouche et al., 2020). We could explain these results in terms of coupling between the cell and the flow. This assumption would explain why at low hydrodynamic stress – where the cell properties dominate the recovery process and where the hydrodynamics can be neglected - we can assume being in an almost static configuration, the recovery time tend toward relaxation time values. In a previous study, we reported that at fixed hydrodynamic stress, shape recovery times of RBCs can be used to discriminate between healthy and mechanically impaired RBCs (Amirouche et al., 2017). In the present paper, we aim at demonstrating that our approach is sensitive enough to discriminate between different membrane modifications.

The repetition of the teeth-like pattern tends to focus cells within the microchannel (see **Supplementary Figure SI.1** in **Supplementary Information**), hence ensuring a symmetrical deformation at the exit of the last narrowing. This prevents them from rotating and imposes that all cells are exposed to the same hydrodynamic stress, all RBCs being aligned on the same flow line. Despite this advantage, the repetition of the constriction could also be a drawback. Indeed, it has been reported in literature (Lee et al., 2004; Simmonds and Meiselman, 2016; Horobin et al., 2017; Qiang et al., 2019) that the application of a stress too high or for a too long period of time can induce a mechanical fatigue of the cells. For example, Simmonds et al. report that RBCs present impaired deformability when exposed to physiological levels of shear stress (Simmonds and Meiselman, 2016) (above 40 Pa) for 1–64 s. Other studies report

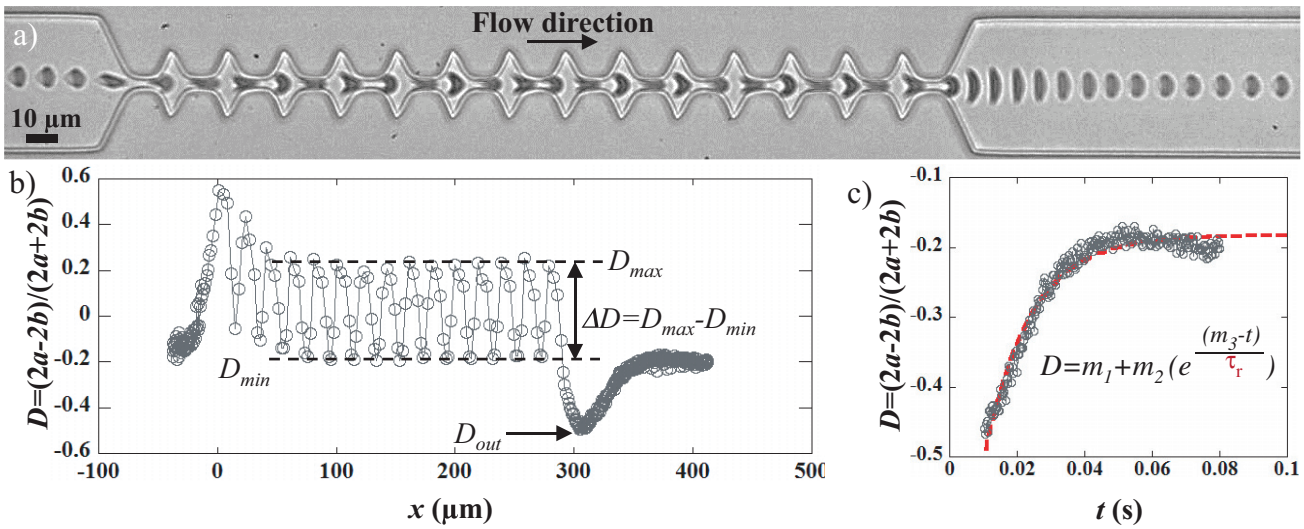

FIGURE 2 | (a) sequence of deformation of a healthy RBC flowing in the geometry at 200 mbar and **(b)** the associated variation of the deformation index D [$D = (2a–2b)/(2a + 2b)$] as a function of the position of the cell center of mass. The origin of the graph has been arbitrarily chosen at the entrance of the first narrowing. The amplitude of deformation ΔD is calculated as $\Delta D = D_{max}–D_{min}$, where D_{max} and D_{min} are the mean of D in the constrictions and the enlargements, respectively. The minimum of the curve corresponds to the large cell elongation at the exit of the last constriction, noted D_{out}. **(c)** representation of D versus time of the previous graph, where only the time window of the cell recovery is reported. The exit of the last narrowing was set to be $t = 0$. The dashed red line is an exponential fit allowing the determination of the recovery time τ_r according to the following equation $D = m_1 + m_2 \exp((m_3–t)/\tau_r)$, where m_1, m_2, and m_3 are constant to be adjusted.

that cyclic mechanical solicitations of RBCs lead to significantly greater loss of membrane deformability, compared to continuous deformation under the same maximum load and duration (Lee et al., 2004). Therefore, we have verified that the repetition of the restriction did not impact the behavior of RBCs exiting the geometry. As presented in **Supplementary Figure SI.2**, the shape recovery time of healthy RBCs was identical after exiting a single 10 µm long constriction and the 15 repetitions of a 10 µm long constriction, hence demonstrating that no fatigue was detected in our experiments.

Chemically Altered RBCs

Two chemical treatments were performed on healthy RBCs in order to affect RBC deformability. For each sample, osmotic gradient ektacytometry was performed (some results are shown on **Figure 3**) and the mechanical responses of RBCs flowing in the microfluidic system were evaluated (**Figure 4** for LPC treated RBCs, and **Figure 5** for diamide treated RBCs). LPC is known to cause a reduction in the surface area of RBCs (Mohandas et al., 1980; Clark et al., 1983). Osmotic gradient ektacytometry experiments performed on LPC treated RBCs at 1.0 µM (**Figure 3**) showed a significant rise in Omin and Ohyper, and a decrease in EImax. These findings confirm the effects of LPC on cell sphericity (decrease of surface-to-volume ratio). The increase in Ohyper could be explained by the slight increase in cell volume upon LPC treatment (MCV were measured to be 87.8 and 103.4 fL for the control and 1.0 µM LPC treated sample, respectively) as already reported (Safeukui et al., 2012). **Figure 4** reports the effect of LPC at various concentrations (from 0.25 to 1 µM) on the RBCs mechanical response while flowing in the geometry. **Figure 4a** shows a typical sequence of deformation of a LPC-treated cell at 1 µM.

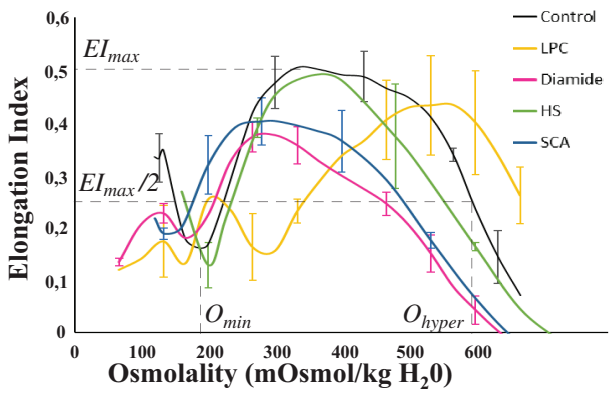

FIGURE 3 | Schematic representation of Osmoscan experiments. Several parameters can be determined on this curve: O_{min} (i.e., the osmolality at which RBC deformability value reaches a minimum in the hypotonic region of the curve), EI_{max} (i.e., the highest RBC deformability) and O_{hyper} which corresponds to the osmolality at half of the EI_{max} on the hypertonic region of the curve. LPC treated RBCs at 1.0 µM show an increase in O_{min} and O_{hyper} and a decrease in EI_{max}. Diamide treated RBCs at 0.5 mM show a decrease in EI_{max} and O_{hyper}. These HS patients have a decreased EI_{max} and O_{hyper} compared to control. O_{min}, O_{hyper} and EI_{max} are decreased in these SCA patients compared to control.

Lysolecithine treated RBCs behaved qualitatively similarly to healthy RBCs. They got compressed and stretched according to the width of the channel, and got elongated by the extensional flow at the exit before recovering a stationary shape. However,

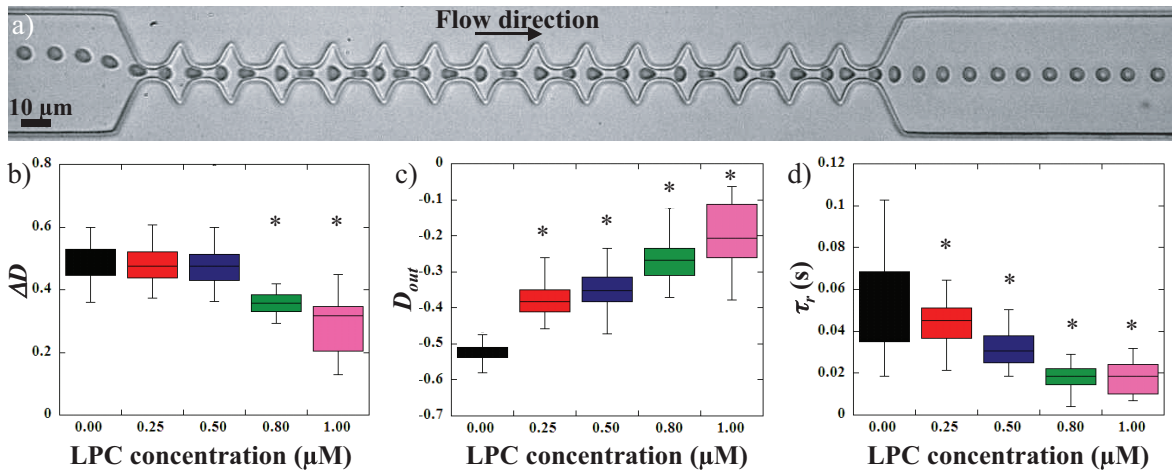

FIGURE 4 | (a) sequence of deformation of a 1 µM LPC treated RBC flowing in the geometry. Evolution of **(b)** the amplitude of deformation ΔD, **(c)** the stretching at the exit D_{out} and **(d)** the recovery time τ_r, versus LPC concentration. *Different from control sample (0 µM), $p < 0.05$.

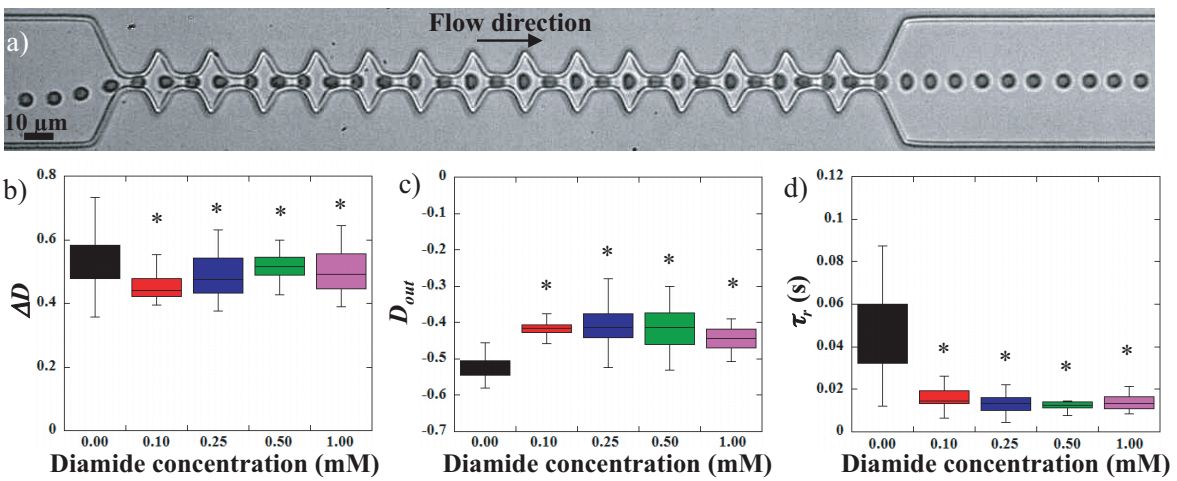

FIGURE 5 | (a) sequence of deformation of a 1 mM diamide treated RBC flowing in the geometry. Evolution of **(b)** the amplitude of deformation ΔD, **(c)** the stretching at the exit D_{out}, and **(d)** τ_r, the recovery time versus diamide concentration. *Different from control sample (0 mM), $p < 0.05$.

a reduction of the amount of deformation experienced by the cells can be visually detected on the picture while undergoing the same amount of stress. These observations are confirmed by the measurements of the amplitude of deformation, ΔD versus LPC concentration upon treatments (**Figure 4b**). LPC treatment at a concentration up to 0.5 µM had no significant impact on the amplitude of deformation of RBCs compared to healthy RBCs. However, treatment with higher concentrations led to a significant reduction of ΔD (**Figure 4b**). **Figures 3d**, **4c** show the evolution of the elongation at the exit, D_{out}, and the recovery time, τ_r, respectively. The stretching at the exit, D_{out}, and the recovery time, τ_r were gradually decreased upon increasing LPC concentration; hence showing that RBCs deformability drops gradually with the concentration of LPC.

Previous works used diamide to rigidify the RBCs membrane (Mohandas et al., 1980; Forsyth et al., 2010; Prado et al., 2015). Indeed, diamide treatment (**Figure 3**) decreased EI_{max} and O_{hyper}. The increase in diamide concentration caused asymmetry in the hump of the osmotic gradient ektacytometry curve with a greater reduction in EI on the hypertonic part of the curve than on the hypotonic side. These findings confirmed the effects of diamide on membrane deformability, i.e., an increased shear modulus caused by the cross-linking between spectrins (Mohandas et al., 1980). **Figure 5** illustrates the effect of diamide treatment with concentrations ranging from 0.1 to 1.0 mM. **Figure 5a** presents the typical sequence of deformation of a diamide treated RBC at 1 mM. As for LPC treatments, RBCs deformability was clearly reduced when the cell was incubated with diamide, although the qualitative behavior of the cells was similar to that of healthy RBCs. Diamide treated cells showed a slight, yet statistically significant, drop in the amplitude of deformation ΔD, as illustrated in **Figure 5b**. Nevertheless, upon incubation

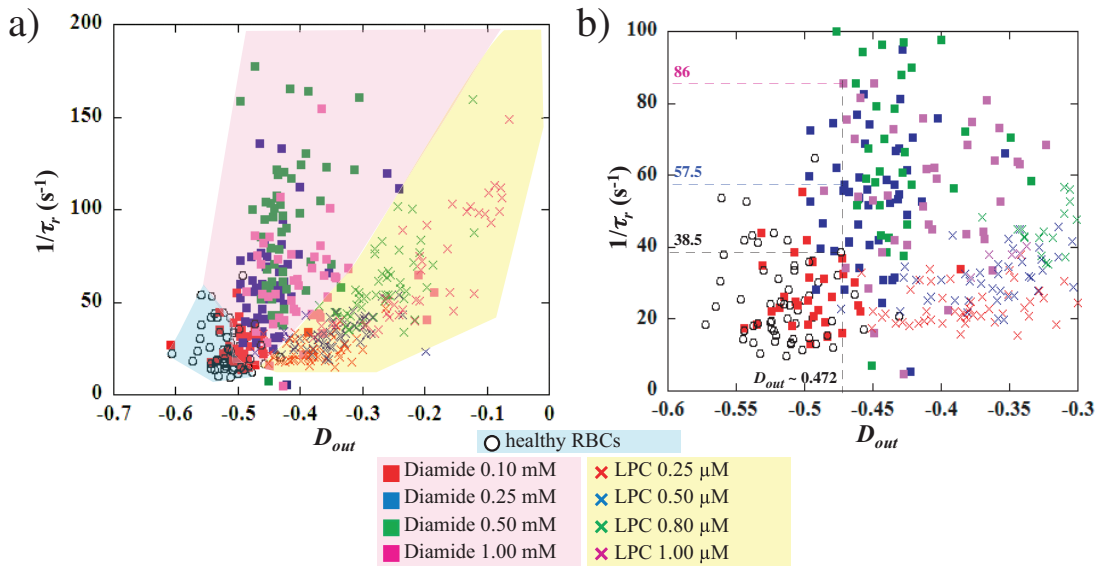

FIGURE 6 | (a) evolution of $1/\tau_r$ versus D_{out} for healthy, Diamide and LPC treated RBCs. **(b)** close-up of the graph in **(a)**. For a given value of the stretching at the exit, D_{out} = –0.472, healthy RBC presents $1/\tau_r$ = 33.5 s^{-1}, 0.25 mM diamide treated cell has $1/\tau_r$ = 57.5 s^{-1} and 1 mM diamide treated cell has $1/\tau_r$ = 86 s^{-1}.

with diamide, elongation at the exit D_{out}, of treated RBCs was reduced (**Figure 5c**), although the measurements were not able to make a distinction between the different diamide concentrations. Diamide treatment also impacted the recovery time τ_r of RBCs as highlighted by the decrease from 0.048 s for healthy RBCs to roughly 0.013 s for diamide treated cells (**Figure 5d**).

From the results presented above, it seems that ΔD is not sensitive enough to clearly detect modifications of the cells mechanical properties. This may be explained by the fact that this parameter is highly impacted by the various off-centered initial positions of the cells when entering the zone of interest.

However, the measurements of the maximum elongation at the exit D_{out} and the RBCs recovery time τ_r can be used to discriminate healthy from chemically treated RBCs. But whether these readouts can differentiate between the different chemical concentrations is unclear. In the case of a visco-elastic object such as a RBC, the relaxation time, and therefore the recovery time, is linked to the deformed state. Indeed, τ_r decreases as D_{out} decreases, i.e., it takes less time to recover from a less elongated shape than from a more elongated one. **Figure 6** represents $1/\tau_r$ versus D_{out}, for the different concentrations of diamide and LPC as well as the healthy samples. It can be clearly observed on the figure that, while healthy RBCs mechanical signature is limited to low $1/\tau_r$ (<50 s^{-1}) values and strong elongation ($D_{out} < -0.5$), chemically rigidified RBCs present lower elongation at the exit associated with shorter recovery time. We can see on **Figure 6b**, that for a given extension at the exit $D_{out} \sim -0.472$, 3 RBCs present three different values of recovery times according to diamide concentration: $1/\tau_r$ = 38.5 s^{-1} for the healthy cell (τ_r ~26 ms), $1/\tau_r$ = 57.5 s^{-1} for the RBC treated with diamide at 0.25 mM (τ_r~17 ms) and $1/\tau_r$ = 86 s^{-1} for 1 mM diamide treated RBC (τ_r~12 ms). These observations suggest that cells treated with diamide (at a concentration above 0.1 mM) exhibit a recovery time smaller than that of healthy ones for an equivalent extension at the exit D_{out}. This representation allows to discriminate easily the chemically rigidified RBCs from the healthy ones (blue zone). Moreover, it is possible to differentiate the two treatments as all the data points associated with LPC treated cells are located in a region (yellow zone) of the graph while diamide treated RBCs are located in another region (pink zone). Although both treatments lead to an increase in the overall cell rigidity, which is traduced by a lower D_{out} and a shorter τ_r, we can distinguish the effect of increased membrane stiffness from the effect of excess surface area.

The results obtained with chemically treated cells highlight that our microsystem is not only able to quantify the RBCs ability to deform, but also to provide a direct signature of the composition and architecture of their membrane. Indeed, we suspect that our microfluidic approach could be useful to differentiate and diagnose different kind of RBC disorders according to the origin of the affection (RBC membrane disorders, changes in surface-to-volume ratio, etc. . .).

Pathological RBCs

In order to evaluate the potential of our microsystem to detect pathological cells, we have studied the mechanical response of HS and SCA RBCs flowing out of our tooth-like pattern. Osmoscan experiments (**Figure 3**) showed a typical signature obtained for HS and SCA RBCs by ektacytometry. **Figure 7** reports the measurements of $1/\tau_r$ as a function of D_{out} for three HS patients, two SCA patients and one healthy donor. In order to help decipher if the two pathological samples are not only different from the healthy sample but also between each other, we decided to represent all pathological data on the same graph. SCA data correspond to the two different patients pooled together. In the same way, the points corresponding to the HS RBCs,

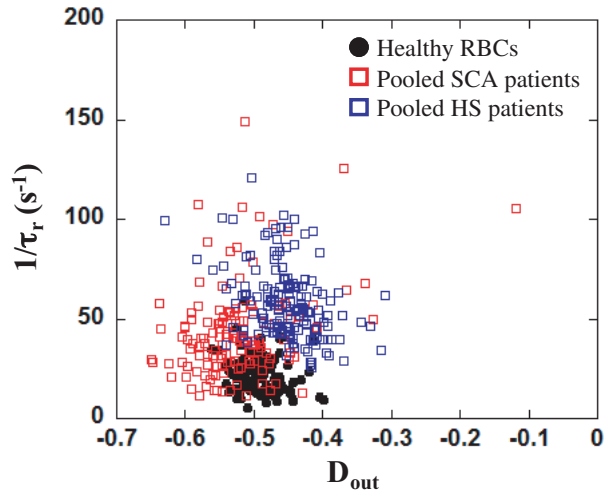

FIGURE 7 | D_{out} versus $1/\tau_r$ for healthy RBCs (solid black circles), pooled SCA patients (open red squares) and pooled HS patients (open blue squares). A MANOVA statistical analysis revealed that the RBCs distribution was significantly different between the three groups ($p < 0.05$ between HS and healthy, $p < 0.05$ between SCA and healthy, and $p < 0.05$ between HS and SCA).

were obtained by pooling the three HS patients. As illustrated on the Figure, RBCs from HS patients showed an increase of $1/\tau_r$ compared to healthy RBCs, while RBCs from SCA patients had both a decrease in D_{out} and a slight increase in $1/\tau_r$. Such increase in $1/\tau_r$ is expected because these diseases are known to increase cell stiffness (Nakashima and Beutler, 1979; Waught and Agre, 1988; Da Costa et al., 2013).

A MANOVA analysis showed that the distribution of RBCs according to D_{out} and $1/\tau_r$ was significantly different between HS, SCA and control individuals ($p < 0.05$). The morphologic signature of HS is the presence of microspherocytes (smaller spherical RBCs), which is caused by loss of RBC membrane surface area, leading to an abnormal osmotic fragility. Although one would have expected to find similar response with HS patients than with LPC treated cells, both being associated with a loss of membrane surface area, other modifications of HS RBCs may explain the difference between the LPC and HS microfluidic signatures. For instance, HS blood also contains dense RBCs (usually more than 4% of RBCs with MCHC > 41 g/dL) which may impact on the microfluidic behavior of the cells (Mohandas et al., 1980; Da Costa et al., 2016). Finally as usual, the inter-cells variability within a blood sample was higher in SCA than in HS. This discrepancy could be attributed to the presence of different sub-populations of more or less dense cells in SCA, suggesting the possibility to retrieve information about the composition of the different sub-populations. Although only few patients were tested, our preliminary results seem to highlight that our microfluidic device could be sensitive enough to make a distinction between healthy and pathological RBCs. Nevertheless, HS patients included in this study were issued from the same family, i.e., presenting the same genetic molecular modifications, and it remains unknown whether our system is able to discriminate RBCs from HS patients with different molecular modifications (ankyrin, α–spectrin, β–spectrin ...). However, in this particular HS family, with the same red cell membrane molecular defect, we reproduced consistently in the three affected relatives the same microfluidic signature.

CONCLUSION

Differences between healthy and chemically treated cells were highlighted by the measurement of both the extension at the exit, D_{out}, and the shape recovery time τ_r. Although the measures were not able to distinguish between the different chemical concentrations, the representation of $1/\tau_r$ versus D_{out} membrane surface area from membrane elasticity. It is able to provide a direct signature of RBCs membrane composition and architecture.

Our preliminary results highlight that the mechanical responses of healthy and pathological RBCs are not only different but also suggest that the discrimination of both diseases could be possible, although more experiments using samples from various RBC disorders are needed. To our knowledge, this is the first attempt to evaluate the specificity of a passive microfluidic approach to perform diagnosis based on the alteration of RBC deformability, although more experiments are necessary to prove it. In addition to is diagnostic potential, further studies including large cohort of patients would be necessary to evaluate the clinical usefulness of our microfluidic approach for various RBC disorders. The single cell approach, while analyzing a statistically relevant population, could also provide complementary information (quantification of the heterogeneity of the cell population) that might be of great importance for the diagnosis and prognosis.

DATA AVAILABILITY STATEMENT

The datasets generated for this study are available on request to the corresponding author.

ETHICS STATEMENT

The studies involving human participants were reviewed and approved by the "Hospices Civils de Lyon – CPP Est" Ethics Committee (L14-127). The patients/participants provided their written informed consent to participate in this study.

AUTHOR CONTRIBUTIONS

MF, CR, PJ, and PC have designed the research. MF and AB have performed the microfluidic experiments. CR and AB have performed the ektacytometry assays. LD and AG included the patients. MF, CR, and PC have analyzed the results. MF has written the main manuscript text and prepared the figures. MF, CR, LD, PJ, AG, and PC have reviewed and approved the final version of the manuscript.

ACKNOWLEDGMENTS

We thank CNRS MITI for financial support. We also thank Julie Galimand and Dr. Odile Fenneteau for their technical help and cytology expertise, respectively.

AUTHOR'S NOTE

‡ The repetition of the tooth-like pattern tends to focus cells at the exit. Such behavior has also been observed at the exit of very long straight constrictions, however, it would need a fairly longer geometry to obtain the same effect.

SUPPLEMENTARY MATERIAL

The Supplementary Material for this article can be found online at: https://www.frontiersin.org/articles/10.3389/fphys.2020.00576/full#supplementary-material

REFERENCES

Amirouche, A., Esteves, J., Ferrigno, R., and Faivre, M. (2020). Dual shape recovery of red blood cells flowing out of a microfluidic constriction. *Biomicrofluidics* 14:024116. doi: 10.1063/5.0005198

Amirouche, A., Ferrigno, R., and Faivre, M. (2017). Impact of channel geometry on the discrimination of mechanically impaired red blood cells in passive microfluidics. *Multidiscip. Digit. Publ. Inst. Proc.* 1:512. doi: 10.3390/proceedings1040512

Antia, M., Herricks, T., and Rathod, P. K. (2008). Microfluidic approaches to malaria pathogenesis. *Cell. Microbiol.* 10, 1968–1974. doi: 10.1111/j.1462-5822.2008.01216.x

Ballas, S. K., and Mohandas, N. (2004). Sickle red cell microrheology and sickle blood rheology. *Microcirculation* 11, 209–225. doi: 10.1080/10739680490279410

Bow, H., Pivkin, I. V., Diez-Silva, M., Goldfless, S. J., Dao, M., Niles, J. C., et al. (2011). A microfabricated deformability-based flow cytometer with application to malaria. *Lab Chip* 11, 1065–1073.

Braunmüller, S., Schmid, L., Sackmann, E., and Franke, T. (2012). Hydrodynamic deformation reveals two coupled modes/time scales of red blood cell relaxation. *Soft Matter* 8, 11240–11248.

Buys, A. V., Van Rooy, M.-J., Soma, P., Van Papendorp, D., Lipinski, B., and Pretorius, E. (2003). Changes in red blood cell membrane structure in type 2 diabetes: a scanning electron and atomic force microscopy study. *Cardiovasc. Diabetol.* 12:25. doi: 10.1186/1475-2840-12-25

Clark, M. R., Mohandas, N., and Shohet, S. B. (1983). Osmotic gradient ektacytometry: comprehensive characterization of red cell volume and surface maintenance. *Blood* 61, 899–910. doi: 10.1182/blood.v61.5.899.bloodjournal615899

Da Costa, L., Galimand, J., Fenneteau, O., and Mohandas, N. (2013). Hereditary spherocytosis, elliptocytosis, and other red cell membrane disorders. *Blood Rev.* 27, 167–178. doi: 10.1016/j.blre.2013.04.003

Da Costa, L., Suner, L., Galimand, J., Bonnel, A., Pascreau, T., Couque, N., et al. (2016). Diagnostic tool for red blood cell membrane disorders: assessment of a new generation ektacytometer. *Blood Cells Mol. Dis.* 56, 9–22. doi: 10.1016/j.bcmd.2015.09.001

Deng, Y., and Chung, A. J. (2016). "Next generation deformability cytometry: fully automated, high-throughput and near real-time cell mechanotyping," in *Proceedings of the 20th International Conference on Miniaturized Systems for Chemistry and Life Sciences*, Dublin, 148–149.

Dondorp, A. M., Angus, B. J., Hardeman, M. R., Chotivanich, K. T., Silamut, K., Ruangveerayuth, R., et al. (1997). The role of reduced red cell deformability in the pathogenesis of severe falciparum malaria and its restoration by blood transfusion. *Am. J. Trop. Med. Hyg.* 57, 507–511. doi: 10.4269/ajtmh.1997.57.507

Duffy, D. C., McDonald, J. C., Schueller, O. J. A., and Whitesides, G. M. (2004). Rapid prototyping of microfluidic systems in poly(dimethylsiloxane). *Anal. Chem.* 70, 4974–4984. doi: 10.1021/ac980656z

Evans, E. A. (1989). Structure and deformation properties of red blood cells: concepts and quantitative methods. *Methods Enzymol.* 1173, 3–35. doi: 10.1016/s0076-6879(89)73003-2

Faustino, V., Pinho, D., Yaginuma, T., Calhelha, R. C., Ferreira, I. C. F. R., and Lima, R. (2014). Extensional flow-based microfluidic device: deformability assessment of red blood cells in contact with tumor cells. *Biochip J.* 8, 42–47. doi: 10.1007/s13206-014-8107-1

Faustino, V., Rodrigues, R. O., Pinho, D., Costa, E., Santos-Silva, A., Miranda, V., et al. (2019). A microfluidic deformability assessment of pathological red blood cells flowing in a hyperbolic converging microchannel. *Micromachines* 10:645. doi: 10.3390/mi10100645

Fischer, T. M., Haest, C. W. M., Stöhr, M., Kamp, D., and Deuticke, B. (1978). Selective alteration of erythrocyte deformability by SH-reagents. Evidence for an involvement of spectrin in membrane shear elasticity. *Biochim. Biophys. Acta* 510, 270–282. doi: 10.1016/0005-2736(78)90027-5

Forsyth, A. M., Wan, J., Ristenpart, W. D., and Stone, H. A. (2010). The dynamic behavior of chemically stiffened red blood cells in microchannel flows. *Microvasc. Res.* 80, 37–43. doi: 10.1016/j.mvr.2010.03.008

Guo, Q., Reiling, S. J., Rohrbach, P., and Ma, H. (2012). Microfluidic biomechanical assay for red blood cells parasitized by *Plasmodium falciparum*. *Lab Chip* 12, 1143–1150.

Hansen, B., Pivkin, I. V., Diez-Silva, M., Goldfless, S. J., Dao, M., Jacquin, C., et al. (2011). A microfabricated deformability-based flow cytometer with application to malaria. *Lab Chip* 11, 1065–1073.

Hauck, T. S., Giri, S., Gao, Y., and Chan, W. C. W. (2010). Nanotechnology diagnostics for infectious diseases prevalent in developing countries. *Adv. Drug Deliv. Rev.* 62, 438–448. doi: 10.1016/j.addr.2009.11.015

Hochmuth, R. M., Worthy, P. R., and Evans, E. A. (1979). Red cell extensional recovery and the determination of membrane viscosity. *Biophys. J.* 26, 101–114. doi: 10.1016/s0006-3495(79)85238-8

Horobin, J. T., Sabapathy, S., and Simmonds, M. J. (2017). Repetitive supra-physiological shear stress impairs red blood cell deformability and induces hemolysis. *Artif. Organs* 41, 1017–1025. doi: 10.1111/aor.12890

Iragorri, M. A. L., El Hoss, S., Brousse, V., Lefevre, S. D., Dussiot, M., Xu, T. Y., et al. (2018). A microfluidic approach to study the effect of mechanical stress on erythrocytes in sickle cell disease. *Lab Chip* 18, 2975–2984. doi: 10.1039/c8lc00637g

Lee, S., Ahn, K. H., Lee, S. J., Sun, K., Goedhart, P. T., and Hardeman, M. R. (2004). Shear induced damage of red blood cells monitored by the decrease of their deformability. *Korea Aust. Rheol. J.* 16, 141–146.

Maciaszek, J. L., and Lykotrafitis, G. (2011). Sickle cell trait human erythrocytes are significantly stiffer than normal. *J. Biomech.* 44, 657–661. doi: 10.1016/j.jbiomech.2010.11.008

Mauritz, J. M. A., Tiffert, T., Seear, R., Lautenschlger, F., Esposito, A., Lew, V. L., et al. (2010). Detection of *Plasmodium falciparum*-infected red blood cells by optical stretching. *J. Biomed. Opt.* 15:030517. doi: 10.1117/1.3458919

Mohandas, N., Clark, M. R., Jacobs, M. S., and Shohet, S. B. (1980). Analysis of factors regulating erythrocyte deformability. *J. Clin. Invest.* 66, 563–573. doi: 10.1172/jci109888

Mohandas, N., and Evans, E. (1994). Mechanical properties of the red cell membrane in relation to molecular structure and genetic defects. *Annu. Rev. Biophys. Biomol. Struct.* 23, 787–818. doi: 10.1146/annurev.bb.23.060194.004035

Nakashima, N., and Beutler, E. (1979). Erythrocyte cellular and membrane deformability in hereditary spherocytosis. *Blood* 53, 481–485. doi: 10.1182/blood.v53.3.481.bloodjournal533481

Nemeth, N., Kiss, F., and Miszti-Blasius, K. (2015). Interpretation of osmotic gradient ektacytometry (osmoscan) data: a comparative study

for methodological standards. *Scand. J. Clin. Lab. Invest.* 75, 213–222. doi: 10.3109/00365513.2014.993695

Prado, G., Farutin, A., Misbah, C., and Bureau, L. (2015). Viscoelastic transient of confined red blood cells. *Biophys. J.* 108, 2126–2136. doi: 10.1016/j.bpj.2015.03.046

Qiang, Y., Liu, J., Dao, M., Suresh, S., and Du, E. (2019). Mechanical fatigue of human red blood cells. *Proc. Natl. Acad. Ssci. U.S.A.* 116, 19828–19834. doi: 10.1073/pnas.1910336116

Safeukui, I., Buffet, P. A., Deplaine, G., Perrot, S., Brousse, V., Ndour, A., et al. (2012). Quantitative assessment of sensing and sequestration of spherocytic erythrocytes by the human spleen. *Blood* 120, 424–430. doi: 10.1182/blood-2012-01-404103

Shelby, J. P., White, J., Ganesan, K., Rathod, P. K., and Chiu, D. T. (2003). A microfluidic model for single-cell capillary obstruction by *Plasmodium falciparum*-infected erythrocytes. *Proc. Natl. Acad. Sci. U.S.A.* 100, 14618–14622. doi: 10.1073/pnas.2433968100

Simmonds, M. J., and Meiselman, H. J. (2016). Prediction of the level and duration of shear stress exposure that induces subhemolytic damage to erythrocytes. *Biorheology* 53, 237–249. doi: 10.3233/bir-16120

Suresh, S. (2007). Biomechanics and biophysics of cancer cells. *Acta Biomater.* 3, 413–438. doi: 10.1016/j.actbio.2007.04.002

Suresh, S., Spatz, J., Mills, J. P., Micoulet, A., Dao, M., Lim, C. T., et al. (2005). Connections between single-cell biomechanics and human disease states: gastrointestinal cancer and malaria. *Acta Biomater.* 1, 15–30. doi: 10.1016/j.actbio.2004.09.001

Tomaiuolo, G. (2014). Biomechanical properties of red blood cells in health and disease towards microfluidics. *Biomicrofluidics* 8:051501. doi: 10.1063/1.4895755

Tomaiuolo, G., Barra, M., Preziosi, V., Cassinese, A., Rotoli, B., and Guido, S. (2011). Microfluidics analysis of red blood cell membrane viscoelasticity. *Lab Chip* 11, 440–454.

Tomaiuolo, G., and Guido, S. (2011). Start-up shape dynamics of red blood cells in microcapillary flow. *Microvasc. Res.* 82, 35–41. doi: 10.1016/j.mvr.2011.03.004

Tsukada, K., Sekizuka, E., Oshio, C., and Minamitani, H. (2001). Direct measurement of erythrocyte deformability in diabetes mellitus with a transparent microchannel capillary model and high-speed video camera system. *Microvasc. Res.* 61, 231–239. doi: 10.1006/mvre.2001.2307

Vilas Boas, L., Faustino, V., Lima, R., Miranda, J. M., Minas, G., Veiga Fernandes, C. S., et al. (2018). Assessment of the deformability and velocity of healthy and artificially impaired red blood cells in narrow polydimethylsiloxane (PDMS) microchannels. *Micromachines* 9:384. doi: 10.3390/mi9080384

Waught, R. E., and Agre, P. (1988). Reductions of erythrocyte membrane viscoelastic coefficients reflect spectrin deficiencies in hereditary spherocytosis. *J. Clim. Invest.* 81, 133–141. doi: 10.1172/jci113284

Zaninoni, A., Fermo, E., Vercellati, C., Consonni, D., Marcello, A. P., Zanella, A., et al. (2018). Use of laser assisted optical rotational cell analyzer (LoRRca MaxSis) in the diagnosis of RBC membrane disorders, enzyme defects, and congenital dyserythropoietic anemias: a monocentric study on 202 patients. *Front. Physiol.* 9:451. doi: 10.3389/fphys.2018.00451

Zheng, Y., Nguyen, J., Wai, Y., and Sun, Y. (2013). Recent advances in microfluidic techniques for single-cell biophysical characterization. *Lab Chip* 13, 2464–2483.

Conflict of Interest: The authors declare that the research was conducted in the absence of any commercial or financial relationships that could be construed as a potential conflict of interest.

frontiers in Physiology

ORIGINAL RESEARCH
published: 10 July 2020
doi: 10.3389/fphys.2020.00821

Micro-Raman Spectroscopy Analysis of Optically Trapped Erythrocytes in Jaundice

Sanu Susan Jacob[1], Aseefhali Bankapur[2], Surekha Barkur[2], Mahendra Acharya[2], Santhosh Chidangil[2], Pragna Rao[3], Asha Kamath[4], R. Vani Lakshmi[4], Prathap M. Baby[5] and Raghavendra K. Rao[1]*

[1] Department of Physiology, Kasturba Medical College-Manipal, Manipal Academy of Higher Education, Manipal, India, [2] Department of Atomic and Molecular Physics, Centre of Excellence for Biophotonics, Manipal Academy of Higher Education, Manipal, India, [3] Department of Biochemistry, Kasturba Medical College-Manipal, Manipal Academy of Higher Education, Manipal, India, [4] Department of Data Science, Prasanna School of Public Health, Manipal Academy of Higher Education, Manipal, India, [5] Department of Physiology, Melaka Manipal Medical College, Manipal Academy of Higher Education, Manipal, India

Derangements in bilirubin metabolism and/or dysfunctions in the hepato-biliary system lead to the unhealthy buildup of bilirubin in blood, resulting in jaundice. During the course of this disorder, circulating red cells are invariably subjected to toxic effects of serum bilirubin and an array of inflammatory compounds. This study aimed to investigate the vibrational spectroscopy of live red cells in jaundice using micro-Raman spectroscopy combined with optical-trap. Red cells from blood samples of healthy volunteers and patients with jaundice were optically immobilized and micro-Raman probed using a 785 nm diode laser. Raman signatures from red cells in jaundice exhibited significant variations from the normal and the spectral-markers were obtained from multivariate analytical methods. This research gives insightful views on how different pathologies can act as "stress-milieus" for red cells in circulation, possibly impeding their normal functions and also exasperating anemia. Raman spectroscopy, an emerging bio-analytical technique, is sensitive in detecting molecular-conformations *in situ*, at cellular-levels and in real-time. This study could pave way in understanding fundamental red cell behavior in different diseases by analyzing Raman markers.

Keywords: red blood cells, jaundice, Raman spectroscopy, bilirubin, hemoglobin

OPEN ACCESS

Edited by:
Richard Van Wijk,
Utrecht University, Netherlands

Reviewed by:
Mauro Magnani,
University of Urbino Carlo Bo, Italy
Norbert Nemeth,
University of Debrecen, Hungary
Christian Wagner,
Saarland University, Germany

****Correspondence:***
Sanu Susan Jacob
sanu.susan@manipal.edu

Specialty section:
This article was submitted to Red Blood Cell Physiology, a section of the journal Frontiers in Physiology

Received: *26 April 2020*
Accepted: *19 June 2020*
Published: *10 July 2020*

Citation:
Jacob SS, Bankapur A, Barkur S, Acharya M, Chidangil S, Rao P, Kamath A, Lakshmi RV, Baby PM and Rao RK (2020) Micro-Raman Spectroscopy Analysis of Optically Trapped Erythrocytes in Jaundice. Front. Physiol. 11:821. doi: 10.3389/fphys.2020.00821

INTRODUCTION

Bilirubin is a yellow pigment produced in the body, primarily as a consequent-by-product of red blood cell (RBC) catabolism (Adamson and Longo, 2012). Senile RBCs at the end of their 120 days' sojourn in circulation, are physiologically detected and hemolysed by the reticulo-endothelial system. This process occurs chiefly in the spleen, causing the release of hemoglobin (Hb), the principle RBC component (Korolnek and Hamza, 2015). When the tetra-pyrrolic moiety of hemoglobin, called heme, breaks down, it generates plasma-insoluble unconjugated bilirubin (UCB) (Schiff et al., 2011). To render it plasma-soluble, UCB is reversibly-bound with plasma albumin and is transported to the liver to undergo a process called conjugation. In the liver, UCB is conjugated

with glucuronic acid (Levitt and Levitt, 2014). Plasma-soluble conjugated bilirubin (CB) is then released through the bile into the intestine, from where it is excreted and eliminated from the body through the bowels and bladder in the form of stercobilinogen (Erlinger et al., 2014).

In any circumstances of increased hemolysis, hepatic dysfunction or even biliary obstruction, there ensues a build-up of bilirubin in blood, resulting in a condition termed hyperbilirubinemia, which is clinical jaundice (Fargo et al., 2017). Normal serum bilirubin levels are not known to pose any implications for general health, rather, is found to be valuable for possessing antioxidant properties in the vasculature (Park, 2016). However, uncontrolled and/or untreated hyperbilirubinemia is toxic and can cause serious deleterious effects that require immediate and appropriate life-saving treatments (Hansen, 2001). Currently, there exist numerous reports that describe the lethal effects of jaundice, but most studies are directed toward its effects on the nervous system (Shapiro, 2003; Shi et al., 2019). There exist fewer reports of bilirubin toxicity on blood components. It has been recognized that bilirubin liberated from RBC destruction, if present in larger than physiological quantities in circulation, can trigger toxic effects on other circulating RBCs. This can result in augmenting the production of more bilirubin, the whole course transitioning into a potentially vicious cycle (Lang et al., 2015). In addition to bilirubin, levels of a multitude of inflammatory markers and acute phase reactants escalate in the serum, such as endotoxins, tumor necrosis factor-α, IL-6, and C-reactive protein (Padillo et al., 2001). These systemic inflammatory cytokines are themselves known to reduce the life-span of RBCs, through a programmed process called eryptosis (Pretorius, 2018).

The focus of this study was to investigate the chemometrics of the Raman spectra of RBCs from blood samples of patients with jaundice, keeping the cells as alive as possible. This required the utility of a tool that demands only the bare minimal sample-preparation procedures, reagents or fixatives, which could themselves be potential sources of cell-injury or cell-modification (Sato et al., 2018). Keeping these viewpoints into consideration, we made use of a home-built micro-Raman spectroscopy system coupled with laser-tweezers to investigate the biochemical characteristics of RBCs (Bankapur et al., 2010). Raman spectroscopy has been gaining popularity in its application in biomedicine as this single-cell technique is tremendously sensitive to very subtle molecular changes within the cell, records vibrations of molecular bonds in its original state instantaneously and does not employ the usage of any chemical markers (Kumamoto et al., 2018). This research aimed to comprehend the molecular changes of RBCs, in a "jaundice" environment.

MATERIALS AND METHODS

Ethics Statement

This study was approved (IEC 02/2002) by the Institutional Ethics Committee of Kasturba Medical College, Manipal Academy of Higher Education, Manipal and all experimental procedures conformed with the Ethical Committee guidelines. Written informed consent was obtained from all the volunteers. Blood samples of confirmed hyperbilirubinemic patients were collected from the laboratory of Clinical Biochemistry. The requirement for informed consent was waived concerning the acquisition of patients' samples.

Blood Sample Collection and RBC Preparation

Four milliliter anticoagulated blood samples were collected in EDTA-containing BD Vacutainers from healthy volunteers (n = 10). Blood samples of hyperbilirubinemic patients (n = 28) in EDTA were collected from the laboratory of Clinical Biochemistry. Whole anticoagulated blood sample was centrifuged (Labinet Spectrafuge 7M) at 5000 rpm for 5 minutes. Following centrifugation, the plasma and buffy-coat layers were aspirated off using a micropipette. One microliter hematocrit (Hct) was pipetted out and suspended in 2 milliliter phosphate-buffered saline (PBS)-filled Eppendorf tube to obtain a suspension of live RBCs. PBS was procured from Sigma Aldrich, India.

One microliter of RBC suspension in PBS was pipetted out from the Eppendorf tube onto the custom-made sample chamber. A total of 379 raw spectra were recorded from 379 individual RBCs, of which 147 spectra were recorded from the blood samples of healthy volunteers and 232 from that of patients with jaundice.

Experimental Set-Up

The illustration of the single-beam micro-Raman spectrometer coupled with optical tweezers has been shown in **Figure 1**. The system comprised of an inverted microscope (Nikon Eclipse Ti-U, Japan) coupled with a 785 nm wavelength-emitting diode laser (Starbright Diode Laser, Denmark) and a spectrograph (Horiba Jobin Yvon iHR320). The expanded laser-beam overfills the back aperture of a 100X, 1.3NA microscope objective (Nikon, Plan Fluor) to create a sharp focal-spot at the sample plane. Single RBCs suspended in PBS were optically-trapped under this focal-spot and simultaneously Raman-excited. The scattered light from the individual RBCs was collected from the very same objective and fed into the spectrograph using f-matching optics. The spectrograph was equipped with a 1200 groves/mm grating and a liquid nitrogen-cooled charged couple device (Symphony CCD-1024x256-OPEN-1LS) detector, with 1024 × 256 pixels. An optical edge-filter (Razor edge LP02-785RU-25, Semrock, United States) was placed just in front of the spectrograph for the removal of Rayleigh scattered radiations. The comprehensive description of the experimental set-up has been published in earlier studies (Bankapur et al., 2010, 2014).

Data Acquisition

Utilizing the above setup, RBCs were optically immobilized and probed using a 785 nm diode laser with an excitation-power of 10mW. RBCs were positioned at the focus

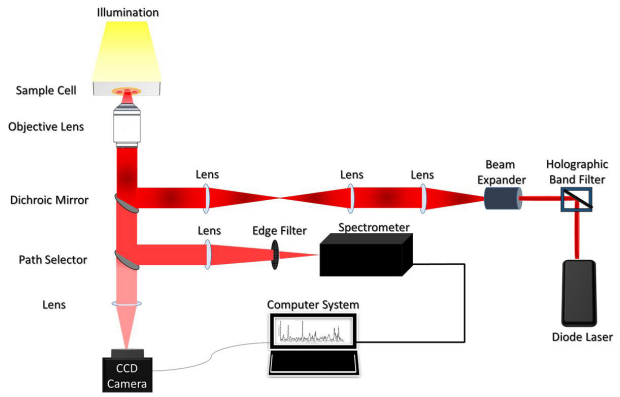

FIGURE 1 | Schematic diagram of the Raman Tweezers set up.

of the laser beam by adjusting the manual stage. Five accumulations were recorded per RBC with the exposure/acquisition time of 60 seconds. Raman spectra of RBCs were procured within the spectral range of ∼600 to 1,800 cm^{-1}. This spin-sensitive-region is observed to deliver maximum information on the "oxygenation-state" of Hb (De Luca et al., 2008).

Data Pre-processing

Origin (OriginLab Corp., Northampton, MA, United States), MATLAB (MATLAB® 7.0) and GRAMS (Grams/AI, PLS Plus IQ) software were employed for the pre-processing of the accrued RBC spectra. 379 raw spectra that included those from the healthy, as well as the jaundice groups, were pre-processed.

The pre-processing steps involved the exclusion of spurious noises/cosmic-spikes, spectral smoothening, baseline-correction, and vector-normalization. The data-points that corresponded to cosmic-spikes were deleted using "Origin." Using GRAMS, the raw spectra were smoothened out by second-order polynomial Savitzky-Golay moving-average-technique. Spectral normalization was accomplished by 2-norm standard-vector normalization (Barkur et al., 2015) using GRAMS. Multiple spectral baseline-correction was effected by employing asymmetric least-squares (AsLS) fitting approach proposed by Eilers (2003).

Statistical Analysis

Multivariate statistical analyses were carried out using GRAMS-AI and CRAN R 3.6.1 (©2019 The R Foundation for Statistical Computing) packages. The intensity of bands in 600–1800 cm^{-1} range of the Raman spectra was analyzed.

The goal was to choose seamless statistical tools for the classification of acquired data, based on variations in spectral features. In this study, for effective categorization, we had performed partial least squares based discriminant analysis (PLS-DA), a supervised diagnostic model, to sharpen variations between the generated principal components (PCs) using Grams IQ spectroscopy software. The PCs were rotated such that a maximum separation among classes was obtained. Additionally, PLS-DA helped to identify the Raman signatures responsible for classification. This was followed by a non-parametric variant of Multivariate ANalysis Of VAriance (MANOVA) to re-affirm the statistically significant difference in the mean value of the measurements captured at different wavelengths across the healthy and jaundice samples. Subsequently, a paired Wilcoxon *post-hoc* test with Bonferonni correction was used to facilitate multiple comparisons. The statistical significance was defined as a $p \leq 0.05$.

RESULTS

Raman Spectra of RBCs From Healthy and Jaundice Blood Samples

The pre-processed spectra were first overlaid together separately for each group (**Supplementary Figure S1**). This exhibited the overall trend of the Raman peaks for the healthy and jaundice groups separately. **Figure 2** gives the overlaid averaged Raman spectra of both the healthy and jaundice groups. The spectral bands were assigned as was described in earlier studies. Since RBCs comprised predominantly of Hb protein, spectral data were dominated primarily by the Raman signatures from heme. There also appeared to be contributions from other organic components as well, such as aromatic amino acids, amide bonds and $-CH/-CH_2$ side-chains of globular proteins.

The averaged spectra exhibited multiple differences in terms of both intensity changes as well as frequency shifts. RBCs from the jaundice group displayed increase in intensity of Raman frequencies at 975, 1,049, 1,123, 1,165, 1,175, 1,212, 1,248, 1,258, 1,264, 1,370, 1,375, 1,389, 1,460, and 1,771 cm^{-1} and a decrease in intensity at wavelengths 752, 788, 999, 1,025, 1,080, 1,223, 1524, 1,545, 1,563, 1,602, 1,617, and 1,636 cm^{-1} when compared to those from RBCs of the healthy group. Additionally, the averaged Raman spectrum in the disease group exhibited a new peak at 663 cm^{-1} and a 2–3 cm^{-1} frequency shift in 975 and 1,248 cm^{-1} bands. The detailed vibrational assignments of the same have been summarized in **Table 1** and **Figure 3** illustrates the detailed chemical structure of heme.

Multivariate PLS-DA and Factor Analysis Approach

Figure 4A displays the two-dimensional plot of the first two PCs: PC_1 and PC_2, and **Figure 4B** gives the 3-dimensional plot of the first three PCs: PC_1, PC_2, and PC_3. Both scores-plots (generated by Grams IQ) exhibited a tight clustering of RBCs from the healthy group, with negligible variance. However, RBCs from the jaundice samples were scattered farther away from those of the healthy group to form a different and wider-distributed group. The variations in the PCs appeared significantly different for classification as healthy and "stressed" due to jaundice. The variance captured in this approach, taking into account all the wavenumbers in the spectra between the groups, was 31.08%.

Subsequently, we performed factor load analysis, taking into consideration the first three factors (**Figure 5**). It was observed

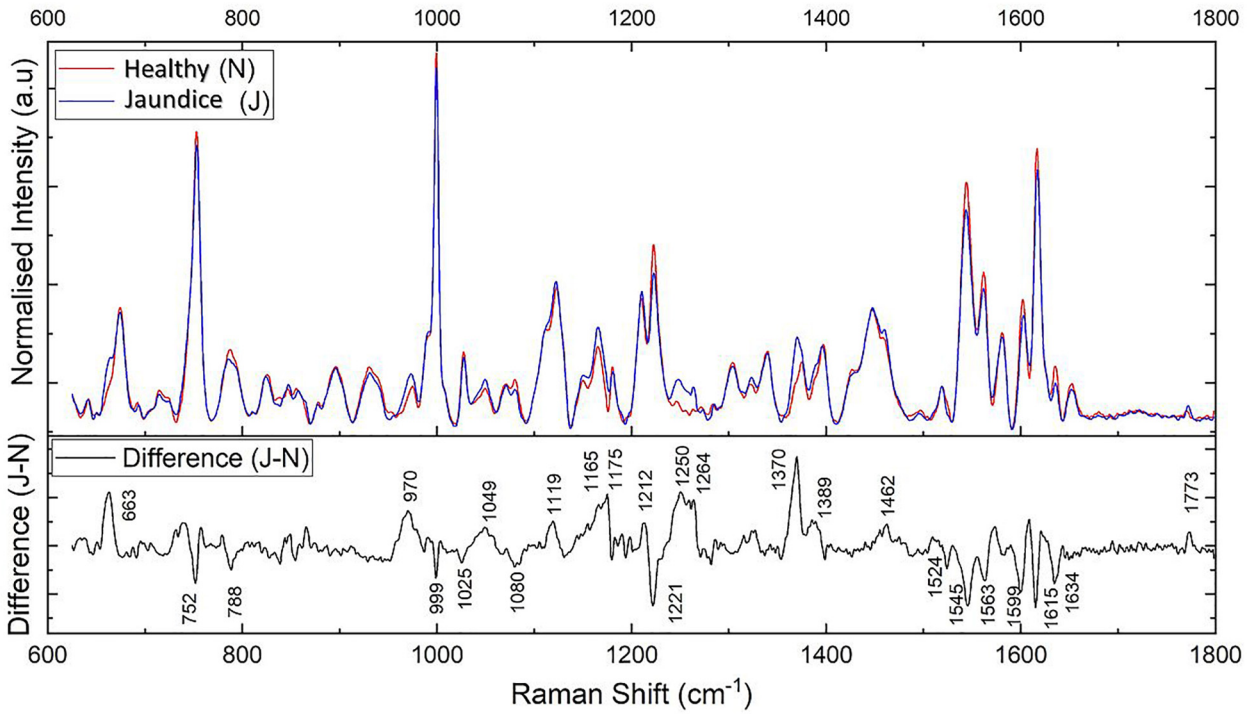

FIGURE 2 | Illustrates the averaged Raman spectra of RBCs from healthy (N) and jaundice (J) samples in the spectral region 600–1,800 cm^{-1} **(on top)** and the difference (J–N) between the averaged spectra between the healthy and jaundice blood samples **(below)**.

that all the Raman peaks that showed positive peaks in Factor-1 loading allied to their corresponding peaks of increased intensities in **Figure 2**. Similarly, all the Raman signals that showed negative peaks in Factor-1 loading allied with their corresponding peaks with decreased intensities in **Figure 2**.

Factors 2 and 3 picked up the next level variations in the spectra, chiefly of Raman peaks at 752, 999, 1,025, and 1,223 cm^{-1}.

RBC Raman Markers Detected in Jaundice

Averaged spectra, PLS-DA and the factor analysis extracted the Raman frequencies that exhibited substantial variations between RBCs from healthy and jaundice blood samples. The observed variations and their assignments have been described below under the four specific band regions, viz., core size/spin-state marker region, pyrrole-ring stretching region, methine C-H deformation region and the low wavenumber region (Wood et al., 2001). It has to be noted that the Raman peaks were assigned based on already existing data from previously conducted studies.

Core Size or Spin State Marker Band: 1,500–1,650 cm^{-1}

This specific band region comprises Raman signatures that were scattered from the C-C bonds in the porphyrin ring and rely on the spin-state of the iron atom (Wood and McNaughton, 2002). It is an important spectral range to explore, as it describes the "oxygenation" (oxy) state of Hb (Lukose et al., 2019). The Raman peaks at 1,524, 1,545, 1,563, 1,602, 1,617, and 1,636 cm^{-1} exhibited a decrease in their intensities in the jaundice samples when compared to their corresponding peaks from the healthy samples. This was an indication that Hb in jaundice was largely present in their "deoxygenated" (deoxy) state, with less bound oxygen (Rao et al., 2009). When iron conforms from the low-spin oxy-state to the deoxy-state, the iron is displaced a few nanometers out of the porphyrin plane as a result of electron withdrawal (Wood et al., 2001; Burchett et al., 2017). This "switch" becomes reflected in the vibrational modes of the porphyrin rings and marks the changes in the above-mentioned peaks. There appeared to be a significant reduction in the intensity of the peak at 1,636 cm^{-1}, a phenomenon attributed to porphyrin-doming (Rao et al., 2009). This peak is considered as the Raman-marker characterizing oxygen-concentration. An intensity decrease of this peak indicates a decline in the oxy-configuration of heme (Luo et al., 2015).

Pyrrole-Ring Stretching Band: 1,300–1,400 cm^{-1}

This Raman band region signifies the "oxidation state" of iron in the pyrrole ring and comprises heme-aggregation bands (Ong et al., 1999). In jaundice, there appeared to be a prominent increase in the intensity of the heme-aggregation Raman peak at 1,370 cm^{-1} (Wood et al., 2005) accompanied by enhanced peaks at 1,375 and 1,389 cm^{-1}. The latter peaks are designated to

TABLE 1 | Assignments of the significantly different Raman peaks of RBCs of healthy and jaundice samples.

Healthy (cm^{-1})	Jaundice (cm^{-1})	Changes	Assignments	*P*-value
–	663	*New Peak*	p:C-S str (gauche)	<0.00001
752	752	↓	pyrrole ring def (out-of-plane), Tryptophan	<0.00001
788	788	↓	pyrrole ring breathing	<0.00001
975	973	↑ and Shift	$\nu(C_c–C_d)$	<0.00001
999	999	↓	Phenylalanine	<0.00001
1,025	1,025	↓	Phenylalanine	<0.00001
1,049	1,049	↑	$\nu(O = O)$, $\delta(= C_bH_2)_{asym}$	<0.00001
1,080	1,080	↓	p: C-N str	<0.00001
1,122	1,123	↑	$\nu(C_\beta – C_1)_{sym}$	<0.00001
1,165	1,165	↑	Pyrrole half-ring vibration	<0.00001
1,175	1,175	↑	Pyrrole half-ring vibration	<0.00001
1,212	1,212	↑	Methine C_m–H def	<0.00001
1,223	1,223	↓	Methine C_m–H def	0.003
1,246	1,248	↑ & Shift	p:Amide III (disordered)	<0.00001
1,258	1,258	↑	p:Amide III (disordered)	<0.00001
1,264	1,264	↑	p:Amide III (disordered)	<0.00001
1,370	1,368, 1,375	↑	Pyrrole half vibration	<0.00001
1,389	1,389	↑	Pyrrole half vibration	<0.00001
1,460	1,460	↑	$\delta(= C_bH_2)_{sym}$, p:$\delta(CH_2)$	<0.00001
1,524	1,524	↓	$\nu(C_\beta – C_\beta)$	<0.00001
1,545	1,545	↓	$\nu(C_\beta – C_\beta)$	<0.00001
1,563	1,563	↓	$\nu(C_\beta – C_\beta)$	<0.00001
1,602	1,602	↓	$\nu(C_\alpha – C_m)_{asym}, \nu(C_a = C_b)_{venyl}$	<0.00001
1,617	1,617	↓	$\nu(C_\alpha – C_m)_{asym}, \nu(C_a = C_b)_{venyl}$	<0.00001
1,636	1,636	↓	$\nu(C_\alpha – C_m)_{asym}$	<0.00001
1,771	1,771	↑	p: C = O str	0.07

p, protein; sy, symmetric; asym, antisymmetric; str, stretch; ν and δ, in-plane modes; str, stretching, def, deformation. RBCs from healthy volunteers and jaundice patients suspended in PBS were optically-trapped and excited with a 785 nm diode laser and their Raman spectra were captured. The given table lists the frequencies of Raman signals that had displayed increased, decreased and shifted peaks. The assignments of the Raman peaks were carried out based on previous studies.

pyrrole deformation/breathing modes (Dybas et al., 2018). This indicated that RBCs in the "jaundice environment" produced heme-aggregates within themselves. There appeared to be a shift in the 1,370 cm^{-1} (oxy state) peak to 1,375 cm^{-1} (deoxy state) in jaundice, ascertaining lesser oxy states in jaundice (Lukose et al., 2019).

Methine C-H Deformation Band: 1,200–1,300 cm^{-1}

This is the spectral zone assigned to methine C-H bonds in heme molecules. These bonds are sensitive to minute changes in Hb conformations and are governed by porphyrin-iron associations. The high sensitivity of these bonds has been described to be because of their juxtaposition with the protein subunits (Wood et al., 2001). Thus, Hb conformational-variations alter the deformation angle of C-H vibrations instantaneously (Wood et al., 2007). In this study, the wavenumbers that displayed enhanced intensity in jaundice were the peaks at 1,212, 1,248, and 1,264 cm^{-1} which were also accompanied by a fall in intensity at the peak 1,223 cm^{-1}, consequent to changes in the methine C-H deformation regions. We also report a shift in the wavenumber 1,246 cm^{-1} to heme aggregation marker 1,248 cm^{-1} in jaundice (Lemler et al., 2014).

Low Wavenumber Band: 600–1,200 cm^{-1}

This spectral region encompasses the bands for pyrrole-breathing, pyrrole-deformation modes and RBC membrane stability. In jaundice, there was a shift of the Raman peak at 973 to 975 cm^{-1} with a significant increase in its intensity along with a shouldering of 675 cm^{-1} pyrrole-deformation band with a new peak at 663 cm^{-1}. These occurrences indicate heme-aggregation, as a consequence of protein denaturation, under "stressful" environments (Wood et al., 2005; Lukose et al., 2019). The 752 cm^{-1} porphyrin breathing mode peak, a crucial spectral-marker that confers the integrity of Hb (Deng et al., 2005), shows reduced intensity in the jaundice group. The peak 788 cm^{-1}, a deoxy Raman marker, has taken a noticeable decrease in its intensity in jaundice samples (Barkur et al., 2017). The 999 and 1,025 cm^{-1} Raman peaks, originating from phenylalanine, exhibited a reduction in their strengths, signifying the breakdown of both Hb (Wu et al., 2011; Raj et al., 2013) as well as cell membranes (Lippert et al., 1975; Goheen et al., 1993). Peak 1,122 cm^{-1}, emanating from the RBC membrane, is caused by the trans conformation vibrations of the C-C frame, the height of which has intensified and so does the peak at 1,080 cm^{-1}, signifying diminished membrane deformability (Lukose et al., 2019). Changes in intensity at 1,165

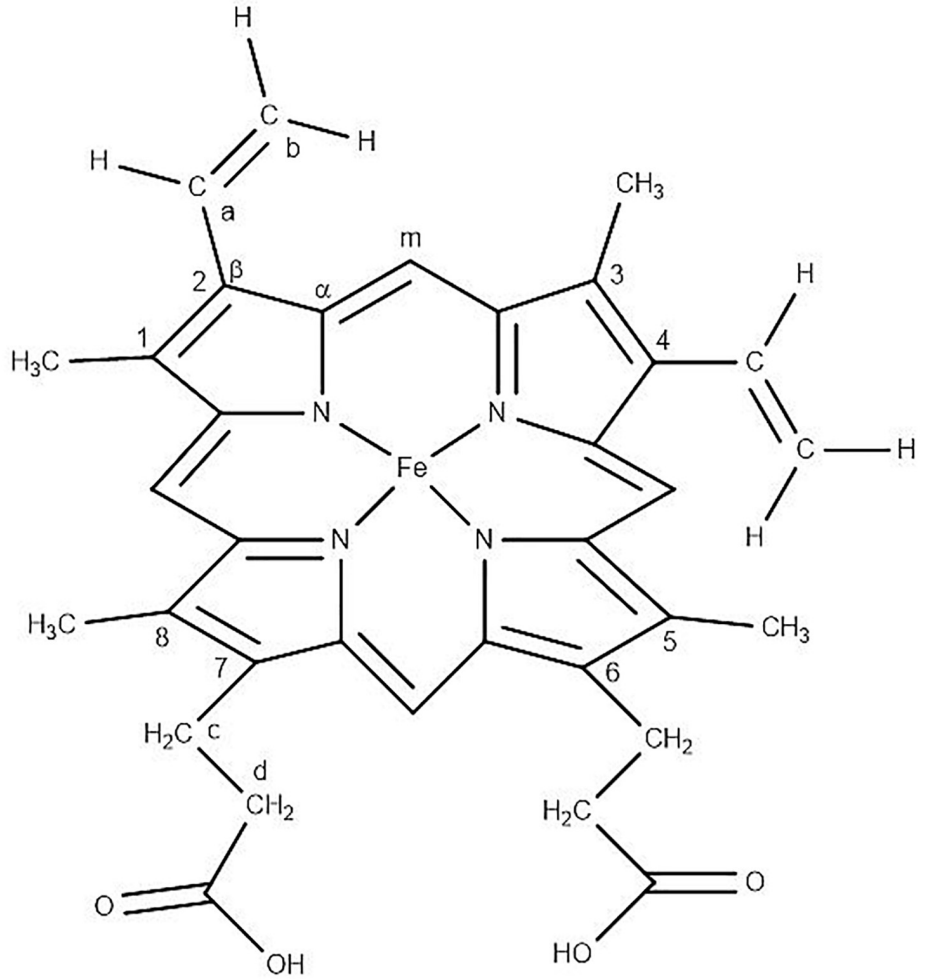

FIGURE 3 | Chemical structure of "heme" in RBC displaying the Fe-protoporphyrin-IX with four pyrrole rings, four methyl (CH_3) groups, two propionate side chains and two vinyl ($-CH = CH_2$) groups.

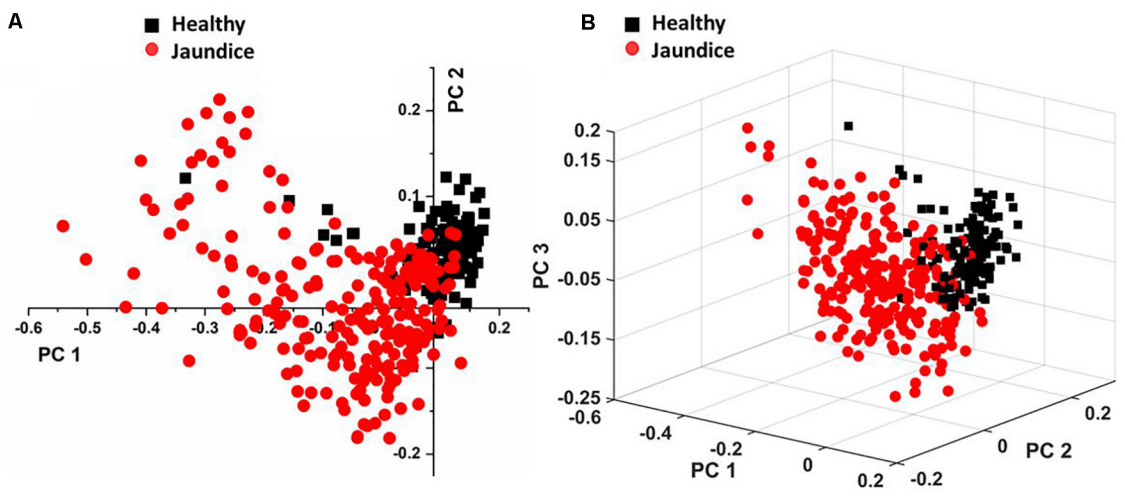

FIGURE 4 | Illustrates PLS-DA scores plots of **(A)** first two PCs and **(B)** first three PCs.

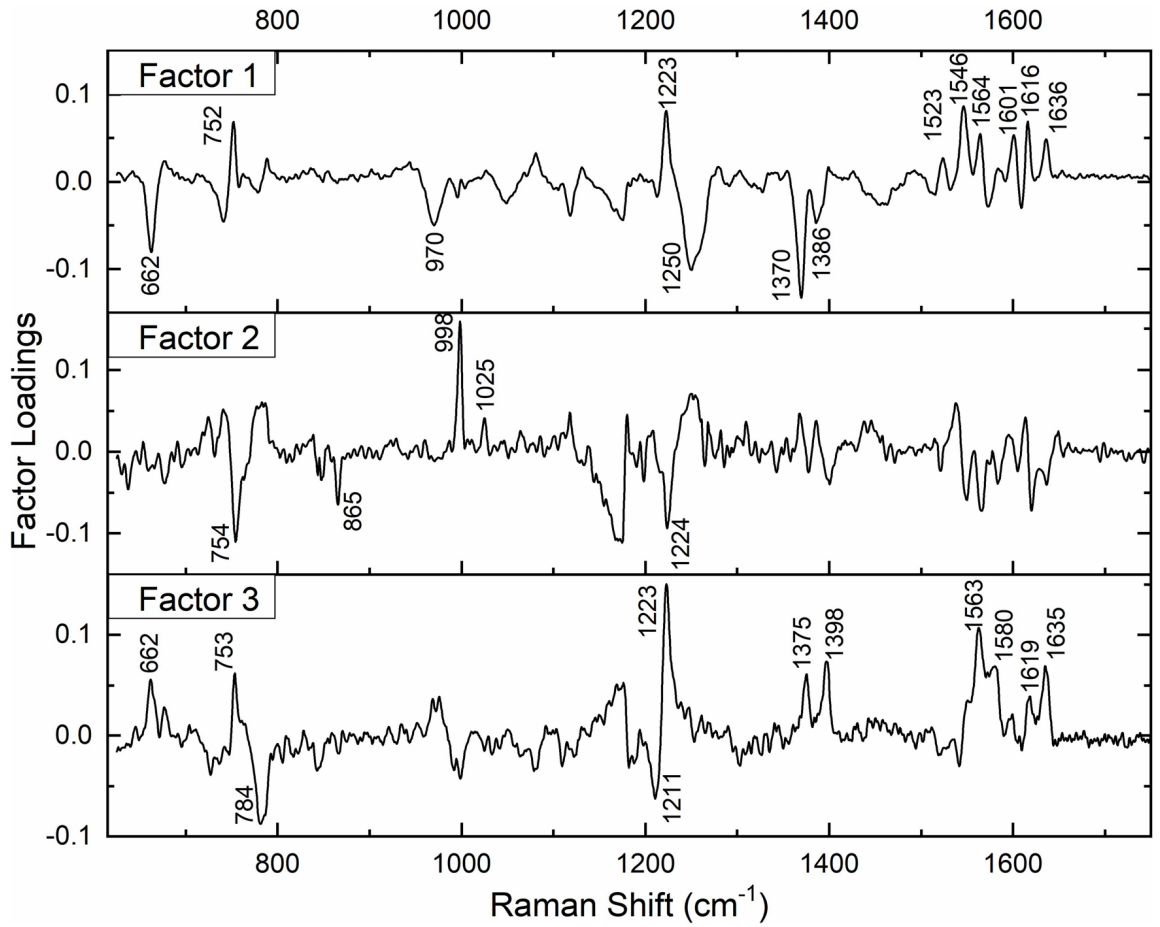

FIGURE 5 | Spectral loadings of PC factors (Factor 1, Factor 2, and Factor 3) between RBCs of healthy and jaundice samples.

and 1,175 cm^{-1} attributes to deformation in pyrrole ring of Hb (Gautam et al., 2018).

PCA of the 26 Detected Wavenumber-Bands

In total, there were 26 Raman bands (**Table 1**) detected by the spectral analysis approach that displayed a substantial difference between the healthy and jaundice samples. Accordingly, PCA was conducted again, taking into consideration the intensity-scores of just these 26 Raman peaks. The analysis captured a variance of 60.54% for the first three PCs, much higher than that obtained (31.08%) when the whole region of the spectra was considered.

Non-parametric MANOVA Approach to Raman Spectral Markers

We then proceeded to explore whether there existed a significant difference in the mean intensity-scores across the two groups for the 26 Raman bands identified in the spectral analysis by a MANOVA-based approach using CRAN 3.6.1. The packages utilized for this analysis were heplots (Fox et al., 2018), npmv (Wood et al., 2007), and MVN (Korkmaz et al., 2014). The advantage of implementing this method was that it made use of dependencies between the wavelengths and enabled joint acceptance or rejection of the hypothesis. When we tested the assumptions of MANOVA, it was observed that the assumptions of multivariate-normality as well as the equality of covariance-matrices that were associated with the two groups were violated. Hence, we made use of a non-parametric variant of MANOVA. Since the data represented intensity-scores across different Raman peaks corresponding to two populations, the McKeon approx. for Lawley Hotelling Test ($p < 0.00001$) was considered. The results indicated a significant difference between the average values of the intensity-scores across the healthy and jaundice samples. As a *post-hoc* analysis, paired Wilcoxon test with Bonferonni corrections was implemented to identify the wavelengths that accounted for significant differences in the intensity-scores across the two populations. The p-values that were derived are presented in **Table 1**.

Excluding Raman peak at 1,223 cm^{-1} ($p = 0.003$), that emanated from the methine C-H deformation band and 1,771 cm^{-1} ($p = 0.07$) from the ν(C = O) peak of proteins, the

intensity scores of all the other Raman bands detected by spectral analysis exhibited a highly significant difference ($p < 0.00001$) between the healthy and jaundice samples.

Therefore, the "vitality" or "normality" of RBCs can be deduced by just analyzing these specific Raman peaks, rather than assessing all the RBC Raman bands across the spectrum. The variations in these peaks convey information regarding deformations/distortions in both cytoplasmic Hb as well as the RBC membrane. This study consequently informs us that under pathologies relating to jaundice, RBCs in circulation, although looking "morphologically" healthy, may not always be "chemometrically" healthy.

DISCUSSION

Jaundice (derived from the French word "jaune" which means yellow) is the yellowish discoloration of the sclera, skin and mucous membrane, caused by the build-up of serum bilirubin, above 2 mg/dL, and nearly always signifies the existence of an underlying infection related to the derangement of bilirubin metabolism. Its persistence is associated with a substantial increase in morbidity and mortality (Anand and Garg, 2015). Our body produces close to 4 mg/kg bilirubin every day (Schiff et al., 2011). Normally, the total serum bilirubin level never exceeds 1 mg/dL, of which UCB is less than 0.8 mg/dL and CB levels is less than 0.3 mg/dL (Zieve et al., 1951; Werner et al., 1970). There exists a myriad of clinical pathologies that results in jaundice. Unconjugated hyperbilirubinemia results primarily due to excessive hemolysis, while hyperbilirubinemia caused by excessive CB, develops in hepatocellular diseases and obstructions of the biliary system. In the latter cases, there can be a rise in both forms of bilirubin (Fargo et al., 2017). In this study, we have included patients diagnosed with hyperbilirubinemia, irrespective of its cause.

Hyperbilirubinemia can be toxic to circulating RBCs, causing morphological and metabolic impairments, eventually leading to further hemolysis, aggravating hyperbilirubinemia and intensifying anemia (Lang et al., 2015). Bilirubin toxicity on RBCs has been found to occur in a concentration and temperature-dependent manner (Brito et al., 2000). During the course of the disease, jaundice is accompanied by elevated levels of several enzymes and inflammatory-cytokines in serum (Padillo et al., 2001). This adds up to the already existing distress on healthy RBCs (Pretorius, 2018). Taking these facets into account, we attempted to examine the biochemical status of live RBCs in jaundice employing Raman spectroscopy. Since this analytical technique is both reagent and fixation-free, it rules out any concerns regarding possible cell modifications or damage caused by the analytical processes itself (Sato et al., 2018). Because RBCs are delicate and extremely sensitive cells, it was very important to ensure utmost care in the management of samples during the procedures that might themselves lead to chemometric variations, hemolysis or even eryptosis. We had also ensured to conduct the experiments immediately on sample-procurement.

Our results showed distinct variations in the biochemical signatures of RBCs in jaundice, when compared to the normal. Since RBCs are simple organelle-less cells with a highly deformable cell membrane that holds abundant cytoplasmic Hb, the obtained Raman spectral features were derived from these two sources. The overlaid averaged Raman spectra from the groups displayed Raman peaks that had their intensities altered and a few peaks that had undergone a shift (**Figure 2** and **Table 1**). It is to be noted that the Raman peaks were assigned to specific biochemical components of the RBC in accordance with earlier studies and in this study we report how these Raman signatures altered in clinical jaundice. Spectral analysis and the various multivariate analytical methods employed in this study indicate chemometric modifications of RBCs in jaundice, when compared to RBCs of the healthy group. The variations (section "RBC Raman Markers Detected in Jaundice") were noted in Raman peaks that represented the "oxygenation status" of Hb. The heme in jaundice exhibited largely a "deoxy" status when compared to the more "oxy" states in the healthy population. This was accompanied by a decline in the frequencies signifying "oxygen saturation" in the jaundice samples. Heme-aggregation-Raman-markers were manifested in jaundice along with a fall in peaks that depicted Hb stability. The spectra also exhibited alterations in Raman peaks portraying RBC membrane stability. The non-parametric MANOVA method served as an aid in the identification of the Raman signatures that could distinctly ($p < 0.00001$) capture the significant differences in the intensity scores across healthy and jaundice populations (**Table 1**). PCA of these identified Raman signatures captured better variance between the groups.

These results exhibit enough evidence to establish that in jaundice, intact and healthy-appearing RBCs in circulation, can experience biochemical alterations similar to those seen when under distress. The probable reasons could be the hostile milieu created by the disease itself such as hyperbilirubinemia, presence of pathogens and/or products related to the immune response that alters the physiological state of blood, thereby experiencing a shortened life-span. The intention of this study was to report the Raman spectroscopy features of RBCs in jaundice and analyze the generated findings, irrespective of the disease or it's cause. An attempt was made to correlate Raman spectral changes with serum bilirubin levels in jaundice. But the results with this group yielded less correlation (**Supplementary Figure S2** and **Supplementary Table S1**). Further exploratory studies are required to investigate the correlation of bilirubin levels and other systemic factors with RBC Raman spectral variations in specific pathologies.

CONCLUSION

It is challenging to unearth the exact biochemical status of RBCs, as existent *in-vivo*, considering their extremely delicate and sensitive nature to even minuscule changes in its environment. Therefore, on a routine basis, RBC pathology is clinically assessed by a collective assemblage of tests that encompasses the estimation of its counts, Hb and bilirubin levels and analysis using peripheral smears. Unlike routine assays or even

other high-end analytical techniques such as flow cytometry, Raman spectroscopy does not demand labels and is unique by being more sensitive and specific. The Raman-scattered-light from a particular substance characterizes its own exclusive "chemical-fingerprint." In recent times this tool has been increasingly employed in hematological research for elucidating structural information from hemes, demonstrating the existence of characteristic molecular signatures from them under different conditions of stress such as oxidation and energy depletion, disorders such as thalassemia and diabetes, and diseases such as malaria and carcinomas. This study is merely a commencement to understand the chemometric behavior of RBCs in jaundice and needs to be extrapolated further to comprehend its characteristics in specific diseases/conditions that lead to it.

DATA AVAILABILITY STATEMENT

The raw data supporting the conclusions of this article will be made available by the authors, without undue reservation, to any qualified researcher.

ETHICS STATEMENT

The studies involving human participants were reviewed and approved by the Institutional Ethics Committee, Kasturba Medical College and Kasturba Hospital Registration no. ECR/146/Inst/KA/2013/RR-16. The participants provided their written informed consent to participate in this study.

AUTHOR CONTRIBUTIONS

SJ, AB, PR, and SC conceived and designed the study. SJ and AB performed the experiments, interpreted the results, and wrote the manuscript. SB and MA contributed to performing the experiments. RR and PB contributed to the conception and design of the project and the interpretation of results. AK and RL contributed to the statistical analysis, interpretation of results, and wrote the manuscript. All authors contributed to the article and approved the submitted version.

FUNDING

The authors acknowledged the financial support by the Department of Biotechnology, Govt. of India for the Raman Tweezers facility through the sanctioned project BT/PR6413/MED/14/80/2005.

ACKNOWLEDGMENTS

We acknowledge the support contributed by the Clinical Biochemistry of Kasturba Hospital-Manipal and also extend special thanks to Dr. Alex Joseph, Associate Professor in Pharmaceutical Chemistry, Manipal College of Pharmaceutical Sciences, Manipal for his contribution in creating figures in ChemDraw and Dr. Prakash P.Y., Associate Professor, Department of Microbiology, Kasturba Medical College-Manipal for his guidance in manuscript review.

SUPPLEMENTARY MATERIAL

The Supplementary Material for this article can be found online at: https://www.frontiersin.org/articles/10.3389/fphys.2020.00821/full#supplementary-material

REFERENCES

Adamson, J., and Longo, D. (2012). *Anemia and Polycythemia. Harrison's Principles of Internal Medicine*, 18th Edn. New York, NY: The McGraw-Hill Companies.

Anand, A. C., and Garg, H. K. (2015). Approach to clinical syndrome of jaundice and encephalopathy in tropics. *J. Clin. Expl. Hepatol.* 5(Suppl. 1), S116–S130. doi: 10.1016/j.jceh.2014.05.007

Bankapur, A., Barkur, S., Chidangil, S., and Mathur, D. (2014). A micro-Raman study of live, single red blood cells (RBCs) treated with AgNO3 nanoparticles. *PLoS One* 9:e103493. doi: 10.1371/journal.pone.0103493

Bankapur, A., Zachariah, E., Chidangil, S., Valiathan, M., and Mathur, D. (2010). Raman tweezers spectroscopy of live, single red and white blood cells. *PLoS One* 4:el0427. doi: 10.1371/journal.pone.0010427

Barkur, S., Bankapur, A., Chidangil, S., and Mathur, D. (2017). Effect of infrared light on live blood cells: role of β-carotene. *J. Photochem. Photobiol. B Biol.* 171, 104–116. doi: 10.1016/j.jphotobiol.2017.04.034

Barkur, S., Bankapur, A., Pradhan, M., Chidangil, S., Mathur, D., and Ladiwala, U. (2015). Probing differentiation in cancer cell lines by single-cell micro-Raman spectroscopy. *J. Biomed. Opt.* 20:085001. doi: 10.1117/1.JBO.20.8.085001

Brito, M. A., Silva, R., Tiribelli, C., and Brites, D. (2000). Assessment of bilirubin toxicity to erythrocytes. Implication in neonatal jaundice management. *Eur. J. Clin. Invest.* 30, 239–247. doi: 10.1046/j.1365-2362.2000.00612.x

Burchett, W. W., Ellis, A. R., Harrar, S. W., and Bathke, A. C. (2017). Nonparametric Inference for multivariate data: the R package npmv. *J. Stat. Softw.* 76, 1–18. doi: 10.18637/jss.v076.i04

De Luca, A. C., Rusciano, G., Ciancia, R., Martinelli, V., Pesce, G., Rotoli, B., et al. (2008). Spectroscopical and mechanical characterization of normal and thalassemic red blood cells by Raman Tweezers. *Opt. Express* 16, 7943–7957. doi: 10.1364/oe.16.007943

Deng, J. L., Wei, Q., Zhang, M. H., Wang, Y. Z., and Li, Y. Q. (2005). Study of the effect of alcohol on single human red blood cells using near-infrared laser tweezers Raman spectroscopy. *J. Raman Spectrosc.* 36, 257–261. doi: 10.1002/jrs.1301

Dybas, J., Grosicki, M., Baranska, M., and Marzec, K. M. (2018). Raman imaging of heme metabolism in situ in macrophages and Kupffer cells. *Analyst* 143, 3489–3498. doi: 10.1039/c8an00282g

Eilers, P. H. (2003). A perfect smoother. *Anal. Chem.* 75, 3631–3636. doi: 10.1021/ac034173t

Erlinger, S., Arias, I. M., and Dhumeaux, D. (2014). Inherited disorders of bilirubin transport and conjugation: new insights into molecular mechanisms and consequences. *Gastroenterology.* 146, 1625–1638. doi: 10.1053/j.gastro.2014.03.047

Fargo, M. V., Grogan, S. P., and Saguil, A. (2017). Evaluation of jaundice in adults. *Am. Fam. Physician* 95, 164–168.

Fox, J., Friendly, M., and Monett, G. (2018). *heplots: Visualizing Tests in Multivariate Linear Models. R package version 1.3-5*.

Gautam, R., Oh, J. Y., Marques, M. B., Dluhy, R. A., and Patel, R. P. (2018). Characterization of storage-induced red blood cell hemolysis using raman spectroscopy. *Lab. Med.* 49, 298–310. doi: 10.1093/labmed/lmy018

Goheen, S. C., Lis, L. J., Kucuk, O., Westerman, M. P., and Kauffman, J. W. (1993). Compositional dependence of spectral features in the Raman spectra of erythrocyte membranes. *J. Raman Spectrosc.* 24, 275–279. doi: 10.1002/jrs.1250240503

Hansen, T. W. J. (2001). Bilirubin brain toxicity. *Perinatology* 21(Suppl. 1), S48–S51. doi: 10.1038/sj.jp.7210634

Korkmaz, S., Goksuluk, D., and Zararsiz, G. (2014). MVN: an R package for assessing multivariate normality. *R J.* 6, 151–162. doi: 10.32614/rj-2014-031

Korolnek, T., and Hamza, I. (2015). Macrophages and iron trafficking at the birth and death of red cells. *Blood* 125, 2893–2897. doi: 10.1182/blood-2014-12-567776

Kumamoto, Y., Harada, Y., Takamatsu, T., and Tanaka, H. (2018). Label-free molecular imaging and analysis by raman spectroscopy. *Acta Histochem. Cytochem.* 51, 101–110. doi: 10.1267/ahc.18019

Lang, E., Gatidis, S., Freise, N. F., Bock, H., Kubitz, R., Lauermann, C., et al. (2015). Conjugated bilirubin triggers anemia by inducing erythrocyte death. *Hepatology* 61, 275–284. doi: 10.1002/hep.27338

Lemler, P., Premasiri, W. R., DelMonaco, A., and Ziegler, L. D. (2014). NIR Raman spectra of whole human blood: effects of laser-induced and in vitro hemoglobin denaturation. *Anal. Bioanal. Chem.* 406, 193–200. doi: 10.1007/s00216-013-7427-7

Levitt, D. G., and Levitt, M. D. (2014). Quantitative assessment of the multiple processes responsible for bilirubin homeostasis in health and disease. *Clin. Exp. Gastroenterol.* 7, 307–328. doi: 10.2147/CEG.S64283

Lippert, J. L., Gorczyca, L. E., and Meiklejohn, G. (1975). A laser Raman spectroscopic investigation of phospholipid and protein configurations in hemoglobin-free erythrocyte ghosts. *Biochim. Biophys. Acta* 382, 51–57. doi: 10.1016/0005-2736(75)90371-5

Lukose, J., Mithun, N., Mohan, G., Shastry, S., and Chidangil, S. (2019). Normal saline-induced deoxygenation of red blood cells probed by optical tweezers combined with the micro-Raman technique. *RSC Adv.* 9, 7878–7884. doi: 10.1039/c8ra10061f

Luo, M., Huang, Y. Y., Su, B. C., Shi, Y. F., Zhang, H., and Ye, X. D. (2015). Study on RBC Oxygen-Carrying Function with the Incubation Time. *Guang Pu Xue Yu Guang Pu Fen Xi* 35, 3350–3355.

Ong, C. W., Shen, Z. X., Ang, K. K. H., Kara, U. A. K., and Tang, S. H. (1999). Resonance Raman microspectroscopy of normal erythrocytes and plasmodium berghei-infected erythrocytes. *Appl. Spectrosc.* 53, 1097–1101. doi: 10.1366/0003702991947874

Padillo, F. J., Andicoberry, B., Muntane, J., Lozano, J. M., Miño, G., Sitges-Serra, A., et al. (2001). Cytokines and acute-phase response markers derangements in patients with obstructive jaundice. *Hepato Gastroenterol.* 48, 378–381.

Park, T. H. (2016). Bilirubin: a promising antioxidant for ischaemia/reperfusion injury. *Int. Wound J.* 13:1040. doi: 10.1111/iwj.12362

Pretorius, E. (2018). Erythrocyte deformability and eryptosis during inflammation, and impaired blood rheology. *Clin. Hemorheol. Microcirc.* 69(Suppl. 1), 1–6. doi: 10.3233/CH-189205

Raj, S., Wojdyla, M., and Petrov, D. (2013). Studying single red blood cells under a tunable external force by combining passive microrheology with Raman spectroscopy. *Cell Biochem. Biophys.* 65, 347–361. doi: 10.1007/s12013-012-9439-x

Rao, S., Bálint, S., Cossins, B., Guallar, V., and Petrov, D. (2009). Raman study of mechanically induced oxygenation state transition of red blood cells using optical tweezers. *Biophys. J.* 96, 209–216. doi: 10.1529/biophysj.108.139097

Sato, H., Ishigaki, M., Taketani, A., and Andriana, B. B. (2018). Raman spectroscopy and its use for live cell and tissue analysis. *Biomed. Spectrosc. Imaging* 7, 97–104. doi: 10.3233/BSI-180184

Schiff, E. R., Maddrey, W. C., and Sorrell, M. F. (2011). *Schiff's Diseases of the Liver*, 11th Edn. Hoboken, GB: Wiley-Blackwell.

Shapiro, S. M. (2003). M Bilirubin toxicity in the developing nervous system. *Rev. Pediatr. Neurol.* 29, 410–421. doi: 10.1016/j.pediatrneurol.2003.09.011

Shi, H. S., Lai, K., Yin, X. L., Liang, M., Ye, H. B., Shi, H. B., et al. (2019). Ca2+-dependent recruitment of voltage-gated sodium channels underlies bilirubin-induced overexcitation and neurotoxicity. *Cell Death Dis.* 10:774. doi: 10.1038/s41419-019-1979-1971

Werner, M., Tolls, R. E., Hultin, J. V., and Mellecker, J. (1970). Influence of sex and age on the normal range of eleven serum constituents. *Z. Klin. Chem. Klin. Biochem.* 8, 105–115. doi: 10.1515/cclm.1970.8.2.105

Wood, B. R., Caspers, P., Puppels, G. J., Pandiancherri, S., and McNaughton, D. (2007). Resonance Raman spectroscopy of red blood cells using near-infrared laser excitation. *Anal. Bioanal. Chem.* 387, 1691–1703. doi: 10.1007/s00216-006-0881-8

Wood, B. R., Hammer, L., Davis, L., and McNaughton, D. (2005). Raman microspectroscopy and imaging provides insights into heme aggregation and denaturation within human erythrocytes. *J. Biomed. Opt.* 10:014005. doi: 10.1117/1.1854678

Wood, B. R., and McNaughton, D. (2002). Micro-Raman characterization of high- and low-spin heme moieties within single living erythrocytes. *Biopolymers* 67, 259–262. doi: 10.1002/bip.10120

Wood, B. R., Tait, B., and McNaughton, D. (2001). Micro-Raman characterisation of the R to T state transition of haemoglobin within a single living erythrocyte. *Biochim. Biophys. Acta* 1539, 58–70. doi: 10.1016/s0167-4889(01)00089-1

Wu, H., Volponi, J. V., Oliver, A. E., Parikh, A. N., Simmons, B. A., and Singh, S. (2011). In vivo lipidomics using single-cell Raman spectroscopy. *Proc. Natl. Acad. Sci. U.S.A.* 108, 3809–3814. doi: 10.1073/pnas.1009043108

Zieve, L., Hill, E., Hanson, M., Falcone, A. B., and Watson, C. J. (1951). Normal and abnormal variations and clinical significance of the one-minute and total serum bilirubin determinations. *J. Lab. Clin. Med.* 38, 446–469.

Conflict of Interest: The authors declare that the research was conducted in the absence of any commercial or financial relationships that could be construed as a potential conflict of interest.

frontiers in Physiology

BRIEF RESEARCH REPORT
published: 31 July 2020
doi: 10.3389/fphys.2020.00958

Inside Out Integrin Activation Mediated by PIEZO1 Signaling in Erythroblasts

*Francesca Aglialoro, Naomi Hofsink, Menno Hofman, Nicole Brandhorst and Emile van den Akker**

Sanquin Research and Landsteiner Laboratory, Department of Haematopoiesis, Amsterdam UMC, University of Amsterdam, Amsterdam, Netherlands

The non-selective mechanosensitive ion channel PIEZO1 controls erythrocyte volume homeostasis. Different missense gain-of-function mutations in *PIEZO1* gene have been identified that cause Hereditary Xerocytosis (HX), a rare autosomal dominant haemolytic anemia. PIEZO1 expression is not limited to erythrocytes and expression levels are significantly higher in erythroid precursors, hinting to a role in erythropoiesis. During erythropoiesis, interactions between erythroblasts, central macrophages, and extracellular matrix within erythroblastic islands are important. Integrin α4β1 and α5β1 present on erythroblasts facilitate such interactions in erythroblastic islands. Here we found that chemical activation of PIEZO1 using Yoda1 leads to increased adhesion to VCAM1 and fibronectin in flowing conditions. Integrin α4, α5, and β1 blocking antibodies prevented this PIEZO1-induced adhesion suggesting inside-out activation of integrin on erythroblasts. Blocking the Ca^{2+} dependent Calpain and PKC pathways by using specific inhibitors also blocked increased erythroid adhesion to VCAM1 and fibronectins. Cleavage of Talin was observed as a result of Calpain and PKC activity. In conclusion, PIEZO1 activation results in inside-out integrin activation, facilitated by calcium-dependent activation of PKC and Calpain. The data introduces novel concepts in Ca^{2+} signaling during erythropoiesis with ramification on erythroblastic island homeostasis in health and disease like Hereditary Xerocytosis.

Keywords: PIEZO1, integrins, calcium signaling, integrin α4β1, erythroblastic island

OPEN ACCESS

Edited by:
Richard Van Wijk,
Utrecht University, Netherlands

Reviewed by:
Iolascon Achille,
University of Naples Federico II, Italy
Guizouarn Helene,
Centre National de la Recherche Scientifique (CNRS), France

***Correspondence:**
Emile van den Akker
e.vandenakker@sanquin.nl

Specialty section:
This article was submitted to Red Blood Cell Physiology, a section of the journal Frontiers in Physiology

Received: *15 May 2020*
Accepted: *15 July 2020*
Published: *31 July 2020*

Citation:
Aglialoro F, Hofsink N, Hofman M, Brandhorst N and van den Akker E (2020) Inside Out Integrin Activation Mediated by PIEZO1 Signaling in Erythroblasts. Front. Physiol. 11:958. doi: 10.3389/fphys.2020.00958

INTRODUCTION

Human erythropoiesis occurs in the bone marrow in a specific niche called the erythroblastic island, composed of a central macrophage surrounded by differentiating erythrocyte precursors (Bessis, 1958; for review see Chasis and Mohandas, 2008; Manwani and Bieker, 2008; Heideveld et al., 2018). The interaction between the erythroblast and the macrophage is regulating erythroid maturation, proliferation, and survival (Manwani and Bieker, 2008). In addition, central macrophage phagocytes the extruded pyrenocyte (the extruded nucleus surrounded by a plasma membrane) left behind by the newly formed reticulocyte. Interactions between erythroid cells and macrophages are mediated by several adhesion molecules. During erythropoiesis, multiple adhesion molecules are expressed that mediate cell-cell and cell-extracellular matrix interactions, among which specific integrins (Chow et al., 2011; Palis, 2016; Seu et al., 2017). Integrin α4β1

[very late antigen 4 (VLA-4)] and α5β1 [very late antigen 5 (VLA-5)] expressed on erythroblasts can bind to counter-receptor vascular cell adhesion protein 1 (VCAM1, CD106) present on central macrophages or extracellular matrix (ECM) protein fibronectin, respectively (Sadahira et al., 1995; Chasis and Mohandas, 2008; Tanaka et al., 2009; Chow et al., 2013; Spring et al., 2013; Belay et al., 2017). Treatment with anti VLA-4 resulted in disruption of the island integrity *in vitro* and induces anemia in a mouse model and defects in stress erythropoiesis (Sadahira et al., 1995; Hamamura et al., 1996; Lee et al., 2006) clearly indicating the important role of these niche interactions. The activation state of integrins can be controlled by various processes including regulation via intracellular signaling, so called inside-out activation (Kim et al., 2003; Abram and Lowell, 2009; Hu and Luo, 2013) potentially providing a regulatory point to control erythroid-macrophage interactions. Inside-out activation of integrins is, among other mechanism, also controlled by intracellular Ca^{2+} concentration, with increased Ca^{2+} concentration leading to integrin activation (Jaconi et al., 1991; Schwartz et al., 1993; Shankar et al., 1993; Coppolino et al., 1997; Rowin et al., 1998; Bye et al., 2020; Shu et al., 2020). Several Ca^{2+} responsive proteins have been identified that control this inside-out integrin activation. For instance, the Ca^{2+} dependent Calpain unmasks the β-integrin binding motif of Talins leading to integrin activation (Goksoy et al., 2008; Mchugh et al., 2010). Inside out integrin activation is also mediated by Ca^{2+}-dependent Protein kinase C (PKC; Kirchhofer et al., 1991; Harburger and Calderwood, 2009). One mechanism through which PKC operates is by activating the small GTPase Rap1 facilitating the formation of a complex with Rap1 effector Rap-1 interacting molecule (RIAM) and Talin, which causes integrin activation (Bos, 2005; Watanabe et al., 2008).

We and others have recently identified, a role for the non selective mechanosensitive cation channel, PIEZO1 during erythropoiesis (Caulier et al., 2020) as well as in *in vitro* cultured reticulocytes (Moura et al., 2019). Activation of PIEZO1 leads to Ca^{2+} influx and activation of Ca^{2+} dependent signal transduction among which NFATs, Calcineurin, MAPK, and calcium dependent PKCs (Von Lindern et al., 2000; Lanuti et al., 2006). Besides a role during erythropoiesis, PIEZO1 expression is maintained on erythrocytes where it regulates volume homeostasis. Indeed, activating mutations within PIEZO1 lead to dehydrated erythrocytes termed Hereditary Xerocytosis (HX; Andolfo et al., 2013; Bagriantsev et al., 2014; Cahalan et al., 2015). In endothelial cells activation of PIEZO1 has been associated with integrin activation and increased cell adhesion resulting in integrin-dependent focal adhesion kinase (FAK) signaling in flowing conditions (Albarran-Juarez et al., 2018). Concomitantly, reduced integrin activation was observed in an endothelium-specific PIEZO1 deficient mouse model (Albarran-Juarez et al., 2018). In agreement with this, depletion of PIEZO1 in small lung cancer cell lines also caused decreased integrin activation (Mchugh et al., 2012). PIEZO1 localization at focal adhesion induced integrin activation and FAK signaling regulated by the ECM (Chen et al., 2018). PIEZO1, located at the endoplasmic reticulum (ER), has been associated with integrin activation in epithelial cells (Mchugh et al., 2010). Inactivation of integrin β1 was observed in PIEZO1 siRNA knockdown in epithelial cells, resulting in reduced cell adhesion. Activation of Ca^{2+}-protease Calpain and cleavage of its target Talin was demonstrated after PIEZO1 activation in epithelial cells (Mchugh et al., 2010). Here, we show that activation of PIEZO1 on erythroblasts using the selective agonist Yoda1 causes activation of downstream Ca^{2+}-mediators Calpain and PKC, resulting in inside-out activation of integrins leading to increased adhesive properties of erythroblasts. The results give new insights into the regulation of integrin activation in erythroblasts, which will have consequences for erythroblastic island homeostasis.

MATERIALS AND METHODS

Human Blood Sample

Human blood mononuclear cells were purified by density separation, following manufacturer's protocol (GE Healthcare, Chicago, IL, United States). Informed consent was given in accordance with the Declaration of Helsinki, the Dutch National and Sanquin Internal Ethic Boards.

Erythroblast Cell Culture and Differentiation

Erythroblasts were expanded as previously described (Heshusius et al., 2019). In short, cells were cultured and expanded in presence of EPO (2 UI/mL; ProSpec, East Brunswick, NJ, United States), human recombinant Stem Cell Factor (100 ng/mL, supernatant SCF producing cell line), and dexamethasone (1 μM; Sigma, St. Louis, MO, United States).

Flow Adhesion Assay

Channels of the μ-Slide $VI^{0.4}$ (Ibidi) were coated with 10 μg/ml recombinant human VCAM-1 (R&D systems, Minneapolis, MN, United States) or fibronectin (Sigma Aldrich, St. Louis, Missouri, United States) for 30 min at room temperature. The flow chambers were placed at room temperature on an inverted microscope. Tubes connected a syringe pump, containing CellQuin medium, with one side of the channel and the other side of the channel with a waste reservoir. Tubes and channels were washed with CellQuin medium at a flow speed of 7,5 ml/h. Samples consisted of 4×10^6 erythroblasts and were incubated 10 min at 37°C with or without PKC inhibitor Gö6976 (Tocris, Bristol, United Kingdom), Calpain 1 and 2 inhibitor (Sigma), integrin α4 antibody (1 μg/ml, BD Biosciences, San Josè, CA, United States), β1 (0,5 μg/ml, Abcam, Cambridge, United Kingdom), and α5 (1 μg/ml, BD Biosciences, San Josè, CA, United States), GsMTx4 (Tocris, Bristol, United Kingdom), or Yoda1 (Sigma Aldrich, St. Louis, Missouri, United States). After incubation, samples were injected into the flow with a syringe and the pump was left running for 15 min unless otherwise stated. Nine pictures were taken across the channel after 15 min and attached erythroblasts were counted with ImageJ. Tubes were washed with water and fresh CellQuin medium in between samples. Data was analyzed with Prism 8 (GraphPad, San Diego, CA, United States). Unpaired

student *t* test was used to calculate statistical significance between each condition. D'Agostino-Pearson test was used to assess the normality of the samples' distribution.

Flow Cytometry

Erythroblasts were treated with or without inhibitor, Yoda1, or Manganese (Mn^{2+}). Samples were taken at different time points, each containing 200.000 erythroblasts in a volume of 200 μl, and were stained in a 96-well plate. The samples were kept on ice after treatment and during staining. Erythroblasts were incubated for 10 min at 37°C with or without PKC inhibitor Gö6976 (500 nM) or Calpain inhibitor 1 and 2 (1 mM) with gentle mixing. Samples were taken and resuspended into ice-cold PBS. Remaining erythroblasts were incubated at 37°C with or without Yoda1 or Manganese (II) chloride dihydrate solution in water (2 mM, Sigma Aldrich, St. Louis, MO, United States). Samples were taken after 10 and 30 min of incubation and were resuspended into ice-cold PBS. Staining was performed with 30 min incubation in FACS buffer (PBS, 0.5% BSA) with the following antibodies antiCD71 (Miltenyi Biotec, Bergisch Gladbach, Germany), antiCD235a OriGene Technologies, Inc., Rockville, MD, United States), antiCD49d (α4 integrin; BD Biosciences, San Jose, CA, United States), anti β1 integrin unconjugated (Abcam, Cambridge, United Kingdom). Staining was followed by two washing steps with FACS buffer, followed or not by staining with secondary antibody. After the last staining and wash, the cells were resuspended into 200 μl of FACS buffer. Cells were transferred to FACS tubes before measurement on FACSCanto II (BD Biosciences, San Josè, CA, United States). Data was analyzed with FlowJo® software (BD Biosciences, San Josè, CA, United States) and Prism 8 (GraphPad, San Diego, CA, United States).

Calpain Activity Assay

Calpain activity was measured with the Calpain Activity Fluorometric Assay Kit (Sigma Aldrich, St. Louis, MO, United States), following manufacturer protocol. Samples were measured in triplicates. In short, the amount of 2×10^6 erythroblasts was taken per sample. Samples were incubated with or without Yoda1 (1 μM or 5 μM, 10 min, 37°C). After centrifugation, samples were washed in PBS and resuspended into 100 μl Extraction Buffer. Samples were incubated (20 min, on ice) and spun down (10.000 *g*, 1 min). Cell lysate was transferred to a new tube and kept on ice. 10x Reaction buffer and Calpain substrate was added to 85 μl cell lysate and samples were transferred to 96-well plate. After incubation in the dark (1 h, 37°C), samples were measured with 400 nm excitation filter and 505 nm emission filter with a plate reader (BioTek, Winooski, VT, United States). Positive control (1 μl Active Calpain) and negative control (1 μl Calpain inhibitor) were taken along. Data was analyzed with Prism 8. Two-way ANOVA was used to calculate statistical significance between samples.

Western Blot

Cells were lysed in CARIN lysis buffer (20 mM Tris–HCl pH 8.0, 138 mM NaCl, 10 mM EDTA, 100 mM NaF, 1% Nonidet P-40, and 10% glycerol). Following Bradford protein quantification (Bio-Rad Laboratories, Hercules, CA, United States), lysates were boiled in Laemmli sample buffer [2% sodium dodecyl sulfate (SDS) wt/vol, 10% glycerol, 5%2-mercaptoethanol, 60 mM Tris–HCl pH6.8, and trace amount brome-phenol blue; 3 min, 95°C], subjected to SDS-polyacrylamide gel electrophoresis, blotted using iBlot-PVDF blotting system (Thermo Fisher Scientific, Bleiswijk, Netherlands), and stained as indicated in the figure legends.

Fluorescent Microscopy Imaging

Expression of integrin β1 on erythroblasts was determined with live imaging. Erythroblasts, 25×10^5 in 0.5 ml CellQuin, were incubated with integrin β1 antibody [1:100, clone (P5D2), Abcam, Cambridge, United Kingdom, Alexa Fluor 488], DRAQ5™ (1:2500, Abcam, Cambridge, United Kingdom), and CD235a (Glycophorin A, 1:200, PB, Miltenyi, Bergisch Gladbach, Germany). Microscopy images were taken with an Axiovert 200 microscope (Zeiss, Oberkochen, Germany) with bright field, DAPI, Alexa Fluor 488, and Alexa Fluor 647 filters using 40x/1.3 oil objective. Software ZEN2.3 (Zeiss, Oberkochen, Germany) was used to analyze and convert images.

RESULTS

Integrin Subunits Are Differently Expressed in Erythroblasts

We have previously reported membrane expression of ITGA4 and ITGB1 (VLA-4) in our *in vitro* cultured erythroid cells (Heideveld et al., 2018). To further evaluate the expression of integrin subunits present on erythroblasts, we data-mined RNA-sequencing that we reported previously containing RNA-expression profiles of CD71+/CD235+ erythroblasts (Heshusius et al., 2019). This analysis showed mRNA expression of eleven integrin subunits: six α subunits (*ITGA*) and five β subunits (*ITGB*; **Figure 1A**). At the erythroblast stage mRNA expression of integrin subunits α2B (*ITGA2B*), α4 (*ITGA4*), α5 (*ITGA5*), αE (*ITGAE*), αV (*ITGAV*), α6 (ITGA6), and subunits β1 (*ITGB1*), β2 (*ITGB2*), β3 (*ITGB3*), and β4 (*ITGB4*) were observed albeit with significantly different expression levels (**Figure 1A**). At the stage where erythroblast are CD71+/CD235+ (**Figure 1B**), α4 and β1 RNAs are most abundantly expressed followed by *ITGAIIB*, *ITGAE*, *ITGA5, ITGB4,* while *ITGAV, ITGB3, ITGB2, and ITG6* are lowly expressed. This confirms the presence of α4β1 (VLA-4; Heideveld et al., 2018) and would further allow α5β1 (VLA-5) and low expression of αVβ1, α6β1, αIIbβ3 (GPIIb/IIIa), αVβ3 (CD61), and αVβ5. Integrins αIIbβ3 (GPIIb/IIIa) and αVβ3 (CD61) are associated with megakaryopoiesis and platelet homeostasis and expression of the beta partner ITGB3 (β3) is significantly downregulated during differentiation (Heshusius et al., 2019). Of note, no interaction partners for the subunits ITGAE, ITGB4, and ITGB2 were detected (**Supplementary Figure 1A**). Expression of the most abundant integrin subunits α4, and β1 was confirmed by flow cytometry in three donors (**Figure 1B** and **Supplementary Figure 1B**) and imaging (**Figure 1B** and **Supplementary Figure 1C**).

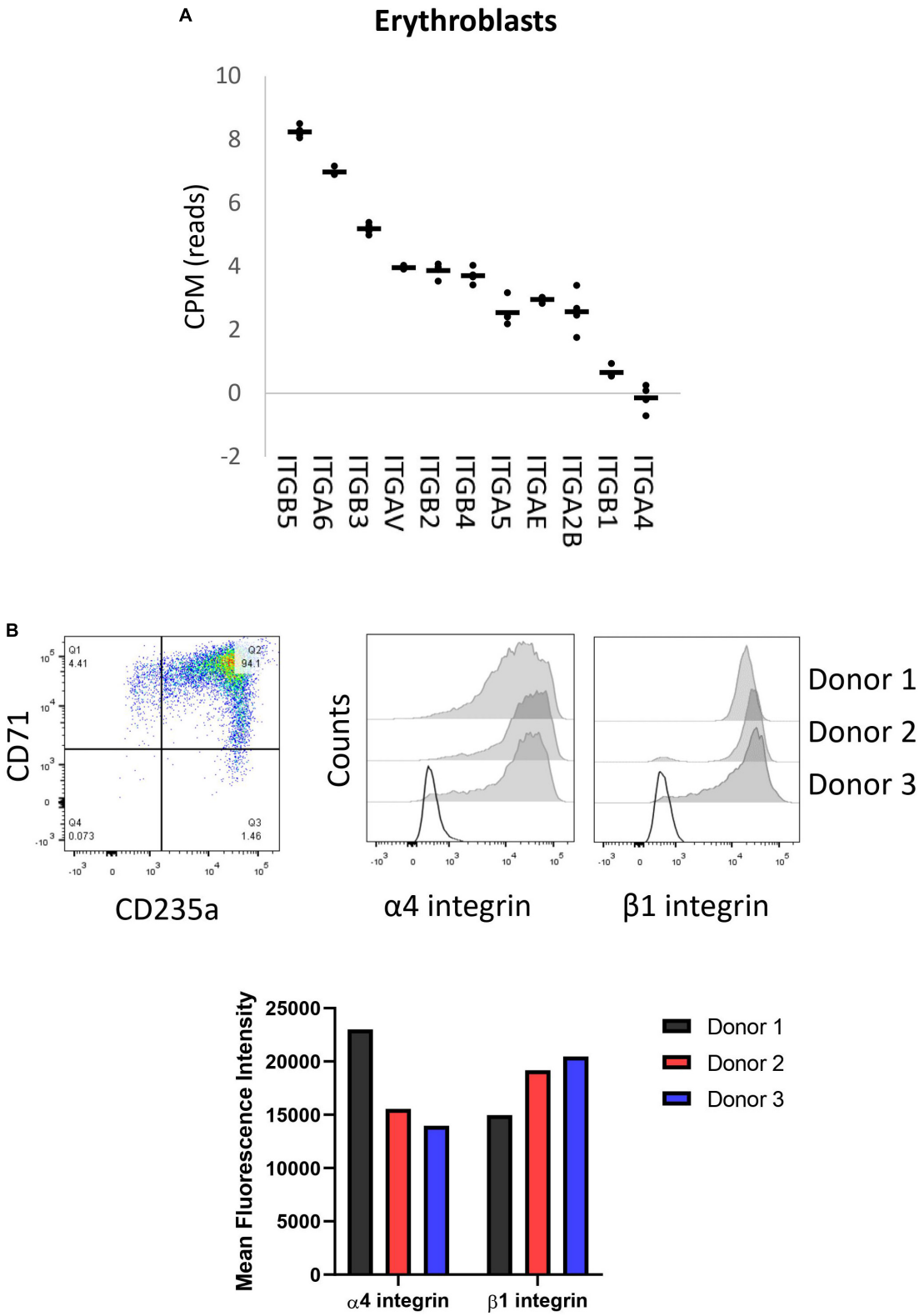

FIGURE 1 | Erythroblasts integrin expression. **(A)** Integrin mRNA expression (count per million) in CD71+/CD235a+ erythroblasts; data mined from Heshusius et al. (2019). Gene expression was found for 11 integrin subunits: six α sub-units (*ITGA*) and five β sub-units (*ITGB*; $n = 4$). **(B)** Dot plot showing a representative CD71/CD235 expression plot depicting the erythroblast stage of analysis. Right histograms and bar graph indicate expression of α4 integrin and β1 integrin in CD71+CD235a+ erythroblasts in 3 donors as measured by flow cytometry.

Activation of PIEZO1 With Yoda1 Leads to Integrin Activation and Increases Erythroblasts Adhesion

Activation of mechanosensitive PIEZO1 has been shown to lead to inside out integrin activation on non-hematopoietic cells and specific Ca^{2+} dependent signal transduction in erythroblasts (Rowin et al., 1998; Mchugh et al., 2010; Caulier et al., 2020). The high abundant integrin subunit β1 in combination with α4 (VLA-4) and α5 (VLA-5) on erythroblasts can bind VCAM1 and fibronectin, respectively. The effect of chemical activation of PIEZO1 on integrin activation and adhesion of CD71HighCD235aHigh erythroblasts to VCAM-1 and fibronectin was assessed. Erythroblasts were activated by 2 mM Mn^{2+}, a strong integrin activator, or with different concentration of the PIEZO1 agonist Yoda1 in presence of soluble VCAM1. Compared to untreated, incubation with Mn^{2+} or Yoda1 increased binding to anti-VCAM1 antibody, albeit that activation with Yoda1 was lower compared to Mn^{2+} (**Supplementary Figure 2A**). Note that the expression of total integrin β1 remained unchanged throughout the different treatments (**Supplementary Figure 2B**). To assess the adhesive properties of erythroblasts, a flow adhesion assay in which the erythroblasts are flowed within a flow cell that is coated with VCAM1 or fibronectin was used. Increased adhesion to VCAM1 (**Figure 2A**) and fibronectin (**Figure 2B**) was observed when erythroblasts were incubated with the PIEZO1 agonist Yoda1 (**Supplementary Figure 3A**). Of note, a Yoda1 concentration of 1 μM was chosen as short term and long term use of higher concentrations have been shown to be detrimental, both in terms of adhesion to VCAM1 (**Supplementary Figure 3B**), as well as cell viability, respectively (**Supplementary Figure 4**). Of note, different flow speeds did not influence the increased adhesion in Yoda1 treated cells (**Supplementary Figure 3C**). Pre-incubation with an antagonizing β1 antibody thus blocking the common beta integrin subunit within VLA-4 and VLA5 results in a significant reduction of both Yoda1-induced and steady state adhesion to VCAM1 or fibronectin (**Figures 2C,D**). Blocking VLA-4 or VLA-5 specifically using anti-α4 or anti-α5 blocking antibodies, respectively, also led to decreased adhesion (**Figures 2C,D**). Note that blocking VLA-4 using α4-integrin antibodies leads to lower inhibition of adhesion to fibronectin compared to blockage of VLA-5, which has been shown before for mouse erythroblasts (Eshghi et al., 2007). Treatment with GsMTx4, a mechanosensitive ion channel inhibitor, resulted in decreased adhesion following Yoda1 treatment but did not revert the basal adhesion of untreated cells (**Supplementary Figure 5**). In conclusion, the results indicate that erythroblast adhesion to VCAM1 and fibronectin is integrin-dependent and can be increased by activating PIEZO1.

Activation of PIEZO1 Leads to Increased Calpain Activity

Ca^{2+} influx caused by PIEZO1 activation has been shown in endothelial cells, erythroid cells and erythrocytes to lead to activation of calcium dependent pathways, among which the positive regulators of integrin activation calpain, PKC and Talin (Bos, 2005; Watanabe et al., 2008; Mchugh et al., 2010). To demonstrate whether calpain is activated following PIEZO1 activation, cells were treated with 1 μM Yoda1 or 5 μM Yoda1 for 60 min or left untreated. Calpain activity was significantly increased upon Yoda1 treatment compared to untreated cells. No significant difference between 1 and 5 μM Yoda1 was observed suggesting that 1 μM Yoda1 is sufficient to activate the pool of calpain within erythroblasts. Of note, short term treatment with 1 μM Yoda1 or 5 μM Yoda1 did not influence cell viability (**Supplementary Figure 4**). Note that Calpain activity is similar between untreated controls and samples treated with a calpain inhibitor 1 and 2, indicating that in erythroblasts basal calpain activity is low (**Figure 3A**). Calpain cleaves Talin to an activated state mediating inside-out integrin activation (Goksoy et al., 2008; Mchugh et al., 2010). Note that 1 μM Yoda1 led to a modest but clear increase in cleaved activated Talin, depicted in western blot as a lower molecular weight migrating band (**Figure 3B**).

Flow-Induced Adhesion to VCAM1 and Fibronectin Is Dependent on PKC and Calpain

Inside-out integrin activation can be mediated by several signaling cascades among which calpain and PKC-dependent pathways. Ca^{2+} influx through PIEZO1 activation by Yoda1, or in patient-derived erythroblasts with specific activation mutations in PIEZO1, causes activation of PKC-dependent signal transduction that can be partly blocked by inhibiting calcium-dependent PKCs (Caulier et al., 2020). Together with the observation that Calpain is activated after PIEZO1 activation we evaluated whether the increased adhesion is a consequence of Calpain and/or PKC activity leading to integrin activation in Yoda1 treated erythroblasts. Pretreatment with Calpain inhibitor or Gö9676 (an inhibitor of Ca^{2+} dependent PKCs) before Yoda1 incubation decreased adhesion of Yoda1 treated erythroblasts to VCAM1 (**Figure 3C**) and fibronectin (**Figure 3B**) to untreated background adhesion levels. Of note, inhibition of the PKC or Calpain pathway does not lead to complete block of adhesion as observed upon blocking integrin subunits (**Figures 3C,D**). The data indicates that PIEZO1 activation leads to both PKC and Calpain dependent integrin activation. Note that the inhibition of adhesion is primarily affecting the Yoda1 mediated increase in adhesion. This is in contrast to blocking specific integrin subunits, which also blocks the basal level of erythroblast adhesion. This is in agreement with the low level of calpain activation in steady state erythroblasts (**Figure 3A**).

DISCUSSION

Ca^{2+} influx has been linked to integrin activation in several cell types (Jaconi et al., 1991; Schwartz et al., 1993; Shankar et al., 1993; Coppolino et al., 1997; Rowin et al., 1998; Bye et al., 2020; Shu et al., 2020). This report identifies for the first time a role of the mechanosensor PIEZO1 in integrin activation in erythroblasts. We found PIEZO1 activation leads to inside-out VLA4 and VLA5 activation in erythroblasts. This activation is dependent on Ca^{2+} activated

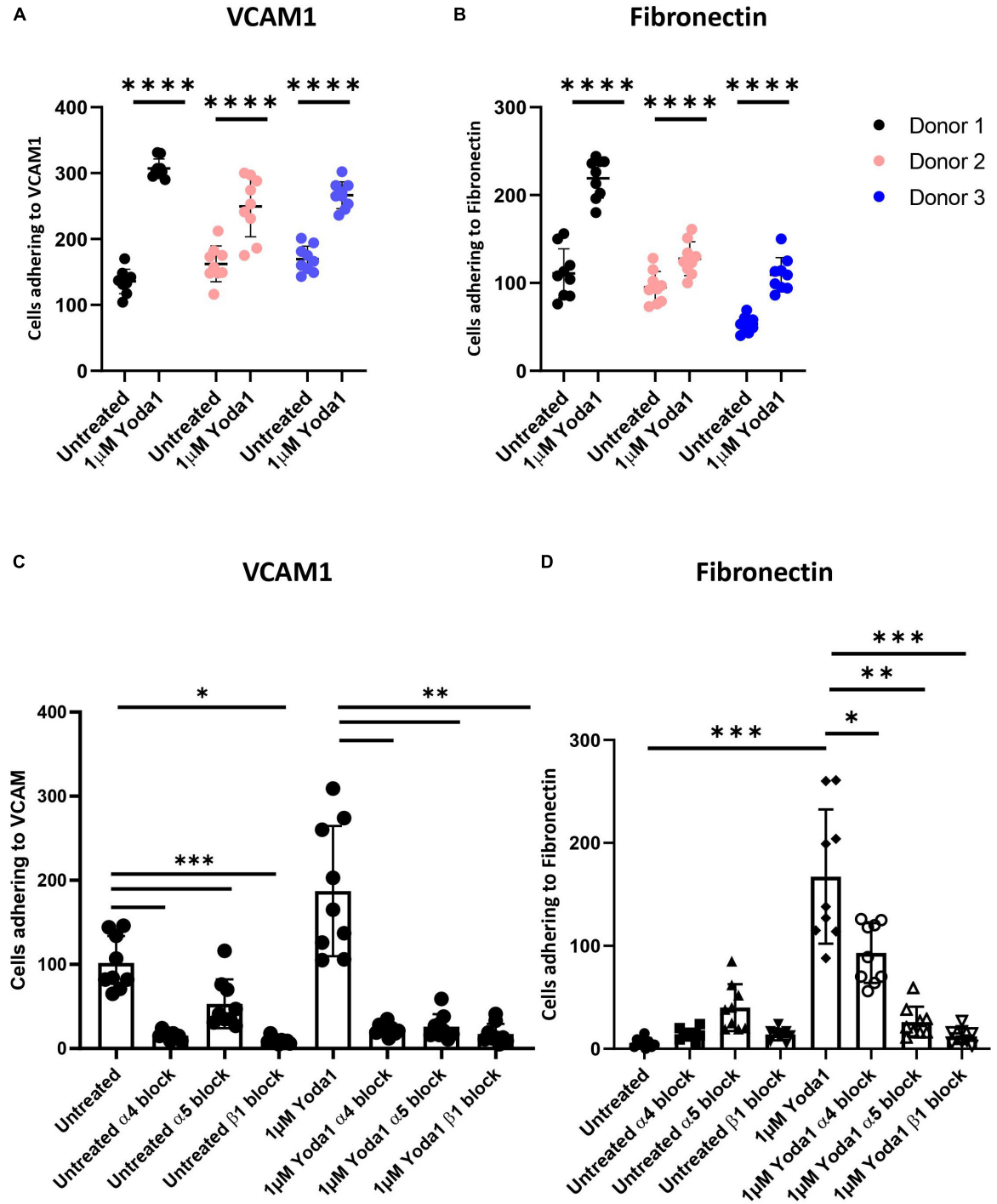

FIGURE 2 | Increased erythroblast binding to VCAM-1 and fibronectin after Yoda1 mediated PIEZO1 stimulation. **(A,B)** Erythroblasts were treated or not with 1 μM of Yoda1 for 10 min and subjected to a flow assay as described in Materials and Methods (7.5 ml/h flow rate). Adhesion of erythroblasts to VCAM **(A)** or fibronectin **(B)** was quantified using imageJ (n = 9 pictures of different donors; data depicted as mean ± SD; ****$P < 0.0001$; **C,D**) Erythroblasts were pre-treated with anti-α4, anti-α5, or anti-β1 and stimulated or not with 1 μM Yoda1 (10 min) as indicated and flowed over a surface coated with VCAM **(C)** or fibronectin (**D**; data depicted as mean ± SD mean n = 9 images was used to calculate statistic; *$P < 0.05$, **$P < 0.01$, ***$P < 0.001$, and ****$P < 0.0001$).

PKCs and calpain. Together, the data indicates that erythroid cells can perceive mechanical forces and in response to this activate VLA5 and VLA4. This may have consequences for bone marrow retention and migration, for instance with the central macrophage within the erythroid island, which expresses VCAM1, the ligand of VLA4.

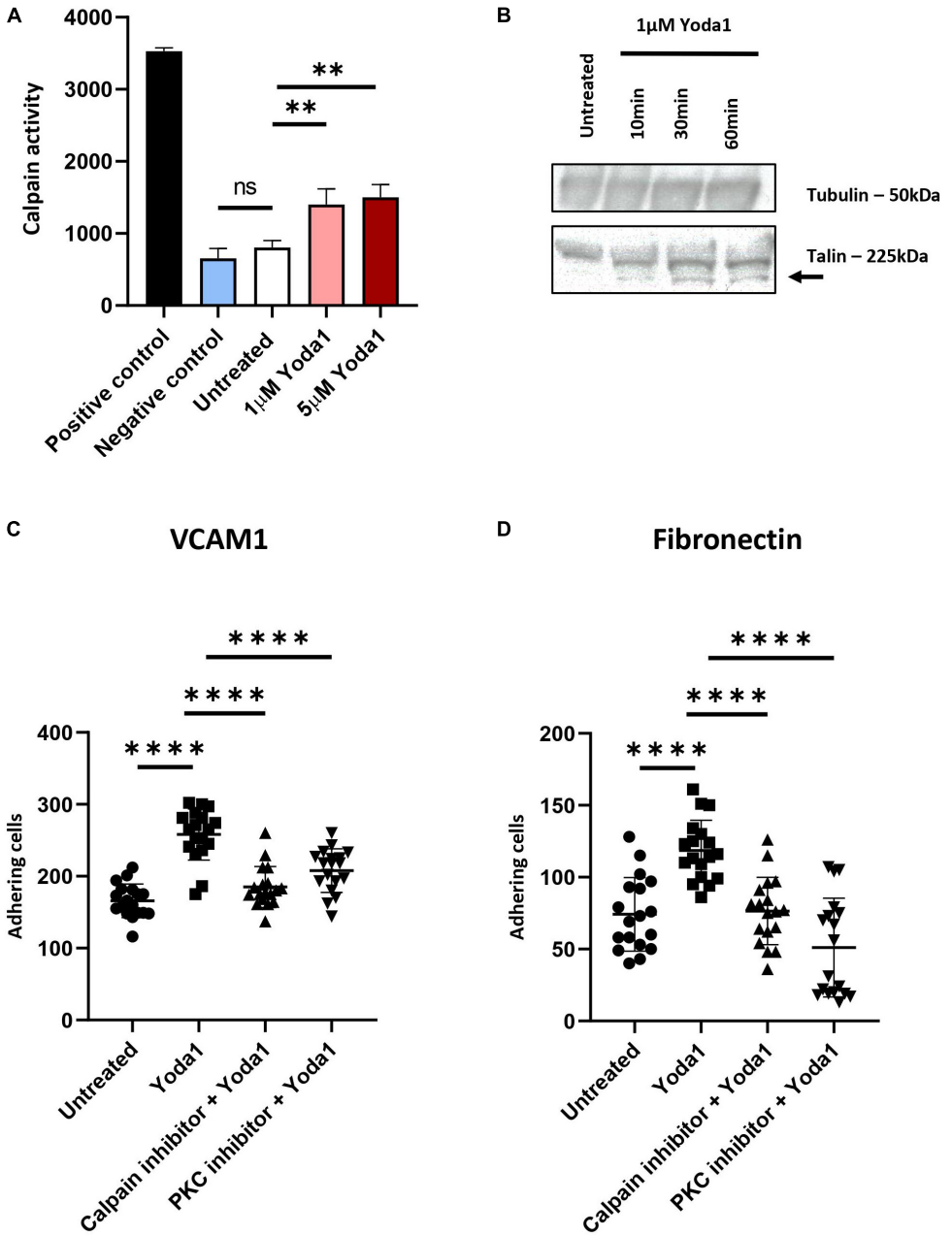

FIGURE 3 | PIEZO1 stimulation with Yoda1 results calpain and PKC dependent integrin activation. **(A)** In untreated and Yoda1 treated erythroblasts, the calpain activity assay measured the absorbance of cleaved calpain substrate at 505 nm, which is quantified using a fluorescence plate reader. Active calpain and inhibited calpain where used as positive and negative controls, respectively ($n = 3$, $^{**}P < 0.01$). **(B)** Expression of Talin (±225 kDa) and the cleavage of Talin (±190 kDa; indicated by arrow) in untreated erythroblasts and erythroblasts incubated with 1 μM Yoda1 for 10, 30, and 60 min. The same amount of protein was loaded and Tubulin (±50 kDa) was used as loading control (representative of $n = 2$). **(C,D)** Erythroblasts were pretreated with PKC inhibitor (500 nM) and calpain inhibitor (1 mM) and stimulated with and without 1 μM Yoda1 (10 min) as indicated and flowed over a surface coated with VCAM **(C)** or fibronectin (**D**; $n = 2$ donors; data depicted as mean ± SD; mean of $n = 18$ images (of two different donors) was used to calculate statistic $^{****}P < 0.0001$).

The semi-solid bone marrow is occupied with a heterogeneous pool of cells that will perceive and induce particular cellular programs upon shear forces from fluid movements, tensile strain, hydrostatic pressure and other physical forces (Meyer et al., 2016; Kim and Bixel, 2020). The consequences of these forces on haematopoiesis are beginning to emerge. For instance, it has been shown that hydrostatic pressure improves the clonogenic potential and CD34+ cell number in ex-vivo cultures (Kim and Bixel, 2020). PIEZO1 may be one of the sensors that could be involved in perceiving these forces and integrating them into a cellular response, for instance through integrin activation as shown here. Indeed, PIEZO1 has been shown to mediate

tissue hydrostatic pressure sensing in various hematopoietic cells including T-cells and monocytes (Solis et al., 2019). More specific to the erythroid system, adhesive interactions facilitated by integrins between (i) the central macrophage and developing erythroblasts, (ii) the erythroblasts themselves, and (iii) the erythroblasts and ECM are important for the support and regulation of erythropoiesis (Vuillet-Gaugler et al., 1990; Hanspal, 1997; Arroyo et al., 1999). Loss of α4 integrin affects erythropoiesis in the mice fetal liver and bone marrow, in terms of decreased cellularity. Moreover, in an *in vitro* system, *ITGA4* null erythroid progenitors display defective proliferation and migration (Arroyo et al., 1999). Ulyanova et al. (2011) observed that *ITGA4*-deficient mice are defective in triggering an optimal stress erythropoiesis response with a decrease in peripheral blood reticulocytes and inability to increase haematocrit after treatment with Phenylhydrazine. The effect was less evident in *ITGA5* deficient mice (Ulyanova et al., 2014). Indeed, integrins have been implicated in regulating the proliferative response of erythroid cells through inhibition of apoptosis by upregulating BCL-XL (Eshghi et al., 2007). Activation of VLA4 and VLA5 via PIEZO1 mechanoactivation in the bone marrow may thus strengthen anti-apoptotic signaling pathways. Interestingly, deletion of α4 integrin caused egress of erythroid cells from the bone marrow during erythroid maturation at homeostasis and during stress erythropoiesis (Ulyanova et al., 2014). This suggests that VLA4 plays a role in maintaining erythroid cells within the bone marrow, which may be strengthened upon PIEZO1-induced VLA4 activation.

The role of PIEZO1 during erythropoiesis has been investigated only recently. Increased activation of PIEZO1 was followed by activation of specific (Ca^{2+} dependent) pathways including NFAT and MAPK (Caulier et al., 2020). We found involvement of the PIEZO1-induced Ca^{2+} dependent Calpain and PKC activation in erythroblasts, which were both essential for PIEZO1-induced VLA4 and VLA5 activation. Although we found increased proteolysis of the calpain target Talin upon Yoda1 treatment, more research needs to be done to identify the intermediate steps between calpain, PKC activation and VLA4/VLA5 activation. We found that erythroblast display a basal level of adhesion toward VCAM1 and fibronectin in flow adhesion assays. Blocking α4-integrin or α5-integrin resulted in complete block of adhesion, including the basal adhesion indicating the complete dependence on VLA4 and VLA5 for adhesion to VCAM and Fibronectin. Of note, untreated cells adhered in the same manner independently of the flow speed used, supporting a basal adhesion at steady state (**Supplementary Figure 3C**). We find that erythroblasts treated with GsMTx4 inhibited the Yoda1-induced adhesion of erythroblasts. However, it must be noted that GsMTx4 is a general inhibitor of mechanosensing by cells and not specific for PIEZO1, as it incorporates itself into the lipid layer, and allows for partial relaxation upon mechanical stress (Gnanasambandam et al., 2017). Nevertheless, the experiments show that integrin activation is dependent on mechanosensing. Interestingly, inhibiting PKC, or Calpain reduced adhesion to basal levels but did not fully block adhesion as observed upon using anti- α4-integrin or α5-integrin. This may suggest that the basal activation of VLA4 and VLA5 is dependent on other PKC and calpain independent processes. Indeed, inhibition of calpain does not significantly decrease the total calpain activity in erythroblasts suggesting that basal levels of calpain activity in steady state erythroblasts is low. In conclusion, we show PIEZO1-induced inside-out integrin activation, facilitated by Ca^{2+}-dependent activation of PKC and Calpain. This knowledge could be of crucial importance in the investigation of the role of Ca^{2+} during erythropoiesis, and in particular of the dynamics of the erythroblastic island, both in health and disease (such as HX). Such a condition could lead to stress erythropoiesis (which would explain the reticulocytosis observed in these patients), a situation where support of the erythroblastic island microenvironment has been shown to be important.

DATA AVAILABILITY STATEMENT

All datasets presented in this study are included in the article/**Supplementary Material**.

ETHICS STATEMENT

The studies involving human participants were reviewed and approved by Dutch National and Sanquin Internal Ethic Boards. The patients/participants provided their written informed consent to participate in this study.

AUTHOR CONTRIBUTIONS

FA designed the experimental setup, performed and designed the experiments, and wrote the manuscript. NH, MH, and NB designed and performed the specific experiments. EA designed the experimental setup, and supervised and edited the manuscript. All authors contributed to the article and approved the submitted version.

FUNDING

FA was supported by a Horizon 2020 European Union International Training Network grant termed "RELEVANCE" (H2020-MSCA ITN-2015 and grant agreement no. 675115).

ACKNOWLEDGMENTS

We would like to thank the Sanquin Central Facility for flow cytometry support.

SUPPLEMENTARY MATERIAL

The Supplementary Material for this article can be found online at: https://www.frontiersin.org/articles/10.3389/fphys.2020.00958/full#supplementary-material

REFERENCES

Abram, C. L., and Lowell, C. A. (2009). The ins and outs of leukocyte integrin signaling. *Annu. Rev. Immunol.* 27, 339–362. doi: 10.1146/annurev.immunol.021908.132554

Albarran-Juarez, J., Iring, A., Wang, S., Joseph, S., Grimm, M., Strilic, B., et al. (2018). Piezo1 and Gq/G11 promote endothelial inflammation depending on flow pattern and integrin activation. *J. Exp. Med.* 215, 2655–2672. doi: 10.1084/jem.20180483

Andolfo, I., Alper, S. L., De Franceschi, L., Auriemma, C., Russo, R., De Falco, L., et al. (2013). Multiple clinical forms of dehydrated hereditary stomatocytosis arise from mutations in PIEZO1. *Blood* 121, 3925–3935. doi: 10.1182/blood-2013-02-482489

Arroyo, A. G., Yang, J. T., Rayburn, H., and Hynes, R. O. (1999). Alpha4 integrins regulate the proliferation/differentiation balance of multilineage hematopoietic progenitors in vivo. *Immunity* 11, 555–566. doi: 10.1016/s1074-7613(00)80131-4

Bagriantsev, S. N., Gracheva, E. O., and Gallagher, P. G. (2014). Piezo proteins: regulators of mechanosensation and other cellular processes. *J. Biol. Chem.* 289, 31673–31681. doi: 10.1074/jbc.r114.612697

Belay, E., Hayes, B. J., Blau, C. A., and Torok-Storb, B. (2017). Human cord blood and bone marrow CD34+ cells generate macrophages that support erythroid islands. *PLoS One* 12:e0171096. doi: 10.1371/journal.pone.0171096

Bessis, M. (1958). Erythroblastic island, functional unity of bone marrow. *Rev. Hematol.* 13, 8–11.

Bos, J. L. (2005). Linking rap to cell adhesion. *Curr. Opin. Cell Biol.* 17, 123–128. doi: 10.1016/j.ceb.2005.02.009

Bye, A. P., Gibbins, J. M., and Mahaut-Smith, M. P. (2020). Ca(2+) waves coordinate purinergic receptor-evoked integrin activation and polarization. *Sci. Signal.* 13:eaav7354. doi: 10.1126/scisignal.aav7354

Cahalan, S. M., Lukacs, V., Ranade, S. S., Chien, S., Bandell, M., and Patapoutian, A. (2015). Piezo1 links mechanical forces to red blood cell volume. *eLife* 4:e07370.

Caulier, A., Jankovsky, N., Demont, Y., Ouled-Haddou, H., Demagny, J., Guitton, C., et al. (2020). PIEZO1 activation delays erythroid differentiation of normal and hereditary xerocytosis-derived human progenitor cells. *Haematologica* 105, 610–622. doi: 10.3324/haematol.2019.218503

Chasis, J. A., and Mohandas, N. (2008). Erythroblastic islands: niches for erythropoiesis. *Blood* 112, 470–478. doi: 10.1182/blood-2008-03-077883

Chen, X., Wanggou, S., Bodalia, A., Zhu, M., Dong, W., Fan, J. J., et al. (2018). A feedforward mechanism mediated by mechanosensitive ion channel PIEZO1 and tissue mechanics promotes glioma aggression. *Neuron* 100, 799.e7–815.e7.

Chow, A., Huggins, M., Ahmed, J., Hashimoto, D., Lucas, D., Kunisaki, Y., et al. (2013). CD169(+) macrophages provide a niche promoting erythropoiesis under homeostasis and stress. *Nat. Med.* 19, 429–436. doi: 10.1038/nm.3057

Chow, A., Lucas, D., Hidalgo, A., Mendez-Ferrer, S., Hashimoto, D., Scheiermann, C., et al. (2011). Bone marrow CD169+ macrophages promote the retention of hematopoietic stem and progenitor cells in the mesenchymal stem cell niche. *J. Exp. Med.* 208, 261–271. doi: 10.1084/jem.20101688

Coppolino, M. G., Woodside, M. J., Demaurex, N., Grinstein, S., St-Arnaud, R., and Dedhar, S. (1997). Calreticulin is essential for integrin-mediated calcium signalling and cell adhesion. *Nature* 386, 843–847. doi: 10.1038/386843a0

Eshghi, S., Vogelezang, M. G., Hynes, R. O., Griffith, L. G., and Lodish, H. F. (2007). Alpha4beta1 integrin and erythropoietin mediate temporally distinct steps in erythropoiesis: integrins in red cell development. *J. Cell Biol.* 177, 871–880. doi: 10.1083/jcb.200702080

Gnanasambandam, R., Ghatak, C., Yasmann, A., Nishizawa, K., Sachs, F., Ladokhin, A. S., et al. (2017). GsMTx4: mechanism of inhibiting mechanosensitive ion channels. *Biophys. J.* 112, 31–45. doi: 10.1016/j.bpj.2016.11.013

Goksoy, E., Ma, Y. Q., Wang, X., Kong, X., Perera, D., Plow, E. F., et al. (2008). Structural basis for the autoinhibition of talin in regulating integrin activation. *Mol. Cell* 31, 124–133. doi: 10.1016/j.molcel.2008.06.011

Hamamura, K., Matsuda, H., Takeuchi, Y., Habu, S., Yagita, H., and Okumura, K. (1996). A critical role of VLA-4 in erythropoiesis in vivo. *Blood* 87, 2513–2517. doi: 10.1182/blood.v87.6.2513.bloodjournal8762513

Hanspal, M. (1997). Importance of cell-cell interactions in regulation of erythropoiesis. *Curr. Opin. Hematol.* 4, 142–147. doi: 10.1097/00062752-199704020-00011

Harburger, D. S., and Calderwood, D. A. (2009). Integrin signalling at a glance. *J. Cell Sci.* 122, 159–163. doi: 10.1242/jcs.018093

Heideveld, E., Hampton-O'neil, L. A., Cross, S. J., Van Alphen, F. P. J., Van Den Biggelaar, M., and Van Den Akker, E. (2018). Glucocorticoids induce differentiation of monocytes towards macrophages that share functional and phenotypical aspects with erythroblastic island macrophages. *Haematologica* 103, 395–405. doi: 10.3324/haematol.2017.179341

Heshusius, S., Heideveld, E., Burger, P., Thiel-Valkhof, M., Sellink, E., Varga, E., et al. (2019). Large-scale in vitro production of red blood cells from human peripheral blood mononuclear cells. *Blood Adv.* 3, 3337–3350. doi: 10.1182/bloodadvances.2019000689

Hu, P., and Luo, B. H. (2013). Integrin bi-directional signaling across the plasma membrane. *J. Cell Physiol.* 228, 306–312. doi: 10.1002/jcp.24154

Jaconi, M. E., Theler, J. M., Schlegel, W., Appel, R. D., Wright, S. D., and Lew, P. D. (1991). Multiple elevations of cytosolic-free Ca2+ in human neutrophils: initiation by adherence receptors of the integrin family. *J. Cell Biol.* 112, 1249–1257. doi: 10.1083/jcb.112.6.1249

Kim, J., and Bixel, M. G. (2020). Intravital multiphoton imaging of the bone and bone marrow environment. *Cytometry A* 97, 496–503. doi: 10.1002/cyto.a.23937

Kim, M., Carman, C. V., and Springer, T. A. (2003). Bidirectional transmembrane signaling by cytoplasmic domain separation in integrins. *Science* 301, 1720–1725. doi: 10.1126/science.1084174

Kirchhofer, D., Grzesiak, J., and Pierschbacher, M. D. (1991). Calcium as a potential physiological regulator of integrin-mediated cell adhesion. *J. Biol. Chem.* 266, 4471–4477.

Lanuti, P., Bertagnolo, V., Gaspari, A. R., Ciccocioppo, F., Pierdomenico, L., Bascelli, A., et al. (2006). Parallel regulation of PKC-alpha and PKC-delta characterizes the occurrence of erythroid differentiation from human primary hematopoietic progenitors. *Exp. Hematol.* 34, 1624–1634. doi: 10.1016/j.exphem.2006.07.018

Lee, G., Lo, A., Short, S. A., Mankelow, T. J., Spring, F., Parsons, S. F., et al. (2006). Targeted gene deletion demonstrates that the cell adhesion molecule ICAM-4 is critical for erythroblastic island formation. *Blood* 108, 2064–2071. doi: 10.1182/blood-2006-03-006759

Manwani, D., and Bieker, J. J. (2008). The erythroblastic island. *Curr. Top. Dev. Biol.* 82, 23–53. doi: 10.1016/s0070-2153(07)00002-6

Mchugh, B. J., Buttery, R., Lad, Y., Banks, S., Haslett, C., and Sethi, T. (2010). Integrin activation by Fam38A uses a novel mechanism of R-Ras targeting to the endoplasmic reticulum. *J. Cell Sci.* 123, 51–61. doi: 10.1242/jcs.056424

Mchugh, B. J., Murdoch, A., Haslett, C., and Sethi, T. (2012). Loss of the integrin-activating transmembrane protein Fam38A (Piezo1) promotes a switch to a reduced integrin-dependent mode of cell migration. *PLoS One* 7:e40346. doi: 10.1371/journal.pone.0040346

Meyer, M. B., Benkusky, N. A., Sen, B., Rubin, J., and Pike, J. W. (2016). Epigenetic plasticity drives adipogenic and osteogenic differentiation of marrow-derived mesenchymal stem cells. *J. Biol. Chem.* 291, 17829–17847. doi: 10.1074/jbc.m116.736538

Moura, P. L., Hawley, B. R., Dobbe, J. G. G., Streekstra, G. J., Rab, M. A. E., Bianchi, P., et al. (2019). PIEZO1 gain-of-function mutations delay reticulocyte maturation in hereditary xerocytosis. *Haematologica* 105, e268–e271. doi: 10.3324/haematol.2019.231159

Palis, J. (2016). Interaction of the macrophage and primitive erythroid lineages in the mammalian embryo. *Front. Immunol.* 7:669. doi: 10.3389/fimmu.2016.00669

Rowin, M. E., Whatley, R. E., Yednock, T., and Bohnsack, J. F. (1998). Intracellular calcium requirements for beta1 integrin activation. *J. Cell. Physiol.* 175, 193–202. doi: 10.1002/(sici)1097-4652(199805)175:2<193::aid-jcp9>3.0.co;2-j

Sadahira, Y., Yoshino, T., and Monobe, Y. (1995). Very late activation antigen 4-vascular cell adhesion molecule 1 interaction is involved in the formation of erythroblastic islands. *J. Exp. Med.* 181, 411–415. doi: 10.1084/jem.181.1.411

Schwartz, M. A., Brown, E. J., and Fazeli, B. (1993). A 50-kDa integrin-associated protein is required for integrin-regulated calcium entry in endothelial cells. *J. Biol. Chem.* 268, 19931–19934.

Seu, K. G., Papoin, J., Fessler, R., Hom, J., Huang, G., Mohandas, N., et al. (2017). Unraveling macrophage heterogeneity in erythroblastic islands. *Front. Immunol.* 8:1140. doi: 10.3389/fimmu.2017.01140

Shankar, G., Davison, I., Helfrich, M. H., Mason, W. T., and Horton, M. A. (1993). Integrin receptor-mediated mobilisation of intranuclear calcium in rat osteoclasts. *J. Cell Sci.* 105(Pt 1), 61–68.

Shu, X., Li, N., Huang, D., Zhang, Y., Lu, S., and Long, M. (2020). Mechanical strength determines Ca(2+) transients triggered by the engagement of beta2 integrins to their ligands. *Exp. Cell Res.* 387:111807. doi: 10.1016/j.yexcr.2019.111807

Solis, A. G., Bielecki, P., Steach, H. R., Sharma, L., Harman, C. C. D., Yun, S., et al. (2019). Mechanosensation of cyclical force by PIEZO1 is essential for innate immunity. *Nature* 573, 69–74. doi: 10.1038/s41586-019-1485-8

Spring, F. A., Griffiths, R. E., Mankelow, T. J., Agnew, C., Parsons, S. F., and Anstee, D. J. (2013). Tetraspanins CD81 and CD82 facilitate alpha4beta1-mediated adhesion of human erythroblasts to vascular cell adhesion molecule-1. *PLoS One* 8:e62654. doi: 10.1371/journal.pone.0062654

Tanaka, R., Owaki, T., Kamiya, S., Matsunaga, T., Shimoda, K., Kodama, H., et al. (2009). VLA-5-mediated adhesion to fibronectin accelerates hemin-stimulated erythroid differentiation of K562 cells through induction of VLA-4 expression. *J. Biol. Chem.* 284, 19817–19825. doi: 10.1074/jbc.m109.009860

Ulyanova, T., Jiang, Y., Padilla, S., Nakamoto, B., and Papayannopoulou, T. (2011). Combinatorial and distinct roles of alpha(5) and alpha(4) integrins in stress erythropoiesis in mice. *Blood* 117, 975–985. doi: 10.1182/blood-2010-05-283218

Ulyanova, T., Padilla, S. M., and Papayannopoulou, T. (2014). Stage-specific functional roles of integrins in murine erythropoiesis. *Exp. Hematol.* 42, 404.e–409.e.

Von Lindern, M., Parren-Van Amelsvoort, M., Van Dijk, T., Deiner, E., Van Den Akker, E., Van Emst-De Vries, S., et al. (2000). Protein kinase C alpha controls erythropoietin receptor signaling. *J. Biol. Chem.* 275, 34719–34727.

Vuillet-Gaugler, M. H., Breton-Gorius, J., Vainchenker, W., Guichard, J., Leroy, C., Tchernia, G., et al. (1990). Loss of attachment to fibronectin with terminal human erythroid differentiation. *Blood* 75, 865–873. doi: 10.1182/blood.v75.4.865.bloodjournal754865

Watanabe, N., Bodin, L., Pandey, M., Krause, M., Coughlin, S., Boussiotis, V. A., et al. (2008). Mechanisms and consequences of agonist-induced talin recruitment to platelet integrin alphaIIbbeta3. *J Cell Biol.* 181, 1211–1222. doi: 10.1083/jcb.200803094

Conflict of Interest: The authors declare that the research was conducted in the absence of any commercial or financial relationships that could be construed as a potential conflict of interest.

frontiers in Physiology

METHODS
published: 15 September 2020
doi: 10.3389/fphys.2020.569289

Improving the EMA Binding Test by Using Commercially Available Fluorescent Beads

Andreas Glenthøj[1], Alaa Sharfo[1], Christian Brieghel[2], Amina Nardo-Marino[1], Henrik Birgens[1] and Jesper Brix Petersen[1]*

[1] Danish Center for Hemoglobinopathies, Department of Hematology, Copenhagen University Hospital, Herlev and Gentofte Hospital, Herlev, Denmark, [2] Department of Hematology, Rigshospitalet, Copenhagen, Denmark

Hereditary spherocytosis (HS) is a common anemia caused by germline mutations in red blood cell cytoskeleton proteins. The flow cytometry-based eosin-5′-maleimide (EMA) binding test is most frequently employed for reliable diagnostics. To perform this test, a number of healthy and ideally also age-matched controls are required, which can be challenging and complicates interlaboratory comparisons. To overcome this limitation, we modified the EMA binding test by replacing healthy controls with commercially available fluorescent beads. Blood samples from 289 individuals with suspected HS were analyzed using the EMA binding test with fluorescent beads and benchmarked against regular EMA binding test using two control samples. Using osmotic gradient ektacytometry as validation, 112 individuals (38.8%) were diagnosed with HS. Performance of the modified EMA binding test was not compromised (accuracy 90.3%) compared to EMA binding test using matched controls (accuracy 88.6%). Based on these findings, we conclude that the modified EMA binding test with fluorescent beads is an attractive alternative, especially in laboratories without easy access to matched controls. Furthermore, as fluorescent beads are stable and easily commutable, they could facilitate both interlaboratory comparisons and quality assessment programs.

Keywords: hereditary spherocytosis, EMA binding test, hemolysis, anemia, membranopathy, ektacytometry

OPEN ACCESS

Edited by:
Richard Van Wijk,
Utrecht University, Netherlands

Reviewed by:
Satheesh Chonat,
Emory University, United States
Elisa Fermo,
IRCCS Ca' Granda Foundation Maggiore Policlinico Hospital, Italy
Rob Van Zwieten,
Sanquin Diagnostic Services, Netherlands

****Correspondence:***
Andreas Glenthøj
andreas.glenthoej@regionh.dk

Specialty section:
This article was submitted to Red Blood Cell Physiology, a section of the journal Frontiers in Physiology

Received: *03 June 2020*
Accepted: *21 August 2020*
Published: *15 September 2020*

Citation:
Glenthøj A, Sharfo A, Brieghel C, Nardo-Marino A, Birgens H and Petersen JB (2020) Improving the EMA Binding Test by Using Commercially Available Fluorescent Beads. Front. Physiol. 11:569289. doi: 10.3389/fphys.2020.569289

INTRODUCTION

Hereditary spherocytosis (HS) is one of the most frequent hereditary hemolytic disorders in Caucasians, affecting approximately 1:2000. Typically, affected individuals present with direct antiglobulin test (DAT) negative hemolytic anemia, increased mean corpuscular hemoglobin concentration (MCHC), and palpable splenomegaly, as well as a known family history of hemolytic anemia and gallbladder disease. In severe cases, transfusions are required from early childhood. Splenectomy is the main therapeutic option for symptomatic patients (Iolascon et al., 2017).

For decades, the laboratory diagnosis of HS was based on the manual osmotic fragility (OF) test. This obsolete test measures the degree of hemolysis after exposing red blood cells (RBCs) to a salt solution of diminishing tonicity, a procedure that is laborious. Sensitivity and specificity of the

OF test are limited, and it has been estimated that approximately 20% of mild cases of HS remain undiagnosed when using only OF test (Perrotta et al., 2008). Most laboratories have now replaced the OF test with new and more technically demanding methods such as the flow cytometry-based eosin-5′-maleimide (EMA) binding test and osmotic gradient ektacytometry.

Osmotic gradient ektacytometry is the gold standard for measuring RBC deformability. In most laboratories, however, ektacytometry has not been accessible until recently. A new generation of ektacytometers is now available, enabling this diagnostic principle to be applied on a broader scale (Da Costa et al., 2016; Llaudet-Planas et al., 2018). Osmotic gradient ektacytometry relies on laser diffraction analysis and allows for a direct and accurate measurement of alterations in the deformability of RBCs under a predetermined shear stress. Unfortunately, the test does not distinguish between HS and other spherocytic conditions such as autoimmune hemolytic anemia (Lazarova et al., 2017) and a DAT is needed to differentiate these.

In most cases, HS is caused by germline mutations in genes encoding RBC cytoskeleton proteins such as α-spectrin, β-spectrin, band 3, ankyrin, and protein 4.2. Even so, upfront genetic diagnostics rarely assists diagnostic workup and is only employed on a case-by-case basis (King et al., 2015). This is due to low sensitivity, difficulties with interpretation of identified – often private -variants, and high costs. As a result, functional testing of RBCs remains the gold standard.

Most laboratories rely on the EMA binding test as the primary screening test for HS. This test provides excellent sensitivity and specificity of >86% and often even >95% (King et al., 2000; Bianchi et al., 2012; Park et al., 2014; Joshi et al., 2016; Arora et al., 2018). The principle of the EMA binding test is measurement of RBC fluorescence intensity after incubation with EMA; a fluorescent substance that binds to RBC membrane-associated proteins, mainly band 3 (King et al., 2004). In individuals with HS, the reduced membrane surface area of the RBCs, and thereby the amount of band 3, is typically reduced (Perrotta et al., 2008). Thus, RBCs from individuals with HS can be distinguished from normal RBCs due to lower mean fluorescence intensity (MFI). The EMA binding test is relatively simple to perform, and results are available within a few hours. Generally, the MFI of the RBCs in individuals with suspected HS is compared to that of normal controls, typically three to six healthy individuals (Hunt et al., 2015). Ideally, but not mandatory, blood from healthy controls should be age-matched and drawn at the same time as the diagnostic blood sample (Falay et al., 2018). Unfortunately, this approach is often not feasible as many laboratories rely on control samples from blood donors, hospital personal, and even leftover blood samples from patients considered hematologically healthy. Especially in children, finding normal age-matched controls can be a challenge. The use of variable and non-commutable reference materials greatly complicate definition of reference ranges, interlaboratory comparisons, and quality assessment programs (Miller et al., 2011; King et al., 2015).

In this study, we investigate the performance and robustness of a modified EMA binding test by replacing fresh blood samples from healthy controls with commercially available fluorescent beads, in order to simplify HS diagnostics.

METHODS

Samples

We included blood samples from all patients referred to our laboratory with suspected HS between February 6, 2017 and September 4, 2019. The Danish Center for Hemoglobinopathies covers >75% of the Danish population and performs the vast majority of membranopathy diagnostics in the country. Travel control was in general not included due to local practices. Samples older than 48 h were discarded.

To derive a calibration factor (CF), we further obtained blood samples from 71 healthy participants in the Copenhagen General Population Study (Warny et al., 2020).

All blood samples were analyzed by osmotic gradient ektacytometry and EMA binding test as described below. Samples were transported and stored cold.

DAT was performed locally. As osmotic gradient ektacytometry is not able to distinguish between immune hemolysis and HS (Da Costa et al., 2016), we considered patients with a positive DAT to have immune hemolysis. Clinical information was only scarcely available.

Eosin-5′-Maleimide Binding Test

The EMA binding test was performed on EDTA-stabilized blood within 48 h of sampling. All EMA binding tests were performed on a FACS Canto II (BD Biosciences, Franklin Lakes, NJ, United States) using standard filter options (530/30).

The labeling of RBCs with EMA and flow cytometry was performed as previously described by others (King et al., 2000, 2004). Albeit, instead of using six healthy age-matched controls, we compared samples to commercially available fluorescent beads.

In detail, each sample was included in an EMA-experiment which, in addition to two control samples, also included two types of commercially available fluorescent beads. Firstly, one drop of FluoroSpheres K0110 beads (calibration beads; Agilent Technologies Inc., Palo Alto, CA, United States) diluted in 500 μL phosphate-buffered saline solution (PBS) was used in every experiment to calibrate the photo multiplier setting of the flow cytometer to a constant value. This was done to ensure that the fluorescence level from all experiments was comparable. Secondly, each sample was compared to one drop of mid-range FL1 Rainbow Fluorescent Particle beads (Rainbow beads; BD Biosciences) diluted in 500 μL PBS.

Eosin-5′-maleimide for the individual patient was calculated as:

$$\mathrm{EMA}_{\mathrm{beads}}\,(\%) = \left(1 - \frac{\mathrm{MFI}_{\mathrm{patient}}}{\mathrm{MFI}_{\mathrm{rainbow}} \times \mathrm{CF}}\right) \times 100\%$$

Rainbow bead MFI was slightly higher than the average fluorescence level of controls. Therefore, a constant CF was

calculated based on the average of control samples from 71 healthy controls:

$$CF = \text{Mean}\left(\frac{MFI_{healthycontrols}}{MFI_{rainbow}}\right)$$

The reason for this CF is solely to ensure that the EMA value obtained can be compared with the EMA values stated in the literature. New lots of rainbow beads should be calibrated toward the previous to ensure consistency of the EMA values calculated. Otherwise, a new CF should be calculated.

Two healthy controls were routinely included with each sample as an extra safety measure and a more traditional EMA value was calculated using these parameters:

$$EMA_{controls}\ (\%) = \left(1 - \frac{MFI_{patient}}{\text{Mean}(MFI_{control1} + MFI_{control2})}\right) \times 100\%$$

Consequently, the value of $EMA_{controls}$ was calculated using only two controls contrary to the six usually employed.

A detailed step-by-step protocol is freely available online at https://www.protocols.io/view/eosin-5-maleimide-ema-binding-test-with-fluorecent-bigdkbs6 (Glenthøj and Petersen, 2020).

Osmotic Gradient Ektacytometry

Osmotic gradient ektacytometry was performed within 48 h of sampling. All analyses were performed on a LoRRca ektacytometer (RR Mechatronics, Zwaag, Netherlands) as previously described (Da Costa et al., 2016).

Statistical Analyses

We used linear regression with Pearson correlation to evaluate linear modeling. We used Fisher's exact test to compare baseline characteristics of categorical variables and Wilcoxon signed rank test to compare numerical variables. Statistical analyses were performed in 'R' version 4.0.0 (R Core Team, 2017) using the ggplot2 package for charts, tableone baseline characteristics, pROC (Robin et al., 2011) and plotROC packages for receiver operating characteristic (ROC) analyses, and caret package for accuracy calculations.

RESULTS

EMA With Fluorescent Beads in Healthy Controls

Characteristics of the 71 control subjects from the Copenhagen General Population Study are shown in **Table 1**. Blood samples from healthy controls were subjected to EMA binding test with rainbow beads and osmotic gradient ektacytometry (**Figure 1A**). Neither EMA (MFI reduction) nor osmotic gradient ektacytometry [decreased osmotic resistance and elongation index (Llaudet-Planas et al., 2018)] indicated a membranopathy in any of the 71 subjects, when compared to the other 70 subjects (data not shown). Mean $MFI_{controls}$ was 12,068 ± 599 (SD) and mean $MFI_{rainbow}$ was 14,900 ± 96 (SD). CF was thus 0.81 (12,068/14,900).

EMA With Fluorescent Beads for Diagnostics of HS

We included blood samples from 289 individuals with suspected HS. In accordance with our inability to find age-matched controls, individuals with suspected HS were significantly younger than the healthy controls (**Table 1**). DAT was available in 187 of the 289 patients (64.7%). Based on osmotic gradient ektacytometry [decreased osmotic resistance, decreased elongation index and no positive DAT (Llaudet-Planas et al., 2018)], 112 individuals were diagnosed with HS (**Figure 1B**). Patient characteristics are summarized in **Table 1**. Patients with HS were significantly younger with fewer available DAT as compared to individuals without HS.

Linearity of the fluorescence was evaluated by changing the photo multiplier of the flow cytometer settings to alter the $MFI_{patient}$ from the standard value to 0.1 and 10 times this value. The difference in $MFI_{patient}/MFI_{rainbow}$ ratio was negligible over

TABLE 1 | Characteristics of healthy controls from the Copenhagen General Population Study used for calculating a calibration factor as well as 289 patients with samples sent to our laboratory for diagnostics of hereditary spherocytosis (HS).

	Control	HS	Not HS	*P*
N	71	112	177	
Sex = Male (%)	36 (50.7)	59 (52.7)	71 (40.1)	0.078
resistance and elongation	67.80 [56.35, 75.35]	19.85 [1.70, 43.92]	37.70 [13.30, 62.00]	<0.001
DAT available, n (%)	0 (0.0)	48 (42.9)	139 (78.5)	<0.001
EI_{min}, mean (SD)	0.15 (0.04)	0.13 (0.03)	0.14 (0.04)	0.007
O_{min}, mean (SD)	148.99 (5.68)	177.33 (13.04)	158.19 (14.30)	<0.001
EI_{max}, mean (SD)	0.61 (0.01)	0.55 (0.03)	0.60 (0.02)	<0.001
O_{max}, mean (SD)	299.08 (13.69)	339.04 (23.98)	321.85 (23.64)	<0.001
EI_{hyper}, mean (SD)	0.30 (0.00)	0.28 (0.02)	0.30 (0.01)	<0.001
O_{hyper}, mean (SD)	455.48 (13.05)	455.50 (26.21)	468.43 (23.59)	<0.001
Area, mean (SD)	167.66 (5.33)	139.80 (14.02)	162.11 (10.04)	<0.001

Age is shown as median with interquartile range (IQR). The two controls per patient are not shown. Sex, age, and DAT were compared using Kruskal–Wallis Rank Sum Test. Ektacytometry parameters (EI_{min}, O_{min}, EI_{max}, O_{max}, EI_{hyper}, O_{hyper}, and Area) were compared using t-test.

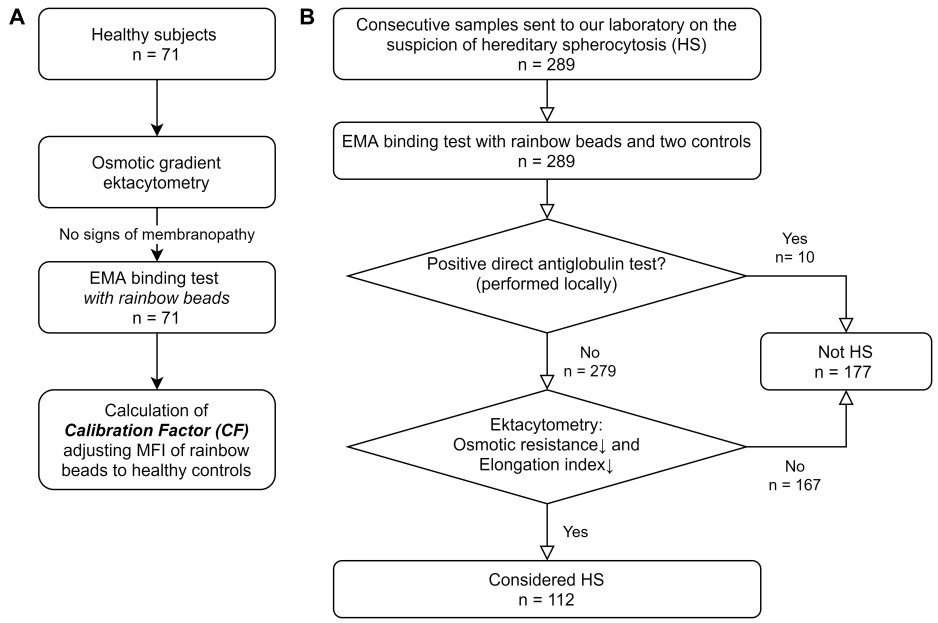

FIGURE 1 | Study flowchart **(A)** Healthy subjects participating in the Copenhagen General Population Study were subjected to osmotic gradient ektacytometry and EMA binding test with rainbow beads. These subjects were only used to calculate a constant Calibration Factor (CF) normalizing mean fluorescent intensity (MFI) of rainbow beads to the mean of healthy controls. **(B)** 289 patients had samples sent to our laboratory on suspicion of hereditary spherocytosis (HS). EMA binding test and osmotic gradient ektacytometry was performed. Patients without a positive direct antiglobulin test and spherocytosis on osmotic gradient ektacytometry were labeled as HS to test the accuracy of the EMA test.

this range, indicating that minute adjustments of photo multiplier may not be necessary (data not shown).

A comparison between EMA_{beads} and traditional $EMA_{controls}$ showed excellent correlation between the two methods [**Figure 2**; Pearson correlation coefficient = 0.93 (95% CI: 0.91–0.94)].

Receiver operating characteristic analysis was performed for EMA_{beads} and $EMA_{controls}$ (**Figure 3**) with an optimal cut-off value of −11.6 and −9.7%, respectively (**Figure 2A**). Rainbow beads showed slightly better specificity, positive predictive value, and accuracy compared to using two healthy controls (**Tables 2**, **3**).

The MFI of the two controls differed by more than 1000 in 87 patients which may have caused low performance when calculating $EMA_{controls}$. After excluding these patients, we found no substantial change in the correlation between EMA_{beads} and $EMA_{controls}$ [**Supplementary Figure S1**; Pearson correlation coefficient = 0.95 (95% CI: 0.93–0.98)], the ROC analysis (**Supplementary Figure S2**), or the accuracy of the $EMA_{controls}$ test (**Supplementary Tables S1, S2**).

DISCUSSION

In this study, we assessed whether commercially fluorescent beads can replace the need for numerous control samples in the EMA binding test with the aim of simplifying HS diagnostics. Our laboratory, and likely many other laboratories, struggles to find suitable control samples for the EMA test and even with age-matched controls, variation is often considerable. Fluorescent beads are easily accessible and could facilitate interlaboratory comparisons as well as quality assessment programs without the potential errors associated with the use of controls.

Using fluorescent beads, we demonstrate that EMA binding test without readily available healthy controls is feasible and non-inferior to a traditional approach (**Figure 2** and **Tables 2**, **3**). We choose to include a CF, which translate the EMA ratio between the MFI of the patient and the rainbow beads into values familiar from the traditional EMA binding test. Theoretically, this is not necessary and the uncorrected MFI ratio between a patient and the rainbow beads could just as well be used for diagnostics.

Due to our decade long standard practice of fluorescent bead EMA, we only use two healthy controls as an extra safety control. As three to six controls are normally employed, this may have weakened the performance of the traditional EMA test in this study (Hunt et al., 2015). We tried to minimize this weakness in our study by removing patients, where the controls differed considerably. This did not substantially alter our results (**Supplementary Figures S1, S2 and Table S1**). Additionally, clinical information was generally not available to assist the diagnosis of HS. Thus, for the purpose of this study, the reference diagnosis of HS was based on osmotic gradient ektacytometry supplemented by locally performed DAT (Llaudet-Planas et al., 2018). Differential diagnoses include immune hemolysis avoiding detection by a traditional DAT and non-HS membranopathies such as congenital dyserythropoietic anemia type II. Nonetheless, the purpose of our study was not to cement the already established diagnostic sensitivity and specificity of the

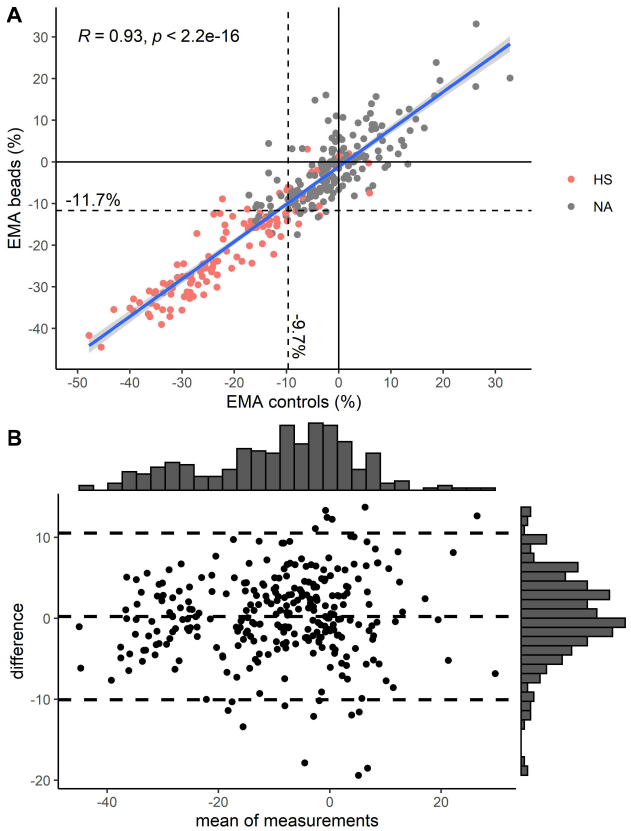

FIGURE 2 | (A) Comparison of EMA using two controls vs. EMA using rainbow beads. Pearson correlation (R) is depicted in upper left corner. Color indicates diagnosis of hereditary spherocytosis (HS) by osmotic gradient ektacytometry (**Figure 1B**). **(B)** Modified Bland-Altman plot for EMA using two controls vs. EMA using rainbow beads. Unit on both axes is percent mean fluorescence intensity compared to healthy controls. Striped lines indicate mean and 1.96 standard deviations above and below that. Histograms are depicted on top and right axes.

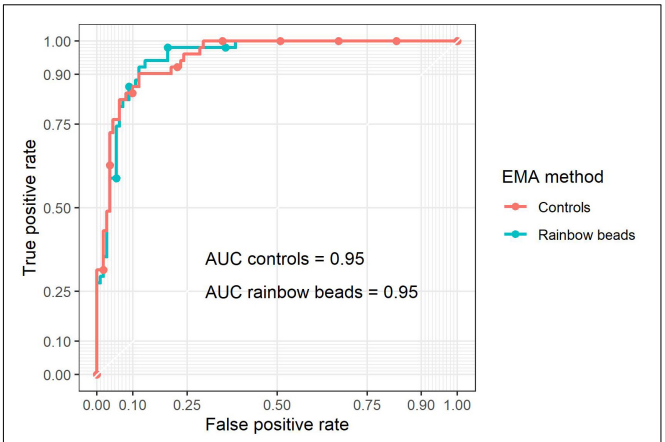

FIGURE 3 | Receiver operating characteristic (ROC) curves of EMA binding test by either two controls (red) or rainbow beads (blue) using osmotic gradient ektacytometry as the gold standard (**Figure 1B**).

TABLE 2 | Confusion matrix for EMA binding test with either **(A)** rainbow beads or **(B)** two controls.

(A)

		Ektacytometry		
EMA rainbow		**HS**	**Not HS**	
	HS	97	13	110
	Not HS	15	164	179
		112	177	

(B)

		Ektacytometry		
EMA controls		**HS**	**Not HS**	
	HS	99	20	119
	Not HS	13	157	170
		112	177	

TABLE 3 | Sensitivity, specificity, positive predictive value (PPV), negative predictive value (NPV), and accuracy for EMA binding test with either rainbow beads or two controls.

	Sensitivity	Specificity	PPV	NPV	Accuracy
EMA rainbow	0.866	0.927	0.882	0.916	0.903
EMA controls	0.884	0.887	0.832	0.924	0.886

EMA binding test (Bianchi et al., 2012), but to demonstrate a non-inferior approach to the EMA test in which healthy controls are replaced by commercially available fluorescent beads.

While replacing control samples with fluorescent beads is an attractive alternative, this approach requires regular calibration to ensure that the ratio between the beads and healthy controls does not change. We routinely perform such reviews after changing batches of the fluorescent beads or EMA. Fluorescence of the EMA dye should be stable up to 6 months at −80°C (Mehra et al., 2015). In our diagnostic setting, acquiring healthy controls for quality checks scheduled months apart is more easily implemented than retrieving suitable controls for each EMA binding test. This is particularly difficult with young patients, and we suspect that many other laboratories have similar difficulties obtaining age-matched control blood from healthy children.

In conclusion, our results indicate that commercially available fluorescent beads can eliminate the need for samples from healthy controls in the EMA binding test without compromising test performance. These results require external validation before employing into clinical practice.

DATA AVAILABILITY STATEMENT

The raw data supporting the conclusions of this article will be made available by the authors, without undue reservation.

ETHICS STATEMENT

Use of blood from healthy controls from the Copenhagen General Population Study was used in accordance with approval from the Danish Ethical Committee (H-KF-01–144/01). Written informed consent was obtained from all participants. All patients or their parents consented to diagnostic tests for hemolytic anemia including tests for hereditary spherocytosis. Data was stored and handled in according with permission from the Danish Data Protection Agency (10122009 HEH-L.HB).

AUTHOR CONTRIBUTIONS

HB, AN-M, JP, and AG planned this study. JP performed EMA and ektacytometry analyses. AS, CB, JP, and AG performed the statistical analyses. AG and JP analyzed data and wrote the manuscript. AG prepared the figures. All authors contributed to the final approved version of this report.

FUNDING

The study was funded by the Danish Center for Hemoglobinopathies.

SUPPLEMENTARY MATERIAL

The Supplementary Material for this article can be found online at: https://www.frontiersin.org/articles/10.3389/fphys.2020.569289/full#supplementary-material

FIGURE S1 | 87 of the 289 patients had controls with mean fluorescence intensity difference >1000 and were discarded. **(A)** Comparison of EMA using two controls vs. EMA using rainbow beads. Pearson correlation (R) is depicted in upper left corner. Color indicates diagnosis of hereditary spherocytosis (HS) by osmotic gradient ektacytometry (**Figure 1B**). **(B)** Modified Bland-Altman plot for EMA using two controls vs. EMA using rainbow beads. Unit on both axes is percent mean fluorescence intensity compared to healthy controls. Striped lines indicate mean and 1.96 standard deviations above and below that. Histograms are depicted on top and right axes.

FIGURE S2 | Receiver operating characteristic (ROC) curves of EMA binding test either two controls or rainbow beads using osmotic gradient ektacytometry as gold standard (**Figure 1B**). 87 of the 289 patients had controls with mean fluorescence intensity difference >1000 and were discarded.

TABLE S1 | Confusion matrix for EMA binding test with either **(A)** rainbow beads or **(B)** two controls. Contrary to **Table 2**, patients where the controls differed the most in mean fluorescence intensity difference (>1000; 87 of the 289 patients) were discarded.

TABLE S2 | Sensitivity, specificity, positive predictive value (PPV), negative predictive value (NPV), and accuracy for EMA test with either rainbow beads or two controls for EMA binding test with either rainbow beads or two controls in patients. Contrary to **Table 3**, patients where the controls differed the most in mean fluorescence intensity difference (>1000; 87 of the 289 patients) were discarded.

REFERENCES

Arora, R. D., Dass, J., Maydeo, S., Arya, V., Radhakrishnan, N., Sachdeva, A., et al. (2018). Flow cytometric osmotic fragility test and eosin-5′-maleimide dye-binding tests are better than conventional osmotic fragility tests for the diagnosis of hereditary spherocytosis. *Int. J. Lab. Hematol.* 40, 335–342. doi: 10.1111/ijlh.12794

Bianchi, P., Fermo, E., Vercellati, C., Marcello, A. P., Porretti, L., Cortelezzi, A., et al. (2012). Diagnostic power of laboratory tests for hereditary spherocytosis: a comparison study in 150 patients grouped according to molecular and clinical characteristics. *Haematologica* 97, 516–523. doi: 10.3324/haematol.2011.052845

Da Costa, L., Suner, L., Galimand, J., Bonnel, A., Pascreau, T., Couque, N., et al. (2016). Diagnostic tool for red blood cell membrane disorders: assessment of a new generation ektacytometer. *Blood Cells Mol. Dis.* 56, 9–22. doi: 10.1016/j.bcmd.2015.09.001

Falay, M., Ulusan, G. E., Şenes, M., and Acar, I. O. (2018). Are the reference ranges and cutoff values of eosin-5′-Maleimide (EMA) binding test for hereditary spherocytosis specific for each age group? *Clin. Lab.* 64, 1101–1103. doi: 10.7754/Clin.Lab.2018.180124

Glenthøj, A., and Petersen, J. B. (2020). Eosin-5′-maleimide (EMA) binding test with fluorecent beads.Br. *J. Heamatol.* 124, 106–113. doi: 10.1046/j.1365-2141.2003.04730.x

Hunt, L., Greenwood, D., Heimpel, H., Noel, N., Whiteway, A., and King, M. J. (2015). Toward the harmonization of result presentation for the eosin-5′-maleimide binding test in the diagnosis of hereditary spherocytosis. *Cytom. Part B Clin. Cytom.* 88, 50–57. doi: 10.1002/cyto.b.21187

Iolascon, A., Andolfo, I., Barcellini, W., Corcione, F., Garçon, L., De Franceschi, L., et al. (2017). Recommendations regarding splenectomy in hereditary hemolytic anemias. *Haematologica* 102, 1304–1313. doi: 10.3324/haematol.2016.161166

Joshi, P., Aggarwal, A., Jamwal, M., Sachdeva, M. U. S., Bansal, D., Malhotra, P., et al. (2016). A comparative evaluation of Eosin-5′-maleimide flow cytometry reveals a high diagnostic efficacy for hereditary spherocytosis. *Int. J. Lab. Hematol.* 38, 520–526. doi: 10.1111/ijlh.12533

King, M. J., Behrens, J., Rogers, C., Flynn, C., Greenwood, D., and Chambers, K. (2000). Rapid flow cytometric test for the diagnosis of membrane cytoskeleton-associated haemolytic anaemia. *Br. J. Haematol.* 111, 924–933. doi: 10.1046/j.1365-2141.2000.02416.x

King, M. J., Garçon, L., Hoyer, J. D., Iolascon, A., Picard, V., Stewart, G., et al. (2015). ICSH guidelines for the laboratory diagnosis of nonimmune hereditary red cell membrane disorders. *Int. J. Lab. Hematol.* 37, 304–325. doi: 10.1111/ijlh.12335

King, M. J., Smythe, J. S., and Mushens, R. (2004). Eosin-5-maleimide binding to band 3 and Rh-related proteins forms the basis of a screening test for hereditary spherocytosis. *Br. J. Haematol.* 124, 106–113. doi: 10.1046/j.1365-2141.2003.04730.x

Lazarova, E., Gulbis, B., Oirschot, B., and Van Wijk, R. (2017). Next-generation osmotic gradient ektacytometry for the diagnosis of hereditary spherocytosis: Interlaboratory method validation and experience. *Clin. Chem. Lab. Med.* 55, 394–402. doi: 10.1515/cclm-2016-0290

Llaudet-Planas, E., Vives-Corrons, J. L., Rizzuto, V., Gómez-Ramírez, P., Sevilla Navarro, J., Coll Sibina, M. T., et al. (2018). Osmotic gradient ektacytometry: a valuable screening test for hereditary spherocytosis and other red blood cell membrane disorders. *Int. J. Lab. Hematol.* 40, 94–102. doi: 10.1111/ijlh.12746

Mehra, S., Tyagi, N., Dorwal, P., Pande, A., Jain, D., Sachdev, R., et al. (2015). Stability of eosin-5′-maleimide dye used in flow cytometric analysis for red cell membrane disorders. *Blood Res.* 50, 109–112. doi: 10.5045/br.2015.50.2.109

Miller, W. G., Myers, G. L., Gantzer, M., Lou Kahn, S. E., Schönbrunner, E. R., Thienpont, L. M., et al. (2011). Roadmap for harmonization of clinical laboratory measurement procedures. *Clin. Chem.* 57, 1108–1117. doi: 10.1373/clinchem.2011.164012

Park, S. H., Park, C. J., Lee, B. R., Cho, Y. U., Jang, S., Kim, N., et al. (2014). Comparison study of the eosin-5′-maleimide binding test, flow cytometric osmotic fragility test, and cryohemolysis test in the diagnosis of hereditary spherocytosis. *Am. J. Clin. Pathol.* 142, 474–484. doi: 10.1309/AJCPO7V4OGXLIIPP

Perrotta, S., Gallagher, P. G., and Mohandas, N. (2008). Hereditary spherocytosis. *Lancet* 372, 1411–1426. doi: 10.1016/S0140-6736(08)61588-61583

R Core Team (2017). *R: A Language and Environment for Statistical Computing*. Vienna: R Foundation for Statistical Computing.

Robin, X., Turck, N., Hainard, A., Tiberti, N., Lisacek, F., Sanchez, J. C., et al. (2011). pROC: An open-source package for R and S+ to analyze and compare ROC curves. *BMC Bioinform.* 12:77. doi: 10.1186/1471-2105-12-77

Warny, M., Helby, J., Nordestgaard, B. G., Birgens, H., and Bojesen, S. E. (2020). Incidental lymphopenia and mortality: a prospective cohort study. *CMAJ* 192, E25–E33. doi: 10.1503/cmaj.191024

Conflict of Interest: The authors declare that the research was conducted in the absence of any commercial or financial relationships that could be construed as a potential conflict of interest.

frontiers in Physiology

ORIGINAL RESEARCH
published: 23 October 2020
doi: 10.3389/fphys.2020.593841

ZOOMICS: Comparative Metabolomics of Red Blood Cells From Old World Monkeys and Humans

Lorenzo Bertolone[1], Hye K. Shin[2], Davide Stefanoni[1], Jin Hyen Baek[2], Yamei Gao[2], Evan J. Morrison[1], Travis Nemkov[1], Tiffany Thomas[3], Richard O. Francis[3], Eldad A. Hod[3], James C. Zimring[4], Tatsuro Yoshida[5], Matthew Karafin[6,7], Joseph Schwartz[3], Krystalyn E. Hudson[3], Steven L. Spitalnik[3], Paul W. Buehler[8,9†] and Angelo D'Alessandro[1,10*†]*

[1] Department of Biochemistry and Molecular Genetics, University of Colorado Denver – Anschutz Medical Campus, Aurora, CO, United States, [2] Center for Biologics Evaluation and Research, Food and Drug Administration, Silver Spring, MD, United States, [3] Department of Pathology and Cell Biology, Columbia University, New York, NY, United States, [4] Department of Pathology, University of Virginia, Charloteseville, VA, United States, [5] Hemanext, Inc., Lexington, MA, United States, [6] Blood Center of Wisconsin, Milwaukee, WI, United States, [7] Department of Pathology and Laboratory Medicine, Milwaukee, WI, United States, [8] Department of Pathology, University of Maryland School of Medicine, Baltimore, MD, United States, [9] Department of Pediatrics, Center for Blood Oxygen Transport and Hemostasis, University of Maryland School of Medicine, Baltimore, MD, United States, [10] Division of Hematology, Department of Medicine, University of Colorado Denver – Anschutz Medical Campus, Aurora, CO, United States

As part of the ZOOMICS project, we set out to investigate common and diverging metabolic traits in the blood metabolome across various species by taking advantage of recent developments in high-throughput metabolomics. Here we provide the first comparative metabolomics analysis of fresh and stored human (n = 21, 10 males, 11 females), olive baboon (n = 20), and rhesus macaque (n = 20) red blood cells at baseline and upon 42 days of storage under blood bank conditions. The results indicated similarities and differences across species, which ultimately resulted in a differential propensity to undergo morphological alterations and lyse as a function of the duration of refrigerated storage. Focusing on purine oxidation, carboxylic acid, fatty acid, and arginine metabolism further highlighted species-specific metabolic wiring. For example, through a combination of steady state measurements and $^{13}C_6{}^{15}N_4$-arginine tracing experiments, we report an increase in arginine catabolism into ornithine in humans, suggestive of species-specific arginase 1 activity and nitric oxide synthesis—an observation that may impact the translatability of cardiovascular disease studies carried out in non-human primates (NHPs). Finally, we correlated metabolic measurements to storage-induced morphological alterations via scanning electron microscopy and hemolysis, which were significantly lower in human red cells compared to both NHPs.

Keywords: comparative biology, red blood cell, metabolomics, blood storage, transfusion

OPEN ACCESS

Edited by:
Paola Bianchi,
Foundation IRCCS Ca' Granda Ospedale Maggiore Policlinico, Italy

Reviewed by:
Mauro Magnani,
University of Urbino Carlo Bo, Italy
Neema Jamshidi,
UCLA Health System, United States

****Correspondence:***
Paul W. Buehler
pbuehler@som.umaryland.edu
Angelo D'Alessandro
angelo.dalessandro@ucdenver.edu

† These authors have contributed equally to this work and share last/senior authorship

Specialty section:
This article was submitted to Red Blood Cell Physiology, a section of the journal Frontiers in Physiology

Received: *11 August 2020*
Accepted: *29 September 2020*
Published: *23 October 2020*

Citation:
Bertolone L, Shin HK, Stefanoni D, Baek JH, Gao Y, Morrison EJ, Nemkov T, Thomas T, Francis RO, Hod EA, Zimring JC, Yoshida T, Karafin M, Schwartz J, Hudson KE, Spitalnik SL, Buehler PW and D'Alessandro A (2020) ZOOMICS: Comparative Metabolomics of Red Blood Cells From Old World Monkeys and Humans. Front. Physiol. 11:593841. doi: 10.3389/fphys.2020.593841

INTRODUCTION

Mere scientific curiosity has historically led science to the discovery of novel natural phenomena that turned out to be mechanistically relevant to our understanding of human biology. From Linnaeus' taxonomical efforts to order nature into separate categories, to modern day DNA-based phylogenetic classifications, scientists have leveraged comparative biology to unravel Nature's mysteries and learn more about humankind as a species. Embracing this philosophy, we embarked on the ZOOMICS project: by taking advantage of recent developments in high-throughput metabolomics (Nemkov et al., 2017; Reisz et al., 2019), we set out to investigate common and diverging metabolic traits in the blood metabolome across various species. The choice to focus on this matrix and, specifically, on red blood cells (RBCs), stems from an appreciation that blood offers a window into systems metabolism. From classical clinical biochemistry to early clinical metabolomics approaches (D'Alessandro et al., 2012), studies on RBC metabolism have furthered our understanding of systemic responses to aging, inflammation, and physiological (e.g., high altitude) or pathological (e.g., hemorrhage, ischemia) hypoxia. RBC metabolism modulates hemoglobin oxygen binding and off-loading and, in so doing, modulates metabolic activity of the rest of bodily cells that, unlike RBCs, contain mitochondria (Nemkov et al., 2018a). As such, it is unlikely that understanding RBC metabolic variance across multiple species will turn out to be nothing more than a sophisticated exercise in technical metabolomics proficiency. Even if ignoring the relevance of such studies to the standpoint of veterinary medicine, we propose that a metabolomics effort in cataloging RBC metabolomes across species will be relevant to the design and interpretation of research studies that rely on these animals as models for human health and disease.

Animal models have contributed significantly to the fields of hematology and transfusion medicine. Rodent [e.g., mice (Howie et al., 2019), rats (Williams et al., 2019), guinea pigs (Baek et al., 2017)], canine (Klein, 2017), and swine (Clendenen et al., 2017) models have been extensively adopted in blood research for years. However, being genotypically closest to humans, non-human primate (NHP) biology is most phenotypically comparable to human biology. Among all NHPs, baboons (e.g., *Papio anubis*, olive baboon) and macaques (e.g., *Macaca mulatta*, Rhesus macaque, hereon referred to as macaques) are the most frequently studied for biomedical research (VandeBerg et al., 2009; Cox et al., 2013). While both species are equally distant phylogenetically from *Homo sapiens* (Siepel, 2009) (∼93% of DNA sequence homology) (Rhesus Macaque Genome Sequencing and Analysis Consortium, Gibbs et al., 2007; Cox et al., 2013), baboon size and anatomy makes them more phenotypically similar to humans and, thus, preferred for some comparative research studies, including blood research (Valeri and Ragno, 2006). For example, similar to humans, the hematocrit is 39–45% in macaques and 33–46% in baboons (Valeri et al., 1981b), with corresponding Hb levels of 13.1 ± 0.9 and 12.5 ± 0.2 g/dl in male and female macaques, and 12.6 ±1.2 and 12.5 ±1.0 g/dl in male and female baboons (Harewood et al., 1999), respectively (Chen et al., 2009). In addition, RBC distribution widths are 13.0 ± 0.7 and 12.9 ±1.0% in macaques and baboons (Mahaney et al., 2005), respectively, similar to human RBCs (Chen et al., 2009). The mean circulatory life span of macaque RBCs is 98 ± 21 days (Fonseca et al., 2016, 2018), comparable to humans (100–120 days), and significantly longer than mice (55–60 days) (Kaestner and Minetti, 2017). Fresh baboon RBCs also have a similar lifespan to humans (∼100 days) (Valeri et al., 2002), and hydrogen peroxide-damaged baboon RBCs have increased levels of spectrin–hemoglobin complexes facilitating more rapid removal from circulation (McKenney et al., 1990). Further, RBCs in both humans and baboons respond to altitude (D'Alessandro et al., 2016) or hemorrhagic hypoxia (Reisz et al., 2017) by promoting synthesis of 2,3-diphosphoglycerate, thereby enhancing hemoglobin transition state responsiveness to pH and carbon dioxide; this process promotes hemoglobin's T state conformation (right shift of the hemoglobin oxygen-dissociation curve), oxygen off-loading, and restoration of tissue oxygen homeostasis (Herman et al., 1971).

Studying baboon RBCs in the context of transfusion medicine is not novel. For example, when stored for 3 weeks in citrate phosphate dextrose (CPD) followed by washing, baboon and human RBCs had comparable post-transfusion recoveries (i.e., ∼77%) (Valeri et al., 1981a). This suggested that baboon RBCs were a candidate animal model for blood storage, *in vivo* recovery, and, potentially, for transfusion outcomes. Subsequent studies in 2005 suggested that storing baboon RBCs for 42 days in CPD combined with Additive Solution-1 (i.e., CPD-ADSOL) yielded inferior post-transfusion recoveries, compared to human RBCs. The interspecies differences were even more significant after 49 days of storage, but not at earlier time points (i.e., 74% for both species at storage day 35) (Valeri and Ragno, 2005), suggesting some limitations regarding the translational relevance of baboons as a model for human RBC storage. Further, both young and older baboons demonstrated comparable RBC storage and post-transfusion recoveries based on ^{59}Fe-labeling studies (Valeri et al., 1985); interestingly, this observation is not consistent with human data (Tuo et al., 2014) suggesting that RBCs from older donors are more susceptible to the "storage lesion" when compared to those from younger donors. Although not directly related to RBC storage, recent studies have explored the differentiation of baboon-induced pluripotent stem cells (iPSCs) into enucleated mature RBCs (Olivier et al., 2019), as a novel therapeutic approach that may become relevant for transfusion medicine.

Despite several studies, little is known about the metabolism of baboon RBCs, especially how they compare to fresh and stored macaque and human RBCs. Recently, we extensively described the metabolic phenotypes of fresh RBCs from humans and macaques (*Macaca mulatta*), as well as along a weekly continuum in 42-day storage studies (Stefanoni et al., 2020). These experiments identified significant metabolic differences between macaque and human RBCs regarding purine deamination, glutathione metabolism (especially the gamma-glutamyl cycle),

arginine metabolism, and membrane phosphatidylserines as a function of storage duration (Stefanoni et al., 2020). Herein, we provide a comparative metabolomics analysis of fresh and stored RBCs from humans and two old-world monkeys, olive baboons (*Papio anubis*) and macaques.

Based on defining RBC metabolic processes that may affect blood storage, disease progression, and translational research, the current work identifies parallel and divergent metabolomics in three primate species (n = 20 per group, equally distributed by sex), with several unique and storage-dependent similarities and differences in non- and human–primate RBC metabolism. Notably, a cross-species dimorphism in arginine metabolism was identified in a non-targeted analysis and further validated using stable isotope-labeled arginine tracing. We highlight this pathway, given the importance of nitric oxide (NO) as an RBC-transported signaling molecule that modulates vascular responsiveness to hypoxia (Doctor and Stamler, 2011); in addition, NO depletion may be a relevant component of the storage lesion that affects transfusion efficacy (Bennett-Guerrero et al., 2007; Kanias et al., 2013; Reynolds et al., 2018). Further, in the context of cardiovascular disease (CVD), RBC imbalances in arginase and NO synthase suggest that increased RBC arginase-1 activity decreases NO bioavailability, superoxide production, endothelial dysfunction, and enhances post-ischemic cardiac failure (Yang et al., 2018; Mahdi et al., 2019; Pernow et al., 2019). Nonetheless, to our knowledge no studies have examined RBC metabolomes of multiple, closely related, primate species, particularly regarding arginine metabolism. This "ZOOmics" study of RBC metabolism may critically affect the design and interpretation of CVD studies focusing on NO signaling and metabolism in humans and NHP models (Havel et al., 2017). Such models may be important for studying communication between RBCs and the vasculature in the progression of CVD, and of RBC transfusion quality-based outcomes that are affected by dysregulated metabolic RBC communication.

MATERIALS AND METHODS

Since all the methods used in this study have been described in prior work, extensive analytical details and related references to methodological papers and their application to recent RBC storage studies are provided in the **Supplementary File—Materials** and Methods extended.

Ethical Statement

All experimental protocols were approved by named institutional committees. Specifically, animal studies were performed according to FDA White Oak Animal Care and Use protocol 2018-31. Human blood was collected under informed consent according to NIH study IRB #99-CC-0168 "Collection and Distribution of Blood Components from Healthy Donors for In Vitro Research Use" under an NIH-FDA material transfer agreement and in compliance with the Declaration of Helsinki.

Blood Collection, Processing, and Storage

Blood was collected into a syringe using a 20-G needle from the femoral vein of 5-year-old rhesus macaques (*Macaca mulatta*—n = 20; 10 males/10 females) and olive baboons (*Papio anubis*—n = 20; 10 males/10 females) under ketamine/dexmedotomidine (7 mg/kg/0.2 mg/kg) anesthesia according to FDA White Oak Animal Care and Use protocol 2018-31. All blood donor macaques originated from the same colony located at Morgan Island, South Carolina, while blood donor olive baboons originated from Southwest National Primate Research Center, San Antonio, Texas, prior to arrival at FDA's White Oak Campus, Silver Spring, Maryland. Donor blood collections for both species were obtained from basal animals prior to their allocation in other, unrelated studies. Human donor blood was collected into a syringe using a 16-G needle from the median cubital vein of 30- to 75-year-old human volunteers (n = 21; 11 males/10 females) under informed consent according to NIH study IRB #99-CC-0168 "Collection and Distribution of Blood Components from Healthy Donors for In Vitro Research Use" under an NIH-FDA material transfer agreement. Blood was collected into acid citrate dextrose, leukofiltered, and stored in AS-3 in pediatric-sized bags designed to hold 20-ml volumes and mimicking the composition of standard full-sized units [i.e., incorporating polyvinylchloride (PVC) and phthalate plasticizers]. RBCs were stored at 4–6°C for 42 days. RBCs and supernatants were separated via centrifugation upon sterile sampling of each unit on days 0, 7, 14, 21, 28, 35, and 42.

Tracing Experiments With $^{13}C_6{}^{15}N_4$-Arginine

All available RBC lysates from the three species were incubated for 5 min and 24 h at 37°C in AS-3 supplemented with 5 mM stable isotope-labeled $^{13}C_6{}^{15}N_4$-arginine (product no: CNLM-539-H-0.05, Cambridge Isotopes).

Ultrahigh-Pressure Liquid Chromatography-Mass Spectrometry Metabolomics, Lipidomics, and Arginine Tracing Experiments

A volume of 50 μl of frozen RBC aliquots was extracted 1:10 in ice cold extraction solution (methanol:acetonitrile:water 5:3:2 *v/v/v*) (Reisz et al., 2019). Samples were vortexed and insoluble material pelleted, as described (Nemkov et al., 2016). Analyses were performed using a Vanquish UHPLC coupled online to a Q Exactive mass spectrometer (Thermo Fisher, Bremen, Germany). Samples were analyzed using a 3-min isocratic condition (Nemkov et al., 2017) or a 5-, 9-, and 17-min gradient, as described (Fu et al., 2016; D'Alessandro et al., 2017b). While this method is not directly comparable to classic methods for quantitation of high-energy phosphate compounds (e.g., ATP and DPG), which require acidic extraction, it still affords ac comprehensive overview of (stored) RBC metabolism (Nemkov et al., 2016). For targeted quantitative experiments,

extraction solutions were supplemented with stable isotope-labeled standards, and endogenous metabolite concentrations were quantified against the areas calculated for heavy isotopologs for each internal standard (Fu et al., 2016; D'Alessandro et al., 2017b). For arginine tracing experiments, ^{13}C and ^{15}N tracing into arginine, ornithine, and citrulline was performed as previously described (Seim et al., 2019), through the auxilium of the software El-MAVEN (Agrawal et al., 2019). Graphs and statistical analyses (either *t*-test or repeated measures ANOVA) were prepared with GraphPad Prism 8.0 (GraphPad Software, Inc, La Jolla, CA, United States), GENE E (Broad Institute, Cambridge, MA, United States), and MetaboAnalyst 4.0 (Chong et al., 2018). Extensive details for this section are provided in the **Supplementary File—Materials** and Methods extended.

Hemolysis Measurements

Percent hemolysis was measured based on % hematocrit, supernatant hemoglobin (Hb) (g/dl), and total (Hb) (supernatant + RBC, g/dl) in 50-μl samples obtained weekly from storage bags. Supernatant and RBCs were separated using a hematocrocrit centrifuge (Thermo Fisher, Frederick, MD, United States). Hematocrit was recorded, and supernatant was separated from RBCs. Supernatant and lysed RBC Hb levels were measured using a Carey 60 UV-visible spectrophotometer (Agilent Technologies, Santa Clara, CA, United States). Oxy ferrous Hb ($HbFe^{2+}O_2$) and ferric Hb ($HbFe^{3+}$) concentrations were determined based on the extinction coefficients for each species. Molar extinction coefficients used to calculate Hb concentrations in heme equivalents were: 15.2 mM^{-1} cm^{-1} at 576 nm for $Hb(O_2)$ and 4.4 mM^{-1} cm^{-1} at 631 nm for ferric Hb using 50 mM potassium phosphate buffer, pH 7.0 at ambient temperature, in both cases. Total heme was calculated by adding these values and converting (heme) (microM) to total (Hb) (g/dl).

Red Blood Cell Morphological Evaluation

Red blood cells were fixed (1% glutaraldehyde in 0.1M phosphate buffer) and post-fixed with 1% osmium tetroxide for 1 h at room temperature, prior to further preparation and evaluation by scanning electron microscopy, as described (Baek et al., 2018).

RESULTS

The Metabolic Phenotypes of Fresh RBCs From NHPs Are More Similar to Each Other Than to Humans

Metabolomics analyses were performed on freshly drawn human (n = 21), baboon (n = 20), and macaque (n = 20) RBCs (**Figure 1A**). All the raw data are extensively reported in tabulated form as **Supplementary Table 1** and as a heat map in **Supplementary Figure 1**. Partial least square-discriminant analysis (PLS-DA; **Figure 1B—Supplementary Table 1** also includes a comparison between PCA and PLS-DA, details of PLS-DA performances, and validation) and hierarchical clustering analyses (**Figure 1C**) were performed on these data, showing that RBC metabolomes of the NHPs were separated from those of humans across principal component (PC) 1, which explained 35.5% of the total variance (**Figure 1B**). This observation is clearer in the heat map in **Figure 1C**, which shows the top 50 significant metabolites by ANOVA from cross-species comparisons. Some metabolites (alanine, threonine, ornithine, $NADP^+$, and urate) were consistently higher in human RBCs, whereas AMP and carnosine were significantly lower in humans compared to NHPs (**Figure 1D**). We also observed metabolic divergences between baboons and macaques. For example, pyridoxal was significantly lower in baboons, whereas macaques had comparable levels to humans (**Figure 1D**). In other cases, metabolic differences that we had previously reported in the comparison of macaques and humans (Stefanoni et al., 2020) (e.g., arginine), were further increased in baboon RBCs and significantly greater than macaques (**Figure 1D**). Other metabolites (e.g., UDP-glucose in the hexosamine pathway) were higher in macaque RBCs than in humans or baboons, which had similar levels of this metabolite (**Figure 1D**).

Species-Specific Metabolic Differences Were Enhanced by Storage Under Blood Bank Conditions

Red blood cell storage in blood banks is critically important for therapeutic purposes; however, RBC storage induces many metabolic changes affecting energy and redox metabolism, membrane function, tissue oxygenation, and cellular communication (Yoshida et al., 2019). Because these pathways differed in humans, compared to NHPs, in fresh RBCs, we hypothesized that they would be further aggravated by storage for 42 days, the shelf-life of packed RBCs in the United States and most European countries. Metabolomics analyses were performed on samples collected weekly by sterile docking of units from Storage Day 0 through 42 (**Figure 2A**). Analyses were performed on 854 samples [n = 61 (20 baboons, 20 macaques, and 21 humans) each for seven storage time points for RBCs and supernatants], which were clustered on the basis of their metabolic phenotypes in the PCA (**Figure 2B**). PC1 showed a significant impact of storage duration (from left to right—storage days 0–42; **Figure 2B**), explaining 24.5% of the total variance. However, PC2 and PC3 still explained > 14% of the residual variance, with human RBCs clustering closer to macaques than baboons throughout storage.

In the heat map in **Figure 2C**, the most significant metabolites and time-dependent %hemolysis comparisons were evaluated by repeated measures two-way ANOVA (**Supplementary Table 1**) and were grouped by general metabolic pathways. Further comparisons between baboon and human %hemolysis were evaluated using a Student's *t*-test or a by one-way ANOVA with Holm–Sidak's multiple-comparison test to compare %hemolysis across the three species. A vectorial version of this figure is provided as **Supplementary Figures 2**, **3** for RBCs and supernatants, along with metabolite names. Major patterns in these time-series data as a function of the species were identified via ANOVA simultaneous component analysis (ASCA—**Supplementary Table 1**). Some of the metabolites that are differentially impacted across

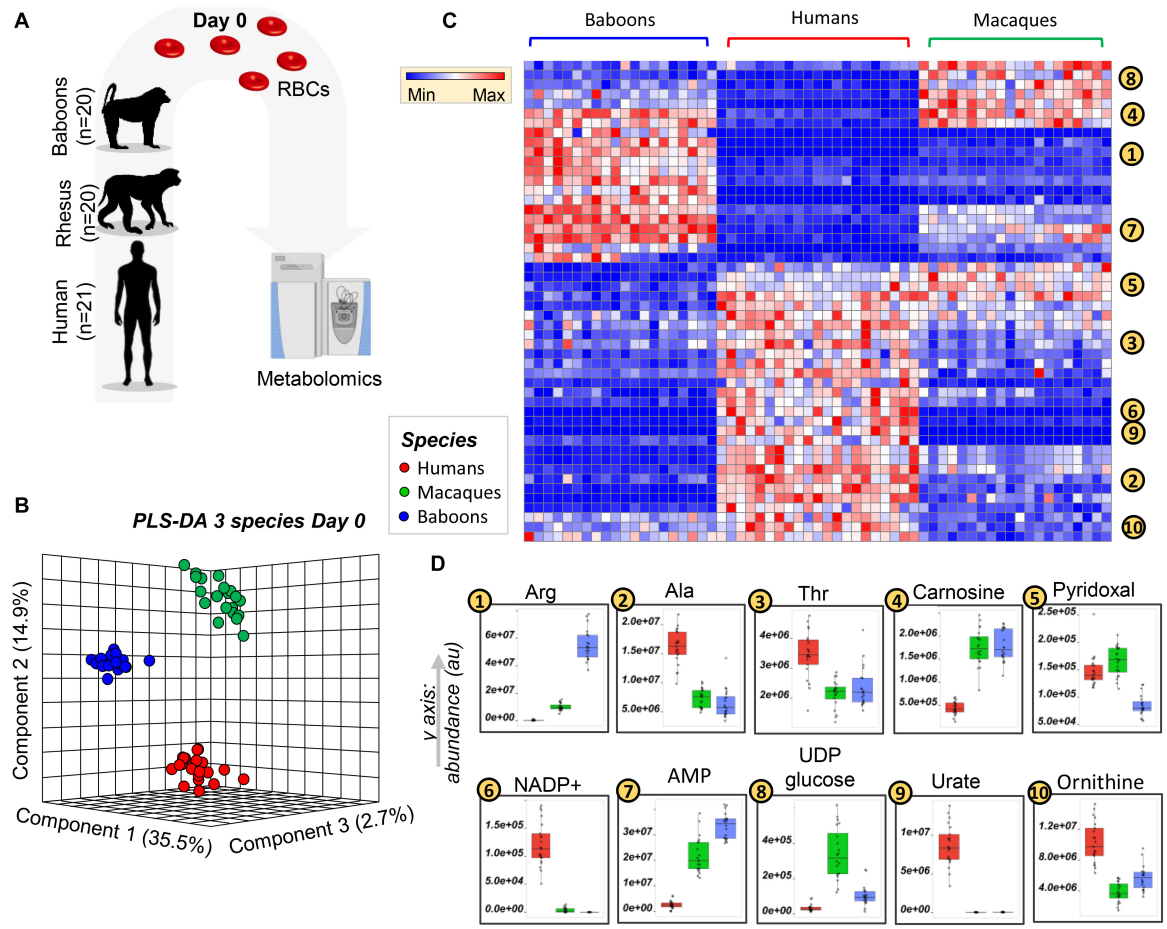

FIGURE 1 | Metabolic phenotypes of freshly drawn human (red), macaque (green), and baboon (blue) red blood cells (RBCs) were tested via ultrahigh-pressure liquid chromatography-mass spectrometry (UHPLC-MS)-based metabolomics approaches **(A)**. Partially supervised partial least square-discriminant analysis (PLS-DA; **B**) and hierarchical clustering analysis **(C)** of the metabolomics data indicate a significant difference between human and NHP RBCs (PC1: 35.5% of the total variance), and between macaque and baboon RBCs (PC2: 14.9% of the total variance; **B**). **(D)** Several representative metabolites, among the top significant changes at baseline, across species, as determined by ANOVA.

species as a function of storage are representatively grouped into classes in **Figure 2C**. While intracellular fatty acids and phosphatidylethanolamines were comparable across species during storage, supernatant levels of lipids were the lowest in humans and highest (and increased during storage) in macaques; nonetheless, baboons unexpectedly had the highest levels of carnitine-conjugated fatty acids in the supernatants (**Figure 2C**).

Species-Specific Metabolic Changes Throughout Storage

To expand on the unsupervised analyses described above, line plots (median $\pm$ quartile ranges) were plotted for human (red), baboon (blue), and macaque (green) RBCs for different pathways, including glycolysis and glutamine/glutathione metabolism (**Figure 3**), purine, arginine, and carboxylic acid/transaminase metabolism (**Figures 4A–C**, respectively), and fatty acids and acyl-carnitines (**Figure 5**). Detailed statistics including fold changes, ANOVA, and ASCA analyses are reported in **Supplementary Table 1**.

Baboon RBCs had the lowest levels of glucose, glycolytic, and pentose phosphate pathway intermediates and byproducts (lactate and ribose phosphate isomers) throughout storage, whereas humans had the highest (though not significantly higher than macaques; **Figure 3**). Human RBCs had the highest levels of reduced glutathione (GSH) and the lowest of oxidized glutathione (GSSG), which was significantly higher in macaques compared to baboons (**Figure 3**). In contrast, baboons had the highest levels of 5-oxoproline, an activation marker of the gamma-glutamyl cycle (**Figure 3**). Compared to humans, baboons and macaques both had significantly higher markers of glutaminolysis (low extracellular glutamine, high intracellular or extracellular glutamate for baboons and macaques, respectively). Further alterations in sulfur metabolism were noted in NHPs. For example, levels of the antioxidant taurine were highest in baboons throughout storage; however, methionine and *S*-adenosylmethionine levels were significantly lower in baboons,

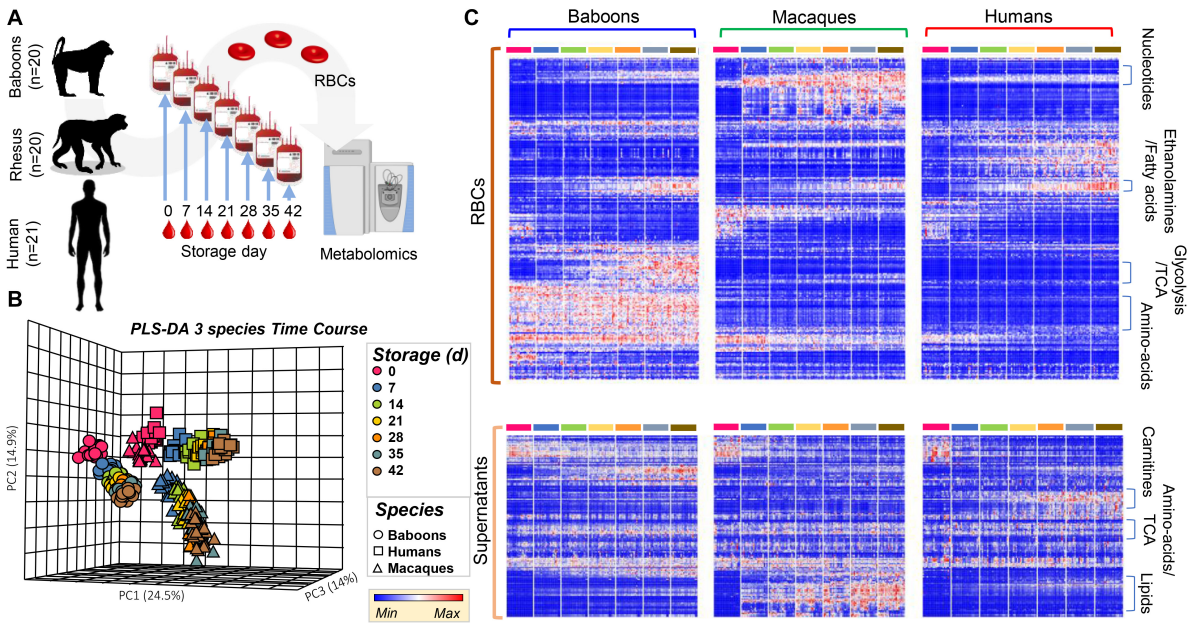

FIGURE 2 | Metabolic phenotypes of human (red), macaque (green), and baboon (blue) RBCs and supernatants during refrigerated storage under blood bank conditions **(A)**. Units were tested weekly, from storage day 0 until the end of the shelf-life (storage day 42). Partially supervised PLS-DA **(B)** and hierarchical clustering analysis **(C)** of the metabolomics data indicate a significant difference between human and non-human primate (NHP) RBCs (PC1: 24.5% of the total variance), and between macaque and baboon RBCs (PC2: 14.9%) and storage duration (14%; **B**). In **(C)**, heat maps indicate significant metabolic changes during storage across species, as determined by repeated measures ANOVA, for RBCs (top) and supernatants (bottom).

suggesting a decreased capacity to repair isoaspartyl damage compared to human and macaque RBCs (**Figure 3**). Analysis of purine metabolism revealed significantly higher levels of methylthioadenosine in baboons, compared to the other species, suggesting an increased activation of salvage pathway *S*-adenosyl metabolites. Conversely, humans had the highest levels of deaminated purine products: IMP, urate [a potent antioxidant (Tzounakas et al., 2015), which was barely detectable in NHPs], 5-hydroxyisourate, and allantoate, with the notable exception of hypoxanthine, which was highest in NHPs (**Figure 4A**). Although we previously reported an effect of sex on this pathway in macaques and humans (Stefanoni et al., 2020) (e.g., the hypoxanthine guanosine phosphoribosyl transferase gene X-linked), only minor, but significant, sex-associated differences were noted in hypoxanthine and allantoate levels in baboons (female > male) during storage (**Supplementary Figure 4A**).

The most notable metabolic change was that baboons had the highest levels of arginine, citrulline, ornithine, and creatine (**Figure 4B**), with ornithine/arginine (a marker of arginase activity) (D'Alessandro et al., 2019a) and citrulline/arginine ratios (a marker of nitric oxide synthase activity) (Kleinbongard et al., 2006) being higher in females and males, respectively (**Supplementary Figure 4B**). Despite having the lowest levels of arginine, human RBCs consistently had the second highest levels of citrulline throughout storage and the highest citrulline/arginine ratios (a marker of nitric oxide synthase activity). To validate this observation further, fresh RBC lysates from these species were incubated with 5 mM $^{13}C_6{}^{15}N_4$-arginine for 5 min and 24 h at 37°C (**Supplementary Figure 5A**). As expected, no residual urea cycle activity was observed in any species (i.e., no isotopolog $^{13}C_5{}^{15}N_2$-citrulline was detected), consistent with the absence of mitochondria in mature RBCs. However, significant arginase activity was seen in humans ($^{13}C_5{}^{15}N_2$-ornithine detected as > 80% of the total after 24 h in humans—**Supplementary Figure 5C**) and nitric oxide synthase activity in all species—in particular, macaques (**Supplementary Figure 5C**), were observed, resulting in the generation of $^{13}C_6{}^{15}N_3$-citrulline. Overall, when normalized to the total levels of labeled arginine detected as a percentage of the total (**Supplementary Figure 5C**), our results indicate that human RBCs have significantly higher arginase activity, and lower nitric oxide synthase activity, than macaques and baboons.

Human RBCs also had the highest transaminase activity (as inferred by the levels of the metabolic products of the activity of these enzymes—e.g., alanine, aspartate—and consumption of glutamate), but the lowest levels of carboxylic acid products of transamination reactions (e.g., alpha-ketoglutarate and related citrate and succinate), which were comparable between NHPs (**Figure 4C**). On the other hand, the highest levels of fumarate and malate in human RBCs are consistent with increased purine deamination and, perhaps, salvage in comparison to NHPs (**Figure 4C**). Finally, human RBCs had the highest levels of free carnitine and long-chain acyl-carnitines (14 carbon atoms or longer) throughout storage, followed by baboons (**Figure 5A**), especially males (**Supplementary Figure 6**). Although macaque RBCs had significantly lower levels of acyl-carnitines throughout storage, they had the highest levels of free fatty acids, from 7 to 18 carbon atoms (**Figure 5A**). In

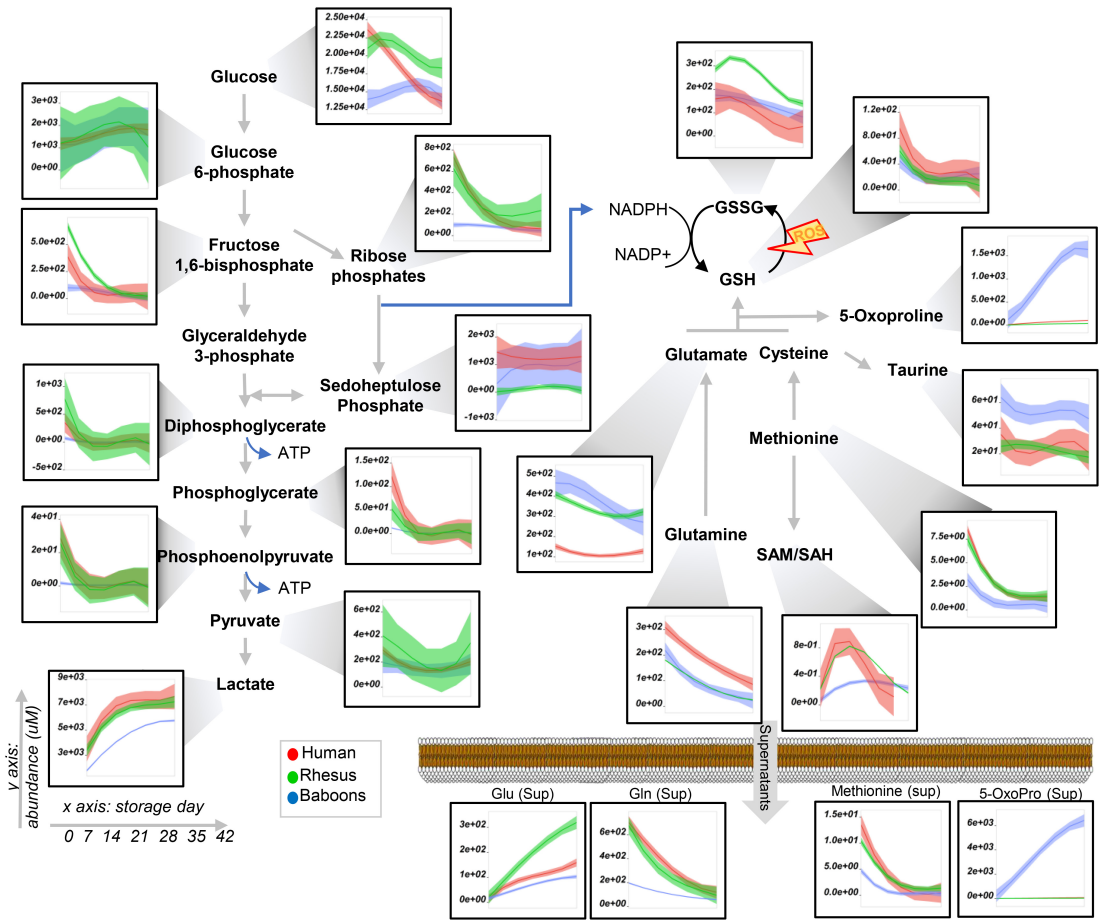

FIGURE 3 | Glycolysis and pentose phosphate pathway, glutathione, and methionine metabolism in human (red), macaques (green), or baboon (blue) RBCs from storage days 0 to 42. Line plots indicate median (n = 20) ± quartile ranges for all the groups. Y axis represents peak areas (arbitrary units) normalized to the median of week 0 measurement for each independent species. Extensive statistical analyses, including fold changes and repeated measures ANOVA, are provided in **Supplementary Table 1**.

contrast, human RBCs had increased levels of polyunsaturated fatty acids and lower levels of oxylipins, which were highest in baboons [hydroxyeicosatetraenoic acids (HETEs)] and macaques [hydroxyoctadecenoic acids (HODEs)] (**Figure 5B**). Macaque and human RBCs had the highest levels of sphingosine 1-phosphate (**Figure 5C**).

Human RBCs Are Characterized by Lower Storage Hemolysis and Morphological Alterations

Considering the differences in lipid metabolism in stored RBCs and supernatants across these species, we anticipated a lower rate of vesiculation and a lower severity of the storage lesion (based on RBC morphology and hemolysis *in vitro*) with human RBCscompared to NHPs. Storage hemolysis increased progressively in baboons, with more than half demonstrating hemolysis levels ≥ 1% at storage day 42 (i.e., above the Food and Drug Administration quality threshold; **Figure 6A**). This was similar in baboons and macaques, whereas all human RBC samples had 42-day hemolysis values of < 1% (**Figure 6B**). By scanning electron microscopy, by storage day 42, > 70% of baboon RBCs had lost their discocytic phenotype (**Figure 6C**). Macaque RBCs were similar, with 80% loss of the discocytic phenotype by storage day 42 (**Supplementary Figure 7**). Unlike the NHPs, human RBCs had a better-preserved morphology, with > 70% discocytes on storage day 42 (**Supplementary Figure 7**), consistent with the patterns of storage hemolysis across these three species.

Common and Divergent Metabolic Correlates to Species-Specific Hemolysis

We performed correlation analyses (**Figure 7A**) of end of storage metabolites with storage hemolysis (**Figure 7B**). This metabolic linkage analysis (D'Alessandro et al., 2017a) provides further, unsupervised, data-driven insights into the metabolic wiring of RBCs evaluated in this study and provides additional correlative evidence of their potential contributions to RBC

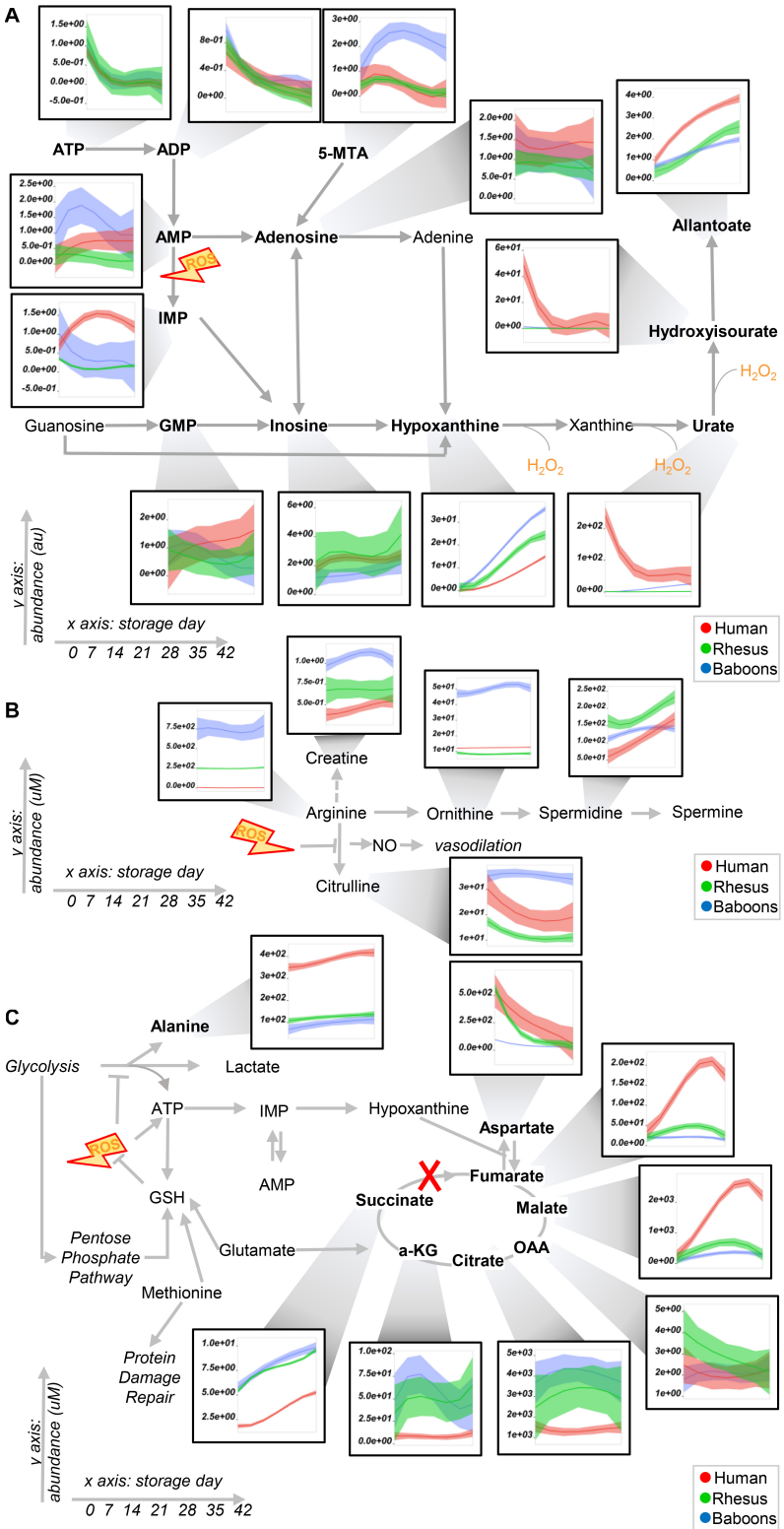

FIGURE 4 | Purine **(A)** and arginine **(B)** metabolism, transaminases, and carboxylic acids **(C)** in human (red), macaque (green), or baboon (blue) RBCs from storage days 0 to 42. Line plots indicate median (n = 20) ± quartile ranges for all the groups. Y axis represents peak areas (arbitrary units) normalized to the median of week 0 measurement for each independent species. Extensive statistical analyses, including fold changes and repeated measures ANOVA are provided in **Supplementary Table 1**.

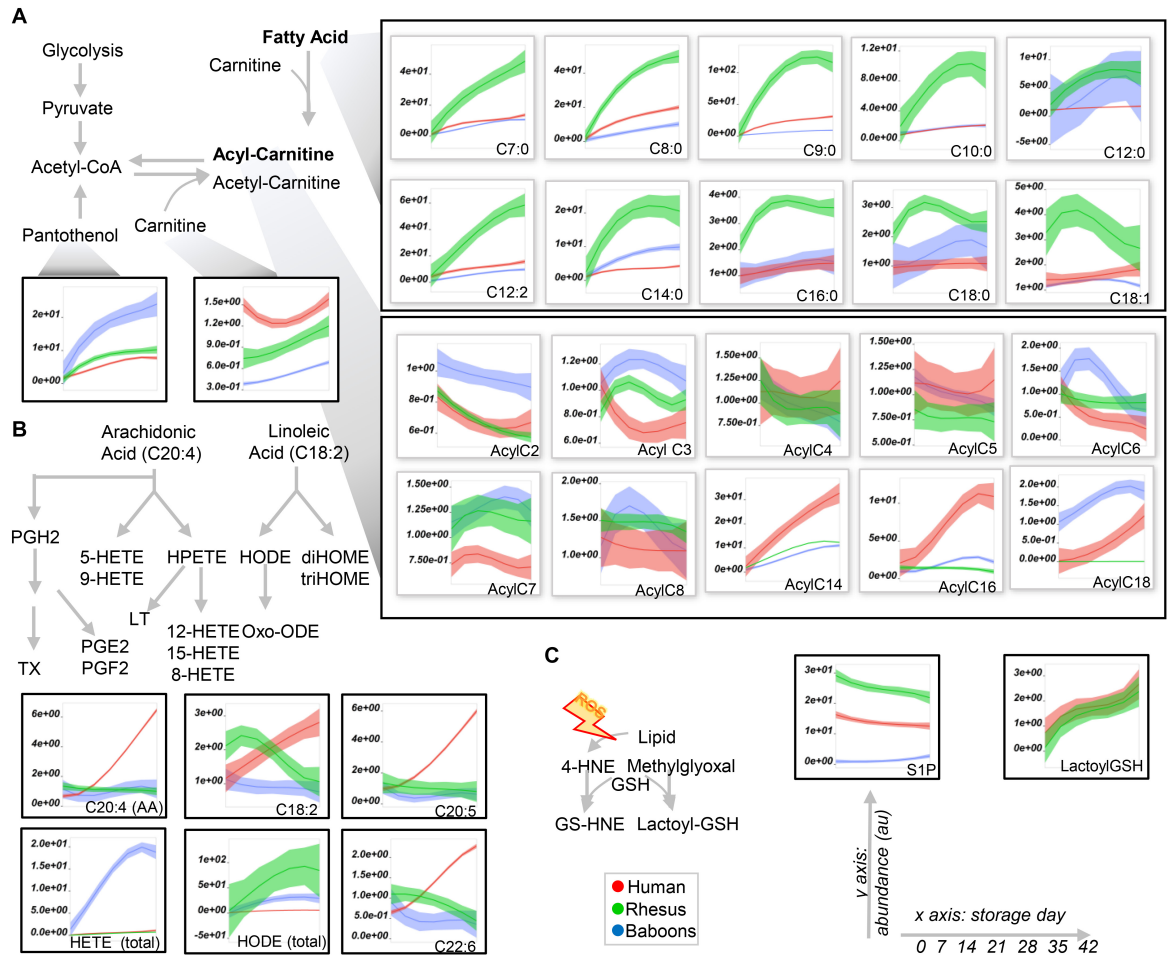

FIGURE 5 | Fatty acid (top), acyl-carnitine (bottom; **A**), eicosanoids **(B)**, and glyoxylate and sphingosine 1-phosphate (S1P) metabolism in human (red), macaque (green), or baboon (blue) RBs from storage days 0 to 42. In **(A,B)**, abbreviations indicate the length in carbon atoms (**C**) of the fatty acid chain and the number of desaturations. The prefix "Acyl-" is used to denote acyl-carnitines in **(A)**. Line plots indicate median (n = 20) ± quartile ranges for all the groups. Y axis represent peak areas (arbitrary units) normalized to the median of week 0 measurement for each independent species. Extensive statistical analyses, including fold changes and repeated measures ANOVA are provided in **Supplementary Table 1**.

hemolysis mechanisms. Thus, in human and macaque RBCs, strong correlations were preserved between the metabolite levels involved in *S*-adenosylmethionine-dependent protein damage repair mechanisms, purine metabolism (except for urate), and glutathione and pentose phosphate pathway homeostasis (**Figure 7C**). In contrast, human RBCs were more comparable to baboons regarding short-chain fatty acid metabolism, whereas long-chain and polyunsaturated fatty acid metabolism was similar between macaques and baboons (**Figure 7C**, bottom half). These observations are consistent with our prior findings identifying several polyunsaturated fatty acids among the top negative correlates of storage hemolysis (**Figure 7D**). Therefore, this was further leveraged in **Figure 7C** to rank species-specific metabolic correlates to hemolysis (in tabular form in **Supplementary Table 1**). Notably, as in our prior studies, deaminated purines, including IMP, positively correlated with hemolysis in human RBCs, while urate negatively correlated (**Figure 7E**). However, this observation was only partially recapitulated in baboons and macaques, with a positive correlation of hypoxanthine with hemolysis in both species, but a negative correlation with the hypoxanthine precursor, IMP, or the downstream oxidation product, urate, in baboon and macaque RBCs, respectively (**Figure 7E**). This suggests species-specific biochemistry (at the structural, expression, or functional level) in xanthine dehydrogenase oxidase, AMP deaminase 3 (AMDP3), or hypoxanthine guanosine-phosphoribosyltransferase (HGPRT). Although no species-specific polymorphisms were noted around the active sites in AMPD3 (99% homology across species) and HGPRT (100% sequence homology), some potentially relevant polymorphisms around the active site (residues 803E and 881R) were seen in XDH, despite ∼97% sequence homology across the three species (**Supplementary Figure 8**). Similar changes in correlation trends to storage hemolysis across these species were seen with carboxylic acids, such as malate and fumarate (positive correlation with hemolysis in humans, but negative correlations

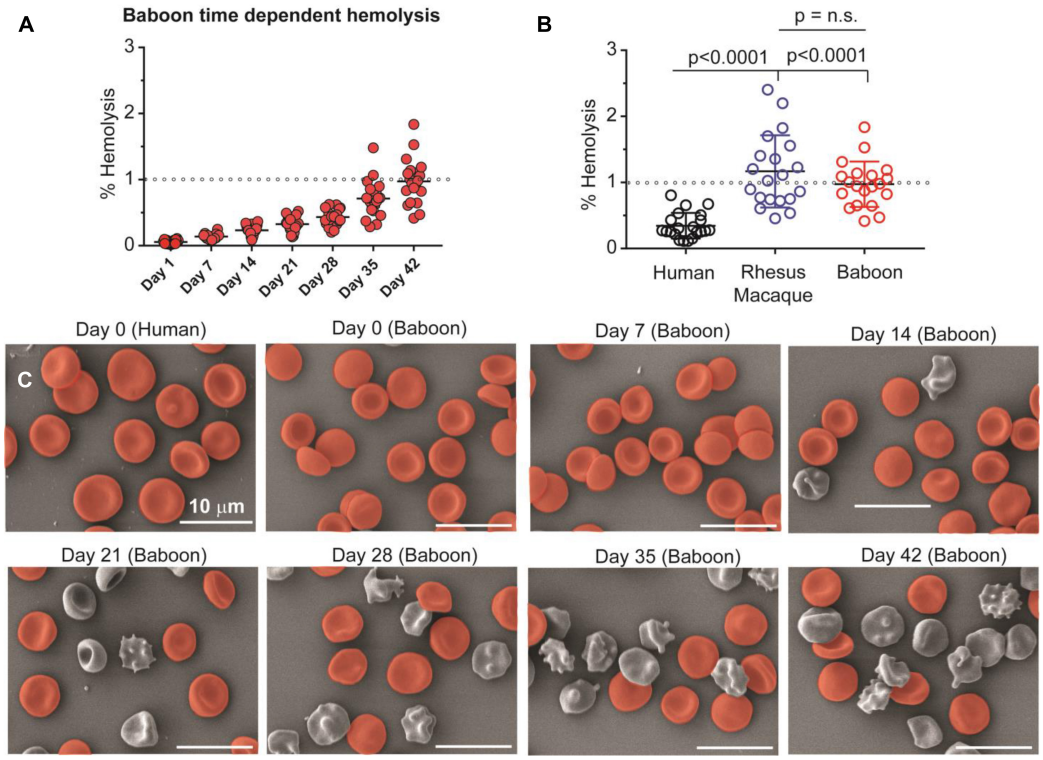

FIGURE 6 | Spontaneous hemolysis as a function of storage duration in baboons **(A)** and an interspecies comparison of end of storage hemolysis **(B)**. NHPs have significantly higher end-of-storage hemolysis than humans, with individual macaques showing the most variability and the greatest maximum individual hemolysis levels. Collectively, mean hemolysis levels between baboons and macaques were similar (p = 0.231, n.s.). Scanning electron micrographs **(C)** are shown for human (day 0) and baboon (weekly) RBCs as a function of storage duration (discocytes in red; echinocytes, spheroechinocytes, acanthocytes, stomatocytes, and spherocytes in gray). Days 0 and 42 equivalent micrographs for human and macaque RBCs are provided as **Supplementary Figure 6**.

in NHPs). Additionally, polyunsaturated fatty acids negatively correlated with hemolysis in human and baboon RBCs, but were positively correlated in macaques (**Figure 7F**).

DISCUSSION

The present study describes significant metabolic, morphological, and storage hemolysis changes between fresh and stored RBCs from human donors and old-world monkeys, specifically olive baboons and rhesus macaques. Baseline metabolic changes were further enhanced by refrigerated storage under standard blood bank conditions. In prior studies, we showed that RBCs undergo alterations to energy and redox metabolism during refrigerated storage (Cancelas et al., 2015; Rolfsson et al., 2017; D'Alessandro et al., 2018). The so-called metabolic "storage lesion" varies across blood donors (D'Alessandro et al., 2019b), with RBCs from some donors being more susceptible to hemolysis *in vitro* or upon oxidant, mechanical, or osmotic challenge applied at the end of their shelf-life (Kanias et al., 2017). The metabolic storage lesion ultimately impacts the tissue metabolome of healthy autologous transfusion recipients (D'Alessandro et al., 2019a) or in sickle-cell disease patients undergoing RBC exchange transfusion (Gehrke et al., 2019). These observations were phenocopied in rodent models of blood storage and transfusion (Howie et al., 2019), providing evidence *in vivo* of the dysregulation of RBC viability, recovery, systemic iron exposure, and redox metabolism in the initial 24 h after transfusion (Gehrke et al., 2019). Further, storage-induced alteration of purine deamination, and subsequent metabolism by AMP deaminase 3 and xanthine dehydrogenase/oxidase, predicted the ability of transfused RBCs to circulate in the recipient (Nemkov et al., 2018b). Although prestorage levels of urate, a major circulating antioxidant, were associated with improved RBC storage quality (Tzounakas et al., 2015), the levels of its precursor (i.e., hypoxanthine) were negatively associated with the preservation of energy metabolism in stored RBCs and predict accelerated RBC removal post-transfusion (Nemkov et al., 2018b). In the present study, metabolites of the purine deamination pathway were the most divergent when comparing human and NHP RBCs; human RBCs had an order of magnitude higher levels of urate both at baseline and after refrigerator storage. Of note, although such differences had been reported in plasma studies (Misra et al., 2018) involving baboons, the impact of this RBC phenotype change had not been described in relation to RBC storage quality. This observation can be explained by species-specific peculiarities in urate metabolism, which would end up affecting the circulating levels of this metabolite and, as a consequence, RBC urate concentration

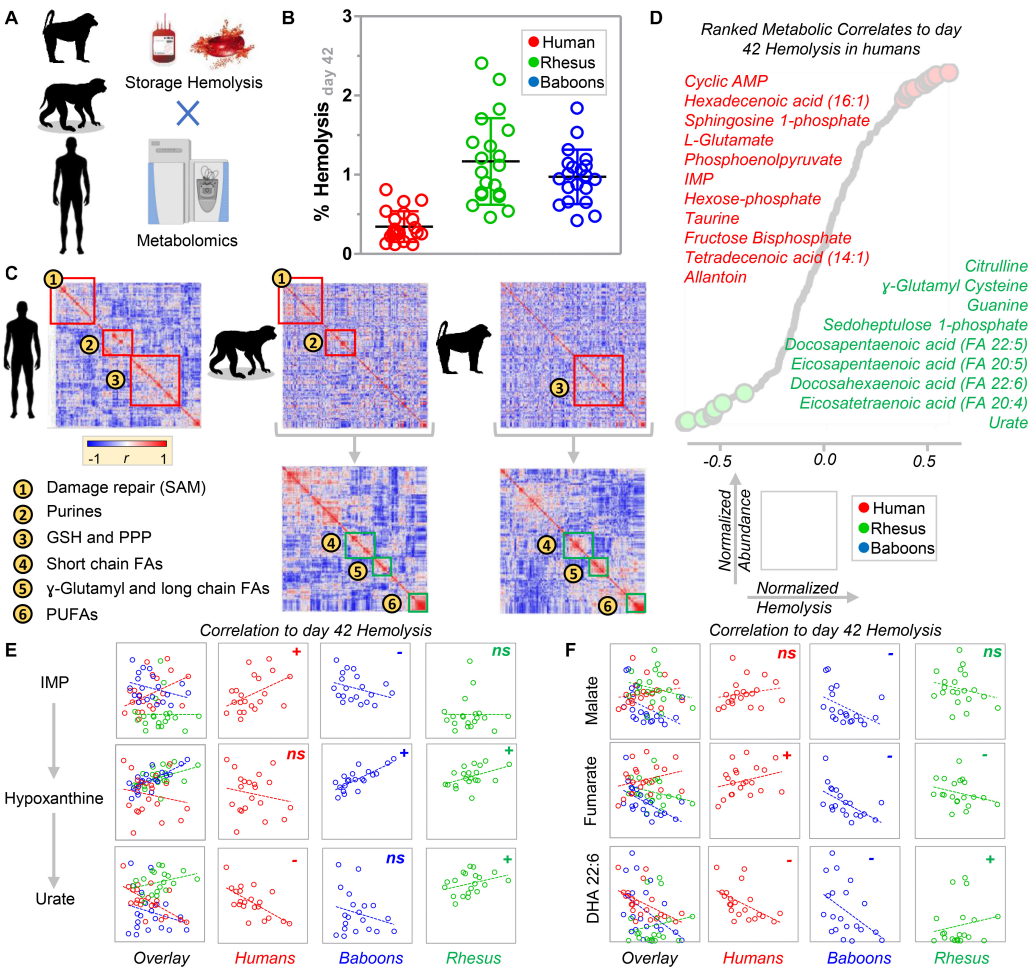

FIGURE 7 | Determination of species-specific metabolic correlates to end of storage hemolysis in baboons, macaques, and humans **(A)**. **(B)** A side-by-side comparison of end of storage hemolysis across the three species. Significantly lower hemolysis was observed in human RBCs. **(C)** Metabolic linkage analysis (i.e., correlation of metabolites to metabolites) in humans, macaques, and baboons [the latter two maintaining the clustered order from human metabolic linkage analyses (i.e., top) or performing species-specific correlations (i.e., bottom)]. These analyses highlighted groups of metabolites and related metabolic pathways that are preserved between humans and macaques, humans and baboons, or baboons and humans. **(D)** A ranked list of metabolic correlates to hemolysis in humans. Based on the analyses described above, a few representative metabolites were plotted that significantly correlated to hemolysis in one species, but not (or inversely correlated) in both of the other two species tested, including purine oxidation metabolites **(E)**, carboxylic acids, and polyunsaturated fatty acids **(F)**.

at the time of blood drawn. In addition, since one of the enzymes involved in hypoxanthine recycling into guanosine (i.e., HGPRT) is encoded by an X-linked gene, it is interesting to note a marginal, but significant, effect of sex on hypoxanthine accumulation across the primate species evaluated here and in previous comparisons between human and macaque RBCs (Stefanoni et al., 2020).

A possible explanation of the divergencies in this pathway across these species is provided by appreciating the polymorphisms in the genes coding for xanthine oxidase in old-world monkeys, compared to humans, as indicated by polymorphisms that mapped within 20 amino acids the active sites of this enzyme (E803 and R881). Increases in carboxylic acid metabolites in macaque and baboon RBCs, compared to humans, along with increases in 5-methylthioadenosine, are consistent with greater purine salvage reactions in NHPs, which may explain the observed decreases in purine deamination products.

Prior studies of macaque RBC storage observed alterations in free fatty acids, acyl-carnitines, and phosphatidylserines, compared in stored human RBCs. Herein, we expanded on these findings by confirming increases in storage-induced hemolysis and morphologic changes in this species, compared to humans. In addition to confirming similar metabolic, hemolytic, and morphological dysregulation in baboon RBCs, we identified unique alterations of lipid oxidation and remodeling (e.g., via carnitine conjugation and the Lands cycle) (Wu et al., 2016) between baboons and macaques. Alterations in this pathway (especially with respect to fatty acyl-compositions) may at least be in part explained by species-specific diets (Stefanoni et al., 2020).

Perhaps one of the most translationally relevant observations in this study is the divergent metabolism of arginine in

human RBCs, compared to baboons and macaques. Arginine conversion to citrulline by an RBC-specific nitric oxide synthase (Kleinbongard et al., 2006) was proposed to contribute to system-wide NO metabolism and, thus, vasodilation. Conversely, arginine metabolism by arginase 1, which is also present and functional in mature RBCs (D'Alessandro et al., 2019a), generates ornithine without the net production of vasoactive NO. Increased arginase-1 activity in the RBCs of patients with Type 2 diabetes is associated with superoxide production and accelerated endothelial dysfunction (Yang et al., 2018; Mahdi et al., 2019; Pernow et al., 2019), suggesting a link between increased RBC arginase-1 activity and CVD. We previously showed that macaque RBCs had significantly higher levels of arginine and its catabolites, compared to human RBCs. To understand this observation further, herein we combined steady state measurements and metabolic tracing with $^{13}C^{15}N$-arginine to show that baboon RBCs have an order of magnitude higher levels of arginine, creatine, and ornithine than macaque RBCs. However, human RBCs had significantly higher steady state levels of citrulline than macaques and significantly higher labeled ornithine (suggestive of higher arginase activity), compared to both NHPs. This observation is critical in light of the central role of this pathway in cardiovascular studies, suggesting caution when interpreting (Havel et al., 2017) CVD studies focusing on NO signaling in baboons and macaques. In addition, these observations cannot be explained by polymorphisms in arginase 1 (>98% sequence homology across the three species) or NO synthase. On the other hand, expression levels and/or activity of arginase may vary across these species as a result of regulatory alterations that has evolved under positive pressure, as classic comparative biology studies report a 957 ± 206 μmol urea/g of hemoglobin/h arginase activity in human RBCs compared to < 1 in *Papio* baboon species (Spector et al., 1985). Moreover, sex dimorphisms in this pathway that were seen previously in human tissues (Reckelhoff et al., 1998) and RBCs (Contreras-Zentella et al., 2019), and macaque RBCs (Stefanoni et al., 2020), are also observed in baboons.

Finally, levels of amino acids involved in transamination reactions were increased in human RBCs, compared to NHPs, with increased glutaminolysis and glutamate consumption in stored human RBCs as storage progressed. Similarly, human and macaque RBCs showed comparable levels of methionine (a marker of oxidant stress and protein isoaspartyl damage-repair in mature RBCs) (Reisz et al., 2018). In contrast, baboon RBCs coped with oxidant stress through activating the gamma-glutamyl cycle (5-oxoproline levels were two orders of magnitude higher in this species compared to macaques and humans) and taurine, a dietary antioxidant that only lower mammals (e.g., rodents, cats) are thought to be capable of synthesizing (Ripps and Shen, 2012).

CONCLUSION

Despite the observational nature of the study, we provide the first comparative metabolomics analysis of fresh and stored human, baboon, and macaque RBCs. The results indicated similarities and differences across species, which ultimately resulted in a differential propensity to undergo morphological alterations and lyse as a function of the duration of refrigerated storage. Focusing on purine oxidation and carboxylic acids, fatty acids, and arginine metabolism, we further highlighted species-specific metabolic wiring (e.g., increased arginine catabolism into citrulline and ornithine in humans) and correlations with storage-induced hemolysis. Notably, while RBCs from these NHPs had been reported to have similar *in vivo* lifespan to human RBCs (Valeri et al., 2002; Kaestner and Minetti, 2017), the increased susceptibility to hemolysis during storage may result from the appreciation that current storage additives have been optimized for human RBCs, a caveat that may be relevant for future transfusion medicine studies using NHPs as a model.

DATA AVAILABILITY STATEMENT

All datasets generated for this study are included in the article/**Supplementary Material**.

ETHICS STATEMENT

The studies involving human participants were reviewed and approved by NIH study IRB #99-CC-0168 "Collection and Distribution of Blood Components from Healthy Donors for In Vitro Research Use" under an NIH-FDA material transfer agreement and in compliance with the Declaration of Helsinki. The patients/participants provided their written informed consent to participate in this study. The animal study was reviewed and approved by FDA White Oak Animal Care and Use protocol 2018-31.

AUTHOR CONTRIBUTIONS

HS, JB, and PB collected and stored the samples. TY, SS, PB, and AD'A provided the essential materials and methods to perform the study. PB and YG performed the hemolysis and SEM evaluation of RBCs. LB, EM, DS, TN, and AD'A performed the metabolomics analyses (untargeted and targeted quantitative) and tracing experiments. LB and AD'A performed the data analysis and prepared the figures and tables. AD'A, PB, and SS wrote and modified the first draft of the manuscript, which was revised by all the other authors, including MK, JS, TT, JZ, EH, RF, and KH. All the authors contributed to the finalizing of the manuscript.

FUNDING

Research reported in this publication was supported by funds from the Boettcher Webb-Waring Investigator Award (AD'A, JZ, and SS), RM1GM131968 by the National Institute of General Medical Sciences (AD'A), R01HL146442, R01HL149714, and

R01HL148151 by the National Heart, Lung and Blood Institute (AA, JZ, and SS). Zoomics was part of the project MIRAGES: Metabolic Investigation of Red blood cells as a function of Aging, Genetics and Environment sponsored by the National Heart, Lung and Blood Institute (R21HL150032 to AD'A).

SUPPLEMENTARY MATERIAL

The Supplementary Material for this article can be found online at: https://www.frontiersin.org/articles/10.3389/fphys.2020.593841/full#supplementary-material

REFERENCES

Agrawal, S., Kumar, S., Sehgal, R., George, S., Gupta, R., Poddar, S., et al. (2019). El-MAVEN: a fast, robust, and user-friendly mass spectrometry data processing engine for metabolomics. *Methods Mol. Biol. Clifton N. J.* 1978, 301–321. doi: 10.1007/978-1-4939-9236-2_19

Baek, J. H., Yalamanoglu, A., Gao, Y., Guenster, R., Spahn, D. R., Schaer, D. J., et al. (2017). Iron accelerates hemoglobin oxidation increasing mortality in vascular diseased guinea pigs following transfusion of stored blood. *JCI Insight* 2:e93577. doi: 10.1172/jci.insight.93577

Baek, J. H., Yalamanoglu, A., Moon, S.-E., Gao, Y., and Buehler, P. W. (2018). Evaluation of renal oxygen homeostasis in a preclinical animal model to elucidate difference in blood quality after transfusion. *Transfusion* 58, 1474–1485. doi: 10.1111/trf.14560

Bennett-Guerrero, E., Veldman, T. H., Doctor, A., Telen, M. J., Ortel, T. L., Reid, T. S., et al. (2007). Evolution of adverse changes in stored RBCs. *Proc. Natl. Acad. Sci. U.S.A.* 104, 17063–17068. doi: 10.1073/pnas.0708160104

Cancelas, J. A., Dumont, L. J., Maes, L. A., Rugg, N., Herschel, L., Whitley, P. H., et al. (2015). Additive solution-7 reduces the red blood cell cold storage lesion. *Transfusion* 55, 491–498. doi: 10.1111/trf.12867

Chen, Y., Qin, S., Ding, Y., Wei, L., Zhang, J., Li, H., et al. (2009). Reference values of clinical chemistry and hematology parameters in rhesus monkeys (*Macaca mulatta*). *Xenotransplantation* 16, 496–501. doi: 10.1111/j.1399-3089.2009.00554.x

Chong, J., Soufan, O., Li, C., Caraus, I., Li, S., Bourque, G., et al. (2018). MetaboAnalyst 4.0: towards more transparent and integrative metabolomics analysis. *Nucleic Acids Res.* 46, W486–W494. doi: 10.1093/nar/gky310

Clendenen, N., Nunns, G. R., Moore, E. E., Reisz, J. A., Gonzalez, E., Peltz, E., et al. (2017). Hemorrhagic shock and tissue injury drive distinct plasma metabolome derangements in swine. *J. Trauma Acute Care Surg.* 83, 635–642. doi: 10.1097/TA.0000000000001504

Contreras-Zentella, M. L., Sánchez-Sevilla, L., Suárez-Cuenca, J. A., Olguín-Martínez, M., Alatriste-Contreras, M. G., García-García, N., et al. (2019). The role of oxidant stress and gender in the erythrocyte arginine metabolism and ammonia management in patients with type 2 diabetes. *PLoS One* 14:e0219481. doi: 10.1371/journal.pone.0219481

Cox, L. A., Comuzzie, A. G., Havill, L. M., Karere, G. M., Spradling, K. D., Mahaney, M. C., et al. (2013). Baboons as a model to study genetics and epigenetics of human disease. *ILAR J.* 54, 106–121. doi: 10.1093/ilar/ilt038

D'Alessandro, A., Giardina, B., Gevi, F., Timperio, A. M., and Zolla, L. (2012). Clinical metabolomics: the next stage of clinical biochemistry. *Blood Transfus.* 10, s19–s24. doi: 10.2450/2012.005S

D'Alessandro, A., Nemkov, T., Reisz, J., Dzieciatkowska, M., Wither, M. J., and Hansen, K. C. (2017a). Omics markers of the red cell storage lesion and metabolic linkage. *Blood Transfus.* 15, 137–144. doi: 10.2450/2017.0341-16

D'Alessandro, A., Nemkov, T., Yoshida, T., Bordbar, A., Palsson, B. O., and Hansen, K. C. (2017b). Citrate metabolism in red blood cells stored in additive solution-3. *Transfusion* 57, 325–336. doi: 10.1111/trf.13892

D'Alessandro, A., Nemkov, T., Sun, K., Liu, H., Song, A., Monte, A. A., et al. (2016). AltitudeOmics: red blood cell metabolic adaptation to high altitude hypoxia. *J. Proteome Res.* 15, 3883–3895. doi: 10.1021/acs.jproteome.6b00733

D'Alessandro, A., Reisz, J. A., Culp-Hill, R., Korsten, H., van Bruggen, R., and de Korte, D. (2018). Metabolic effect of alkaline additives and guanosine/gluconate in storage solutions for red blood cells. *Transfusion* 58, 1992–2002. doi: 10.1111/trf.14620

D'Alessandro, A., Reisz, J. A., Zhang, Y., Gehrke, S., Alexander, K., Kanias, T., et al. (2019a). Effects of aged stored autologous red blood cells on human plasma metabolome. *Blood Adv.* 3, 884–896. doi: 10.1182/bloodadvances.2018029629

D'Alessandro, A., Zimring, J. C., and Busch, M. (2019b). Chronological storage age and metabolic age of stored red blood cells: are they the same? *Transfusion* 59, 1620–1623. doi: 10.1111/trf.15248

Doctor, A., and Stamler, J. S. (2011). Nitric oxide transport in blood: a third gas in the respiratory cycle. *Compr. Physiol.* 1, 541–568. doi: 10.1002/cphy.c090009

Fonseca, L. L., Alezi, H. S., Moreno, A., Barnwell, J. W., Galinski, M. R., and Voit, E. O. (2016). Quantifying the removal of red blood cells in *Macaca mulatta* during a Plasmodium coatneyi infection. *Malar. J.* 15:410. doi: 10.1186/s12936-016-1465-5

Fonseca, L. L., Joyner, C. J., Saney, C. L., Moreno, A., Barnwell, J. W., Galinski, M. R., et al. (2018). Analysis of erythrocyte dynamics in Rhesus macaque monkeys during infection with Plasmodium cynomolgi. *Malar. J.* 17:410. doi: 10.1186/s12936-018-2560-6

Fu, X., Felcyn, J. R., Odem-Davis, K., and Zimring, J. C. (2016). Bioactive lipids accumulate in stored red blood cells despite leukoreduction: a targeted metabolomics study. *Transfusion* 56, 2560–2570. doi: 10.1111/trf.13748

Gehrke, S., Shah, N., Gamboni, F., Kamyszek, R., Srinivasan, A. J., Gray, A., et al. (2019). Metabolic impact of red blood cell exchange with rejuvenated red blood cells in sickle cell patients. *Transfusion* 59, 3102–3112. doi: 10.1111/trf.15467

Harewood, W. J., Gillin, A., Hennessy, A., Armistead, J., Horvath, J. S., and Tiller, D. J. (1999). Biochemistry and haematology values for the baboon (Papio hamadryas): the effects of sex, growth, development and age. *J. Med. Primatol.* 28, 19–31. doi: 10.1111/j.1600-0684.1999.tb00085.x

Havel, P. J., Kievit, P., Comuzzie, A. G., and Bremer, A. A. (2017). Use and importance of nonhuman primates in metabolic disease research: current state of the field. *ILAR J.* 58, 251–268. doi: 10.1093/ilar/ilx031

Herman, C. M., Rodkey, F. L., Valeri, C. R., and Fortier, N. L. (1971). Changes in the oxyhemoglobin dissociation curve and peripheral blood after acute red cell mass depletion and subsequent red cell mass restoration in baboons. *Ann. Surg.* 174, 734–743. doi: 10.1097/00000658-197111000-00002

Howie, H. L., Hay, A. M., de Wolski, K., Waterman, H., Lebedev, J., Fu, X., et al. (2019). Differences in Steap3 expression are a mechanism of genetic variation of RBC storage and oxidative damage in mice. *Blood Adv.* 3, 2272–2285. doi: 10.1182/bloodadvances.2019000605

Kaestner, L., and Minetti, G. (2017). The potential of erythrocytes as cellular aging models. *Cell Death Differ.* 24, 1475–1477. doi: 10.1038/cdd.2017.100

Kanias, T., Lanteri, M. C., Page, G. P., Guo, Y., Endres, S. M., Stone, M., et al. (2017). Ethnicity, sex, and age are determinants of red blood cell storage and stress hemolysis: results of the REDS-III RBC-Omics study. *Blood Adv.* 1, 1132–1141. doi: 10.1182/bloodadvances.2017004820

Kanias, T., Wang, L., Lippert, A., Kim-Shapiro, D. B., and Gladwin, M. T. (2013). Red blood cell endothelial nitric oxide synthase does not modulate red blood cell storage hemolysis. *Transfusion* 53, 981–989. doi: 10.1111/j.1537-2995.2012.03850.x

Klein, H. G. (2017). The red cell storage lesion(s): of dogs and men. *Blood Transfus.* 15, 107–111. doi: 10.2450/2017.0306-16

Kleinbongard, P., Schulz, R., Rassaf, T., Lauer, T., Dejam, A., Jax, T., et al. (2006). Red blood cells express a functional endothelial nitric oxide synthase. *Blood* 107, 2943–2951. doi: 10.1182/blood-2005-10-3992

Mahaney, M. C., Brugnara, C., Lease, L. R., and Platt, O. S. (2005). Genetic influences on peripheral blood cell counts: a study in baboons. *Blood* 106, 1210–1214. doi: 10.1182/blood-2004-12-4863

Mahdi, A., Jiao, T., Yang, J., Kövamees, O., Alvarsson, M., von Heijne, M., et al. (2019). The effect of glycemic control on endothelial and cardiac dysfunction induced by red blood cells in type 2 diabetes. *Front. Pharmacol.* 10:861. doi: 10.3389/fphar.2019.00861

McKenney, J., Valeri, C. R., Mohandas, N., Fortier, N., Giorgio, A., and Snyder, L. M. (1990). Decreased in vivo survival of hydrogen peroxide-damaged baboon red blood cells. *Blood* 76, 206–211.

Misra, B. B., Bassey, E., Bishop, A. C., Kusel, D. T., Cox, L. A., and Olivier, M. (2018). High resolution GC/MS metabolomics of non-human primate serum. *Rapid Commun. Mass Spectrom.* 32, 1497–1506. doi: 10.1002/rcm.8197

Nemkov, T., Hansen, K. C., and D'Alessandro, A. (2017). A three-minute method for high-throughput quantitative metabolomics and quantitative tracing experiments of central carbon and nitrogen pathways. *Rapid Commun. Mass Spectrom.* 31, 663–673. doi: 10.1002/rcm.7834

Nemkov, T., Hansen, K. C., Dumont, L. J., and D'Alessandro, A. (2016). Metabolomics in transfusion medicine. *Transfusion* 56, 980–993. doi: 10.1111/trf.13442

Nemkov, T., Reisz, J. A., Xia, Y., Zimring, J. C., and D'Alessandro, A. (2018a). Red blood cells as an organ? How deep omics characterization of the most abundant cell in the human body highlights other systemic metabolic functions beyond oxygen transport. *Expert Rev. Proteomics* 15, 855–864. doi: 10.1080/14789450.2018.1531710

Nemkov, T., Sun, K., Reisz, J. A., Song, A., Yoshida, T., Dunham, A., et al. (2018b). Hypoxia modulates the purine salvage pathway and decreases red blood cell and supernatant levels of hypoxanthine during refrigerated storage. *Haematologica* 103, 361–372. doi: 10.3324/haematol.2017.178608

Olivier, E. N., Wang, K., Grossman, J., Mahmud, N., and Bouhassira, E. E. (2019). Differentiation of baboon (*Papio anubis*) induced-pluripotent stem cells into enucleated red blood cells. *Cells* 8:1282. doi: 10.3390/cells8101282

Pernow, J., Mahdi, A., Yang, J., and Zhou, Z. (2019). Red blood cell dysfunction: a new player in cardiovascular disease. *Cardiovasc. Res.* 115, 1596–1605. doi: 10.1093/cvr/cvz156

Reckelhoff, J. F., Hennington, B. S., Moore, A. G., Blanchard, E. J., and Cameron, J. (1998). Gender differences in the renal nitric oxide (NO) system. *Am. J. Hypertens.* 11, 97–104. doi: 10.1016/S0895-7061(97)00360-9

Reisz, J. A., Nemkov, T., Dzieciatkowska, M., Culp-Hill, R., Stefanoni, D., Hill, R. C., et al. (2018). Methylation of protein aspartates and deamidated asparagines as a function of blood bank storage and oxidative stress in human red blood cells. *Transfusion* 58, 2978–2991. doi: 10.1111/trf.14936

Reisz, J. A., Slaughter, A. L., Culp-Hill, R., Moore, E. E., Silliman, C. C., Fragoso, M., et al. (2017). Red blood cells in hemorrhagic shock: a critical role for glutaminolysis in fueling alanine transamination in rats. *Blood Adv.* 1, 1296–1305. doi: 10.1182/bloodadvances.2017007187

Reisz, J. A., Zheng, C., D'Alessandro, A., and Nemkov, T. (2019). Untargeted and semi-targeted lipid analysis of biological samples using mass spectrometry-based metabolomics. *Methods Mol. Biol. Clifton N. J.* 1978, 121–135. doi: 10.1007/978-1-4939-9236-2_8

Reynolds, J. D., Jenkins, T., Matto, F., Nazemian, R., Farhan, O., Morris, N., et al. (2018). Pharmacologic targeting of red blood cells to improve tissue oxygenation. *Clin. Pharmacol. Ther.* 104, 553–563. doi: 10.1002/cpt.979

Rhesus Macaque Genome Sequencing and Analysis Consortium, Gibbs, R. A., Rogers, J., Katze, M. G., Bumgarner, R., Weinstock, G. M., et al. (2007). Evolutionary and biomedical insights from the rhesus macaque genome. *Science* 316, 222–234. doi: 10.1126/science.1139247

Ripps, H., and Shen, W. (2012). Review: taurine: a "very essential" amino acid. *Mol. Vis.* 18, 2673–2686.

Rolfsson, Ó, Sigurjonsson, ÓE., Magnusdottir, M., Johannsson, F., Paglia, G., Guðmundsson, S., et al. (2017). Metabolomics comparison of red cells stored in four additive solutions reveals differences in citrate anticoagulant permeability and metabolism. *Vox Sang.* 112, 326–335. doi: 10.1111/vox.12506

Seim, G. L., Britt, E. C., and Fan, J. (2019). Analysis of arginine metabolism using LC-MS and isotopic labeling. *Methods Mol. Biol. Clifton N. J.* 1978, 199–217. doi: 10.1007/978-1-4939-9236-2_13

Siepel, A. (2009). Phylogenomics of primates and their ancestral populations. *Genome Res.* 19, 1929–1941. doi: 10.1101/gr.084228.108

Spector, E. B., Rice, S. C., Hendrickson, R., and Cederbaum, S. D. (1985). Comparison of arginase activity in red blood cells of lower mammals, primates, and man: evolution to high activity in primates. *Am. J. Hum. Genet.* 7, 138–145.

Stefanoni, D., Shin, H. K. H., Baek, J. H., Champagne, D. P., Nemkov, T., Thomas, T., et al. (2020). Red blood cell metabolism in Rhesus macaques and humans: comparative biology of blood storage. *Haematologica.* 105, 2174–2186. doi: 10.3324/haematol.2019.229930

Tuo, W.-W., Wang, D., Liang, W.-J., and Huang, Y.-X. (2014). How cell number and cellular properties of blood-banked red blood cells of different cell ages decline during storage. *PLoS One* 9:e105692. doi: 10.1371/journal.pone.0105692

Tzounakas, V. L., Georgatzakou, H. T., Kriebardis, A. G., Papageorgiou, E. G., Stamoulis, K. E., Foudoulaki-Paparizos, L. E., et al. (2015). Uric acid variation among regular blood donors is indicative of red blood cell susceptibility to storage lesion markers: a new hypothesis tested. *Transfusion* 55, 2659–2671. doi: 10.1111/trf.13211

Valeri, C. R., Ellis, A., Donahue, K., Curran, T., and Pivacek, L. (1985). The viability of young and old baboon red cells stored in the liquid state at 4 C. *Prog. Clin. Biol. Res.* 195, 429–441.

Valeri, C. R., Lindberg, J. R., Contreras, T. J., Pivacek, L. E., Austin, R. M., Valeri, D. A., et al. (1981a). Liquid preservation of baboon red blood cells in acid-citrate-dextrose or citrate-phosphate-dextrose anticoagulant: effects of washing liquid-stored red blood cells. *Am. J. Vet. Res.* 42, 1011–1013.

Valeri, C. R., Lindberg, J. R., Contreras, T. J., Pivacek, L. E., Austin, R. M., Valeri, D. A., et al. (1981b). Measurement of red blood cell volume, plasma volume, and total blood volume in baboons. *Am. J. Vet. Res.* 42, 1025–1029.

Valeri, C. R., Pivacek, L. E., Cassidy, G. P., and Ragno, G. (2002). Volume of RBCs, 24- and 48-hour posttransfusion survivals, and the lifespan of (51)Cr and biotin-X-N-hydroxysuccinimide (NHS)-labeled autologous baboon RBCs: effect of the anticoagulant and blood pH on (51)Cr and biotin-X-NHS elution in vivo. *Transfusion* 42, 343–348. doi: 10.1046/j.1537-2995.2002.00071.x

Valeri, C. R., and Ragno, G. (2005). The 24-hour posttransfusion survival of baboon red blood cells preserved in citrate phosphate dextrose/ ADSOL (CPD/AS-1) for 49 days. *Contemp. Top. Lab. Anim. Sci.* 44, 38–40.

Valeri, C. R., and Ragno, G. (2006). The survival and function of baboon red blood cells, platelets, and plasma proteins: a review of the experience from 1972 to 2002 at the naval blood research Laboratory, Boston, Massachusetts. *Transfusion* 46, 1–42. doi: 10.1111/j.1537-2995.2006.00922.x

VandeBerg, J. L., Williams-Blangero, S., and Tardif, S. D. (eds) (2009). *The Baboon in Biomedical Research*. New York, NY: Springer-Verlag, doi: 10.1007/978-0-387-75991-3

Williams, A. T., Jani, V. P., Nemkov, T., Lucas, A., Yoshida, T., Dunham, A., et al. (2019). Transfusion of anaerobically or conventionally stored blood after hemorrhagic shock. *Shock Augusta Ga.* 53, 352–362. doi: 10.1097/SHK.0000000000001386

Wu, H., Bogdanov, M., Zhang, Y., Sun, K., Zhao, S., Song, A., et al. (2016). Hypoxia-mediated impaired erythrocyte Lands' Cycle is pathogenic for sickle cell disease. *Sci. Rep.* 6:29637. doi: 10.1038/srep29637

Yang, J., Zheng, X., Mahdi, A., Zhou, Z., Tratsiakovich, Y., Jiao, T., et al. (2018). Red blood cells in type 2 diabetes impair cardiac post-ischemic recovery through an arginase-dependent modulation of nitric oxide synthase and reactive oxygen species. *JACC Basic Transl. Sci.* 3, 450–463. doi: 10.1016/j.jacbts.2018.03.006

Yoshida, T., Prudent, M., and D'alessandro, A. (2019). Red blood cell storage lesion: causes and potential clinical consequences. *Blood Transfus.* 17, 27–52. doi: 10.2450/2019.0217-18

Conflict of Interest: Though unrelated to the contents of this manuscript, the authors declare that AD'A and TN are founders of Omix Technologies, Inc., and Altis Biosciences LLC. AD'A and SS are consultants for Hemanext, Inc. SS is also a consultant for Tioma, Inc. PB is a consultant for KaloCyte, Inc. AD'A and JZ are consultants for Rubius Inc. AD'A is a consultant for Forma, Inc.

The remaining authors declare that the research was conducted in the absence of any commercial or financial relationships that could be construed as a potential conflict of interest.

frontiers in Physiology

BRIEF RESEARCH REPORT
published: 12 November 2020
doi: 10.3389/fphys.2020.581386

A Novel ALAS2 Missense Mutation in Two Brothers With Iron Overload and Associated Alterations in Serum Hepcidin/Erythroferrone Levels

Acaynne Lira Zidanes[1,2†], Giacomo Marchi[1,2†], Fabiana Busti[1,2], Alessandro Marchetto[3], Elisa Fermo[4], Alejandro Giorgetti[3], Alice Vianello[1,2], Annalisa Castagna[1,2], Oliviero Olivieri[1,2], Paola Bianchi[4] and Domenico Girelli[1,2]*

[1] Section of Internal Medicine, Department of Medicine, University of Verona, Verona, Italy, [2] EuroBloodNet Referral Center for Rare Disorders of Iron Metabolism, University Hospital of Verona, Verona, Italy, [3] Department of Biotechnology, University of Verona, Verona, Italy, [4] Hematology and Pathophysiology of Anemias Unit, Istituto di Ricovero e Cura a Carattere Scientifico (IRCSS) Ca' Granda Foundation, Policlinico Milano, Milan, Italy

OPEN ACCESS

Edited by:
Alan N. Schechter, National Institutes of Health (NIH), United States

Reviewed by:
Tomas Ganz, UCLA David Geffen School of Medicine, United States
Sylvia S. Bottomley, University of Oklahoma Health Sciences Center, United States

***Correspondence:**
Domenico Girelli
domenico.girelli@univr.it

[†] These authors have contributed equally to this work

Specialty section:
This article was submitted to Red Blood Cell Physiology, a section of the journal Frontiers in Physiology

Received: 08 July 2020
Accepted: 01 October 2020
Published: 12 November 2020

Citation:
Lira Zidanes A, Marchi G, Busti F, Marchetto A, Fermo E, Giorgetti A, Vianello A, Castagna A, Olivieri O, Bianchi P and Girelli D (2020) A Novel ALAS2 Missense Mutation in Two Brothers With Iron Overload and Associated Alterations in Serum Hepcidin/Erythroferrone Levels. Front. Physiol. 11:581386. doi: 10.3389/fphys.2020.581386

Iron loading anemias are characterized by ineffective erythropoiesis and iron overload. The prototype is non-transfusion dependent ß-thalassemia (NTDT), with other entities including congenital sideroblastic anemias, congenital dyserythropoietic anemias, some hemolytic anemias, and myelodysplastic syndromes. Differential diagnosis of iron loading anemias may be challenging due to heterogeneous genotype and phenotype. Notwithstanding the recent advances in linking ineffective erythropoiesis to iron overload, many pathophysiologic aspects are still unclear. Moreover, measurement of hepcidin and erythroferrone (ERFE), two key molecules in iron homeostasis and erythropoiesis, is scarcely used in clinical practice and of uncertain utility. Here, we describe a comprehensive diagnostic approach, including next-generation sequencing (NGS), *in silico* modeling, and measurement of hepcidin and erythroferrone (ERFE), in two brothers eventually diagnosed as X-linked sideroblastic anemia (XLSA). A novel pathogenic *ALAS2* missense mutation (c.1382T>A, p.Leu461His) is described. Hyperferritinemia with high hepcidin-25 levels (but decreased hepcidin:ferritin ratio) and mild-to-moderate iron overload were detected in both patients. ERFE levels were markedly elevated in both patients, especially in the proband, who had a more expressed phenotype. Our study illustrates how new technologies, such as NGS, *in silico* modeling, and measurement of serum hepcidin-25 and ERFE, may help in diagnosing and studying iron loading anemias. Further studies on the hepcidin-25/ERFE axis in additional patients with XLSA and other iron loading anemias may help in establishing its usefulness in differential diagnosis, and it may also aid our understanding of the pathophysiology of these genetically and phenotypically heterogeneous entities.

Keywords: XLSA, ERFE, hepcidin, *ALAS2* gene, next-generation sequencing, *in silico* modeling, iron-loading anemias

INTRODUCTION

Iron loading anemias are anemias characterized by ineffective erythropoiesis and iron overload (Camaschella and Nai, 2016). They include non-transfusion dependent ß-thalassemia (NTDT) (Musallam et al., 2012), congenital sideroblastic anemias (Fujiwara and Harigae, 2019), congenital dyserythropoietic anemias (Iolascon et al., 2013), some hemolytic anemias, and myelodysplastic syndromes (Tanno and Miller, 2010; Camaschella and Nai, 2016; Brissot et al., 2018). X-linked sideroblastic anemias (XLSA), which can be referred also to the group of atypical microcytic anemias (Donker et al., 2014), can be suspected starting from simple blood exams showing microcytic anemia with paradoxically high ferritin after easily discarding more frequent conditions such as thalassemia and anemia of inflammation (Camaschella, 2013; Donker et al., 2014). Regarding the pathogenesis of iron overload in iron loading anemias, the hepcidin/erythroferrone (ERFE) axis seems to play a crucial role, also representing a promising new therapeutic target (Arezes et al., 2020). Hepcidin is the master regulator of systemic iron homeostasis, which acts by controlling intestinal iron absorption and macrophage iron recycling through the inhibition of the iron exporter ferroportin (Ganz, 2011; Girelli et al., 2016). The recently described hormone ERFE is produced by erythroblasts in response to erythropoietin (EPO) and acts by suppressing hepcidin, thereby increasing iron absorption and mobilization for erythropoiesis demand (Kautz et al., 2014; Coffey and Ganz, 2018). ERFE, likely in addition to other mediators, is thus thought to contribute to secondary iron overload in iron loading anemias. With the advent of next generation sequencing (NGS) techniques, genes responsible for sideroblastic anemias are often included in panels designed for diagnosing hereditary anemias, allowing for detection of an increasing number of cases, reducing misdiagnosis, and highlighting the phenotypic variability of this group of disorders.

X-linked sideroblastic anemia (XLSA; OMIM 301300) is caused by loss-of-function mutations in the erythroid-specific 5-aminolevulinate synthase gene (*ALAS2*) (Cotter et al., 1994). *ALAS2* gene encodes for mitochondrial 5-aminolevulinate synthase (ALAS2), the first enzyme in heme biosynthetic pathway in erythroid cells (Bishop et al., 1990; Cox et al., 1990). ALAS2 catalyzes the condensation of glycine and succinyl-CoA into 5-aminolevulinic acid (ALA), using pyridoxal 5′-phosphate (PLP) as a cofactor (Ducamp et al., 2011). To date, more than 80 different mutations in *ALAS2* gene have been reported in patients with XLSA (Ducamp and Fleming, 2019) (Human Genome Mutation database[1]). Most of these are missense mutations located within a conserved region (encoded by exons 5–11), leading to a reduced ALAS2 activity and/or stability (Ducamp and Fleming, 2019). Mutations in the *ALAS2* regulatory region, such as the promoter and intron 1, have also been reported, resulting in decreased *ALAS2* expression (Bekri et al., 2003; Campagna et al., 2014).

XLSA is the most common subtype of Congenital Sideroblastic Anemia (CSA) and typically affects hemizygous males, who often show a mild to moderate anemia since childhood with complications related to iron overload in adulthood. The anemia is hypochromic and microcytic in males, with a mean corpuscular volume (MCV) between 60 and 70 fL and accompanying laboratory signs of iron overload, i.e., high ferritin and transferrin saturation (Bergmann et al., 2010), but almost always normocytic or macrocytic in females. However, severity varies widely depending on the effect of the mutation in ALAS2 protein and additional factors. The phenotypic expression of XLSA is variable between families and also within relatives of a given affected family (Cazzola and Malcovati, 2015; Brissot et al., 2018). Although patients with XLSA are predominantly males, because of hemizygosity of the X-linked defect, many cases of female patients with the heterozygous *ALAS2* mutation have also been reported (Fujiwara and Harigae, 2019), and this is usually due to an age-related skewing of X chromosome inactivation. Additional genetic or somatic mutations and environmental factors may contribute to phenotypic variability (Donker et al., 2014). For example, co-inheritance of HFE mutations may worsen the degree of iron overload in hemizygous males (Cotter et al., 1999). XLSA treatment is focused on two aspects: anemia and iron overload. Most patients are not transfusion-dependent; however, they may develop a transfusion need with increasing age. Anemia and ineffective erythropoiesis often benefit from pyridoxine treatment, although pyridoxine-responsiveness is lower in the case of iron overload (Cotter et al., 1999). Low-regimen phlebotomies (e.g., 200–250 mL every 2 weeks) or iron chelating agents are used in the case of iron overload (Cazzola and Malcovati, 2015).

This report illustrates how new technologies, such as NGS and measurement of serum hepcidin-25 and ERFE, may help in diagnosing and studying iron loading anemias. We describe the paradigmatic case of a male proband diagnosed with XLSA through NGS, who had a novel *ALAS2* missense mutation. His brother also carried the same mutation; however, his phenotypic expression was slightly different. We also provide the *in silico* modeling of the novel mutation and measurements of serum hepcidin-25 and serum ERFE as possible tools for better understanding the pathophysiology of iron overload in XLSA.

METHODS

Patients

Informed consent was obtained before conducting the experimental analysis. All the procedures performed in this study were in accordance with the ethical standards of our Ethical Committee and with the 1964 Helsinki declaration and its later amendments.

DNA samples were collected from both patients, who gave written informed consent to DNA analysis, according to study protocols approved by the local Ethical Committee.

ALAS2 Gene Analysis

Genomic DNA was extracted from peripheral blood leukocytes through salting out method (Miller et al., 1988) using the Wizard

[1] www.hgmd.cf.ac.uk

TABLE 1 | Clinical characteristics of the two brothers.

Laboratory data	Proband (M, 56 years old)	Younger brother (M, 53 years old)	(Reference range)
Hb (g/L)	103	134	(130–170)
RBCs ($\times 10^{12}$)	5.2	6.14	*(4.50–5.80)*
MCV (fL)	73.3	69.2	(79–96)
MCH (pg)	19.8	21.8	(27–33)
Reticulocytes ($\times 10^{9}$)	54	/	(27–99)
WBCs ($\times 10^{9}$)	5.9	8.3	(4–10)
PLTs ($\times 10^{9}$)	286	305	(150–400)
Ferritin (μg/L)	1,493	890	(30–300)
Transferrin saturation (%)	63	28.6	(20–50)
GOT (U/L)	38	24	(5–40)
GPT (U/L)	58	40	(10–65)
Bilirubin (mg/dL)	0.8	0.3	*(0.0–1.2)*
Creatinine (mg/dL)	0.7	0.9	*(0.6–1.4)*
Folate (ng/mL)	> 20	2.7	*(3.8–20)*
Vitamin B12 (pg/mL)	499	483	(197–866)
Ringed sideroblasts in bone marrow	8–10%	n.a.	(Absence)
Erythroferrone (ng/mL)	75.51	14.47	*(0.32–1.80)*
Hepcidin-25 (nM/L)	27.65	10.34	*(1.8–9.2)*
Hepcidin:Ferritin ratio (pM/μg)	18.5	11.6	*(20.9–25.3)*
MRI-LIC (liver iron content) (μM/g)	295	96	*(<36)*
MRI-SIC (spleen iron content) (μM/g)	134	127	(Unvalidated)
MRI-Pancreas T2/T2* (ms)	24.6	n.a.	*(>26)*
MRI-Heart T2/T2* (ms)	43	n.a.	*(>20)*
Spleen volume estimated on MRI (mL)	562	265	(110–340)
HFE sequencing	Negative for C282Y and H63D mutations	Negative for C282Y and H63D mutations	(No mutations)
ALAS2 sequencing	Novel mutation (c.1382T>A p.Leu461His)	Novel mutation (c.1382T>A p.Leu461His)	(No mutations)
Transfusion-dependency	No	No	
Number of packed red blood cells transfused in life	5	0	
Comorbidities	Allergic asthma, obesity, hypertension	None	
Subsequent treatment	Pyridoxine, folate, deferasirox	Pyridoxine, folate, low regimen phlebotomies	
Outcome	Iron-depletion; Hb 103 → 114 g/L, MCV 73 → 75 fL	Iron-depletion; Hb 134 → 137 g/L, MCV 69 → 75 fL	

Genomic DNA purification kit (Promega). The DNA extraction was performed according to the manufacturer's instructions.

The DNA sample of the proband was analyzed on an NGS-targeted panel SureDesign software (Agilent Technologies, Santa Clara, United States) containing 40 genes associated with congenital hemolytic anemia and modifier genes (Rotordam et al., 2019). Libraries were obtained by HaloPlexHS Target Enrichment System Kit and sequenced on a MiSeq platform (Illumina, San Diego, United States). Targeted filtering and annotation of protein-changing variants were performed using the wANNOVAR web tool[2].

The mutation identified was confirmed by Sanger method (ABI PRISM 310 Genetic Analyzer, Applied Biosystems, Warrington, United Kingdom) using the Big Dye Terminator Cycle Sequencing Kit (Applied Biosystems, Warrington, United Kingdom).

Sequence Analysis and *in silico* Modeling

In silico predictions of missense variants' pathogenicity was performed using SIFT (Kumar et al., 2009) and Polyphen-2 (Adzhubei et al., 2010) bioinformatics tools. Reviewed ALAS2 sequences from different species were retrieved from the UniProtKB/Swiss-Prot database and aligned using the MUSCLE (Edgar, 2004) program for multiple sequence alignments. Conservation analysis and alignment visualization were performed by Jalview software (version 2)[3] (Waterhouse et al., 2009) and they are available from IronGenes website[4].

[2]http://wannovar.wglab.org/

[3]www.jalview.org

[4]http://molsim.sci.univr.it/marchetto/alas2/alas2info.php

The structural analysis of the missense variants was made based on the available human ALAS2 crystallographic structure (Bailey et al., 2020) (PDB accession code: 5QQQ, crystallographic resolution: 1.93 Å).

The Consurf server (Ashkenazy et al., 2016) was used to map conservation features on the structure. The prediction of the putative effects of the variants in the structure/function of the protein was performed also by visual inspection using the Chimera program. The wild-type residues and the modeled mutant were included in the publicly accessible IronGenes database[5].

Hepcidin and Erythroferrone Measurement

Hepcidin measurement was performed using an updated and validated Mass-Spectrometry (MS)-based assay (Castagna et al., 2009). This analysis allowed the quantification of the mature bioactive circulating isoform (hepcidin-25) and two smaller isoforms (hepcidin-24 and hepcidin-20), using a chromatography-tandem mass spectrometry (LC-MS/MS) approach (van der Vorm et al., 2016). Hepcidin-25 synthetic standards (the native and the isotopic labeled internal standard), and standards for hepcidin-24 and hepcidin-20 isoforms, were purchased from Peptide International (Lousiville, United States). Briefly, an internal standard was added in all samples, and the calibration curve was created. Blank serum, deprived of hepcidin, was prepared using charcoal treatment. The calibration curve was prepared with the blank serum and a known concentration of standards of each hepcidin isoform. Samples were treated by solid-phase extraction using Oasis hydrophilic-lipophilic balanced reversed-phase (HLB) cartridges (Waters, Italia). High-performance LC was performed using an X-Terra MS C18 2.5 mm column (Waters, Italia), and detection was obtained using a Triple Quad LC-MS/MS (Agilent Technologies). The results were evaluated according to previously obtained reference ranges for males and females at different ages (Traglia et al., 2011).

Erythroferrone analysis was performed using the Erythroferrone IE^{TM} ELISA kit (Intrinsic Lifesciences-The BioIron Company^{TM}), a double monoclonal antibody sandwich ELISA method, according to manufacturer instructions. The concentration of human ERFE was obtained from the mean absorbance of the standard curve. The reference range (0.32–1.80 ng/mL) was obtained from a recent publication that evaluated ERFE levels using the same ELISA kit in 78 males with median age 47 years (Appleby et al., 2020).

Magnetic Resonance Imaging

Organ iron distribution was not-invasively studied with Magnetic Resonance Imaging (MRI), according to Gandon's protocol (Gandon et al., 2004) to define liver iron content (LIC) and spleen iron content (*SIC*) and with T2/T2* sequences (Garbowski et al., 2014). Spleen volume was estimated based on a three-axis approach (Prassopoulos et al., 1997).

[5]http://molsim.sci.univr.it/marchetto/php/gene_detail.php?geneId=ALAS2#tabellaInit

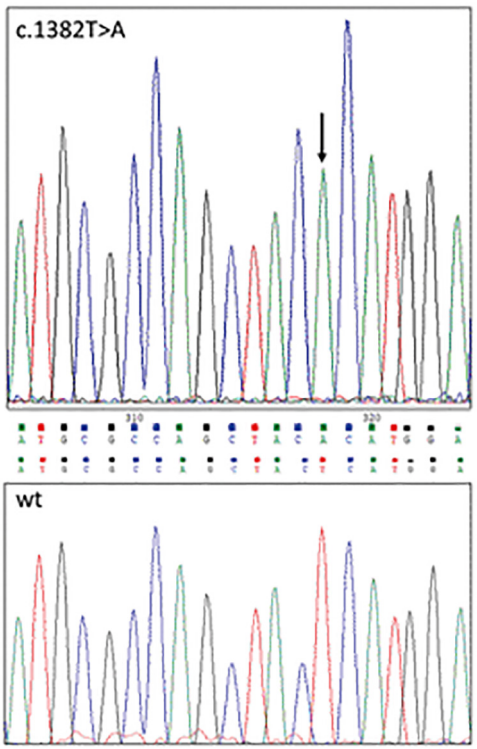

FIGURE 1 | The ALAS2 c.1382T>A mutation confirmed by Sanger sequencing.

RESULTS

The proband was a 56 years-old male, referred to our Center because of a microcytic anemia known since childhood and hyperferritinemia. Personal history and physical examination revealed allergic asthma treated with inhalers, obesity (BMI 33 Kg/m^2), hypertension, and splenomegaly. He only received five units of packed red blood cells in his life during a hospitalization for a transient severe drop of Hb levels. First-level laboratory analysis showed Hb 103 g/L, MCV 73.3 fL, ferritin 1,493 ng/mL, transferrin saturation 63%; no signs of hemolysis, chronic hepatitis, or inflammation were detected. The bone marrow smear showed erythroid hyperplasia with dyserythropoiesis and 2–3% of blasts, ringed sideroblasts were 8–10%. A review of historical complete blood counts (CBCs) in the proband showed Hb values around 110–120 g/L. He had a younger brother who also had microcytosis and low to normal Hb levels (around 130 g/L in historical CBCs series).

Patients' characteristics are reported in **Table 1**, including laboratory and instrumental data at the time of diagnosis.

ALAS2 Mutation and *in silico* Modeling

A novel missense mutation in *ALAS2* gene (c.1382T>A, p.Leu461His, NM_000032.5), located in exon 9 was identified in the proband by targeted NGS, and confirmed by Sanger sequencing in both the proband and the brother (**Figure 1**).

No other pathogenic variants associated with congenital anemias were detected.

The new mutation was not been previously reported in XLSA patients and was predicted to be probably damaging using five predictive tools: Mutation Taster[6], Polyphen-2[7], SIFT[8], MutPred[9], and SNPs&GO[10]. Splice site prediction tools showed no evidence of slicing site abnormalities (NetGene2[11]; NNSplice[12]; MutPred Splice[13]).

The variant was neither found in ExAC nor gnomAD and classified as likely pathogenic according to ACMG Standards and Guidelines (Richards et al., 2015).

Targeted NGS analysis also excluded concomitant presence of mutations in HFE gene associated with hemochromatosis.

In position 461, the leucine residue appears well conserved (58.1%) in our multiple sequence alignment (see footnote 4). Moreover, the presence of a hydrophobic residue (Leu, Ala, and Val) at that position is ensured for more than 90% of the sequences, indicating the need of a hydrophobic residue able to stabilize that protein region locally. Indeed, our *in silico* analysis of the amino acids around the mutated residue points in this direction. **Figure 2** shows that Leu461 is surrounded by a bunch of hydrophobic residues, i.e., L460, M457, V533, and I476 among others, and that its mutation into a histidine residue may hamper the formation of this hydrophobic network (**Figure 2**) (see footnote 5). Indeed, the I476 residue has been shown to reduce the enzymatic activity when mutated into Asn, likely by altering the local folding of the mutant enzyme (Cotter et al., 1992). Similarly to the I476N mutation (rs137852299), the L461H mutation introduces a polar residue in a hydrophobic environment. We therefore cannot exclude a similar effect on the local folding of the enzyme.

[6]http://www.mutationtaster.org/

[7]http://genetics.bwh.harvard.edu/pph2/

[8]https://sift.bii.a-star.edu.sg/

[9]http://mutpred.mutdb.org/index.html

[10]https://snps.biofold.org/snps-and-go/snps-and-go.html

[11]http://www.cbs.dtu.dk/services/NetGene2/

[12]https://www.fruitfly.org/seq_tools/splice.html

[13]http://www.mutdb.org/mutpredsplice/about.htm

Serum Hepcidin and Erythroferrone

High hepcidin-25 levels were found in both patients, especially in the proband (27.65 vs. 10.34 nM/L, normal range 1.8–9.2 nM/L). Ferritin levels were increased in both patients and higher in the proband (1,493 vs. 890 μg/L, normal range 30–300 μg/L). The hepcidin:ferritin ratio was decreased in both patients (18.5 and 11.6, respectively, normal range 20.9–25.3). ERFE levels in the proband, who had the more expressed phenotype, were markedly higher than reference range (75.51 ng/mL, reference range 0.32–1.80 ng/mL) and about five times higher than those of his brother (14.47 ng/mL) (**Table 1**).

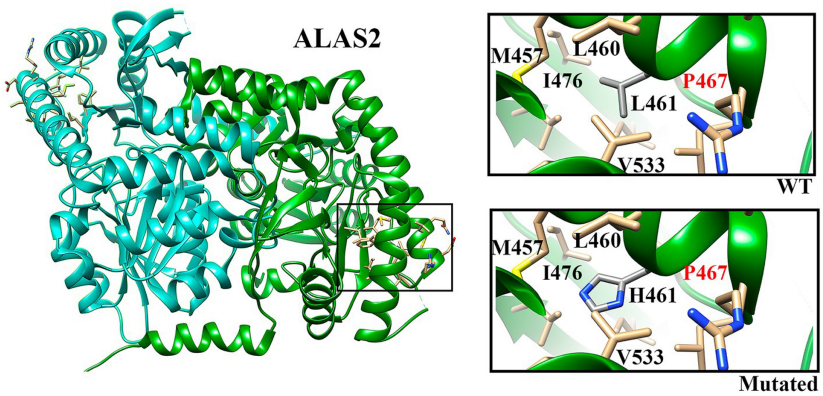

FIGURE 2 | ALAS2 structure. Chains A and B are indicated in green and cyan, respectively. The selected region (square) indicates the localization of L461 residue. In the insights we show the WT residue (upper) and the mutated residue (lower) with the closest neighbors.

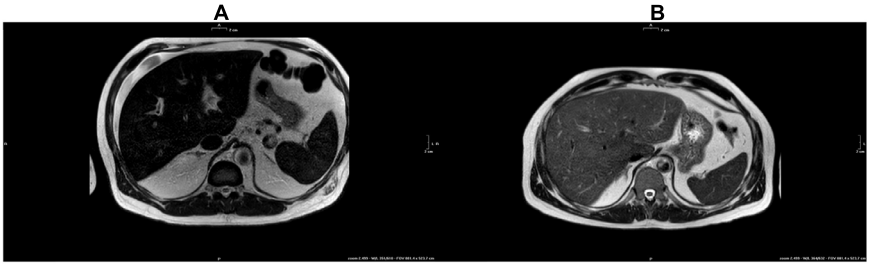

FIGURE 3 | (A) T2-w MRI of the proband. **(B)** T2-w of the younger brother.

Magnetic Resonance Imaging

In the proband, Magnetic Resonance Imaging (MRI) demonstrated a significant iron accumulation in liver (LIC 295 μM/g), and a mild accumulation in spleen (*SIC* 134 μM/g) and pancreas (T2/T2* 24.6 ms) (**Figure 3A** and **Table 1**), whereas no accumulation was detected in heart (T2/T2* 43 ms). The younger brother had a mild accumulation in liver (LIC 96 μM/g) and spleen (*SIC* 127 μM/g) (**Figure 3B** and **Table 1**). Only the proband had splenomegaly (562 vs. 265 mL).

DISCUSSION AND CONCLUSION

Our targeted NGS panel analysis revealed a novel *ALAS2* missense mutation c.1382T>A (p.Leu461His) in exon 9 in the two brothers. Although Sanger sequencing is usually the first choice in patients presenting with classical features of X-linked sideroblastic anemia due to low costs, we choose performing a NGS panel analysis due to our experience on a not negligible prevalence of digenic inheritance in iron overload disorders (Badar et al., 2016), as well as because of the slightly different phenotype in the two brothers. Leu461 is located in an α-helix, which in turn is located in the central catalytic domain, the most evolutionary conserved domain of ALAS2. Indeed, our sequence alignment analysis revealed that Leu461 (or a hydrophobic residue) is highly conserved across different species. Previously described pathogenic mutations were found in the same highly conserved domain of the protein (Cotter et al., 1992). Indeed, our *in silico* modeling showed that the mutant residue (His) is bigger than the wild type residue (Leu), and with very different physicochemical properties. The inclusion of a polar/charged amino acid in a highly hydrophobic environment (**Figure 2**) (see footnote 5) could, with high probability, cause alterations in the local folding of the protein (alpha-helix structure) by disrupting the local hydrophobic core network of interactions.

Iron homeostasis in the two affected brothers was studied, linking biochemical parameters, serum hepcidin-25 and ERFE, MRI organ iron distribution, and clinical characteristics. Both patients had a mild-to-moderate iron overload, with some differences. The proband had a more expressed phenotype with lower Hb and higher ferritin, TSAT, LIC and spleen volume. His ERFE and hepcidin levels were higher compared to reference range and to the younger brother. However, when hepcidin was studied in relation to ferritin levels, the hepcidin:ferritin ratio was decreased in both patients, indicating that hepcidin levels were not as high as they would be expected for the ferritin levels. Indeed, since hepcidin is physiologically regulated by body iron stores, the usefulness of hepcidin:ferritin ratio is to assess whether or not hepcidin production is appropriate for the degree of iron overload. Surprisingly, the younger brother, who had the milder phenotype and milder iron overload, had the lower hepcidin:ferritin ratio. According to current hypothesis, in iron loading anemias, erythroid signals override signals from the replete stores, causing and perpetuating iron overload, with ERFE being the major candidate erythroid regulator of hepcidin production (Kautz and Nemeth, 2014; Camaschella and Nai, 2016). In humans it has been showed that blood loss or EPO administration increase serum ERFE concentrations, and that patients with both NTDT and transfusion-dependent β-thalassemia have very high serum ERFE levels, which decrease after blood transfusion (Ganz et al., 2017). ERFE levels in our two patients with XLSA were quite higher than normal, resembling levels found in NTDT patients (Ganz et al., 2017). This suggests the presence of a significant erythroid stimulus affecting iron metabolism notwithstanding a relatively mild XLSA phenotype. Nonetheless, further studies are needed in additional patients with XLSA, other sideroblastic anemias, and other iron loading anemias.

Our study has the obvious limitation that, given the rarity and the molecular heterogeneity of mutations in *ALAS2* gene, no other cases carrying this mutation have been described so far. The different clinical severity observed in the two brothers raised the possibility of concomitant causes of anemia or iron overload, here excluded by targeted-NGS panel analysis. Furthermore, it must be taken into account that environmental factors, like obesity in the proband, may have influenced the phenotype.

In conclusion, our report illustrates how new methods, like NGS panels, hepcidin-25 and ERFE measurement, may help in differential diagnosis of iron loading anemias. Further studies on the hepcidin-25/ERFE axis in additional patients with XLSA and other iron loading anemias may help in establishing its usefulness in the differential diagnosis as well as to better understand pathophysiology of these genetically and phenotypically heterogeneous entities.

DATA AVAILABILITY STATEMENT

The sequencing data has been deposited into the ClinVar database (accession: SCV001433006).

ETHICS STATEMENT

The studies involving human participants were reviewed and approved by the Comitato etico per la Sperimentazione Clinica (CESC) delle Province di Verona e Rovigo. The patients/participants provided their written informed consent to participate in this study.

AUTHOR CONTRIBUTIONS

AL, GM, and DG conceived the study. GM, FB, and AV collected the clinical data. AL, AC, AM, and AG carried out the experimental studies. EF and PB carried out the genetic study. AL and GM analyzed the data and wrote the manuscript. OO and DG critically revised the manuscript. All authors have approved the final version of the manuscript.

FUNDING

This work was financially supported by the Fondazione IRCCS Ca' Granda Policlinico Milano, Project number RC2020 175/05.

ACKNOWLEDGMENTS

This study was performed (in part) in the LURM (Laboratorio Universitario di Ricerca Medica) Research Center, University of Verona.

REFERENCES

Adzhubei, I. A., Schmidt, S., Peshkin, L., Ramensky, V. E., Gerasimova, A., Bork, P., et al. (2010). A method and server for predicting damaging missense mutations. *Nat. Methods* 7, 248–249. doi: 10.1038/nmeth0410-248

Appleby, S., Chew-Harris, J., Troughton, R. W., Richards, A. M., and Pemberton, C. J. (2020). Analytical and biological assessment of circulating human erythroferrone. *Clin. Biochem.* 79, 41–47. doi: 10.1016/j.clinbiochem.2020.02.001

Arezes, J., Foy, N. J., McHugh, K., Quinkert, D., Benard, S., Sawant, A., et al. (2020). Antibodies against the erythroferrone N-terminal domain prevent hepcidin suppression and ameliorate murine thalassemia. *Blood* 135, 547–557. doi: 10.1182/blood.2019003140

Ashkenazy, H., Abadi, S., Martz, E., Chay, O., Mayrose, I., Pupko, T., et al. (2016). ConSurf 2016: an improved methodology to estimate and visualize evolutionary conservation in macromolecules. *Nucleic Acids Res.* 44, W344–W350. doi: 10.1093/nar/gkw408

Badar, S., Busti, F., Ferrarini, A., Xumerle, L., Bozzini, P., Capelli, P., et al. (2016). Identification of novel mutations in hemochromatosis genes by targeted next generation sequencing in Italian patients with unexplained iron overload. *Am. J. Hematol.* 91, 420–425. doi: 10.1002/ajh.24304

Bailey, H. J., Bezerra, G. A., Marcero, J. R., Padhi, S., Foster, W. R., Rembeza, E., et al. (2020). Human aminolevulinate synthase structure reveals a eukaryotic-specific autoinhibitory loop regulating substrate binding and product release. *Nat. Commun.* 11:2813. doi: 10.1038/s41467-020-16586-x

Bekri, S., May, A., Cotter, P. D., Al-Sabah, A. I., Guo, X., Masters, G. S., et al. (2003). A promoter mutation in the erythroid-specific 5-aminolevulinate synthase (ALAS2) gene causes X-linked sideroblastic anemia. *Blood* 102, 698–704. doi: 10.1182/blood-2002-06-1623

Bergmann, A. K., Campagna, D. R., McLoughlin, E. M., Agarwal, S., Fleming, M. D., Bottomley, S. S., et al. (2010). Systematic molecular genetic analysis of congenital sideroblastic anemia: evidence for genetic heterogeneity and identification of novel mutations. *Pediatr. Blood Cancer* 54, 273–278. doi: 10.1002/pbc.22244

Bishop, D. F., Henderson, A. S., and Astrin, K. H. (1990). Human delta-aminolevulinate synthase: assignment of the housekeeping gene to 3p21 and the erythroid-specific gene to the X chromosome. *Genomics* 7, 207–214. doi: 10.1016/0888-7543(90)90542-3

Brissot, P., Bernard, D. G., Brissot, E., Loreal, O., and Troadec, M. B. (2018). Rare anemias due to genetic iron metabolism defects. *Mutat. Res.* 777, 52–63. doi: 10.1016/j.mrrev.2018.06.003

Camaschella, C. (2013). How I manage patients with atypical microcytic anaemia. *Br. J. Haematol.* 160, 12–24. doi: 10.1111/bjh.12081

Camaschella, C., and Nai, A. (2016). Ineffective erythropoiesis and regulation of iron status in iron loading anaemias. *Br. J. Haematol.* 172, 512–523. doi: 10.1111/bjh.13820

Campagna, D. R., de Bie, C. I., Schmitz-Abe, K., Sweeney, M., Sendamarai, A. K., Schmidt, P. J., et al. (2014). X-linked sideroblastic anemia due to ALAS2 intron 1 enhancer element GATA-binding site mutations. *Am. J. Hematol.* 89, 315–319. doi: 10.1002/ajh.23616

Castagna, A., Campostrini, N., Zaninotto, F., and Girelli, D. (2009). Hepcidin assay in serum by SELDI-TOF-MS and other approaches. *J. Proteom.* 73, 527–536. doi: 10.1016/j.jprot.2009.08.003

Cazzola, M., and Malcovati, L. (2015). Diagnosis and treatment of sideroblastic anemias: from defective heme synthesis to abnormal RNA splicing. *Hematol. Am. Soc. Hematol. Educ. Program.* 2015, 19–25. doi: 10.1182/asheducation-2015.1.19

Coffey, R., and Ganz, T. (2018). Erythroferrone: an erythroid regulator of hepcidin and Iron metabolism. *Hemasphere* 2:e35. doi: 10.1097/HS9.0000000000000035

Cotter, P. D., Baumann, M., and Bishop, D. F. (1992). Enzymatic defect in "X-linked" sideroblastic anemia: molecular evidence for erythroid delta-aminolevulinate synthase deficiency. *Proc. Natl. Acad. Sci. U.S.A.* 89, 4028–4032. doi: 10.1073/pnas.89.9.4028

Cotter, P. D., May, A., Li, L., Al-Sabah, A. I., Fitzsimons, E. J., Cazzola, M., et al. (1999). Four new mutations in the erythroid-specific 5-aminolevulinate synthase (ALAS2) gene causing X-linked sideroblastic anemia: increased pyridoxine responsiveness after removal of iron overload by phlebotomy and coinheritance of hereditary hemochromatosis. *Blood* 93, 1757–1769.

Cotter, P. D., Rucknagel, D. L., and Bishop, D. F. (1994). X-linked sideroblastic anemia: identification of the mutation in the erythroid-specific delta-aminolevulinate synthase gene (ALAS2) in the original family described by Cooley. *Blood* 84, 3915–3924.

Cox, T. C., Bawden, M. J., Abraham, N. G., Bottomley, S. S., May, B. K., Baker, E., et al. (1990). Erythroid 5-aminolevulinate synthase is located on the X chromosome. *Am. J. Hum. Genet.* 46, 107–111.

Donker, A. E., Raymakers, R. A., Vlasveld, L. T., van Barneveld, T., Terink, R., Dors, N., et al. (2014). Practice guidelines for the diagnosis and management of microcytic anemias due to genetic disorders of iron metabolism or heme synthesis. *Blood* 123, 3873–3886. doi: 10.1182/blood-2014-01-548776

Ducamp, S., and Fleming, M. D. (2019). The molecular genetics of sideroblastic anemia. *Blood* 133, 59–69. doi: 10.1182/blood-2018-08-815951

Ducamp, S., Kannengiesser, C., Touati, M., Garcon, L., Guerci-Bresler, A., Guichard, J. F., et al. (2011). Sideroblastic anemia: molecular analysis of the ALAS2 gene in a series of 29 probands and functional studies of 10 missense mutations. *Hum. Mutat.* 32, 590–597. doi: 10.1002/humu.21455

Edgar, R. C. (2004). MUSCLE: multiple sequence alignment with high accuracy and high throughput. *Nucleic Acids Res.* 32, 1792–1797. doi: 10.1093/nar/gkh340

Fujiwara, T., and Harigae, H. (2019). Molecular pathophysiology and genetic mutations in congenital sideroblastic anemia. *Free Radic. Biol. Med.* 133, 179–185. doi: 10.1016/j.freeradbiomed.2018.08.008

Gandon, Y., Olivie, D., Guyader, D., Aube, C., Oberti, F., Sebille, V., et al. (2004). Non-invasive assessment of hepatic iron stores by MRI. *Lancet* 363, 357–362. doi: 10.1016/S0140-6736(04)15436-6

Ganz, T. (2011). Hepcidin and iron regulation, 10 years later. *Blood* 117, 4425–4433. doi: 10.1182/blood-2011-01-258467

Ganz, T., Jung, G., Naeim, A., Ginzburg, Y., Pakbaz, Z., Walter, P. B., et al. (2017). Immunoassay for human serum erythroferrone. *Blood* 130, 1243–1246. doi: 10.1182/blood-2017-04-777987

Garbowski, M. W., Carpenter, J. P., Smith, G., Roughton, M., Alam, M. H., He, T., et al. (2014). Biopsy-based calibration of T2* magnetic resonance for estimation of liver iron concentration and comparison with R2 Ferriscan. *J. Cardiovasc. Magn. Reson.* 16:40. doi: 10.1186/1532-429X-16-40

Girelli, D., Nemeth, E., and Swinkels, D. W. (2016). Hepcidin in the diagnosis of iron disorders. *Blood* 127, 2809–2813. doi: 10.1182/blood-2015-12-639112

Iolascon, A., Heimpel, H., Wahlin, A., and Tamary, H. (2013). Congenital dyserythropoietic anemias: molecular insights and diagnostic approach. *Blood* 122, 2162–2166. doi: 10.1182/blood-2013-05-468223

Kautz, L., Jung, G., Valore, E. V., Rivella, S., Nemeth, E., and Ganz, T. (2014). Identification of erythroferrone as an erythroid regulator of iron metabolism. *Nat. Genet.* 46, 678–684. doi: 10.1038/ng.2996

Kautz, L., and Nemeth, E. (2014). Molecular liaisons between erythropoiesis and iron metabolism. *Blood* 124, 479–482. doi: 10.1182/blood-2014-05-516252

Kumar, P., Henikoff, S., and Ng, P. C. (2009). Predicting the effects of coding non-synonymous variants on protein function using the SIFT algorithm. *Nat. Protoc.* 4, 1073–1081. doi: 10.1038/nprot.2009.86

Miller, S. A., Dykes, D. D., and Polesky, H. F. (1988). A simple salting out procedure for extracting DNA from human nucleated cells. *Nucleic Acids Res.* 16:1215. doi: 10.1093/nar/16.3.1215

Musallam, K. M., Cappellini, M. D., Wood, J. C., and Taher, A. T. (2012). Iron overload in non-transfusion-dependent thalassemia: a clinical perspective. *Blood Rev.* 26(Suppl. 1), S16–S19. doi: 10.1016/S0268-960X(12)70006-1

Prassopoulos, P., Daskalogiannaki, M., Raissaki, M., Hatjidakis, A., and Gourtsoyiannis, N. (1997). Determination of normal splenic volume on computed tomography in relation to age, gender and body habitus. *Eur. Radiol.* 7, 246–248. doi: 10.1007/s003300050145

Richards, S., Aziz, N., Bale, S., Bick, D., Das, S., Gastier-Foster, J., et al. (2015). Standards and guidelines for the interpretation of sequence variants: a joint consensus recommendation of the American College of Medical genetics and genomics and the association for molecular pathology. *Genet. Med.* 17, 405–424. doi: 10.1038/gim.2015.30

Rotordam, M. G., Fermo, E., Becker, N., Barcellini, W., Bruggemann, A., Fertig, N., et al. (2019). A novel gain-of-function mutation of Piezo1 is functionally affirmed in red blood cells by high-throughput patch clamp. *Haematologica* 104, e179–e183. doi: 10.3324/haematol.2018.201160

Tanno, T., and Miller, J. L. (2010). Iron loading and overloading due to ineffective erythropoiesis. *Adv. Hematol.* 2010:358283. doi: 10.1155/2010/358283

Traglia, M., Girelli, D., Biino, G., Campostrini, N., Corbella, M., Sala, C., et al. (2011). Association of HFE and TMPRSS6 genetic variants with iron and erythrocyte parameters is only in part dependent on serum hepcidin concentrations. *J. Med. Genet.* 48, 629–634. doi: 10.1136/jmedgenet-2011-100061

van der Vorm, L. N., Hendriks, J. C. M., Laarakkers, C. M., Klaver, S., Armitage, A. E., Bamberg, A., et al. (2016). Toward worldwide hepcidin assay harmonization: identification of a commutable secondary reference material. *Clin. Chem.* 62, 993–1001.

Waterhouse, A. M., Procter, J. B., Martin, D. M., Clamp, M., and Barton, G. J. (2009). Jalview Version 2–a multiple sequence alignment editor and analysis workbench. *Bioinformatics* 25, 1189–1191. doi: 10.1093/bioinformatics/btp033

Conflict of Interest: The authors declare that the research was conducted in the absence of any commercial or financial relationships that could be construed as a potential conflict of interest.

frontiers in Physiology

REVIEW
published: 22 December 2020
doi: 10.3389/fphys.2020.613559

Genetics and Genomics Approaches for Diagnosis and Research Into Hereditary Anemias

Roberta Russo[1,2], Roberta Marra[1,2], Barbara Eleni Rosato[1,2], Achille Iolascon[1,2] and Immacolata Andolfo[1,2]**

[1] Department of Molecular Medicine and Medical Biotechnologies, University of Naples Federico II, Naples, Italy, [2] CEINGE Biotecnologie Avanzate, Naples, Italy

The hereditary anemias are a relatively heterogeneous set of disorders that can show wide clinical and genetic heterogeneity, which often hampers correct clinical diagnosis. The classical diagnostic workflow for these conditions generally used to start with analysis of the family and personal histories, followed by biochemical and morphological evaluations, and ending with genetic testing. However, the diagnostic framework has changed more recently, and genetic testing is now a suitable approach for differential diagnosis of these patients. There are several approaches to this genetic testing, the choice of which depends on phenotyping, genetic heterogeneity, and gene size. For patients who show complete phenotyping, single-gene testing remains recommended. However, genetic analysis now includes next-generation sequencing, which is generally based on custom-designed targeting panels and whole-exome sequencing. The use of next-generation sequencing also allows the identification of new causative genes, and of polygenic conditions and genetic factors that modify disease severity of hereditary anemias. In the research field, whole-genome sequencing is useful for the identification of non-coding causative mutations, which might account for the disruption of transcriptional factor occupancy sites and *cis*-regulatory elements. Moreover, advances in high-throughput sequencing techniques have now resulted in the identification of genome-wide profiling of the chromatin structures known as the topologically associating domains. These represent a recurrent disease mechanism that exposes genes to inappropriate regulatory elements, causing errors in gene expression. This review focuses on the challenges of diagnosis and research into hereditary anemias, with indications of both the advantages and disadvantages. Finally, we consider the future perspectives for the use of next-generation sequencing technologies in this era of precision medicine.

Keywords: hereditary anemias, next generation sequencing, differential diagnosis, chromatin 3D architecture, genetic test

OPEN ACCESS

Edited by:
Richard Van Wijk,
Utrecht University, Netherlands

Reviewed by:
Elisa Fermo,
IRCCS Ca 'Granda Foundation Maggiore Policlinico Hospital, Italy
Andrew Charles Perkins,
Monash University, Australia

****Correspondence:***
Roberta Russo
roberta.russo@unina.it
Immacolata Andolfo
andolfo@ceinge.unina.it

Specialty section:
This article was submitted to Red Blood Cell Physiology, a section of the journal Frontiers in Physiology

Received: *02 October 2020*
Accepted: *03 December 2020*
Published: *22 December 2020*

Citation:
Russo R, Marra R, Rosato BE, Iolascon A and Andolfo I (2020) Genetics and Genomics Approaches for Diagnosis and Research Into Hereditary Anemias. Front. Physiol. 11:613559. doi: 10.3389/fphys.2020.613559

INTRODUCTION

The hereditary anemias (HAs) represent a particularly heterogeneous group of disorders with rare to low frequency that are characterized by complex genotype–phenotype correlations that remain to be explained. It has only been in recent years that major advances have been made in our understanding of the genetic basis and the pathophysiology of HAs. Indeed, more than 70 genes involved in red blood cell (RBC) physiology have been identified as causative of HAs to date.

Based on clinical manifestations and morphological RBC alterations, HAs can be broadly classified into four different subtypes: (i) disorders of hemoglobin (Hb) synthesis, such as thalassemia and hemoglobinopathies; (ii) hyporegenerative anemias, such as Diamond-Blackfan anemia and congenital dyserythropoietic anemias; (iii) RBC membrane defects that are due to either altered structural organization of their membranes, such as hereditary spherocytosis and hereditary elliptocytosis, or to alterations to membrane transport functions, such as hereditary stomatocytosis; and (iv) non-spherocytic hemolytic anemias due to RBC enzyme defects.

In the last few years, much time and effort has been spent on the identification of the genes and mutations that underlie HAs. The rapid evolution in the diagnostic and research technologies involved now needs to be taken into account. The use of such new techniques has changed the ways in which both diagnosis and research are carried out.

This review focuses on the past, present, and future genetics and genomics approaches for establishment of correct differential diagnosis among these conditions, and for research into new causative/modifier genes and new pathogenetic mechanisms.

CLASSIFICATION OF THE HEREDITARY ANEMIAS

Initially, we will briefly describe the main hallmarks, both clinical and molecular, of the various subtype of HAs. Specific guidance on the pathway to establish correct diagnosis for these conditions has been extensively reviewed elsewhere (Da Costa et al., 2013; Andolfo et al., 2016, 2018b; Gambale et al., 2016; Taher et al., 2018; Bianchi et al., 2019; Grace et al., 2019a; Iolascon et al., 2019, 2020), and so this will not be discussed in any detail in the present review.

Disorders of Hemoglobin Synthesis

The globin disorders can generally be classified as quantitative (e.g., thalassemias) and qualitative (e.g., hemoglobinopathies) defects that lead to hemolysis, and that are defined according to the globin chains. Thalassemia has been shown to be one of the most common genetic disorders worldwide, and it arises as a result of mutations in the α-globin or β-globin genes (Taher et al., 2018). The mutations associated with thalassemia now number over 1,530, and these range from single-nucleotide variations to large genome rearrangements (Higgs et al., 2012; Zhao et al., 2020). α-Thalassemia arises from deletions in the *HBA* genes in ∼95% of patients, while the remaining cases arise from point mutations. In contrast, some 95% of β-thalassemias arise either from *HBB* gene point mutations that result in disruption of RNA transcription, processing or stability, or from nonsense mutations that result in the production of abnormal proteins or in nonsense-mediated decay of RNA. Many of the aspects of β-thalassemia pathophysiology are now explained by excess production of α-globin chains, with the result that they can precipitate in RBC precursors (resulting in ineffective erythropoiesis) and mature RBCs (resulting in hemolysis). Structural variants of the globin genes are associated with sickle-cell anemia, hemolysis caused by the unstable Hb, the altered oxygen affinity of Hb, and Hb where the ferrous (Fe^{2+}) state of the iron cannot be maintained (Rees et al., 1999; Sabath, 2017). The use of various electrophoretic techniques to separate the various Hb states has become the mainstay for the diagnosis of these Hb disorders.

Hypo-Regenerative and Hypo-Productive Anemias

These represent a heterogeneous group of disorders that have effects on the normal differentiation–proliferation pathways at the different steps through the erythroid lineage, and that mainly result in monolinear cytopenia.

Diamond-Blackfan anemia (DBA) is defined by macrocytic moderate or severe anemia that can occur in association with hyporegenerative bone marrow and with reticulocytopenia. Almost half of these patients have physical abnormalities, with 50% showing craniofacial anomalies, and 38% showing defects of the upper limb and hand, which mainly include the thumb. This disease shows mutations in 20 genes for ribosomal proteins, of a total of 80 genes that encode the complete ribosome. For six of these 20 causative genes (i.e., *RPS19*, *RPS24*, *RPS26*, *RPL5*, *RPL11*, *RPL35a*), the mutations and deletions comprise 70% of all DBA patients (Da Costa et al., 2018). There is strong evidence that suggests that erythroid blockage occurs between the BFU-e and CFU-e erythroid development stages, although the exact stage remains to be fully defined (Ohene-Abuakwa et al., 2005).

Congenital dyserythropoietic anemias (CDAs) are a large group of hypo-productive anemias that have been classified into five subtypes: types I, II and III CDAs; CDAs related to transcription factors; and variant CDAs. The most common forms are CDA types I and II (Heimpel et al., 2010), which are caused by bi-allelic mutations in the *CDAN1/CDIN1* genes for CDAI (Dgany et al., 2002; Babbs et al., 2013), and in the *SEC23B* gene for CDAII (Bianchi et al., 2009; Schwarz et al., 2009). For many years, the main diagnostic features of these CDAs were morphological abnormalities of bone marrow (e.g., erythroid hyperplasia with binuclearity) or late erythroblast multinuclearity. However, these particular features of CDAs are not always specific; in particular, they are also seen for other acquired conditions that involve erythropoietic stress, including iron deficiency and preterm birth (Iolascon et al., 2020).

Red Blood Cell Membrane Disorders

RBC membrane disorders consist of hemolytic anemias, which can show wide differences in their clinical, morphological, laboratory, and molecular aspects. The main effects that these genetic alterations have relate to lowered RBC deformability and shortened RBC survival (Iolascon et al., 2019). Among these, there are hereditary spherocytosis, hereditary elliptocytosis, hereditary pyropoikilocytosis, and Southeast Asian ovalocytosis, which are caused by altered membrane structural organization. Hereditary spherocytosis is the most frequent form, and it is characterized by phenotypic, locus, and allelic heterogeneity. Indeed, mutations in five genes that encode proteins that are involved in interactions between the cytoskeleton and the RBC phospholipid bilayer are associated with these conditions: *ANK1*, *SPTA1*, *SPTB*, *SLC4A1*, and *EPB42* (Iolascon et al., 2019). The clinical manifestations can range from symptom-free carriers

to patients with severe hemolysis, jaundice, reticulocytosis, splenomegaly, and cholelithiasis (Da Costa et al., 2013; Andolfo et al., 2016). Conversely, hereditary RBC membrane disorders can arise from genetic defects of RBC transport proteins, which leads to abnormal cation permeability, and the consequent changes in RBC hydration. Hereditary stomatocytosis represents this wide spectrum of diseases, among which the most frequent form is dehydrated hereditary stomatocytosis (DHS). Cation leaks cause dysregulation of cellular volume, which leads in turn to morphological abnormalities of RBCs, with stomatocytes seen for peripheral blood smears, and the consequent leftward shift in the osmolarity curve seen by ektacytometry for patients with mutation of the *PIEZO1* gene (Andolfo et al., 2018a). As generally seen for all hemolytic conditions, the key symptoms include pallor, fatigue, jaundice, gallstones, and splenomegaly. DHS is an autosomal dominant disease that is caused by gain-of-function mutations in *PIEZO1* (DHS type I) and in *KCNN4*, also known as 'Gardos channelopathy' due to its peculiar characteristics, which include lack of clear signs of RBC dehydration and normal ektacytometric curve (Zarychanski et al., 2012; Andolfo et al., 2013a, 2018b; Rapetti-Mauss et al., 2015; Picard et al., 2019).

Non-sperocytic Hemolytic Anemias Due to RBC Enzyme Defects

Mature RBCs rely exclusively on glycolysis for their energy production. Indeed, mutations to almost any of the glycolytic enzymes can result in hemolytic anemias (van Wijk and van Solinge, 2005). The most common human defect is deficiency of glucose-6-phosphate dehydrogenase (G6PD). About 140 mutations in the *G6PD* gene that have X-linked inheritance can cause G6PD functional variants, with many biochemical and clinical phenotypes seen. Of the clinical phenotypes, the main ones are neonatal jaundice and acute hemolytic anemia; this latter is generally triggered by exogenous agents (Luzzatto et al., 2016). Similarly, pyruvate kinase deficiency is generally the cause of chronic non-spherocytic hemolytic anemia, which is an autosomal recessive disease. More than 250 mutations in the *PKLR* gene that encodes the liver and RBC pyruvate kinase isoforms are known to be causative of this condition. Pyruvate kinase deficiency is characterized by a highly variable clinical spectrum (Grace et al., 2018), with patients with two non-missense mutations more severely affected (Bianchi et al., 2020). Furthermore, there are other more rare enzyme defects that are associated with HAs that involve the following: adenylate kinase, aldolase, phosphofructokinase, phosphoglycerate kinase, glucose phosphate isomerase, glutathione reductase, glutathione synthetase, hexokinase, pyrimidine-50-nucleotidase, and triosephosphate isomerase (Koralkova et al., 2014).

PAST, CURRENT, AND FUTURE OF MOLECULAR TESTING FOR DIAGNOSIS OF HEREDITARY ANEMIAS

Here, we will briefly describe the past, current, and future methodologies for genetic testing of HAs, and highlight the strengths and limitations of these different approaches.

First-Generation Sequencing: Sanger Method

The conventional workflow for diagnosis of these conditions started as first line of investigation with positive familial history, complete blood count, and peripheral blood smear. Then specialized biochemical tests, and eventually bone-marrow aspirate, were required. Finally, genetic testing by Sanger sequencing served as the confirmatory test. Very often, no mutations in the candidate gene were identified by this approach for the genetic heterogeneity of the conditions, which led to confusing or lacking molecular diagnoses.

Currently, genetic testing is used early in the diagnostic workflow of HAs, which removes the need for some of the specialized tests, such as bone marrow biopsies (Roy and Babbs, 2019), especially when the clinical data for the patients are not informative, or when the patient is transfusion dependent. Sanger sequencing was also our starting point, while we now use second-generation sequencing (i.e., NGS), which allows us to move from a monogenic approach to an oligo/multigenic approach (**Figure 1**). For many years, monogenic approaches were used for diagnosis and identification of new causative genes of HAs. For mapping to define the causative gene, there was the need to find families with confirmed Mendelian inheritance that preferably involves multiple generations. The use of linkage approaches associated with the functional mapping of the candidate genes was used to successfully identify the mutations responsible for several HAs, such as in the *SEC23B* gene for CDAII, or in *CDAN1* for CDAI, and in *ABCB6* for familial pseudohyperkalemia (Dgany et al., 2002; Schwarz et al., 2009; Andolfo et al., 2013b).

A critical aspect here is that this traditional approach still has great value, mainly in the diagnostic field. Indeed, the testing of single genes is preferred when: (i) the patient's clinical features are typical of a specific HA; (ii) an association has been established between the disorder and the specific gene; and (iii) there is complete phenotyping (i.e., at the clinical, biochemical, and morphological levels). For example, for G6PD deficiency, starting with single-gene analysis is usually still preferred, because in most of the cases an assured clinical diagnosis can be obtained, and *G6PD* is the only causative gene of this condition. Such single-gene tests show high clinical sensitivity because the phenotype and further findings indicate a single disorder associated with a single gene. Furthermore, one particular interpretive advantage of this single-gene approach is that there is minimal likelihood of uncovering multiple confounding variants that have unknown clinical significance. On the other hand, for many other HAs, the clinical variability and the heterogeneity of the genetic locus are significant enough such that a custom targeting panel and/or whole-exome sequencing (WES) are the most appropriate for efficient and timely molecular diagnosis.

Second-Generation Sequencing: NGS Short Reads

Next-generation sequencing has revolutionized the framework of HA diagnosis (**Figure 1**). Although WES or WGS can provide more information (e.g., identification of non-coding causative mutations, or new causative genes), a drawback remains in that

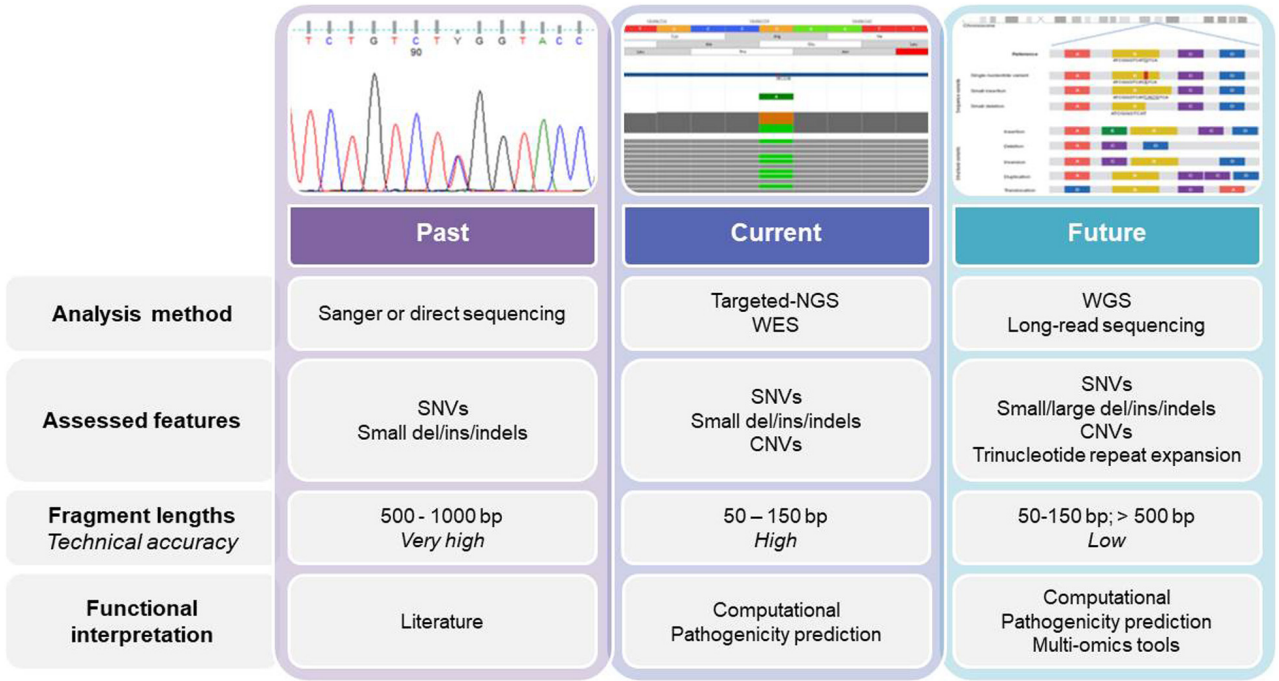

FIGURE 1 | The past, present, and future of genetics and genomics technologies for the diagnosis of and research into hereditary anemias. The diagram shows the current analysis methods for DNA sequencing, while also highlighting the main differences among them. WES, whole-exome sequencing; WGS, whole-genome sequencing; SNV, single nucleotide variant; CNV, copy number variation.

the overall complexity of the data analysis includes a number of variants of unknown significance. The functional tests are therefore crucial to assess the pathogenicity of new variants detected by NGS. Moreover, further problems can arise from the need for adequate coverage of the genes when there are copy number variants and GC−rich regions with low−complexity (Rets et al., 2019). Currently, a targeted-NGS approach is preferred in the diagnostic work-up for these disorders (Agarwal et al., 2016; Del Orbe Barreto et al., 2016; Niss et al., 2016; Roy et al., 2016; Russo et al., 2018; Choi et al., 2019; Kedar et al., 2019; Svidnicki et al., 2020). Custom panels for HAs include variable numbers of genes (e.g., 50–200) that can provide diagnostic yields of 38–87%, which depends on how many and what types of genes are included, and on the depth of the phenotypic assessment (**Table 1**). The main limitation of the targeted NGS approach is the need for continuous updating of the gene list for each panel, to include all recently identified causative genes. Indeed, the targeted NGS approach does not allow for the identification of new genes, by design. Moreover, the cost of WES is now similar to the cost of the large panels that are required to cover

TABLE 1 | Case series of hereditary anemias diagnosed by targeted next-generation sequencing.

Hereditary anemia subtypes	Families (n)	Patients (n)	Genes (n)	Diagnostic yield (%)‡	References
CDA; DBA; sideroblastic anemia; RBC enzymatic defects	57	57	33	38.6	Roy et al., 2016
RBC membrane defects; CDA; RBC enzymatic defects	10	10	40	100§	Del Orbe Barreto et al., 2016
RBC membrane defects; RBC enzymatic defects	15	15	28	86.7	Agarwal et al., 2016
RBC membrane defects	13	15	12	100§	Niss et al., 2016
RBC membrane defects; CDA; DBA; RBC enzymatic defects	62	74	71	64.9	Russo et al., 2018
RBC membrane defects; CDA; DBA; RBC enzymatic defects	21	21	76	61.9	Shefer Averbuch et al., 2018
BMFS; CDA; RBC enzymatic defects; hematological malignancies	21	21	76	81.0	Kedar et al., 2019
RBC membrane defects; RBC enzymatic defects; hereditary anemia modifiers	59	59	43	84.7	Choi et al., 2019
CDA; RBC membrane defects; RBC enzymatic defects	26	36	35	72.2	Svidnicki et al., 2020

‡*Ratio of number of diagnosed patients/numbers of tested patients.* §*These studies reported only the number of diagnosed patients. CDA, congenital dyserythropoietic anemia; DBA, Diamond-Blackfan anemia; RBC, red blood cell; BMFS, bone marrow failure syndrome.*

the full gamut of potential gene mutations that underpin HAs. Therefore, in the near future, WES with the use of managed variant lists that contain known pathogenic variants will become the most appropriate diagnostic approach for investigation of HAs (excluding the hemoglobinopathies, which require more specialized tests).

The exome is believed to represent 1–2% of the genome; however, it also contains 85% of the mutations that are known to cause disease. WES has been reported to have a diagnostic yield of ∼30–50% when used in clinical diagnostics, which depends on detailed phenotyping (Alkan et al., 2011; Sankaran et al., 2012; Rehm et al., 2013; Hamada et al., 2018). Thus, ∼30–50% of cases will remain undiagnosed following NGS testing. This arises mainly because of incomplete phenotyping of the patients, which reduces the specificity of the data, as supported by a report of the numerous variants of unknown significance (Trujillano et al., 2017). Contrary to the targeted-NGS and WES approaches, no estimate of the diagnostic rate of WGS for HAs has been established yet. In a prospective study with 100 patients referred to a pediatric genetics service, genetic variants that met the clinical diagnostic criteria were identified by WGS in 34% of cases (Stavropoulos et al., 2016).

Next-generation sequencing has many advantageous aspects, which include the low cost and the high speed and yield. Conversely, there are some intrinsic limitations of NGS that can have significant impact on accuracy of these analyses. Considering these as bottlenecks, the most noticeable drawback is the short read length. Short read length has been shown to limit precision in a number of biological studies, in particular for genome assembly and transcriptome analyses. Here, NGS short reads are liable for unresolved complexities that can arise from heterozygosity, GC-rich regions, transposable elements, tandem repeats, and repetitive regions (10 kb–10 Mb or more) interspersed in the genome (Alkan et al., 2011). The use of NGS to sequence polymorphic tandem repeats in the genome can be severely impaired by read length (Mousavi et al., 2019).

Considering the analysis of complex chromosomal rearrangements and structural variants, the analytical approaches of comparative genomic hybridization and multiplex ligation-dependent probe amplification are still widely used for detection of copy-number changes (Minervini et al., 2020). For instance, these techniques are crucial for β-thalassemia diagnosis. Indeed, most β-thalassemia alleles (∼90%) are point mutations, and are thus easily identified through Sanger sequencing or other dedicated methods. As the remaining 10% of the alleles are deletions, these are detectable by comparative genomic hybridization arrays or multiplex ligation-dependent probe amplification (Joly et al., 2014). It is important, however, that the application of all of these techniques should not be considered as mutually exclusive or as consecutive, but rather as synergistic. Indeed, several cases of apparent recessive inheritance due to uniparental isodisomy in probands with homozygous recessive mutations where only one parent is heterozygous for the same variant have been described among patients with HAs (Bogardus et al., 2014; Andolfo et al., 2020).

Third-Generation Sequencing: NGS Long Reads

The use of NGS with improved read lengths represents a milestone in the study of the genetics of HAs. This so-called third-generation sequencing now has two advantages that are crucial: single molecules can be sequenced without the need for PCR amplification, which thus avoids any PCR bias; and secondly, this also generates read lengths that are longer (Furst et al., 2020). The two main systems that are based on this third-generation NGS are from Pacific Biosystems[1] and from Oxford Nanopore Technologies[2]. These both have the advantage of long read lengths, although they also share the disadvantage of high randomly distributed error rates (∼5–20%). Indeed, despite their advantages, such methods that provide long reads can also show high error rates, thus reducing the accuracy of this genome sequencing (Minervini et al., 2020). Recently, nanopore sequencing has been used in a number of fields, such as genomics, epigenomics, and transcriptomics. The third-generation NGS approach overcomes the problems of (i) sequencing of tandem repeats; (ii) detection of complex chromosomal rearrangements and structural variants; (iii) RNA sequencing for detection of alternative splicing/transcripts or RNA isoforms; and (iv) direct sequencing of epigenetic/methylation markers. The direct detection of epigenetic modifications or RNA molecules can remove the need for reverse transcription for RNA sequencing and for bisulfite treatment to decipher methylation. Of note, a strong limitation arising from long reads and their analysis is the computational requirements. During the process of genome assembly, as the number of reads increases, an exponential increase is seen for the number of overlaps computed between the reads. For these reasons, many studies have demonstrated that even with the long reads technologies that have been developed, the relevance of short reads has not been lost yet. Indeed, the long reads approach is not yet used in the diagnosis of HAs.

APPLICATION OF GENETICS AND GENOMICS TO DIFFERENTIAL DIAGNOSIS OF HEREDITARY ANEMIAS: CLINICAL AND THERAPEUTIC IMPLICATIONS

Although the diagnostic workflow for HAs is part of normal clinical practice, it is often very difficult to obtain differential diagnosis and classification. Indeed, there is a wide range of unspecific phenotypes and overlapping phenotypes in patients with different genetic backgrounds. For instance, CDAI/CDAII and DHS share several clinical aspects (such as low reticulocyte counts, and dyserythropoietic features of the bone marrow) and are thus often misdiagnosed, as also for CDAII and hereditary spherocytosis (Andolfo et al., 2018a). Such incorrect diagnosis can critically impact on the follow-up and therapy of these patients. Splenectomy is the most effective surgical

[1] www.pacb.com

[2] www.nanoporetech.com

treatment for hereditary spherocytosis, although it might not be necessary for a patient with CDAII, or even worst, it can be contraindicated in DHS because of the risk of severe thrombotic events (Stewart et al., 1996; Iolascon et al., 2017; Andolfo et al., 2018a; Picard et al., 2019).

Next-generation sequencing-based diagnosis has resulted in the modification of initial clinical diagnoses for 10–40% of patients investigated (Iolascon et al., 2020). Moreover, a recent study showed that 45.5% of patients with CDAs had conclusive diagnosis of chronic anemia arising from enzymatic defects, mainly in terms of pyruvate kinase deficiency (Russo et al., 2018). Of note, most of these cases were transfusion-dependent patients, where a classical laboratory approach (e.g., pyruvate kinase enzyme assay) was not performed or was not available. A few years ago, it was demonstrated that an allosteric activator of wild-type and mutant pyruvate kinases, AG-348 (also known as mitapivat) can increase enzymatic activities in the RBCs of these patients, and thus it has been proposed as a novel therapeutic approach for this disease (Kung et al., 2017). Indeed, a phase 2 study of patients with pyruvate kinase deficiency treated with mitapivat was recently completed (ClinicalTrials.gov: NCT02476916), which indicated that the correct identification of these patients might be valuable for guiding their treatment (Grace et al., 2019b). Co-inheritance of multiple conditions or multiple disease-associated variants are further issues that increase the complex scenario of the diagnosis of HAs. For instance, even though ektacytometry is the gold standard for DHS diagnosis, the co-inheritance of β-thalassemia or the splenectomy might modify the shape of the ektacytometry curve, thereby resulting in misdiagnosis (Lazarova et al., 2017; Zaninoni et al., 2018).

APPLICATION OF GENETICS AND GENOMICS TO THE IDENTIFICATION OF HIDDEN DISEASE MECHANISMS

In this section, we will briefly present the main advances and the future perspectives for the use of NGS technologies for identification of genetic modifier variants, non-coding regulatory variants, and genomic structural variants in the erythroid genes. Currently, this is an active and interesting field of research, but it is still far from application to routine clinical diagnostics.

Polygenic Conditions and Genetic Modifiers

Identification of new causative genes has provided improved knowledge of disease etiology; however, there remains the need for better understanding of the genetic factors that can modify HA disease severity. Even diseases that are simple to diagnose can show clinical variability, and it might be that this variability itself involves genetic factors, as so-called "modifier genes" (Genin et al., 2008). One of the major advantages of the NGS approach is the identification of both the polygenic conditions and the modifier variants associated with causative mutations. Although there is no unique definition, we would define such a modifier as a gene that changes the expression of another gene at a different locus that affects the phenotypic expression of another gene, or that can modify the phenotypic manifestation of a mutant gene while not showing any effects on the normal condition (Genin et al., 2008).

In a recent study, an analysis of patients with CDAII that used a target panel of 81 genes for modifier genes identified modifier variants that could explain the clinical variability of these patients, and even among patients who shared the same pathogenic variants. Among these variants, an *ERFE* gene recurrent low-frequency variant, A260S, was shown in 12.5% of patients with CDAII who had severe phenotypes. *ERFE* encodes erythroferrone, which is a soluble protein that is secreted by erythroid precursors and that suppresses expression of hepcidin. Increased levels of ERFE are associated with the ERFE-A260S variant, which results in large impairment of the regulation pathways for iron at the level of the liver. ERFE-A260S functional characterization in a hepatic cell system showed that it has a modifier role in iron overload through the BMP/SMAD pathway. This was the first description of ERFE polymorphism as a genetic modifier variant (Andolfo et al., 2019).

Next-generation sequencing technologies allowed the identification of co-inheritance of multiple disease genotypes in a patient with DHS1 who had severe iron overload that was caused by bi-allelic mutations in *SEC23B* that had been co-inherited with a *PIEZO1* mutation (Russo et al., 2018). *PIEZO1* is a highly polymorphic gene that shows high tolerance to variations. Recently, we provided evidence that the *de novo* R1864H mutation in the *PIEZO1* gene has a phenotype modifier role that co-segregates with the inherited E2492_L2493dup, where the severe phenotype was seen for a proband with DHS1. Of note, the effects that are mediated by R1864H are mainly evident in modulation of the RBC hydration status. Indeed, we were able to show that this rare missense variant resulted in augmented K^+ efflux when it was co-inherited with the duplication, which led in turn to the disease taking on a more severe clinical presentation (Andolfo et al., 2018c).

A recent study on 73 Asian families in an investigated that used NGS-based diagnostic approaches demonstrated that co-inherited G6PD deficiency was seen for 15% of patients with hereditary spherocytosis. *G6PD* variants worsen the phenotype by increasing the transfusion rate. Additionally, *UGT1A1* promoter variant homozygosity (Gilbert syndrome) was shown to lead to a significantly greater mean bilirubin levels, with high frequency of cholelithiasis (30% of the patients with hereditary spherocytosis analyzed) (Aggarwal et al., 2020). Hence, these new genetic technologies have provided useful tools to fill some of the gaps in our understanding of the genetic factors that modify HA disease severity.

Non-coding Genetic Variants: Transcription Factor Binding Sites and *Cis*-Regulatory Elements

Increased knowledge of how transcription factors and *cis*-regulatory elements influence and guide the fine-tuned processes of erythroid differentiation is critical for translation of these

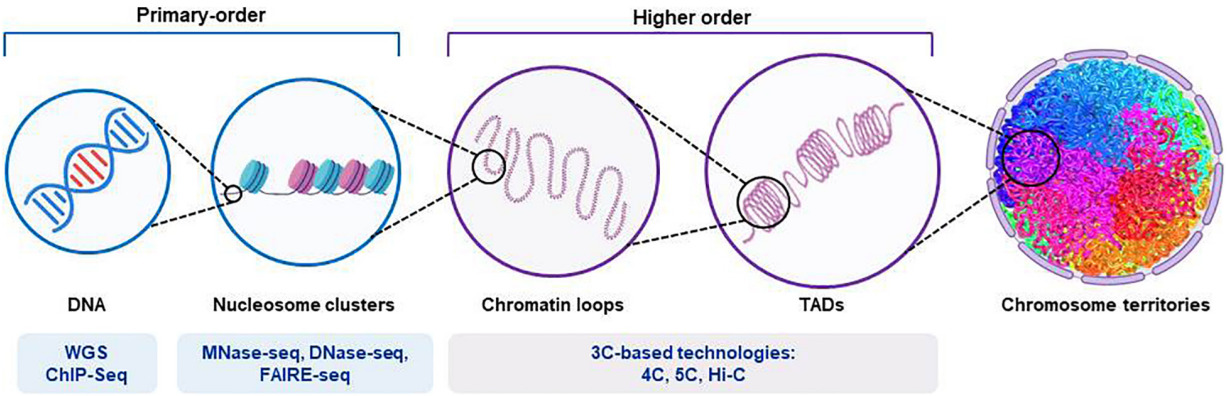

FIGURE 2 | Representation of the structure of chromosomal DNA and the technical procedures for the assessment of chromatin hierarchy. The diagram shows the main features of the organization of chromatin, from those of higher order to those of primary order. The different next-generation-sequencing-based techniques used for each order degree are shown. Whole-genome sequencing (WGS) applications allow identification of both coding and non-coding regulatory variants. Chromatin immunoprecipitation sequencing (ChIP-seq) provides identification of binding sites of DNA-associated proteins, which can be used to map the global binding sites for any given protein (e.g., transcription factors). Endo-exonuclease sequencing (MNase-seq) allows identification of closed chromatin by using an endo-exonuclease to cleave the linker DNA between nucleosomes. DNase I endonuclease sequencing (DNase-seq) identifies open chromatin regions, as accessible regions of the genome are hypersensitive to this activity. Sequencing through formaldehyde-assisted isolation of regulatory elements (FAIRE-seq) is a similar method that identifies open regions of the genome. The chromosome conformation capture (3C)-based technologies (e.g., 4C, 5C, and their variants [Hi-C]) incorporate next-generation sequencing and can provide quantitative measures for intra (*cis*)-chromosomal and inter (*trans*)-chromosomal interactions. TADs, topologically associated domains.

findings from research to possible future diagnosis and treatment of HAs. Although both targeted NGS and WES are currently used in the diagnostic workflow for these disorders, WGS might be useful in the research field to identify the presence of putative non-coding causative mutations (**Figure 2**). Indeed, the mutational disruption of transcription factor occupancy sites has been shown to be a pathogenic mechanism in several hematological disorders. For instance, mutations of the GATA1-binding *cis*-element in an intron of the *ALAS2* gene account for X-linked sideroblastic anemia (Kaneko et al., 2014). Similarly, disruption of the consensus binding motif for GATA1 in the promoter of *PKLR* results in severe pyruvate kinase deficiency (Manco et al., 2000; van Wijk and van Solinge, 2005).

As well as non-coding causative mutations, single nucleotide polymorphisms within *cis*-elements might also result in significant inter-individual differences in hematological parameters, and might influence therapeutic strategies. Genome-wide association studies have identified motif-disrupting single nucleotide polymorphisms in the enhancer of *BCL11A*, a critical repressor of fetal Hb levels that is associated with decreased *BCL11A* expression and elevated fetal Hb (Bauer et al., 2013). Indeed, they proposed the CRISPR–Cas9-mediated *BCL11A* enhancer editing approach in hematopoietic stem cells, as a practicable therapeutic strategy to produce durable fetal Hb in patients with β-hemoglobinopathies (Wu et al., 2019). Similarly, a polymorphism in the 5' upstream region of *GATA1* was described as a genetic modifier in patients with CDAII (Russo et al., 2017).

Along with time-dependent regulation of erythroid gene expression, several studies have described the fine regulation that underlies tissue specificity. Thirty-five percent of genes expressed in erythroid cells have many distinct alternative promoters and first exons (Tan et al., 2006) that regulate tissue-specific isoform selection. For erythrocytes, a high number of cytoskeletal proteins and transcription factors have alternative first exons that can be upstream, positioned close together (e.g., *NRF1*) or tens of kilobases apart (e.g., *EPB4.1*), or downstream of one or more internal coding exons (e.g., *ANK1*). Of note, a 2-kb upstream region of the *ANK1* erythroid promoter leads to selective activation of its transcription in erythroid cells, while this is silent in cell types where alternative tissue-specific *ANK1* promoters are active (Gallagher et al., 2010). This sheds light on the possible pathogenic roles of mutations that do not alter coding sequences, but reduce and alter the transcription of specific isoforms (Yocum et al., 2012).

Genomic Structural Variants: Topologically Associating Domains and Chromatin Occupancy

The assembly of DNA and proteins in chromatin is compact and organized, with the three-dimensional structure showing intricate folding. The chromosomal DNA structure is defined as 'higher order' and 'primary order' based on this folding complexity (Chang et al., 2018). The human genome is characterized by architectural features that are conserved, which include chromatin loops and domains, and nuclear bodies. It also shows non-random patterns, as seen for the location of genes and chromosomes in three-dimensional space (Misteli, 2020). With the advances seen for high-throughput sequencing, profiling of chromatin structures on a genome-wide basis has been made possible. **Figure 2** briefly summarizes the main NGS-based application for the assessment of chromatin hierarchy. Generally, intra-chromosomal interactions are within regions that are known as megabase-sized topologically associating

domains (TADs). These TADs have been identified as large-scale (>100 kb), highly self-interacting regions that are in spatial proximity, and that constrain the spread of heterochromatin within the same region. CCCTC-binding factor (CTCF) is enriched at the TAD boundaries, and this transcriptional repressor or insulator prevents communication between different TADs (Dixon et al., 2012). The so-called 'loop extrusion mechanism' that is mediated by binding of cohesin to sites on CTCF was proposed as the formation process for TADs (Fudenberg et al., 2016; Oudelaar et al., 2018; Vian et al., 2018). It is now established that disruption of the TAD boundaries is a recurrent disease mechanism that promotes aberrant gene expression due to exposure of genes to inappropriate regulatory elements (Lupianez et al., 2015; Gonzalez-Sandoval and Gasser, 2016; Sikorska and Sexton, 2020).

Genomic structural variants have been extensively studied for the globin *loci*. Hay and colleagues characterized the mouse α-globin super-enhancer, which contains five enhancer-like elements flanked by two pairs of CTCF binding sites, which define a single TAD (Hay et al., 2016).

Although TADs are strongly conserved between species, a systematic comparative analysis of chromatin occupancy of master regulators between mouse and human was performed, in the transcriptional landscape of erythroid differentiation. It was shown that transcription factor occupancy sites are well conserved across proerythroblasts and cell lines of the same species (e.g., human proerythroblasts *versus* human K562 cells) but less across different species, according to previous observations regarding the differences in timing and expression levels of some constituent erythroid genes (Pishesha et al., 2014). Conversely, substantial divergence across the mouse and human epigenomes have been reported, as demonstrated for *SEC23A* (paralog of *SEC23B*) transcription factor occupancy and histone state. Human *SEC23A* and the surrounding region are in a general state of heterochromatin, whereas the mouse *sec23a* region is open for transcription. This finding provides evidence for why hematopoietic deficiency for *SEC23B* in mice does not result in anemia or other CDAII characteristics, while it does in humans (Khoriaty et al., 2014). Moreover, the SEC23B deficient phenotype in mice can be completely rescued by expression of SEC23A from the endogenous *Sec23b* locus, which indicates that *SEC23A* and *SEC23B* have functional overlap (Khoriaty et al., 2018). In agreement with this overlap in erythroid cells, a report has shown a milder phenotype in two CDAII patients with higher SEC23A levels compared to one CDAII patient with lower SEC23A levels (Russo et al., 2013). These studies also emphasize the importance of looking at differences in chromatin occupancy between species during the development of a disease model (Ulirsch et al., 2014).

WHERE NEXT FOR GENETICS AND GENOMICS IN HEREDITARY ANEMIAS?

The advent of high-throughput sequencing techniques has provided increased knowledge of the genetic and genomic differences that can be found among individuals. This has gradually led to changes in clinical management and therapeutic plans, which have moved from population-based approaches to providing personalized therapies for individual patients. Genetic approaches now form a routine part of studies of HAs, and they are becoming widespread in clinical practice. On the other hand, the study of non-coding genetic variants and genomic structural variants is very interesting and promising in the search for new pathogenetic mechanisms, but these remain far from being applied in clinical diagnosis.

Testing based on NGS can now provide time-effective diagnosis, while also identifying polygenic conditions and modifier variants. With our increasing knowledge of the genetic features combined with detailed phenotyping of patients with HA, this will facilitate the diagnosis of these patients, to improve their personalized clinical management, while also generating advanced telemedicine tools (Tornador et al., 2019). Third-generation sequencing still represents a revolution for NGS technologies. In terms of HAs, these approaches are still far from diagnostic applications, but they provide a valid approach for the discovery of new pathogenic mechanisms.

In the near future, this transition to personalized medicine provided by the use of genomics for HAs, as in other fields of medicine, should result in the use of individualized treatments through the targeting of the right medication to the right person at the right time, based on their unique profile.

AUTHOR CONTRIBUTIONS

RR, IA, RM, and BR reviewed the literature data and wrote the manuscript. AI revised the manuscript. RR designed the figures. All authors contributed to the article and approved the submitted version.

FUNDING

This research was funded by Programme STAR, financially supported by UniNA and Compagnia di San Paolo (to RR); by Junior Research Grant 2018, 3978026 of European Hematology Association (EHA) to IA.

REFERENCES

Agarwal, A. M., Nussenzveig, R. H., Reading, N. S., Patel, J. L., Sangle, N., Salama, M. E., et al. (2016). Clinical utility of next-generation sequencing in the diagnosis of hereditary haemolytic anaemias. *Br. J. Haematol.* 174, 806–814. doi: 10.1111/bjh.14131

Aggarwal, A., Jamwal, M., Sharma, P., Sachdeva, M. U. S., Bansal, D., Malhotra, P., et al. (2020). Deciphering molecular heterogeneity of Indian families with hereditary spherocytosis using targeted next-generation sequencing: first south asian study. *Br. J. Haematol.* 188, 784–795. doi: 10.1111/bjh.16244

Alkan, C., Sajjadian, S., and Eichler, E. E. (2011). Limitations of next-generation genome sequence assembly. *Nat. Methods* 8, 61–65. doi: 10.1038/nmeth.1527

Andolfo, I., Alper, S. L., De Franceschi, L., Auriemma, C., Russo, R., De Falco, L., et al. (2013a). Multiple clinical forms of dehydrated hereditary stomatocytosis arise from mutations in PIEZO1. *Blood* 121, S3912–S3921.

Andolfo, I., Alper, S. L., Delaunay, J., Auriemma, C., Russo, R., Asci, R., et al. (2013b). Missense mutations in the ABCB6 transporter cause dominant familial pseudohyperkalemia. *Am. J. Hematol.* 88, 66–72. doi: 10.1002/ajh.23357

Andolfo, I., Manna, F., De Rosa, G., Rosato, B. E., Gambale, A., Tomaiuolo, G., et al. (2018c). PIEZO1-R1864H rare variant accounts for a genetic phenotype-modifier role in dehydrated hereditary stomatocytosis. *Haematologica* 103, e94–e97.

Andolfo, I., Martone, S., Ribersani, M., Bianchi, S., Manna, F., Genesio, R., et al. (2020). Apparent recessive inheritance of sideroblastic anemia type 2 due to uniparental isodisomy at the SLC25A38 locus. *Haematologica* 2020:258533.

Andolfo, I., Rosato, B. E., Marra, R., De Rosa, G., Manna, F., Gambale, A., et al. (2019). The BMP-SMAD pathway mediates the impaired hepatic iron metabolism associated with the ERFE-A260S variant. *Am. J. Hematol.* 94, 1227–1235. doi: 10.1002/ajh.25613

Andolfo, I., Russo, R., Gambale, A., and Iolascon, A. (2016). New insights on hereditary erythrocyte membrane defects. *Haematologica* 101, 1284–1294. doi: 10.3324/haematol.2016.142463

Andolfo, I., Russo, R., Gambale, A., and Iolascon, A. (2018a). Hereditary stomatocytosis: an underdiagnosed condition. *Am. J. Hematol.* 93, 107–121. doi: 10.1002/ajh.24929

Andolfo, I., Russo, R., Rosato, B. E., Manna, F., Gambale, A., Brugnara, C., et al. (2018b). Genotype-phenotype correlation and risk stratification in a cohort of 123 hereditary stomatocytosis patients. *Am. J. Hematol.* 93, 1509–1517. doi: 10.1002/ajh.25276

Babbs, C., Roberts, N. A., Sanchez-Pulido, L., McGowan, S. J., Ahmed, M. R., Brown, J. M., et al. (2013). Homozygous mutations in a predicted endonuclease are a novel cause of congenital dyserythropoietic anemia type I. *Haematologica* 98, 1383–1387. doi: 10.3324/haematol.2013.089490

Bauer, D. E., Kamran, S. C., Lessard, S., Xu, J., Fujiwara, Y., Lin, C., et al. (2013). An erythroid enhancer of *BCL11A* subject to genetic variation determines fetal hemoglobin level. *Science* 342, 253–257. doi: 10.1126/science.1242088

Bianchi, P., Fermo, E., Glader, B., Kanno, H., Agarwal, A., Barcellini, W., et al. (2019). Addressing the diagnostic gaps in pyruvate kinase deficiency: consensus recommendations on the diagnosis of pyruvate kinase deficiency. *Am. J. Hematol.* 94, 149–161. doi: 10.1002/ajh.25325

Bianchi, P., Fermo, E., Lezon-Geyda, K., van Beers, E. J., Morton, H. D., Barcellini, W., et al. (2020). Genotype-phenotype correlation and molecular heterogeneity in pyruvate kinase deficiency. *Am. J. Hematol.* 95, 472–482.

Bianchi, P., Fermo, E., Vercellati, C., Boschetti, C., Barcellini, W., Iurlo, A., et al. (2009). Congenital dyserythropoietic anemia type II (CDAII) is caused by mutations in the SEC23B gene. *Hum. Mutat.* 30, 1292–1298. doi: 10.1002/humu.21077

Bogardus, H., Schulz, V. P., Maksimova, Y., Miller, B. A., Li, P., Forget, B. G., et al. (2014). Severe nondominant hereditary spherocytosis due to uniparental isodisomy at the SPTA1 locus. *Haematologica* 99, e168–e170.

Chang, P., Gohain, M., Yen, M. R., and Chen, P. Y. (2018). Computational methods for assessing chromatin hierarchy. *Comput. Struct. Biotechnol. J.* 16, 43–53. doi: 10.1016/j.csbj.2018.02.003

Choi, H. S., Choi, Q., Kim, J. A., Im, K. O., Park, S. N., Park, Y., et al. (2019). Molecular diagnosis of hereditary spherocytosis by multi-gene target sequencing in Korea: matching with osmotic fragility test and presence of spherocyte. *Orphanet. J. Rare Dis.* 14:114.

Da Costa, L., Galimand, J., Fenneteau, O., and Mohandas, N. (2013). Hereditary spherocytosis, elliptocytosis, and other red cell membrane disorders. *Blood Rev.* 27, 167–178. doi: 10.1016/j.blre.2013.04.003

Da Costa, L., Narla, A., and Mohandas, N. (2018). An update on the pathogenesis and diagnosis of diamond-Blackfan anemia. *F1000Res.* 7:F1000.

Del Orbe Barreto, R., Arrizabalaga, B., De la Hoz, A. B., García-Orad, Á, Tejada, M. I., Garcia-Ruiz, J. C., et al. (2016). Detection of new pathogenic mutations in patients with congenital haemolytic anaemia using next-generation sequencing. *Int. J. Lab. Hematol.* 38, 629–638. doi: 10.1111/ijlh.12551

Dgany, O., Avidan, N., Delaunay, J., Krasnov, T., Shalmon, L., Shalev, H., et al. (2002). Congenital dyserythropoietic anemia type I is caused by mutations in codanin-1. *Am. J. Hum. Genet.* 71, 1467–1474.

Dixon, J. R., Selvaraj, S., Yue, F., Kim, A., Li, Y., Shen, Y., et al. (2012). Topological domains in mammalian genomes identified by analysis of chromatin interactions. *Nature* 485, 376–380. doi: 10.1038/nature11082

Fudenberg, G., Imakaev, M., Lu, C., Goloborodko, A., Abdennur, N., and Mirny, L. A. (2016). Formation of chromosomal domains by loop extrusion. *Cell Rep.* 15, 2038–2049. doi: 10.1016/j.celrep.2016.04.085

Furst, D., Tsamadou, C., Neuchel, C., Schrezenmeier, H., Mytilineos, J., and Weinstock, C. (2020). Next-generation sequencing technologies in blood group typing. *Transfus. Med. Hemother.* 47, 4–13. doi: 10.1159/000504765

Gallagher, P. G., Steiner, L. A., Liem, R. I., Owen, A. N., Cline, A. P., Seidel, N. E., et al. (2010). Mutation of a barrier insulator in the human ankyrin-1 gene is associated with hereditary spherocytosis. *J. Clin. Invest.* 120, 4453–4465. doi: 10.1172/jci42240

Gambale, A., Iolascon, A., Andolfo, I., and Russo, R. (2016). Diagnosis and management of congenital dyserythropoietic anemias. *Expert. Rev. Hematol.* 9, 283–296. doi: 10.1586/17474086.2016.1131608

Genin, E., Feingold, J., and Clerget-Darpoux, F. (2008). Identifying modifier genes of monogenic disease: strategies and difficulties. *Hum. Genet.* 124, 357–368. doi: 10.1007/s00439-008-0560-2

Gonzalez-Sandoval, A., and Gasser, S. M. (2016). On TADs and LADs: spatial control over gene expression. *Trends Genet.* 32, 485–495. doi: 10.1016/j.tig.2016.05.004

Grace, R. F., Bianchi, P., van Beers, E. J., Eber, S. W., Glader, B., Yaish, H. M., et al. (2018). Clinical spectrum of pyruvate kinase deficiency: data from the pyruvate kinase deficiency natural history study. *Blood* 131, 2183–2192.

Grace, R. F., Mark Layton, D., and Barcellini, W. (2019a). How we manage patients with pyruvate kinase deficiency. *Br. J. Haematol.* 184, 721–734. doi: 10.1111/bjh.15758

Grace, R. F., Rose, C., Layton, D. M., Galacteros, F., Barcellini, W., Morton, D. H., et al. (2019b). Safety and efficacy of mitapivat in pyruvate kinase deficiency. *N. Engl. J. Med.* 381, 933–944. doi: 10.1056/nejmoa1902678

Hamada, M., Doisaki, S., Okuno, Y., Muramatsu, H., Hama, A., Kawashima, N., et al. (2018). Whole-exome analysis to detect congenital hemolytic anemia mimicking congenital dyserythropoietic anemia. *Int. J. Hematol.* 108, 306–311. doi: 10.1007/s12185-018-2482-7

Hay, D., Hughes, J. R., Babbs, C., Davies, J. O. J., Graham, B. J., Hanssen, L., et al. (2016). Genetic dissection of the alpha-globin super-enhancer in vivo. *Nat. Genet.* 48, 895–903. doi: 10.1038/ng.3605

Heimpel, H., Matuschek, A., Ahmed, M., Bader-Meunier, B., Colita, A., Delaunay, J., et al. (2010). Frequency of congenital dyserythropoietic anemias in europe. *Eur. J. Haematol.* 85, 20–25.

Higgs, D. R., Engel, J. D., and Stamatoyannopoulos, G. (2012). Thalassaemia. *Lancet* 379, 373–383.

Iolascon, A., Andolfo, I., Barcellini, W., Corcione, F., Garcon, L., De Franceschi, L., et al. (2017). Recommendations regarding splenectomy in hereditary hemolytic anemias. *Haematologica* 102, 1304–1313. doi: 10.3324/haematol.2016.161166

Iolascon, A., Andolfo, I., and Russo, R. (2019). Advances in understanding the pathogenesis of red cell membrane disorders. *Br. J. Haematol.* 187, 13–24. doi: 10.1111/bjh.16126

Iolascon, A., Andolfo, I., and Russo, R. (2020). Congenital dyserythropoietic anemias. *Blood* 136, 1274–1283. doi: 10.1182/blood.2019000948

Joly, P., Pondarre, C., and Badens, C. (2014). [Beta-thalassemias: molecular, epidemiological, diagnostical and clinical aspects]. *Ann. Biol. Clin.* 72, 639–668. doi: 10.1684/abc.2014.1015

Kaneko, K., Furuyama, K., Fujiwara, T., Kobayashi, R., Ishida, H., Harigae, H., et al. (2014). Identification of a novel erythroid-specific enhancer for the ALAS2 gene and its loss-of-function mutation which is associated with congenital sideroblastic anemia. *Haematologica* 99, 252–261. doi: 10.3324/haematol.2013.085449

Kedar, P. S., Harigae, H., Ito, E., Muramatsu, H., Kojima, S., Okuno, Y., et al. (2019). Study of pathophysiology and molecular characterization of congenital anemia in India using targeted next-generation sequencing approach. *Int. J. Hematol.* 110, 618–626. doi: 10.1007/s12185-019-02716-9

Khoriaty, R., Hesketh, G. G., Bernard, A., Weyand, A. C., Mellacheruvu, D., Zhu, G., et al. (2018). Functions of the COPII gene paralogs SEC23A and SEC23B are interchangeable in vivo. *Proc. Natl. Acad. Sci. U S A.* 115, E7748–E7757.

Khoriaty, R., Vasievich, M. P., Jones, M., Everett, L., Chase, J., Tao, J., et al. (2014). Absence of a red blood cell phenotype in mice with hematopoietic deficiency of SEC23B. *Mol. Cell. Biol.* 34, 3721–3734. doi: 10.1128/mcb.00287-14

Koralkova, P., van Solinge, W. W., and van Wijk, R. (2014). Rare hereditary red blood cell enzymopathies associated with hemolytic anemia - pathophysiology, clinical aspects, and laboratory diagnosis. *Int. J. Lab. Hematol.* 36, 388–397. doi: 10.1111/ijlh.12223

Kung, C., Hixon, J., Kosinski, P. A., Cianchetta, G., Histen, G., Chen, Y., et al. (2017). AG-348 enhances pyruvate kinase activity in red blood cells from patients with pyruvate kinase deficiency. *Blood* 130, 1347–1356. doi: 10.1182/blood-2016-11-753525

Lazarova, E., Gulbis, B., Oirschot, B. V., and van Wijk, R. (2017). Next-generation osmotic gradient ektacytometry for the diagnosis of hereditary spherocytosis: interlaboratory method validation and experience. *Clin. Chem. Lab. Med.* 55, 394–402.

Lupianez, D. G., Kraft, K., Heinrich, V., Krawitz, P., Brancati, F., Klopocki, E., et al. (2015). Disruptions of topological chromatin domains cause pathogenic rewiring of gene-enhancer interactions. *Cell* 161, 1012–1025. doi: 10.1016/j.cell.2015.04.004

Luzzatto, L., Nannelli, C., and Notaro, R. (2016). Glucose-6-phosphate dehydrogenase deficiency. *Hematol. Oncol. Clin. North Am.* 30, 373–393.

Manco, L., Ribeiro, M. L., Maximo, V., Almeida, H., Costa, A., Freitas, O., et al. (2000). A new PKLR gene mutation in the R-type promoter region affects the gene transcription causing pyruvate kinase deficiency. *Br. J. Haematol.* 110, 993–997. doi: 10.1046/j.1365-2141.2000.02283.x

Minervini, C. F., Cumbo, C., Orsini, P., Anelli, L., Zagaria, A., Specchia, G., et al. (2020). Nanopore sequencing in blood diseases: a wide range of opportunities. *Front. Genet.* 11:76. doi: 10.3389/fgene.2020.00076

Misteli, T. (2020). The self-organizing genome: principles of genome architecture and function. *Cell* 183, 28–45. doi: 10.1016/j.cell.2020.09.014

Mousavi, N., Shleizer-Burko, S., Yanicky, R., and Gymrek, M. (2019). Profiling the genome-wide landscape of tandem repeat expansions. *Nucleic Acids Res.* 47:e90. doi: 10.1093/nar/gkz501

Niss, O., Chonat, S., Dagaonkar, N., Almansoori, M. O., Kerr, K., Rogers, Z. R., et al. (2016). Genotype-phenotype correlations in hereditary elliptocytosis and hereditary pyropoikilocytosis. *Blood Cells Mol. Dis.* 61, 4–9. doi: 10.1016/j.bcmd.2016.07.003

Ohene-Abuakwa, Y., Orfali, K. A., Marius, C., and Ball, S. E. (2005). Two-phase culture in diamond blackfan anemia: localization of erythroid defect. *Blood* 105, 838–846. doi: 10.1182/blood-2004-03-1016

Oudelaar, A. M., Davies, J. O. J., Hanssen, L. L. P., Telenius, J. M., Schwessinger, R., Liu, Y., et al. (2018). Single-allele chromatin interactions identify regulatory hubs in dynamic compartmentalized domains. *Nat. Genet.* 50, 1744–1751. doi: 10.1038/s41588-018-0253-2

Picard, V., Guitton, C. I, Thuret, I., Rose, C., Bendelac, L., Ghazal, K., et al. (2019). Clinical and biological features in PIEZO1-hereditary xerocytosis and Gardos channelopathy: a retrospective series of 126 patients. *Haematologica* 104, 1554–1564. doi: 10.3324/haematol.2018.205328

Pishesha, N., Thiru, P., Shi, J., Eng, J. C., Sankaran, V. G., and Lodish, H. F. (2014). Transcriptional divergence and conservation of human and mouse erythropoiesis. *Proc. Natl. Acad. Sci. U S A.* 111, 4103–4108. doi: 10.1073/pnas.1401598111

Rapetti-Mauss, R., Lacoste, C., Picard, V., Guitton, C., Lombard, E., Loosveld, M., et al. (2015). A mutation in the Gardos channel is associated with hereditary xerocytosis. *Blood* 126, 1273–1280. doi: 10.1182/blood-2015-04-642496

Rees, D. C., Porter, J. B., Clegg, J. B., and Weatherall, D. J. (1999). Why are hemoglobin F levels increased in HbE/beta thalassemia? *Blood* 94, 3199–3204. doi: 10.1182/blood.v94.9.3199.421k19_3199_3204

Rehm, H. L., Bale, S. J., Bayrak-Toydemir, P., Berg, J. S., Brown, K. K., Deignan, J. L., et al. (2013). ACMG clinical laboratory standards for next-generation sequencing. *Genet. Med.* 15, 733–747.

Rets, A., Clayton, A. L., Christensen, R. D., and Agarwal, A. M. (2019). Molecular diagnostic update in hereditary hemolytic anemia and neonatal hyperbilirubinemia. *Int. J. Lab. Hematol.* 41, 95–101. doi: 10.1111/ijlh.13014

Roy, N. B., Wilson, E. A., Henderson, S., Wray, K., Babbs, C., Okoli, S., et al. (2016). A novel 33-Gene targeted resequencing panel provides accurate, clinical-grade diagnosis and improves patient management for rare inherited anaemias. *Br. J. Haematol.* 175, 318–330. doi: 10.1111/bjh.14221

Roy, N. B. A., and Babbs, C. (2019). The pathogenesis, diagnosis and management of congenital dyserythropoietic anaemia type I. *Br. J. Haematol.* 185, 436–449. doi: 10.1111/bjh.15817

Russo, R., Andolfo, I., Gambale, A., De Rosa, G., Manna, F., Arillo, A., et al. (2017). GATA1 erythroid-specific regulation of SEC23B expression and its implication in the pathogenesis of congenital dyserythropoietic anemia type II. *Haematologica* 102, e371–e374. doi: 10.3324/haematol.2016.162966

Russo, R., Andolfo, I., Manna, F., Gambale, A., Marra, R., Rosato, B. E., et al. (2018). Multi-gene panel testing improves diagnosis and management of patients with hereditary anemias. *Am. J. Hematol.* 93, 672–682. doi: 10.1002/ajh.25058

Russo, R., Langella, C., Esposito, M. R., Gambale, A., Vitiello, F., Vallefuoco, F., et al. (2013). Hypomorphic mutations of SEC23B gene account for mild phenotypes of congenital dyserythropoietic anemia type II. *Blood Cells Mol. Dis.* 51, 17–21. doi: 10.1016/j.bcmd.2013.02.003

Sabath, D. E. (2017). Molecular diagnosis of thalassemias and hemoglobinopathies: an ACLPS critical review. *Am. J. Clin. Pathol.* 148, 6–15. doi: 10.1093/ajcp/aqx047

Sankaran, V. G., Ghazvinian, R., Do, R., Thiru, P., Vergilio, J. A., Beggs, A. H., et al. (2012). Exome sequencing identifies GATA1 mutations resulting in diamond-blackfan anemia. *J. Clin. Invest.* 122, 2439–2443. doi: 10.1172/jci63597

Schwarz, K., Iolascon, A., Verissimo, F., Trede, N. S., Horsley, W., Chen, W., et al. (2009). Mutations affecting the secretory COPII coat component SEC23B cause congenital dyserythropoietic anemia type II. *Nat. Genet.* 41, 936–940. doi: 10.1038/ng.405

Shefer Averbuch, N., Steinberg-Shemer, O., Dgany, O., Krasnov, T., Noy-Lotan, S., Yacobovich, J., et al. (2018). Targeted next generation sequencing for the diagnosis of patients with rare congenital anemias. *Eur. J. Haematol.* 101, 297–304. doi: 10.1111/ejh.13097

Sikorska, N., and Sexton, T. (2020). Defining functionally relevant spatial chromatin domains: it is a TAD complicated. *J. Mol. Biol.* 432, 653–664. doi: 10.1016/j.jmb.2019.12.006

Stavropoulos, D. J., Merico, D., Jobling, R., Bowdin, S., Monfared, N., Thiruvahindrapuram, B., et al. (2016). Whole genome sequencing expands diagnostic utility and improves clinical management in pediatric medicine. *NP.J. Genom. Med.* 1:15012.

Stewart, G. W., Amess, J. A., Eber, S. W., Kingswood, C., Lane, P. A., Smith, B. D., et al. (1996). Thrombo-embolic disease after splenectomy for hereditary stomatocytosis. *Br. J. Haematol.* 93, 303–310. doi: 10.1046/j.1365-2141.1996.4881033.x

Svidnicki, M., Zanetta, G. K., Congrains-Castillo, A., Costa, F. F., and Saad, S. T. O. (2020). Targeted next-generation sequencing identified novel mutations associated with hereditary anemias in Brazil. *Ann. Hematol.* 99, 955–962. doi: 10.1007/s00277-020-03986-8

Taher, A. T., Weatherall, D. J., and Cappellini, M. D. (2018). Thalassaemia. *Lancet* 391, 155–167.

Tan, J. S., Mohandas, N., and Conboy, J. G. (2006). High frequency of alternative first exons in erythroid genes suggests a critical role in regulating gene function. *Blood* 107, 2557–2561. doi: 10.1182/blood-2005-07-2957

Tornador, C., Sánchez-Prados, E., Cadenas, B., Russo, R., Venturi, V., Andolfo, I., et al. (2019). CoDysAn: a telemedicine tool to improve awareness and diagnosis for patients with congenital dyserythropoietic anemia. *Front. Physiol.* 10:1063. doi: 10.3389/fphys.2019.01063

Trujillano, D., Bertoli-Avella, A. M., Kumar Kandaswamy, K., Weiss, M. E., Köster, J., Marais, A., et al. (2017). Clinical exome sequencing: results from 2819 samples reflecting 1000 families. *Eur. J. Hum. Genet.* 25, 176–182. doi: 10.1038/ejhg.2016.146

Ulirsch, J. C., Lacy, J. N., An, X., Mohandas, N., Mikkelsen, T. S., and Sankaran, V. G. (2014). Altered chromatin occupancy of master regulators underlies evolutionary divergence in the transcriptional landscape of erythroid differentiation. *PLoS Genet* 10:e1004890. doi: 10.1371/journal.pgen.1004890

van Wijk, R., and van Solinge, W. W. (2005). The energy-less red blood cell is lost: erythrocyte enzyme abnormalities of glycolysis. *Blood* 106, 4034–4042. doi: 10.1182/blood-2005-04-1622

Vian, L., Pekowska, A., Rao, S. S. P., Kieffer-Kwon, K. R., Jung, S., Baranello, L., et al. (2018). The energetics and physiological impact of cohesin extrusion. *Cell* 173, 1165–1178.

Wu, Y., Zeng, J., Roscoe, B. P., Liu, P., Yao, Q., Lazzarotto, C. R., et al. (2019). Highly efficient therapeutic gene editing of human hematopoietic stem cells. *Nat. Med.* 25, 776–783.

Yocum, A. O., Steiner, L. A., Seidel, N. E., Cline, A. P., Rout, E. D., Lin, J. Y., et al. (2012). A tissue-specific chromatin loop activates the erythroid ankyrin-1 promoter. *Blood* 120, 3586–3593. doi: 10.1182/blood-2012-08-450262

Zaninoni, A., Fermo, E., Vercellati, C., Consonni, D., Marcello, A. P., Zanella, A., et al. (2018). Use of laser assisted optical rotational cell analyzer (LoRRca MaxSis) in the diagnosis of rbc membrane disorders, enzyme defects, and congenital dyserythropoietic anemias: a monocentric study on 202 patients. *Front. Physiol.* 9:451. doi: 10.3389/fphys.2018.00451

Zarychanski, R., Schulz, V. P., Houston, B. L., Maksimova, Y., Houston, D. S., Smith, B., et al. (2012). Mutations in the mechanotransduction protein PIEZO1 are associated with hereditary xerocytosis. *Blood* 120, 1908–1915. doi: 10.1182/blood-2012-04-422253

Zhao, J., Li, J., Lai, Q., and Yu, Y. (2020). Combined use of gap-PCR and next-generation sequencing improves thalassaemia carrier screening among premarital adults in china. *J. Clin. Pathol.* 73, 488–492. doi: 10.1136/jclinpath-2019-206339

Conflict of Interest: The authors declare that the research was conducted in the absence of any commercial or financial relationships that could be construed as a potential conflict of interest.

frontiers in Physiology

ORIGINAL RESEARCH
published: 13 January 2021
doi: 10.3389/fphys.2020.603633

Red Blood Cell Morphodynamics: A New Potential Marker in High-Risk Patients

Benedetta Porro[1†], Edoardo Conte[1†], Anna Zaninoni[2], Paola Bianchi[2], Fabrizio Veglia[1], Simone Barbieri[1], Susanna Fiorelli[1], Sonia Eligini[1], Alessandro Di Minno[1‡], Saima Mushtaq[1], Elena Tremoli[1], Viviana Cavalca[1] and Daniele Andreini[1,3]*

[1]Centro Cardiologico Monzino, Istituto di Ricovero e Cura a Carattere Scientifico (IRCCS), Milan, Italy, [2]Fondazione IRCCS Ca' Granda Ospedale Maggiore Policlinico Milano, Unità Operativa Complessa (UOC) Ematologia, Unità Operativa Semplice (UOS) Fisiopatologia delle Anemie, Milan, Italy, [3]Department of Clinical Sciences and Community Health, Cardiovascular Section, University of Milan, Milan, Italy

OPEN ACCESS

Edited by:
Angelo D'Alessandro, University of Colorado Denver, United States

Reviewed by:
Joan-lluis Vives-Corrons, Josep Carreras Leukaemia Research Institute (IJC), Spain
Travis Nemkov, University of Colorado Anschutz Medical Campus, United States

***Correspondence:**
Viviana Cavalca
viviana.cavalca@ccfm.it

[†]These authors have contributed equally to this work

[‡]Present address:
Alessandro Di Minno, Department of Pharmacy, Federico II University Naples, Naples, Italy

Specialty section:
This article was submitted to Red Blood Cell Physiology, a section of the journal Frontiers in Physiology

Received: *07 September 2020*
Accepted: *16 December 2020*
Published: *13 January 2021*

Citation:
Porro B, Conte E, Zaninoni A, Bianchi P, Veglia F, Barbieri S, Fiorelli S, Eligini S, Di Minno A, Mushtaq S, Tremoli E, Cavalca V and Andreini D (2021) Red Blood Cell Morphodynamics: A New Potential Marker in High-Risk Patients. Front. Physiol. 11:603633. doi: 10.3389/fphys.2020.603633

In the last years, a substantial contribution of red blood cells (RBCs) in cardiovascular homeostasis has been evidenced, as these cells are able to regulate cardiovascular function by the export of adenosine triphosphate and nitric oxide as well as to maintain redox balance through a well-developed antioxidant system. Recently a link between high-risk plaque (HRP) features and myocardial ischemia, in the absence of severe lumen stenosis, has been evidenced. Nonobstructive coronary artery disease (nonob CAD) has been associated in fact with a greater 1-year risk of myocardial infarction and all-cause mortality compared with no apparent CAD. This new evidence increases interest in searching new triggers to identify these high-risk patients, in the absence/or on top of traditional hazard markers. In this study, we investigated the existence of any association between RBC morphodynamics and HRP features in individuals with different grades of coronary stenosis detected by coronary computed tomography angiography (CCTA). Ninety-one consecutive individuals who underwent CCTA [33 no CAD; 26 nonobstructive (nonob), and 32 obstructive (ob) CAD] were enrolled. RBC morphodynamic features, i.e., RBC aggregability and deformability, were analyzed by means of Laser Assisted Optical Rotation Cell Analyzer (LoRRca MaxSis). The putative global RBC morphodynamic (RMD) score and the related risk chart, associating the extent of HRP (e.g., the non-calcified plaque volume) with both the RMD score and the max % stenosis were computed. In nonob CAD group only positive correlations between RBC rigidity, osmotic fragility or aggregability and HRP features (plaque necrotic core, fibro-fatty and fibro-fatty plus necrotic core plaque volumes) were highlighted. Interestingly, in this patient cohort three of these RBC morphodynamic features result to be independent predictors of the presence of non-calcified plaque volume in this patients group. The risk chart created shows that only in nonob CAD plaque vulnerability increases according to the score quartile. Findings of this work, by evidencing the association between erythrocyte morphodynamic characteristics assessed by LoRRca and plaque instability in a high-risk cohort of nonob CAD, suggest the use of these blood cell features in the identification of high-risk patients, in the absence of severe coronary stenosis.

Keywords: red blood cell morphodynamics, non-obstructive coronary artery disease, high-risk plaque, coronary computed tomography angiography, risk chart

INTRODUCTION

Coronary artery disease (CAD) is one of the major causes of morbidity and mortality in the western countries (Montalescot et al., 2013). Specific anatomic plaque features have been established as fundamental to the process leading to acute coronary thrombosis and, among them, plaque burden, thin-cap fibroatheroma, positive arterial remodeling, necrotic cores, spotty calcifications, and macrophage infiltration play a central role (Virmani et al., 2006).

Although the diagnosis of obstructive (ob) CAD is the milestone for risk stratification in cardiac disease, non-obstructive (nonob) CAD is a relatively common feature, occurring in 10–25% of patients undergoing coronary angiography (Bugiardini and Bairey Merz, 2005), and its presence has been defined as "insignificant" or "no significant CAD" in the medical literature so far (Hung and Cherng, 2003; Patel et al., 2006). Nevertheless, a high number of atheromatous plaques that are not flow limiting are responsible for acute coronary syndromes (ACS; Finn et al., 2010).

The need for improved methods and new markers beyond stenosis for high-risk plaque (HRP) identification follows from these premises.

In the last years, coronary computed tomography angiography (CCTA) has emerged as a non-invasive method for accurate detection and/or exclusion of the presence of CAD (Al-Mallah et al., 2015). Specifically, a high extent of literature evidenced the ability of CCTA to identify not only ob CAD but also early atherosclerotic lesions (Min et al., 2011; Andreini et al., 2012). As before the "CCTA era" patients with nonob CAD and without signs of inducible ischemia were included in the same group of those without evident disease, now with the aid of this imaging technique, we are able, in this patient group, to discriminate between individuals with low-risk plaque morphology and subjects in whom plaque characteristics are associated with an increased risk of future events (Libby, 2013; Conte et al., 2017).

These methodological improvements enhanced a new interest in the evaluation of atherosclerosis determinants, from lumen stenosis to myocardial ischemia. In this context, a new and emerging factor is red blood cell (RBC), not only the transporter of oxygen to tissues but also a cell able to modulate blood flow behavior. Several factors related to RBCs are associated with CAD including erythrocyte sedimentation rate, hemoglobin levels, hematocrit (Hct), and red blood cell distribution width (RDW; Danesh et al., 2000). In particular, it has been demonstrated that men who had the erythrocyte sedimentation rate in the upper quintile had more than twice the risk of coronary heart disease (CHD) death (Gillum et al., 1995). As regards hemoglobin, an observational study conducted on 2,059 patients undergoing coronary artery bypass surgery revealed that individuals with a preoperative hemoglobin concentration of 100 g/L or less had a five-fold higher in-hospital mortality rate after surgery than those with a higher hemoglobin concentration (Zindrou et al., 2002). Opposite results were published on the correlation between Hct and the risk of CHD, with high Hct level associated with an increased risk of myocardial infarction, coronary insufficiency, or CHD death (Sorlie et al., 1981). Recently, the role of RDW in identifying mortality and cardiovascular risk among patients with CAD has been highlighted, being high RDW levels associated with increased risk of mortality and cardiovascular disease (CVD) events in patients with established CAD (Su et al., 2014). However, scarce knowledge is available nowadays regarding their functional profile in relation to morphodynamic features.

An increase in RBC aggregation has been described in patients with acute myocardial infarction (Lakshmi et al., 2011) and was associated with different cardiovascular risk factors, i.e., age (Vaya et al., 2013), obesity (Wiewiora et al., 2007), or diabetes mellitus (Martinez et al., 1998).

A reduced RBC deformability was reported in different vessel types (Baskurt and Meiselman, 2003; Keymel et al., 2011) and linked with pathological states related to microcirculatory disorders such as CAD (Pytel et al., 2013), hypertension (Odashiro et al., 2015), hypercholesterolemia (Kohno et al., 1997), and diabetes mellitus (Jain and Lim, 2000).

However, no data are available about the existence of a relation between RBC rheological properties and high-risk atherosclerotic plaque features.

In this study, we investigated the morphodynamic features of erythrocytes of individuals with different grades of coronary stenosis by means of Laser Assisted Optical Rotational Cell Analyzer (LoRRca MaxSis) in order to find any association between RBC features and plaque characteristics.

MATERIALS AND METHODS

Study Population and Blood Collection

In this study, we prospectively enrolled 91 consecutive patients who underwent CCTA between March 2016 and February 2018 for suspected but unknown stable CAD. In all patients, blood sample was obtained before CCTA and collected into EDTA tubes. Based on CCTA evaluation, patients were defined as having no apparent CAD in the absence of any plaque in the coronary tree (0% stenosis and no luminal irregularities, namely no CAD). Nonobstructive disease was defined as the presence of limited atherosclerotic disease demonstrated by a stenosis <50% (1–49%, named nonob CAD). When the atherosclerotic disease was associated with a stenosis ≥50%, patients were classified as ob CAD.

All patients were further evaluated for the presence of traditional cardiovascular risk factors such as diabetes mellitus (fasting glucose level of 126 mg/dl or higher and/or the need for insulin or oral hypoglycemic agents), hypercholesterolemia (total cholesterol level >200 mg/dl, or treatment with lipid-lowering drugs), hypertension, smoking attitude, and family history of CAD.

This observational study was carried out in accordance with the Declaration of Helsinki and approved by the local ethics research committee of Centro Cardiologico Monzino. Written informed consent to participate was obtained from all subjects.

Coronary Computed Tomography Angiography Scan Protocol, Images Reconstruction, and Analysis

Before CT scan, patients were treated with intravenous beta-blocker (Metoprolol up to 20 mg) to optimize heart rate and

with a standard dose of sublingual nitrates. CCTAs were performed using a last generation 256-CT scanner (Revolution CT GE Healthcare, Milwaukee, WI, USA) with prospective ECG-triggering. A BMI-adapted scanning protocol was used: BMI < 20 Kg/m^2, tube voltage and tube current of 100 kVp and 500 mA, respectively; 20 ≤ BMI < 25 Kg/m^2, tube voltage and tube current of 100 kVp and 550 mA, respectively; 25 ≤ BMI < 30 Kg/m^2, tube voltage and tube current of 100 kVp and 600 mA, respectively; 30 ≤ BMI < 35 Kg/m^2, tube voltage and tube current of 120 kVp and 650 mA, respectively. Patients received a 50-ml (for BMI ≤ 25 Kg/m^2) or 60-ml (for BMI > 25 Kg/m^2) bolus of contrast medium (Iomeron 400 mg/ml, Bracco, Milan, Italy) through an antecubital vein at an infusion rate of 5 ml/s, followed by 50 ml of saline solution. The imaging was performed using bolus tracking technique.

Image CCTA datasets were evaluated using vessel analysis software (CardioQ3 Package - GE Healthcare).

Coronary plaques were defined as structures of at least 1 mm^2 area adjacent to coronary lumen, clearly distinguishable from the vessel lumen and surrounded by pericardial tissue; tissue with signal intensity below 40 HU was considered a pericardial fat and excluded from analysis. Normal coronary arteries were defined when no atherosclerotic plaque (including focal and eccentric calcified plaques) could be detected in any segment within the coronary artery wall or lumen.

Advanced coronary atherosclerosis evaluation were performed as follows: arterial remodeling index assessed using vessel area = lesion plaque area/reference area, plaque burden = (lesion plaque area-lesion lumen area)/lesion plaque area, napkin ring sign defined as the presence of a semi-circular thin enhancement around the plaque along the outer contour of the vessel, and small spotty calcifications as any discrete calcification ≤3 mm in length and occupying ≤90° arc when viewed in short axis, low-attenuation plaque defined as the presence of any plaque voxel <30 HU 11. Total plaque volume was evaluated and reported in mm^3 as previously described (Conte et al., 2020b). Non-calcified fibro-fatty plaque volume was expressed as the amount of plaque <150 HU, reported in mm^3.

Measurement of Morphodynamic RBC Characteristics

The analysis of RBC morphodynamic features was performed by means of Laser Assisted Optical Rotational Red Cell Analyzer (LoRRca MaxSis, Mechatronics, Hoorn, The Netherlands) according to the manufacturer's instructions and detailed below.

Osmotic gradient dependent RBC deformability: 250 µl of whole blood was suspended in 5 ml of polyvinylpyrrolidone buffer (Mechatronics, Hoorn, The Netherlands) and used for the analysis. The osmotic gradient curve generated by the instrument shows the variation in deformability as a continuous function of the osmolality of the solution in which RBCs are dissolved. The following parameters were evaluated: the elongation index (EI)max, corresponding to the maximal deformability or elongation obtained near the isotonic osmolality and is an expression of the membrane surface; the EImin, corresponding to the osmolality at which the deformability reaches its minimum and represents the 50% of the RBCs hemolysis in conventional osmotic fragility assays, reflecting mean cellular surface-to-volume ratio; the osmolality (O)EImax or Omin, corresponding to the osmolality value at which the deformability reaches its EImax or EImin; the area under the curve (AUC, reported in the text as Area), defined in the provided software as the AUC beginning from a starting point in the hypo-osmolar region and an ending point in the hyper-osmolar region (instrument settings 500 mOsm/kg; Baskurt and Meiselman, 2004; Baskurt et al., 2009).

Red blood cells aggregation and disaggregation: 1 ml of oxygenated blood was placed into a preheated (37°C) Couette system consisting of two cylinders. A photo diode, integrated in the fixed inner cylinder, detects the intensity of the backscattered light during the RBC aggregation and disaggregation processes. A syllectogram curve was generated at the end of the assay and the following parameters were automatically calculated: the amplitude (Amp), showing the total extent of aggregation; the aggregation index (AI), calculated as integral of the total syllectogram curve; and the aggregation halftime (t1/2), reflecting the kinetics of RBC aggregation.

Statistical Analysis

Continuous variables were presented as mean ± SD or as median with interquartile range [IQR: 25°–75°], if more appropriate. Continuous variables normally distributed were compared using the Student's *t*-test for independent samples. When the variable distribution was not normal, Mann-Whitney U tests for independent samples were used. Variables with positively skewed distributions were log-transformed before analysis. The proportion of the categorical variables was compared using a χ^2 analysis or Fisher exact test, as appropriate. A value of $p < 0.05$ was considered statistically significant.

Logistic regression analysis was used in order to evaluate the relationship between biological variables and CCTA advanced coronary atherosclerosis characteristics (i.e., plaque volume and HRP features).

For every biological variable associated with CCTA finding with a $p < 0.10$ at logistic regression analysis, a receiver operating characteristic (ROC) curve and a correlation analysis were performed.

The association between RBC morphodynamics and HRP features was assessed by multivariable general linear models, after stratifying the population into the three mentioned groups. The hypothesis that RBC morphodynamics is predictive of a HRP in nonob CAD patients but not in ob ones was tested by computing the appropriate interaction terms. The different RBC morphodynamics variables were tested individually and by multiple regression. Statistical analysis and graphics were produced with MedCalc (version 11.6.1.0, Med-Calc Software; 1993–2011) and by SAS v. 9.4 statistical package (SAS Inc. Cary NC, USA).

Global RBC Morphodynamic (RMD) Score

In order to summarize the potential association of the different RBC morphodynamic variables with HRP in nonob CAD patients, we created a RMD score with the following procedure: first, we ran a multiple regression with non-calcified plaque

volume as dependent variable and the RBC morphodynamic variables as predictors; then, the score was computed as the sum of the variables that were independent predictors of non-calcified plaque volume in the multivariable analysis, each weighted by the beta coefficient. The strength of the associations of the individual variables and of the score with HRP was quantified by the partial R-square.

RESULTS

Population Features

A total of 91 patients were consecutively enrolled. Male prevalence was 68.1% (62 out of 91) and mean age was 61.07 ± 10.9 years. The presence of plaque was excluded in 33 patients (36.3%), while 26 patients had nonob CAD (28.6%) and 32 patients had at least one obstructive coronary stenosis (35.2%).

All demographic and clinical characteristics of the study population were reported in **Table 1**.

Patients with ob CAD were older compared to individuals without CAD. This difference is reflected in a low number of platelets in ob CAD individuals. Interestingly, both ob and nonob CAD patients showed higher mean corpuscular hemoglobin (MCH) and mean corpuscular hemoglobin concentration (MCHC) values compared to no CAD individuals. Prevalence of traditional risk factors and medical therapy at the time of cardiac CCTA were similar throughout the entire enrolled population.

CCTA Characteristics

In **Table 2**, the main features of atherosclerotic lesions detected by CCTA have been reported.

Total coronary plaque volume was 88.5 ± 128.2 mm^3 in the whole cohort of patients enrolled in the study and resulted to be significantly higher in patients with ob CAD when compared to those with nonob disease ($p < 0.0001$). Similarly, non-calcified plaque volume resulted to be significantly higher in patients with ob CAD than in nonob CAD ones. In 26 of

TABLE 1 | Demographic and clinical characteristics of the study population.

Variables	All patients *N* = 91	no CAD *N* = 33	nonob CAD *N* = 26	ob CAD *N* = 32	*p*
Demographic and clinical characteristics					
Age, years	61.07 ± 10.9	57.1 ± 11.5	60.68 ± 10	65.48 ± 9.7*	0.007
Male, *n* (%)	62 (68.1)	18 (54.5)	20 (76.9)	24 (75)	0.07
BMI, kg/m^2	25.42 ± 3.8	25.5 ± 4.5	25.01 ± 3.6	25.66 ± 3.3	0.80
WBC, $10^3/\mu l$	7.41 ± 2.2	7.78 ± 2.5	7.3 ± 1.9	7.11 ± 2.2	0.46
Platelet, $10^3/\mu l$	221.34 ± 61.8	242.76 ± 70	213.69 ± 55.7	205.47 ± 52*	0.04
MPV, fl	10.36 ± 1.4	10.55 ± 0.8	10.23 ± 0.9	10.27 ± 2	0.60
RBC, $10^6/\mu l$	4.75 ± 0.6	4.69 ± 0.5	4.83 ± 0.5	4.75 ± 0.8	0.72
Hb, g/dl	14.3 [13.2–15.2]	13.7 [13–14.6]	14.5 [13.9–15.6]	14.4 [13.4–15.4]	0.05
Hct, %	41.48 ± 4.6	40.4 ± 3.2	42.33 ± 3.7	41.91 ± 6.2	0.22
MCV, fl	87.56 ± 4.5	86.39 ± 5.5	88 ± 4.5	88.41 ± 3.1	0.17
MCH, pg	30.22 ± 1.8	29.49 ± 2.1	30.5 ± 1.9*	30.75 ± 1.2*	0.01
MCHC, %	34.51 ± 0.9	34.13 ± 1	34.66 ± 0.9*	34.78 ± 0.8*	0.01
RDW-CV, %	13.17 ± 0.9	13.22 ± 0.9	13.12 ± 0.7	13.15 ± 0.9	0.90
RDW-SD, fl	41.32 ± 2.8	40.84 ± 2.1	41.58 ± 3	41.59 ± 3.2	0.47
Total cholesterol, mg/dl	197.8 ± 39.5	196.3 ± 35.2	187.9 ± 46.8	206.8 ± 36.1	0.22
LDL cholesterol, mg/dl	118.5 ± 35.1	116.9 ± 29.1	106.7 ± 42.5	129.3 ± 31.4	0.05
HDL cholesterol, mg/dl	57.4 ± 15.1	60.2 ± 14.8	57.2 ± 18.6	54.8 ± 12.3	0.36
Triglycerides, mg/dl	104.77 ± 49.1	97.61 ± 47.6	103.19 ± 50.8	113.44 ± 49.5	0.43
Basal glucose, mg/dl	99.5 ± 16.7	103.3 ± 19.7	93 ± 10.4	100.8 ± 16.2	0.05
Hypertension, *n* (%)	43 (47.3)	14 (42.4)	12 (46.2)	17 (53.1)	0.39
Family history of CVD, *n* (%)	36 (39.6)	10 (30.3)	15 (57.7)	11(34.4)	0.65
Dyslipidaemia, *n* (%)	37 (40.6)	13 (39.4)	14 (53.8)	10 (31.2)	0.51
Diabetes, *n* (%)	5 (5.5)	2 (6.1)	1 (3.8)	2 (6.2)	0.98
Active smokers, *n* (%)	20 (21.9)	5 (15.2)	9 (34.6)	6 (18.7)	0.17
Past smokers, *n* (%)	16 (17.6)	7 (21.2)	2 (7.7)	7 (21.8)	0.28
Pharmacological treatments					
β-blockers, *n* (%)	55 (60.4)	16 (48.5)	19 (71.1)	20 (62.5)	0.24
ACE-inhibitors, *n* (%)	18 (19.8)	6 (18.2)	6 (23.1)	6 (18.7)	0.95
Angiotensin receptor blockers, *n* (%)	16 (17.6)	4 (12.1)	5 (19.2)	7 (21.8)	0.30
Diuretics, *n* (%)	13 (16.3)	4 (12.1)	1 (3.8)	8 (25)	0.14
Aspirin, *n* (%)	20 (21.9)	8 (24.4)	4 (15.4)	8 (25)	0.95
Statins, *n* (%)	30 (32.9)	7 (21.1)	13 (50)	10 (31.2)	0.38

BMI, body mass index; CVD, cardiovascular disease; Hb, hemoglobin; Hct, hematocrit; HDL, high-density lipoprotein; LDL, low-density lipoprotein; MCH, mean corpuscular hemoglobin; MCHC, mean corpuscular hemoglobin concentration; MCV, mean corpuscular volume; MPV, mean platelet volume; RBC, red blood cell; RDW-CV, red blood cell distribution width-coefficient of variation; RDW-SD, red blood cell distribution width-standard deviation; WBC, white blood cell.
$^*p < 0.05$ vs. no CAD; $^†p < 0.05$ vs. nonob CAD.

TABLE 2 | CCTA characteristics of the study population.

Parameters	All patients *N* = 91	no CAD *N* = 33	nonob CAD *N* = 26	ob CAD *N* = 32	*p*
Total plaque volume, mm^3	88.5 ± 128.2	-	99.6 ± 126.7*	170.7 ± 139.1*,†	<0.001
Non-calcified plaque volume, mm^3	25.2 ± 40.7	-	25.9 ± 35.6*	50.7 ± 49.3*,†	<0.001
High risk plaque features >2, *n* (%)	26 (28.6)	0	6 (23.1)	20 (62.5)*,†	<0.001
Non-calcified plaque volume HQ, *n* (%)	23 (25.3)	0	6 (23.1)	17 (53.1)*,†	<0.001
Total plaque volume HQ, *n* (%)	23 (25.3)	0	5 (19.2)	18 (56.3)*,†	<0.001

CAD, coronary artery disease; CCTA, coronary computed tomography angiography; HQ, high quartile.
**p < 0.05 vs. no CAD; †p < 0.05 vs. nonob CAD.*

TABLE 3 | RBC morphodynamic parameters in the study population.

Parameters	All patients *N* = 91	no CAD *N* = 33	nonob CAD *N* = 26	ob CAD *N* = 32	*p*
Deformability					
Elmax	0.63 ± 0.02	0.62 ± 0.02	0.63 ± 0.01	0.63 ± 0.02	0.54
Elmin	0.12 ± 0.01	0.12 ± 0.01	0.12 ± 0.01	0.12 ± 0.01	0.96
O Elmax, mOsm/kg	290.85 ± 19.5	290.96 ± 18.4	285.95 ± 17.1	294.84 ± 22.1	0.31
Omin, mOsm/kg	134.81 ± 8.4	134.23 ± 7.8	133.81 ± 8.5	136.24 ± 9.1	0.57
Area	149.93 ± 5.2	152.02 ± 5.3	149.45 ± 4.9	148.14 ± 4.7*	0.02
Aggregation					
AI, %	64.76 ± 10.4	66.69 ± 8.7	61.81 ± 11.2	65.54 ± 10.8	0.24
Amp, au	37.09 ± 9.5	37.02 ± 11.6	39.79 ± 5.2	34.94 ± 10	0.19
$t_{1/2}$, sec	1.8 [1.5–2.5]	1.8 [1.3–2.3]	2.2 [1.6–2.5]	1.8 [1.3–2.4]	0.17
RMD score	−47.2 [−47.6, −47.0]	−47.1 [−47.6, −46.9]	−47.2 [−47.5, −47.0]	−47.3 [−48.1, −46.7]	0.75

AI, aggregation index; Amp, amplitude of the aggregate; CAD, coronary artery disease; Elmax, maximal elongation index; Elmin, minimum elongation index; O Elmax, osmolality corresponding to maximal elongation index; Omin osmolality corresponding to minimum elongation index; RMD, RBC morphodynamic; t1/2, aggregation halftime.
**p < 0.05 vs. no CAD.*

91 patients (28.6%) more than two HRP features were identified; as expected, an high prevalence of HRP features was recorded among patients with ob CAD [6 (23.1%) vs. 20 (62.5%), value of $p < 0.0001$ for nonob vs. ob CAD patients].

RBC Morphodynamics

In our study population, the analysis of RBC morphodynamic characteristics in relation to the degree of stenosis did not evidence any difference. The only parameter altered in ob CAD patients compared to no CAD is the Area (value of $p = 0.024$, **Table 3**), evidencing a reduced ability of erythrocytes to modify their shape in response to an osmotic gradient curve in patients with a severe stenosis.

RBC Morphodynamics and Atherosclerotic Plaque Features at CCTA

While no statistically significant association between RBC morphodynamic characteristics assessed by LoRRca and HRP features was found in patients with severe stenosis, in nonob CAD group, several relationships were evidenced.

In particular, we highlighted a positive correlation between RBC osmotic fragility (evaluated using the Omin value from the osmoscan curve) and two HRP features: fibro-fatty (**Figure 1A**) and fibro-fatty plus necrotic core plaque (**Figure 1B**) volumes. In parallel with increased fragility, we found correlations between RBC rigidity (assessed by a reduction in the Area of the osmoscan graph), defined by the inability of cell to change its shape under various osmotic conditions, and necrotic core (**Figure 1C**), fibro-fatty (**Figure 1D**) and fibro-fatty plus necrotic core (**Figure 1E**) plaque volumes.

In addition, RBC from nonob CAD patients with a high necrotic core plaque volume displayed an increased kinetics of aggregation (**Figure 1F,G**).

In accordance to these findings, we evidenced only in nonob CAD group the existence of an interaction among all these morphodynamic RBC characteristics and fibro-fatty plus necrotic core plaque volume (value of $p = 0.005$).

In this patient group, the non-calcified plaque volume resulted to be inversely associated with the degree of RBC resistance to lysis (Omin; **Figure 2A**) and positively correlated with the Area (**Figure 2B**), while no association was found with the total plaque volume (**Figures 2C,D**), an index of the extent of atherosclerosis.

Of interest, neither Omin nor Area or RBC aggregation parameters resulted to be significantly correlated to HRP features among patients with ob CAD (**Supplementary Figures S1, S2**).

To corroborate the existence of a relationship between RBC morphodynamic characteristics and HRP features specifically in nonob CAD population, in this patient group, we found an apparent linear relation between five RBC morphodynamic features and non-calcified plaque volume. Although the correlation was significant only for O EImax, the pattern was similar for all features, with a concomitant totally flat relation in patients with severe stenosis (ob CAD; **Figures 3A–E**).

Most importantly, in a multivariable analysis, three morphodynamic RBC variables were independent predictors of non-calcified plaque volume in nonob CAD patients, i.e.,

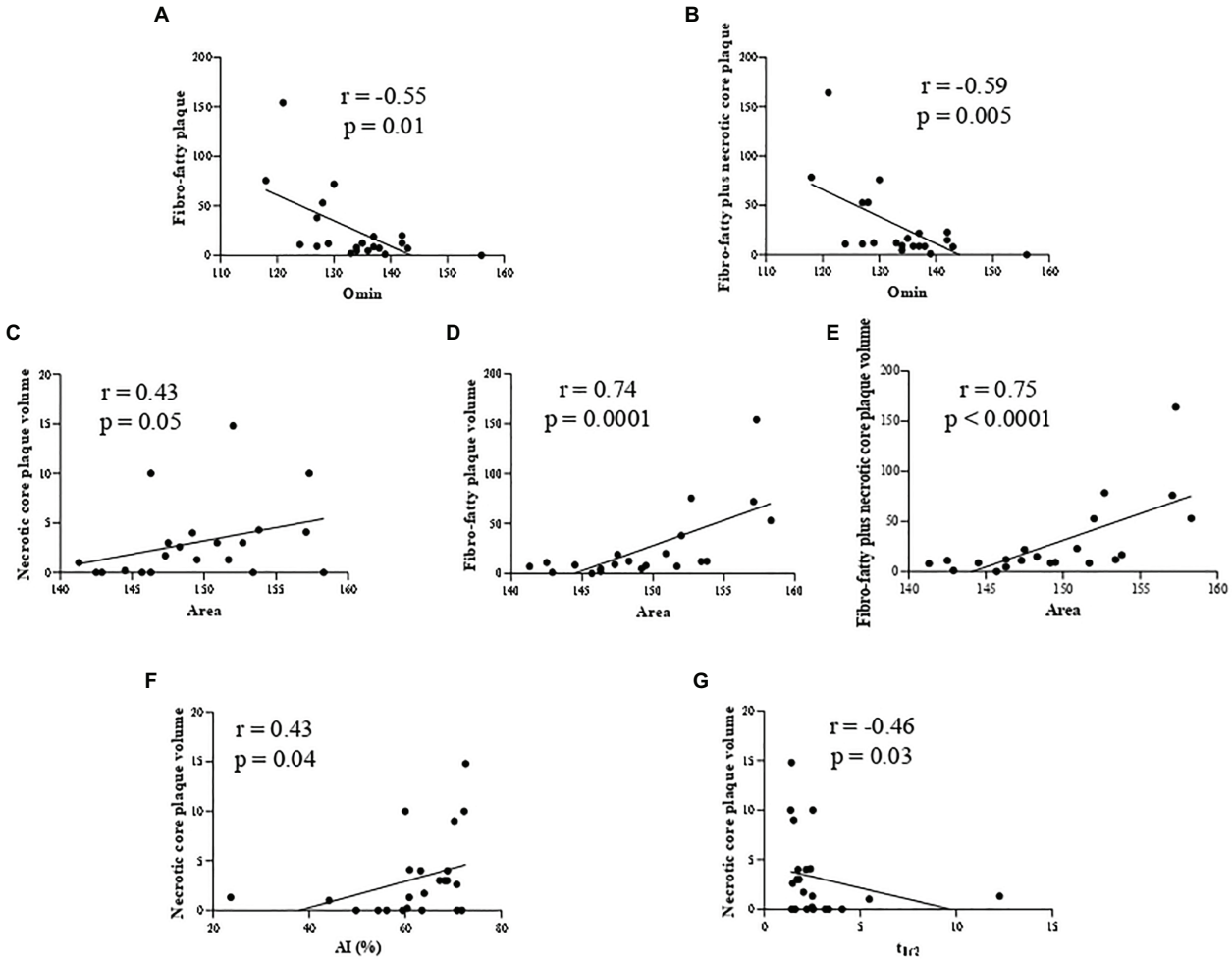

FIGURE 1 | Correlation analysis in nonob CAD patients revealing the association between: RBC osmotic fragility (evaluated using the Omin value from the osmoscan curve) and two HRP features (fibro-fatty **(A)** and fibro-fatty plus necrotic core plaque **(B)** volumes) and between RBC rigidity (assessed by a reduction in the Area of the osmoscan graph) and necrotic core **(C)**, fibro-fatty **(D)** and fibro-fatty plus necrotic core **(E)** plaque volumes. RBC from nonob CAD with a high necrotic core plaque volume displayed an increased kinetics of aggregation [displayed by AI **(F)** and $t_{1/2}$ **(G)**]. AI, aggregation index; Area, area under the elongation index-related osmolality curve; CAD, coronary artery disease; HRP, high-risk plaque; nonob CAD, non-obstructive coronary artery disease; Omin, minimal osmolality; RBC, red blood cell; $t_{1/2}$, aggregation half time.

EImax, O EImax and $t_{1/2}$ (**Table 4**). These variables were included in the putative global RMD score, which was computed using the following formula:

$$\text{RMD score} = 22.6 \times \log(\text{EImax}) + 17.2 \times \log(\text{O EImax}) + 1.6 \times \log(\text{t1}/2)$$

The RMD score was not associated with the presence or degree of CAD (**Table 3**), but it strongly correlated with the extent of HRP (such as the non-calcified plaque volume) in the nonob CAD group (**Figure 4A**). Therefore, the RMD score could be utilized in clinical practice to illustrate its potential use, we created a risk chart, relating three variables: the RMD score (in quartiles), the max % stenosis, and the non-calcified plaque volume (**Figure 4B**). This chart shows that only in nonob CAD patients the plaque instability increases according to RMD score quartile. Of note, a significant interaction between the RMD score and patient group was found (value of $p = 0.001$), with an R-square (i.e., the proportion of the variability of non-calcified plaque volume explained by the score) in the nonob CAD group equal to 0.38, whereas in the ob CAD was 0.008.

DISCUSSION

In this study, we highlighted the presence of changes in morphodynamic features of RBCs from patients with nonob CAD assessed by means of LoRRca. In this clinical setting, RBC alterations correlate well with HRP features detected by CCTA, suggesting the existence of a possible link between erythrocyte morphodynamics and the increased risk of acute coronary events.

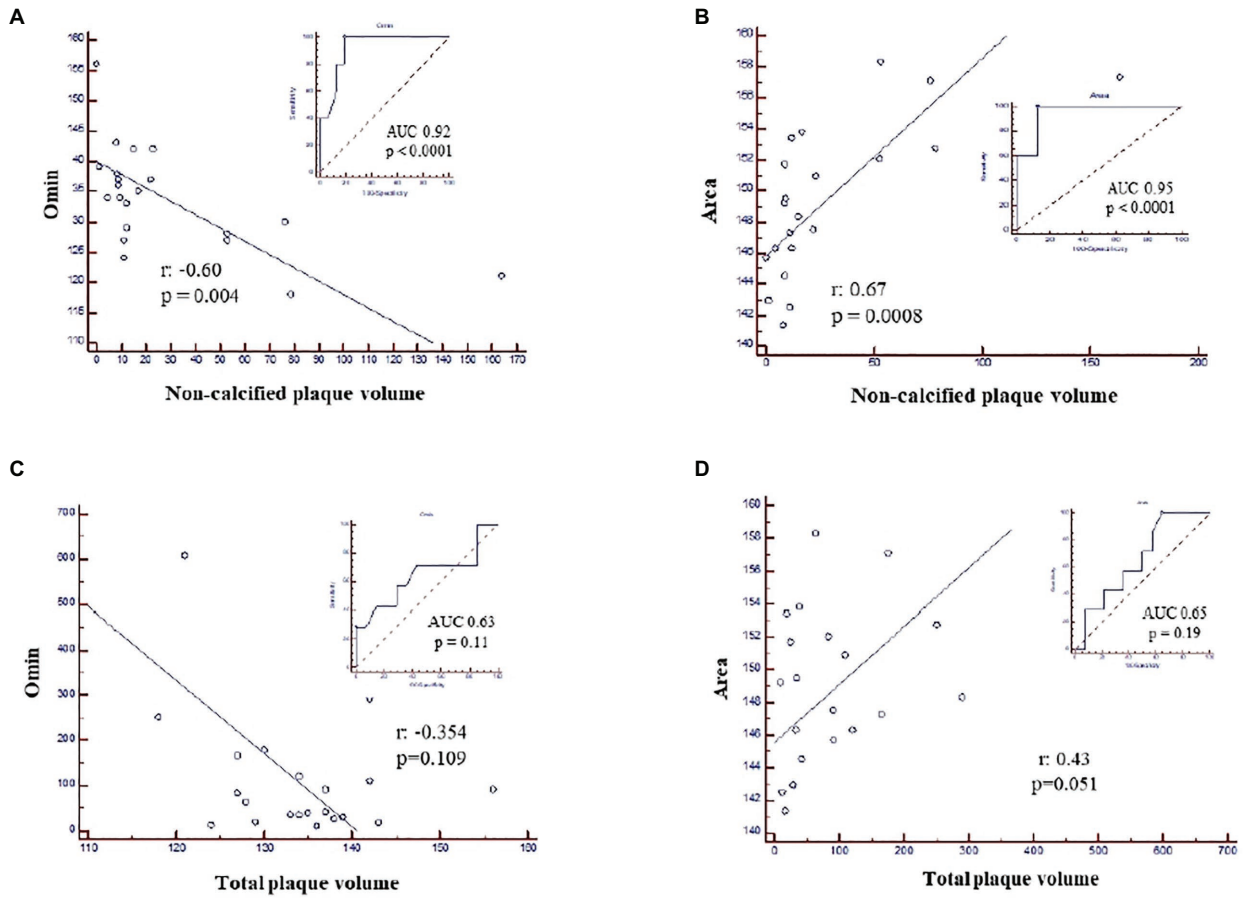

FIGURE 2 | ROC curves and correlation analysis in nonob CAD patients showing the association between non-calcified plaque volume and **(A)** Omin, corresponding to the degree of RBC resistance to lysis; **(B)** the Area and the absence of any correlation between total plaque volume and Omin **(C)** and the Area **(D)**. Area, area under the elongation index-related osmolality curve; CAD, coronary artery disease; nonob CAD, non-obstructive coronary artery disease; Omin, minimal osmolality; RBC, red blood cell; ROC, Receiver Operating Characteristic.

In the last decade, a high number of reports highlighted the presence of acute coronary syndrome (ACS) in the contest of nonob CAD. Up to now, the identification of HRPs is demanded to CCTA and, even if preliminary data on the CAPIRE study may suggest a potential association between HRP features and inflammatory markers (Conte et al., 2020a), the lack of circulating biomarkers associated with plaque instability constitutes a critical diagnostic issue.

Our findings, highlighting the existence of a connection between the erythrocyte morphodynamic behavior and plaque instability, turns on new lights on this circulating cell, moving the attention from the instable plaque to the instable patient.

During its long lifespan of 120 days, RBCs pass through the entire circulatory system where they play a key role in blood flow regulation and the consequent tissue perfusion (Yedgar et al., 2002). Even if up to now the precise mechanism underlining the involvement of this blood cell in the control of circulatory processes is not well described, some hypotheses can be formulated. In particular, it has been recognized the role of ATP release from RBC in modulating vasomotor tone in the microcirculation through a diffusive mechanism toward endothelial cells. This mechanical-dependent release is sensitive to several stimuli and, between them, low oxygen level, shear stress, and shape deformation and is believed to play an important role in the microcirculation, characterized by high levels of shear stress and shape deformation degree (Sprague et al., 1998; Dietrich et al., 2000; Wan et al., 2008; Forsyth et al., 2011). Another key mechanism through which RBCs regulate vascular function is NO production and release (Simmonds et al., 2014). Specifically, thanks to the internal compartmentalization of hemoglobin, RBCs are able to maintain hemostasis through the well-regulated delivery of oxygen and the balance of NO scavenging and production (Helms et al., 2018).

It becomes evident the importance of RBC regulatory role in vascular function in pathological states able to compromise the RBC membrane integrity leading to conditions of increased oxidative stress, hypertension, thrombosis, and vaso-occlusion.

In this regard, RBC aggregation and adherence to the endothelial wall were described to be influenced by both blood cellular and plasma factors, as this is a reversible process that depends on the concentration of high molecular weight proteins such as

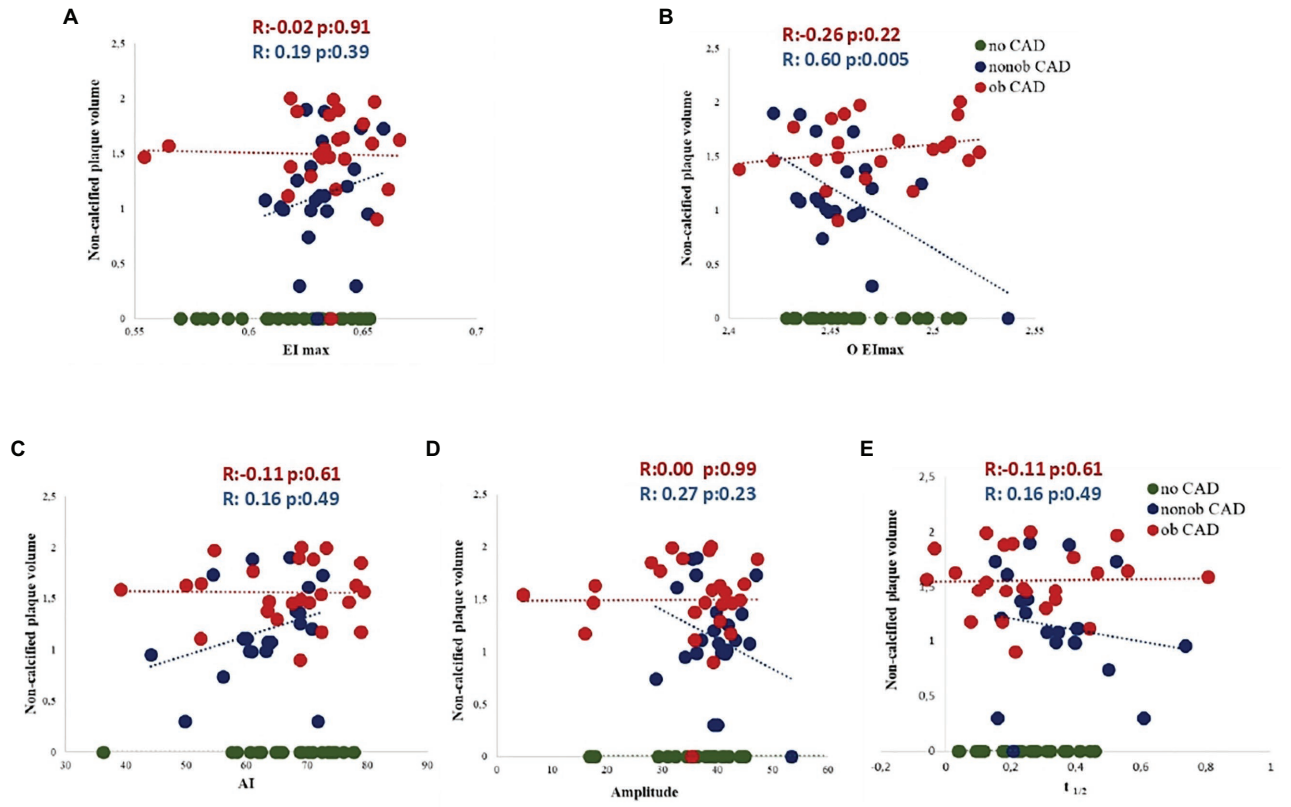

FIGURE 3 | Association between five RBC morphodynamic characteristics (AI, **A**; Amp, **B**; $t_{1/2}$, **C**; Elmax, **D**; O Elmax, **E**) and non-calcified plaque volume in nonob CAD (red dots), ob CAD (green dots) and no CAD (blue dots) patients. AI, aggregation index; Amp, amplitude of RBC aggregation; CAD, coronary artery disease; Elmax, maximal elongation index; nonob CAD, non-obstructive coronary artery disease; O Elmax, osmolality for Elmax; ob CAD, obstructive coronary artery disease; RBC, red blood cell; $t_{1/2}$, aggregation half time.

TABLE 4 | Morphodynamic RBC variables that are independent predictors of non-calcified plaque volume in nonob CAD patients.

Variable (log-transformed)	Beta coefficient	SE	*p*
Elmax	22.6	7.7	0.011
O Elmax	17.2	2.8	<0.0001
$t_{1/2}$	1.6	0.5	0.004

El max, maximal elongation index; O Elmax, osmolality corresponding to maximal elongation index; SE, standard error; t1/2, aggregation halftime.

fibrinogen (Baskurt, 2007). In this regard, it has been demonstrated that RBC aggregates strength directly correlates to the inflammatory state (Ami et al., 2001). Specifically, the RBC aggregation parameters considered in the study conducted by Ami and colleagues (i.e., the average aggregate size, the distribution of the RBC population into aggregate size ranges, the shear stress required to obtain 50% of RBC population in the small range of aggregate size, and the area under the curve (AUC) of the plot as a function of shear stress) correlated with the inflammatory indexes C reactive protein and fibrinogen in patients with cardiovascular and infectious conditions associated with an inflammatory response, regardless of the specific pathological state and despite the variability of symptoms. In addition, RBC deformability was found to be able to control platelet-vessel interaction (Aarts et al., 1984). In this context, the morphodynamic characteristics we evidenced in RBCs of patients with nonob CAD could be the result of the interaction among RBC and cell components or humoral factors derived from plaque or are consequent to the alteration of the erythrocyte itself that negatively influences plaque progression (Aarts et al., 1984).

It could be expected HRP features to be associated to RBC dysfunctionality also in ob CAD patients. These data might be explained by the diffuse endothelial dysfunction that characterizes patients with ob CAD that could mask the interplay between atherosclerosis and RBC alterations. Of interest, when comparing individuals with or without ob stenosis, no difference in RBC morphodynamics was observed as total plaque volume was not associated with erythrocyte features, suggesting that overall atherosclerosis burden is a sub-optimal marker of atherosclerosis disease activity at least in the early stages.

Thus, it can be hypothesized that RBC could be mainly involved in the early phase of atherosclerosis process (nonob CAD), rather than in the more advanced stages (ob CAD).

Our data have also to be considered in view of the results of the CAPIRE study that specifically identified high non-calcified

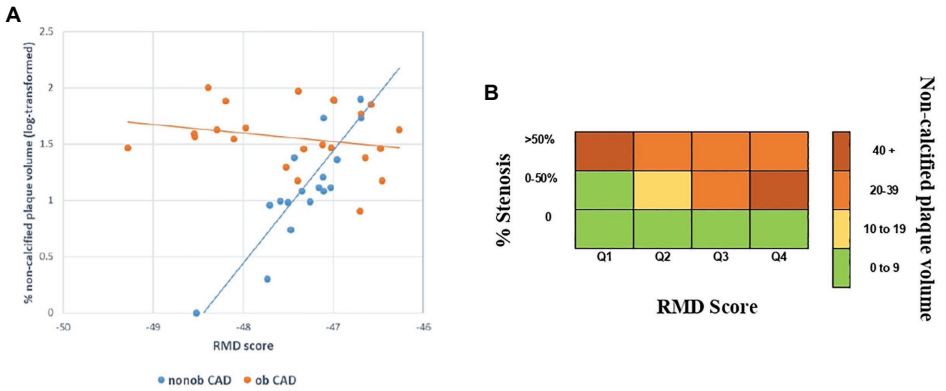

FIGURE 4 | Association between HRP (such as the non-calcified plaque volume) and the RMD score in nonob and ob CAD groups **(A)**. Risk chart, relating the RMD score and the maximal percentage of stenosis with the extent of HRP feature (i.e., the non-calcified plaque volume), showing the existence of a strong relationship in nonob CAD group. The strong association is depicted in dark red, while the weak one in green **(B)**. CAD, coronary artery disease; HRP, high-risk plaque; nonob CAD, non-obstructive coronary artery disease; ob CAD, obstructive coronary artery disease; RMD, RBC morphodynamic; RBC, red blood cell.

plaque volume as the most ACS-predictive parameter in CAD patients. The underlined association between RBC dysfunction indexes and adverse plaque features (i.e., non-calcified plaque volume) can be proposed as a new systemic non-invasive marker for the identification of high risk patients (Andreini et al., 2019).

In this context, one possible pathophysiological model to explain the correlation between elevated non-calcified plaque volume and RBC rigidity could be identified in the role of cholesterol in determining RBC deformability. More precisely, as previously described (Banerjee et al., 1998; Cicco and Pirrelli, 1999; Ercan et al., 2002), higher amount of cholesterol in RBC structure positively correlates with their hemorheological parameters and especially with rigidity. In our clinical setting, the decrease in the area under the curve (AUC) value in ob CAD vs. no CAD could be the result of increased cholesterol (Banerjee et al., 1998), as in our patient group, the levels of LDL cholesterol show a trend to increase, moving from nonob CAD to no CAD and to ob CAD. We cannot exclude that the absence of a difference in the EI max value can be attributable to the pharmacological treatment with statins, present in the 50% of nonob CAD and in the 31.2% of ob CAD.

Similarly, tissue with low CT attenuation are commonly considered as lipid rich and low-attenuation coronary plaque in CCTA could be considered as a diagnostic for lipid-core unstable plaque (Chen et al., 2010; Schlett et al., 2013). This pathophysiological hypothesis, even if of speculative nature, well fits with the widely recognized role of dyslipidemia as a major cardiovascular risk factor.

Another factor able to augment RBC rigidity is an increase in intracellular viscosity because of increased MCHC. Specifically, a variation in MCHC values as a result of a different hydrating states of erythrocytes is able to induce a modification in the osmotic deformability profile (and consequently in the area) without affecting the EImax (Clark et al., 1983). According to these findings, in our study population we registered a significant increase in MCHC values from no CAD to ob CAD that could explain in part this result.

As clinical tool, the morphodynamic characteristics combined into the RMD score could be used in a risk chart. This is a simple, cheap and non-invasive procedure that will allow identifying high risk patients in the early stage of atherosclerosis. The use of this chart in the clinical practice could help in better identifying patients who may merit CCTA, even if asymptomatic, and in the long-term follow-up of non-obstructive patients with a high probability of experiencing acute events.

Several limitations warrant discussion. This study was conducted on a small number of subjects. The RMD score and its relative risk chart here obtained have not to be considered as substitutes of CCTA. Moreover, further studies are needed before our findings could be used in clinical practice for early identification of asymptomatic patients who may merit screening CCTA, that nowadays remains not indicated.

CONCLUSION

In nonob CAD patients the HRP features correlated with an altered RBC morphodynamic behavior highlighted by means of LoRRca. Three of the erythrocyte flow-affecting properties analyzed are independent predictors of the extent of the non-calcified plaque volume in this population. The RMD score and the related risk chart clearly highlighted the rise of acute events probability with the increase of erythrocyte altered features.

Further studies are needed to validate this chart in a large cohort of subjects in order to define its potential use in patient identification and management, with the final goal of slowing the disease progression.

DATA AVAILABILITY STATEMENT

The raw data supporting the conclusions of this article will be made available by the authors, without undue reservation.

ETHICS STATEMENT

The studies involving human participants were reviewed and approved by Local ethics research committee of Centro Cardiologico Monzino. The patients/participants provided their written informed consent to participate in this study.

AUTHOR CONTRIBUTIONS

BP, EC, VC, and DA designed the study. BP, AZ, AM, and SF performed the ektacytometry assays. EC and SM enrolled patients. BP, EC, PB, DA, and VC interpreted the results. FV and SB performed statistical analysis. BP and EC wrote the manuscript. BP, EC, AZ, PB, FV, SB, SF, SE, AM, SM, ET, VC, and DA reviewed and approved the final version of the manuscript.

FUNDING

This research was funded by Italian Ministry of Health, grant number RC-2016 BIO03.

SUPPLEMENTARY MATERIAL

The Supplementary Material for this article can be found online at: https://www.frontiersin.org/articles/10.3389/fphys.2020.603633/full#supplementary-material

REFERENCES

Aarts, P. A., Heethaar, R. M., and Sixma, J. J. (1984). Red blood cell deformability influences platelets--vessel wall interaction in flowing blood. *Blood* 64, 1228–1233.

Al-Mallah, M. H., Aljizeeri, A., Villines, T. C., Srichai, M. B., and Alsaileek, A. (2015). Cardiac computed tomography in current cardiology guidelines. *J. Cardiovasc. Comput. Tomogr.* 9, 514–523. doi: 10.1016/j.jcct.2015.09.003

Ami, R. B., Barshtein, G., Zeltser, D., Goldberg, Y., Shapira, I., Roth, A., et al. (2001). Parameters of red blood cell aggregation as correlates of the inflammatory state. *Am. J. Physiol. Heart Circ. Physiol.* 280, H1982–H1988. doi: 10.1152/ajpheart.2001.280.5.H1982

Andreini, D., Magnoni, M., Conte, E., Masson, S., Mushtaq, S., Berti, S., et al. (2019). Coronary plaque features on CTA can identify patients at increased risk of cardiovascular events. *JACC Cardiovasc. Imaging* 13, 1704–1717. doi: 10.1016/j.jcmg.2019.06.019

Andreini, D., Pontone, G., Mushtaq, S., Bartorelli, A. L., Bertella, E., Antonioli, L., et al. (2012). A long-term prognostic value of coronary CT angiography in suspected coronary artery disease. *JACC Cardiovasc. Imaging* 5, 690–701. doi: 10.1016/j.jcmg.2012.03.009

Banerjee, R., Nageshwari, K., and Puniyani, R. R. (1998). The diagnostic relevance of red cell rigidity. *Clin. Hemorheol. Microcirc.* 19, 21–24.

Baskurt, O. K. (2007). *Handbook of Hemorheology and Hemodynamics*. IOS Press.

Baskurt, O. K., Hardeman, M. R., Uyuklu, M., Ulker, P., Cengiz, M., Nemeth, N., et al. (2009). Parameterization of red blood cell elongation index—shear stress curves obtained by ektacytometry. *Scand. J. Clin. Lab. Invest.* 69, 777–788. doi: 10.3109/00365510903266069

Baskurt, O. K., and Meiselman, H. J. (2003). Blood rheology and hemodynamics. *Semin. Thromb. Hemost.* 29, 435–450. doi: 10.1055/s-2003-44551

Baskurt, O. K., and Meiselman, H. J. (2004). Analyzing shear stress-elongation index curves: comparison of two approaches to simplify data presentation. *Clin. Hemorheol. Microcirc.* 31, 23–30.

Bugiardini, R., and Bairey Merz, C. N. (2005). Angina with "normal" coronary arteries: a changing philosophy. *J. Am. Med. Assoc.* 293, 477–484. doi: 10.1001/jama.293.4.477

Chen, Z., Ichetovkin, M., Kurtz, M., Zycband, E., Kawka, D., Woods, J., et al. (2010). Cholesterol in human atherosclerotic plaque is a marker for underlying disease state and plaque vulnerability. *Lipids Health Dis.* 9:61. doi: 10.1186/1476-511X-9-61

Cicco, G., and Pirrelli, A. (1999). Red blood cell (RBC) deformability, RBC aggregability and tissue oxygenation in hypertension. *Clin. Hemorheol. Microcirc.* 21, 169–177.

Clark, M. R., Mohandas, N., and Shohet, S. B. (1983). Osmotic gradient ektacytometry: comprehensive characterization of red cell volume and surface maintenance. *Blood* 61, 899–910.

Conte, E., Andreini, D., Magnoni, M., Masson, S., Mushtaq, S., Berti, S., et al. (2020a). Association of high-risk coronary atherosclerosis at CCTA with clinical and circulating biomarkers: insight from CAPIRE study. *J. Cardiovasc. Comput. Tomogr.* doi: 10.1016/j.jcct.2020.03.005 [Epub ahead of print]

Conte, E., Annoni, A., Pontone, G., Mushtaq, S., Guglielmo, M., Baggiano, A., et al. (2017). Evaluation of coronary plaque characteristics with coronary computed tomography angiography in patients with non-obstructive coronary artery disease: a long-term follow-up study. *Eur. Heart J. Cardiovasc. Imaging* 18, 1170–1178. doi: 10.1093/ehjci/jew200

Conte, E., Mushtaq, S., Pontone, G., Li Piani, L., Ravagnani, P., Galli, S., et al. (2020b). Plaque quantification by coronary computed tomography angiography using intravascular ultrasound as a reference standard: a comparison between standard and last generation computed tomography scanners. *Eur. Heart J. Cardiovasc. Imaging* 21, 191–201. doi: 10.1093/ehjci/jez089

Danesh, J., Collins, R., Peto, R., and Lowe, G. D. (2000). Haematocrit, viscosity, erythrocyte sedimentation rate: meta-analyses of prospective studies of coronary heart disease. *Eur. Heart J.* 21, 515–520. doi: 10.1053/euhj.1999.1699

Dietrich, H. H., Ellsworth, M. L., Sprague, R. S., and Dacey, R. G. Jr. (2000). Red blood cell regulation of microvascular tone through adenosine triphosphate. *Am. J. Physiol. Heart Circ. Physiol.* 278, H1294–H1298. doi: 10.1152/ajpheart.2000.278.4.H1294

Ercan, M., Konukoglu, D., Erdem, T., and Onen, S. (2002). The effects of cholesterol levels on hemorheological parameters in diabetic patients. *Clin. Hemorheol. Microcirc.* 26, 257–263.

Finn, A. V., Nakano, M., Narula, J., Kolodgie, F. D., and Virmani, R. (2010). Concept of vulnerable/unstable plaque. *Arterioscler. Thromb. Vasc. Biol.* 30, 1282–1292. doi: 10.1161/ATVBAHA.108.179739

Forsyth, A. M., Wan, J., Owrutsky, P. D., Abkarian, M., and Stone, H. A. (2011). Multiscale approach to link red blood cell dynamics, shear viscosity, and ATP release. *Proc. Natl. Acad. Sci. U. S. A.* 108, 10986–10991. doi: 10.1073/pnas.1101315108

Gillum, R. F., Mussolino, M. E., and Makuc, D. M. (1995). Erythrocyte sedimentation rate and coronary heart disease: the NHANES I epidemiologic follow-up study. *J. Clin. Epidemiol.* 48, 353–361. doi: 10.1016/0895-4356(94)00156-k

Helms, C. C., Gladwin, M. T., and Kim-Shapiro, D. B. (2018). Erythrocytes and vascular function: oxygen and nitric oxide. *Front. Physiol.* 9:125. doi: 10.3389/fphys.2018.00125

Hung, M. J., and Cherng, W. J. (2003). Comparison of white blood cell counts in acute myocardial infarction patients with significant versus insignificant coronary artery disease. *Am. J. Cardiol.* 91, 1339–1342. doi: 10.1016/s0002-9149(03)00325-4

Jain, S. K., and Lim, G. (2000). Lipoic acid decreases lipid peroxidation and protein glycosylation and increases $(Na^{(+)} + K^{(+)})$- and $Ca^{(++)}$-ATPase activities in high glucose-treated human erythrocytes. *Free Radic. Biol. Med.* 29, 1122–1128. doi: 10.1016/s0891-5849(00)00410-x

Keymel, S., Heiss, C., Kleinbongard, P., Kelm, M., and Lauer, T. (2011). Impaired red blood cell deformability in patients with coronary artery disease and diabetes mellitus. *Horm. Metab. Res.* 43, 760–765. doi: 10.1055/s-0031-1286325

Kohno, M., Murakawa, K., Yasunari, K., Yokokawa, K., Horio, T., Kano, H., et al. (1997). Improvement of erythrocyte deformability by cholesterol-lowering therapy with pravastatin in hypercholesterolemic patients. *Metabolism* 46, 287–291.

Lakshmi, A. B., Uma, P., Venkatachalam, C., and Nageswar Rao, G. S. (2011). A simple slide test to assess erythrocyte aggregation in acute ST-elevated myocardial infarction and acute ischemic stroke: its prognostic significance. *Indian J. Pathol. Microbiol.* 54, 63–69. doi: 10.4103/0377-4929.77327

Libby, P. (2013). Mechanisms of acute coronary syndromes and their implications for therapy. *N. Engl. J. Med.* 368, 2004–2013. doi: 10.1056/NEJMra1216063

Martinez, M., Vaya, A., Server, R., Gilsanz, A., and Aznar, J. (1998). Alterations in erythrocyte aggregability in diabetics: the influence of plasmatic fibrinogen and phospholipids of the red blood cell membrane. *Clin. Hemorheol. Microcirc.* 18, 253–258.

Min, J. K., Dunning, A., Lin, F. Y., Achenbach, S., Al-Mallah, M., Budoff, M. J., et al. (2011). Age- and sex-related differences in all-cause mortality risk based on coronary computed tomography angiography findings results from the International Multileft CONFIRM (Coronary CT angiography evaluation for clinical outcomes: an international Multileft registry) of 23,854 patients without known coronary artery disease. *J. Am. Coll. Cardiol.* 58, 849–860. doi: 10.1016/j.jacc.2011.02.074

Montalescot, G., Sechtem, U., Achenbach, S., Andreotti, F., Arden, C., Budaj, A., et al. (2013). 2013 ESC guidelines on the management of stable coronary artery disease: the task force on the management of stable coronary artery disease of the European Society of Cardiology. *Eur. Heart J.* 34, 2949–3003. doi: 10.1093/eurheartj/eht296

Odashiro, K., Saito, K., Arita, T., Maruyama, T., Fujino, T., and Akashi, K. (2015). Impaired deformability of circulating erythrocytes obtained from nondiabetic hypertensive patients: investigation by a nickel mesh filtration technique. *Clin. Hypertens.* 21:17. doi: 10.1186/s40885-015-0030-9

Patel, M. R., Chen, A. Y., Peterson, E. D., Newby, L. K., Pollack, C. V. Jr., Brindis, R. G., et al. (2006). Prevalence, predictors, and outcomes of patients with non-ST-segment elevation myocardial infarction and insignificant coronary artery disease: results from the Can Rapid risk stratification of Unstable angina patients Suppress ADverse outcomes with Early implementation of the ACC/AHA guidelines (CRUSADE) initiative. *Am. Heart J.* 152, 641–647. doi: 10.1016/j.ahj.2006.02.035

Pytel, E., Olszewska-Banaszczyk, M., Koter-Michalak, M., and Broncel, M. (2013). Increased oxidative stress and decreased membrane fluidity in erythrocytes of CAD patients. *Biochem. Cell Biol.* 91, 315–318. doi: 10.1139/bcb-2013-0027

Schlett, C. L., Ferencik, M., Celeng, C., Maurovich-Horvat, P., Scheffel, H., Stolzmann, P., et al. (2013). How to assess non-calcified plaque in CT angiography: delineation methods affect diagnostic accuracy of low-attenuation plaque by CT for lipid-core plaque in histology. *Eur. Heart J. Cardiovasc. Imaging* 14, 1099–1105. doi: 10.1093/ehjci/jet030

Simmonds, M. J., Detterich, J. A., and Connes, P. (2014). Nitric oxide, vasodilation and the red blood cell. *Biorheology* 51, 121–134. doi: 10.3233/BIR-140653

Sorlie, P. D., Garcia-Palmieri, M. R., Costas, R. Jr., and Havlik, R. J. (1981). Hematocrit and risk of coronary heart disease: the Puerto Rico Health Program. *Am. Heart J.* 101, 456–461. doi: 10.1016/0002-8703(81)90136-8

Sprague, R. S., Ellsworth, M. L., Stephenson, A. H., Kleinhenz, M. E., and Lonigro, A. J. (1998). Deformation-induced ATP release from red blood cells requires CFTR activity. *Am. J. Phys.* 275, H1726–H1732. doi: 10.1152/ajpheart.1998.275.5.H1726

Su, C., Liao, L. Z., Song, Y., Xu, Z. W., and Mei, W. Y. (2014). The role of red blood cell distribution width in mortality and cardiovascular risk among patients with coronary artery diseases: a systematic review and meta-analysis. *J. Thorac. Dis.* 6, 1429–1440. doi: 10.3978/j.issn.2072-1439.2014.09.10

Vaya, A., Alis, R., Romagnoli, M., Perez, R., Bautista, D., Alonso, R., et al. (2013). Rheological blood behavior is not only influenced by cardiovascular risk factors but also by aging itself. Research into 927 healthy Spanish Mediterranean subjects. *Clin. Hemorheol. Microcirc.* 54, 287–296. doi: 10.3233/CH-131734

Virmani, R., Burke, A. P., Farb, A., and Kolodgie, F. D. (2006). Pathology of the vulnerable plaque. *J. Am. Coll. Cardiol.* 47 (Suppl. 8), C13–C18. doi: 10.1016/j.jacc.2005.10.065

Wan, J., Ristenpart, W. D., and Stone, H. A. (2008). Dynamics of shear-induced ATP release from red blood cells. *Proc. Natl. Acad. Sci. U. S. A.* 105, 16432–16437. doi: 10.1073/pnas.0805779105

Wiewiora, M., Sosada, K., Wylezol, M., Slowinska, L., and Zurawinski, W. (2007). Red blood cell aggregation and deformability among patients qualified for bariatric surgery. *Obes. Surg.* 17, 365–371. doi: 10.1007/s11695-007-9066-6

Yedgar, S., Koshkaryev, A., and Barshtein, G. (2002). The red blood cell in vascular occlusion. *Pathophysiol. Haemost. Thromb.* 32, 263–268. doi: 10.1159/000073578

Zindrou, D., Taylor, K. M., and Bagger, J. P. (2002). Preoperative haemoglobin concentration and mortality rate after coronary artery bypass surgery. *Lancet* 359, 1747–1748. doi: 10.1016/S0140-6736(02)08614-2

Conflict of Interest: The authors declare that the research was conducted in the absence of any commercial or financial relationships that could be construed as a potential conflict of interest.

frontiers in Physiology

BRIEF RESEARCH REPORT
published: 14 January 2021
doi: 10.3389/fphys.2020.602109

Rapid Gardos Hereditary Xerocytosis Diagnosis in 8 Families Using Reticulocyte Indices

Véronique Picard[1,2], Corinne Guitton[3], Lamisse Mansour-Hendili[4], Bernard Jondeau[1], Laurence Bendélac[1], Maha Denguir[5], Julien Demagny[6], Valérie Proulle[1], Frédéric Galactéros[7] and Loic Garçon[1,6]*

[1] Service d'Hématologie Biologique, Assistance Publique-Hôpitaux de Paris, Hôpital Bicêtre, Hôpitaux Universitaires Paris-Saclay, Le Kremlin-Bicêtre, France, [2] Faculté de Pharmacie, Université Paris-Saclay, Châtenay-Malabry, France, [3] Service de Pédiatrie Générale, Assistance Publique-Hôpitaux de Paris, Hôpital Bicêtre, Filière MCGRE, Hôpitaux Universitaires Paris-Saclay, Le Kremlin-Bicêtre, France, [4] Department of Molecular Genetics, Assistance Publique-Hôpitaux de Paris, Henri Mondor University Hospital, Créteil, France, [5] Service de Biochimie, Assistance Publique-Hôpitaux de Paris, Bicêtre Hospital, Le Kremlin-Bicêtre, France, [6] Service d'Hématologie Biologique, CHU Amiens, EA 4666 HEMATIM-UPJV, Amiens, France, [7] Centre de Référence des Syndromes Drépanocytaires Majeurs, Hôpital Henri-Mondor, AP-HP, Créteil, France

OPEN ACCESS

Edited by:
Richard Van Wijk, Utrecht University, Netherlands

Reviewed by:
Roberta Russo, University of Naples Federico II, Italy
Hitoshi Kanno, Tokyo Women's Medical University, Japan
Egee Stéphane, UMR 8227 Laboratoire de Biologie Intégrative des Modèles Marins, France

***Correspondence:**
Véronique Picard
veronique.picard@aphp.fr

Specialty section:
This article was submitted to Red Blood Cell Physiology, a section of the journal Frontiers in Physiology

Received: *02 September 2020*
Accepted: *11 December 2020*
Published: *14 January 2021*

Citation:
Picard V, Guitton C, Mansour-Hendili L, Jondeau B, Bendélac L, Denguir M, Demagny J, Proulle V, Galactéros F and Garçon L (2021) Rapid Gardos Hereditary Xerocytosis Diagnosis in 8 Families Using Reticulocyte Indices. Front. Physiol. 11:602109. doi: 10.3389/fphys.2020.602109

Gardos channelopathy (Gardos-HX) or type 2 stomatocytosis/xerocytosis is a hereditary hemolytic anemia due to mutations in the *KCNN4* gene. It is rarer than inherited type 1 xerocytosis due to *PIEZO1* mutations (Piezo1-HX) and its diagnosis is difficult given the absence of a specific clinical or biological phenotype. We report here that this diagnosis can be sped up using red blood cell (RBC) indices performed on an ADVIA 2120 (Siemens®) analyzer, which measures reticulocyte mean corpuscular volume (rMCV) and mean corpuscular hemoglobin concentration (rMCHC). We studied reticulocyte indices in 3 new and 12 described patients (8 families) with Gardos-HX, 11 subjects presented the recurrent p.Arg352His mutation, 4 cases (two families) carried a private *KCNN4* mutation. They were compared to 79 described patients (49 families) with Piezo1-HX. Surprisingly, in Gardos-HX cases, rMCV revealed to be smaller than MCV and rMCHC higher than MCHC, in contrast with normal or Piezo1-HX RBC. Consequently, ΔMCV (rMCV-MCV) was -0.9 ± 5 fL vs. 19.8 ± 3 fL ($p < 0.001$) in Gardos compared with Piezo1-HX and ΔMCHC (rMCHC-MCHC) was 18.7 ± 13 vs. -50 ± 8.7 g/L ($p < 0.001$). A threshold of 8.6 fL for ΔMCV and −5.5 g/L for ΔMCHC could discriminate between Gardos and Piezo1-HX with 100% sensitivity and specificity, regardless of age, mutation or splenectomy status. Consequently, we showed that reticulocytes indices are useful to suggest Gardos-HX on blood count results, allowing to rapidly target these patients for gene analysis. In addition, these parameters may prove useful as a 'functional tool' in interpreting new *KCNN4* variants.

Keywords: reticulocytes, Piezo1, xerocytosis, Gardos, red cell indices

Gardos hereditary xerocytosis (Gardos-HX) is the most recently described hereditary hemolysis, also known as dehydrated stomatocytosis type II, or Gardos channelopathy (Glogowska et al., 2015; Rapetti-Mauss et al., 2015). Hereditary xerocytosis (HX) are rare dominant red cell membrane disorders initially characterized by K^+ leak leading to decreased intracellular cationic content, loss of water and red cell dehydration (Delaunay, 2004). In most cases, HX is associated with

gain of function heterozygous mutations in *PIEZO1* (Piezo1-HX). Piezo1 is a mechanosensitive cation channel that translates a mechanical force into a biological signal, mainly through a Ca^{2+} influx into red cells (Zarychanski et al., 2012; Albuisson et al., 2013; Andolfo et al., 2013). Gardos-HX is caused by heterozygous activating mutations in *KCNN4*, encoding the Ca^{2+}-dependent K^+ exporter Gardos channel. Functional studies have suggested that Gardos channel activation is the common effector of red cell dehydration, triggered either directly by *KCNN4* activating mutation or indirectly by Piezo1-dependant intracellular Ca^{2+} increase (Rapetti-Mauss et al., 2017; Caulier et al., 2018).

Gardos-HX diagnosis is difficult and often delayed because of the absence of typical clinical and biological phenotype. Indeed, it presents as a chronic hemolysis with negative red cell phenotypic investigations including osmolar gradient ektacytometry, which is normal or not specific. Diagnosis is made by genetic analysis, often performed after ruling out many other causes of hemolysis (King et al., 2015). It is important to distinguish Piezo1- and Gardos-HX because of several distinct clinical issues: non-spherocytic chronic hemolysis and risk of iron overload are common to both disorders, however, post-splenectomy thrombotic events and perinatal edemas without anemia are observed in Piezo1-HX, whereas anemia –including pre/neonatal anemia – are more severe in Gardos-HX (Fermo et al., 2017; Andolfo et al., 2018; Picard et al., 2019).

We report here that diagnosis of Gardos-channelopathy can be substantially sped up using reticulocyte indices. In a previous retrospective study including 12 Gardos and 91 Piezo1-HX cases, we have already described red cell parameters – Hb level, reticulocytes count, mean cell volume (MCV), mean cell hemoglobin concentration (MCHC) – in Gardos and Piezo1-HX (Picard et al., 2019). Specifically, we showed that MCV was not significantly different in both disorders, however, MCHC, which is in the normal range in subjects with Gardos channelopathy, was significantly higher in Piezo1-HX (Picard et al., 2019). These observations were also reported by others, they are consistent with data from osmotic gradient ektacytometry assays since these curves show a characteristic left-shifted dehydrated profile in Piezo1-HX but not in Gardos-HX indicating the absence of clear red cell dehydration features (Rapetti-Mauss et al., 2015; Picard et al., 2019). Here, we have extended these observations by analyzing reticulocyte indices in an enlarged series of 15 KCNN4-mutated cases (three new subjects, 12 already described) aged 1–59 years from eight families (two new families), that were compared to 79 Piezo1-HX subjects (49 families) with complete blood count records from the described cohort (Picard et al., 2019). Our primary objective was to better define how red cell and/or reticulocyte indices could be used in diagnosing HX. All patients gave their informed consent according to the Helsinki protocol, and this report followed the French regulations in terms of non-interventional retrospective study. HX diagnosis was based on clinical and biological data and a typical ektacytometry curve for the 79 Piezo1-HX patients, all of them carried at least one rare (MAF < 0.01) *PIEZO1* mutation, this mutation may be already described as associated with HX or not. In the 15 Gardos-HX patients, the ektacytometric profile was normal ($n = 10$) or atypical ($n = 5$) and therefore not contributive for diagnosis, genetic testing identified a *KCNN4* mutation that segregated with the disease in the eight families. Six Gardos-HX families (12 patients) were already described, one patient was found to carry a new KCNN4 mutation (c.965C > T, p.Ala322Val), in addition, three unreported subjects from two novel families were found to carry the recurrent p.Arg352His mutation. Overall, 11 cases from six families carried the recurrent p.Arg352His substitution and 4 cases from two families carried private KCNN4 mutations. The clinical, biological and genetic characteristics of KCNN4-mutated cases are summarized in **Supplementary Table 1**. All subjects had a complete blood count performed in the same lab on EDTA-blood samples within a 24 h/4°C delay

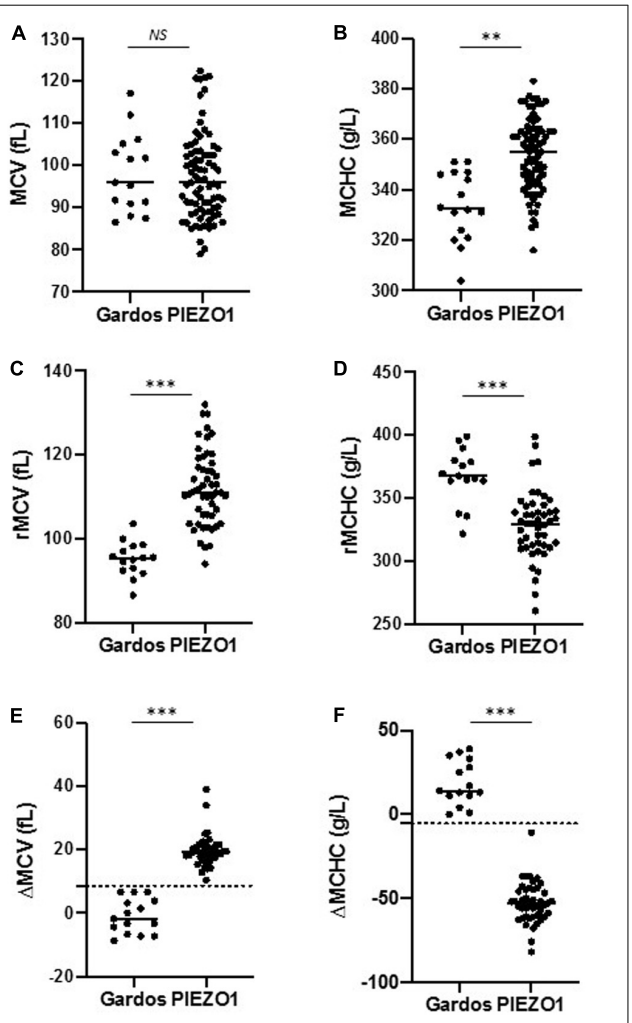

FIGURE 1 | Red cell and reticulocytes indices in Piezo1- and Gardos-HX. **(A,B)** Comparison of MCV (fL) and MCHC (g/L) of all red blood cells (mature + reticulocytes) in Piezo1-HX ($n = 79$) and Gardos-HX ($n = 15$). **(C,D)** Comparison of MCV (fL) and MCHC (g/L) of reticulocytes in Piezo1-HX ($n = 79$) and Gardos-HX ($n = 15$). **(E,F)** ΔMCV (rMCV – mMCV) and ΔMCHC (rMCHC – mMCHC) parameters could discriminate between Gardos and Piezo1-HX, with cut-off values of 8.6 fL and –5.5 g/L, respectively (dashed line). *NS,* non-significant; $^{**}p < 0.01$, $^{***}p < 0.001$ as analyzed by Student *t* test. Normal range: MCV: 80–100 fL, MCHC: 310–360 g/L, rMCV: 92–120 fL, rMCHC: 270–330 g/L.

TABLE 1 | Comparison of red cell, reticulocyte and differential indices in splenectomized vs. non-splenectomized Gardos and Piezo1-HX cases (mean ± SEM, *p*: student *T* test).

	Normal range	Gardos-HX (*n* = 15)			Piezo1-HX (*n* = 79)		
		Splenectomy			Splenectomy		
		Yes	No	*p*	Yes	No	*p*
N		7	8		8	71	
Hb (g/L)	120–160 (female) 130–180 (male)	91 ± 8.7	112 ± 1.1	< 0.05	123.7 ± 17	124.8 ± 12	0.24
Reticulocyte (G/L)	20–120	341 ± 15	174 ± 62	0.07	284 ± 135	307 ± 100	0.78
MCV	80–100	107 ± 4.2	92 ± 2.7	< 0.001	103 ± 11	96 ± 7.1	0.25
rMCV (fL)	92–120	96.8 ± 5.3	93.6 ± 3.8	0.27	114 ± 10	111 ± 7	0.66
mMCHC (g/L)	310–360	343 ± 12	353 ± 23	0.5	365 ± 37	370 ± 21	0.84
rMCHC (g/L)	270–330	372 ± 13	364 ± 17	0.1	305 ± 29	334 ± 18	0.1
ΔMCV (fL)	–	−5.8 ± 1.9	3.5 ± 2.5	< 0.001	16.3 ± 6	19.6 ± 6	0.05
ΔMCHC (g/L)	–	28 ± 9	10 ± 6	< 0.001	−65.4 ± 14	−52.4 ± 8.6	0.21

In Gardos-HX, ΔMCV was significantly lower and MCV and ΔMCHC were significantly higher in splenectomized subjects, in splenectomized or non-splenectomized cases, the differential indices remained discriminant for Gardos or Piezo1-HX.

after blood harvesting using an ADVIA2120 (Siemens®) analyzer, that provided specialized red cell and reticulocyte parameters. The ADVIA2120 analyzer measures MCV and MCHC using single cell analysis by dual angle laser scattering cytometry. On one channel, MCV and MCHC indices are measured on red cells, including reticulocytes as well as mature cells. On a second channel using a different set of reagents, reticulocyte counts and indices (rMCV, rMCHC) are distinguished from mature red cells (mMCV, mMCHC) by using oxazine 750 staining. All statistical analyses were performed using two-tailed *p* value and parametric tests. Statistical significance used was $\alpha = 0.05$. For quantitative variables, we used Student's *t*-test or one-way ANOVA test and Tukey *post hoc* analysis for multiparametric analysis. All numeric values were expressed as mean values ± SEM.

As already described, mean hemoglobin level was lower in Gardos vs. Piezo1-HX (103 ± 16 vs. 134 ± 19 g/L, respectively), MCV was not significantly different (98.8 ± 9 vs. 97.7 ± 8 fL), and MCHC was lower in Gardos compared to Piezo1-HX subjects (332 ± 13 vs. 354 ± 24 g/L, Student's *t*-test, $p < 0.01$) (**Figures 1A,B**; Picard et al., 2019). Now, a focus on reticulocytes indices indicated that, quite surprisingly, Gardos-HX reticulocytes appeared smaller than expected compared with total red cells (95.1 ± 3 vs. 98.8 ± 9 fL) and their MCHC was higher (367 ± 16 vs. 332 ± 13 g/L). This was not the case in Piezo1-HX, where, as expected, reticulocytes were larger than red cells with a lower MCHC (113.7 ± 7 vs. 97.7 ± 8 fL and 329 ± 20 vs. 354 ± 24 g/L). Therefore, Gardos-HX reticulocytes appeared significantly smaller and had a significantly higher MCHC compared with Piezo1-HX (95.1 ± 3 vs. 113.7 ± 7 fL and 367 ± 16 vs. 329 ± 20 g/L, respectively) (**Figures 1C,D**). As a consequence, the differential MCV between reticulocytes and mature red cells ΔMCV (rMCV – mMCV) was −0.9 ± 5 in Gardos vs. 19.8 ± 3 fL in Piezo1-HX ($p < 0.001$), and the ΔMCHC (rMCHC – mMCHC) was 18.7 ± 3 in Gardos vs. −50 ± 8.7 g/L in Piezo1-HX ($p < 0.001$) (**Figures 1E,F**). We then used ROC curves to analyze the performance of these reticulocyte parameters in differentiating Gardos or Piezo1-mutated cases. The ΔMCHC and ΔMCV were found to be the best parameters (**Supplementary Figure 1**). Indeed, a value of 8.6 fL for ΔMCV and −5.5 g/L for ΔMCHC could discriminate both genotypes with a 100% sensitivity and 100% specificity with no overlap in this small series (**Figures 1E,F**). Because of the low number of Gardos-HX cases, these parameters should be further tested and validated in other labs before use in routine testing. Interestingly, these observations revealed correct for each individual subject, whatever the age, whether they carry the p.Arg352His recurrent mutation or a private mutation. We have not tested subjects carrying the p.Val282Met or p.Val282Glu substitutions, both associated with Gardos-HX, reticulocyte indices in these patients deserve to be investigated (Glogowska et al., 2015).

Then, since 7/15 Gardos vs. 8/79 Piezo1-HX cases were splenectomized, we asked whether splenectomy might influence red cell indices. As shown in **Table 1**, there was no

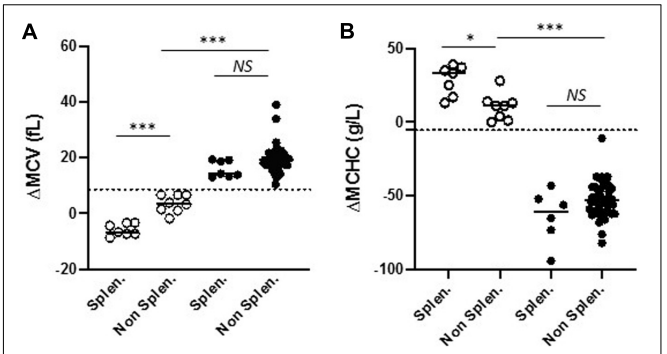

FIGURE 2 | Comparison of ΔMCV **(A)** and ΔMCHC **(B)** in splenectomized and non-splenectomized patients in Gardos-HX (o) and Piezo1-HX (•). The cut-off value of 8.6 fL and –5.5 g/L, respectively are indicated (dashed line). These differential indices could discriminate between Gardos and Piezo1-HX whether subjects were splenectomized or not. *NS,* non-significant; $^{*}p < 0.05$, $^{***}p < 0.001$ as measured by one-way ANOVA test and Tukey *post hoc* analysis for multiparametric analysis.

significant difference in terms of rMCV and rMCHC between splenectomized and non-splenectomized subjects in both disorders. We observed that Gardos-HX splenectomized subjects had an increased MCV compared to non-splenectomized subjects (MCV: 107 ± 4 vs. 92 ± 3 fL, $p < 0.001$). Nonetheless, ΔMCV and ΔMCHC remained highly suggestive of Gardos-HX whether patients were splenectomized or not (**Table 1** and **Figure 2**). In our setting, these new parameters revealed highly useful and reliable in order to target patients for *KCNN4* gene analysis as soon as the blood count was performed.

Reticulocyte indices are not widely used in diagnosis, although reticulocytes hemoglobin content measured by most hematology analyzers has proved to be helpful in diagnosis of iron deficient anemia (Brugnara et al., 2006; David et al., 2006). Reticulocytes are immature cells, their volume is larger compared with mature red cells and their hemoglobin concentration lower, consistent with rMCV and rMCHC reference range provided by the manufacturer (rMCV: 92.0–120.0 fL, rMCHC: 270–330 g/L in adults) (Thomas, 2008). Currently, most blood cell analyzers do not measure rMCV and rMCHC. Whether red cell indices obtained on other systems using different optic or impedance-based technologies might allow to target Gardos-HX should be evaluated. The ADVIA® technology measures individual red cell volume and hemoglobin content by cell light scattering after isovolumetric spherization. In this setting, Gardos-HX reticulocytes appeared small and dehydrated, they react differently from reticulocytes in Piezo1-HX or in other hemolytic anemia, acquired or hereditary, whether they are related to hemoglobin, enzyme or other membrane defects. This specific behavior of Gardos-HX reticulocytes might be due to an ionic imbalance induced by the *KCNN4* mutation *per se* or due to other differences in the membrane structure or composition. A difference in Gardos channel concentration at the membrane in reticulocytes compared with mature red cells might also account for this observation, to our knowledge, this point has not been studied before. Alternately, the interaction of the Gardos channel with proteins present at a different level in reticulocytes may be involved. Finally, we cannot rule out a possible *in vitro* artifact due to the ADVIA® technology. Although we cannot infer that this *in vitro* observation does reflect reticulocytes properties *in vivo*, we hypothesize that dehydration predominates in immature cells, i.e., reticulocytes in Gardos-HX while mild or absent in mature red cells. Because reticulocytes represent a minor fraction of circulating red cells, this would account for the normal MCHC reported by several teams in Gardos-HX as well as the non-dehydrated ektacytometry profile. In Piezo1-HX, we propose that dehydration predominates in mature red cells and accounts for the observed high MCHC and dehydrated ektacytometric profile.

In conclusion, these data revealed a new feature distinguishing Gardos and Piezo1-HX. That a simple analysis of red cell and reticulocyte indices on a blood count were able to target each individual Gardos-HX subject was quite unexpected. Although the cause of this specific behavior of Gardos-HX remains to be established, it provides a very useful and cost-free tool for labs using ADVIA analyzers in order to suggest Gardos-HX and speed up diagnosis by *KCNN4* gene analysis. In addition, ΔMCV and ΔMCHC may prove useful as a "functional tool" in interpreting new *KCNN4* variants when Gardos-HX is suspected.

DATA AVAILABILITY STATEMENT

The original contributions presented in the study are included in the article/**Supplementary Material**, further inquiries can be directed to the corresponding author.

ETHICS STATEMENT

The studies involving human participants were reviewed and approved by the French National Commission on Informatics and Liberty (CNIL). Written informed consent to participate in this study was provided by the participants' legal guardian/next of kin.

AUTHOR CONTRIBUTIONS

VPi and LG designed the study and wrote the manuscript. LB and LM-H performed genetic studies. VPi, MD, VPr, BJ, and JD analyzed the data. LG, CG, and FG followed patients. All authors contributed to the article and approved the submitted version.

ACKNOWLEDGMENTS

We wish to thank the patients, their family, the clinicians, and the French Cohort of Hereditary Stomatocytosis, as well as the technicians and biologists of the Hematology Laboratory of Hôpital Bicêtre and Mme Hélène Ponsin, for excellent resource management, and ARFH (Association Recherche et Formation en Hematopathologie) for financial support.

SUPPLEMENTARY MATERIAL

The Supplementary Material for this article can be found online at: https://www.frontiersin.org/articles/10.3389/fphys.2020.602109/full#supplementary-material

REFERENCES

Albuisson, J., Murthy, S. E., Bandell, M., Coste, B., Louis-Dit-Picard, H., Mathur, J., et al. (2013). Dehydrated hereditary stomatocytosis linked to gain-of-function mutations in mechanically activated PIEZO1 ion channels. *Nat. Commun.* 4:1884.

Andolfo, I., Alper, S. L., De Franceschi, L., Auriemma, C., Russo, R., De Falco, L., et al. (2013). Multiple clinical forms of dehydrated hereditary stomatocytosis arise from mutations in PIEZO1. *Blood* 121, 3925–3935. doi: 10.1182/blood-2013-02-482489

Andolfo, I., Russo, R., Rosato, B. E., Manna, F., Gambale, A., Brugnara, C., et al. (2018). Genotype-phenotype correlation and risk stratification in a cohort of

123 hereditary stomatocytosis patients. *Am. J. Hematol.* 93, 1509–1517. doi: 10.1002/ajh.25276

Brugnara, C., Schiller, B., and Moran, J. (2006). Reticulocyte hemoglobin equivalent (Ret He) and assessment of iron-deficient states. *Clin. Lab. Haematol.* 28, 303–308. doi: 10.1111/j.1365-2257.2006.00812.x

Caulier, A., Rapetti-Mauss, R., Guizouarn, H., Picard, V., Garçon, L., and Badens, C. (2018). Primary red cell hydration disorders: pathogenesis and diagnosis. *Int. J. Lab. Hematol.* 40, 68–73. doi: 10.1111/ijlh.12820

David, O., Grillo, A., Ceoloni, B., Cavallo, F., Podda, G., Biancotti, P. P., et al. (2006). Analysis of red cell parameters on the Sysmex XE 2100 and ADVIA 120 in iron deficiency and in uraemic chronic disease. *Scand. J. Clin. Lab. Invest.* 66, 113–120. doi: 10.1080/00365510500406910

Delaunay, J. (2004). The hereditary stomatocytoses : disorders of the red cell membrane permeability to monovalent cations. *Semin. Hematol.* 41, 165–172. doi: 10.1053/j.seminhematol.2004.02.005

Fermo, E., Bogdanova, A., Petkova-Kirova, P., Zaninoni, A., Marcello, A. P., Makhro, A., et al. (2017). 'Gardos Channelopathy': a variant of hereditary Stomatocytosis with complex molecular regulation. *Sci. Rep.* 7:1744.

Glogowska, E., Lezon-Geyda, K., Maksimova, Y., Schulz, V. P., and Gallagher, P. G. (2015). Mutations in the Gardos channel (KCNN4) are associated with hereditary xerocytosis. *Blood* 126, 1281–1284. doi: 10.1182/blood-2015-07-657957

King, M. J., Garçon, L., Hoyer, J. D., Iolascon, A., Picard, V., Stewart, G., et al. (2015). International Council for Standardization in Haematology. ICSH guidelines for the laboratory diagnosis of nonimmune hereditary red cell membrane disorders. *Int. J. Lab. Hematol.* 37, 304–325. doi: 10.1111/ijlh.12335

Picard, V., Guitton, C., Thuret, I., Rose, C., Bendelac, L., Ghazal, K., et al. (2019). Clinical and biological features in *PIEZO1* -hereditary xerocytosis and Gardos channelopathy: a retrospective series of 126 patients. *Haematologica* 104, 1554–1564. doi: 10.3324/haematol.2018.205328

Rapetti-Mauss, R., Lacoste, C., Picard, V., Guitton, C., Lombard, E., Loosveld, M., et al. (2015). A mutation in the Gardos channel is associated with hereditary xerocytosis. *Blood* 126, 1273–1280. doi: 10.1182/blood-2015-04-642496

Rapetti-Mauss, R., Picard, V., Guitton, C., Ghazal, K., Proulle, V., Badens, C., et al. (2017). Red blood cell Gardos channel (KCNN4): the essential determinant of erythrocyte dehydration in hereditary xerocytosis. *Haematologica* 102, e415–e418.

Thomas, L. (2008). *Labor und Diagnose, 7. Auflage*. Frankfurt: TH-books Verlagsgesellschaft mbH.

Zarychanski, R., Schulz, V. P., Houston, B. L., Maksimova, Y., Houston, D. S., Smith, B., et al. (2012). Mutations in the mechanotransduction protein PIEZO1 are associated with hereditary xerocytosis. *Blood* 120, 1908–1915. doi: 10.1182/blood-2012-04-422253

Conflict of Interest: The authors declare that the research was conducted in the absence of any commercial or financial relationships that could be construed as a potential conflict of interest.

frontiers in Physiology

ORIGINAL RESEARCH
published: 05 February 2021
doi: 10.3389/fphys.2021.628236

Usefulness of NGS for Diagnosis of Dominant Beta-Thalassemia and Unstable Hemoglobinopathies in Five Clinical Cases

*Valeria Rizzuto[1,2,3], Tamara T. Koopmann[4], Adoración Blanco-Álvarez[5], Barbara Tazón-Vega[5], Amira Idrizovic[1], Cristina Díaz de Heredia[6], Rafael Del Orbe[7], Miriam Vara Pampliega[7], Pablo Velasco[6], David Beneitez[8], Gijs W. E. Santen[4], Quinten Waisfisz[9], Mariet Elting[9], Frans J. W. Smiers[10], Anne J. de Pagter[10], Jean-Louis H. Kerkhoffs[11], Cornelis L. Harteveld[4] and Maria del Mar Mañú-Pereira[1]**

[1] Translational Research in Child and Adolescent Cancer – Rare Anemia Disorders Research Laboratory, Vall d'Hebron Research Institute, ERN-EuroBloodNet Member, Barcelona, Spain, [2] Josep Carreras Leukaemia Research Institute, Badalona, Spain, [3] Department of Medicine, Universitat de Barcelona, Barcelona, Spain, [4] Department of Clinical Genetics, Leiden University Medical Center, ERN-EuroBloodNet Member, Leiden, Netherlands, [5] Hematologic Molecular Genetics Unit, Hematology Department, Hospital Universitari Vall d'Hebron, ERN-EuroBloodNet Member, Barcelona, Spain, [6] Oncohematologic Pediatrics Department, Hospital Universitari Vall d'Hebron, ERN-EuroBloodNet Member, Barcelona, Spain, [7] Hematology Department, Hospital Universitario Cruces, Barakaldo, Spain, [8] Red Blood Cell Disorders Unit, Hematology Department, Hospital Universitari Vall d'Hebron, ERN-EuroBloodNet Member, Barcelona, Spain, [9] Department of Clinical Genetics, VU Medical Center, Amsterdam, Netherlands, [10] Department of Pediatric Hematology, Leiden University Medical Center, Leiden, Netherlands, [11] Department of Hematology, HAGA City Hospital, The Hague, Netherlands

OPEN ACCESS

Edited by:
Paola Bianchi, IRCCS Ca' Granda Foundation Maggiore Policlinico Hospital, Italy

Reviewed by:
James Hoyer, Mayo Clinic, United States
Theodosia A. Kalfa, Cincinnati Children's Hospital Medical Center, United States

***Correspondence:**
Maria del Mar Mañú-Pereira
mar.manu@vhir.org

Specialty section:
This article was submitted to Red Blood Cell Physiology, a section of the journal Frontiers in Physiology

Received: *11 November 2020*
Accepted: *13 January 2021*
Published: *05 February 2021*

Citation:
Rizzuto V, Koopmann TT, Blanco-Álvarez A, Tazón-Vega B, Idrizovic A, Díaz de Heredia C, Del Orbe R, Pampliega MV, Velasco P, Beneitez D, Santen GWE, Waisfisz Q, Elting M, Smiers FJW, de Pagter AJ, Kerkhoffs J-LH, Harteveld CL and Mañú-Pereira MdM (2021) Usefulness of NGS for Diagnosis of Dominant Beta-Thalassemia and Unstable Hemoglobinopathies in Five Clinical Cases. Front. Physiol. 12:628236. doi: 10.3389/fphys.2021.628236

Unstable hemoglobinopathies (UHs) are rare anemia disorders (RADs) characterized by abnormal hemoglobin (Hb) variants with decreased stability. UHs are therefore easily precipitating, causing hemolysis and, in some cases, leading to dominant beta-thalassemia (dBTHAL). The clinical picture of UHs is highly heterogeneous, inheritance pattern is dominant, instead of recessive as in more prevalent major Hb syndromes, and may occur *de novo*. Most cases of UHs are not detected by conventional testing, therefore diagnosis requires a high index of suspicion of the treating physician. Here, we highlight the importance of next generation sequencing (NGS) methodologies for the diagnosis of patients with dBTHAL and other less severe UH variants. We present five unrelated clinical cases referred with chronic hemolytic anemia, three of them with severe blood transfusion dependent anemia. Targeted NGS analysis was performed in three cases while whole exome sequencing (WES) analysis was performed in two cases. Five different UH variants were identified correlating with patients' clinical manifestations. Four variants were related to the beta-globin gene (Hb Bristol—Alesha, Hb Debrousse, Hb Zunyi, and the novel Hb Mokum) meanwhile one case was caused by a mutation in the alpha-globin gene leading to Hb Evans. Inclusion of alpha and beta-globin genes in routine NGS approaches for RADs has to be considered to improve diagnosis' efficiency of RAD due to UHs. Reducing misdiagnoses and underdiagnoses of UH variants, especially of the severe forms leading to dBTHAL would also facilitate the early start of intensive or curative treatments for these patients.

Keywords: unstable hemoglobinopathies, dominant beta-thalassemia, next generation sequencing, whole exome sequencing, rare anemia disorders

INTRODUCTION

Beta-thalassemia major (BTHAL) is a well-known life-threatening condition characterized by severe transfusion-dependent anemia. BTHAL is an autosomal recessive disorder presenting with high frequencies in populations from the Mediterranean area. Currently, up to 257 genetic variants in the beta-globin gene (*HBB*) have been identified as BTHAL disease-causing, leading to a total or partial reduction of beta-globin chain synthesis. The clinical severity of BTHAL is related to the extent of imbalance between the alpha and non-alpha-globin chains, while clinical management consists of regular life-long red blood cell (RBC) transfusions and iron chelation therapy. At present, the only definitive cure is bone marrow transplant (Efremov, 2007; Galanello and Origa, 2010). Both BTHAL patients and carriers are usually easily diagnosed through routine laboratory tests. However, there is an ultra-rare condition overlapping BTHAL clinical manifestations known as dominant beta-thalassemia (dBTHAL), which is caused by the presence of certain unstable (UH) or hyper unstable (HUH) hemoglobinopathies.

UHs are a group of congenital disorders caused by mutations in globin genes leading to destabilization of hemoglobin (Hb) molecules as a consequence of (a) amino acid substitutions within the heme pocket, (b) disruption of secondary structure, (c) substitution in the hydrophobic interior of the subunit, (d) amino acid deletions, and (e) elongation of the subunit. Thus, altering any of the steps in globin processing, including subunit folding, heme interaction, dimerization, or tetramerization (Bunn and Forget, 1986). These abnormal Hb variants undergo rapid denaturation followed by precipitation, leading to the formation of Heinz bodies, which cause hemolysis of RBCs. Clinical manifestations may vary from asymptomatic to severely affected forms. Treatment is mainly symptomatic and based on transfusion requirements as for BTHAL (Steinberg et al., 2009; Thom et al., 2013).

UHs are dominantly inherited with a significant rate of *de novo* mutations. They generally do not separate from normal Hb using standard methods. Thus, diagnosis of dBTHAL can be challenging since it requires a high index of suspicion and the diagnosis may be delayed for years hampering the access to timely treatment interventions.

The study we present herein confirms the relevance of including globin genes in next generation sequencing (NGS) approaches for the diagnosis of rare anemia disorders (RADs), especially for cases with no family history in which the anemia is not easily explained.

PATIENTS AND METHODS

Clinical Reports

Here we present five clinical cases diagnosed with UH after NGS analysis. Clinical data and laboratory findings are shown in **Table 1**.

The first case is a male pediatric patient referred with severe chronic blood dependent anemia since he was 4-month-old, asthenia, jaundice, and short stature. No family history of hemolytic anemia. Examination of blood smear revealed polychromasia, anisopoikilocytosis, basophil stippling, Cabot rings, schistocytes, and spherocytes. Separation and quantification of Hb fractions did not reveal any extraordinary peak and showed normal values for HbA_2 and HbF. At 5-year-old he underwent splenectomy. After the surgery, Heinz bodies were present (**Figures 1**, **2**) and isopropanol stability test, performed according to standard methodology, appeared positive (**Figure 3**). Family studies in both parents were strictly normal, including evaluation of Hb fractions. Enzyme activity assays, EMA-binding test, and osmotic gradient ectacytometry (LoRRca MaxSis) were performed to rule out hemolytic anemia due to RBC defects other than hemoglobinopathy. Results, although not strictly normal, did not reveal any RBC defect. However, they should be taken with caution since the patient was intensively transfused. Genetic analysis was performed on *PKLR* and *G6PD* genes failing to reveal any disease-causing mutation.

The second case is a female adult patient with mild chronic compensated hemolysis referred for diagnosis when she was 20 years old. The father also presented with mild compensated hemolysis. No further examinations were performed before referral. Although the presence of extravascular hemolysis, the examination of blood smear was not informative. Separation and quantification of Hb fractions did not reveal any extra peaks and Heinz body and stability tests were normal. Further laboratory tests were performed to rule out hemolytic anemia due to RBC enzyme and membrane defects, including enzyme activity assays, EMA-binding test, and osmotic gradient ectacytometry (LoRRca MaxSis). All of them showed normal values.

The third case is a male adult patient. He presented with several episodes of hemolytic crises during childhood requiring blood transfusion on two occasions. He underwent splenectomy at the age of 25-year-old. The patient was diagnosed with hereditary spherocytosis (HS) following a previous HS diagnosis of his mother and the absence of abnormal Hb peaks by conventional electrophoresis.

Patients who underwent splenectomy neither clinically improved nor presented complications as pulmonary hypertension, thrombosis or increased hemolysis during 10-year follow-up.

The last two cases are two unrelated children who presented with macrocephaly and severe congenital anemia. The parents of both patients had no family history for abnormal Hb or thalassemia and had normal hematological features. Therefore, conventional testing for abnormal Hb was not performed. All siblings were unaffected.

The first of these two unrelated children is a male patient presenting with large head circumference and hepatosplenomegaly. Congenital dyserythropoietic anemia was suspected. However, no genetic analysis was performed for confirmation. He underwent successfully bone marrow transplant at the age of 4.

The second child is a female patient presenting with frontal bossing, macrocephaly, and severe anemia at the age of 2. Congenital dyserythropoietic anemia was suspected. Therefore, genetic analysis of *CDAN1* and *SEC23B* genes was

TABLE 1 | Overview on clinical and genetic data of the five reported clinical cases.

Parameters	Case 1	Case 2	Case 3	Case 4	Case 5
Gender/Age	**Male/Pediatric**	**Female/Adult**	**Male/Adult**	**Male/Pediatric**	**Female/Pediatric**
Hb (120–170 g/L)	70–80	119	141	82	79
MCV (80–100 fL)	110–115	97.8	102.3	83	Not done
MCHC (27–33.5 g/dL)	28	32.1	30.8	Not done	Not done
Reticulocyte count (50–100 · 10^9/L)	900	293	331	810	Not done
Reticulocyte count (%)	34	7.71	7.39	Not done	Not done
Lactate dehydrogenase-LDH (U/L)	4,500–5,000	243	145	186	259
Hb Fractions	Normal	Normal	Normal	Not done	Not done
Heinz bodies	Positive	Negative	Positive	Not done	Not done
Stability test	Positive	Negative	Positive	Not done	Not done
Age of onset (months)	4	Unknown	Unknown	Unknown	2
Family history	No family history	Father presents mild compensated hemolysis	Mother diagnosed with hereditary spherocytosis	No family history	No family history
Transfusion need	8 U/Year	No	2 times	Multiple	Multiple
Splenectomy	Yes (5 y)	No	Yes (25 y)	No	No
Stem cell transplant (age years)	No	No	No	Yes (4 y)	Yes (3 y)
Genotype	*HBB*c.202G > A (p.Val67Met)	*HBA1*c.187G > A (p.Val62Met)	*HBB*c.290T > C (p.Leu96Pro)	*HBB*c.442T > C (p.Ter147Glnext*21)	*HBB*c.442T > A (p.Ter147Lysext*21)
Hb variant name	Hb Bristol-Alesha	Hb Evans	Hb Debrousse	Hb Zunyi	Hb Mokum

**Performed after the diagnosis of UH.*

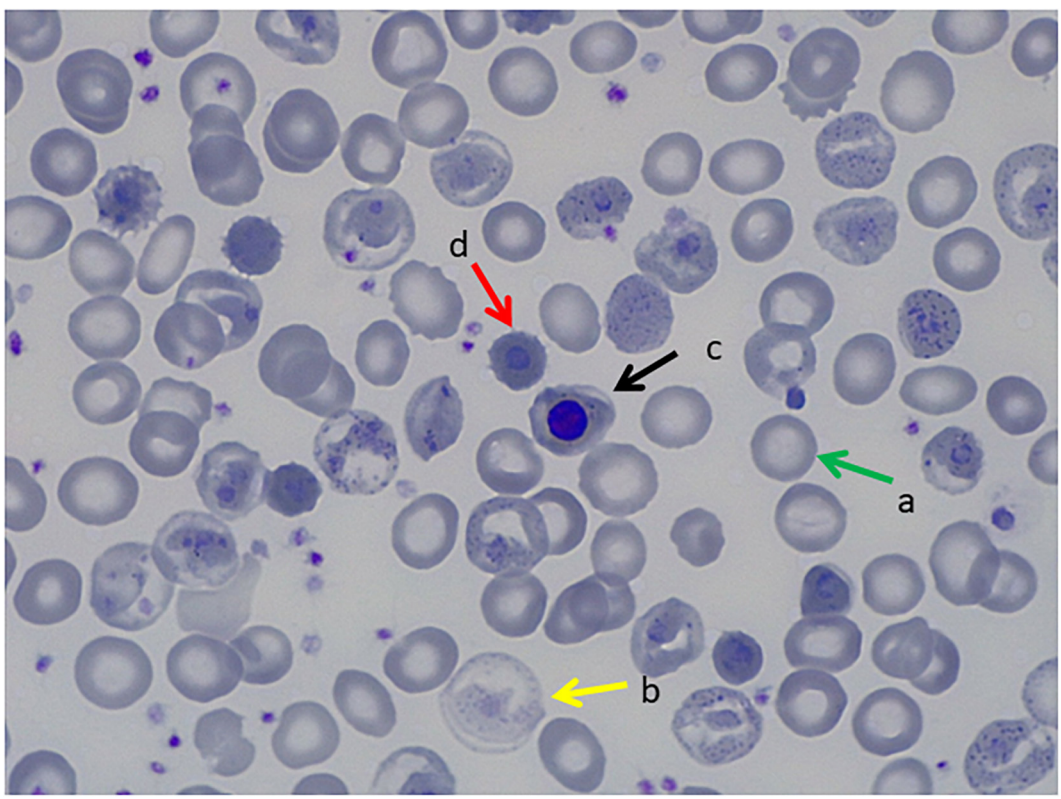

FIGURE 1 | Peripheral Blood Smear, May Grunwald Giemsa Stain. **(a)** Transfused red blood cells, **(b)** non-transfused red blood cells with hemoglobinization abnormalities, **(c)** orthochromatic erythroblast, **(d)** erythrocitary inclusions that correspond to Heinz bodies.

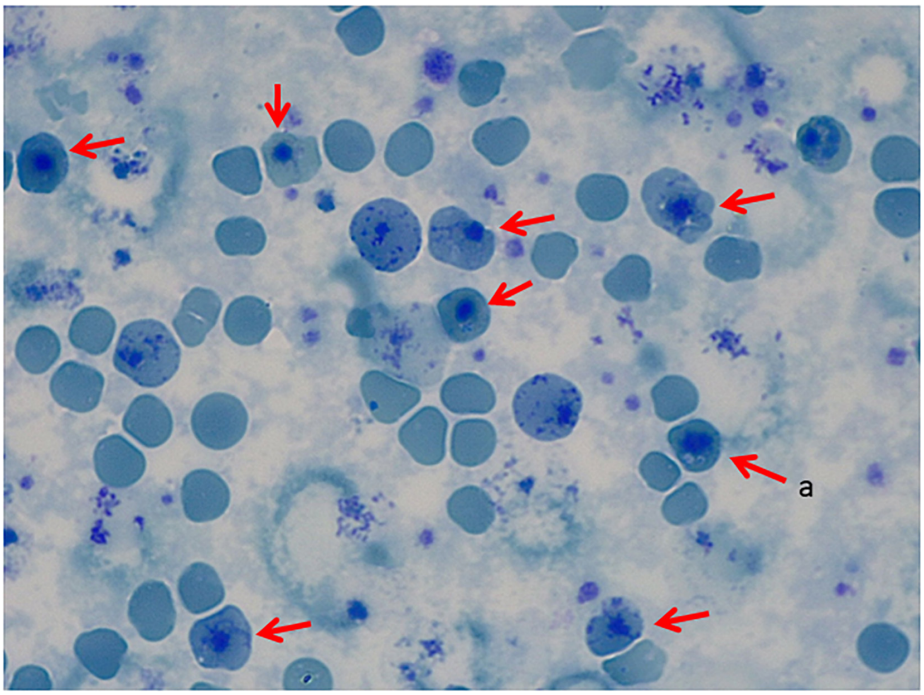

FIGURE 2 | Peripheral Blood Smear, Brilliant Cresyl Blue Stain. **(a)** Heinz bodies.

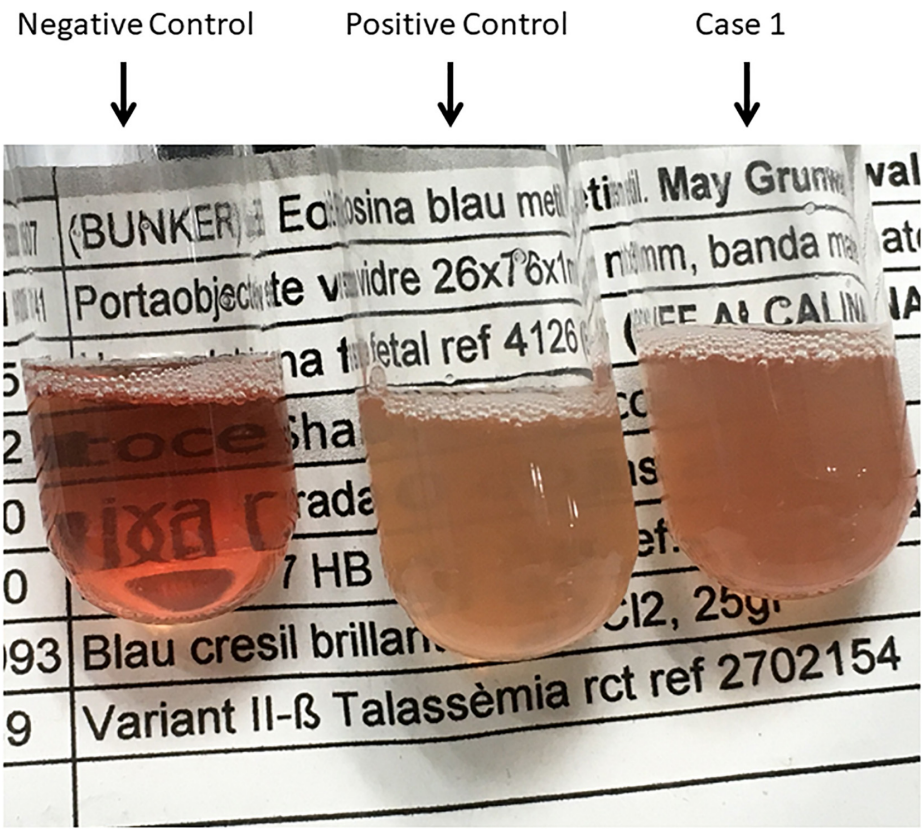

FIGURE 3 | Isopropanol Test_01. Negative control (Hb AS), Positive control (Hb F), and Case 1.

TABLE 2 | List of genes included in the t-NGS approach.

Symbol	Phenotype MIM number	Gene/Locus MIM number	Category	Description
ADA	102700	608958	Enzymopathy	Adenosine deaminase
AK1	103000	103000	Enzymopathy	Adenylate kinase 1
ALDOA	611881	103850	Enzymopathy	Aldolase, fructose-bisphosphate a
ANK1	616089	612641	Membranopathy	Ankyrin 1
ATRX	301040	300032	Alpha-thalassemia myelodysplasia syndrome, somatic; Alpha-thalassemia/mental retardation syndrome; Mental retardation-hypotonic facies syndrome, X-linked	Helicase 2, x-linked
BPGM	222800	613896	Erythrocytosis and methemoglobinemia due to enzyme alteration	Bisphosphoglycerate mutase
C15orf41	615631	615626	Congenital dyserythropoietic anemia	Chromosome 15 open reading frame 41
CDAN1	224120	224120	Congenital dyserythropoietic anemia	Codanin 1
CYB5R3	250800	613213	Methemoglobinemia, type I; Methemoglobinemia, type II	Cytochrome b5 reductase 3
EPB41	611804	130500	Membranopathy	Erythrocyte membrane protein band 4.1
EPB42	612690	177070	Membranopathy	Erythrocyte membrane protein band 4.2
EPO	617907	133170	Erythropoiesis modulator	Erythropoietin
EPOR	133100	133171	Erythropoiesis modulator	Erythropoietin receptor
G6PD	300908	305900	Enzymopathy	Glucose-6-phosphate dehydrogenase
GAPDH	*	138400	Enzymopathy	Glyceraldehyde-3-phosphate dehydrogenase
GATA1	300835	305371	Congenital dyserythropoietic anemia	Gata binding protein 1 (globin transcription factor 1)
GCLC	230450	606857	Enzymopathy	Glutamate-cysteine ligase, catalytic subunit
GPI	613470	172400	Enzymopathy	Glucose-6-phosphate isomerase
GSR	618660	138300	Enzymopathy	Glutathione reductase
GSS	266130	601002	Enzymopathy	Glutathione synthetase
GYPC	616089	110750	Membranopathy	Glycophorin c (gerbich blood group)
HBA1	617981	141800	Hemoglobinopathy	Hemoglobin–alpha locus 1
HBA2	617981	141850	Hemoglobinopathy	Hemoglobin–alpha locus 2
HBB	617980	141900	Hemoglobinopathy	Hemoglobin subunit beta
HBD	*	142000	Thalassemia due to Hb Lepore; Thalassemia, delta-	Hemoglobin–delta locus
HBG1	141900	141749	Fetal hemoglobin quantitative trait locus 1	Hemoglobin, gamma a
HBG2	613977	142250	Cyanosis, transient neonatal; Fetal hemoglobin quantitative trait locus 1	Hemoglobin, gamma g
HK1	235700	142600	Enzymopathy	Hexokinase 1
KCNN4	616689	602754	Membranopathy	Potassium channel, calcium activated intermediate/small conductance subfamily n alpha, member 4
KIF23	*	605064	Congenital dyserythropoietic anemia	Kinesin family member 23
KLF1	613673	600599	Congenital dyserythropoietic anemia	Kruppel-like factor 1 (erythroid)
NT5C3A	266120	606224	Enzymopathy	5′-nucleotidase, cytosolic iiia
PFKL	*	171860	Hemolytic anemia due to phosphofructokinase deficiency	Phosphofructokinase, liver type
PFKM	232800	610681	Enzymopathy	Phosphofructokinase, muscle
PGD	*	172200	Enzymopathy	6-phosphogluconate dehydrogenase, erythrocyte
PGK1	300653	311800	Enzymopathy	Phosphoglycerate kinase 1
PIEZO1	616089	611184	Membranopathy	Piezo-type mechanosensitive ion channel component 1
PKLR	266200	609712	Enzymopathy	Pyruvate kinase, liver and rbc
RHAG	185000	180297	Membranopathy	rh-associated glycoprotein
SEC23B	224100	610512	Congenital dyserythropoietic anemia	Sec23 homolog b, copii coat complex component

(Continued)

TABLE 2 | Continued

Symbol	Phenotype MIM number	Gene/Locus MIM number	Category	Description
SLC2A1	606777	138140	Membranopathy	Solute carrier family 2 (facilitated glucose transporter), member 1
SLC4A1	612653	109270	Membranopathy	Solute carrier family 4 (anion exchanger), member 1 (diego blood group)
SPTA1	130600	182860	Membranopathy	Spectrin alpha, erythrocytic 1
SPTB	616649	182870	Membranopathy	Spectrin beta, erythrocytic
TPI1	615512	190450	Enzymopathy	Triosephosphate isomerase 1
UGT1A1	237900	191740	Gilbert syndrome	udp glucuronosyltransferase 1 family, polypeptide a1

**Not available.*

performed not revealing any disease-causing mutation. She underwent successfully bone marrow transplant when she was almost 3-year-old.

In all cases, RAD due to Hb variant was not suspected mainly due to the fact that parents did not present family history of RADs, except for case 3, RBC parameters were found to be normal and abnormal Hb fractions were absent when analyzed. Therefore, genetic testing was performed for genes associated with RADs other than globin genes, failing to show a conclusive diagnosis.

Genetics Analysis

Written informed consent was obtained from cases or legal guardian. Targeted NGS (t-NGS) analysis was performed in cases 1, 2, and 3 while whole exome sequencing (WES) analysis was performed in cases 4 and 5. For all the patients, genomic DNA was extracted from peripheral blood. For patients who underwent bone marrow transplant, DNA samples were previously stored.

The designed t-NGS panel covered 46 genes described as disease causing for RADs, including genes responsible for membrane disorders, enzyme defects, congenital dyserytrhopoietic anemia and the *HBA1*/*HBA2* and *HBB* genes responsible for alpha and beta-globin chains, respectively. The full list of genes included is shown in **Table 2**. Exon and exon/intron boundaries were capture using a NimbleGen SeqCap EZ HyperCap (Roche) solution-based capture system followed by next generation sequencing on the MySeq (Illumina) with 150 bp paired-end reads. For the bioinformatics analysis, alignment to the hg38 genome was performed with BWA-MEM (Li H. 203 arXIV:1303.3997v2) and detection of changes with GATK[1]. Obtained variants were filtered and annotated based on variant effect, coverage (>30) and MAF (>0.05). Resulting variants were assessed for technique pitfalls through IGV. The nomenclature used was the recommended by HGVS[2]. Finally, disease-causing variants were prioritized based on inheritance pattern and VarSome[3] for previous evidence as disease causing mutations or predictions score information. Variants were reported according to American College of Medical Genetics (ACMG) guidelines.

For case 4, WES was performed in a trio approach (patient and both parents). Libraries were prepared using the Kapa HTP kit (Illumina, San Diego, CA, United States) and capture was performed using the SeqCap EZ Human Exome Library v3.0 (Roche NimbleGen Madison, WI, United States). Sequencing was done on an Illumina HiSeq2500 HTv4 (Illumina, San Diego, CA, United States) with paired-end 125-bp reads. Read alignment to hg19 and variant calling were done with a pipeline based on BWA-MEM0.7 and GATK 3.3.0. The median coverage of the captured target region was at least 98×. Variant annotation and prioritizing were done using Cartagenia Bench Lab NGS (Agilent Technologies). Variants located outside the exons and intron/exon boundaries and variants with a minor allele frequency (MAF) of >1% in control databases, including dbSNP137[4], 1000 Genomes Project (phase 3)[5], and Exome Variant Server (EVS), NHLBI Exome Sequencing Project National Heart, Lung, and Blood Institute GO Exome Sequencing Project (ESP6500 release)[6] and in-house exome controls were excluded. Variants that fitted with a *de novo* or recessive mode of inheritance were further prioritized based on literature, predicted (deleterious) effects on protein function by e.g., truncating the protein, affecting splicing, amino acid change, and evolutionary conservation.

For case 5, WES was performed in a trio approach (patient and both parents). Exomes were captured using the Agilent SureSelectXT Human All Exon v5 (Agilent, Santa Clara, CA, United States) accompanied by Illumina paired-end sequencing on the HiSeq2000 (Illumina, San Diego, CA, United States). The in-house sequence analysis pipeline Modular GATK-Based Variant Calling Pipeline (MAGPIE) (LUMC Sequencing Analysis Support Core, LUMC) was used to call the SNVs/indels. LOVDplus (Leiden Genome Technology Center, LUMC, Leiden) was used for interpretation of variants.

RESULTS

Genetic variants in globin genes responsible for UH or HUH were found in all five cases as shown in **Table 1**. All variants were confirmed by Sanger sequencing.

In case 1, variant *HBB*:c.202G > A (p.Val67Met) was found in exon 2 in the heterozygous state. This *HBB* variant is known as Hb Bristol-Alesha, a UH associated with moderate-severe hemolytic anemia. The variant was not found in the parents, suggesting a *de novo* variant in the patient.

[1]https://software.broadinstitute.org/gatk/

[2]http://www.hgvs.org

[3]https://varsome.com

[4]http://www.ncbi.nlm.nih.gov/projects/SNP

[5]http://www.internationalgenome.org/

[6]http://evs.gs.washington.edu/EVS/

In case 2, variant *HBA1*:c.187G > A (p.Val62Met) was found in exon 2 in the heterozygous state. This *HBA1* variant is known as Hb Evans and is associated wild with mild hemolytic anemia and classified as UH. Parents were not sequenced.

In Case 3, variant *HBB*:c.290T > C (p.Leu96Pro) was found in in exon 2 in the heterozygous state. This *HBB* variant is known as Hb Debrousse and is described as a moderate UH. Parents were not sequenced. Nevertheless, antecedents of hemolytic anemia are present in the mother, suggesting a dominant inheritance pattern.

In cases 4 and 5, two missense stop-loss mutations at position 422 of the *HBB* gene were found. The first variant *HBB*:c.442T > C (p.Ter147Glnext*21), found in case 4, is known as Hb Zunyi, while the second variant *HBB*:c.442T > A (p.Ter147Lysnext*21), found in case 5, constitutes a novel variant which was called Hb Mokum. Both variants cause the loss of a stop codon and elongation of the translated beta-globin chain of 21 amino acids due to a new stop codon in the 3′ untranslated region (3′UTR) of the *HBB* gene. The variants were not found in the parents suggesting *de novo* variants in the patients.

According to the ACMG guidelines, all the variants were classified as pathogenic (Richards et al., 2015).

DISCUSSION

We highlight the importance of including globin genes in the NGS analysis of RAD for enabling the diagnosis of UH. We present five clinical cases affected with RAD due to UH variants, four are related to the beta-globin gene (Hb Bristol—Alesha, Hb Debrousse, Hb Zunyi, and the novel Hb Mokum), meanwhile, one is related to the alpha-globin gene (Hb Evans). The use of NGS has been crucial for the final conclusive diagnosis.

The severity of RADs due to UHs depends on the mutation's impact on protein stability and consequently on the degree of hemolysis and inefficient erythropoiesis. Patients' RBCs typically display abnormal but unspecific morphology with microcytosis, hypochromia, moderate to severe anisopoikilocytosis, basophilic stippling, and inclusions that may become particularly prominent following splenectomy (Steinberg et al., 2009; Kent et al., 2014). UHs are commonly inherited in a dominant way or presented as *de novo*, although there are some examples of recessive inheritance leading to mild phenotypes. According to results obtained through the HbVar Query page (dated 14th January 2020), 1,534 Hb variants have been described so far due to mutations on either *HBA1*/*HBA2* or the *HBB* genes. Up to 251 variants (16.4%) are classified as UH or HUH based on heat or isopropanol stability tests and/or low Hb abundancy (Giardine et al., 2007, 2014). It is worthy to highlight that all the HUH variants involving the *HBB* gene reported positive stability tests, meanwhile in most of the HUH involving the alpha-globin genes, hyper instability has been only deduced from low abundance. This must be cautiously taken since mutations in alpha-globin genes are lower expressed (<25%) than in beta-globin gene due to the existence of duplicated alpha-globin genes, *HBA1* and *HBA2*, especially in mutations involving the *HBA2* gene, as it encodes a 2-3–fold higher level of mRNA than *HBA1* (Liebhaberts et al., 1986). Thus, the beta-globin gene is the first option to investigate for disease-causing mutations leading to RADs due to UHs/HUHs especially in cases with moderate to severe phenotypes.

Interestingly, Hb Bristol-Alesha is classified as a UH variant, not as a HUH as we expected based on the severity of the patient's clinical picture. The change to methionine at position 67 of the beta-globin chain alters the hydrophobic heme pocket causing the instability of the protein (Kano et al., 2004). As described in previous clinical reports, at physical examination, splenomegaly and jaundice may be found. Iron overload and gallstones may develop due to the rapid turnover of RBCs.

Hb Debrousse, reported twice in literature, is a UH characterized by well-compensated chronic hemolytic anemia due to its high oxygen affinity. Hb Debrousse is caused by leucine to proline substitution at position 96 involving the hydrophobic environment of the proximal side of the heme. In the previously reported cases, Hb Debrousse discovery was possible after a Parvovirus B19 infection that caused a hemolytic crisis (Lacan et al., 1996). Indeed, since affected patients show a chronic well-compensated hemolytic anemia, the diagnosis of such a variant is unlikely until the globin genes are investigated. Such a study is usually performed only when some complications occur.

Hb Zunyi was recently reported for the first time as a *de novo* mutation in a Chinese child with severe anemia requiring blood transfusion, malnutrition, growth delay, splenomegaly and hepatomegaly (Su et al., 2019). In the study herein, we identified both Hb Zunyi and Hb Mokum as *de novo* mutations in the heterozygous state. Hb Zunyi and the novel Hb Mokum are stop-loss mutations at position 442 in *HBB*, resulting in an elongated beta-globin chain leading to HUHs. The extra amino acids in the elongated beta-globin chain (169 a.a.) are probably affecting its helical sequence, interfering with its tertiary structure and causing an unstable tetramer. Frameshift mutations in the *HBB* gene, resulting in the elongated beta-globin chain, have been described before but resulted in shorter beta-chains (max. 157 aa.) and milder phenotypes than the mutations described here (Su et al., 2019).

Finally, Hb Evans is classified as UH. It is consequence of a valine to methionine substitution at position 62 of the alpha2-globin chain encoding gene *HBA2*. Hb Evans has been reported in patients presenting with mild hemolytic anemia that was getting worse particularly in case of stress (Wilson et al., 1989).

The standard tests to detect abnormal anemias are High Precision Liquid Chromatography (HPLC) or conventional or capillary electrophoresis (CE). However, UHs/HUHs do not normally appear in the peak-patterns or appear as small peaks that may be mistaken for degradation products. In three of the five UH cases reported here, extra peaks were not detected. More confined methods are Heinz Bodies test or stability tests as isopropanol precipitation or heat stability tests, which are affordable screening techniques for UHs/HUHs variants. In the patient with Hb Bristol-Alesha, Heinz bodies were detected and heat stability test was positive only after splenectomy (**Figures 1**, **2**), while in the other patients, Heinz bodies and heat stability test

were not performed. Genetic analysis of globin genes should be performed for diagnosis confirmation. Inclusion of *HBA1/HBA2* and *HBB* in NGS approaches will facilitate timely conclusive diagnosis. as a screening tool for hemolytic anemias will assist in reaching a definitive diagnosis sooner.

Furthermore, the occurrence of *de novo* mutations causing UHs/HUHs should also be considered in the analysis of genetic variants.

The usefulness of NGS in improving the diagnosis of RADs has already been demonstrated in several studies as well as its relevance in new gene discovery (Shang et al., 2017; Duez et al., 2018). In the case of overlapping phenotypes, which frustrate proper diagnosis, the use of NGS may be beneficial for ultra-rare RADs. In a recent publication, 36% of patients initially diagnosed with congenital dyserytrhopoietic anemia, received a final diagnosis of pyruvate kinase deficiency after NGS analysis (Russo et al., 2018). Nevertheless, in the majority of the t-NGS panels reported, globin genes are not included, since globin genes are quite short and molecular diagnosis of most common Hb disorders, such as sickle cell disease (SCD) and thalassemia syndromes, is well-established through Sanger sequencing and GAP-PCR/MLPA. Therefore, dBTHAL disorders due to UH/HUH may also benefit from NGS approaches for RADs by including globin genes, as presented herein.

Current literature on dBTHAL and UH/HUH variants is mainly composed of retrospective case reports, which makes evidenced-based management of this RAD unlikely. In addition, to benefit from the most adequate management it is necessary to achieve a diagnosis as early as possible. In conclusion, this study confirms the importance of NGS as a fundamental tool to early identify and treat UH/HUH in patients with RAD without an established diagnosis after standard methodologies.

Future challenges include a better understanding of disease characteristics and management, and consideration of bone marrow transplant as a curative option. Therefore, we encourage that these patients are referred to expert Units in referral centers for enabling basic and clinical research taking advantage of the already established European Reference Networks for rare hematological disorders, ERN-EuroBloodNet.

DATA AVAILABILITY STATEMENT

The datasets generated for this study can be found in the online repositories. The names of the repository/repositories and accession number(s) can be found below: www.ithanet.eu and https://ithanet.eu/db/ithagenes?ithaID=3697.

ETHICS STATEMENT

Written informed consent was obtained from the cases/legal guardian for the publication of any potentially identifiable images or data included in this article.

AUTHOR CONTRIBUTIONS

VR, MM-P, CLH, TK, and DB wrote the manuscript. All authors critically revised the manuscript.

FUNDING

This study was supported by funding from the authors' institutions and the European Commission H2020-MSCA-ITN-2019, Grant Agreement N860436, "EVIDENCE."

ACKNOWLEDGMENTS

This work was generated within the European Reference Network on Rare Hematological Diseases (ERN-EuroBloodNet, FPA 739541).

REFERENCES

Bunn, H. F., and Forget, B. G. (1986). *Hemoglobin: Molecular, Genetic and Clinical Aspects*. Philadelphia, PA: W. B. Saunders Company, doi: 10.1016/0092-8674(87)90069-9

Duez, J., Carucci, M., Garcia-Barbazan, I., Corral, M., Perez, O., Luis Presa, J., et al. (2018). High-throughput microsphiltration to assess red blood cell deformability and screen for malaria transmission-blocking drugs. *Nat. Protoc.* 13, 1362–1376. doi: 10.1038/nprot.2018.035

Efremov, G. D. (2007). Dominantly inherited β-Thalassemia. *Hemoglobin* 31, 193–207. doi: 10.1080/03630260701290092

Galanello, R., and Origa, R. (2010). Beta-Thalassemia. *Orphanet J. Rare Dis.* 5:11. doi: 10.1186/1750-1172-5-11

Giardine, B., Borg, J., Viennas, E., Pavlidis, C., Moradkhani, K., Joly, P., et al. (2014). Updates of the hbvar database of human hemoglobin variants and Thalassemia Mutations. *Nucleic Acids Res.* 42, 1063–1069. doi: 10.1093/nar/gkt911

Giardine, B., van Baal, S., Kaimakis, P., Riemer, C., Miller, W., Samara, M., et al. (2007). HbVar database of human hemoglobin variants and thalassemia mutations: 2007 update. *Hum. Mutat.* 28:206. doi: 10.1002/humu.9479

Kano, G., Morimoto, A., Hibi, S., Tokuda, C., Todo, S., and Sugimoto, T. (2004). Hb Bristol-Alesha presenting Thalassemia-Type hyperunstable hemoglobinopathy. *Int. J. Hematol.* 80, 410–415. doi: 10.1532/IJH97.04048

Kent, M. W., Oliveira, J. L., Hoyer, J. D., Swanson, K. C., Kluge, M. L., Dawson, D. B., et al. (2014). Hb grand junction (HBB: C.348-349delinsG; P.His117IlefsX42): a new hyperunstable hemoglobin variant. *Hemoglobin* 38, 8–12. doi: 10.3109/03630269.2013.853672

Lacan, P., Kister, J., Francina, A., Souillet, G., Galactéros, F., Delaunay, J., et al. (1996). Hemoglobin debrousse (B96[FG3]Leu → Pro): a new unstable hemoglobin with twofold increased oxygen affinity. *Am. J. Hematol.* 51, 276–281. doi: 10.1002/(SICI)1096-8652(199604)51:4<276::AID-AJH5<3.0.CO;2-T

Liebhaberts, S. A., Cash, F. E., Ballad, S. K., and Human Gene Expression (1986). Human A-Globin gene expression. The dominant role of the Alpha 2-Locus in MRNA and protein synthesis. *J. Biol. Chem.* 261, 15327–15333.

Richards, S., Aziz, S., Bale, S., Bick, D., Das, S., Acmg Laboratory Quality Assurance Committee, et al. (2015). Standards and guidelines standards and guidelines for the interpretation of sequence variants: a joint consensus recommendation of the American College of Medical Genetics and Genomics and the Association for Molecular Pathology. *Genet. Med.* 17, 405–424. doi: 10.1038/gim.2015.30

Russo, R., Manna, F., Gambale, A., Marra, R., Rosato, B. E., Caforio, P., et al. (2018). Multi-Gene panel testing improves diagnosis and management of patients with Hereditary Anemias. *Am. J. Hematol.* 93, 672–682. doi: 10.1002/ajh.25058

Shang, X., Peng, Z., Ye, Y., Asan, Zhang, X., Chen, Y., et al. (2017). Rapid targeted next-generation sequencing platform for molecular screening and clinical genotyping in subjects with hemoglobinopathies. *EBioMedicine* 23, 150–159. doi: 10.1016/j.ebiom.2017.08.015

Steinberg, M. H., Forget, B. G., Higgs, D. R., and Weatherall, D. J. (2009). *Disorders of Hemoglobin: Genetics, Pathophysiology, and Clinical Management, Second Edition*, Vol. 94. Cambridge: Cambridge University Press, i–iv. doi: 10.1017/CBO9780511596582

Su, Q., Chen, S., Wu, L., Tian, R., Yang, X., Huang, X., et al. (2019). Severe thalassemia caused by Hb Zunyi [B147(HC3)Stop→Gln; HBB: C.442T>C)] on the β-Globin gene. *Hemoglobin* 43, 7–11. doi: 10.1080/03630269.2019.1582430

Thom, C. S., Dickson, C. F., Gell, D. A., and Weiss, M. J. (2013). Hemoglobin variants: biochemical properties and clinical correlates. *Cold Spring Harb. Perspect. Med.* 3, 1–22. doi: 10.1101/cshperspect.a011858

Wilson, J. B., Webber, B. B., Kutlar, A., Reese, A. L., Mckie, V. C., Lutcher, C. L., et al. (1989). Hb evans or A262(E11)Val→metβ2; an unstable hemoglobin causing a mild hemolytic anemia. *Hemoglobin* 13, 557–566. doi: 10.3109/03630268908993106

Conflict of Interest: The authors declare that the research was conducted in the absence of any commercial or financial relationships that could be construed as a potential conflict of interest.

frontiers in Physiology

ORIGINAL RESEARCH
published: 23 February 2021
doi: 10.3389/fphys.2021.638027

Impaired Cytoskeletal and Membrane Biophysical Properties of Acanthocytes in Hypobetalipoproteinemia – A Case Study

*Anne-Sophie Cloos[1†], Laura G. M. Daenen[2†], Mauriane Maja[1], Amaury Stommen[1], Juliette Vanderroost[1], Patrick Van Der Smissen[1], Minke Rab[3], Jan Westerink[4], Eric Mignolet[5], Yvan Larondelle[5], Romano Terrasi[6], Giulio G. Muccioli[6], Andra C. Dumitru[5], David Alsteens[5], Richard van Wijk[3] and Donatienne Tyteca[1]**

[1] CELL Unit & PICT Imaging Platform, de Duve Institute, UCLouvain, Brussels, Belgium, [2] Department of Hematology, University Medical Center Utrecht, Utrecht University, Utrecht, Netherlands, [3] Central Diagnostic Laboratory – Research, University Medical Center Utrecht, Utrecht University, Utrecht, Netherlands, [4] Department of Vascular Medicine, University Medical Center Utrecht, Utrecht University, Utrecht, Netherlands, [5] Louvain Institute of Biomolecular Science and Technology, UCLouvain, Ottignies-Louvain-la-Neuve, Belgium, [6] Bioanalysis and Pharmacology of Bioactive Lipids Research Group, Louvain Drug Research Institute, UCLouvain, Brussels, Belgium

OPEN ACCESS

Edited by:
Giampaolo Minetti,
University of Pavia, Italy

Reviewed by:
Gregory Barshtein,
Hebrew University of Jerusalem, Israel
Liana C. Silva,
University of Lisbon, Portugal

***Correspondence:**
Donatienne Tyteca
donatienne.tyteca@uclouvain.be

[†]These authors share first authorship

Specialty section:
This article was submitted to Red Blood Cell Physiology, a section of the journal Frontiers in Physiology

Received: 04 December 2020
Accepted: 25 January 2021
Published: 23 February 2021

Citation:
Cloos A-S, Daenen LGM, Maja M, Stommen A, Vanderroost J, Van Der Smissen P, Rab M, Westerink J, Mignolet E, Larondelle Y, Terrasi R, Muccioli GG, Dumitru AC, Alsteens D, van Wijk R and Tyteca D (2021) Impaired Cytoskeletal and Membrane Biophysical Properties of Acanthocytes in Hypobetalipoproteinemia – A Case Study. Front. Physiol. 12:638027. doi: 10.3389/fphys.2021.638027

Familial hypobetalipoproteinemia is a metabolic disorder mainly caused by mutations in the *apolipoprotein B* gene. In its homozygous form it can lead without treatment to severe ophthalmological and neurological manifestations. In contrast, the heterozygous form is generally asymptomatic but associated with a low risk of cardiovascular disease. Acanthocytes or thorny red blood cells (RBCs) are described for both forms of the disease. However, those morphological changes are poorly characterized and their potential consequences for RBC functionality are not understood. Thus, in the present study, we asked whether, to what extent and how acanthocytes from a patient with heterozygous familial hypobetalipoproteinemia could exhibit altered RBC functionality. Acanthocytes represented 50% of the total RBC population and contained mitoTracker-positive surface patches, indicating the presence of mitochondrial fragments. While RBC osmotic fragility, calcium content and ATP homeostasis were preserved, a slight decrease of RBC deformability combined with an increase of intracellular free reactive oxygen species were observed. The spectrin cytoskeleton was altered, showing a lower density and an enrichment in patches. At the membrane level, no obvious modification of the RBC membrane fatty acids nor of the cholesterol content were detected but the ceramide species were all increased. Membrane stiffness and curvature were also increased whereas transversal asymmetry was preserved. In contrast, lateral asymmetry was highly impaired showing: (i) increased abundance and decreased functionality of sphingomyelin-enriched domains; (ii) cholesterol enrichment in spicules;

and (iii) ceramide enrichment in patches. We propose that oxidative stress induces cytoskeletal alterations, leading to increased membrane stiffness and curvature and impaired lipid lateral distribution in domains and spicules. In addition, ceramide- and spectrin-enriched patches could result from a RBC maturation defect. Altogether, the data indicate that acanthocytes are associated with cytoskeletal and membrane lipid lateral asymmetry alterations, while deformability is only mildly impaired. In addition, familial hypobetalipoproteinemia might also affect RBC precursors leading to disturbed RBC maturation. This study paves the way for the potential use of membrane biophysics and lipid vital imaging as new methods for diagnosis of RBC disorders.

Keywords: acanthocytosis, lipidomics, lipid domains, membrane biophysical properties, reactive oxygen species, ceramide, mitochondria, erythropoiesis

INTRODUCTION

Abetalipoproteinemia and familial homozygous hypobetalipoproteinemia are two very rare metabolic disorders which are clinically indistinguishable (Biemer, 1980). Abetalipoproteinemia is provoked by mutations of both alleles of the *microsomal triglyceride transfer protein* (*MTP*) encoding gene (Calzada et al., 2013). MTP allows the transfer of triglycerides, cholesteryl ester and phospholipids onto the apolipoprotein B (ApoB). Familial hypobetalipoproteinemia is considered as autosomal codominant and most frequently caused by mutations affecting directly the *ApoB* gene leading to truncated forms of the protein (Clarke et al., 2006). In both abetalipoproteinemia and familial homozygous hypobetalipoproteinemia the consequence of gene mutations is failure of release of ApoB-containing lipoproteins, especially chylomicrons and very low density lipoproteins (VLDL) (Burnett and Hooper, 2015). As a result, lipid and lipid soluble vitamin absorption is disturbed, clinically manifesting by extremely low plasma cholesterol and triacylglycerol levels, vitamin A, E, and K levels as well as an almost complete lack of circulating chylomicrons, VLDL and low density lipoproteins (LDL) (Granot and Kohen, 2004). Patients suffering from these diseases present early in life a series of gastroenterological complications including fat malabsorption, steatorrhea, vomiting, abdominal distension and failure to thrive. Later in life, neurological and ophthalmological manifestations, due to lipid soluble vitamin deficiency, as well as non-alcoholic fatty liver disease (NAFLD) become part of the clinical picture (Burnett and Hooper, 2015). For this reason, therapy implies, besides of a strict low fat diet, a life-long supplementation with vitamins A and E (Granot and Kohen, 2004).

Besides abetalipoproteinemia and familial homozygous hypobetalipoproteinemia, a heterozygous form of familial hypobetalipoproteinemia has also been described. Patients are often asymptomatic but frequently associated with NAFLD and in rare cases with neurological disorders (Musialik et al., 2020). Despite the frequently asymptomatic appearance of the heterozygous form of familial hypobetalipoproteinemia, strongly reduced plasma ApoB and LDL-cholesterol levels combined eventually with vitamin E levels below or at the limit of reference values are typical clinical features (Clarke et al., 2006). This heterozygous form is also associated with a low risk of cardiovascular disease (Whitfield et al., 2004).

More surprisingly, acanthocytes (or thorny red blood cells, RBCs) are usually observed on blood smears from patients with abetalipoproteinemia and familial homozygous hypobetalipoproteinemia and to a lesser extent in the heterozygous form (Whitfield et al., 2004; Cuerq et al., 2018). Acanthocytes are RBCs with few membrane projections varying in length and presenting a non-uniform distribution along the RBC surface, in contrast to echinocytes which exhibit more regular membrane projections that are evenly distributed on the RBC membrane. Acanthocytes are, however, not specific to the above mentioned metabolic disorders but are also associated with a series of other pathologies and disorders including chorea-acanthocytosis, McLeod phenotype, In(Lu) phenotype, hereditary spherocytosis with a β-spectrin deficiency, alcoholic cirrhosis, uremia, vitamin E deficiency, anorexia nervosa and hypothyroidism (Wong, 2004).

Such acanthocyte shape could lead to alteration of RBC deformability, which mainly results from the RBC typical biconcave shape as determined by a membrane surface area to cytoplasmatic volume excess. Besides, RBC deformability is also determined by a finely regulated cytoplasmic viscosity controlled by hemoglobin (Hb) concentration and a cytoskeleton composed of a meshwork of spectrin tetramers linked to the membrane by the 4.1R- and ankyrin-based anchorage complexes (Salomao et al., 2008; Baines, 2010). RBC deformation also depends on the intracellular ATP content, the antioxidant defense, the ion balance and subsequent volume control regulated by ion channels, symporters, antiporters and pumps. Among ion channels, the mechanosensitive non-selective cation channel PIEZO1 has been recently identified as the link between mechanical forces, calcium influx and RBC volume homeostasis. The calcium-activated K^+ channel (named Gardos), the Cl^-/HCO_3^- antiporter Band3 and the plasma membrane calcium ATPase pump (PMCA) are also essential for the RBC homeostasis. For instance, the transient increase in intracellular calcium upon deformation activates Gardos channels, leading to cell dehydration and favoring local membrane:cytoskeleton uncoupling (Bogdanova et al., 2013; Cahalan et al., 2015; Lew and Tiffert, 2017; Kaestner et al., 2020). In addition, RBC membrane lipid

composition and distribution are also important for RBC deformation. Actually, the RBC plasma membrane exhibits a high cholesterol content as compared to other cells and shows lipid clustering in domains (Carquin et al., 2016). Three types of lipid domains coexist at the RBC outer membrane leaflet (D'Auria et al., 2013; Carquin et al., 2014, 2015; Leonard et al., 2017b; Conrard et al., 2018). The first, associated with high-curvature membrane areas, is mainly enriched in cholesterol and gathers and/or stabilizes high curvature membrane areas upon RBC deformation. The second and third domains are associated with low-curvature membrane areas. They are, respectively, enriched in ganglioside GM1, phosphatidylcholine and cholesterol (hereafter named GM1-enriched domains) and in sphingomyelin, phosphatidylcholine and cholesterol (hereafter named sphingomyelin-enriched domains). Both GM1- and sphingomyelin-enriched domains seem to participate in calcium exchanges during RBC deformation as GM1-enriched domain abundance increases upon calcium influx after PIEZO1 activation while sphingomyelin-enriched domain abundance increases during calcium efflux (Leonard et al., 2017b; Conrard et al., 2018). A fourth type of lipid domain, mainly enriched in ceramide and associated to the membrane inner leaflet, has been recently identified (Cloos et al., 2020).

In the present study, we asked whether, to what extent and how acanthocytes from a patient with heterozygous familial hypobetalipoproteinemia (pHypoβ) could exhibit alteration of RBC deformability. For this purpose, the RBCs of the patient, who presented a high number of acanthocytes on blood smears, were analyzed for the main features associated with RBC deformability, i.e., RBC morphology, the spectrin cytoskeleton integrity, the intracellular ATP content, the antioxidant defense, the ion balance and the RBC membrane lipid composition and biophysical properties.

The experimental approaches were chosen based on our previous work (Carquin et al., 2014, 2015; Leonard et al., 2017a; Pollet et al., 2018, 2020; Cloos et al., 2020): (i) for RBC morphology: blood smears, optical microscopy of living RBCs and scanning electron microscopy (SEM) of fixed RBCs; (ii) for RBC deformability: osmotic fragility through Hb release and deformability upon shear stress by ektacytometry; (iii) for cytoskeleton integrity: spectrin confocal imaging; (iv) for intracellular ATP content: a biochemical assay; (v) for the antioxidant defense: extent of oxidative stress through measurement of free intracellular reactive oxygen species (ROS) content, lipid peroxidation and Hb oxidation; (vi) for the ion balance: intracellular calcium content evaluated by flow cytometry; (vii) for membrane lipid composition: determination of fatty acids (FA), cholesterol, sphingolipids and phospholipids content; and (viii) for membrane biophysical properties: evaluation of elastic modulus by atomic force microscopy (AFM), curvature by optical microscopy of living RBCs in suspension, transversal asymmetry by phosphatidylserine (PS) surface exposure and lateral asymmetry by vital confocal imaging using validated fluorescent lipid analogs or toxin fragments specific to endogenous lipids. We finally explored whether impairments resulted from defects during RBC maturation or from acceleration of aging. Our findings improve our understanding of hypobetalipoproteinemia and might be extended to other RBC diseases.

MATERIALS AND METHODS

Blood Collection and Preparation

The study was approved by the Medical Ethics Committee of UCLouvain and University Medical Center Utrecht (Study 17–450). After informed consent, blood from the patient and 4 healthy volunteers was collected by venipuncture into K^+/EDTA-coated tubes at the University Medical Center Utrecht. Whenever possible, healthy donors were selected to be age- and gender-matched. After collection, the tubes were transferred to the research laboratory at UCLouvain. Two splenectomised healthy donors were included in the study. Before experiments, RBCs were collected through 10-fold blood dilution in a glucose- and HEPES-containing medium [Dulbecco's modified eagle medium (DMEM), Invitrogen]. Diluted blood was centrifugated at 200 *g* for 2 min, the supernatant removed and RBCs suspended in medium. RBCs were washed a second time by centrifugation at 200 *g* for 2 min and resuspended, as in Cloos et al. (2020). The number of RBCs used for experiments were as follows: (i) Hb release, 12.5×10^6; (ii) intracellular ATP content, 5×10^6; (iii) calcium and ROS contents, 15×10^6; (iv) lipidomic and FA analyses, $2.5–6 \times 10^8$; (v) PS surface exposure, 0.5×10^6; (vi) cholesterol assay, 37.5×10^6; and (vii) fluorescence imaging, 12.5×10^6.

RBC Chemical Treatments

Chemical treatments were performed on washed RBCs. To activate calcium entry through PIEZO1, RBCs were incubated with 0.1 μM Yoda1 (Bio-Techne) for 30 s at RT. To deplete the intracellular calcium content, RBCs were preincubated in a calcium-free medium containing 1mM EGTA (Sigma-Aldrich) for 10 min at RT and maintained during the experiment. To induce oxidative stress, RBCs were submitted to 100 mM H_2O_2 for 60 min at 37°C.

RBC Morphology Determination

RBC morphology was determined (i) on blood smears, (ii) upon suspension of living RBCs in μ-dish IBIDI chambers, (iii) by SEM on fixed RBCs, and (iv) after immobilization of living RBCs on poly-L-lysine (PLL)-coated coverslips. For the RBCs in suspension, washed RBCs were diluted 24-fold in DMEM, deposed in μ-dish IBIDI chambers and observed with a wide-field fluorescence microscope (Observer.Z1; plan-Apochromat 100× 1.4 oil Ph3 objective). For SEM microscopy experiments, RBCs were prepared and analyzed exactly as in Cloos et al. (2020). For RBC immobilization, PLL was deposed on coverslips for 30 min at 37°C and then washed. RBCs were then spread on the PLL-coated coverslip during 4 min and the coverslip was then placed upside down in a medium-filled LabTek chamber (Fisher Scientific). RBCs were observed with the fluorescence microscope Observer.Z1 as above.

RBC Hemoglobin Release Measurement

Washed RBCs were incubated for 10 min at RT in isotonic (320 mOsm, DMEM) or increasingly hypotonic media (264–0 mOsm, DMEM mixed with water to obtain the desired osmolarity) and then pelleted by centrifugation at 200 *g* for 2 min. Supernatants and pellets broken with 0.2% (*w*/*v*) Triton X-100 were both assessed for Hb at 450 nm in 96-well plates (SpectraCount^{TM}, Packard BioScience Co.). Hb release in the supernatant was expressed as percentage of the total Hb present in the sample.

Ektacytometry

Deformability of RBCs was measured with the Laser Optical Rotational Red Cell Analyzer (Lorrca, RR Mechatronics, Zwaag, Netherlands). In this ektacytometer, RBCs are exposed to shear stress in a viscous solution (Elon-Iso, RR Mechatronics), forcing the cells to elongate in an elliptical shape. The diffraction pattern, that is generated by a laser beam, is measured by a camera. The vertical axis (A) and the horizontal axis (B) of the ellipse are used to calculate the elongation index (EI) by the formula $(A - B)/(A + B)$. The EI reflects the deformability of the total population of RBCs. Two different forms of ektacytometry were used: osmotic gradient ektacytometry and cell membrane stability test (CMST). Osmotic gradient ektacytometry measurements of RBCs were obtained using the osmoscan module, according to the manufacturer's instructions and as described elsewhere (Da Costa et al., 2016; Lazarova et al., 2017). Briefly, 250 µl whole blood was standardized to a fixed RBC count of $1000*10^6$ and mixed with 5 ml of Elon-Iso. RBCs in polyvinylpyrrolidone (PVP) were exposed to an osmolarity gradient from approximately 60–600 mOsmol/L, whereas shear stress was kept constant (30 Pa). The CMST was performed using the CMST module on the ektacytometer. To perform a CMST, 50 µl of whole blood was standardized to a fixed RBC count of $200*10^6$ and mixed with 5 ml of Elon-Iso. In the CMST, RBCs are exposed to a shear stress of 100 Pa for 3,600 s (1 h) while the EI is continuously measured. The change in the elongation index (ΔEI) was calculated by determining the median of the first and the last 100 s of the CMST and subsequently calculating the difference between the medians. The ΔEI depicts the capacity of the RBCs to shed membrane and resist shear stress.

Intracellular ATP Measurement

The intracellular ATP level was determined by a chemiluminescence assay kit (Abcam) as described in Conrard et al. (2018) and Cloos et al. (2020). ATP levels were then reported to the corresponding Hb content measured by spectrophotometry.

Intracellular Calcium Determination

Intracellular calcium content was determined by RBC labeling with Fluo4-AM (Invitrogen) as in Cloos et al. (2020). Labeled RBCs were then either analyzed by flow cytometry (FACSVerse, BD Biosciences) or fluorimetry (GloMax; Promega; λ_{exc} of 490 nm and λ_{em} of 520 nm). Flow cytometry data, obtained by medium flow rate on 10.000 events, was analyzed with the software FlowJo to determine the median fluorescence intensity (MFI) of analyzed RBCs. Fluorimetry data were normalized to the global Hb content determined spectrophotometrically as above.

RBC Fatty Acid Content

RBC FA composition was assessed exactly as described in Cloos et al. (2020).

RBC Lipid Composition

The cholesterol content of washed RBCs was determined with a fluorescent assay kit (Invitrogen) as in Cloos et al. (2020) and reported to the global Hb content as described above. The membrane composition in phospholipids, lysophospholipids, sphingolipids and oxysterols was analyzed by lipidomics according to Guillemot-Legris et al. (2016) and Mutemberezi et al. (2016), as described in Cloos et al. (2020).

Oxidative Stress Measurements

Intracellular free ROS were assessed by RBC labeling with 2,7-dichlorodihydrofluoresceindiacetate (H_2DCFDA) in Krebs–Ringer–Hepes (KRH) solution for 30 min at 37°C. MFI of the whole RBC population was acquired as explained above for Fluo4-AM. Lipid peroxidation was evaluated by measurement of malondialdehyde (MDA) with a lipid peroxidation assay kit (Abcam) according to the high sensitivity protocol as in Cloos et al. (2020). Methemoglobin (metHb) was analyzed in RBC lysates, produced through repeated freeze–thaw cycles, with a sandwich Elisa kit (Lifespan Biosciences) as described in Cloos et al. (2020). Both MDA levels and metHb contents were reported to the global Hb content.

Membrane Lipid Imaging on Living RBCs

Endogenous cholesterol was evidenced through living RBC labeling with mCherry-Theta toxin fragment followed by immobilization on PLL-coated coverslips (Cloos et al., 2020). To visualize GM1 ganglioside, sphingomyelin and ceramide, living RBCs were spread onto PLL-coated coverslips and then labeled by trace insertion in the plasma membrane of BODIPY fluorescent analogs of those lipids (Invitrogen) as described in Conrard et al. (2018). Coverslips with living immobilized RBCs were placed in medium-filled LabTek chambers and observed with the wide-field fluorescence microscope (Observer.Z1; plan-Apochromat 100× 1.4 oil Ph3 objective).

Mitochondria Fragment Imaging on Living RBCs

To determine the presence of mitochondria fragments in RBCs, washed RBCs were labeled with 100 nM mitoTracker (Invitrogen) at RT for 30 min, washed, placed on PLL-coated coverslips and observed with the wide-field fluorescence microscope Observer.Z1.

Membrane Curvature on Living RBCs

RBCs were placed into IBIDI chambers as described above for RBC morphology in suspension. Microscopy images were then analyzed with the last version of Shape Analysis by Fourier

Descriptors computation plugging for ImageJ as in Leonard et al. (2017b) and Pollet et al. (2020).

Membrane Transversal Asymmetry on Living RBCs

Exposure of PS was assessed by RBC labeling with Annexin-V coupled to FITC (Invitrogen) and analyzed by flow cytometry as in Cloos et al. (2020). The proportion of PS-exposing RBCs was then determined with the FlowJo software by positioning the cursor at the edge of the healthy RBC population.

Force Distance-Based Atomic Force Microscopy on Living RBCs

AFM experiments were performed with a Bioscope Resolve AFM (Bruker) at ∼25–30°C in DMEM. PeakForce QNM Live Cell probes (Bruker) with spring constants of 0.10 ± 0.02 N m^{-1} and tip radius of curvature of 65 nm were used. The spring constant of the cantilevers was calibrated with a vibrometer (OFV-551, Polytec, Waldbronn) by the manufacturer. The pre-calibrated spring constant was used to determine the deflection sensitivity (Schillers et al., 2017) using the thermal noise method (Hutter and Bechhoefer, 1993) before each experiment. In fast indentation experiments (Dumitru et al., 2018), the AFM was operated in PeakForce QNM mode and Force-distance (FD)-based multiparametric maps were acquired using a force setpoint of 300 pN. The AFM cantilever was oscillated vertically at 0.25 kHz with a peak-to-peak oscillation amplitude of 500 nm. Height and Young's modulus maps were recorded using a scan rate of 0.2 Hz and 256 pixels per line. Slow indentation experiments were performed in Force-Volume (FV) mode. Individual FD curves were recorded in contact mode on the RBC surface with a force setpoint of 300 pN, using ramp speeds of 2 μm s^{-1} for a 2 μm ramp size. Measurements were performed in the central region of RBCs to avoid substrate effects. Indentations ranged between 300 nm and 1 μm depending on cell type.

RBC Spectrin Immunofluorescence

Immunolabeling of spectrin was performed as in Cloos et al. (2020) and Pollet et al. (2020). All coverslips were mounted with Dako and examined with a Zeiss Cell Observer Spinning Disk (COSD) confocal microscope using a plan-Apochromat 100× NA 1.4 oil immersion objective and the same settings for illumination.

Image Analysis, Data Quantification and Statistical Analyses

RBC membrane area, RBC curvature and spectrin intensity/occupation were determined using the Fiji software. Lipid domain abundance was determined by manual counting and expressed by reference to the hemi-RBC projected area. The proportion of spiculated RBCs and of RBCs presenting lipid- or mitoTracker-enriched vesicles, patches or spicules was also assessed by manual counting on fluorescence images. For AFM, at least 64 FD curves were recorded per cell and analyzed using the Nanoscope Analysis v9.1 software (Bruker). Hertz model was used to extract Young's modulus values from individual FD curves. Whole RBC elasticity was analyzed from Slow indentation experiments in FD-AFM mode, by fitting the repulsive part of FD curves with the Hertz model. To analyze the contribution of the plasma membrane and cytoskeleton to the cellular mechanical behavior, two different fit ranges were defined in the repulsive part of FD curves obtained in Fast indentation experiments (PeakForce QNM mode). Plasma membrane elastic contribution was estimated for indentations $\delta < 50$ nm and cytoskeleton elasticity was extracted from δ between 50 and 100 nm. Data are expressed as means ± SEM when the number of independent experiments was $n \geq 3$ or means ± SD if $n \leq 2$. For all experiments, statistical tests were performed only when $n \geq 3$. Tests were non-parametrical Mann–Whitney test or Kruskal–Wallis followed by Dunn's comparison test, except for AFM and membrane curvature data for which two sample *t*-tests were applied as RBCs were analyzed individually and data obtained for all RBCs are presented. To evaluate the effect of chemical agents, the paired data were analyzed by paired non-parametrical tests (Wilcoxon matched-pairs signed rank tests). ns, not significant; $^{*}p < 0.05$, $^{**}p < 0.01$, $^{****}p < 0.0001$.

RESULTS

Case Presentation

The patient pHypoβ is a 49 year-old adult. Due to idiopathic thrombocytopenic purpura, his spleen has been removed at the age of 17 as a curative treatment. He has no additional treatment. The transaminases are increased (**Supplementary Table 1**) but he has no anemia and is otherwise healthy. He exhibits since more than 30 years a high number of acanthocytes on blood smears (**Figure 1A**), which was suspected to result from hypobetalipoproteinemia. The patient also presented a vitamin E level close to the lower reference limit (**Supplementary Table 1**). Despite of acanthocytosis, reticulocyte count, RBC mean corpuscular volume and Hb levels are within the normal range (**Supplementary Table 1**).

pHypoβ Presents a Nucleotide Deletion in *APOB* Resulting in a Truncated ApoB

Next-Generation Sequencing of pHypoβ revealed a heterozygous single nucleotide deletion in *APOB*, the gene encoding ApoB. It concerns the deletion of adenosine at nucleotide 2,534 in exon 17, which leads to a shift in the reading frame and consequent premature end of translation at residue 862 (Human Gene Mutation Database, CD051293). Nonsense-mediated mRNA decay likely will prevent translation of such mutant *APOB* mRNA into a severely truncated protein. This mutation has already been identified (Fouchier et al., 2005), but consequences for RBC morphology, cytoskeletal and biophysical properties as well as functionality were not evaluated.

pHypoβ Exhibits a High Proportion of Acanthocytes

We started by confirming the presence of spiculated RBCs detected on a blood smear (**Figure 1A**) by optical microscopy

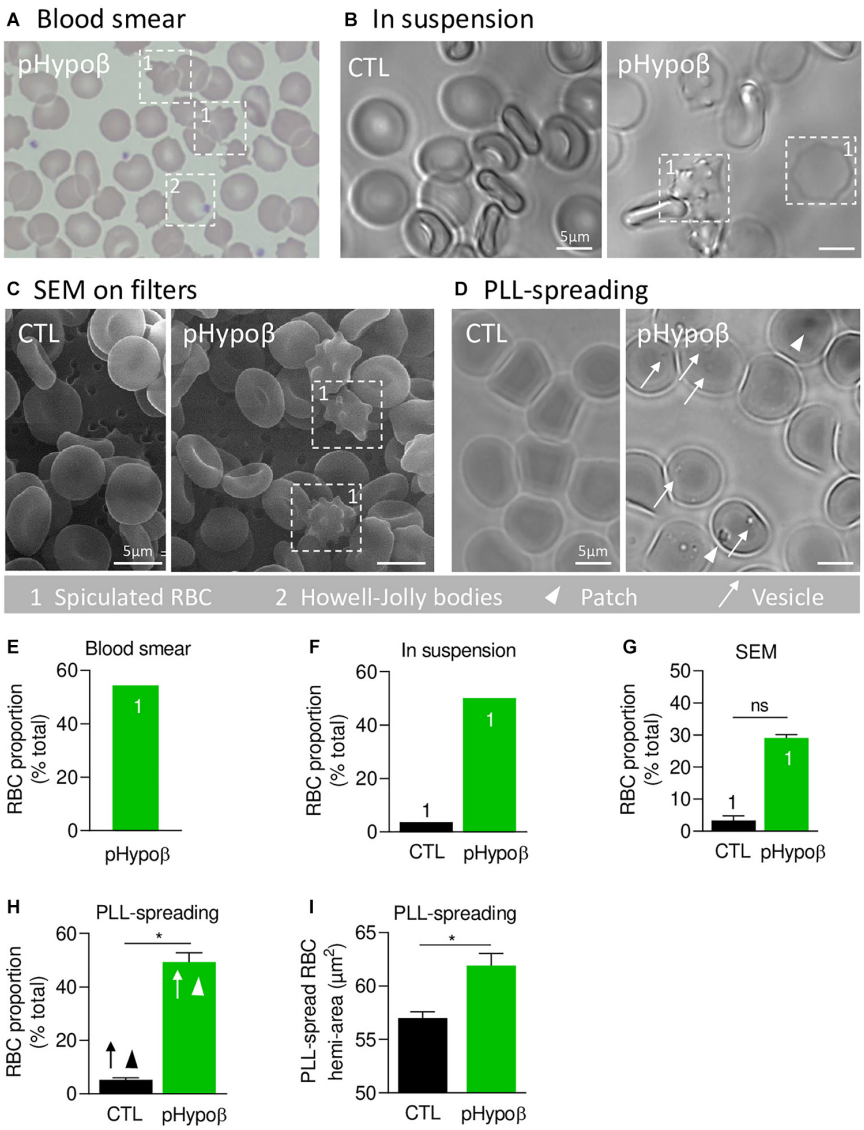

FIGURE 1 | A high proportion of acanthocytes is visible on pHypoβ blood smears and RBCs in suspension while patches and small vesicles are evidenced upon RBC spreading. The morphology of RBCs of the patient with hypobetalipoproteinemia (pHypoβ; green columns) was compared to those of healthy donors (CTL; black columns), either on blood smear **(A)**, on RBCs in suspension **(B,C)**, or upon spreading on poly-L-lysine (PLL)-coated coverslips **(D)**. Then, the proportion of RBCs with spicules (indicated with 1; **E–G**), patches (arrowheads, **H**) and/or vesicles (arrows, **H**) and the RBC membrane area were determined **(I)**. **(A)** May–Grünwald Giemsa-stained blood smear. 1, spiculated RBCs; 2, Howell-Jolly bodies. **(B)** Light microscopy of living RBCs in suspension in IBIDI chambers. Images are representative of 2 independent experiments. **(C)** Scanning electron microscopy of glutaraldehyde-fixed RBCs on filters. Images are representative of 2 experiments with 3 filters each. **(D)** Light microscopy of living RBCs spread on PLL-coated coverslips. Images are representative of at least 10 experiments. **(E–G)** Quantification of the abundance of spiculated RBCs, expressed as % of total RBCs. Data are means from 1 experiment for **(E,F)** and means ± SEM of 3–4 filters in **(G)**. Mann–Whitney test; ns, not significant. **(H)** Quantification of the proportion of PLL-spread RBCs presenting patches and/or vesicles. Data are means ± SEM of 3–6 independent experiments. Mann–Whitney test; $^*p < 0.05$. **(I)** Quantification of the membrane surface area of PLL-spread RBCs. Data are means ± SEM of 6–7 independent experiments. Mann–Whitney test; $^*p < 0.05$.

of living RBCs in suspension and by SEM of fixed RBCs on filters (**Figures 1B,C**). Quantification indicated that spiculated RBCs represented ∼50% of all pHypoβ RBCs in blood smear and optical microscopy images and ∼30% in electron microscopy images while they accounted only for a minority of RBCs from healthy donors (**Figures 1E–G**). Discrepancies regarding the proportion of spiculated RBCs detected by electron and optical microscopy could result from the shear stress induced by filtration during RBC preparation for SEM, eventually leading to hemolysis of spiculated RBCs.

When RBCs were spread on PLL-coated coverslips, spiculated RBCs could still be distinguished from other RBCs as they presented big dark patches and smaller clearer vesicles at their surface (arrowheads and arrows at **Figure 1D**). The proportion

of such RBCs was significantly increased in pHypoβ (**Figure 1H**) and corresponded exactly to the proportion determined above for non-spread RBCs. RBC morphological alterations were accompanied by an increased membrane area of spread RBCs (**Figure 1I**) and by the presence of Howell-Jolly bodies on blood smears (**Figure 1A**), compatible with splenectomy. In contrast, the increase of membrane area did not result from splenic absence since a healthy splenectomised donor did not show such a membrane surface area increase (**Supplementary Figure 1A**).

pHypoβ RBCs Show no Evidence for Increased Osmotic Fragility nor Modifications of ATP and Calcium Homeostasis but a Reduced Ability to Shed Membrane Upon Shear Stress

Despite the high proportion of pHypoβ RBCs with a modified morphology, their resistance to hemolysis was similar to healthy controls (splenectomised or not), as shown by Hb release after RBC incubation in isotonic and increasingly hypotonic media (**Figures 2A,B** and **Supplementary Figure 1B**). Nevertheless, the more sensitive osmotic gradient ektacytometry test revealed that the O_{min} value was slightly increased in pHypoβ (153 vs. 125–148 in healthy donors), indicative of a slight decrease in surface area-to-volume ratio and a slight increase in osmotic fragility (**Figure 2C**). Moreover, the EI_{max}, and therefore the surface area, were slightly decreased in pHypoβ RBCs (0.566 vs. 0.585–0.607). This decrease *a priori* contrasted with the increased surface area determined by optical microscopy on spread RBCs which could result from the increase of the outer leaflet membrane area specifically (**Figure 1I**). Those changes did not result from splenectomy since all osmotic gradient ektacytometry-derived parameters were normal in the healthy splenectomized control (**Figure 2C**). To further investigate pHypoβ RBC deformability, the CMST was performed to assess the RBC ability to shed membrane when exposed to prolonged supraphysiological shear stress force. This is a physiological property of healthy RBCs and the decrease in EI that occurs under these circumstances is proposed to be a measure of membrane health. pHypoβ RBCs showed a ΔEI of −0.144, which was considerably less than the ΔEI of −0.187 from the healthy splenectomized control, and even more less than the ΔEI of −0.208 seen in healthy donors (**Figure 2D**). These results indicated that splenectomy on itself was accompanied with loss of the ability to shed membrane upon shear stress, but that this loss was more pronounced in pHypoβ RBCs. We also evaluated the intracellular contents in ATP and calcium, two key parameters for RBC functionality and deformation (Bogdanova et al., 2013; Conrard et al., 2018). The intracellular ATP content was slightly increased but the calcium content remained unchanged (**Figures 2E,F**).

pHypoβ RBCs Exhibit Normal Membrane Fatty Acid Profile and Cholesterol Content but Increased Ceramide Species

As acanthocytotic RBCs in abetalipoproteinemia and homozygous familial hypobetalipoproteinemia are associated with profound alterations of membrane lipid composition (Biemer, 1980; Barenholz et al., 1981; Gheeraert et al., 1988), we then determined whether RBC morphology alterations in pHypoβ could be associated with modified membrane composition in FAs (**Figures 3A–E**), cholesterol (**Figure 3F**), phospholipids and/or sphingolipids (**Figure 4**). The relative proportion of saturated (SFA), monounsaturated (MUFA) and polyunsaturated (PUFA) FAs was unchanged in pHypoβ RBCs (**Figure 3A**). Closer examination of major SFAs and MUFAs did not reveal more changes (**Figures 3B,C**). For PUFAs, however, the proportion of long chain C22 PUFAs appeared to decrease in favor of PUFAs with shorter C18 or C20 chains (**Figure 3D**). The increase of C18 and C20 PUFAs appeared to result from the higher relative contents in linoleic (C18:2) and arachidonic (C20:4) acids (**Figure 3E**).

Since the plasmatic cholesterol content was decreased in pHypoβ (**Supplementary Table 1**), we then evaluated the RBC membrane cholesterol content. Surprisingly, it was not modified in the patient as compared to the healthy donors (**Figure 3F**). Sphingomyelin species were also largely maintained (**Figure 4A**) whereas all ceramide and dihydroceramide species, whatever their fatty acid length and unsaturation number, were increased by 1.5- to 2-fold in pHypoβ (**Figure 4B**). Among phospholipids, no obvious change was detected for PS and phosphatidylinositol (PI) but phosphatidylcholine (PC) species were decreased and phosphatidylethanolamine (PE) species were very slightly increased (**Figures 4C,E,G,I**). In agreement with the heightened proportion of PE, four lysoPE species were also increased. The other lysophospholipids remained unaffected in pHypoβ (**Figures 4D,F,H,J**).

pHypoβ RBCs Have Increased Free Reactive Oxygen Species but No Modification of Phospholipid, Cholesterol and Hemoglobin Oxidation

As the proportion of long chain PUFAs was decreased, we investigated whether pHypoβ RBCs could suffer from oxidative stress due to low circulating vitamin E levels (**Supplementary Table1**), eventually leading to lipid and protein oxidation. We started by measuring ROS using H_2DCFDA. A significant twofold increase of free ROS was observed in pHypoβ RBCs (**Figure 5A**) but not in a healthy donor without spleen (**Supplementary Figure 1C**), indicating that the ROS increase in pHypoβ was not due to splenectomy.

The extent of lipid peroxidation, determined through the level of MDA, was not modified in pHypoβ RBCs (**Figure 5B**). This might seem surprising because increased lipid peroxidation could be detected in HDL and platelets of patients with abetalipoproteinemia (Calzada et al., 2013). Nevertheless, only a slight increase was observed even for healthy RBCs treated with H_2O_2 (**Figure 5B**) and might be explained by the fact that MDA is not the only end product of lipid peroxidation. Nevertheless, oxysterol species were

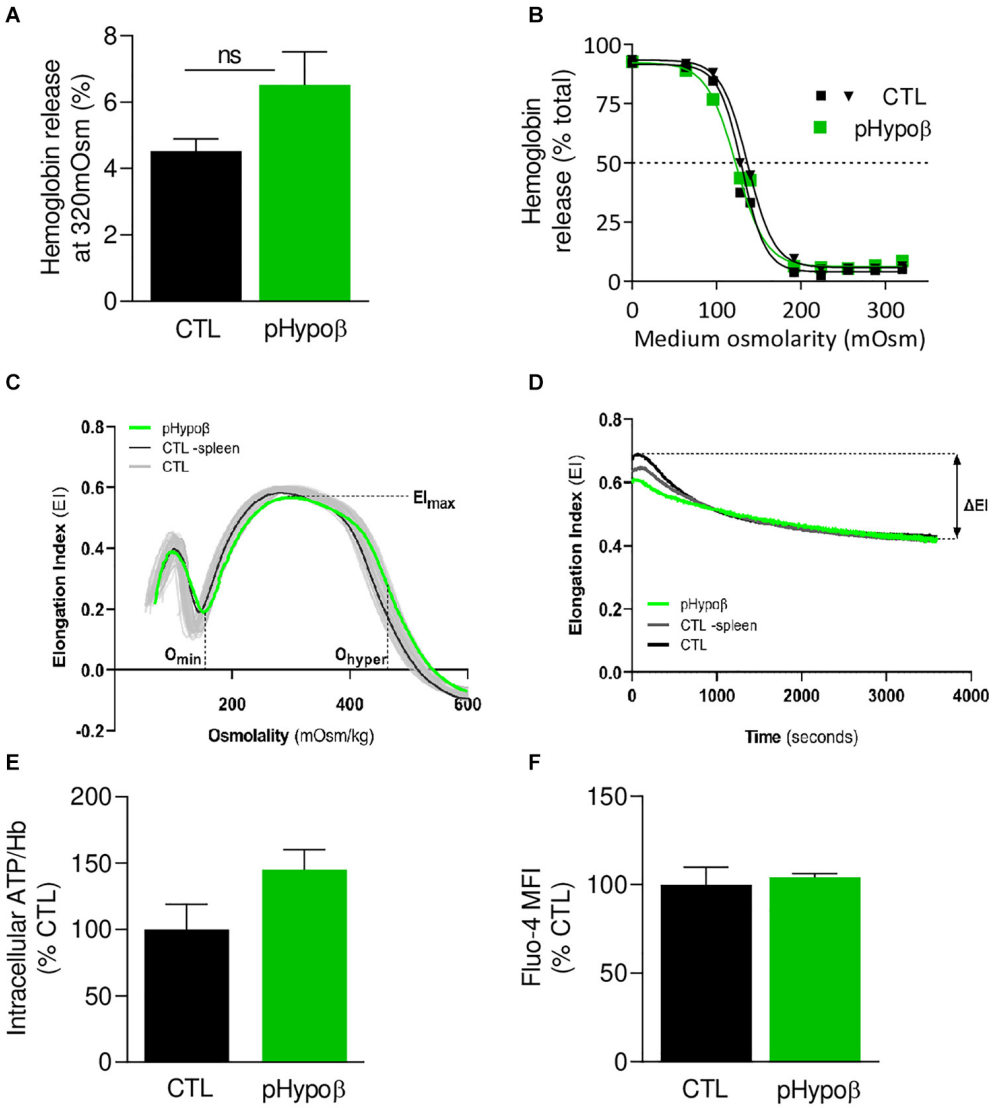

FIGURE 2 | The extent of hemoglobin release and the intracellular calcium and ATP levels are preserved in pHypoβ RBCs while deformability upon shear stress is slightly decreased. RBCs from healthy donors (black and gray in panel **C**) or pHypoβ (green) were evaluated for osmotic fragility **(A,B)**, deformability **(C,D)**, intracellular ATP **(E)** and calcium content **(F)**. **(A,B)** RBC osmotic fragility. RBCs were incubated in isotonic **(A)** or increasingly hypotonic **(B)** media and then centrifugated. Hemoglobin (Hb) in supernatants and in RBC pellets was assessed spectrophotometrically to determine hemolysis. The horizontal dotted line in **(B)** indicates the medium osmolarity at which 50% of the RBCs were lysed. Data are means ± SEM of 4 independent experiments for **(A)** and are representative for 2 independent experiments in **(B)**. Mann–Whitney test; ns, not significant. **(C,D)** RBC deformability. **(C)** Osmotic gradient ektacytometry curve and derived EI_{max}, O_{min}, and O_{hyper} parameters, which, respectively, reflect membrane surface area, surface area-to-volume ratio and cellular hydration. pHypoβ RBCs (green curve) were compared to healthy controls (gray curves obtained from 25 healthy subjects) and a healthy splenectomized control (black curve). **(D)** Cell membrane stability test (CMST) curve and the derived ΔEI parameter which depicts the capacity of the RBCs to shed membrane and resist shear stress. Data are representative of 2 experiments in **(C)** and 1 experiment in **(D)**. **(E)** Intracellular ATP. ATP levels were determined with a kit based on the activity of the firefly luciferase in presence of ATP and the consequent light emission in presence of luciferin. Intracellular ATP levels were normalized to Hb and expressed as percentage of the CTL RBCs. Data are means ± SD of triplicates from 1 experiment. **(F)** RBC calcium content. RBCs were labeled with the non-fluorescent Fluo4-AM which is transformed in RBCs into the fluorescent Fluo4 after de-esterification and interaction with calcium ions. Labeled RBCs were analyzed by flow cytometry for median fluorescence intensity (MFI) and then expressed as percentage of CTLs. Data are means ± SD of triplicates from 1 experiment.

also maintained at levels similar to those found in healthy RBCs (**Figure 5C**).

Besides lipids, Hb is also a major target of oxidative stress in RBCs, generating metHb and eventually hemichromes (Mohanty et al., 2014). By ELISA we showed that pHypoβ RBCs exhibited a very slight metHb increase, comparable to the one obtained upon treatment of healthy RBCs with H_2O_2 (**Figure 5D**). All those data suggested that, despite major morphological changes

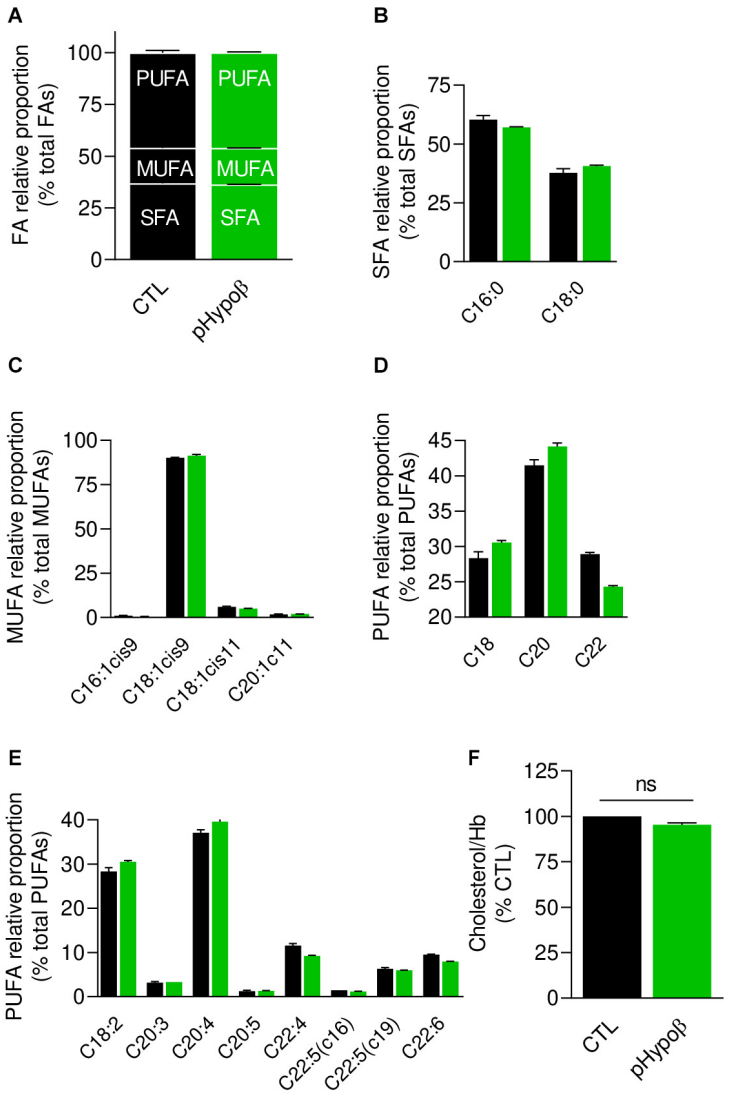

FIGURE 3 | Membrane fatty acid and cholesterol contents are largely preserved in pHypoβ RBCs. RBCs from healthy donors (black columns) or pHypoβ (green columns) were evaluated for membrane fatty acid (FA) content **(A–E)** and cholesterol level **(F)**. **(A–E)** RBC FA composition. Lipids were extracted from isolated RBCs and prepared for gas chromatography to analyze FA content. **(A)** Relative proportion of saturated (SFA), monounsaturated (MUFA) and polyunsaturated (PUFA) FAs expressed as percentage of total FAs. **(B)** Relative proportion of the two major SFAs (C16:0 and C18:0). **(C)** Relative proportion of the four major MUFAs (C16 and C18 with one double bond on position 9 and C18 and C20 with one double bound on position 11). **(D)** Relative proportion of PUFA according to the carbon chain length (chains of 18, 20, or 22C). **(E)** Relative proportion of the major PUFAs (chains of 18–22C and 2–6 double bonds). All data are means ± SD of triplicates from 1 experiment. **(F)** Cholesterol content. Lysed RBCs were evaluated for their cholesterol content through a fluorescent assay kit which uses several enzymatic reactions starting with cholesterol and ending with the transformation of Amplex Red into fluorescent resofurin. Cholesterol content was normalized to Hb content and expressed as percentage of the CTL RBCs. Data are means ± SEM of 3 independent experiments. Mann–Whitney test; ns, not significant.

and increase of free ROS, no obvious alterations in lipid and Hb oxidation appeared to occur in pHypoβ RBCs.

pHypoβ RBCs Are Altered for Their Spectrin Network, Showing Either a Lower Density or a Patchy or Vesiculated Pattern

We next evaluated by immunofluorescence the distribution of spectrin, another major target of oxidative stress (Voskou et al., 2015). Although the spectrin network was homogeneous in ∼99% of healthy RBCs, this proportion was significantly reduced to ∼75% in pHypoβ (population 1 at **Figures 6A,B**). Closer examination of this population indicated a tendency to decrease of the spectrin occupancy per RBC surface combined with a lower variance of spectrin occupancy (**Figures 6C,D**), suggesting that the spectrin network at the surface of pHypoβ RBCs was less dense than in healthy RBCs. Besides, the patient exhibited two additional populations with differential spectrin patterns, namely spectrin-enriched patches and vesicles (populations 2 and 3 at

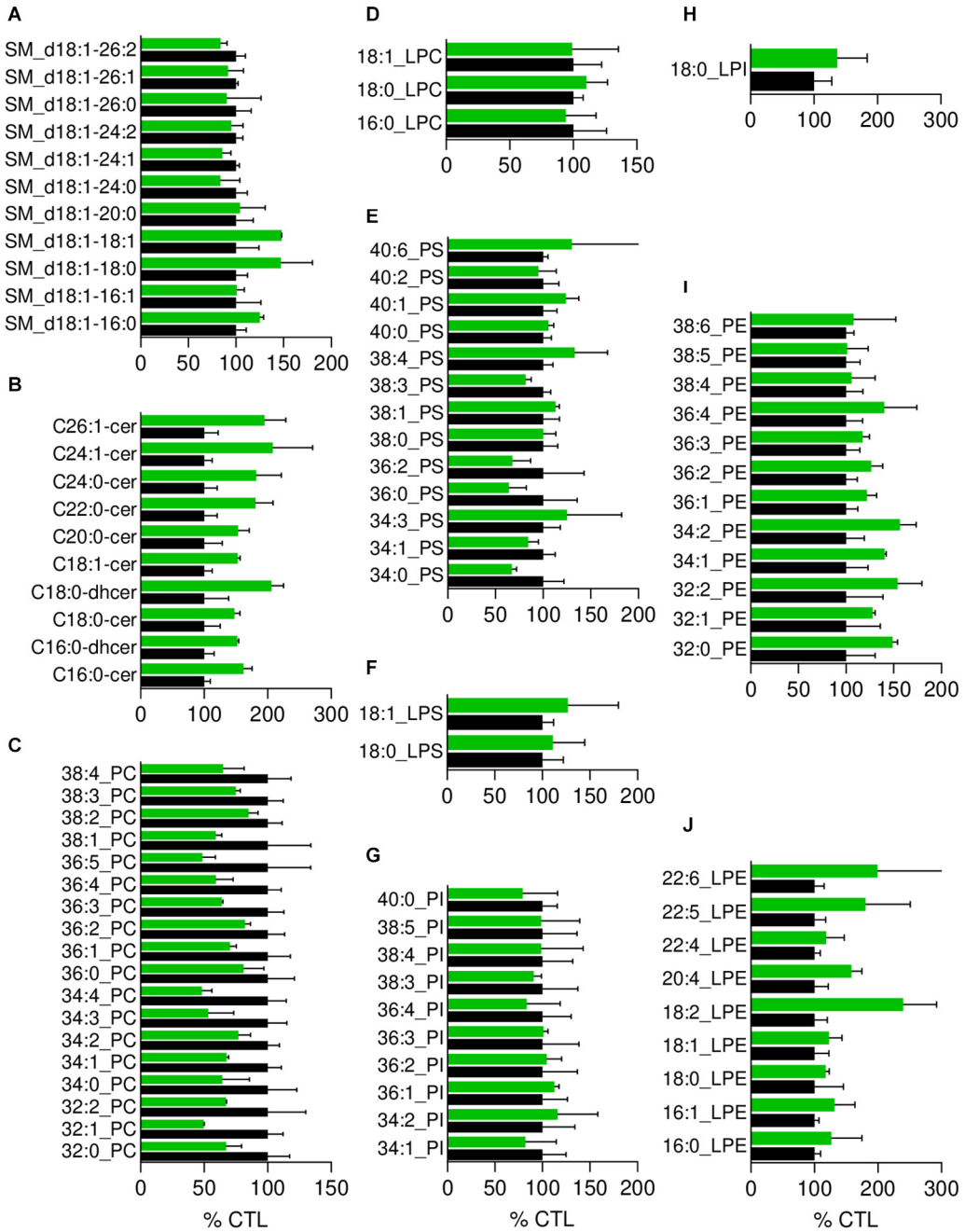

FIGURE 4 | The most obvious membrane lipid changes in pHypoβ RBCs are an increase of ceramide species and a decrease of phosphatidylcholine species. Lipid species were assessed by HPLC-MS on washed, lysed and lipid-extracted RBCs. Content in sphingomyelin (d18:1 D-erythro-sphingosine backbone, SM; **A**), ceramide (Cer) and dihydroceramide (dhcer; **B**), phosphatidylcholine (PC; **C**), lysophosphatidylcholine (LPC; **D**), phosphatidylserine (PS; **E**), lysophosphatidylserine (LPS; **F**), phosphatidylinositol (PI; **G**), lysophosphatidylinositol (LPI; **H**), phosphatidylethanolamnine (PE; **I**) and lysophosphatidylethanolamine (LPE; **J**). Results are expressed as percentage of controls (CTL, mean of 4 donors). Data are means ± SD of 2 independent experiments.

Figure 6A). The proportion of those two populations together increased by ∼25-fold as compared to healthy RBCs (populations 2 and 3 at **Figure 6B**). In conclusion, the spectrin cytoskeleton was altered in pHypoβ RBCs, ∼25% of them showing a patchy and vesiculated pattern and the remaining ∼75% exhibiting a less dense network.

RBC Whole Stiffness and Curvature in Low and High Curvature Areas Are Increased in pHypoβ

To determine whether spectrin cytoskeleton modifications were accompanied by altered membrane biophysical properties, we

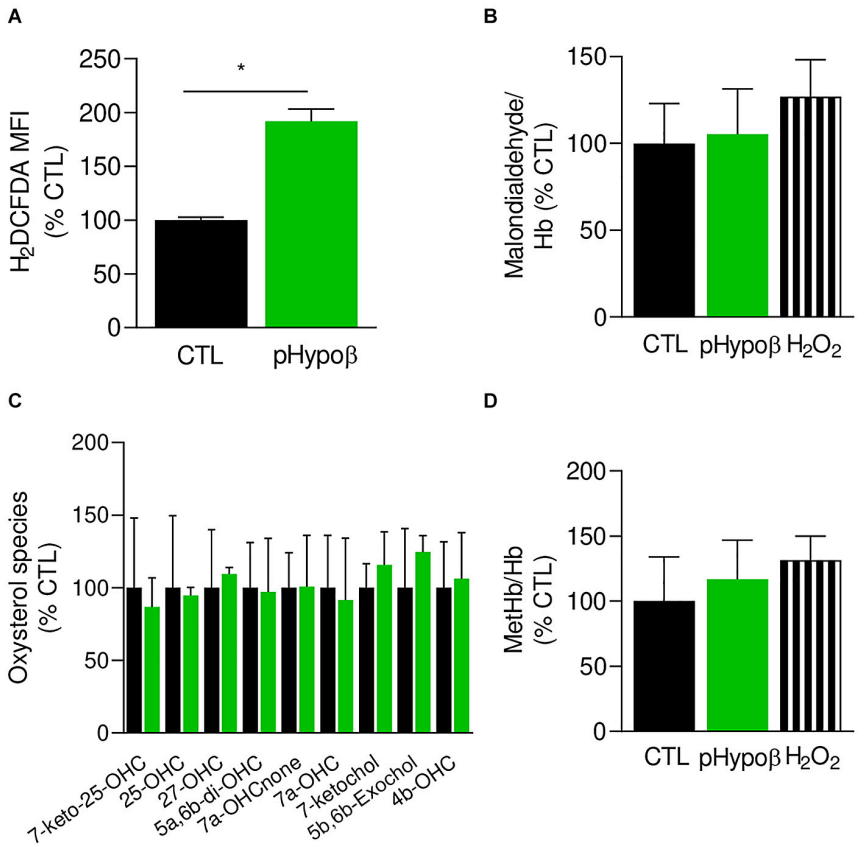

FIGURE 5 | Accumulation of free reactive oxygen species in pHypoβ RBCs is not accompanied by lipid or hemoglobin oxidation. RBCs from healthy donors (black columns) or pHypoβ (green columns) were evaluated for free reactive oxygen species (ROS) accumulation **(A)**, lipid peroxidation **(B)**, oxysterol content **(C)**, and methemoglobin (MetHb) accumulation **(D)**. Hydrogen peroxide was used as positive control in **(B,D)** (hatched columns). All data are expressed as percentage of healthy untreated RBCs. **(A)** Intracellular ROS accumulation. RBCs were labeled with the non-fluorescent H_2DCFDA which is transformed into fluorescent DCF inside the RBCs after de-esterification and interaction with ROS. Flow cytometry analysis allowed to determine the MFI of the global RBC population. Data are means ± SEM of 3–6 independent experiments. Mann–Whitney test; $^*p < 0.05$. **(B)** Lipid peroxidation. Malondialdehyde (MDA), one final product of lipid peroxidation, was detected through interaction with thiobarbituric acid forming a fluorescent adduct. MDA levels were normalized to Hb content and data are means ± SD of triplicates from 2 independent experiments. **(C)** Membrane content in oxysterols. RBCs were washed, lysed, extracted for lipids and determined for 7-Keto-25-hydroxycholesterol (7-keto-25-OHC), 25-hydroxycholesterol (25-OHC), 27-hydroxycholesterol (27-OHC), 5α,6β-dihydroxycholesterol (5α,6β-diOHC), 7α-hydroxycholestenone (7α-OHCnone), 7α-hydroxycholesterol (7α-OHC), 7-ketocholesterol (7-ketochol), 5β,6β-epoxycholesterol (5β,6β-exochol) and 4β-hydroxycholesterol (4β-OHC). Results are expressed as percentage of control RBCs and are means ± SD of 2 independent experiments. **(D)** MetHb content. MetHb was determined using a sandwich Elisa and reported to the global Hb content. Data are means ± SD of triplicates from 1 experiment.

analyzed RBC membrane stiffness and curvature. AFM at SLOW indentation revealed that pHypoβ RBCs were stiffer than healthy RBCs (**Figure 7A**). Since our previous experiments on RBCs treated with cytoskeleton-depolymerizing drugs using the same indentation approach revealed changes in the Young's modulus, we inferred that the main contribution in the whole Young's modulus originated from the cytoskeleton even if some contribution from the cytoplasmic viscosity cannot be discarded. To further test the contribution of the cytoskeleton in the whole RBC Young's modulus vs. the plasma membrane stiffness, RBCs were analyzed at Fast indentation. Plasma membrane elasticity was similar in CTL and pHypoβ RBCs, while a stiffening of the cytoskeleton was observed for pHypoβ RBCs (**Figure 7B**). Hence, a higher variability of measurements was observed for the patient than healthy donors, which might reflect the presence of both acanthocytes and discocytes that were difficult to discriminate after RBC spreading. Interestingly, for both control and pHypoβ RBCs, the highest plasma membrane elastic modulus corresponded to the highest cytoskeleton stiffness (**Supplementary Figure 2**), suggesting that in diseased RBCs both the plasma membrane and the cytoskeleton were altered.

Because it was not possible to discriminate between spiculated and non-spiculated RBCs in AFM due to spreading we then used chambers compatible with RBC morphology preservation and quantified the membrane curvature of the non-spiculated RBCs (**Figure 7C**, population 1). Although the differential curvature between high (HC) and low curvature (LC) areas was preserved in the patient, curvature in both HC and LC areas was increased (**Figures 7C,D**). This latter increase was in good agreement with the lower spectrin occupancy per RBC surface in pHypoβ. Of

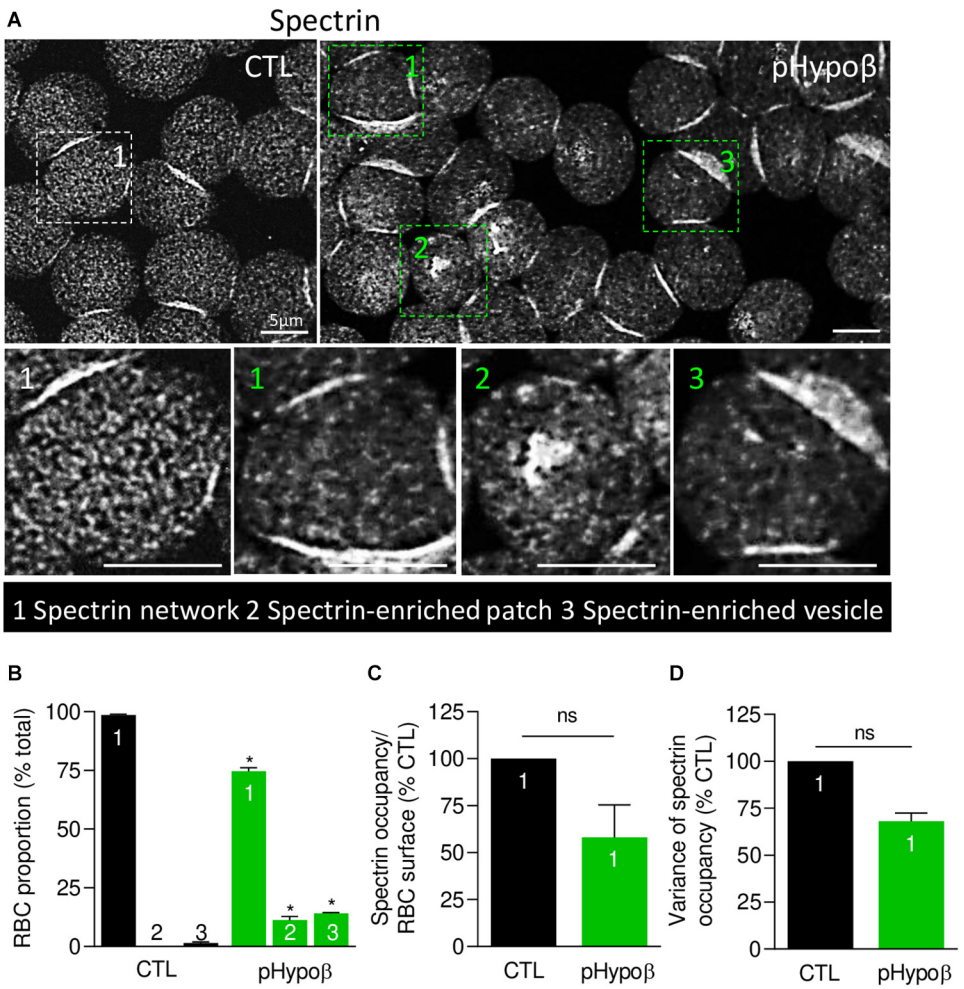

FIGURE 6 | The spectrin network is altered in pHypoβ RBCs, showing either a lower density or a patchy or vesiculated pattern. RBCs from healthy donors (CTL, black) or pHypoβ (green) were spread onto PLL-coated coverslips, fixed/permeabilized, immunolabelled for spectrin and visualized by confocal fluorescence microscopy using the same settings for sample illumination. **(A)** Representative general views and zooms of RBCs with homogenous spectrin network (1), spectrin-enriched patches (2) and spectrin-enriched vesicles (3). **(B)** Quantification of the relative proportion of RBCs with homogenous spectrin network (1), spectrin-enriched patches (2) or spectrin-enriched vesicles (3). Data are means ± SEM of 3–6 independent experiments. Mann–Whitney tests to compare each RBC population in healthy vs. pHypoβ RBCs. $^*p < 0.05$. **(C,D)** Quantification of spectrin occupancy normalized to the RBC surface **(C)** and variance of the spectrin labeling **(D)** in RBCs with homogenous spectrin network (population 1). Data are expressed as percentage of CTLs and are means ± SEM of 3 independent experiments. Mann–Whitney tests; ns, not significant.

note, no modification of membrane curvature was detected for RBCs from a healthy splenectomised donor (**Supplementary Figure 1D**). Altogether our data indicated that the cytoskeleton alteration in pHypoβ RBCs was accompanied by increased stiffness and curvature. To further analyze the potential alteration of the plasma membrane in the disease, we determined the membrane asymmetry both at the transversal and lateral levels.

The Proportion of RBCs Exhibiting Phosphatidylserine Surface Exposure Is Preserved in pHypoβ

RBC PS exposure, a measure of membrane transversal asymmetry integrity loss, was not increased in pHypoβ RBCs as compared to healthy RBCs. As internal control, we used blood stored for 2 weeks in K^+/EDTA tubes at 4°C, which we previously validated as a model of accelerated RBC aging *in vitro* based on morphological, biophysical and biochemical storage lesions, including PS surface exposure (Cloos et al., 2020). Thus, according to our previous work, a strong increase of PS surface exposure was observed in this condition (**Figure 7E**).

Sphingomyelin-Enriched Domains at the pHypoβ RBC Surface Increase in Abundance and Do Not Respond to Intracellular Calcium Depletion

We then took benefit from our expertise in submicrometric lipid domain organization at the RBC outer plasma membrane

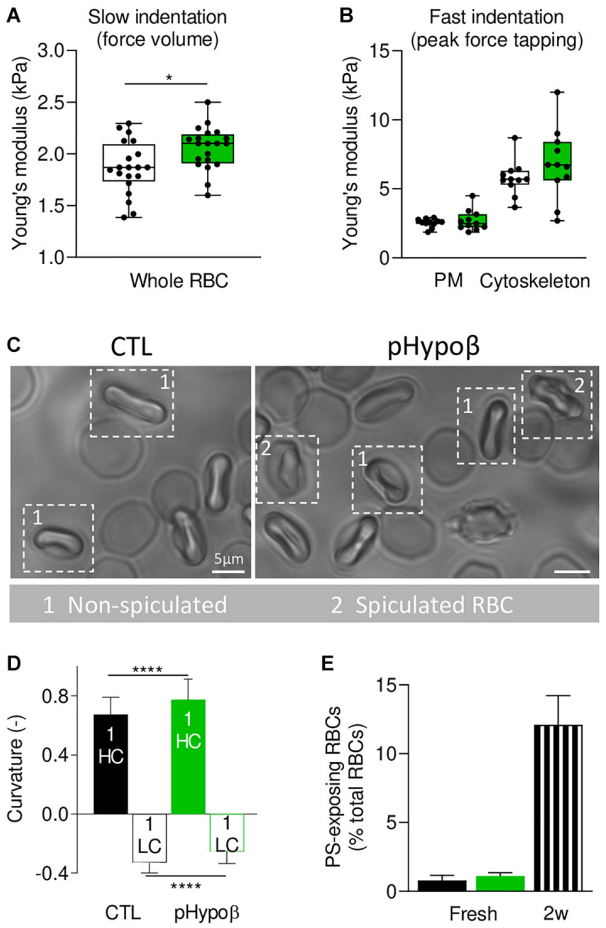

FIGURE 7 | Membrane stiffness and curvature are increased in pHypoβ RBCs whereas membrane transversal asymmetry is not modified. RBCs from healthy donors (CTL, black) or pHypoβ (green) were evaluated for membrane stiffness **(A,B)**, curvature **(C,D)** and transversal asymmetry **(E)**. **(A,B)** Membrane stiffness. **(A)** Young's modulus values extracted for CTL and pHypoβ RBCs in Slow indentation experiments, where the whole RBC mechanical behavior was analyzed. **(B)** Young's modulus of CTL and pHypoβ RBCs obtained in Fast indentation experiments, where the elastic contribution of the plasma membrane (PM) and cytoskeleton were evaluated separately. Each data point represents the mean Young's modulus value calculated for one RBC. Box plots depict 25th–75th percentiles, horizontal lines and cantered squares show mean values and error bars indicate SD. 20 RBCs were analyzed in **(A)** and 11 RBCs in **(B)**. Two-sample *t*-test. $*p < 0.05$. **(C,D)** Membrane curvature. RBCs were diluted, dropped off in IBIDI chambers and immediately observed by microscopy. Spiculated RBCs (indicated by 2) were distinguished from non-spiculated RBCs (indicated by 1) and the latter were then quantified for curvature in high curvature maxima (HC) and low curvature maxima (LC). 110 RBCs were analyzed for healthy donors and 50 RBCs for pHypoβ. Two-sample *t*-test. $****p < 0.0001$. **(E)** Membrane transversal asymmetry. RBCs were labeled with fluorescent Annexin-V and then analyzed with FlowJo to determine the proportion of phosphatidylserine (PS)-exposing cells by positioning the cursor at the edge of the healthy fresh RBC population. RBCs from blood stored for 2 weeks at 4°C (2w) were used as positive control. Data are means ± SD of triplicates from 1 experiment.

to evaluate the respective abundance of cholesterol-, GM1- and sphingomyelin-enriched domains, which contribute to the RBC deformation process (Leonard et al., 2017b; Conrard et al., 2018). Indeed, global quantitative analyses at the whole cell level may not reveal more localized alterations of acanthocyte membranes. Moreover, lipid domain abundance depends on membrane:cytoskeleton anchorage (Conrard et al., 2018). To visualize lipid domains, RBCs were labeled with a mCherry-toxin fragment specific to endogenous cholesterol or BODIPY fluorescent analogs of GM1 and sphingomyelin. Although the three types of lipid domains showed a tendency to increase in pHypoβ, only the abundance of sphingomyelin-enriched domains per hemi-RBC was significantly increased by 2.5-fold (**Figures 8A,B**). In contrast, no modifications of lipid domain abundance could be observed for RBCs from healthy splenectomised donors (**Supplementary Figure 1E**).

As GM1- and sphingomyelin-enriched domains were proposed to be implicated in calcium exchanges necessary for RBC deformation, we investigated their functionality in pHypoβ by stimulation of RBCs with Yoda1 and EGTA in a calcium-free medium to induce calcium entry and intracellular depletion, respectively. RBC incubation with Yoda1 led to an increased abundance of GM1-enriched domains in healthy RBCs, as previously shown (Conrard et al., 2018), and the same amplitude of response could be observed for pHypoβ RBCs (**Figure 8C**). In contrast, after intracellular calcium depletion, a heightened abundance of sphingomyelin-enriched domains was detected for healthy RBCs, as expected (Conrard et al., 2018), but not for pHypoβ RBCs (**Figure 8D**).

pHypoβ RBCs Show Low Curvature-Associated Ceramide-Enriched Patches and High Curvature-Associated Cholesterol-Enriched Spicules

Besides well-defined submicrometric lipid domains, larger lipid-enriched patches (arrowheads at **Figure 8A**) and peripheral spicules (open arrows at **Figure 8A**) were seen in pHypoβ RBCs. We quantified the proportion of those lipid-enriched patches and spicules and their potential relationship with the patches and vesicles observed by contrast phase microscopy (see **Figure 1D**). Although none of the patches were enriched in cholesterol or GM1 ganglioside (white arrowheads at **Figure 9A**), some sphingomyelin-enriched patches were observed (red arrowheads at **Figure 9A**). However, their abundance was non-significantly different from the one in healthy RBCs (**Figure 9B**) and represented a low proportion of the patches evidenced at **Figure 1D**.

Intrigued by the increased content of ceramide and dihydroceramide species in pHypoβ (**Figure 4B**), we wondered if the patches could be enriched in ceramide. A ∼30-fold increase of the number of RBCs presenting ceramide-enriched patches was observed (red arrowheads at **Figure 9A** and quantification at **Figure 9C**). A heightened proportion of RBCs with ceramide-enriched patches was

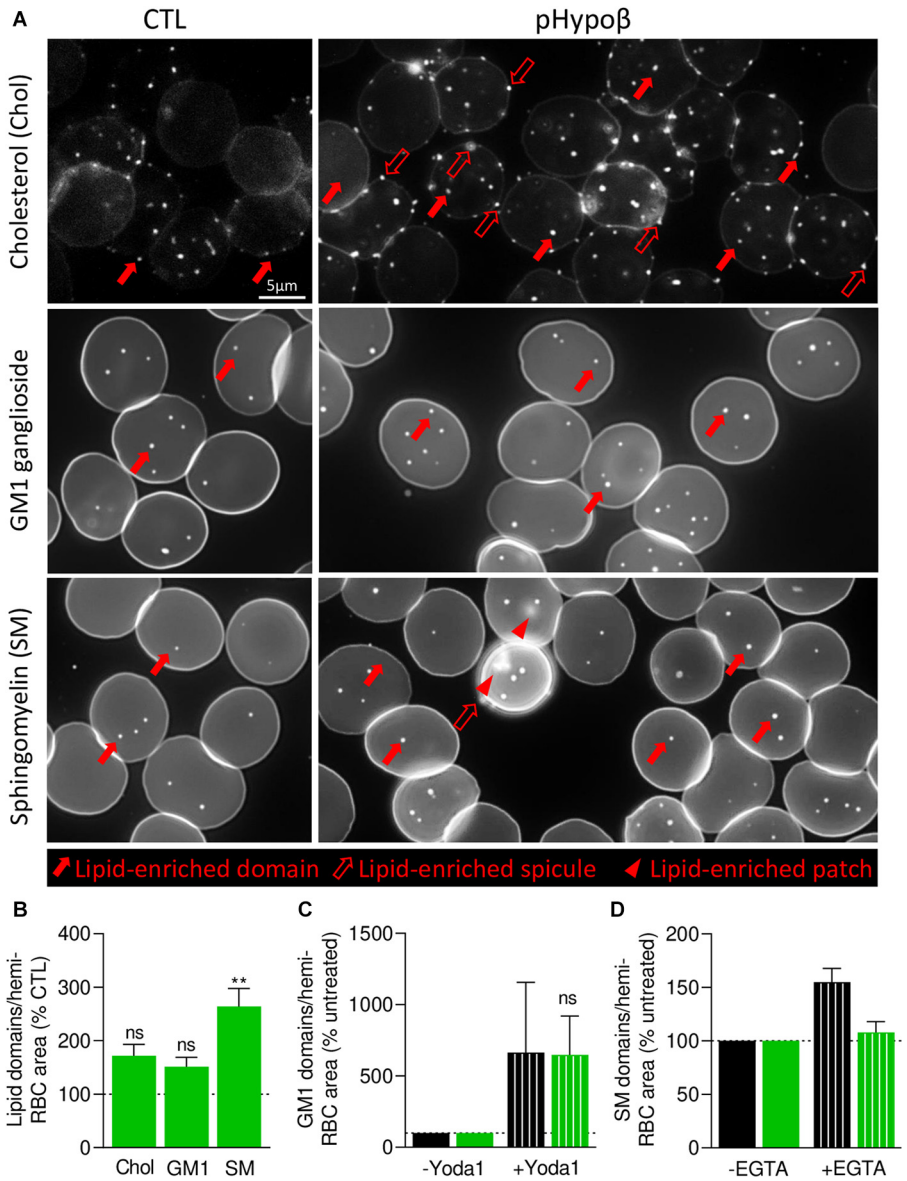

FIGURE 8 | In contrast to cholesterol- and GM1-enriched domains, those enriched in sphingomyelin are modified in abundance and functionality at the pHypoβ RBC surface. RBCs from healthy donors (CTL, black columns) or pHypoβ (green columns) were either left untreated (not-hatched columns) or incubated with Yoda1 for 30 s (hatched columns in **C**) or EGTA for 10 min in a calcium-free medium (hatched columns in **D**). All RBCs were then either labeled with the fluorescent Theta toxin fragment specific to endogenous cholesterol and then immobilized on PLL-coated coverslips (Chol; **A,B**); or immobilized on PLL-coated coverslips and then labeled with fluorescent BODIPY analogs of GM1 ganglioside (GM1; **A–C**) or sphingomyelin (SM; **A,B,D**). All coverslips were then directly observed by vital fluorescence microscopy. **(A)** Representative images of Chol-, GM1-, and SM-enriched domains, spicules or patches in untreated RBCs. Large filled arrows, lipid-enriched domains; large open arrows, lipid-enriched spicules; arrowheads, lipid-enriched patches. **(B–D)** Quantification of lipid domain abundance in RBCs either untreated or treated with Yoda1 or EGTA to, respectively, activate PIEZO1 **(C)** or induce intracellular calcium depletion **(D)**. In **(D)** the calcium-free medium containing EGTA is maintained all along the experiment. Data are normalized to the hemi-RBC area and are means ± SEM of 4–5 independent experiments **(B)** or means ± SD/SEM of 2–3 independent experiments **(C,D)**. Kruskal–Wallis test followed by Dunn's comparison test **(B)** and Wilcoxon matched-pairs signed rank tests **(C)**. ns, not significant; $^{**}p < 0.01$.

also observed for a healthy splenectomised donor but those RBCs accounted only for ∼10% of all RBCs compared to ∼35% for pHypoβ (**Figure 9C** and **Supplementary Figure 1F**). This could suggest that those patches are normally eliminated by the spleen.

Besides patches, ceramide-enriched vesicles can also be found but they did not significantly increase in abundance as compared to healthy RBCs (**Figure 9C**). The same was true for sphingomyelin-enriched vesicles (**Figure 9B**). In contrast, cholesterol-enriched spicules were observed at the edges of

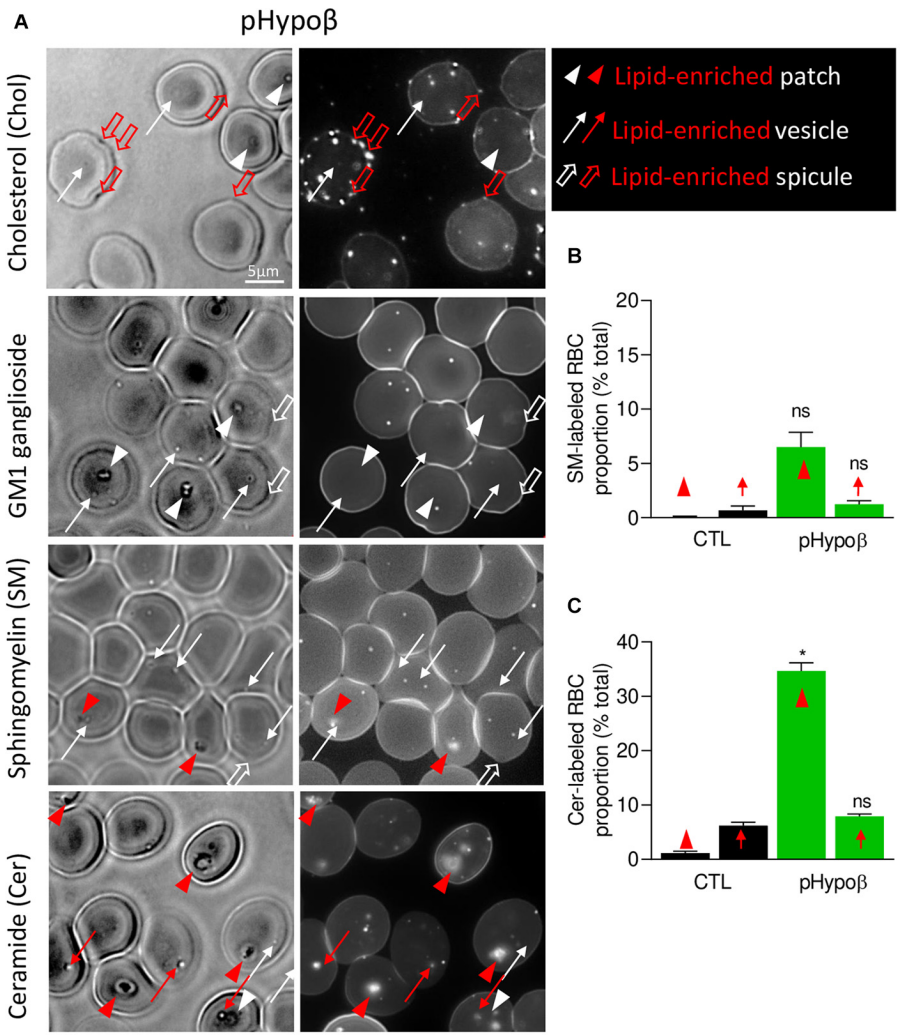

FIGURE 9 | The spicules at the pHypoβ surface are mainly enriched in cholesterol whereas the patches and vesicles are mainly enriched in ceramide. RBCs from healthy donors (black columns) or pHypoβ (green columns) were either labeled with the fluorescent Theta toxin fragment specific to endogenous cholesterol and then immobilized on PLL-coated coverslips (Chol; **A**) or immobilized on PLL-coated coverslips and then labeled with fluorescent BODIPY analogs of GM1 ganglioside (GM1; **A**), sphingomyelin (SM; **A,B**); or ceramide (Cer; **A,C**). All coverslips were then directly observed by vital fluorescence microscopy. **(A)** Representative images of pHypoβ RBCs. Left, transmission microscopy image; right, fluorescence microscopy image. Lipid-enriched (red) or non-enriched (white) patches (arrowheads), vesicles (arrows), spicules (large open arrows) detected on the RBC surface on transmission images. **(B,C)** Quantification of the proportion of RBCs presenting SM- **(B)** or cer- **(C)** enriched patches or vesicles. Data are expressed as means ± SEM of 3–6 independent experiments. Mann–Whitney tests to compare enriched structures at the surface of healthy vs. pHypoβ RBCs; ns, not significant; $^*p < 0.05$.

pHypoβ RBCs. As for patches, GM1 was enriched neither in vesicles nor in spicules (**Figure 9A**, white thin and thick arrows).

pHypoβ RBCs Do Not Represent an Accelerated Model of RBC Aging

Altogether, our data indicated that pHypoβ RBCs were spiculated and showed enhanced ROS content, altered spectrin cytoskeleton integrity as well as increased membrane stiffness and curvature and abundance of sphingomyelin-enriched domains. These elements are consistent with the RBC morphological and biochemical storage lesions we previously revealed upon blood storage in K^+/EDTA tubes for up to 4 weeks at 4°C as a model of accelerated RBC aging *in vitro* (Cloos et al., 2020). On the other hand, pHypoβ had increased membrane surface area and proportion of ceramide-enriched patches, rather consistent with reticulocyte properties (Ney, 2011). To therefore evaluate whether morphological, biochemical and biophysical alterations of pHypoβ RBCs could result from acceleration of RBC aging, RBCs from pHypoβ and healthy donors were stored for up to 3 weeks at 4°C and compared for morphology, fragility, functionality and biophysical properties. After 1 week of storage, the proportion of pHypoβ RBCs with patches did not increase any more (**Figure 10A**) and the differences in RBC membrane area and Hb release between pHypoβ and healthy donors seen in fresh RBCs were both abrogated (**Figures 10B,C**). The increase of

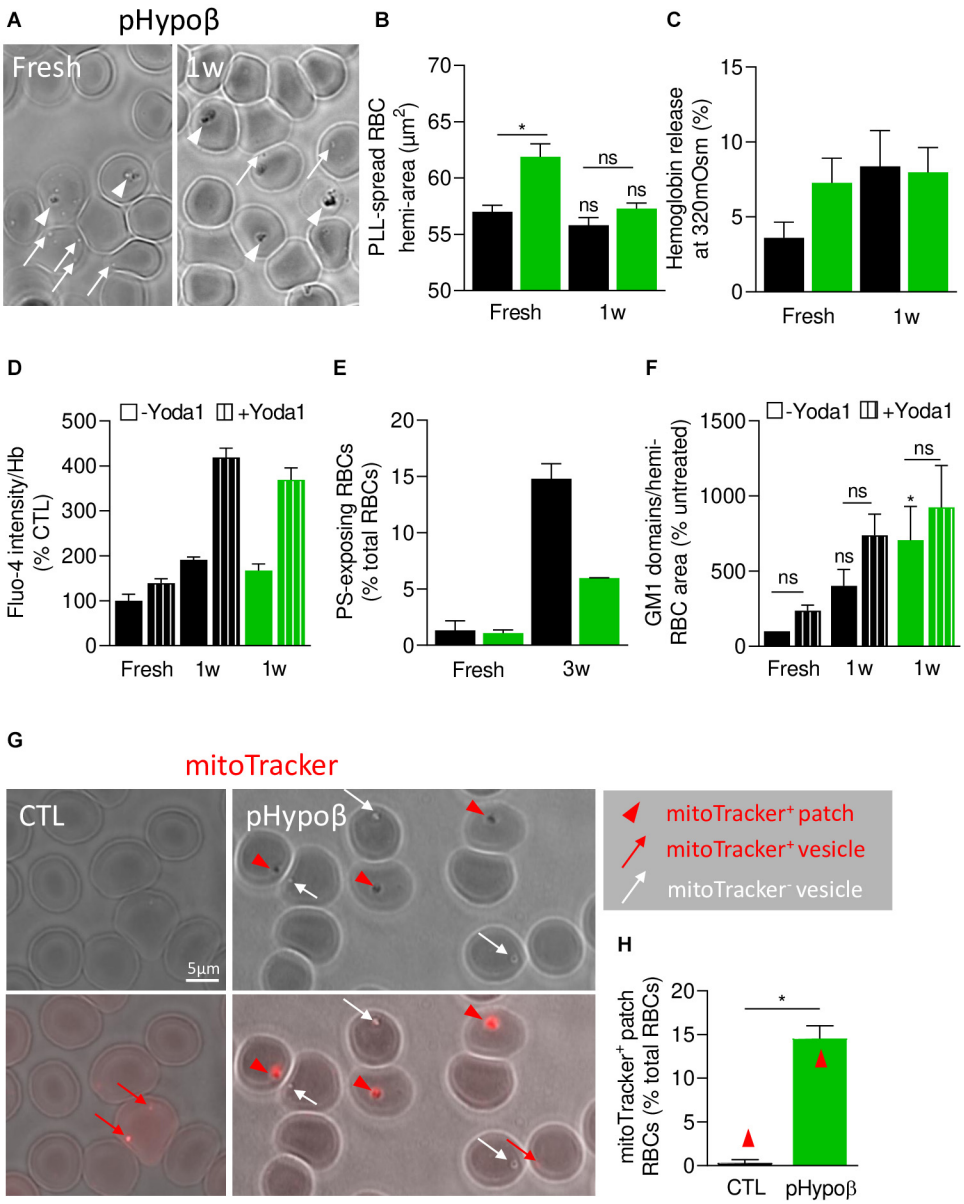

FIGURE 10 | pHypoβ RBCs partly resist to RBC aging upon blood storage in K^+/EDTA tubes at 4°C but exhibit a high abundance of residual mitochondrial fragments. RBCs from healthy donors (black columns) or pHypoβ (green columns) were either stored for 1–3 weeks at 4°C (1-3w) and assessed for RBC morphology and surface area **(A,B)**, osmotic fragility **(C)**, calcium content **(D)**, PS surface exposure **(E)** and GM1-enriched domain abundance **(F)**; or freshly analyzed for the presence of mitochondria remnants **(G,H)**. **(A–F)** RBC morphology and functionality upon storage at 4°C. **(A)** Morphology of fresh and 1 week-stored pHypoβ RBCs immobilized on PLL-coated coverslips as in **Figure 1D**. Images are representative of 3 experiments. **(B)** RBC surface determined as in **Figure 1I**. Data are means ± SEM of 3–7 independent experiments. Wilcoxon matched-pairs signed rank tests and Mann–Whitney test; ns, not significant; *$p < 0.05$. **(C)** RBC fragility determined as in **Figure 2A**. Data are means ± SD of triplicates from 1 experiment. **(D)** RBC calcium content. RBCs were labeled with Fluo4-AM as in **Figure 2F**, incubated with Yoda1 (hatched columns) and analyzed by fluorimetry. Data are normalized to Hb content and are means ± SD of triplicates from 1 experiment. **(E)** RBC PS exposure assessed as in **Figure 7E**. Data are means ± SD of triplicates from 1 experiment. **(F)** GM1-enriched domain abundance on RBCs at resting state and upon stimulation with Yoda1 (hatched columns), determined as in **Figure 8C**. Data are means ± SEM of 3 independent experiments. Kruskal–Wallis test followed by Dunn's comparison test and Wilcoxon matched-pairs signed rank tests for the effect of Yoda1. ns, not significant; *$p < 0.05$. **(G,H)** RBC evaluation for the presence of mitochondrial remnants. RBCs were incubated for 30 min with a fluorescent mitoTracker, washed, dropped on PLL-coated coverslips and immediately observed by fluorescence microscopy. **(G)** Representative images. Upper panels, transmission; lower panels, transmission with fluorescence. Red arrowheads, mitoTracker-positive patches; red arrows, mitoTracker-positive vesicles; white arrows, mitotracker-negative vesicles. **(H)** Relative proportion of RBCs presenting mitoTracker-labeled patches as percentage of total RBCs. Data are means ± SEM of 3–6 independent experiments. Mann–Whitney test. *$p < 0.05$.

intracellular calcium content measured after 1 week of storage in untreated and Yoda1-treated conditions were similar in pHypoβ and healthy donors (**Figure 10D**). Quite surprisingly, the extent of PS surface exposure measured after 3 weeks of storage increased three times less in pHypoβ than in healthy donors (**Figure 10E**). Regarding GM1-enriched domains, they increased in healthy RBCs after 1 week as expected from our previous data (Cloos et al., 2020), but this increase was even more pronounced and significant in pHypoβ RBCs. However, the increase of GM1-enriched domain abundance resulting from Yoda1 stimulation was lower in pHypoβ than healthy RBCs which might be due to the fact that GM1-enriched domain abundance was already higher at the surface of 1 week-stored pHypoβ RBCs than healthy RBCs stored for the same time (**Figure 10F**). We conclude that pHypoβ RBCs did not appear to represent an accelerated model of RBC aging.

pHypoβ Shows a Very High Proportion of RBCs With Mitochondrial Fragments

We therefore evaluated the alternative possibility of a maturation defect of pHypoβ RBCs by labeling with a fluorescent mitoTracker. The proportion of pHypoβ RBCs presenting mitoTracker-positive patches at their surface increased by ∼40-fold as compared to healthy RBCs (**Figures 10G,H**). Importantly, the presence of those patches cannot be explained by the absence of spleen (**Supplementary Figure 1G**).

DISCUSSION

We here describe a case of familial hypobetalipoproteinemia, resulting from a heterozygosity for the pathogenic Gln845Argfs*18 mutation in the *ApoB* gene. Similar to most patients with familial hypobetalipoproteinemia, pHypoβ presented reduced plasma cholesterol and ApoB levels, heightened plasmatic liver enzymes as well as a vitamin E level close to the lower reference limit (Clarke et al., 2006; Musialik et al., 2020). More surprisingly, a high proportion of acanthocytes was detected in this patient, most likely corresponding to the RBCs with surface patches and/or vesicles upon spreading on PLL-coated coverslips. Although those morphology changes were not accompanied by altered resistance to osmotic stress and cellular homeostasis, RBC deformability, oxidative stress, and membrane cytoskeletal and biophysical properties (curvature and stiffness) were impaired. Hence, a deeper imaging analysis revealed (i) heterogeneous spectrin cytoskeleton distribution in patches and vesicles; (ii) ceramide-enrichment and mitoTracker-partitioning in patches, suggesting the presence of mitochondria fragments resulting from RBC maturation defect; (iii) cholesterol-enrichment in spicules; and (iv) sphingomyelin-enriched domain increased abundance and decreased functionality.

Extent of Acanthocytosis in Heterozygous Hypobetalipoproteinemia

Acanthocytes provide a typical clinical feature of abetalipoproteinemia, representing 50–90% of total RBCs (Biemer, 1980). In contrast, the proportion of acanthocytes and their existence are more debated for homozygous and heterozygous familial hypobetalipoproteinemia. In homozygous familial hypobetalipoproteinemia, while it has been stated that acanthocytes are as numerous as in abetalipoproteinemia Biemer (1980) and Tamura et al. (1988) reported two patients suffering from this disease with acanthocytes representing only 10–15% of all RBCs. For the heterozygous form of the disease, their presence is less frequently detected but not excluded (Biemer, 1980; Hardie, 1989; Clarke et al., 2006). Actually, splenectomy could be partly responsible for the unusual high proportion of spiculated RBCs detected for pHypoβ as (i) in some cases, acanthocytes can be observed post-splenectomy (Shah and Hamad, 2020); and (ii) the absence of the spleen in this patient could prevent hemolysis of acanthocytes normally provoked through splenic sequestration. Even if the post-splenectomy hypothesis could be supported by Howell–Jolly bodies observed on pHypoβ blood smears, it seems more likely that reduced RBC elimination as consequence of the absence of a spleen contributes to the abundance of acanthocytes in pHypoβ as no spiculated RBCs could be detected for a heathy splenectomised donor and acanthocytosis is part of the usual clinical picture of lipoprotein disorders and vitamin E deficiencies (Wong, 2004).

Oxidative Stress, Cytoskeleton Defects and Membrane Stiffness Contribute to the RBC Phenotype in Heterozygous Hypobetalipoproteinemia

Vitamins E and A are important antioxidants and their supplementation is part of therapy for patients with homozygous familial hypobetalipoproteinemia and abetalipoproteinemia in order to prevent neurological and ophthalmological disorders (Granot and Kohen, 2004). This is not the case for heterozygous familial hypobetalipoproteinemia even if vitamin E levels below the normal range were detected (Burnett and Hooper, 2015). Regarding pHypoβ, although vitamin A was within the normal range, vitamin E was at the lower level. Clarke et al. actually detected reduced plasma vitamin E levels combined with reduced alpha-tocopherol content in RBCs of 9 patients suffering from heterozygous hypobetalipoproteinemia (Clarke et al., 2006). For patients suffering from abetalipoproteinemia and supplemented with liposoluble vitamins, observations differ. According to Granot and Kohen (2004), no signs for oxidative stress can be detected in the plasma of those patients while Calzada et al. (2013) reported decreased alpha-tocopherol levels in both platelets and HDLs of these patients combined with increased lipid peroxidation, consistent with the fact that vitamin E is a potent inhibitor of lipid peroxidation (Burnett and Hooper, 2015).

A high amount of free ROS was measured in pHypoβ RBCs but was not accompanied by increase in lipid peroxidation and metHb. However, it remains unclear where these ROS are coming from. Actually, vitamin K is not the typical antioxidant but it has nevertheless been shown to prevent oxidative stress in neurons (Li et al., 2003). Plasma levels of the latter were very low in pHypoβ. Taken together with low vitamin E levels, oxidative balance could be disturbed in pHypoβ RBCs because of reduced

amount in circulating antioxidant vitamins eventually sufficient to avoid important lipid peroxidation but not to totally prevent RBC oxidative stress.

Besides membrane lipids and Hb, spectrin and several membrane:cytoskeleton anchorage proteins such as Band3 also represent targets of oxidative stress (Voskou et al., 2015). In pHypoß RBCs, we provided several lines of evidence supporting the role of the altered cytoskeleton in RBC morphology alteration. First, the abundance of RBCs with a homogenously dense spectrin network was decreased at the benefit of RBCs presenting spectrin-enriched patches and/or vesicles. Second, in the RBCs with an homogeneous spectrin network, the spectrin membrane occupancy was decreased, which could reflect a reduced membrane:cytoskeleton anchorage and lead to increased stiffness. Third, the latter increase in pHypoβ RBCs was confirmed by AFM.

The cytoskeleton alterations found in pHypoβ were in agreement with the literature. First, spectrin enrichment in the thorny projections of acanthocytes was already described by electron microscopy (Siegl et al., 2013). Second, spectrin modification through treatment with urea combined with lysophosphatidylcholine membrane insertion has been shown to induce the transformation of discocytes into acanthocytes (Khodadad et al., 1996). Third, cytoskeletal alterations and abnormalities of Band3 immunolabeling have been revealed in neuro-acanthocytosis (Wong, 2004; Adjobo-Hermans et al., 2015). Acanthocytes could be actually formed by alterations in Band3 conformation similar to echinocytes in which the ratio of outward and inward facing Band3 is responsible for the morphological alteration (Wong, 2004). Thus, spectrin but also Band3 could be the target of ROS in pHypoβ RBCs, leading to decreased membrane:cytoskeleton anchorage and to acanthocytes with spectrin-enriched projections. However, the role of Band3 in the disease remains to be explored.

Alteration of Membrane Lipid Lateral Distribution Represents a New Contributor to the Acanthocytosis Seen in Heterozygous Hypobetalipoproteinemia

Analysis of the whole pHypoβ RBC population revealed no modification in the total cholesterol content in agreement with findings from other groups obtained on RBCs from patients with heterozygous hypobetalipoproteinemia (Biemer, 1980; Gheeraert et al., 1988). In abetalipoproteinemia and homozygous hypobetalipoproteinemia, observations are less consistent. Some groups reported increased cholesterol-to-phospholipid ratios (McBride and Jacob, 1970; Biemer, 1980; Barenholz et al., 1981) while others detected increased total cholesterol content without any increase in the cholesterol-to-phospholipid ratio (Iida et al., 1984) and still others described no alterations at all of the total cholesterol amount (Simon and Ways, 1964). Fatty acid composition was also largely maintained in pHypoβ RBCs, except for the slight increase of the linoleic and arachidonic acids, which could be related to specific dietary intake (Takkunen et al., 2013; Ford et al., 2016). To the best of our knowledge, the fatty acid content has not been studied in heterozygous hypobetalipoproteinemia. Abetalipoproteinemia and homozygous hypobetalipoproteinemia are instead generally associated with decreased linoleic acid content together with lower membrane fluidity. Besides, an increased sphingomyelin/lecithin or sphingomyelin/phosphatidylcholine ratio is also seen in RBCs of those patients (Ways et al., 1963; Simon and Ways, 1964; Cooper et al., 1977; Biemer, 1980; Barenholz et al., 1981; Iida et al., 1984). An increased sphingomyelin/phosphatidylcholine ratio resulting from a reduced abundance of phosphatidylcholine species was also evidenced in pHypoß. A higher (dihydro)ceramide content was also seen in pHypoβ RBCs in agreement with the increased ceramide-enriched patches. More surprisingly, a specific increase of lysophosphatidylethanolamine species was revealed while lysophosphatidylcholine is generally described to be associated with RBC morphological transformation into acanthocytes or echinocytes (Fujii and Tamura, 1984; Khodadad et al., 1996).

Lipid distribution at the RBC surface was analyzed in parallel to evaluate whether local changes in lipid domains could be revealed. We showed three types of membrane lipid distribution alterations. First, the abundance of sphingomyelin-enriched domains increased by 2.5-fold at the surface of pHypoβ RBCs. As membrane sphingomyelin content was not altered, the decreased membrane to cytoskeletal anchorage in pHypoβ RBCs could be responsible for this increase. This hypothesis is based on the observation by Conrard et al. that impairment of the membrane:cytoskeleton anchorage by PKC activation leads to an increase of sphingomyelin-enriched domains (Conrard et al., 2018). Second, ∼35 and ∼7% of pHypoβ RBCs presented ceramide- and sphingomyelin-enriched patches, respectively. Third, a high number of RBCs presented cholesterol-enriched spicules. The evident changes in membrane lipid organization stressed the importance of combining quantitative lipidomic analyses with qualitative lipid imaging to better understand diseases characterized by a variable- not systematically inventoried- amount of acanthocytes.

RBC Functionality Is Poorly Affected in Heterozygous Hypobetalipoproteinemia

Quite surprisingly at first glance, only slight modifications of pHypoβ RBC functionality were observed. First, although no modification was seen in the poorly sensitive osmotic fragility test, osmotic gradient ektacytometry indicated a slight increase in surface area-to-volume ratio and therefore of osmotic fragility. Those observations were in accordance with the literature as for other models of acanthocytotic RBCs no modification in osmotic fragility is detected (Cooper, 1969; McBride and Jacob, 1970). Second, the intracellular calcium and ATP contents were normal. Third, the response of GM1-enriched domains to PIEZO1 activation through Yoda1 in fresh RBCs was similar in the patient and healthy donors.

Nevertheless, a deeper analysis indicated that the number of GM1-enriched domains was increased- although not significantly- in fresh RBCs and significantly in 1 week-old RBCs. Likewise, the abundance of sphingomyelin-enriched

domains was enhanced and their response to intracellular calcium depletion through EGTA was abrogated. Thus, a fine analysis of the RBC surface both upon resting state and upon stimulation of calcium exchanges revealed functionality impairments in pHypoβ. Those alterations were not accompanied by altered calcium content or large increases in fragility probably because those measurements were made on the whole RBC population without any distinction between acanthocytes and discocytes. Interestingly, Ohsaka et al. reported on a patient with acute myelodysplasia with myelofibrosis who presented acanthocytes a heightened calcium uptake in RBCs combined with normal calcium levels (Ohsaka et al., 1989). In agreement with slight but detectable functionality impairment in pHypoβ, a loss of deformability after prolonged exposure to high shear stress was observed. Since this loss could only be partly explained by splenectomy, this observation revealed a slight reduction of membrane health of pHypoβ RBCs. This conclusion was further supported by alterations of RBC membrane biophysical properties.

Defective RBC Maturation May Be a Novel Feature of Heterozygous Hypobetalipoproteinemia

In this study, we showed that the proportion of pHypoβ RBCs presenting mitoTracker-enriched patches, and thus mitochondrial fragments, increased by ∼40-fold as compared to healthy RBCs and represented ∼15% of total RBCs in pHypoβ. Moreover, ∼35% of pHypoβ RBCs presented ceramide-enriched patches. We propose that those ceramide-enriched patches corresponded to mitochondrial fragments, since (i) the increased abundance of those two types of patches in pHypoβ was similar; (ii) ceramides are known to be enriched in the outer mitochondrial membrane (Siskind, 2005); and (iii) mitoTracker and BODIPY-ceramide double-labeling in RBCs from patients with hereditary spherocytosis showed high colocalization (our unpublished data).

Besides the high number of mitochondria-positive RBCs, the RBC maturation defect in pHypoβ is further supported by (i) the increased membrane area measured after RBC spreading, normally reduced by vesiculation upon reticulocyte maturation (Trakarnsanga et al., 2017); (ii) the higher oxidative stress, as lipid peroxidation and activity of antioxidant enzymes are increased in reticulocytes as compared to mature RBCs (Sailaja et al., 2003); (iii) the increased abundance of GM1-enriched domains, as those domains are related to calcium influx in RBCs and calcium uptake is heightened in reticulocytosis (Ohsaka et al., 1989); and (iv) the threefold reduction in stored RBCs of surface exposure of PS, a lipid normally found in autophagic vesicles upon reticulocyte maturation (Trakarnsanga et al., 2017). Actually, the resistance to PS surface exposure has also been reported by Siegl et al. (2013) in chorea-acanthocytosis after RBC stimulation with lysophosphatidic acid. Thus, pHypoβ has a high proportion of acanthocytes which could result from a maturation defect during the R1 reticulocyte stage known to undergo significant rearrangements in reticulocyte membrane and intracellular components via several mechanisms including exosome release and mitophagy (Minetti et al., 2018, 2020).

Experimental Strategy Strengths and Weaknesses

In this study, a wide range of research methods was used to evaluate morphological, biochemical and biophysical changes and their potential consequences for RBC functionality in hypobetalipoproteinemia. Moreover, thanks to a deep imaging analysis, we were able to reveal local changes in lipid composition and cytoskeleton distribution in acanthocytes. Nevertheless, our experimental strategy also presents some drawbacks that are inherent to the low prevalence of heterozygous hypobetalipoproteinemia with a high proportion of acanthocytes on one hand and to the study of membrane lipid lateral organization on the other hand. However, those limitations were minimized, based on the following evidences. First, although generalization of observations based on only one patient is difficult, our findings are in agreement with literature data on diseases associated with acanthocytosis. In fact, altered membrane composition and biophysical properties have also been demonstrated in a patient suffering from hereditary elliptocytosis and a series of patients suffering from hereditary spherocytosis, two diseases associated with increased membrane fragility due to cytoskeleton defects (Pollet et al., 2020; unpublished data), thereby supporting the importance of membrane:cytoskeleton interplay in RBC morphology and functionality. Second, although fluorescent lipid analogs were extensively used and validated in previous researches, their validity as *bona fide* surrogates of endogenous lipid counterparts is debated in view of the bulk fluorophore which can deeply modify biophysical properties. To minimize difficulties, we extensively validated all the lipid probes we used. For information regarding BODIPY-sphingomyelin and -GM1, we refer the reader to our previous papers (Tyteca et al., 2010; D'Auria et al., 2011, 2013; Carquin et al., 2016; Leonard et al., 2017b). For BODIPY-ceramide, the following lines of evidences supported a distribution as endogenous ceramides: (i) the fluorescent BODIPY-ceramide labeling correlated with the endogenous ceramide content measured by lipidomics both in pHypoβ and in RBCs upon blood storage at 4°C (Cloos et al., 2020); (ii) BODIPY-ceramide accumulates in the Golgi complex in nucleated cells (Tyteca et al., 2010) and in mitochondria remnants in RBCs from patients suffering from familial hypobetalipoproteinemia and from hereditary spherocytosis (data not shown), indicating that the lipid probe is able to join the intracellular compartments enriched in endogenous ceramide (Pagano et al., 1991); (iii) in the Golgi complex, BODIPY-ceramide can be efficiently converted into BODIPY-sphingomyelin, demonstrating the "one molecule at a time" conversion by the selectivity of the catalytic site of sphingomyelin synthase (Tyteca et al., 2010); (iv) BODIPY-ceramide accumulates in the inner plasma membrane leaflet, as revealed by resistance to back-exchange by BSA (Pollet et al., 2020) and demonstrating ability of the probe incorporated into the outer leaflet to flip to the inner one, as natural ceramide

(Contreras et al., 2010); (v) BODIPY-ceramide-enriched domain abundance correlates with the ceramide content, as revealed by the decrease of ceramide-enriched domain abundance at the RBC membrane and the concomitant enrichment of ceramide species in RBC-derived extracellular vesicles at the end of the blood storage period in K^+/EDTA tubes at 4°C (Cloos et al., 2020). Besides extensive validation of fluorescent lipid analogs, we developed the use of fluorescent Lysenin and Theta toxin fragments specific to endogenous sphingomyelin and cholesterol. However, it should be noted that, as fluorescent lipid analogs, toxin fragments also present drawbacks (Carquin et al., 2014, 2015, 2016) and it is therefore crucial to use complementary unrelated lipid probes to target one lipid, once possible. Third, regarding the imaging method used, although confocal microscopy offers several advantages such as vital imaging, multiple labeling and 3D-reconstruction, the size of observed lipid domains could have been overestimated.

Conclusion and Overall Significance

In a case of familial hypobetalipoproteinemia, resulting from heterozygosity for the pathogenic Gln845Argfs*18 mutation in the *ApoB* gene, we showed that the resulting acanthocytes exhibited impaired cytoskeleton and membrane biophysical properties without significant loss of RBC functionality as assessed by functional tests applied on the total RBC population, without any distinction between acanthocytes and discocytes (e.g., osmotic fragility test, intracellular calcium measurement). In contrast, more sensitive tests (e.g., ektacytometry) and assays aimed at investigating specific RBC populations (e.g., lipid domains, membrane curvature) did demonstrate functional impairments in pHypoβ.

Although our findings were generated from only one patient, the observed cytoskeleton and membrane alterations were consistent with literature data on diseases associated with acanthocytosis. Indeed, cytoskeletal alterations and abnormalities of Band3 immunolabeling have been shown in neuro-acanthocytosis (Wong, 2004; Adjobo-Hermans et al., 2015). The resistance to PS surface exposure has also been reported in chorea-acanthocytosis after RBC stimulation with lysophosphatidic acid (Siegl et al., 2013). The modest alterations of pHypoβ RBC functionality agreed with the absence of modification in osmotic fragility in other models of acanthocytotic RBCs (Cooper, 1969; McBride and Jacob, 1970).

From a more global point-of-view, altered membrane composition and biophysical properties have also been demonstrated in two RBC disorders associated with altered cytoskeleton function and a large diversity of RBC morphological changes and deformability alterations (Pollet et al., 2020; unpublished data), indicating the close membrane:cytoskeleton interplay and its role in RBC morphology and functionality. More specifically, a parallelism could be established with the patients with hereditary spherocytosis exhibiting a high proportion of spiculated RBCs (our unpublished data).

Our study demonstrates that evaluation of membrane biophysical properties and membrane lipid distribution could be of benefit in the diagnosis and better understanding of RBC disorders.

DATA AVAILABILITY STATEMENT

The original contributions generated for this study are included in the article/**Supplementary Material**, further inquiries can be directed to the corresponding author.

AUTHOR CONTRIBUTIONS

A-SC and DT designed the experiments, analyzed and interpreted the data, and wrote the manuscript. LGMD and JW identified the patient and established the diagnosis. MM, AS, and JV collected, analyzed, and quantified lipid imaging data. PVDS did the electron microscopy experiments. MR and RW performed ektacytometry measurements. EM and YL were responsible for fatty acid analysis while RT and GM performed lipidomics. ACD and DA generated and analyzed AFM data. All authors reviewed the final version of the manuscript.

FUNDING

This work was supported by grants from UCLouvain (FSR and Actions de Recherches Concertées, ARC), the F.R.S-FNRS and the Salus Sanguinis Foundation. DT and DA are Research Associate of the F. R. S.-FNRS. ACD is postdoctoral fellow of the F. R. S.-FNRS.

ACKNOWLEDGMENTS

We thank Drs. A. Miyawaki, M. Abe, T. Kobayashi (Riken Brain Science Institute, Saitama, Japan & University of Strasbourg, France), and H. Mizuno (KU Leuven, Belgium) for the Dronpa-theta-D4 plasmid. The MASSMET platform (UCLouvain, Belgium) is acknowledged for the access to the LC-MS for lipid analysis.

SUPPLEMENTARY MATERIAL

The Supplementary Material for this article can be found online at: https://www.frontiersin.org/articles/10.3389/fphys.2021.638027/full#supplementary-material

Supplementary Figure 1 | Except for a slight increase in ceramide-enriched patches, RBCs from a healthy splenectomised donor exhibit similar morphology, biophysical properties, functionality and maturation than healthy non-splenectomised donors. RBCs from healthy non-splenectomised (+spleen; black columns) donors and a healthy splenectomised (−spleen; gray columns) donor were compared for RBC membrane area **(A)**, osmotic fragility **(B)**, ROS intracellular content **(C)**, curvature **(D)**, lipid domain abundance **(E)**, and proportion of RBCs with ceramide (cer)- or mitoTracker-enriched patches and vesicles **(F,G)**. **(A)** RBC membrane area assessed as in **Figure 1I**. Data are means ± SEM of 5 independent experiments. Mann–Whitney test. Ns, not significant. **(B)** RBC osmotic fragility determined as in **Figure 2B**. Data from 1 experiment. **(C)** ROS content evaluated as in **Figure 5A**. Data are means ± SD of triplicates from 1 experiment. **(D)** RBC curvature determined on RBCs in suspension as in **Figure 2B**. Representative images of 2 independent experiments.

(E) Lipid domain abundance determined as in **Figure 8B**. Data are means ± SEM of 4–5 independent experiments. Kruskal–Wallis test followed by Dunn's comparison test. Ns, not significant. **(F)** Proportion of RBCs with cer-enriched patches and vesicles determined as in **Figure 9C**. Upper panel, representative image of RBCs from the splenectomised donor; lower panel, quantification of cer-enriched patches (red arrowheads) and vesicles (red arrows) in RBCs from non-splenectomised (black columns) and splenectomised (gray columns) donors. Data are means ± SEM of 3–6 independent experiments. Mann–Whitney tests to compare non-splenectomised vs. splenectomised RBCs; ns, not significant; $*p < 0.05$. **(G)** MitoTracker labeling as in **Figure 10G**. Upper panels, transmission; lower panels, transmission combined with fluorescence. MitoTracker-positive vesicles are indicated with red arrows. Images are representative of 3 experiments.

Supplementary Figure 2 | Relation between RBC plasma membrane and cytoskeleton elastic modulus in the fast indentation experiments. RBCs from healthy donors or pHypoβ were evaluated for both plasma membrane and cytoskeleton Young's modulus. Each dot depicts one RBC measured for plasma membrane and cytoskeleton Young's modulus. Experimental data are from **Figure 7B**.

Supplementary Table 1 | pHypoβ clinical data. Clinical parameters were assessed for pHypoβ after blood collection. MCV, mean corpuscular volume; MCH, mean corpuscular hemoglobin; Gamma-GT, Gamma-glutamyltransferase; ASAT, aspartate transaminase; ALAT, alanine transaminase; LD, lactate dehydrogenase. Values upon or under the reference values are indicated in red or blue, respectively.

REFERENCES

Adjobo-Hermans, M. J., Cluitmans, J. C., and Bosman, G. J. (2015). Neuroacanthocytosis: Observations, Theories and Perspectives on the Origin and Significance of Acanthocytes. *Tremor. Other. Hyperkinet. Mov.* 5:328. doi: 10.5334/tohm.271

Baines, A. J. (2010). The spectrin-ankyrin-4.1-adducin membrane skeleton: adapting eukaryotic cells to the demands of animal life. *Protoplasma* 244, 99–131. doi: 10.1007/s00709-010-0181-1

Barenholz, Y., Yechiel, E., Cohen, R., and Deckelbaum, R. J. (1981). Importance of cholesterol-phospholipid interaction in determining dynamics of normal and abetalipoproteinemia red blood cell membrane. *Cell Biophys.* 3, 115–126. doi: 10.1007/bf02788128

Biemer, J. J. (1980). Acanthocytosis–biochemical and physiological considerations. *Ann. Clin. Lab. Sci.* 10, 238–249.

Bogdanova, A., Makhro, A., Wang, J., Lipp, P., and Kaestner, L. (2013). Calcium in red blood cells-a perilous balance. *Int. J. Mol. Sci.* 14, 9848–9872. doi: 10.3390/ijms14059848

Burnett, J. R., and Hooper, A. J. (2015). Vitamin E and oxidative stress in abetalipoproteinemia and familial hypobetalipoproteinemia. *Free Radic. Biol. Med.* 88, 59–62. doi: 10.1016/j.freeradbiomed.2015.05.044

Cahalan, S. M., Lukacs, V., Ranade, S. S., Chien, S., Bandell, M., and Patapoutian, A. (2015). Piezo1 links mechanical forces to red blood cell volume. Elife, e07370. doi: 10.7554/eLife.07370

Calzada, C., Vericel, E., Colas, R., Guillot, N., El Khoury, G., Drai, J., et al. (2013). Inhibitory effects of in vivo oxidized high-density lipoproteins on platelet aggregation: evidence from patients with abetalipoproteinemia. *FASEB J.* 27, 2855–2861. doi: 10.1096/fj.12-225169

Carquin, M., Conrard, L., Pollet, H., Van Der Smissen, P., Cominelli, A., Veiga-Da-Cunha, M., et al. (2015). Cholesterol segregates into submicrometric domains at the living erythrocyte membrane: evidence and regulation. *Cell. Mol. Life Sci.* 72, 4633–4651. doi: 10.1007/s00018-015-1951-x

Carquin, M., D'auria, L., Pollet, H., Bongarzone, E. R., and Tyteca, D. (2016). Recent progress on lipid lateral heterogeneity in plasma membranes: From rafts to submicrometric domains. *Prog. Lipid. Res.* 62, 1–24. doi: 10.1016/j.plipres.2015.12.004

Carquin, M., Pollet, H., Veiga-Da-Cunha, M., Cominelli, A., Van Der Smissen, P., N'kuli, F., et al. (2014). Endogenous sphingomyelin segregates into submicrometric domains in the living erythrocyte membrane. *J. Lipid Res.* 55, 1331–1342. doi: 10.1194/jlr.m048538

Clarke, M. W., Hooper, A. J., Headlam, H. A., Wu, J. H., Croft, K. D., and Burnett, J. R. (2006). Assessment of tocopherol metabolism and oxidative stress in familial hypobetalipoproteinemia. *Clin. Chem.* 52, 1339–1345. doi: 10.1373/clinchem.2006.068692

Cloos, A. S., Ghodsi, M., Stommen, A., Vanderroost, J., Dauguet, N., Pollet, H., et al. (2020). Interplay Between Plasma Membrane Lipid Alteration, Oxidative Stress and Calcium-Based Mechanism for Extracellular Vesicle Biogenesis From Erythrocytes During Blood Storage. *Front. Physiol.* 11:712. doi: 10.3389/fphys.2020.00712

Conrard, L., Stommen, A., Cloos, A. S., Steinkuhler, J., Dimova, R., Pollet, H., et al. (2018). Spatial Relationship and Functional Relevance of Three Lipid Domain Populations at the Erythrocyte Surface. *Cell Physiol. Biochem.* 51, 1544–1565. doi: 10.1159/000495645

Conrard, L., and Tyteca, D. (2019). Regulation of Membrane Calcium Transport Proteins by the Surrounding Lipid Environment. *Biomolecules* 9:513. doi: 10.3390/biom9100513

Contreras, F. X., Sanchez-Magraner, L., Alonso, A., and Goni, F. M. (2010). Transbilayer (flip-flop) lipid motion and lipid scrambling in membranes. *FEBS Lett.* 584, 1779–1786. doi: 10.1016/j.febslet.2009.12.049

Cooper, R. A. (1969). Anemia with spur cells: a red cell defect acquired in serum and modified in the circulation. *J. Clin. Invest.* 48, 1820–1831. doi: 10.1172/jci106148

Cooper, R. A., Durocher, J. R., and Leslie, M. H. (1977). Decreased fluidity of red cell membrane lipids in abetalipoproteinemia. *J. Clin. Invest.* 60, 115–121. doi: 10.1172/jci108747

Cuerq, C., Henin, E., Restier, L., Blond, E., Drai, J., Marcais, C., et al. (2018). Efficacy of two vitamin E formulations in patients with abetalipoproteinemia and chylomicron retention disease. *J. Lipid Res.* 59, 1640–1648. doi: 10.1194/jlr.m085043

Da Costa, L., Suner, L., Galimand, J., Bonnel, A., Pascreau, T., Couque, N., et al. (2016). Diagnostic tool for red blood cell membrane disorders: Assessment of a new generation ektacytometer. *Blood Cells Mol. Dis.* 56, 9–22. doi: 10.1016/j.bcmd.2015.09.001

D'Auria, L., Fenaux, M., Aleksandrowicz, P., Van Der Smissen, P., Chantrain, C., Vermylen, C., et al. (2013). Micrometric segregation of fluorescent membrane lipids: relevance for endogenous lipids and biogenesis in erythrocytes. *J. Lipid. Res.* 54, 1066–1076. doi: 10.1194/jlr.m034314

D'Auria, L., Van Der Smissen, P., Bruyneel, F., Courtoy, P. J., and Tyteca, D. (2011). Segregation of fluorescent membrane lipids into distinct micrometric domains: evidence for phase compartmentation of natural lipids? *PLoS One* 6:e17021. doi: 10.1371/journal.pone.0017021

Dumitru, A. C., Poncin, M. A., Conrard, L., Dufrêne, Y. F., Tyteca, D., and Alsteens, D. (2018). Nanoscale membrane architecture of healthy and pathological red blood cells. *Nanoscale Horiz.* 3, 293–304. doi: 10.1039/c7nh00187h

Ford, R., Faber, M., Kunneke, E., and Smuts, C. M. (2016). Dietary fat intake and red blood cell fatty acid composition of children and women from three different geographical areas in South Africa. *Prostagl. Leukot Essent Fatty Acids* 109, 13–21. doi: 10.1016/j.plefa.2016.04.003

Fouchier, S. W., Sankatsing, R. R., Peter, J., Castillo, S., Pocovi, M., Alonso, R., et al. (2005). High frequency of APOB gene mutations causing familial hypobetalipoproteinaemia in patients of Dutch and Spanish descent. *J. Med. Genet.* 42:e23. doi: 10.1136/jmg.2004.029454

Fujii, T., and Tamura, A. (1984). Shape change of human erythrocytes induced by phosphatidylcholine and lysophosphatidylcholine species with various acyl chain lengths. *Cell. Biochem. Funct.* 2, 171–176. doi: 10.1002/cbf.290020311

Gheeraert, P., De Buyzere, M., Delanghe, J., De Scheerder, I., Bury, J., and Rosseneu, M. (1988). Plasma and erythrocyte lipids in two families with heterozygous hypobetalipoproteinemia. *Clin. Biochem.* 21, 371–377. doi: 10.1016/s0009-9120(88)80020-1

Granot, E., and Kohen, R. (2004). Oxidative stress in abetalipoproteinemia patients receiving long-term vitamin E and vitamin A supplementation. *Am. J. Clin. Nutr.* 79, 226–230. doi: 10.1093/ajcn/79.2.226

Guillemot-Legris, O., Masquelier, J., Everard, A., Cani, P. D., Alhouayek, M., and Muccioli, G. G. (2016). High-fat diet feeding differentially affects the

development of inflammation in the central nervous system. *J. Neuroinfl.* 13:206.

Hardie, R. J. (1989). Acanthocytosis and neurological impairment–a review. *Q. J. Med.* 71, 291–306.

Hutter, J. L., and Bechhoefer, J. (1993). Calibration of atomic−force microscope tips. *Rev. Scient. Instrum.* 64, 1868–1873. doi: 10.1063/1.1143970

Iida, H., Takashima, Y., Maeda, S., Sekiya, T., Kawade, M., Kawamura, M., et al. (1984). Alterations in erythrocyte membrane lipids in abetalipoproteinemia: phospholipid and fatty acyl composition. *Biochem. Med.* 32, 79–87. doi: 10.1016/0006-2944(84)90010-3

Kaestner, L., Bogdanova, A., and Egee, S. (2020). Calcium Channels and Calcium-Regulated Channels in Human Red Blood Cells. *Adv. Exp. Med. Biol.* 1131, 625–648. doi: 10.1007/978-3-030-12457-1_25

Khodadad, J. K., Waugh, R. E., Podolski, J. L., Josephs, R., and Steck, T. L. (1996). Remodeling the shape of the skeleton in the intact red cell. *Biophys. J.* 70, 1036–1044. doi: 10.1016/s0006-3495(96)79649-2

Lazarova, E., Gulbis, B., Oirschot, B. V., and Van Wijk, R. (2017). Next-generation osmotic gradient ektacytometry for the diagnosis of hereditary spherocytosis: interlaboratory method validation and experience. *Clin. Chem. Lab. Med.* 55, 394–402.

Leonard, C., Alsteens, D., Dumitru, A., Mingeot-Leclercq, M., and Tyteca, D. (2017a). "Lipid domains and membrane (re)shaping : from biophysics to biology," in *The role of the physical properties of membranes in influencing biological phenomena*, eds J. Ruysschaert and R. Epand (Netherland: Springer), 121–175. doi: 10.1007/978-981-10-6244-5_5

Leonard, C., Conrard, L., Guthmann, M., Pollet, H., Carquin, M., Vermylen, C., et al. (2017b). Contribution of plasma membrane lipid domains to red blood cell (re)shaping. *Sci. Rep.* 7:4264.

Lew, V. L., and Tiffert, T. (2017). On the Mechanism of Human Red Blood Cell Longevity: Roles of Calcium, the Sodium Pump, PIEZO1, and Gardos Channels. *Front. Physiol.* 8:977. doi: 10.3389/fphys.2017.00977

Li, J., Lin, J. C., Wang, H., Peterson, J. W., Furie, B. C., Furie, B., et al. (2003). Novel role of vitamin k in preventing oxidative injury to developing oligodendrocytes and neurons. *J. Neurosci.* 23, 5816–5826. doi: 10.1523/jneurosci.23-13-05816.2003

McBride, J. A., and Jacob, H. S. (1970). Abnormal kinetics of red cell membrane cholesterol in acanthocytes: studies in genetic and experimental abetalipoproteinaemia and in spur cell anaemia. *Br. J. Haematol.* 18, 383–397. doi: 10.1111/j.1365-2141.1970.tb01452.x

Minetti, G., Achilli, C., Perotti, C., and Ciana, A. (2018). Continuous Change in Membrane and Membrane-Skeleton Organization During Development From Proerythroblast to Senescent Red Blood Cell. *Front. Physiol.* 9:286. doi: 10.3389/fphys.2018.00286

Minetti, G., Bernecker, C., Dorn, I., Achilli, C., Bernuzzi, S., Perotti, C., et al. (2020). Membrane Rearrangements in the Maturation of Circulating Human Reticulocytes. *Front. Physiol.* 11:215. doi: 10.3389/fphys.2020.00215

Mohanty, J. G., Nagababu, E., and Rifkind, J. M. (2014). Red blood cell oxidative stress impairs oxygen delivery and induces red blood cell aging. *Front. Physiol.* 5:84. doi: 10.3389/fphys.2014.00084

Musialik, J., Boguszewska-Chachulska, A., Pojda-Wilczek, D., Gorzkowska, A., Szymanczak, R., Kania, M., et al. (2020). A Rare Mutation in The APOB Gene Associated with Neurological Manifestations in Familial Hypobetalipoproteinemia. *Int. J. Mol. Sci.* 21:1439. doi: 10.3390/ijms21041439

Mutemberezi, V., Masquelier, J., Guillemot-Legris, O., and Muccioli, G. G. (2016). Development and validation of an HPLC-MS method for the simultaneous quantification of key oxysterols, endocannabinoids, and ceramides: variations in metabolic syndrome. *Anal. Bioanal. Chem.* 408, 733–745. doi: 10.1007/s00216-015-9150-z

Ney, P. A. (2011). Normal and disordered reticulocyte maturation. *Curr. Opin. Hematol.* 18, 152–157. doi: 10.1097/moh.0b013e328345213e

Ohsaka, A., Yawata, Y., Enomoto, Y., Takahashi, A., Sato, Y., Sakamoto, S., et al. (1989). Abnormal calcium transport of acanthocytes in acute myelodysplasia with myelofibrosis. *Br. J. Haematol.* 73, 568–570. doi: 10.1111/j.1365-2141.1989.tb00301.x

Pagano, R. E., Martin, O. C., Kang, H. C., and Haugland, R. P. (1991). A novel fluorescent ceramide analogue for studying membrane traffic in animal cells: accumulation at the Golgi apparatus results in altered spectral properties of the sphingolipid precursor. *J. Cell. Biol.* 113, 1267–1279. doi: 10.1083/jcb.113.6.1267

Pollet, H., Cloos, A. S., Stommen, A., Vanderroost, J., Conrard, L., and Paquot, A. (2020). Aberrant Membrane Composition and Biophysical Properties Impair Erythrocyte Morphology and Functionality in Elliptocytosis. *Biomolecules* 10:1120. doi: 10.3390/biom10081120

Pollet, H., Conrard, L., Cloos, A. S., and Tyteca, D. (2018). Plasma Membrane Lipid Domains as Platforms for Vesicle Biogenesis and Shedding? *Biomolecules* 8:94. doi: 10.3390/biom8030094

Sailaja, Y. R., Baskar, R., and Saralakumari, D. (2003). The antioxidant status during maturation of reticulocytes to erythrocytes in type 2 diabetics. *Free Radic. Biol. Med.* 35, 133–139. doi: 10.1016/s0891-5849(03)00071-6

Salomao, M., Zhang, X., Yang, Y., Lee, S., Hartwig, J. H., Chasis, J. A., et al. (2008). Protein 4.1R-dependent multiprotein complex: new insights into the structural organization of the red blood cell membrane. *Proc. Natl. Acad. Sci. U. S. A.* 105, 8026–8031. doi: 10.1073/pnas.0803225105

Schillers, H., Rianna, C., Schäpe, J., Luque, T., Doschke, H., Wälte, M., et al. (2017). Standardized Nanomechanical Atomic Force Microscopy Procedure (SNAP) for Measuring Soft and Biological Samples. *Sci. Rep.* 7:5117.

Shah, P. R., and Hamad, H. (2020). *Acanthocytosis," in StatPearls*. Treasure Island, FL: StatPearls.

Siegl, C., Hamminger, P., Jank, H., Ahting, U., Bader, B., Danek, A., et al. (2013). Alterations of red cell membrane properties in neuroacanthocytosis. *PLoS One* 8:e76715. doi: 10.1371/journal.pone.0076715

Simon, E. R., and Ways, P. (1964). Incubation Hemolysis and Red Cell Metabolism in Acanthocytosis. *J. Clin. Invest.* 43, 1311–1321. doi: 10.1172/jci105006

Siskind, L. J. (2005). Mitochondrial ceramide and the induction of apoptosis. *J. Bioenerg. Biomembr.* 37, 143–153. doi: 10.1007/s10863-005-6567-7

Takkunen, M., Agren, J., Kuusisto, J., Laakso, M., Uusitupa, M., and Schwab, U. (2013). Dietary fat in relation to erythrocyte fatty acid composition in men. *Lipids* 48, 1093–1102. doi: 10.1007/s11745-013-3832-0

Tamura, A., Keiji, K., Fiujii, T., Harano, Y., Harada, M., Nakano, T., Hidaka, H., et al. (1988). Abnormalities in the Membrane of Erythrocytes from Two Patients Homozygous for Familial Hypobetalipoproteinemia. *J. Clin. Biochem. Nutr.* 5, 103–108. doi: 10.3164/jcbn.5.103

Trakarnsanga, K., Griffiths, R. E., Wilson, M. C., Blair, A., Satchwell, T. J., Meinders, M., et al. (2017). An immortalized adult human erythroid line facilitates sustainable and scalable generation of functional red cells. *Nat. Commun.* 8:14750.

Tyteca, D., D'auria, L., Der Smissen, P. V., Medts, T., Carpentier, S., Monbaliu, J. C., et al. (2010). Three unrelated sphingomyelin analogs spontaneously cluster into plasma membrane micrometric domains. *Biochim. Biophys. Acta* 1798, 909–927. doi: 10.1016/j.bbamem.2010.01.021

Voskou, S., Aslan, M., Fanis, P., Phylactides, M., and Kleanthous, M. (2015). Oxidative stress in beta-thalassaemia and sickle cell disease. *Redox. Biol.* 6, 226–239. doi: 10.1016/j.redox.2015.07.018

Ways, P., Reed, C. F., and Hanahan, D. J. (1963). Red-Cell and Plasma Lipids in Acanthocytosis. *J. Clin. Invest.* 42, 1248–1260. doi: 10.1172/jci104810

Whitfield, A. J., Barrett, P. H., Van Bockxmeer, F. M., and Burnett, J. R. (2004). Lipid disorders and mutations in the APOB gene. *Clin. Chem.* 50, 1725–1732. doi: 10.1373/clinchem.2004.038026

Wong, P. (2004). A basis of the acanthocytosis in inherited and acquired disorders. *Med. Hypotheses* 62, 966–969. doi: 10.1016/j.mehy.2003.12.032

Conflict of Interest: The authors declare that the research was conducted in the absence of any commercial or financial relationships that could be construed as a potential conflict of interest.

frontiers in Physiology

METHODS
published: 25 March 2021
doi: 10.3389/fphys.2021.636609

Automated Oxygen Gradient Ektacytometry: A Novel Biomarker in Sickle Cell Anemia

*Alina Sadaf[1], Katie G. Seu[1,2], Elizabeth Thaman[1,2], Rose Fessler[1,2], Diamantis G. Konstantinidis[1,2], Holly A. Bonar[1,3], Jennifer Korpik[1,4], Russell E. Ware[1,2,5], Patrick T. McGann[1,2,5], Charles T. Quinn[1,2,4,5] and Theodosia A. Kalfa[1,2,4,5]**

[1]Cancer and Blood Diseases Institute, Cincinnati Children's Hospital Medical Center, Cincinnati, OH, United States, [2]Division of Hematology, Cincinnati Children's Hospital Medical Center, Cincinnati, OH, United States, [3]Immunopathology Laboratory, Cincinnati Children's Hospital Medical Center, Cincinnati, OH, United States, [4]Erythrocyte Diagnostic Laboratory, Cincinnati Children's Hospital Medical Center, Cincinnati, OH, United States, [5]Department of Pediatrics, College of Medicine, University of Cincinnati, Cincinnati, OH, United States

Sickle cell anemia (SCA) is a hereditary hemoglobinopathy with a variable phenotype. There is no single biomarker that adequately predicts disease severity and can be used to monitor treatment response in patients in clinical trials and clinical care. The use of clinical outcomes, such as vaso-occlusive crises (VOC), requires long and expensive studies, sometimes with inconclusive results. To address these limitations, there are several biomarkers under study to improve the ability to predict complications and assess treatment response in both clinical and research settings. Oxygen gradient ektacytometry, also called as oxygenscan, is an assay that measures the effects of deoxygenation and reoxygenation on red blood cell (RBC) deformability and is gaining popularity in SCA research, because it captures the dynamic sickling capacity of a patient's RBCs as they are subjected to an oxygen gradient under steady shear stress. We describe here the oxygenscan methodology and evaluate the correlation between oxygenscan parameters and more well-known biomarkers of SCA such as fetal hemoglobin (HbF), F-cells, and dense red blood cells (DRBCs). Our data indicate that the oxygenscan curve is affected by all these parameters and the result incorporates the effects of %HbF, %F-cells, RBC hydration, and RBC membrane deformability.

Keywords: sickle cell anemia, erythrocyte, oxygen gradient ektacytometry, oxygenscan, fetal hemoglobin, F-cell, dense red blood cells, red blood cell

OPEN ACCESS

Edited by:
Richard Van Wijk, Utrecht University, Netherlands

Reviewed by:
Wassim El Nemer, Institut National de la Santé et de la Recherche Médicale (INSERM), France
Ozlem Yalcin, Koç University, Turkey

****Correspondence:***
Theodosia A. Kalfa
theodosia.kalfa@cchmc.org

Specialty section:
This article was submitted to Red Blood Cell Physiology, a section of the journal Frontiers in Physiology

Received: *01 December 2020*
Accepted: *05 March 2021*
Published: *25 March 2021*

Citation:
Sadaf A, Seu KG, Thaman E, Fessler R, Konstantinidis DG, Bonar HA, Korpik J, Ware RE, McGann PT, Quinn CT and Kalfa TA (2021) Automated Oxygen Gradient Ektacytometry: A Novel Biomarker in Sickle Cell Anemia. Front. Physiol. 12:636609. doi: 10.3389/fphys.2021.636609

INTRODUCTION

Sickle cell disease (SCD) is an umbrella term for a group of inherited hemoglobinopathies. A single nucleotide mutation in the *HBB* gene, which encodes the β-globin chain of hemoglobin, results in the sickle hemoglobin allele β^S. Sickle cell anemia (SCA) is used to describe sickle cell disease caused by homozygosity for β^S (SS) or compound heterozygosity for β^S and a β^0-thalassemia mutation ($S\beta^0$). HbS polymerizes upon deoxygenation causing the red blood cell (RBC) to acquire a "sickle" shape (Steinberg and Rodgers, 2001). Sickle RBCs are markedly less deformable than normal RBCs (Clark et al., 1980), have an increased

transit time in the microcirculation of tissues (Vargas and Blackshear, 1982; Du et al., 2015), and demonstrate increased adherence to the vascular endothelium (Mohandas and Evans, 1984, 1985; Papageorgiou et al., 2018). These processes contribute to the major complications of SCD including vaso-occlusive crises (VOC) and chronic organ damage. However, there is wide phenotypic variability in SCD even between patients with the same genotype (Quinn, 2016); therefore, there is a need to develop biomarkers that can reliably identify the risk of complications and assess treatment response (Hoots and Shurin, 2012).

Ektacytometry is a technique for measuring RBC deformability that is used for the diagnosis of RBC cytoskeleton and hydration disorders such as hereditary spherocytosis and xerocytosis (Bessis et al., 1980; Da Costa et al., 2016; Risinger and Kalfa, 2020). In this technique, RBCs suspended in a liquid of known viscosity are subjected to increasing shear stress, or in the case of osmotic gradient ektacytometry (osmoscan), RBCs are suspended in a medium of varying osmolality and subjected to a steady shear stress. RBCs scatter light from a laser beam directed at the suspension, generating a diffraction pattern that can be analyzed to quantify RBC deformability. Under conditions of normal oxygen saturation (normoxia), RBC deformability in SCA is decreased due to the altered cytoskeleton mechanics of irreversibly sickled cells (ISCs), while the osmotic fragility is decreased due to increased surface-to-volume ratio of the dense or dehydrated cells (Clark et al., 1980). Because the percentage of ISCs and dense cells varies between steady state and during VOC, RBC osmoscan also varies in patients over time (Clark et al., 1983; Ballas et al., 1988; Lande et al., 1988; Ballas and Smith, 1992; Lemonne et al., 2013; Parrow et al., 2017). As sickling is caused by deoxygenation, the study of RBC deformability under varying oxygen saturation is promising to be of physiologic relevance. Oxygen gradient ektacytometry, referred to as the oxygenscan, is a next-generation functional assay that measures RBC deformability through an automated cycle of deoxygenation and reoxygenation, demonstrating characteristic features of sickle RBCs (Rab et al., 2019a). As use of the oxygenscan is increasing in sickle cell research, there is a need for standardization of methodology, clinical validation, and correlation with known SCA biomarkers such as fetal hemoglobin (HbF) and dense red blood cells (DRBCs; Rab et al., 2019b, 2020a).

One of the main drivers of polymerization is the intracellular HbS concentration in RBCs (Noguchi et al., 1983). Cellular dehydration mediated by cell membrane cation channels may increase HbS concentration (Brugnara, 2003). Other factors, such as membrane damage due to oxidation (Aslan et al., 2000) and phosphorylation changes (Noomuna et al., 2020), also affect deformability and accelerate RBC lysis. HbF is known to inhibit deoxygenation-induced HbS polymerization (Poillon et al., 1993) and improve RBC deformability likely by improving membrane mechanics and decreasing the number of ISCs (Parrow et al., 2017). However, because HbF is typically unevenly distributed across the population of sickle RBCs, HbF levels do not accurately capture phenotype variability. A fraction of the RBC population with HbF content of 20–25% can survive up to three times longer than RBCs that do not have HbF (Franco et al., 1998). Although low HbF levels have been correlated with increased mortality in SCA (Leikin et al., 1989), the wide variability of F-cells genetically and in response to HbF-inducing medications, may limit the ability of each one of these biomarkers to estimate severity of SCA (Steinberg, 2005; Steinberg et al., 2014; Quinn, 2016).

DRBCs, another biomarker in SCA, are defined as RBCs with density >1.11 g/ml (Fabry and Nagel, 1982) as measured by density-gradient fractionation methods, or percentage of RBCs with a measured mean corpuscular hemoglobin concentration (MCHC) >41 g/dl (Clark et al., 1980). In adults with SCA, %DRBCs have been associated with increased frequency of leg ulcers, priapism, and renal dysfunction, and their decline with hydroxyurea therapy was shown to be independent of the effect of hydroxyurea on HbF levels (Bartolucci et al., 2012).

The oxygenscan curve is a novel laboratory assay that directly measures the sickling propensity of an entire RBC population when challenged with deoxygenation and reoxygenation. Here, we describe its use as a reproducible functional biomarker, demonstrate and discuss the correlation of main oxygenscan parameters with %HbF levels, %F-cells, and %DRBCs, and illustrate results from patients with SCD (all with SS genotype except one).

MATERIALS AND METHODS

All procedures were approved by the Institutional Review Board (IRB) at the Cincinnati Children's Hospital Medical Center and were in accordance with the Declaration of Helsinki. IRB numbers of the studies that provided samples are 2018-0759 and 2018-5,182.

Oxygen Gradient Ektacytometry

General Principles

The Laser Optical Rotational Red Cell Analyzer (Lorrca®, RR Mechatronics, Zwaag, The Netherlands) oxygenscan measures RBC deformability in terms of the elongation index (EI), which is based on the height and width of an elliptical diffraction pattern (**Figures 1A**,**B**). A standardized number of RBCs is suspended in a liquid medium of known viscosity, as detailed below, and exposed to constant shear stress of 30 Pa. The RBC suspension is subjected to one cycle of deoxygenation (1,300 s) through the slow introduction of nitrogen gas followed by rapid reoxygenation (280 s) *via* passive diffusion of ambient air. EI is plotted on a curve against the partial pressure of oxygen (pO_2; **Figure 1C**). EI_{max} is the maximum EI measured at full oxygenation (pO_2 100–150 mmHg) and represents baseline RBC deformability in arterial circulation. EI_{min} is the minimum EI measured at the lowest oxygen saturation (pO_2 < 20 mmHg) and represents RBC deformability in post capillary venules. The Point of Sickling (PoS) is the pO_2 at which the EI_{max} decreases by 5% as deoxygenation proceeds. The PoS represents the

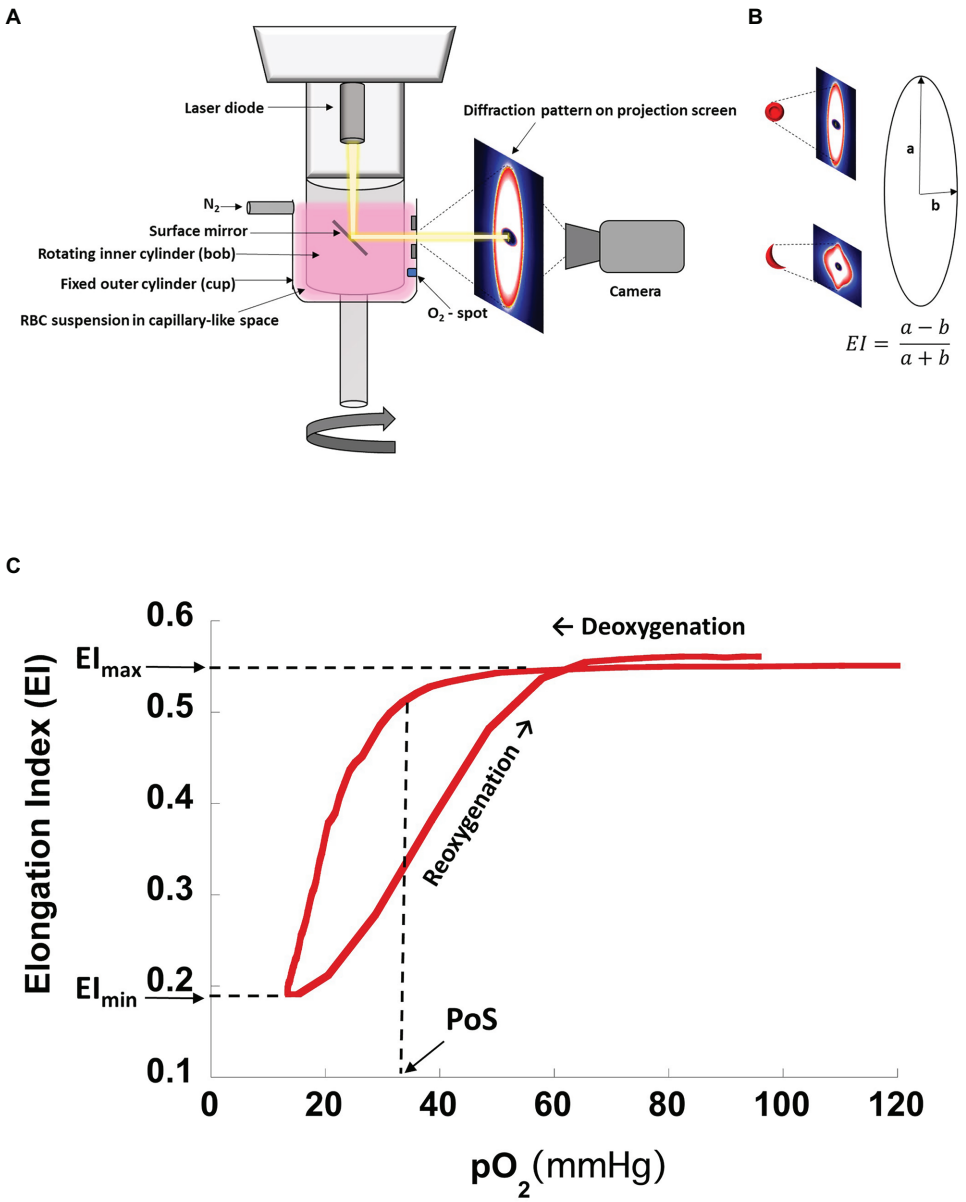

FIGURE 1 | Schematic drawing of oxygenscan setup with representative curve. **(A)** Schematic drawing of oxygenscan. **(B)** Representative diffraction pattern of RBCs in suspension. With deoxygenation and shear stress (30 Pa) in the capillary-like space between the cup and bob, RBCs containing HbS tend to deform to sickled shapes causing the diffraction pattern to change from an elliptical to a rhomboid pattern. Elongation index (EI) is calculated as a ratio of radii along the long and short axis of the diffraction pattern. **(C)** Representative oxygenscan curve of HbS RBCs. Maximum elongation index, EI_{max}, is the EI measured at full oxygenation (pO_2 100–150 mmHg) and represents baseline RBC deformability in arterial circulation. Minimum elongation index, EI_{min}, is the EI measured at the lowest oxygen saturation (pO_2 < 20 mmHg) and represents RBC deformability in post capillary venules. Point of sickling, PoS, is the pO_2 at which the EI decreases to 95% of EI_{max} during deoxygenation and represents a patient/disease-status-specific pO_2 at which HbS polymerization is accelerated and drives the sickling of RBCs that were deformable at normoxia. "Recovery," i.e., the percentage of EI_{max} reached after reoxygenation (Rab et al., 2019b), may be >100% for certain patients, reaching an EI_{max} value that is higher than the EI_{max} prior to deoxygenation. This is likely related to lysis of less deformable RBCs during the assay, which results in an overall increase in deformability of the RBC population.

patient-specific pO_2, where HbS polymerization is accelerated and drives the sickling of RBCs that are deformable at normoxia (Rab et al., 2019a). Recovery is calculated as the percentage of EI_{max} reached during reoxygenation and represents the capacity to reverse sickling with reoxygenation.

Sample Collection, Storage, and Processing

Peripheral blood samples (at least 1 ml) from patients with SCD were obtained by venipuncture and collected in EDTA tubes. Samples were stored at 4°C overnight, for at least 16 h and at most 32 h, prior to analysis. Twenty-six percent of the samples

were processed within 24 h of sample collection. Samples obtained at an outside institution were shipped overnight at 4°C. Care was taken to process samples immediately after removal from 4°C storage.

Prior to analysis, the EDTA tube was gently inverted to allow mixing of plasma with cellular components. RBC count of the sample was determined using the ADVIA® 2120i hematology analyzer (Siemens, Munich, Germany). Next, the volume of whole blood that would yield 200 × 10^6 RBCs per sample was determined using the following formula.

$$Volume\ of\ sample(\mu L) = 200 / \left(\frac{RBC\ count\ of\ sample}{\left(\mathrm{x}\,10^6\ cells / \mu L \right)} \right)$$

Sample volume was then added to 5 ml of polyvinylpyrrolidone (PVP) buffer, Iso Oxy (osmolarity 282–286 mOsm/kg, pH 7.35–7.45) with known viscosity of approximately 28 Pa·s. The RBC suspension was gently inverted to allow homogenization. Using a syringe, the sample was drawn up and air bubbles were removed before injection into the machine for analysis. Temperature of the bob (internal cylinder of the Lorrca® oxygenscan) was fixed at 37°C. Camera gain was adjusted to capture the entire diffraction pattern (**Figures 1A**,**B**).

Fetal Hemoglobin

HbF levels were quantified using capillary zone electrophoresis (Sebia Capillarys 2 Flex Piercing System®, Lisses, France). F-cell analysis was performed using an adaptation of a previously described method using multiparametric flow cytometry (Davis and Davis, 2004). Whole blood samples were fixed, permeabilized, and labeled with antibodies to HbF (Invitrogen, Waltham, MA, United States) and CD235a (Glycophorin A, BD Biosciences, San Jose, CA, United States). Flow cytometric analysis was performed using the BD FACSLyric Clinical System (BD Biosciences). Patient samples were accompanied by two separate control samples: a healthy adult and a manufactured high HbF control. F-cell population was quantified as percentage of the total RBCs.

Dense Red Blood Cells

%DRBCs were measured using an automated analyzer (ADVIA 2120i system), which quantifies %DRBCs by estimating the percentage of RBCs with a measured MCHC >41 g/dl.

Statistical Analysis

Data from the oxygenscan were exported into R (v i386 4.0.2) to generate curves and determine EI_{min}, EI_{max}, and PoS. Linear correlations between %HbF, %F-cells, and %DRBCs with oxygenscan parameters were also obtained in R. Oxygenscan profiles were created for individual SCD patients for illustrative results using KaleidaGraph® v 4.1 (Synergy Software).

RESULTS

Characteristics of the 38 patients with SCD whose samples were tested in this study are summarized in **Table 1**. All patients were transfusion free for at least 3 months prior to testing. The pediatric cohort of 27 patients, aged from 6 months to 16 years, were not on hydroxyurea. The 11 adult patients were on hydroxyurea therapy with variable compliance. Linear correlation graphs of %HbF, %F-cells, and %DRBCs with EI_{max}, EI_{min}, and PoS are shown in **Figure 2** and results are summarized in **Table 2**.

TABLE 1 | Characteristics of patients evaluated by oxygen-gradient ektacytometry.

	Mean ± SD (range)
Age range (years)	6 months to 48 years
HbSS, *n* (%)	37 (97%)
HbSβ⁺-Thalassemia, *n* (%)	1 (3%)
HbF (%)	23 ± 11.5 [5.6–50.6]
F-cells (%)	67.7 ± 23.1 [24–99.2]
Hb (g/dl)	9 ± 1.2 [6.9–11.4]
RBC (×10^6/μl)	3.2 ± 0.7 [1.7–4.5]
DRBCs (%)	1.2 ± 1.5 [0–4.8]

EI_{max} demonstrated a positive linear correlation with %HbF (r = 0.6675) and %F-cells (r = 0.6494), and a strong negative linear correlation with %DRBCs (r = −0.8152; **Figures 2A–C**). Of note, samples with no DRBC had an EI_{max} that approached 0.6, which is the maximum EI of normal RBCs. When %HbF was more than 20% and %F-cells were more than 70%, the EI_{max} approached the normal maximum value (approximately 0.6), while at lower percentage of F-cells and HbF, a variable decrease of EI_{max} was observed.

EI_{min} showed a positive linear correlation with increasing %HbF levels (r = 0.6310) and %F-cells (r = 0.5855) and a negative correlation with %DRBCs (r = −0.6988; **Figures 2D–F**). As expected, PoS had a negative correlation with %HbF (r = −0.5596), %F-cells (r = −0.5309), and a positive correlation with %DRBCs (r = 0.7029; **Figures 2G–I**). Absent DRBCs were not always good predictors for a consistently high EI_{min} or consistently low PoS. It appeared that very high values of %HbF (>30%) and %F-cells (>80%) were required for a reliable decline in the PoS to less than 25 mmHg.

Overall, the oxygenscan profile was influenced by the combination of these classically recognized biomarkers of SCA rather than having a strong association with a single biomarker. **Figure 3A** illustrates representative oxygen gradient ektacytometry curves from four patients with SCA with varying %HbF, %F-cells, and %DRBCs. A combined increase in %HbF and %F-cells and associated decrease of %DRBCs is necessary to cause an upward shift of the oxygenscan curve resulting in increased RBC deformability, and a lower PoS, indicating an increased capacity to tolerate deoxygenation before sickling is initiated. In contrast, low %HbF and low %F-cells with increased %DRBCs result in lower EI_{min} and EI_{max}, indicating a decrease in RBC deformability, as well as a higher PoS, signifying decreased ability to tolerate deoxygenation with sickling initiated at an oxygen pressure that can occur in arterioles in normal physiology.

To illustrate the effect of hydroxyurea on the oxygenscan profile, we identified two pairs of patients with similar fetal hemoglobin values with and without hydroxyurea treatment (**Figure 3B**). Hydroxyurea appeared to have beneficial effects

TABLE 2 | Correlations of oxygenscan parameters with fetal hemoglobin, F-cells, and dense red blood cells.

	EI_{min}	EI_{max}	PoS
HbF (%)	0.6310	0.6675	−0.5596
	2.17e-05	**4.70e-06**	**2.60e-04**
F-cells (%)	0.5855	0.6496	−0.5309
	1.13e-04	**1.03e-05**	**6.05e-04**
DRBC (%)	−0.6988	−0.8152	0.7029
	1.07e-06	**4.64e-10**	**8.67e-07**

The correlation coefficients (r) in black and the values of p in bold.

beyond HbF induction in the deformability parameters of EI_{min} and EI_{max} in both high (28%) and relatively low (13%) HbF values.

DISCUSSION

Patients with SCA display a wide variation in phenotype, which is inadequately captured by the currently available biomarkers (Quinn, 2016). HbF, one of the best-studied biomarkers in SCA, is used to predict the risk of disease complications and assess response to treatment with hydroxyurea, which is known to induce HbF production in sickle erythropoiesis. However, HbF distribution and induction is widely variable across individuals with SCA, and it is genetically and epigenetically determined (Steinberg et al., 2014). In young patients with SCA, there are distinct patterns of HbF expression and silencing in RBCs (Meier et al., 2011) that confounds the generalizability of HbF and F-cell analysis across age groups. In addition, there has been an increase in treatments that do not rely on HbF induction, such as the Hb-O_2 affinity modulator voxelotor (Vichinsky et al., 2019), the P-selectin blocker crizanlizumab (Ataga et al., 2017), the amino acid supplement L-glutamine (Anker et al., 2018), as well as cure-targeting strategies such as hematopoietic stem cell transplantation and non-gamma globin-focused gene therapy (Steinberg et al., 2019). The US Food and Drug Administration's (FDA) approvals for crizanlizumab and L-glutamine were based on a reduction in VOCs without the use of a functional (sickling) assay as an endpoint. Reliance on clinical endpoints such as pain, which are subjective, can lead to long and expensive clinical trials, sometimes with inconclusive results. The phase-3 clinical trial of voxelotor, for example, showed a modest increase in Hb concentration but no effect on the frequency of vaso-occlusive complications (Vichinsky et al., 2019). For these reasons, there has been a call for expanding research into SCD phenotyping and the development of laboratory biomarkers by the U.S. National Heart, Lung, and Blood Institute (Yawn et al., 2014).

Oxygen gradient ektacytometry is a laboratory assay designed to mimic *in vivo* RBC physiology in SCA, i.e., stimulation of HbS polymerization on deoxygenation that decreases RBC deformability, allowing for a direct assessment of sickling (Rab et al., 2019a). This is expected to give oxygenscan an advantage over single parameter assessments, such as HbF or DRBCs, as it integrates the composite effects of multiple physiologic changes in the RBCs, including intracellular HbS concentration, RBC hydration, membrane permeability, and mechanical deformability of the cytoskeleton.

The oxygenscan is a rapid, automated test that uses a small amount (<1 ml) of blood. However, there is a need for intra- and inter-laboratory standardization of the methodology as a number of variables may affect the results (Rab et al., 2020a). For example, 2,3-diphosphoglycerate (2,3-DPG) is known to reduce the percentage of oxyhemoglobin S at a given oxygen tension and depletion of 2,3-DPG may reduce sickling (Charache et al., 1970). The intracellular concentration of 2,3-DPG in RBCs is depleted with time (Chanutin and Curnish, 1967), so there is a need to standardize storage time of samples. Although cold storage is important to reduce RBC hemolysis, RBCs stored at 4°C have a minimally increased oxygen affinity after 2 days, which further increases with prolonged storage (Valtis and Kennedy, 1954). Recently, it has been shown that the storage of blood samples at 4°C for greater than 24 h may affect the EI_{max} and EI_{min} in oxygen gradient ektacytometry while the PoS remains fairly stable (Rab et al., 2019a; Boisson et al., 2020). As it was not feasible to process shipped and in-house samples within the same day, we recognize this as a limitation of the current work. To apply uniform conditions, we standardized the analysis time for all samples to 16–32 h from the time of collection (day after the blood draw). We recommend using the same post-collection time for analysis of paired samples when monitoring response to a therapeutic intervention.

During the analysis, the bob is maintained at a physiologic temperature of 37°C. This prevents changes in viscosity caused by variable temperature of the RBC suspension. Oxygen affinity of hemoglobin is also affected by pH with a decrease in oxygen affinity at lower physiologic pH values (Bohr effect; Jensen, 2004). To avoid changes in pH, a standardized PVP buffer, Iso Oxy, is used, which has a physiologic pH of 7.35–7.45. Another important consideration is to use a fixed number of RBCs using the equation described in the methods, because anemia will reduce the viscosity of the RBC suspension. We obtain the RBC count of the sample with an automated flow-cytometry-based hematology analyzer prior to performing the oxygenscan.

The diffraction pattern has an elliptical shape and adjustment of the camera gain is necessary to capture the entire image to determine EI. It should be noted that this approach assumes that as deformability decreases the RBC population acquires a more spherical shape. However, for a population of sickle RBCs, the diffraction pattern on deoxygenation may be rhomboid rather than spherical, so the EI formula may not accurately capture the change in deformability. Further research is needed to better capture the three-dimensional change in diffraction to estimate changes in deformability with greater accuracy.

Rab et al. (2019b) have previously reported on the effects of hydroxyurea treatment and transfusion therapy on oxygenscan parameters. In a mixed cohort of SCD patients with and without hydroxyurea treatment, they demonstrated a significant correlation of oxygenscan parameters with %HbF (EI_{max} $r = 0.650$, $p = 0.009$;

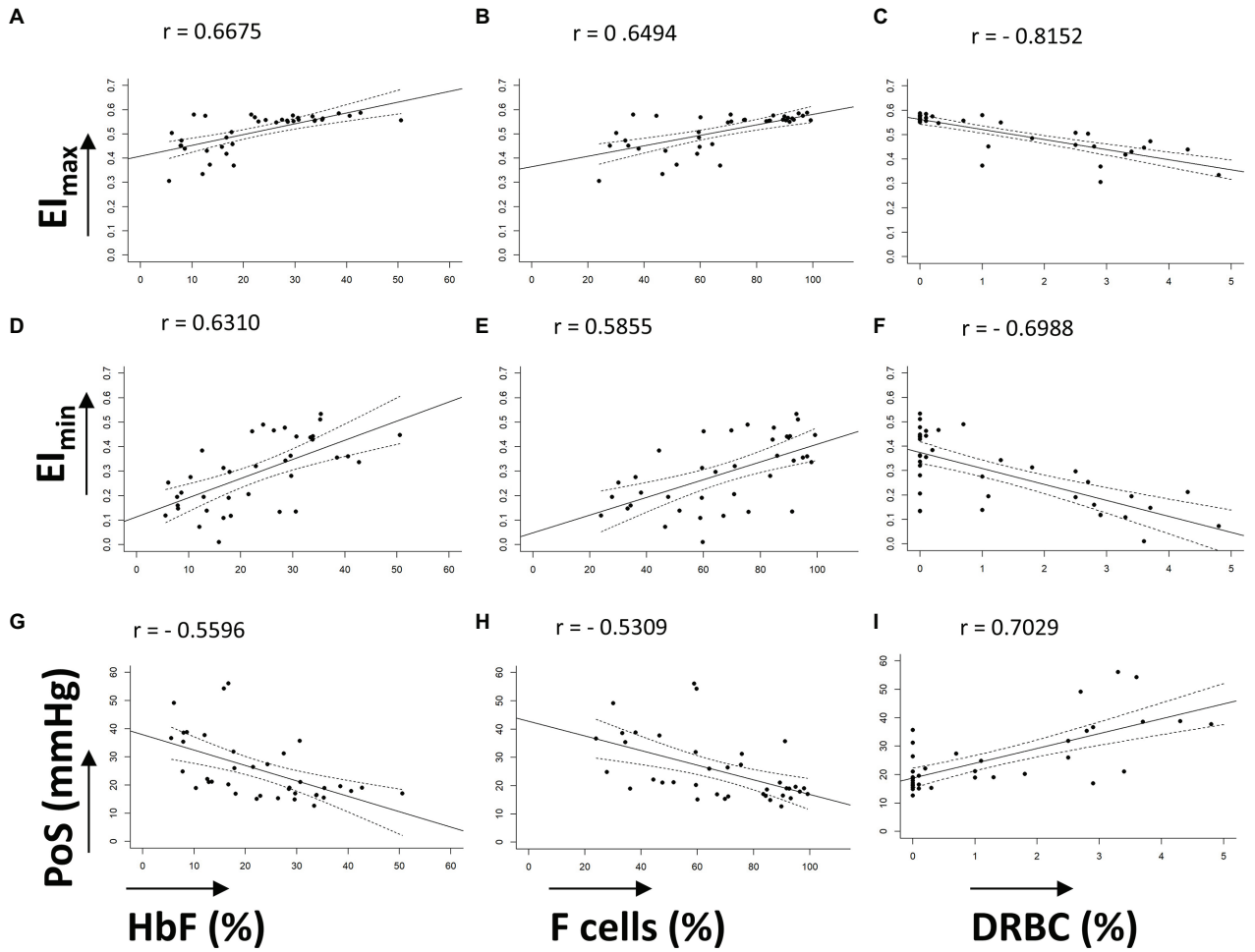

FIGURE 2 | Linear correlations of oxygenscan parameters with known biomarkers. **(A–C)** Linear correlations of EI_{max} with %HbF, %F-cells, and %DRBCs, respectively. **(D–F)** Linear correlations of EI_{min} with %HbF, %F-cells, and %DRBCs, respectively. **(G–I)** Linear correlations of PoS with %HbF, %F-cells, and %DRBCs, respectively. Dashed lines represent 95% CI. All correlations have $p < 0.001$.

EI_{min} $r = 0.833$, $p < 0.001$, PoS $r = 0.574$, $p = 0.025$). Our results on correlation with %HbF are in agreement: EI_{max} $r = 0.6675$, $p < 0.001$; EI_{min} $r = 0.6310$, $p < 0.001$, PoS $r = 0.5596$, $p < 0.001$. The congruence especially for EI_{max} and PoS are striking.

We analyzed data from SCD patients across a wide age range, 6 months to 48 years, and demonstrated correlations of oxygenscan parameters with fetal hemoglobin including %HbF and %F-cells. While %DRBCs have been shown to change independently of HbF in response to hydroxyurea (Bartolucci et al., 2012), we demonstrated a correlation of oxygenscan parameters with both %DRBCs and %HbF. However, although each of the oxygenscan parameters have a linear correlation with each of the known SCD biomarkers examined, the oxygenscan profile is affected by all of them and likely additional ones in a more complex way. For example, patients with similar %HbF with or without hydroxyurea treatment, may have different oxygenscan profiles likely due to changes in RBC hydration caused by hydroxyurea (**Figure 3**).

We noted that very high values of %HbF (>30%) and %F-cells (>80%) were consistently associated with a lower PoS (<25 mmHg). A highly significant correlation between the %F-cells and the log (%HbF) has been shown before (Marcus et al., 1997). This, in combination with our findings, indicates that a goal of 30%HbF and 80% F-cells may be more appropriate for hydroxyurea therapy or γ-globin targeting gene therapy to have the optimal effect. A recent study in pediatric patients with SCA has demonstrated that an early initiation of hydroxyurea using an individualized, pharmacokinetic-guided dosing strategy can achieve this goal in the clinical setting (McGann et al., 2019). Novel medications that increase Hb-O_2 affinity may synergize with hydroxyurea to lower PoS (Brown et al., 2020; Rab et al., 2020a). All patients in our analysis had SS genotype, except one patient with $S\beta^+$-thalassemia. Further work is required to evaluate the oxygenscan profile of patients with other SCD genotypes, such SC and $S\beta^0$-thalassemia, as well as with genetic modifiers such as the hereditary persistence of fetal hemoglobin

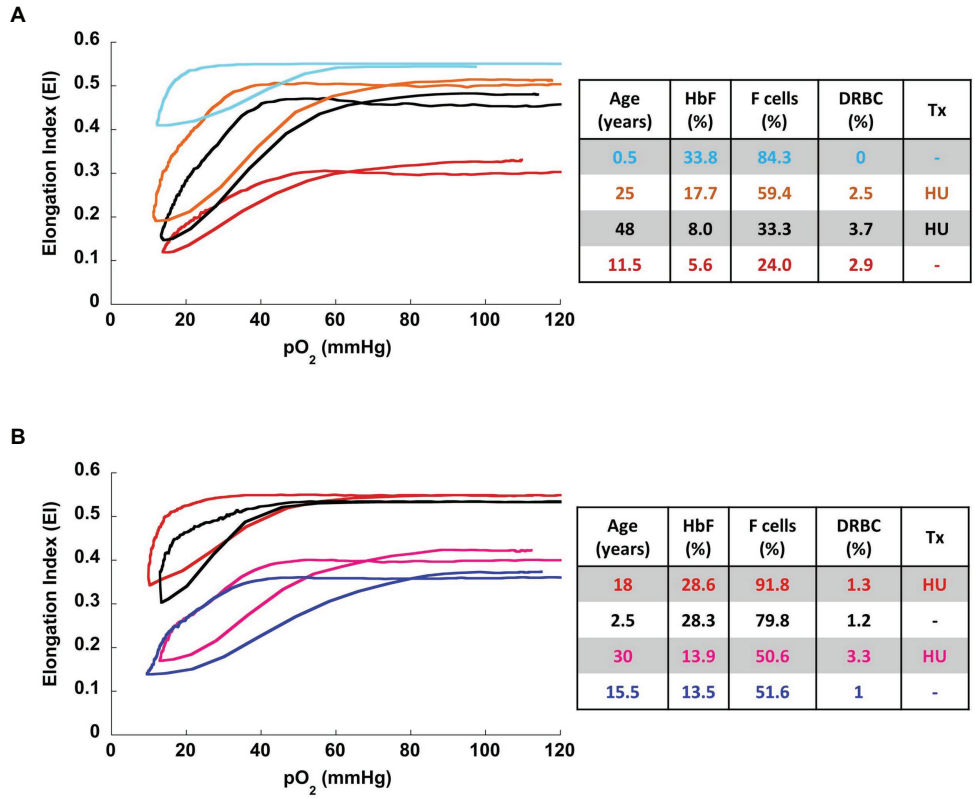

Age (years)	HbF (%)	F cells (%)	DRBC (%)	Tx
0.5	33.8	84.3	0	-
25	17.7	59.4	2.5	HU
48	8.0	33.3	3.7	HU
11.5	5.6	24.0	2.9	-

Age (years)	HbF (%)	F cells (%)	DRBC (%)	Tx
18	28.6	91.8	1.3	HU
2.5	28.3	79.8	1.2	-
30	13.9	50.6	3.3	HU
15.5	13.5	51.6	1	-

FIGURE 3 | Representative oxygenscan curves. **(A)** Four patients with sickle cell disease with corresponding parameters of %HbF, %F-cells, and %DRBCs. In general, increase fetal hemoglobin content (%HbF and %F-cells) and decrease in %DRBC are associated with increase in EI_{max} and EI_{min} and a decrease in PoS. The oxygenscan profile appears to be affected by the combination of these parameters. **(B)** Two pairs of patients with similar HbF, with and without hydroxyurea therapy. At both high HbF (top pair of curves) and low HbF (bottom pair of curves) hydroxyurea is associated with higher EI_{max} and EI_{min}. HU, hydroxyurea; Tx, treatment.

(HPFH) and α-thalassemia trait. In addition, all patients in this analysis were at their steady state at the time of sample collection. Recently, Rab et al. (2020b) described the correlation of oxygenscan parameters with patients who experienced VOC compared to those who did not and demonstrated that oxygenscan parameters had a predictive value for increased VOC frequency, and oxygenscan curve improvement aligned with response to hydroxyurea treatment. Further research is needed to correlate oxygenscan parameters with the various aspects of SCD phenotype and evaluate changes with new medications being developed and used for SCD management.

CONCLUSION

Oxygen-gradient ektacytometry is a reproducible, rapid, and automated functional assay that evaluates the sickling capacity of an erythrocyte population when challenged with deoxygenation and reoxygenation. Although the oxygenscan parameters have an individual relationship with known biomarkers of SCD severity, the oxygenscan profile captures the cumulative effect of those and likely additional factors and may serve as a novel and useful biomarker to evaluate SCD phenotype.

DATA AVAILABILITY STATEMENT

The raw data supporting the conclusions of this article will be made available by the authors, without undue reservation.

ETHICS STATEMENT

The studies involving human participants were reviewed and approved by Institutional Review Board at Cincinnati Children's Hospital Medical Center. Written informed consent to participate in this study was provided by the participants or their legal guardians/next of kin.

AUTHOR CONTRIBUTIONS

AS and TK performed the data analysis, prepared the figures and tables, and wrote the first draft of the manuscript. KS provided expertise in the performance, standardization, and troubleshooting aspects of the oxygenscan assay. RF, ET, and DK performed the oxygenscan assays. JK performed assays for RBC counts, %DRBCs, and %HbF. HB performed the F-cell assays. RW and PM were principal investigators of trials from

which patient samples were obtained. CQ provided expertise in the interpretation of F-cell studies. All authors contributed to the article and approved the submitted version.

FUNDING

Research reported in this publication was supported by the National Center for Advancing Translational Sciences of the National Institutes of Health, under award number 2UL1TR001425-05A1, by the Cincinnati Children's Academic and Research Committee (ARC) award for Sickle Cell Clinical Outreach and Research Excellence (TK and CQ), and by a National Heart, Lung, and Blood Institute Patient-Oriented Career Development award K23HL128885 (PM). The content is the sole responsibility of the authors and does not necessarily represent the official views of the NIH.

ACKNOWLEDGMENTS

We would like to acknowledge all members of the Erythrocyte Diagnostic Laboratory at Cincinnati Children's Hospital Medical Center (CCHMC) for their technical support, the CCHMC hematology clinical research support team, as well as patients and families for donating samples for this study.

REFERENCES

Anker, M. S., Haverkamp, W., and Anker, S. D. (2018). A phase 3 trial of L-glutamine in sickle cell disease. *N. Engl. J. Med.* 379:1879. doi: 10.1056/NEJMc1811050

Aslan, M., Thornley-Brown, D., and Freeman, B. A. (2000). Reactive species in sickle cell disease. *Ann. N. Y. Acad. Sci.* 899, 375–391. doi: 10.1111/j.1749-6632.2000.tb06201.x

Ataga, K. I., Kutlar, A., Kanter, J., Liles, D., Cancado, R., Friedrisch, J., et al. (2017). Crizanlizumab for the prevention of pain crises in sickle cell disease. *N. Engl. J. Med.* 376, 429–439. doi: 10.1056/NEJMoa1611770

Ballas, S. K., Larner, J., Smith, E. D., Surrey, S., Schwartz, E., and Rappaport, E. F. (1988). Rheologic predictors of the severity of the painful sickle cell crisis. *Blood* 72, 1216–1223. doi: 10.1182/blood.V72.4.1216.1216

Ballas, S. K., and Smith, E. D. (1992). Red blood cell changes during the evolution of the sickle cell painful crisis. *Blood* 79, 2154–2163. doi: 10.1182/blood.V79.8.2154.2154

Bartolucci, P., Brugnara, C., Teixeira-Pinto, A., Pissard, S., Moradkhani, K., Jouault, H., et al. (2012). Erythrocyte density in sickle cell syndromes is associated with specific clinical manifestations and hemolysis. *Blood* 120, 3136–3141. doi: 10.1182/blood-2012-04-424184

Bessis, M., Mohandas, N., and Feo, C. (1980). Automated ektacytometry: a new method of measuring red cell deformability and red cell indices. *Blood Cells* 6, 315–327.

Boisson, C., Rab, M. A. E., Nader, E., Renoux, C., van Oirschot, B. A., Joly, P., et al. (2020). Methodological aspects of oxygen gradient ektacytometry in sickle cell disease: effects of sample storage on outcome parameters in distinct patient subgroups. *Clin. Hemorheol. Microcirc.* doi: 10.3233/CH-201037 [Epub ahead of print]

Brown, R. C., Cruz, K., Kalfa, T. A., Kuypers, F. A., Saraf, S. L., Estepp, J. H., et al. (2020). FT-4202, an allosteric activator of pyruvate kinase-r, demonstrates proof of mechanism and proof of concept after a single dose and after multiple daily doses in a phase 1 study of patients with sickle cell disease. *Blood* 136, 19–20. doi: 10.1182/blood-2020-134269

Brugnara, C. (2003). Sickle cell disease: from membrane pathophysiology to novel therapies for prevention of erythrocyte dehydration. *J. Pediatr. Hematol. Oncol.* 25, 927–933. doi: 10.1097/00043426-200312000-00004

Chanutin, A., and Curnish, R. R. (1967). Effect of organic and inorganic phosphates on the oxygen equilibrium of human erythrocytes. *Arch. Biochem. Biophys.* 121, 96–102. doi: 10.1016/0003-9861(67)90013-6

Charache, S., Grisolia, S., Fiedler, A. J., and Hellegers, A. E. (1970). Effect of 2,3-diphosphoglycerate on oxygen affinity of blood in sickle cell anemia. *J. Clin. Invest.* 49, 806–812. doi: 10.1172/JCI106294

Clark, M. R., Mohandas, N., and Shohet, S. B. (1980). Deformability of oxygenated irreversibly sickled cells. *J. Clin. Invest.* 65, 189–196. doi: 10.1172/JCI109650

Clark, M. R., Mohandas, N., and Shohet, S. B. (1983). Osmotic gradient ektacytometry: comprehensive characterization of red cell volume and surface maintenance. *Blood* 61, 899–910. doi: 10.1182/blood.V61.5.899.899

Da Costa, L., Suner, L., Galimand, J., Bonnel, A., Pascreau, T., Couque, N., et al. (2016). Diagnostic tool for red blood cell membrane disorders: assessment of a new generation ektacytometer. *Blood Cells Mol. Dis.* 56, 9–22. doi: 10.1016/j.bcmd.2015.09.001

Davis, B. H., and Davis, K. T. (2004). Enumeration of fetal red blood cells, F cells, and F reticulocytes in human blood. *Curr. Protoc. Cytom.* 6:17. doi: 10.1002/0471142956.cy0617s28

Du, E., Diez-Silva, M., Kato, G. J., Dao, M., and Suresh, S. (2015). Kinetics of sickle cell biorheology and implications for painful vasoocclusive crisis. *Proc. Natl. Acad. Sci. U. S. A.* 112, 1422–1427. doi: 10.1073/pnas.1424111112

Fabry, M. E., and Nagel, R. L. (1982). Heterogeneity of red cells in the sickler: a characteristic with practical clinical and pathophysiological implications. *Blood Cells* 8, 9–15.

Franco, R. S., Lohmann, J., Silberstein, E. B., Mayfield-Pratt, G., Palascak, M., Nemeth, T. A., et al. (1998). Time-dependent changes in the density and hemoglobin F content of biotin-labeled sickle cells. *J. Clin. Invest.* 101, 2730–2740. doi: 10.1172/JCI2484

Hoots, W. K., and Shurin, S. B. (2012). Future directions of sickle cell disease research: the NIH perspective. *Pediatr. Blood Cancer* 59, 353–357. doi: 10.1002/pbc.24180

Jensen, F. B. (2004). Red blood cell pH, the Bohr effect, and other oxygenation-linked phenomena in blood O_2 and CO_2 transport. *Acta Physiol. Scand.* 182, 215–227. doi: 10.1111/j.1365-201X.2004.01361.x

Lande, W. M., Andrews, D. L., Clark, M. R., Braham, N. V., Black, D. M., Embury, S. H., et al. (1988). The incidence of painful crisis in homozygous sickle cell disease: correlation with red cell deformability. *Blood* 72, 2056–2059. doi: 10.1182/blood.V72.6.2056.2056

Leikin, S. L., Gallagher, D., Kinney, T. R., Sloane, D., Klug, P., and Rida, W. (1989). Mortality in children and adolescents with sickle cell disease. Cooperative study of sickle cell disease. *Pediatrics* 84, 500–508.

Lemonne, N., Lamarre, Y., Romana, M., Mukisi-Mukaza, M., Hardy-Dessources, M. D., Tarer, V., et al. (2013). Does increased red blood cell deformability raise the risk for osteonecrosis in sickle cell anemia? *Blood* 121, 3054–3056. doi: 10.1182/blood-2013-01-480277

Marcus, S. J., Kinney, T. R., Schultz, W. H., O'branski, E. E., and Ware, R. E. (1997). Quantitative analysis of erythrocytes containing fetal hemoglobin (F cells) in children with sickle cell disease. *Am. J. Hematol.* 54, 40–46. doi: 10.1002/(SICI)1096-8652(199701)54:1<40::AID-AJH6>3.0.CO;2-4

McGann, P. T., Niss, O., Dong, M., Marahatta, A., Howard, T. A., Mizuno, T., et al. (2019). Robust clinical and laboratory response to hydroxyurea using pharmacokinetically guided dosing for young children with sickle cell anemia. *Am. J. Hematol.* 94, 871–879. doi: 10.1002/ajh.25510

Meier, E. R., Byrnes, C., Weissman, M., Noel, P., Luban, N. L., and Miller, J. L. (2011). Expression patterns of fetal hemoglobin in sickle cell erythrocytes are both patient- and treatment-specific during childhood. *Pediatr. Blood Cancer* 56, 103–109. doi: 10.1002/pbc.22643

Mohandas, N., and Evans, E. (1984). Adherence of sickle erythrocytes to vascular endothelial cells: requirement for both cell membrane changes and plasma factors. *Blood* 64, 282–287. doi: 10.1182/blood.V64.1.282.282

Mohandas, N., and Evans, E. (1985). Sickle erythrocyte adherence to vascular endothelium. Morphologic correlates and the requirement for divalent cations and collagen-binding plasma proteins. *J. Clin. Invest.* 76, 1605–1612. doi: 10.1172/JCI112144

Noguchi, C. T., Torchia, D. A., and Schechter, A. N. (1983). Intracellular polymerization of sickle hemoglobin. Effects of cell heterogeneity. *J. Clin. Invest.* 72, 846–852. doi: 10.1172/JCI111055

Noomuna, P., Risinger, M., Zhou, S., Seu, K., Man, Y., An, R., et al. (2020). Inhibition of band 3 tyrosine phosphorylation: a new mechanism for treatment of sickle cell disease. *Br. J. Haematol.* 190, 599–609. doi: 10.1111/bjh.16671

Papageorgiou, D. P., Abidi, S. Z., Chang, H. Y., Li, X., Kato, G. J., Karniadakis, G. E., et al. (2018). Simultaneous polymerization and adhesion under hypoxia in sickle cell disease. *Proc. Natl. Acad. Sci. U. S. A.* 115, 9473–9478. doi: 10.1073/pnas.1807405115

Parrow, N. L., Tu, H., Nichols, J., Violet, P. C., Pittman, C. A., Fitzhugh, C., et al. (2017). Measurements of red cell deformability and hydration reflect HbF and HbA. *Blood Cells Mol. Dis.* 65, 41–50. doi: 10.1016/j.bcmd.2017.04.005

Poillon, W. N., Kim, B. C., Rodgers, G. P., Noguchi, C. T., and Schechter, A. N. (1993). Sparing effect of hemoglobin F and hemoglobin A2 on the polymerization of hemoglobin S at physiologic ligand saturations. *Proc. Natl. Acad. Sci. U. S. A.* 90, 5039–5043. doi: 10.1073/pnas.90.11.5039

Quinn, C. T. (2016). Minireview: clinical severity in sickle cell disease: the challenges of definition and prognostication. *Exp. Biol. Med.* 241, 679–688. doi: 10.1177/1535370216640385

Rab, M. A. E., Kanne, C. K., Bos, J., Boisson, C., van Oirschot, B. A., Nader, E., et al. (2020a). Methodological aspects of the oxygenscan in sickle cell disease: a need for standardization. *Am. J. Hematol.* 95, E5–E8. doi: 10.1002/ajh.25655

Rab, M. A. E., Kanne, C. K., Bos, J., van Oirschot, B. A., Boisson, C., Houwing, M. E., et al. (2020b). Oxygen gradient ektacytometry derived-biomarkers are associated with vaso-occlusive crises and correlate with treatment response in sickle cell disease. *Am. J. Hematol.* 96, E29–E32. doi: 10.1002/ajh.26031

Rab, M. A. E., van Oirschot, B. A., Bos, J., Kanne, C. K., Sheehan, V. A., van Beers, E. J., et al. (2019a). Characterization of sickling during controlled automated deoxygenation with oxygen gradient ektacytometry. *J. Vis. Exp.* doi: 10.3791/60213

Rab, M. A. E., van Oirschot, B. A., Bos, J., Merkx, T. H., van Wesel, A. C. W., Abdulmalik, O., et al. (2019b). Rapid and reproducible characterization of sickling during automated deoxygenation in sickle cell disease patients. *Am. J. Hematol.* 94, 575–584. doi: 10.1002/ajh.25443

Risinger, M., and Kalfa, T. A. (2020). Red cell membrane disorders: structure meets function. *Blood* 136, 1250–1261. doi: 10.1182/blood.2019000946

Steinberg, M. H. (2005). Predicting clinical severity in sickle cell anaemia. *Br. J. Haematol.* 129, 465–481. doi: 10.1111/j.1365-2141.2005.05411.x

Steinberg, M. H., Chui, D. H., Dover, G. J., Sebastiani, P., and Alsultan, A. (2014). Fetal hemoglobin in sickle cell anemia: a glass half full? *Blood* 123, 481–485. doi: 10.1182/blood-2013-09-528067

Steinberg, M. H., Kumar, S., Murphy, G. J., and Vanuytsel, K. (2019). Sickle cell disease in the era of precision medicine: looking to the future. *Expert Rev. Precis. Med. Drug Dev.* 4, 357–367. doi: 10.1080/23808993.2019.1688658

Steinberg, M. H., and Rodgers, G. P. (2001). Pathophysiology of sickle cell disease: role of cellular and genetic modifiers. *Semin. Hematol.* 38, 299–306. doi: 10.1016/S0037-1963(01)90023-X

Valtis, D. J., and Kennedy, A. C. (1954). Defective gas-transport function of stored red blood-cells. *Lancet* 266, 119–124. doi: 10.1016/s0140-6736(54)90978-2

Vargas, F. F., and Blackshear, G. L. (1982). Vascular resistance and transit time of sickle red blood cells. *Blood Cells* 8, 139–145.

Vichinsky, E., Hoppe, C. C., Ataga, K. I., Ware, R. E., Nduba, V., El-Beshlawy, A., et al. (2019). A phase 3 randomized trial of voxelotor in sickle cell disease. *N. Engl. J. Med.* 381, 509–519. doi: 10.1056/NEJMoa1903212

Yawn, B. P., Buchanan, G. R., Afenyi-Annan, A. N., Ballas, S. K., Hassell, K. L., James, A. H., et al. (2014). Management of sickle cell disease: summary of the 2014 evidence-based report by expert panel members. *JAMA* 312, 1033–1048. doi: 10.1001/jama.2014.10517

Conflict of Interest: The authors declare that the research was conducted in the absence of any commercial or financial relationships that could be construed as a potential conflict of interest.

frontiers in Physiology

ORIGINAL RESEARCH
published: 25 March 2021
doi: 10.3389/fphys.2021.641384

Ektacytometry Analysis of Post-splenectomy Red Blood Cell Properties Identifies Cell Membrane Stability Test as a Novel Biomarker of Membrane Health in Hereditary Spherocytosis

M. C. Berrevoets[1], J. Bos[1], R. Huisjes[1], T. H. Merkx[1], B. A. van Oirschot[1], W. W. van Solinge[1], J. W. Verweij[2], M. Y. A. Lindeboom[2], E. J. van Beers[3], M. Bartels[3†], R. van Wijk[1†] and M. A. E. Rab[1,3]*

[1] Central Diagnostic Laboratory-Research, University Medical Center Utrecht, Utrecht University, Utrecht, Netherlands, [2] Department of Pediatric Surgery, University Medical Center Utrecht, Utrecht University, Utrecht, Netherlands, [3] Van Creveldkliniek, University Medical Center Utrecht, Utrecht University, Utrecht, Netherlands

OPEN ACCESS

Edited by:
Giampaolo Minetti, University of Pavia, Italy

Reviewed by:
Alberto Zanella, IRCCS Ca 'Granda Foundation Maggiore Policlinico Hospital, Italy
Theodosia A. Kalfa, Cincinnati Children's Hospital Medical Center, United States

***Correspondence:**
M. A. E. Rab
m.a.e.rab@umcutrecht.nl

† These authors have contributed equally and share penultimate authorship

Specialty section:
This article was submitted to Red Blood Cell Physiology, a section of the journal Frontiers in Physiology

Received: *14 December 2020*
Accepted: *24 February 2021*
Published: *25 March 2021*

Citation:
Berrevoets MC, Bos J, Huisjes R, Merkx TH, van Oirschot BA, van Solinge WW, Verweij JW, Lindeboom MYA, van Beers EJ, Bartels M, van Wijk R and Rab MAE (2021) Ektacytometry Analysis of Post-splenectomy Red Blood Cell Properties Identifies Cell Membrane Stability Test as a Novel Biomarker of Membrane Health in Hereditary Spherocytosis. Front. Physiol. 12:641384. doi: 10.3389/fphys.2021.641384

Hereditary spherocytosis (HS) is the most common form of hereditary chronic hemolytic anemia. It is caused by mutations in red blood cell (RBC) membrane and cytoskeletal proteins, which compromise membrane integrity, leading to vesiculation. Eventually, this leads to entrapment of poorly deformable spherocytes in the spleen. Splenectomy is a procedure often performed in HS. The clinical benefit results from removing the primary site of destruction, thereby improving RBC survival. But whether changes in RBC properties contribute to the clinical benefit of splenectomy is unknown. In this study we used ektacytometry to investigate the longitudinal effects of splenectomy on RBC properties in five well-characterized HS patients at four different time points and in a case-control cohort of 26 HS patients. Osmotic gradient ektacytometry showed that splenectomy resulted in improved intracellular viscosity (hydration state) whereas total surface area and surface-to-volume ratio remained essentially unchanged. The cell membrane stability test (CMST), which assesses the *in vitro* response to shear stress, showed that after splenectomy, HS RBCs had partly regained the ability to shed membrane, a property of healthy RBCs, which was confirmed in the case-control cohort. In particular the CMST holds promise as a novel biomarker in HS that reflects RBC membrane health and may be used to asses treatment response in HS.

Keywords: hereditary spherocytosis, splenectomy, deformability, ektacytometry, biomarker, red blood cell, hemolytic anemia

INTRODUCTION

Hereditary spherocytosis (HS) is a heterogeneous group of inherited anemias that originates from defective anchoring of transmembrane proteins to the cytoskeletal network of the red blood cell (RBC). The defective anchoring is predominantly caused by a mutation in the genes coding for ankyrin (ANK1), α-spectrin (SPTA1), β-spectrin (SPTB), band-3 (SLC4A1), or protein 4.2 (EPB42) (Perrotta et al., 2008). These mutations compromise the vertical linkages between the lipid bilayer and the cytoskeletal network, leading to destabilization of the membrane, increased

vesiculation and subsequent membrane loss. The progressive membrane loss leads to formation of dense spherical-shaped RBCs (spherocytes) with reduced deformability (Chasis et al., 1988; Eber and Lux, 2004; Huisjes et al., 2018).

The spleen plays an intricate role in the pathophysiology of HS. Normally, this organ functions as a quality control for RBCs. During the 120-day lifespan of healthy RBCs, membrane surface area, surface area-to-volume ratio, and deformability decrease because of release of essentially hemoglobin-free microvesicles. RBCs with increased density and reduced deformability are eventually trapped in the narrow endothelial slits of the spleen, leading to clearance of aged RBCs (Eber and Lux, 2004; Mebius and Kraal, 2005). The compromised vertical linkages in HS accelerate the loss of membrane and deformability, leading to premature destruction of RBCs in the spleen. Therefore, splenectomy is an effective treatment, and removal of the primary site of RBC destruction generally improves clinical symptoms (Musser et al., 1984; Eber and Lux, 2004; Perrotta et al., 2008). Nevertheless, the risks and benefits should be carefully assessed as splenectomy results in a permanently increased risk of infections caused by encapsulated bacteria and long term risk for cardiovascular events (Perrotta et al., 2008; Schilling et al., 2008).

The effects of splenectomy on RBC rheology and RBC related parameters in HS have been studied to a limited extent. It is known that splenectomy improves the RBC count, hemoglobin (Hb) levels, and hematocrit, and that it reduces mean corpuscular hemoglobin concentration (MCHC) and the percentage of reticulocytes (Reliene et al., 2002; Li et al., 2016; Zaninoni et al., 2018; Huisjes et al., 2020). On a cellular level it has been shown that the size of RBCs increases following splenectomy, and that microspherocytes can no longer be detected (Sugihara et al., 1984). However, splenectomy has little effect on correcting the cytoskeletal membrane defect (Reliene et al., 2002). More recent studies have shown that RBC deformability as measured by osmotic gradient ektacytometry was not improved after splenectomy (Zaninoni et al., 2018; Huisjes et al., 2020). An important limitation of these studies was the fact that they compared cohorts of splenectomized and non-splenectomized patients; longitudinal studies on the response to splenectomy of individual HS patients are scarce (Li et al., 2016).

In this study, we investigated individual responses to splenectomy in a group of five HS patients, with particular focus on RBC functional properties as determined by ektacytometry. Our results indicate that the Cell Membrane Stability Test (CMST), which measures the RBCs response to high shear stress, is able to detect substantial functional improvement of the RBC membrane after splenectomy, by showing a partly restored ability to shed membrane, a feature of healthy RBCs. We suggest that the CMST represents a novel biomarker of RBC membrane health in HS, and may be used to assess the efficacy of treatment.

MATERIALS AND METHODS

Patients

Two groups of patients were enrolled in this study. The first group consisted of five patients (one male and four females, aged between 13 and 43 years) diagnosed with HS, and scheduled to undergo splenectomy. Detailed characteristics are provided in **Supplementary Table 1**. Left-over material of blood collected before splenectomy and at different time points after splenectomy (i.e., 1 week, 1 month and $\geq$3 months) was used for laboratory measurements. Informed consent was obtained from all patients and/or legal guardians. The second group consisted of a patient cohort of 26 HS patients: 18 non-splenectomized patients, eight patients who underwent splenectomy $\geq$ 1 year prior to enrollment, and 26 healthy controls (HC). Blood samples of this cohort were obtained after inclusion in the CoMMiTMenT-study which was approved by the Medical Ethical Research Board of the University Medical Center Utrecht, Netherlands (15/426 M) or from anonymized left-over material. Blood from HC individuals was obtained by means of the institutional blood donor service.

Surgical Procedure

Laparoscopic total splenectomy was performed in all five patients. The patients were positioned in right lateral decubitus. Four trocars were used. The lesser sac was entered and the short gastric vessels were divided. After full mobilization of the spleen, the hilar vessels were controlled by using a linear cutting stapler. The spleen was extracted using a retrieval bag.

Laboratory Parameters

Routine hematological laboratory parameters were analyzed on an Abbott Cell-Dyn Sapphire hematology analyzer (Abbott Diagnostics Division, Santa Clara, CA, United States).

Ektacytometry

Deformability of RBCs was measured with the Lorrca (Laser Optical Rotational Red Cell Analyzer, RR Mechatronics, Zwaag, Netherlands). In this ektacytometer, RBCs are exposed to shear stress in a viscous solution (Elon-Iso), forcing the cells to elongate into an elliptical shape. The diffraction pattern that is generated by a laser beam is measured by a camera. The vertical axis (A) and the horizontal axis (B) of the ellipse are used to calculate the elongation index (EI) by the formula (A-B)/(A+B). The EI reflects the deformability of the total population of RBCs.

Osmotic Gradient Ektacytometry

Osmotic gradient ektacytometry measurements of RBCs of HC and HS patients before and after splenectomy were obtained using the osmoscan module on the Lorrca according to the manufacturer's instructions and as described elsewhere (DaCosta et al., 2016; Lazarova et al., 2017). Briefly, whole blood was standardized to a fixed RBC count of 1,000 $\times$ 10^6 and mixed with 5 mL of Elon-Iso (RR Mechatronics). RBCs in the viscous solution (Elon-Iso) were exposed to an osmolarity gradient from approximately 60 mOsmol/L to 600 mOsmol/L, while shear stress was kept constant (30 Pa).

Cell Membrane Stability Test

The CMST was performed using the CMST module on the ektacytometer. To perform a CMST, whole blood was standardized to a fixed RBC count of 200 $\times$ 10^6 and mixed with 5 mL of Elon-Iso. In the CMST RBCs are exposed to a shear stress

of 100 Pa for 3,600 s (1 h) while the EI is continuously measured. The change in the elongation index (ΔEI) was calculated by determining the median of the first and the last 100 s of the CMST and subsequently calculating the difference between the medians. The ΔEI depicts the capacity of the RBCs to shed membrane and resist shear stress.

Microscopic analysis on a subset of samples was performed with the use of a camera microscope (1/1.8″ Sony CMOS Global IMX265LLR imaging sensor, long working distance VS-Technology 50X Plan LWD, VS-MS-COL tube) which was placed on outside of the rotating cup of the Lorrca. A power-LED flash (415 nm) coupled to a fiber-optic, in bright field illumination, from the inside of the cup into a 45 degrees mirror and diffusor lens directed at the microscope, was used for proper lighting of the RBCs. A flash time of 214 ns was used to get less than 1% motion blur. The rotating cup was modified with 15 thin and small glass windows circumferential in the cup. Images were taken with Image Capture software during a CMST measurement.

Density Separation

To assess the effect of splenectomy on the composition of the RBC population a density separation was carried out before splenectomy and approximately 1 month after in one HS patient. A total of 20 mL whole blood was placed on top of three layers with different percentage percoll (GE Healthcare) 1.130 ± 0.005 g/mL in eight different columns (2 mL whole blood/column). RBCs were fractioned according to density (i.e., cellular age) using this density gradient of percoll with addition of HEPES, NaCl, KCL, and NaOH as described in detail elsewhere (Rennie et al., 1979). Cells were centrifuged at 1,665 × *g* for 15 min, after which four fractions could be obtained (**Supplementary Figure 1A**). Fraction 1, containing the RBCs with the lowest density, was present on top of the 59% percoll layer, and was only present and subsequently obtained from the pre-splenectomy blood sample (**Supplementary Figure 1A**). Because of the limited amount of RBCs in fraction 1 only a subset of measurements could be performed. Fraction 2 was obtained from the top of the 70% percoll layer. Fraction 3 was obtained from the top of the 78% percoll layer. The 4th fraction, containing the most dense RBCs was obtained from the bottom of the tube (**Supplementary Figure 1A**).

Digital Microscopy

Peripheral blood smears were analyzed using the CellaVision digital microscope DM96 (software 5.0.1 build11). Analysis was performed using a neuronal network which classifies RBCs based on morphological characteristics such as shape, color, and texture. Spherocytes, microcytes and macrocytes (%) were calculated as a percentage of total RBCs as quantified by the software (Huisjes et al., 2017).

Statistical Analysis

All the data were analyzed using GraphPad Prism version 8.3.0 for Windows (GraphPad Software, San Diego, CA, United States). A paired *T*-test (two-tailed) was used to assess the values before and after splenectomy. An one-way ANOVA, with post-hoc Tukey analysis was used to assess the differences between HC and HS patients, and non-splenectomized and splenectomized HS patients. In addition, a correlation analysis between RBC related parameters and the change in elongation index (ΔEI) was conducted using the Spearman's rank correlation coefficient. A *p*-value below 0.05 was considered statistically significant.

RESULTS

Routine Hematological Parameters Show a Decrease in RBC Density and Increased RBC Homogeneity After Splenectomy

Following splenectomy, routine hematology parameters showed a significant improvement in RBC count, Hb, and reticulocyte count after 1 and ≥3 months (**Figures 1A–C** and **Supplementary Table 1**). Mean corpuscular volume (MCV) increased in the first week after splenectomy, but returned to pre-surgery levels in the following months (**Figure 1D**). This suggests that cell volume is not altered by splenectomy. At the same time, we observed a significant decrease in MCHC and the percentage of hyperchromic cells, indicating a decline in RBC density following splenectomy (**Figures 1E,F**). At the same time, spherocytes and microcytes as assessed by digital microscopy also declined, except for spherocytes in patient 1 (**Supplementary Table 1**). When RBCs of one HS patient were separated according to density (**Supplementary Figure 1A**), we noted that the MCHC before splenectomy seemed determined mainly by density fraction 4, containing the most dense RBCs, whereas after splenectomy density fractions 3 and 4 seem to contribute equally to the MCHC (**Supplementary Figure 1B**), This implies a more homogeneous RBC population after splenectomy, which was also reflected by a more equal distribution of the different fractions after splenectomy (**Supplementary Figure 1A**). Hyperchromic cells were predominantly present in fraction 4 before splenectomy, and their number decreased substantially after splenectomy (**Supplementary Figure 1C**).

Osmotic Gradient Ektacytometry-Derived Parameters Indicate Increased Cellular Hydration After Splenectomy

Osmotic gradient ektacytometry was performed to determine the effect of splenectomy on RBC total surface area (EI_{max}), surface area-to-volume ratio (O_{min}), and RBC hydration state (O_{hyper}). In addition, the area under the curve was calculated (Van Vuren et al., 2019). A representative curve of the effect of splenectomy after 1 month is shown in **Figure 2A**.

Post-splenectomy values for O_{min} and EI_{max} did not change significantly compared to pre-splenectomy values, indicating that after splenectomy HS RBCs still had reduced surface area-to-volume ratio and total surface area (**Figures 2B,C**,

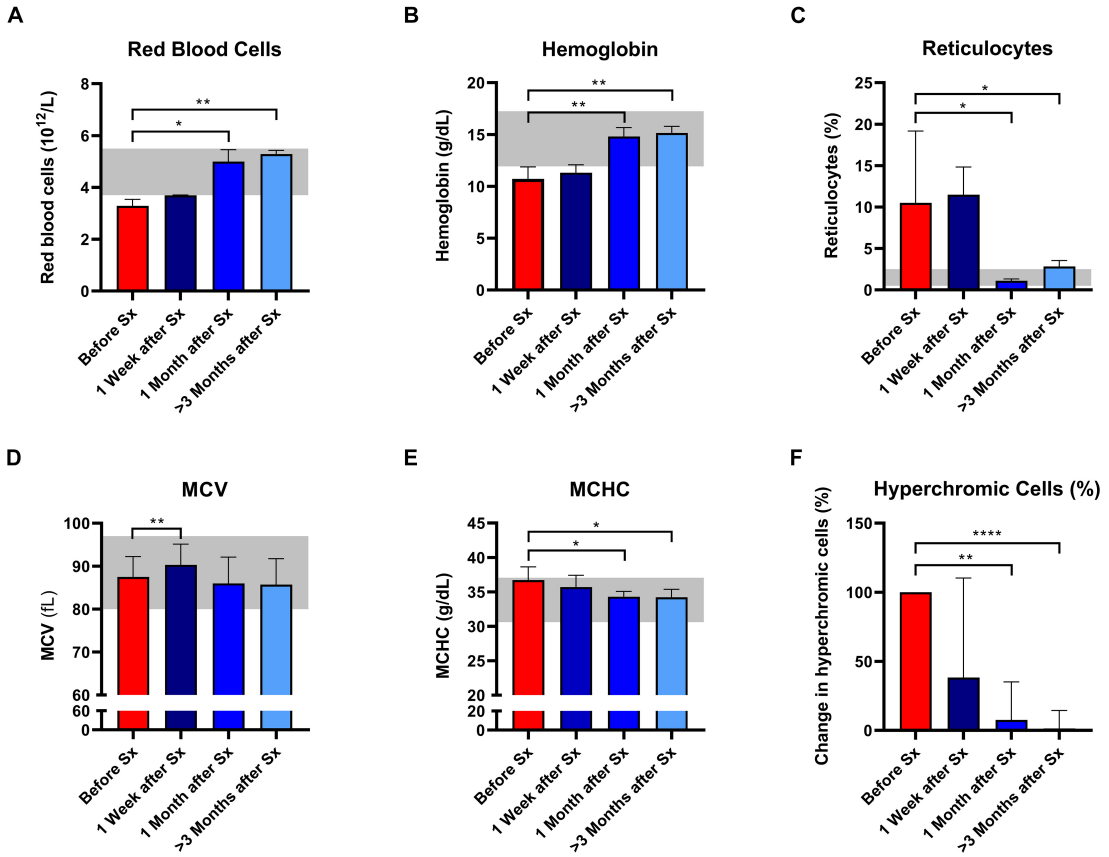

FIGURE 1 | Red blood cell related parameters of patients with hereditary spherocytosis (HS) before and after splenectomy (Sx). Whole blood of HS patients (n = 5) was analyzed before and 1 week, 1 and 3 months after splenectomy. **(A)** Red Blood Cells significantly increased after splenectomy. **(B)** Mean hemoglobin values significantly increased after 1 and 3 months after splenectomy. **(C)** Mean values of reticulocytes decreased 1 and 3 months after splenectomy. **(D)** mean values of mean corpuscular volume (MCV) increased significantly 1 week after splenectomy but decreased 1 and 3 months after splenectomy. **(E)** Mean values of mean corpuscular hemoglobin concentration (MCHC) decreased significantly 1 and 3 months after splenectomy. **(F)** Mean change in hyperchromic cells (%) after splenectomy. The laboratory reference ranges (2SD) of the University Medical Center Utrecht (UMCU) are depicted in the light gray area. Error bars represent standard deviation. ****$p < 0.0001$, ***$p < 0.001$, **$p < 0.01$, and *$p \leq 0.05$.

respectively). In contrast, the hydration state or cytoplasmic viscosity (O_{hyper}) showed a significant increase toward normal values after already 1 week and this was maintained after 1 and ≥3 months (**Figure 2D**). This is in line with the decrease in number of hyperchromic cells and MCHC (**Figures 1E,F**). The increase in O_{hyper} was accompanied by an increase in the AUC, although values remained lower than normal controls (**Figure 2E**).

Additional osmotic gradient ektacytometry measurements on the different density fractions showed that following splenectomy the variability between the curves from each density fraction is less, again indicating a more homogeneous RBC population (**Supplementary Figures 1D,E**). These analyses also showed that only O_{hyper} of density fraction 4 improved. Therefore, the increase in O_{hyper} after splenectomy seemed mainly determined by this fraction, containing the most dense RBCs. O_{hyper} of fractions 2 and 3 decreased after splenectomy, most presumably due to a decrease in reticulocytes in both fractions (**Supplementary Figures 1D–G**).

The Cell Membrane Stability Test Reveals That HS RBCs Have Regained the Ability to Shed Membrane After Splenectomy, Reflecting Improved Membrane Health

We next investigated RBC rigidity and its ability to respond to mechanical stress by performing CMST measurements. The CMST exposes RBCs to a high, supraphysiological, shear stress (100 Pa) for the duration of 1 h. Healthy RBCs showed a gradual decrease in deformability under these conditions (Representative curve, **Figure 3A**), reflected by a negative ΔEI. The loss of deformability likely results from increased vesiculation *in vitro* and consequent membrane loss under shear. In contrast, HS RBCs showed a significantly lower ΔEI before splenectomy compared to HC ($p < 0.01$, **Figure 3B**; representative curve **Figure 3A**). This suggests that RBCs of HS patients are more rigid and less able to shed membrane *in vitro* compared to healthy RBCs. After splenectomy, ΔEI increased until it was no longer significantly different from HC ≥ 3 months after

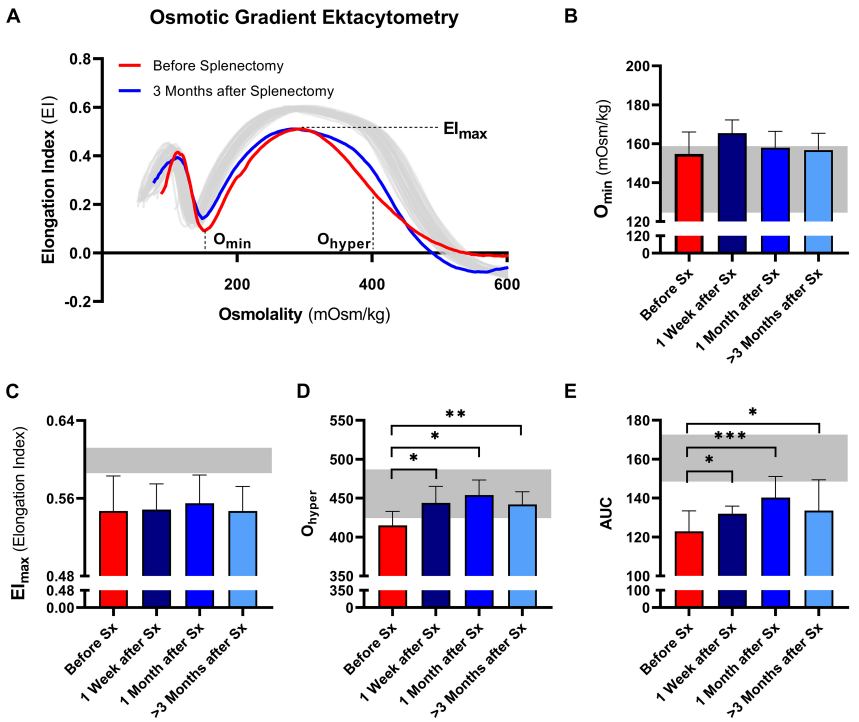

FIGURE 2 | Osmotic gradient ektacytometry curve (Osmoscan) and the corresponding parameters of 5 patients with HS before and after splenectomy (Sx). **(A)** Representative example of the osmotic gradient ektacytometry curve in P03 before and 3 months after splenectomy. The osmotic gradient ektacytometry curves of healthy controls (n = 40) are depicted by the gray lines. The changes in **(B)** the surface area to volume ratio of red blood cells (Omin), **(C)** the maximum deformability (Elmax), **(D)** the hydration state or cytoplasmic viscosity (Ohyper) and **(E)** the area under the curve (AUC) are depicted above. The HS patients (n = 5) were grouped and the results are displayed as the mean (SD) of the combined values. The mean (2SD) of healthy controls (n = 74) are depicted in the light gray area **(B–E)**. Error bars represent standard deviation. ***$p < 0.001$, **$p < 0.01$, *$p \leq 0.05$.

splenectomy (**Figure 3B**). Hence, splenectomy results in a less rigid cell population that has for a large part regained the ability to shed membrane. These findings were strengthened by microscopic analysis of RBCs during the CMST. **Figure 3C** shows how RBCs obtained from a HC were fully elongated and elliptical at the start of the CMST (t = 10 s), then turning into dense and less elongated RBCs at the end of the measurement (t = 3,590 s). In contrast, RBCs of an HS patient without splenectomy were already dense and unable to elongate fully at the start of the CMST, remaining like this throughout the measurement. Notably, reticulocyte count and hyperchromic cells both correlated with ΔEI (r = 0.660, $p < 0.01$ and r = 0.668, $p < 0.01$, respectively, **Figures 3D,E**), indicating that these cells strongly influence the outcome of CMST measurements.

Additional CMST measurements on the density fractions suggest that the increase in ΔEI post-splenectomy are determined by density fractions 2 and 3 (**Supplementary Figure 1H**).

Membrane-Shedding as Measured by the CMST Represents a Novel Pathophysiological Property of HS RBCs

To further explore its added value we performed CMST measurements on a large HS cohort consisting of 18 non-splenectomized, 8 splenectomized patients, and 26 HCs. These results confirmed the findings observed in our longitudinal study, showing that the CMST was able to distinguish splenectomized HS patients from non-splenectomized HS patients (p = 0.028), in addition to the clear distinction between HS patients in general and HCs (both $p < 0.001$). Similarly, also in this large cohort there was a correlation of ΔEI and reticulocyte count (R = 0.606, $p < 0.01$, **Figure 4F**) and hyperchromic cells (R = 0.521, $p < 0.01$ **Figure 4G**).

We next evaluated osmotic gradient ektacytometry measurements in this case-control cohort. In agreement with our findings in the longitudinal study (**Figure 2B**), O_{min} was not different in splenectomized patients (**Figure 4B**). Also EI_{max} and AUC were not significantly different in splenectomized HS patients (**Figures 4C,E**). In contrast, O_{hyper} was the only parameter that showed improvement when comparing splenectomized to non-splenectomized HS patients ($p < 0.01$, **Figure 4D**). Furthermore, O_{hyper} correlated with hyperchromic cells although less clear than ΔEI (R = −0.461, $p < 0.05$, **Supplementary Figure 2**), but not with reticulocyte count (**Figure 4H**). Importantly, ΔEI and O_{hyper} showed no correlation (**Figure 4I**), suggesting that both biomarkers reflect different features of HS RBCs.

Together, these findings confirm that a decreased ability to shed membrane *in vitro* as measured by the CMST is

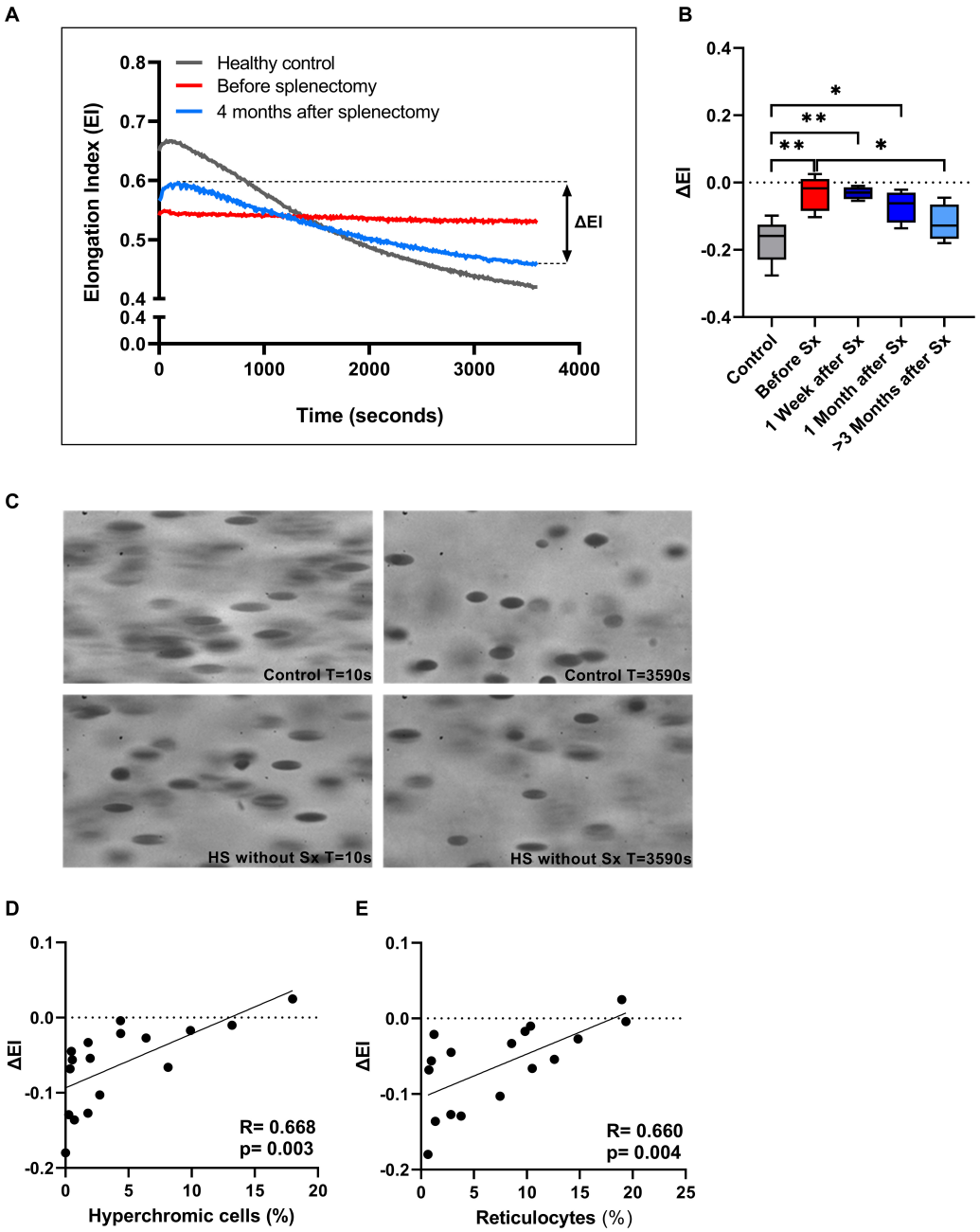

FIGURE 3 | The Cell membrane stability test (CMST) and the calculated parameter (ΔEI) improves after splenectomy in a longitudinal study of 5 HS patients. **(A)** Representative example of the CMST before (red line) and 4 months after splenectomy (light blue line) compared to a healthy control (dark gray line). **(B)** The mean values of ΔEI of HS patients (n = 5) before and after splenectomy. **(C)** Microscopic images of the RBCs in the Lorrca during a CMST. Start of the measurement (T = 10 s) compared to the end of the measurement (T = 3,590 s) in a control and HS patient without splenectomy. **(D)** Correlation between ΔEI and hyperchromic red blood cells. **(E)** Correlation between ΔEI and reticulocytes (%). Error bars represent standard deviation. $^{**}p < 0.01$, $^{*}p \leq 0.05$. Sx, splenectomy; HS, hereditary spherocytosis; T, time; s, seconds.

a novel pathophysiological feature of HS RBCs. It likely reflects membrane health and improves after splenectomy, thereby rendering a novel biomarker that is distinct from the improved density/cell hydration as measured by osmotic gradient ektacytometry.

DISCUSSION

In the present study, we report on the longitudinal effects of splenectomy in five HS patients. We specifically focused on cellular properties related to membrane health with the

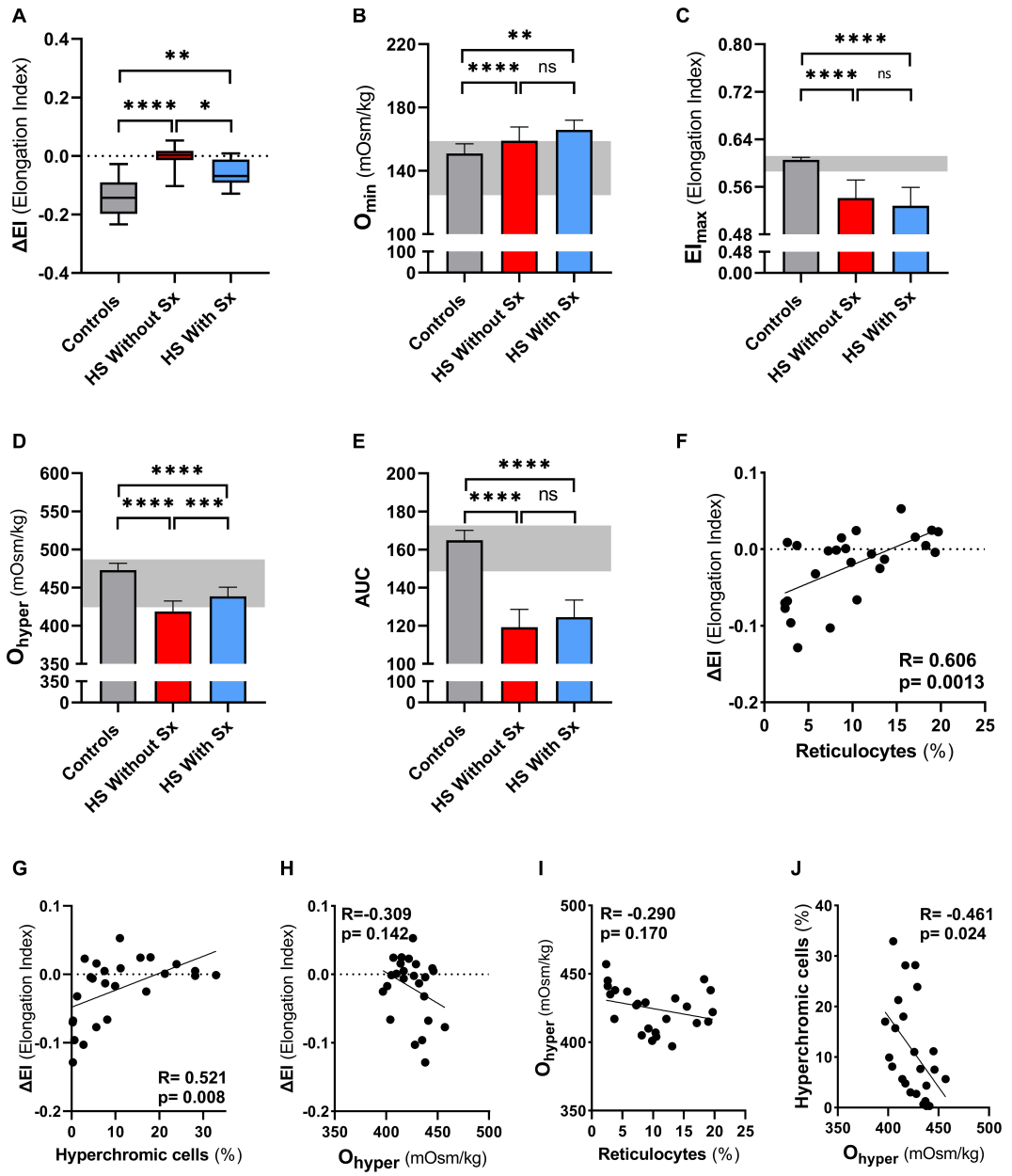

FIGURE 4 | Cell membrane stability test (CMST) and the calculated parameter (ΔEI) shows improvement in splenectomized patients with HS in a case-control study. CMST-derived parameter ΔEI [panels **(A,F,G,H)**], osmotic gradient ektacytometry-derived parameters [panels **(B–E,H,I,J)**], reticulocytes and hyperchromic cells were assessed in 18 non-splenectomized HS patients, 8 non-splenectomized HS patients and 26 healthy controls (HC). **(A)** Mean ΔEI of HS patients without splenectomy compared to patients with splenectomy, both groups were compared to HCs. **(B)** Mean values of Omin are increased in splenectomized patients compared to HCs or non-splenectomized HS. **(C)** Mean values of Elmax are decreased in splenectomized HS patient RBCs, compared to HC and non-splenectomized HS RBCs. **(D)** Mean values of Ohyper are significantly different between the 3 groups mentioned above. **(E)** Mean values of AUC show no significant differences between non-splenectomized and splenectomized HS RBCs. **(F)** Linear correlation between reticulocytes (%) and ΔEI of HS patients. **(G)** Linear correlation between hyperchromic cells (%) and ΔEI of HS patients. **(H)** Linear correlation between Ohyper and ΔEI. **(I)** Linear correlation between reticulocytes (%) and Ohyper. **(J)** Linear correlation between hyperchromic cells and Ohyper. Error bars represent standard deviation. $^{****}p < 0.0001$, $^{***}p < 0.001$, $^{**}p < 0.01$, $^{*}p \leq 0.05$; ns, non-significant. Sx, splenectomy; HS, hereditary spherocytosis; AUC, area under the curve.

use of two different forms of ektacytometry: osmotic gradient ektacytometry and the CMST. In particular the CMST results revealed a novel feature of HS RBCs, i.e., the loss of the ability to shed membrane, and improvement of this *in vitro* cellular property following splenectomy. Membrane-shedding capacity in this test is assessed by the loss of deformability that occurs during prolonged exposure of RBCs to high shear stress. We suggest that improved membrane-shedding capacity after

splenectomy reflects improved RBC membrane health, and ΔEI as measured by the CMST may thus serve as a novel clinically relevant biomarker.

The longitudinally observed increase in RBC count, Hb and reticulocyte count after splenectomy corresponds well with results from previous studies where splenectomized and non-splenectomized patient groups were compared (Zaninoni et al., 2018; Huisjes et al., 2020). In addition, our patients also showed a decrease in MCHC directly after splenectomy, which continued to decrease in the following months. This implicates that the internal viscosity or cellular density of HS RBCs is reduced after splenectomy, which is supported by the reduction in the percentage of hyperchromic cells. Little is known about the effect of splenectomy on *in vivo* RBC vesiculation in HS, an important pathophysiological feature, but previous studies demonstrated that RBC vesiculation caused an increase in internal viscosity (MCHC) through shedding of RBC-derived microvesicles (Bosch et al., 1994; Alaarg et al., 2013; Bosman, 2013). Hence, both the decrease in MCHC and hyperchromic cells could indicate that *in vivo* vesiculation of RBCs in HS is reduced after splenectomy. In turn this could explain the observed improvement in ΔEI in the CMST after splenectomy, which reflects improved ability to shed membrane *in vitro*.

More detailed analysis of the longitudinal effects of splenectomy was obtained by osmotic gradient ektacytometry. This technique is generally considered as the gold standard in the diagnosis of HS (DaCosta et al., 2016; Lazarova et al., 2017; Llaudet-Planas et al., 2018; Zaninoni et al., 2018), and its parameters EI_{max}, O_{min}, and O_{hyper} are considered biomarkers of, respectively, total membrane surface area, surface area to volume ratio, and RBC hydration status. Upon splenectomy most of these parameters were not affected, only O_{hyper} was significantly increased (**Figures 2D**, **4D**). O_{hyper} and MCHC are known to have an inverse correlation with each other (Zaninoni et al., 2018). Both the increase in O_{hyper} and the decrease in MCHC indicate that splenectomy improves the hydration state/intracellular viscosity. In line with this, an increase in the AUC was observed in the longitudinal cohort, whereas AUC remained unchanged after splenectomy in the case-control cohort. Our findings partly contradict with previous studies were both O_{hyper} and AUC remained unaltered after splenectomy (Zaninoni et al., 2018; Huisjes et al., 2020). This could be explained by the non-longitudinal design of these latter studies in which individual differences in response to splenectomy become less apparent.

We next investigated the effect of splenectomy on the ability of HS RBCs to respond to mechanical stress. For this we used the CMST, an ektacytometry based test that was previously used to study membrane stability in HS by studying resealed RBC ghosts (Mohandas et al., 1982; Chasis and Mohandas, 1986). We demonstrate that RBCs from non-splenectomized HS patients show no or only a modest decrease in EI after prolonged exposure to shear stress, in contrast to HC RBCs which display a substantial decrease in EI under these conditions. We hypothesize that HS RBCs from non-splenectomized HS patients are more dense and rigid due to *in vivo* vesiculation that is accelerated by the spleen, and, therefore are less able to shed membrane *in vitro* (Waugh and La Celle, 1980). This is confirmed by the microscopic evaluation of HS RBCs during CMST measurement, which shows that, in contrast to healthy RBCs, HS RBCs do not change morphologically (**Figure 3C**). Further support for this hypothesis is obtained from the significant correlation of ΔEI and hyperchromic cells (**Figure 3D**).

Following splenectomy HS RBCs showed an increase in ΔEI (**Figure 3B**) and after more than 3 months ΔEI was not significantly different compared to HC. This suggests that after splenectomy HS RBCs have regained part of the ability to shed membrane *in vitro*, which may be related to a partly restored ability of HS RBCs for *de novo* synthesis of lipids (Cooper and Jandl, 1969; Sugihara et al., 1984; Takashi and Yoshihito, 1984). The increase in ΔEI could also indicate a change in RBC population due to the absence of the quality control function of the spleen; Instead of shedding micro vesicles *in vivo* in the spleen (i.e., splenic conditioning), this now occurs *in vitro* under the supraphysiological conditions in the CMST. In both cases cellular characteristics as obtained by the CMST measurements indicate an improvement after splenectomy, in a sense that they behave more like normal healthy RBCs. Furthermore, the degree of increase in ΔEI after splenectomy we observed could also be dependent on genetic defect (Ingrosso et al., 1996; Reliene et al., 2002). Our findings were strengthened by CMST results on a large cohort of HS patients that showed that this test was able to discriminate between splenectomized and non-splenectomized HS patients (**Figure 4A**). This implies that the CMST may represent a novel biomarker of HS, which was further supported by the correlation of ΔEI and % reticulocytes ($r = 0.66$, $p = 0.004$). The ability to distinguish splenectomized patients from non-splenectomized patients can be valuable in an era where different types of splenectomy are explored. Partial splenectomy, either through embolization of splenic arteries or through (laparoscopic) removal of a part of the spleen, might ameliorate symptoms and improve anemia while maintaining splenic phagocytic function (Tchernia et al., 1993; Pratl et al., 2008). However, data of several small studies are inconclusive regarding the remaining immunological capacity of the spleen after partial splenectomy even though hemolysis is decreased (Guizzetti, 2016). Larger studies that also include functional analysis of the spleen and functional analysis of RBCs, i.e., the CMST, are warranted to accurately assess the efficacy of (partial) splenectomy or embolization, and to investigate whether changes in RBC properties or the nature of the underlying molecular defect (Ingrosso et al., 1996; Reliene et al., 2002) contribute to the clinical benefit of splenectomy.

In conclusion, we report on the longitudinal effects of splenectomy on HS RBC characteristics and function as studied by ektacytometry. Our data shows that before splenectomy the HS RBC population is more heterogeneous, cells are more rigid, have increased intracellular viscosity and reduced deformability. Functional analysis of HS RBCs using osmotic gradient ektacytometry and CMST further shows that splenectomy improves the hydration state of HS RBCs and allows cells to regain the ability to shed membrane. In particular the CMST reflects an yet-undescribed distinct RBC characteristic and holds promise as a novel biomarker for membrane health

in HS that could be helpful, together with a comprehensive clinical evaluation and appropriate follow-up, to assess the effect of different treatments such as embolization and (partial) splenectomy, and that may be related to clinical severity given the correlation of ΔEI and reticulocyte count. Larger studies are warranted to establish if the CMST can be used to improve the assessment of clinical severity and/or is able to contribute to a better understanding of phenotypic differences in HS.

DATA AVAILABILITY STATEMENT

The raw data supporting the conclusions of this article will be made available by the authors, without undue reservation.

ETHICS STATEMENT

The studies involving human participants were reviewed and approved by METC University Medical Center Utrecht. Written informed consent to participate in this study was provided by the participants' legal guardian/next of kin.

AUTHOR CONTRIBUTIONS

RH, MB, RW, and MR designed the study. RH, JV, ML, MB, EB, and MR collected clinical and laboratory data. JB, RH, TM, BO, and MR performed laboratory experiments. MCB, RW, and MR analyzed the data and wrote the manuscript. All authors edited the manuscript and approved the final version.

FUNDING

The research has received funding from the European Seventh Framework Program under grant agreement number 602121 (CoMMiTMenT) and was partially funded by an unrestricted grant from RR Mechatronics.

ACKNOWLEDGMENTS

The authors would like to thank all patients that donated blood for this study.

SUPPLEMENTARY MATERIAL

The Supplementary Material for this article can be found online at: https://www.frontiersin.org/articles/10.3389/fphys.2021.641384/full#supplementary-material

REFERENCES

Alaarg, A., Schiffelers, R. M., Van Solinge, W. W., and Van Wijk, R. (2013). Red blood cell vesiculation in hereditary hemolytic anemia. *Front. Physiol.* 4:365. doi: 10.3389/fphys.2013.00365

Bosch, F. H., Werre, J. M., Schipper, L., Roerdinkholder-Stoelwinder, B., Huls, T., Willekens, F. L., et al. (1994). Determinants of red blood cell deformability in relation to cell age. *Eur. J. Haematol.* 52, 35–41.

Bosman, G. J. C. G. M. (2013). Survival of red blood cells after transfusion: processes and consequences. *Front. Physiol.* 4:376. doi: 10.3389/fphys.2013.00376

Chasis, J. A., Agre, P., and Mohandas, N. (1988). Decreased membrane mechanical stability and in vivo loss of surface area reflect spectrin deficiencies in hereditary spherocytosis. *J. Clin. Invest.* 82, 617–623. doi: 10.1172/JCI113640

Chasis, J. A., and Mohandas, N. (1986). Erythrocyte membrane deformability and stability: two distinct membrane properties that are independently regulated by skeletal protein associations. *J. Cell Biol.* 103, 343–350. doi: 10.1083/jcb.103.2.343

Cooper, R. A., and Jandl, J. H. (1969). The role of membrane lipids in the survival of red cells in hereditary spherocytosis. *J. Clin. Invest.* 48, 736–744. doi: 10.1172/JCI106031

DaCosta, L., Suner, L., Galimand, J., Bonnel, A., Pascreau, T., Couque, N., et al. (2016). Diagnostic tool for red blood cell membrane disorders: assessment of a new generation ektacytometer. *Blood Cells Mol. Dis.* 56, 9–22. doi: 10.1016/j.bcmd.2015.09.001

Eber, S. W., and Lux, S. E. (2004). Hereditary spherocytosis–defects in proteins that connect the membrane skeleton to the lipid bilayer. *Semin. Hematol.* 41, 118–141.

Guizzetti, L. (2016). Total versus partial splenectomy in pediatric hereditary spherocytosis: a systematic review and meta-analysis. *Pediatr. Blood Cancer* 63, 1713–1722. doi: 10.1002/pbc.26106

Huisjes, R., Bogdanova, A., van Solinge, W. W., Schiffelers, R. M., Kaestner, L., and van Wijk, R. (2018). Squeezing for life - Properties of red blood cell deformability. *Front. Physiol.* 9:656. doi: 10.3389/fphys.2018.00656

Huisjes, R., Makhro, A., Llaudet-Planas, E., Hertz, L., Petkova-Kirova, P., Verhagen, L. P., et al. (2020). Density, heterogeneity and deformability of red cells as markers of clinical severity in hereditary spherocytosis. *Haematologica* 105, 338–347. doi: 10.3324/haematol.2018.188151

Huisjes, R., Solinge, W. W., Levin, M. D., Wijk, R., and Riedl, J. A. (2017). Digital microscopy as a screening tool for the diagnosis of hereditary hemolytic anemia. *Int. J. Lab. Hematol.* 40, 159–168. doi: 10.1111/ijlh.12758

Ingrosso, D., D'Angelo, S., Perrotta, S., d'Urzo, G., Iolascon, A., Perna, A. F., et al. (1996). Cytoskeletal behaviour in spectrin and in band 3 deficient spherocytic red cells: evidence for a differentiated splenic conditioning role. *Br. J. Haematol.* 93, 38–41. doi: 10.1046/j.1365-2141.1996.451990.x

Lazarova, E., Gulbis, B., van Oirschot, B., and van Wijk, R. (2017). Next-generation osmotic gradient ektacytometry for the diagnosis of hereditary spherocytosis: interlaboratory method validation and experience. *Clin. Chem. Lab. Med.* 55, 394–402. doi: 10.1515/cclm-2016-0290

Li, Y., Lu, L., and Li, J. (2016). Topological structures and membrane nanostructures of erythrocytes after splenectomy in hereditary spherocytosis patients via atomic force microscopy. *Cell Biochem. Biophys.* 74, 365–371. doi: 10.1007/s12013-016-0755-4

Llaudet-Planas, E., Vives-Corrons, J. L., Rizzuto, V., Gómez-Ramírez, P., Navarro, J. S., Sibina, M. T. C., et al. (2018). Osmotic gradient ektacytometry: a valuable screening test for hereditary spherocytosis and other red blood cell membrane disorders. *Int. J. Lab. Hematol.* 40, 94–102. doi: 10.1111/ijlh.12746

Mebius, R. E., and Kraal, G. (2005). Structure and function of the spleen. *Nat. Rev. Immunol.* 5, 606–616. doi: 10.1038/nri1669

Mohandas, N., Clark, M. R., Health, B. P., Rossi, M., Wolfe, L. C., Lux, S. E., et al. (1982). A technique to detect reduced mechanical stability of red cell membranes: relevance to elliptocytic disorders. *Blood* 59, 768–774.

Musser, G., Lazar, G., Hocking, W., and Busuttil, W. (1984). Splenectomy for hematologic disease. The UCLA experience with 306 patients. *Ann. Surg.* 200, 40–45. doi: 10.1097/00000658-198407000-00006

Perrotta, S., Gallagher, P. G., and Mohandas, N. (2008). Hereditary spherocytosis. *Lancet* 372, 1411–1426. doi: 10.1016/S0140-6736(08)61588-3

Pratl, B., Benesch, M., Lackner, H., Portugaller, H. R., Pusswald, B., Sovinz, P., et al. (2008). Partial splenic embolization in children with hereditary spherocytosis. *Eur. J. Haematol.* 80, 76–80. doi: 10.1111/j.1600-0609.2007.00979.x

Reliene, R., Mariani, M., Zanella, A., Reinhart, W. H., Ribeiro, M. L., del Giudice, E. M., et al. (2002). Splenectomy prolongs *in vivo* survival of erythrocytes differently in spectrin/ankyrin- and band 3-deficient hereditary spherocytosis. *Blood* 100, 2208–2215. doi: 10.1182/blood.v100.6.2208.h81802002208_2208_2215

Rennie, C. M., Thompson, S., Parker, A. C., and Maddy, A. (1979). Human erythrocyte fractionation in "percoll" density gradients. *Clin. Chim. Acta* 98, 119–125. doi: 10.1016/0009-8981(79)90172-4

Schilling, R. F., Gangnon, R. E., and Traver, M. I. (2008). Delayed adverse vascular events after splenectomy in hereditary spherocytosis. *J. Thromb. Haemost.* 6, 1289–1295. doi: 10.1111/j.1538-7836.2008.03024.x

Sugihara, T., Miyashima, K., and Yawata, Y. (1984). Disappearance of microspherocytes in peripheral circulation and normalization of decreased lipids in plasma and in red cells of patients with hereditary spherocytosis after splenectomy. *Am. J. Hematol.* 17, 129–139.

Takashi, S., and Yoshihito, Y. (1984). Observations on plasma and red cell lipids in hereditary spherocytosis. *Clin. Chim. Acta* 137, 227–232. doi: 10.1016/0009-8981(84)90182-7

Tchernia, G., Gauthier, F., Mielot, F., Dommergues, J. P., Yvart, J., Chasis, J. A., et al. (1993). Initial assessment of the beneficial effect of partial splenectomy in hereditary spherocytosis. *Blood* 81, 2014–2020. doi: 10.1016/B978-0-323-05226-9.50014-1

Van Vuren, A., Van Der Zwaag, B., Huisjes, R., Lak, N., Bierings, M., Gerritsen, E., et al. (2019). The complexity of genotype-phenotype correlations in hereditary spherocytosis: a cohort of 95 patients: genotype-phenotype correlation in hereditary spherocytosis. *HemaSphere* 3:e276. doi: 10.1097/HS9.0000000000000276

Waugh, R. E., and La Celle, P. L. (1980). Abnormalities in the membrane material properties of hereditary spherocytes. *J. Biomech. Eng.* 102:240. doi: 10.1115/1.3149580

Zaninoni, A., Fermo, E., Vercellati, C., Consonni, D., Marcello, A. P., Zanella, A., et al. (2018). Use of laser assisted optical rotational cell analyzer (LoRRca MaxSis) in the diagnosis of RBC membrane disorders, enzyme defects, and congenital dyserythropoietic anemias: a monocentric study on 202 patients. *Front. Physiol.* 9:451. doi: 10.3389/fphys.2018.00451

Conflict of Interest: The authors declare that the research was conducted in the absence of any commercial or financial relationships that could be construed as a potential conflict of interest.

frontiers in Physiology

ORIGINAL RESEARCH
published: 21 May 2021
doi: 10.3389/fphys.2021.684569

Targeted Next Generation Sequencing and Diagnosis of Congenital Hemolytic Anemias: A Three Years Experience Monocentric Study

*Elisa Fermo[1], Cristina Vercellati[1], Anna Paola Marcello[1], Ebru Yilmaz Keskin[2], Silverio Perrotta[3], Anna Zaninoni[1], Valentina Brancaleoni[4], Alberto Zanella[1], Juri A. Giannotta[1], Wilma Barcellini[1] and Paola Bianchi[1]**

[1] UOS Fisiopatologia delle Anemie, UOC Ematologia, Fondazione IRCCS Ca' Granda Ospedale Maggiore Policlinico, Milan, Italy, [2] Department of Pediatric Hematology and Oncology, Suleyman Demirel University, Isparta, Turkey, [3] Dipartimento della Donna, del Bambino e di Chirurgia Generale e Specialistica, Università degli Studi della Campania "Luigi Vanvitelli," Naples, Italy, [4] UOC Medicina Generale, Fondazione IRCCS Ca' Granda Ospedale Maggiore Policlinico, Milan, Italy

OPEN ACCESS

Edited by:
Angelo D'Alessandro, University of Colorado Denver, United States

Reviewed by:
Tiffany Thomas, Columbia University Irving Medical Center, United States
Marianna H. Antonelou, National and Kapodistrian University of Athens, Greece

***Correspondence:**
Paola Bianchi
paola.bianchi@policlinico.mi.it

Specialty section:
This article was submitted to Red Blood Cell Physiology, a section of the journal Frontiers in Physiology

Received: *23 March 2021*
Accepted: *27 April 2021*
Published: *21 May 2021*

Citation:
Fermo E, Vercellati C, Marcello AP, Keskin EY, Perrotta S, Zaninoni A, Brancaleoni V, Zanella A, Giannotta JA, Barcellini W and Bianchi P (2021) Targeted Next Generation Sequencing and Diagnosis of Congenital Hemolytic Anemias: A Three Years Experience Monocentric Study. Front. Physiol. 12:684569. doi: 10.3389/fphys.2021.684569

Congenital hemolytic anemias (CHAs) are heterogeneous and rare disorders caused by alterations in structure, membrane transport, metabolism, or red blood cell production. The pathophysiology of these diseases, in particular the rarest, is often poorly understood, and easy-to-apply tools for diagnosis, clinical management, and patient stratification are still lacking. We report the 3-years monocentric experience with a 43 genes targeted Next Generation Sequencing (t-NGS) panel in diagnosis of CHAs; 122 patients from 105 unrelated families were investigated and the results compared with conventional laboratory pathway. Patients were divided in two groups: 1) cases diagnosed with hematologic investigations to be confirmed at molecular level, and 2) patients with unexplained anemia after extensive hematologic investigation. The overall sensitivity of t-NGS was 74 and 35% for families of groups 1 and 2, respectively. Inside this cohort of patients we identified 26 new pathogenic variants confirmed by functional evidence. The implementation of laboratory work-up with t-NGS increased the number of diagnoses in cases with unexplained anemia; cytoskeleton defects are well detected by conventional tools, deserving t-NGS to atypical cases; the diagnosis of Gardos channelopathy, some enzyme deficiencies, familial siterosterolemia, X-linked defects in females and other rare and ultra-rare diseases definitely benefits of t-NGS approaches.

Keywords: congenital hemolytic anemia, targeted-NGS, pathogenic variants, red blood cells, differential diagnosis

INTRODUCTION

Congenital hemolytic anemias (CHAs) comprise a group of very heterogeneous and rare disorders caused by alterations in structure, transport functions, metabolism, or defective production of red blood cells (RBCs). Since the pathophysiology of some rare forms is poorly understood, these disorders represent a group of diseases that still lack easy-to-apply tools for diagnosis, clinical management, and patient stratification.

The laboratory diagnostic pathway of CHAs was historically based on sequential steps using a panel of functional analyses that investigate the RBC membrane and metabolism. The first diagnostic step relies on hematological tests (complete blood count, red cell indices, hemolysis markers), peripheral blood smear examination, osmotic fragility tests and eosin-5-maleimide (EMA) binding test. The second includes biochemical tests such as quantitative assay of RBC enzymes activity, sodium dodecyl sulphate-polyacrylamide gel electrophoresis (SDS-PAGE) for the diagnosis of membranopathies, and specialized investigations requiring instruments which are available only in reference Centers, as ektacytometry (King et al., 2015; Fermo et al., 2021). The molecular characterization of the affected genes by traditional Sanger sequencing was usually, up to some years ago, the last step allowing the definitive confirmation of the diagnosis. Despite this, even after extensive and complete investigation, the differential diagnosis of these disorders may be difficult, and some patients remain undiagnosed with a consequent negative impact on clinical follow up, risk of inappropriate therapeutic decisions and lack of access to new specific treatments.

The advent and recent progresses on next generation sequencing (NGS) technologies has radically changed the diagnostic approach to CHAs, often placing the genetic analysis as a first line screening tool; different NGS strategies have been developed in the last years including targeted panels and whole exome sequencing (WES), with a progressive reduction of costs that allowed their routinely use (Steinberg-Shemer and Tamary, 2020; Russo et al., 2020). Targeted-NGS panels have been developed and applied by several groups, being currently the preferred approach for the molecular diagnosis of CHAs; custom panels include different numbers of genes and have been reported to have a wide range of diagnostic efficacy (38–90%) depending on the number of genes included and on the characteristics of the patients studied (Agarwal et al., 2016; Del Orbe Barreto et al., 2016; Niss et al., 2016; Roy et al., 2016; Russo et al., 2018; Shefer Averbuch et al., 2018; Choi et al., 2019; Kedar et al., 2019a,b; Svidnicki et al., 2020). In this paper we report the 3 years monocentric experience in targeted-NGS and diagnosis of CHAs, and we compare the efficacy of this methodological approach with the conventional laboratory diagnosis.

MATERIALS AND METHODS

Patients

Among the patients referred to our Institut (Pathophysiology of Anemias Unit, Fondazione IRCCS Ca' Granda Ospedale Maggiore of Milan–Italy) between 2017 and 2019 with a clinical suspect of CHAs we examined a cohort of 122 patients from 105 unrelated families (51% males and 49% females, median age 27 years, range 0–73 years). The inclusion criteria in the study were: a diagnostic indication for congenital hemoltic anemia; the specific request from clinicians to perform/complete diagnosis at molecular level; a specific scientific interest in cases with intra-family variability or atypical presentation; all cases with unexplained phenotype despite extensive investigations; signed informed consent to perform molecular investigations. Samples were collected from patients and controls during diagnostic procedures after obtaining informed consent and approval from the Institutional Human Research Committee. For patients under the age of 18, written informed consent was obtained from the parents. The procedures followed were in accordance with the Helsinki International ethical standards on human experimentation.

All patients but 18 (received after shipping from abroad) underwent extensive hematologic investigations, including: RBC morphology, complete blood count, hemolysis markers, screening for abnormal/unstable hemoglobins, direct antiglobulin test, osmotic fragility tests, EMA binding test (Bianchi et al., 2012), and RBC enzymes activities determination (hexokinase, glucosephosphate isomerase, phosphofructokinase, glyceraldehyde-P-dehydrogenase, phos phoglycerate kinase, pyruvate kinase, glucose-6-phosphate dehydrogenase, 6-phosphogluconate dehydrogenase, adenylate kinase) (Beutler et al., 1977).

In the vast majority of cases we also performed Osmoscan analysis by LoRRca MaxSis (Laser-Assisted Optical Rotational Cell Analyzer, Mechatronics, NL) (Zaninoni et al., 2018, see **Supplementary Materials** for more details), and RBC membrane protein analysis by SDS–PAGE performed according to Laemmli (1970) and Fairbanks et al. (1971) with minor modifications (Mariani et al., 2008).

In the remaining 18 cases (15 families), when possible, a minimum panel of investigation was performed (i.e., EMA binding test, RBC enzyme assay, Osmoscan) and evaluated together with clinical and laboratory information received from the local centers.

In 60 patients from 51 families a definite diagnostic orientation was obtained after first and second level hematological investigations. In particular, 6 were suspected of RBC enzyme defects, 28 of structural membrane defects (hereditary spherocytosis, elliptocytosis, pyropoikilocytosis, HS/HE/HPP), 10 of stomatocytosis and 7 were classified as congenital dyserythropoietic anemia.

In the remaining 62 cases (from 54 families) the laboratory investigations did not allow a clear diagnosis.

NGS Sequencing and Analysis

Genomic DNA was extracted from peripheral blood, using standard manual methods and quantified by Nandrop One (Thermo Scientific, Italy). When available, relatives of affected cases were also enrolled to analyze allelic segregation and correctly assess the pathogenicity of each variant.

Using SureDesign software (Agilent) we created a NGS based panel containing 43 genes already described as disease causing for RBC membrane disorders (n = 14 genes), enzymopathies (n = 18), dyserythropoietic and sideroblastic anemias (n = 11) (**Supplementary Table 1**). For the probe design, coding regions, 5'UTR, 3'UTR, 50 bp flanking splice junctions were selected as regions of interest. Sequence length was set at 150 × 2 nucleotides and the average target coverage was 99.52%. The panel was validated on previously characterized patients affected by CHAs.

Libraries were obtained by HaloPlexHS Target Enrichment System Kit (Agilent) following the instruction's manufacturer. Samples were pooled (average 22 samples) and loaded at 7 pM on MiSeq platform using a v2-300 cycle reagent kit (Illumina). Sequencing reads were aligned against reference genome (UCSC hg19) and variants were called and annotated using the SureCall software (Agilent Technologies).

Filter settings were as follows: variant call quality threshold > 100; minimum number of reads supporting variant allele > 10; mutant allele frequency ≥ 25%; minor allele frequency (MAF) < 1% of the population. Common pathogenic modifiers of hereditary spherocytosis known to be present above the 1% cutoff, e.g., *SPTA1* LELY (Low Expression Lyon) allele (p.L1858V, found in association with the intronic variant c.6531-12 c > t), or the SPTA-Bughill allele (p.A970D) usually found in linkage with the LEPRA (Low Expression PRAgue) allele (SPTA c.4339-99 c > t) were also included.

Targeted filtering and annotation of protein-changing variants were performed using the wANNOVAR web tool[1].

Variants were assessed by mutation prediction and conservation programs including SIFT[2], polyphen-2 (Polymorphism Phenotyping v2)[3] and MutationTaster[4]; pathogenicity was evaluated according to the guidelines of American College of Medical Genetics and Genomics (ACMG) (Richards et al., 2015) using the online tool VarSome[5] (Kopanos et al., 2019).

Variants previously classified as pathogenic by databases such as ClinVar, HGMD, dbSNP, deleterious variants expected to produce truncated or abnormal protein, or splice site variants were considered as causatives. Variants of unknown significance (VUSs) were reported only if found in genes relevant to the primary indication for testing.

The mutations identified were confirmed by Sanger method (ABI PRISM 310 Genetic Analyzer, Applied Biosystems, Warrington, United Kingdom) using the Big Dye Terminator Cycle Sequencing Kit (Applied Biosystems, Warrington, United Kingdom).

Nucleotide numbering reflects cDNA numbering with + 1 corresponding to the A of ATG translation initiation codon in the reference sequence, according to the nomenclature for the description of sequence variants of Human Genome Variation Society[6]. The initiation codon is codon 1.

According with ACMG guidelines, well-established *in vitro* functional studies were performed to assess pathogenicity of VUSs, in particular: spectrophotometric enzyme assay in the suspect of RBC enzyme defects, SDS-PAGE electrophoresis analysis of RBC membrane proteins in the suspect of membrane defects and CDAII, ektacytometry and patch-clamp analysis in case of novel missense variants in *PIEZO1* and *KCNN4* mutations.

[1]http://wannovar.wglab.org/

[2]http://sift.jcvi.org/

[3]http://genetics.bwh.harvard.edu/pph2/

[4]http://www.mutationtaster.org/

[5]https://varsome.com/

[6]www.hgvs.org/mutnomen

RESULTS

The 122 patients examined have been divided in two groups: (1) patients who reached a diagnosis after first and second level hematologic investigations, to be confirmed at molecular level; (2) patients with unexplained chronic hemolytic anemia after extensive hematologic investigations.

Patients belonging to group 1 (60 patients, 51 families) were selected among the entire cohort of patients with CHAs studied between 2017 and 2019 basing on complexity of clinical presentation, intra-family clinical variability or incomplete molecular characterization by Sanger (e.g., enzyme defects or CDA cases). All the available patients who didn't reach a definitive diagnosis in the same period were investigated and included in group 2 (62 cases from 54 families, 39 of them studied in our Center, the other 15 received from abroad).

Group 1

We were able to identify pathogenic variants in 38/51 families belonging to Group 1, with an overall sensitivity of the t-NGS of 74% (**Figure 1A** and **Table 1**).

Enzyme Defects

Eight cases from six families had a biochemical diagnosis of enzyme defect; two were confirmed to have pyruvate kinase (PK) deficiency, three from two families glucose-6-phosphate dehydrogenase (G6PD) deficiency and one was found to have one mutation in *GPI* gene, in compound heterozygosity with the polymorphism c.489A > G (p.Gly163 = rs1801015), possibly associated to splicing alterations (Fermo et al., 2019); in two related cases no mutations in *PKLR* gene were found in spite of a slightly decreased PK activity detected by enzymatic assay.

Among these cases with enzyme defects, in four patients from three families a coinheritance of hereditary stomatocytosis was also suspected due to the presence of stomatocytes at peripheral blood smear and left-shifted Osmoscan curve; only in two of them (5-1 and 5-2) in addition to G6PD deficiency we found a mutation in *PIEZO1* gene causing hereditary stomatocytosis.

Congenital Dyserythropoietic Anaemias (CDAs)

Seven cases had a suspect of congenital dyserythropoietic anemia; five were classified as CDAII on the basis of band 3 deglycosylation at SDS-PAGE analysis, and two had an atypical CDA variant with distinct morphological abnormalities at bone marrow examination. Three out of five CDAII cases displayed biallelic mutations in *SEC23B* gene, whereas in two cases (9-1 and 10-1) we were able to find only one pathogenic variant; in the two cases with the atypical CDA we didn't find any pathological mutation in the genes associated to CDAs included in our panel.

Hereditary Stomatocytosis

Thirteen patients from 10 families had a suspect of hereditary stomatocytosis based on presence of stomatocytes at peripheral blood smear and/or abnormalities at ektacytometric curve; eight of them (from six families) were confirmed to have dehydrated stomatocytosis caused by *PIEZO1* gene pathogenic variants. In one case previously diagnosed as overhydrated stomatocytosis

(11-1) based on a clear right-shifted ektacytometric curve, we found mutations in *ABCG8* gene responsible for sitosterolemia. In the remaining case no pathogenic variants in genes associated with hereditary stomatocytosis were identified.

Membrane Defects

We included in this group chronic hemolytic anemias due to altered RBC membrane structural organization, as HS, HE, HPP; 32 cases from 28 families have received such diagnosis based on first and second level laboratory investigations. In 23 cases from 21 families we found pathogenic variants. One patient with a previous diagnosis of HS was found to be affected by dehydrated stomatocytosis (DHSt); in the remaining cases, mutations in genes responsible for HS and HE were identified. In particular among them we studied 3 families with a complex phenotype: case 38-2 (mixed HS/HE phenotype) carried two variants in *SPTA1* and *SLC4A1*, whereas the brother with typical HE (38-1) had only the *SPTA1* variant. Case 20-1, presenting severe HPP with combined 68% spectrin and 56% ankyrin deficiency, had two different mutations in *SPTA1* gene transmitted by the parents, one of them associated in *cis* with the alpha-LELY allele. Finally, case 19-2 (severe HS with 50% band3 deficiency) had 3 different variants in *SLC4A1* gene, the father (19-1) presenting only one missense mutation, thus justifying intra-family clinical variability (**Figure 2**).

Group 2

Inside this group we were able to identify pathogenic variants in 19/54 families (21/62 patients), with an overall sensitivity of the t-NGS of 35% (**Figure 1B** and **Table 1**).

Ten families were found to have pathogenic variants in RBC enzymes. In five of them (2 PK, 2 G6PD and 1 hexokinase (HK) deficiency, cases 39-1, 40-1, 43-1, 44-1, and 41-1) the enzyme activity was previously tested and found to be normal; in other four cases enzyme activity was not tested for sample unavailability. One case had known G6PD deficiency that was initially not considered during the laboratory screening based on chronic hemolysis. Triosephosphate isomerase (TPI) deficiency was diagnosed in a 7 months old child presenting at the time of the study only hemolytic anemia without neuromuscular manifestations.

Three unrelated cases were found to have pathogenic variants in *KCNN4* gene associated with Gardos channelopathy, two of them carrying the common variant p.R352H and one a private variant p.S314P resulting in channel activation (Fermo et al., 2020).

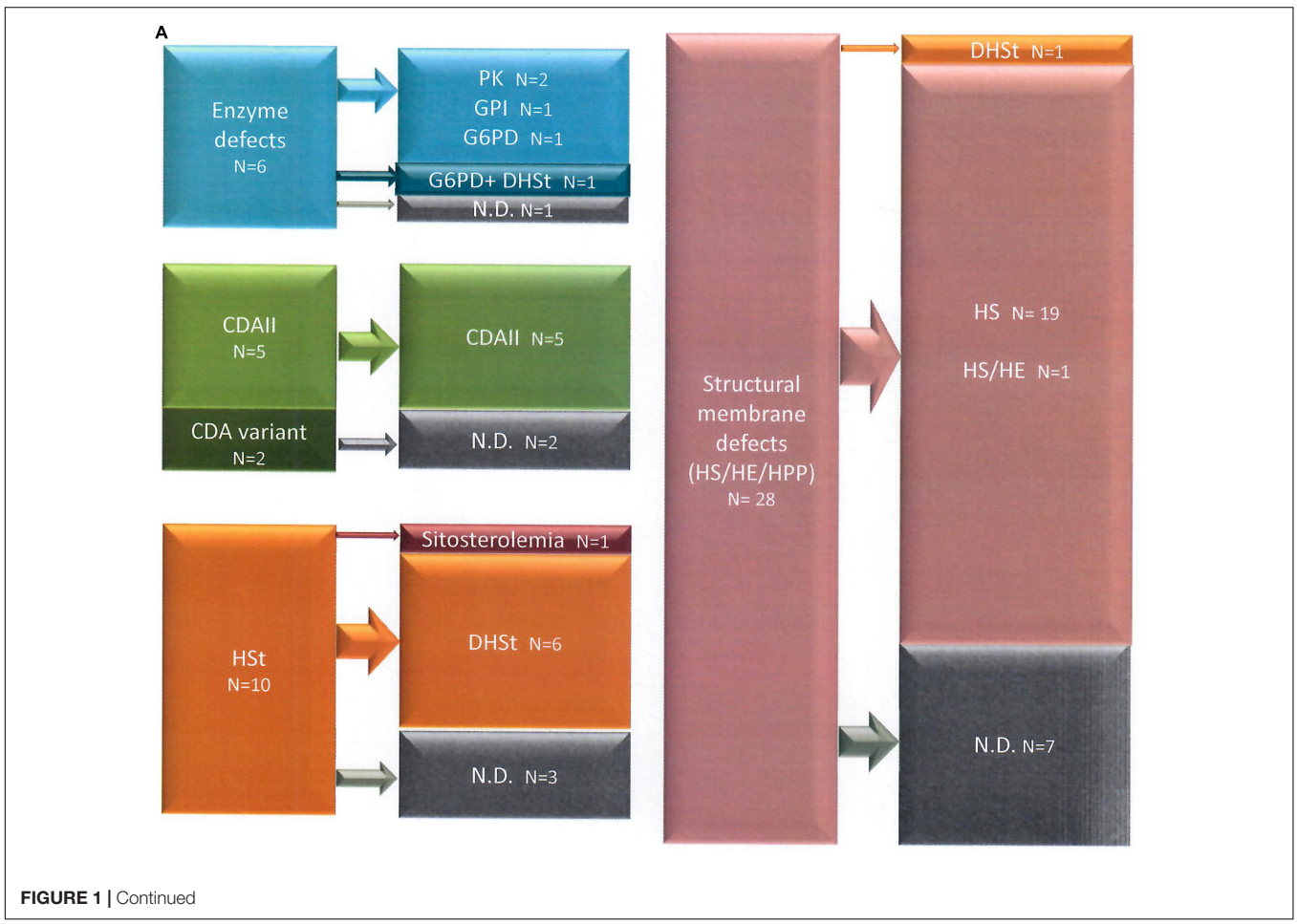

FIGURE 1 | Continued

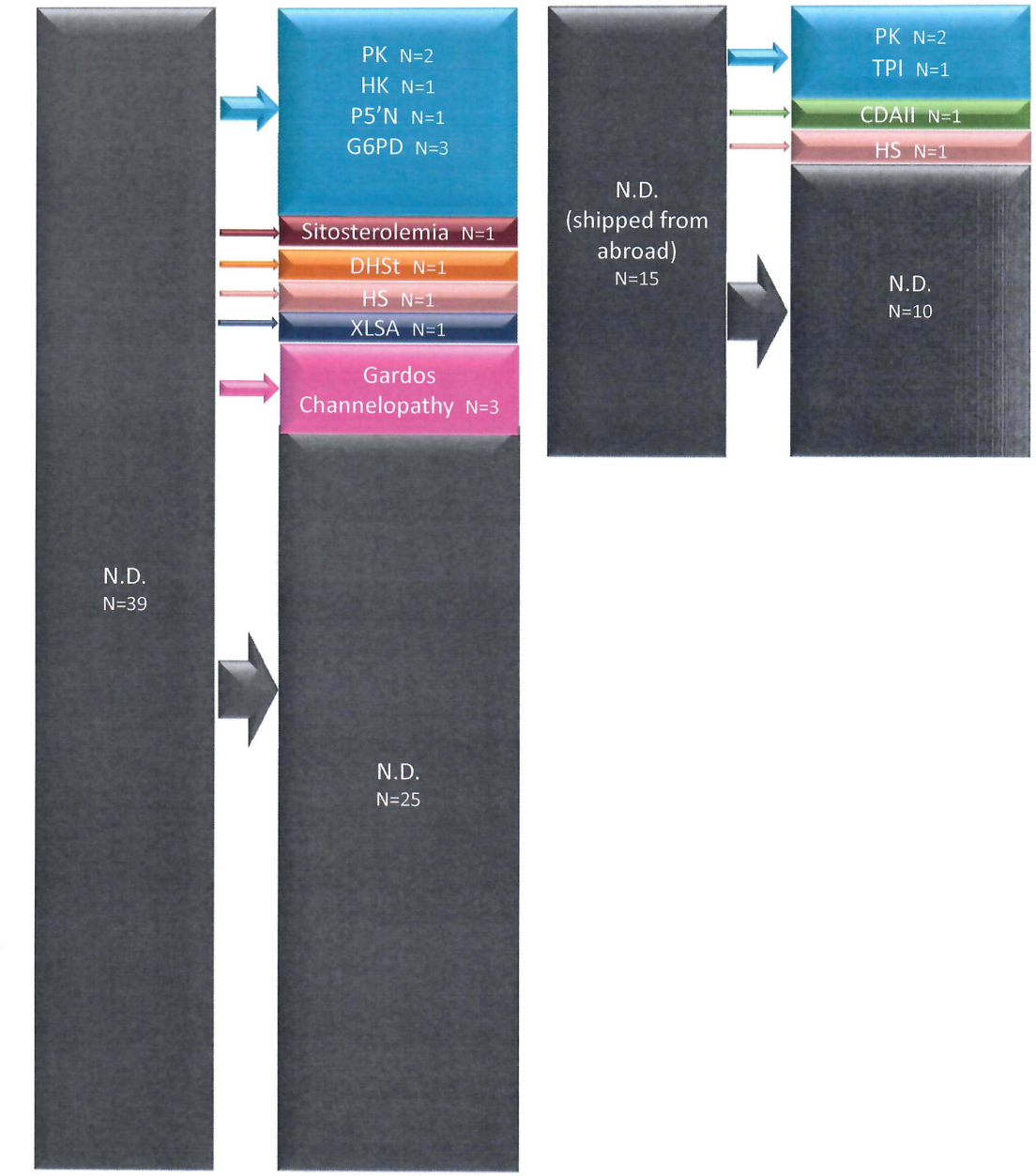

FIGURE 1 | Diagnostic suspect after first and second level laboratory investigation and final diagnosis after t-NGS in Group 1 **(A)** and Group 2 **(B)** patients.

Only one family with two affected siblings (47-1 and 47-2), addressed to our attention in the suspect of PK deficiency in absence of pathogenic variants in *PKLR* gene, carried a PIEZO1 pathogenic variant. Patient 46-1, who had 17% of stomatocytes at peripheral blood smear without any abnormality of the Osmoscan curve, was diagnosed with sitosterolemia due to *ABCG5* mutation p.Y458X. Finally, NGS analysis allowed the diagnosis of X-linked sideroblastic anemia (XLSA) in a woman affected by unexplained macrocytic anemia since birth (case 49-1, *ALAS2* mutation p.H524R). Human androgen receptor gene (HUMARA) analysis showed skewed X-Chromosome inactivation pattern; the mutation was transmitted by the asymptomatic mother.

New Variants Identified

Inside the analyzed cohort we identified 26 new variants, 20 of them associated with structural membrane defects (*SLC4A1*: p.QPLLPQ186Q, p.R870Q, p.T837K, p.K757X, p.G771V, p.S510R, c.1627-1g>t; *SPTB*: p.R52W, p.Q1036PfsX37, p.W1312X, p.Q342X, p.Q760X, p.L883WfsX15, c.4842+1g>c;

TABLE 1 | Results of NGS analysis in 64 patients with congenital hemolytic anemia.

Pt. ID	Laboratory diagnosis	Gene	Transcript	Mutation	Effect	Status	rs	Pathogenicity	Final diagnosis	Additional findings
Group 1										
1-1	Enzyme defect	*PKLR*	NM_000298.5	c.1618 + 2t>c	Abn. splicing	Comp het	rs983394596	5-P	PK deficiency	
		PKLR	NM_000298.5	c.1456C>T	p.R486W	Comp het	rs116100695	5-P		
2-1	Enzyme defect	*PKLR*	NM_000298.5	c.-73G>C	Promoter variant	Comp het		5-P	PK deficiency	*SPTA1* a - lely
		PKLR	NM_000298.5	c.1456C>T	p.R486W	Comp het	rs116100695	5-P		
3-1	Enzyme defect	*GPI*	NM_000175.3	c.1415G>A	p.R472H	Het	rs148811525	5-P	GPI deficiency	
4-1	Enzyme defect	*G6PD*	NM_001042351.1	c.202G>A	p.V68M	Hem	rs1050828	5-P	G6PD deficiency	*SPTA1* a - lely
5-1	Enzyme defect	*G6PD*	NM_001042351.1	c.563C>T	p.S188F	Hom	rs5030868	5-P	G6PD def./DHSt	
		PIEZO1	NM_001142864.3	c.7367G>A	p.R2456H	Het	rs587776988	5-P		
5-2	Enzyme defect	*G6PD*	NM_001042351.1	c.563C>T	p.S188F	Hom	rs5030868	5-P	G6PD def./DHSt	
		PIEZO1	NM_001142864.3	c.7367G>A	p.R2456H	Het	rs587776988	5-P		
6-1	CDAII	*SEC23B*	NM_006363.4	c.40C>T	p.R14W	Comp het	rs121918222	5-P	CDAII	*SPTA1* a - lely
		SEC23B	NM_006363.4	c.689 + 1 g>a	Abn. splicing	Comp het	rs398124226	5-P		
7-1	CDAII	*SEC23B*	NM_006363.4	c.325G>A	p.E109K	Comp het	rs121918221	5-P	CDAII	
		SEC23B	NM_006363.4	c.2270A>C	p.H757P	Comp het	rs1331894607	5-P		
8-1	CDAII	*SEC23B*	NM_006363.4	c.40C>T	p.R14W	Comp het	rs121918222	5-P	CDAII	
		SEC23B	NM_006363.4	c.1821delT	p.H608IfsX7	Comp het		5-P		
9-1	CDAII	*SEC23B*	NM_006363.4	c.235C>T	p.R79X	Het	rs150263014	5-P	CDAII	
10-1	CDAII	*SEC23B*	NM_006363.4	c.40C>T	p.R14W	Het	rs121918222	5-P	CDAII	*SPTA1* a - lely
11-1	HSt	*ABCG8*	NM_022437.2	c.788G>A	p.R263Q	Hom	rs137852990	5-P	Sitosterolemia	
12-1	HSt	*PIEZO1*	NM_001142864.3	c.6574C>A	p.L2192I	Het		4-LP	DHSt	
12-2	HSt	*PIEZO1*	NM_001142864.3	c.6574C>A	p.L2192I	Het		4-LP	DHSt	
13-1	HSt	*PIEZO1*	NM_001142864.3	c.7367G>A	p.R2456H	Het	rs587776988	5-P	DHSt	
14-1	HSt	*PIEZO1*	NM_001142864.3	c.6007G>A	p.A2003T	Het		4-LP	DHSt	
15-1	HSt	*PIEZO1*	NM_001142864.3	c.6328C>T	p.R2110W	Het	rs776531529	5-P	DHSt	*SPTA1* a - lely
16-1	HSt	*PIEZO1*	NM_001142864.3	c.1815G>A	p.M605I	Het		4-LP	DHSt	
16-2	HSt	*PIEZO1*	NM_001142864.3	c.1815G>A	p.M605I	Het		4-LP	DHSt	
17-1	HSt	*PIEZO1*	NM_001142864.3	c.1815G>A	p.M605I	Het		4-LP	DHSt	*SPTA1* a - lely
18-1	Membrane defect	*PIEZO1*	NM_001142864.3	c.1792G>A	p.V598M	Het		4-LP	DHSt	
19-1	Membrane defect	*SLC4A1*	NM_000342.3	c.1469G>A	p.R490H	Het		5-P	HS	
19-2	Membrane defect	*SLC4A1*	NM_000342.3	c.1469G>A	p.R490H	Comp het		5-P	HS	*SPTA1* a - lely
		SLC4A1	**NM_000342.3**	**c.558_572del15bp**	**p.QPLLPQ186Q**	Comp het		4-LP		
		SLC4A1	**NM_000342.3**	**c.1627-1g>t**	**Abn. splicing**	Comp het		5-P		
20-1	Membrane defect	***SPTA1***	**NM_003126.3**	**c.3477 + 1g>c**	**Abn. splicing**	Comp het		5-P	HS	*SPTA1* a - lely
		SPTA1	NM_003126.3	c.3139C>T	p.R1047X	Comp het		5-P		

(Continued)

TABLE 1 | Continued

Pt. ID	Laboratory diagnosis	Gene	Transcript	Mutation	Effect	Status	rs	Pathogenicity	Final diagnosis	Additional findings
21-1	Membrane defect	***SPTB***	**NM_001355436.1**	**c.154C>T**	**p.R52W**	Het		4-LP	HS	*SPTA1* a - lely
22-1	Membrane defect	***SPTB***	**NM_001355436.1**	**c.3106_3107insC**	**p.Q1036Pfs*37**	Het		5-P	HS	*SPTA1* a - lely
23-1	Membrane defect	***SPTB***	**NM_001355436.1**	**c.3936G>A**	**p.W1312X**	Het		5-P	HS	*PKLR* p.R486W
24-1	Membrane defect	*SLC4A1*	NM_000342.3	c.1462G>A	p.V488M	Het	rs28931584	5-P	HS	
25-1	Membrane defect	***SLC4A1***	**NM_000342.3**	**c.2609G>A**	**p.R870Q**	Het	rs746426065	4-LP	HS	*SPTA1* a - lely
26-1	Membrane defect	*SLC4A1*	NM_000342.3	c.2279G>A	p.R760Q	Het	rs121912755	5-P	HS	
27-1	Membrane defect	***SLC4A1***	**NM_000342.3**	**c.2510C>A**	**p.T837K**	Het		4-LP	HS	
28-1	Membrane defect	***SLC4A1***	**NM_000342.3**	**c.2269A>T**	**p.K757X**	Het		5-P	HS	*SEC23B* c.689 + 1G>A *SPTA1* a - lely
29-1	Membrane defect	***ANK1***	**NM_000037.3**	**c.4541delA**	**p.Y1514SfsX33**	Het		5-P	HS	*SPTA1* a - lely
30-1	Membrane defect	***ANK1***	**NM_000037.3**	**c.1430_1431insGTGC**	**p.A478CfsX17**	Het		5-P	HS	
31-1	Membrane defect	***ANK1***	**NM_000037.3**	**c.4057C>T**	**p.Q1353X**	Het		5-P	HS	*SPTA1* a - lely
32-1	Membrane defect	***SPTB***	**NM_001355436.1**	**c.4842 + 1g>c**	**Abn. splicing**	Het		5-P	HS	*SPTA1* a - lely
33-1	Membrane defect	***EPB42***	**NM_000119.2**	**c.922G>C**	**p.V308L/Abn. splicing**	Comp het	rs772330879	4-LP	HS	
		EPB42	**NM_000119.2**	**c.413C>T**	**p.T138I**	Comp het		4-LP		
34-1	Membrane defect	***SLC4A1***	**NM_000342.3**	**c.2312G>T**	**p.G771V/Abn. splicing**	Het		4-LP	HS	
35-1	Membrane defect	*SLC4A1*	NM_000342.3	c.163delC	p.H55TfsX11	Het		5-P	HS	
36-1	Membrane defect	***SPTB***	**NM_001355436.1**	**c.1024C>T**	**p.Q342X**	Het		5-P	HS	
37-1	Membrane defect	*SLC4A1*	NM_000342.3	c.2423G>A	p.R808H	Het	rs866727908	4-LP	HS	
38-1	Membrane defect	*SPTA1*	NM_003126.3	c.460_462dupTTG	p.L155dup	Het	rs757679761	4-LP	HE	
38-2	Membrane defect	*SPTA1*	NM_003126.3	c.460_462dupTTG	p.L155dup	Het	rs757679761	4-LP	HS/HE	
		SLC4A1	**NM_000342.3**	**c.1530C>G**	**p.S510R**	Het		3-VUS		
Group 2										
39-1	n.d	*PKLR*	NM_000298.5	c.1456C>T	p.R486W	Comp het	rs116100695	5-P	PK deficiency	
		PKLR	NM_000298.5	c.1151C>T	p.T384M	Comp het	rs74315362	5-P		
40-1	n.d	*PKLR*	NM_000298.5	c.1456C>T	p.R486W	Comp het	rs116100695	5-P	PK deficiency	*SPTA1* a - lely
		PKLR	NM_000298.5	c.958G>A	p.V320M	Comp het		5-P		
41-1	n.d	***HK1***	**NM_033496.2**	**c.34C>T**	**p.R12X**	Comp het	rs756166032	5-P	HK deficiency	
		HK1	**NM_033496.2**	**c.1351G>C**	**p.G451R**	Comp het		4-LP		
42-1	n.d	***NT5C3A***	**NM_016489.12**	**c.64C>T**	**p.R22X**	Hom	rs753346459	5-P	P5'N deficiency	*SPTA1* a - lely
43-1	n.d	*G6PD*	NM_001042351.1	c.563C>T	p.S188F	Het	rs5030868	5-P	G6PD deficiency	
44-1	n.d	*G6PD*	NM_001042351.1	c.1160G>A	p.R387H	Hem	rs137852321	5-P	G6PD deficiency	
45-1	n.d	*G6PD*	NM_001042351.1	c.1180G>C	p.V394L	Hem	rs137852335	5-P	G6PD deficiency	*NT5C3A* p.N178H
46-1	n.d	***ABCG5***	**NM_022436.2**	**c.1374C>G**	**p.Y458X**	Hom		5-P	Sitosterolemia	

(Continued)

TABLE 1 | Continued

Pt. ID	Laboratory diagnosis	Gene	Transcript	Mutation	Effect	Status	rs	Pathogenicity	Final diagnosis	Additional findings
47-1	n.d	*PIEZO1*	NM_001142864.3	c.7367G>A	p.R2456H	Het	rs587776988	5-P	DHSt	
47-2	n.d	*PIEZO1*	NM_001142864.3	c.7367G>A	p.R2456H	Het	rs587776988	5-P	DHSt	
48-1	n.d	***SPTB***	**NM_001355436.1**	**c.2278C>T**	**p.Q760X**	Het		5-P	HS	*SPTA1* a - lely
49-1	n.d	***ALAS2***	**NM_000032.5**	**c.1571A>G**	**p.H524R**	Het		4-LP	XLSA	*SPTA1* a - lely
50-1	n.d	*KCNN4*	NM_002250.2	c.1055G>A	p.R352H	Het	rs774455945	5-P	Gardos channelopathy	*SPTA1* a - lely
51-1	n.d	*KCNN4*	NM_002250.2	c.940T>C	p.S314P	Het		4-LP	Gardos channelopathy	*AK1* p.G50N
52-1	n.d	*KCNN4*	NM_002250.2	c.1055G>A	p.R352H	Het	rs774455945	5-P	Gardos channelopathy	*SPTA1* a - lely
53-1	n.d	*PKLR*	NM_000298.5	c.581G>C	p.R194P	Hom		4-LP	PK deficiency	
54-1	n.d	***PKLR***	**NM_000298.5**	**c.1591C>A**	**p.R531S**	Hom		4-LP	PK deficiency	
55-1	n.d	*TPI1*	NM_000365.5	c.315G>T	p.E105D	Hom	rs121964845	5-P	TPI deficiency	
56-1	n.d	*SEC23B*	NM_006363.4	c.40C>T	p.R14W	Comp het	rs121918222	5-P	CDAII	
		SEC23B	NM_006363.4	c.490delG	p.V164Wfs*3	Comp het	rs776983439	5-P		
57-1	n.d	***SPTB***	**NM_001355436.1**	**c.2647delC**	**p.L883Wfs*15**	Het		5-P	HS	*SPTA1* a - lely
57-2	n.d	***SPTB***	**NM_001355436.1**	**c.2647delC**	**p.L883Wfs*15**	Het		5-P	HS	

Newly detected variants are reported in bold. Het, heterozygous; Comp het, compound heterozygous; Hom, homozygous; Hem, hemizygous; 5-P, pathogenic; 4-LP, likely pathogenic; 3-VUS, variant of uncertain significance; n.d, not determined. The ClinVar accessions for the new variants here reported are SCV001469066-SCV001469086.

ANK1: p.Y1514SfsX33, p.A478CfsX17, p.Q1353X; *SPTA1*: c.3477+1g>c; *EPB42* p.V308L, p.T138I). The remaining new variants were identified in enzyme genes (*PKLR*: p.R531S; *HK1*: p.R12X, p.G451R; *NT5C3A*: p.R22X), and in genes associated with sitosterolemia (*ABCG5*: p.Y458X) and sideroblastic anemia (*ALAS2*: p.H524R). All new variants were classified as pathogenic or likely pathogenic by *in silico* analysis, according with transmission, clinical phenotype and functional laboratory evidences. Only one VUS variant in *SLC4A1* gene was included and considered as pathogenic because clearly fitting with patients phenotype in a family with a suspected combined transmission of HS and HE (case 38-2) (**Figure 2**).

DISCUSSION

The observed sensitivity of NGS in the two groups of patients analyzed is very different, varying from 74% (patients with a specific diagnostic orientation, Group 1) to 35% (hemolytic patients with no diagnosis after laboratory investigations, or not investigated due long shipping conditions, Group 2).

These data are in line with the available literature (Russo et al., 2018; Bianchi et al., 2020; Steinberg-Shemer and Tamary, 2020) and may explain the heterogeneous sensitivity that, independently from the number of genes analyzed, is often reported for these techniques. For example, the overall sensitivity was around 38.6% in a large series of 57 hemolytic patients with no definitive diagnosis (Roy et al., 2016) and 45.8% in a group of undiagnosed hemolytic patients studied with a combination of two-step t-NGS platforms covering about 100 genes (Russo et al., 2018). Different results are found when NGS is performed on well characterized patient subsets, for example in series of HS patients, where the reported sensitivity increased to 70–100% (Chonat et al., 2019; van Vuren et al., 2019; Xue et al., 2019; Vives-Corrons et al., 2021).

In this view, a sensitivity of 75%, as obtained in our Group 1, may be expected for t-NGS, considering some technical limitations of this technique (loss of variant calling, presence of pathogenic variants in not sequenced regions, copy number variations not always revealed), or to the presence of diseases-causing variants in new genes or genes not included in the panels. In such cases, results could be further improved by considering other technical approaches (WES or WGS) (Mansour-Hendili et al., 2020).

In a portion of cases reported in literature up to 45%, the genetic testing changed the initial diagnosis, in particular when transfusion dependence prevented laboratory investigations from being carried out, and the suspect was based only on clinical features (Russo et al., 2018). In our experience, when detailed clinical history is available together with fresh blood samples collected far from transfusions, first and second level laboratory diagnosis for CHAs has a good level of specificity, as demonstrated by the finding of only two patients who changed diagnosis after NGS analysis inside group 1: one patient previously diagnosed as HS had indeed a pathogenic variant in *PIEZO1* gene, and one case with a long-lasting diagnosis of overhydrated stomatocytosis (done on morphological bases, with

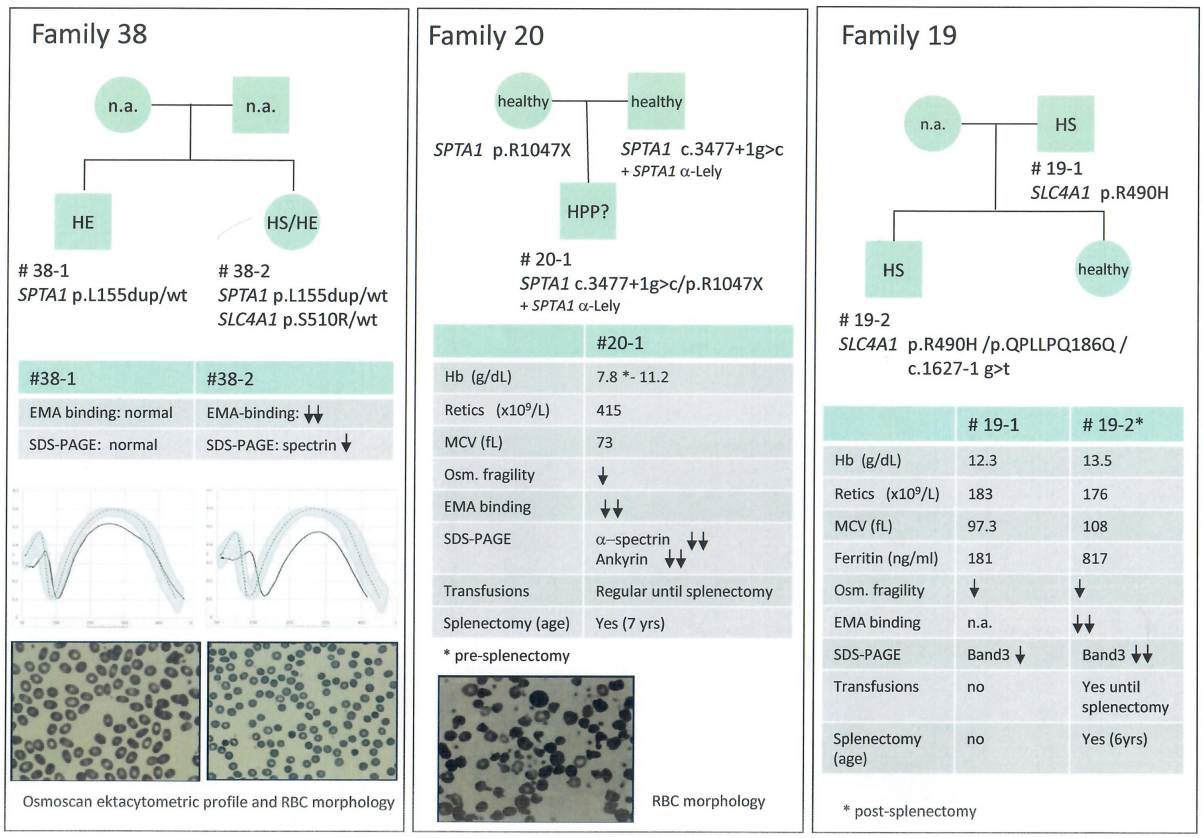

FIGURE 2 | Families with erythrocyte membrane defects and complex phenoptypes and/or intrafamily variability.

18% of stomatocytes and right shift of ektacytometry curve) was indeed a case of familial sitosterolemia with homozygous mutation p.R263Q in *ABCG8* gene (Berge et al., 2000). In both cases the molecular diagnosis changed the clinical management: in the first case the patient was warned about the thrombotic risk associated with splenectomy in hereditary stomatocytosis, and in the second case suggestions were given about dietary reduction of plant sterols consumption, to reduce cardiovascular risk that is associated with familial sitosterolemia (Tzavella et al., 2017). Patients affected by hereditary sitosterolemia may display an extremely variable clinical phenotype, in some cases restricted to abnormal hematological features, leading to misdiagnosis with hereditary stomatocytosis, immune thrombocytopenia (ITP), or Evans syndrome. The mechanisms of hematologic changes in these patients are so far unexplained, and a toxic effect of plant sterols on red blood cells has been hypothezied from *in vitro* experiments (Wang et al., 2012). The finding of two cases in our series, in line with increasing reports of the last years (Wang et al., 2014; Zheng et al., 2019), suggest that sitosterolemia may have an underestimated prevalence, and it should be taken in account in differential diagnosis of CHAs, in particular when stomatocytosis and concomitant macrothrombocytopenia are observed.

Combined defects of red cell membrane and/or metabolism are very rare, and the fact that carriership for a metabolic defect might modify the clinical expression of a membrane defect is still debated (van Zwieten et al., 2015; Fermo et al., 2017). However, the detection of cases with concomitant red cell defects has increased in the last years after the introduction of NGS analysis (Russo et al., 2018; Mansour-Hendili et al., 2020) suggesting that these conditions might not be so rare, also possibly due to protection toward malaria infection. In this series we found the association of G6PD deficiency and *PIEZO1* stomatocytosis in two female patients (mother and daughter) with suspected hereditary stomatocytosis. Among families with membrane defects and complex intra-family phenotypes, we were able to identify a patient with mixed HS/HE who carried two variants in *SPTA1* and *SLC4A1* gene.

Notably, in addition to the disease-causing mutations, four patients also displayed heterozygous variants in other genes associated with hemolytic anemias (see **Table 1**). Although a synergistic effect of heterozygous variants has been hypothesized by some authors (van Zwieten et al., 2015; Pereira et al., 2016), in the presented cases the contribution of these variants to the phenotype remains to be determined.

A careful analysis of Group 2 put in light the limitations of laboratory work-up of CHAs. Only two among the undiagnosed families were found to have HS, suggesting that most of the HS patients can be correctly diagnosed during first and second level screening tools (Fermo et al., 2021). On the

other hand, 10 out of the 19 families belonging to this group had an enzyme defect; in five of them enzymopathies were previously excluded because of normal enzyme activity, in the remaining cases the enzyme assays were not performed due to recent transfusions or unavailability of the appropriate sample. RBC enzyme defects are often detected by NGS in cases of unexplained anemia (Roy et al., 2016) or in patients misdiagnosed as CDAII (Shefer Averbuch et al., 2018; Russo et al., 2018), suggesting that this approach may greatly improve the diagnosis of these disorders.

In this series two PK deficient cases carrying known pathogenic variants (p.R486W, p.T384M, and p.V320M) repeatedly showed normal PK activity (14.7 and 18.8 IU/gHb, respectively, reference range 11.9–16.5), in absence of clear explanation (reticulocyte/WBC contamination excluded). Information on sensitivity of spectrophotometric enzyme assays is scanty, in particular for the rarer defects (Bianchi et al., 2019) but, as shown in the present cohort of patients, it will be possibly available in the next future through the systematic analysis of undiagnosed cases by NGS technologies.

Interestingly, we identified a triosephosphate isomerase deficiency in a 7 month child presenting at the time of the study only hemolytic anemia without neuromuscular manifestations. An early diagnosis allowed to inform and prepare the family and to offer bone marrow transplantation (BMT) as a therapeutic option before that neurological damage became evident (Conway et al., 2018); BMT was refused by the parents and the patient developed neurological signs at the age of 18 months. Early diagnosis in red cell disorders by NGS technologies opens interesting landscapes and perspectives in view of future therapeutic approaches for these diseases

	Laboratory testing	Molecular analysis (t-NGS)
HS	EMA-binding test Ectacytometry Others	High molecular heterogenity Consistency with clinical and laboratory features required
HE	Osmotic fragility tests Ectacytometry RBC morphology	High molecular heterogenity Consistency with clinical and laboratory features required
HSt- *PIEZO1*	Rbc morphology; Ektacytometry Always requiring molecular testing to confirm diagnosis	Highly polymorphic gene Functional tests mandatory in presence of new variants
HSt-*KCNN4*	Absence of specific laboratory markers	
RBC enzyme defects	RBC enzyme assay . Always requiring molecular testing to confirm diagnosis	
Familial sitosterolemia	Complete blood count	
Atypical conditions		

FIGURE 3 | Advandages and limitations of laboratory approach vs. t-NGS technologies in congenital hemolytic anemias. The laboratory tests/parameters specifically useful for diagnosis of different diseases are reported. Brilliant green, exhaustive diagnostic approach; Green, requiring other approaches to confirm the diagnosis; gray, insufficient laboratory markers to reach the diagnosis.

(Garcia-Gomez et al., 2016; Grace et al., 2019; Dessy-Rodriguez et al., 2020; Hrizo et al., 2021).

Among enzymopathies, we also identified 3 cases with undiagnosed G6PD deficiency, an heterozygous woman and two men with G6PD variants associated with chronic hemolysis, conditions in some cases underdiagnosed. A correct diagnosis enabled to give specific recommendation regarding contraindication for drugs associated with hemolytic anemia in G6PD -deficient patients (Luzzatto et al., 2020).

Differently from the *PIEZO1* mutated cases, all the *KCNN4* mutated patients belonged to group 2, confirming that molecular testing, and in particular NGS approaches, are the only diagnostic tools able to identify Gardos channelopathy, given the absence of a specific clinical or biological phenotype in this disorder; in fact, although ektacytometry, and some RBC and reticulocytes indices (Picard et al., 2019, 2021) may help to differentiate *PIEZO1* from *KCNN4* cases, no hematological parameter or specific laboratory test enable to differentiate Gardos channelopathy from other CHAs.

In conclusion, by considering the entire cohort here studied, the implementation of diagnostic work-up with t-NGS analysis increased the number of diagnoses of patients with unexplained anemia up to 35%. As reported in **Figure 3**, cytoskeleton defects (HS/HE) are well diagnosed by laboratory approaches, deserving NGS only to atypical cases; on the other hand, the diagnosis of Gardos channelopathy, some RBC enzyme defects, familial siterosterolemia, X-linked defects in females and other rare and ultra-rare conditions definitely benefits of NGS approaches. However, it should be always considered that a set of functional tests is required to validate the molecular results and assess pathogenicity of the new identified variants, in particular in highly polymorphic genes such as *PIEZO1*.

DATA AVAILABILITY STATEMENT

The datasets presented in this study can be found in online repositories. The names of the repository/repositories and accession number(s) can be found in the article/ **Supplementary Table 1**.

ETHICS STATEMENT

The studies involving human participants were reviewed and approved by Fondazione IRCCS Ca' Granda Ospedale Maggiore Policlinico. Written informed consent to participate in this study was provided by the participants' legal guardian/next of kin.

AUTHOR CONTRIBUTIONS

EF and PB designed the study and performed NGS analysis and molecular studies. CV, AnZ, and AM performed laboratory investigations. WB, AZ, SP, EK, and JG followed-up patients. EF and PB drafted the manuscript, all other authors revised and approved the manuscript. All authors contributed to the article and approved the submitted version.

FUNDING

The study was supported by Fondazione IRCCS Ca' Granda Policlinico Milano, Project number RC2020 175/05 and was generated in line with the European Reference Network on Rare Hematological Diseases (ERN-EuroBloodNet) FPA 739541.

SUPPLEMENTARY MATERIAL

The Supplementary Material for this article can be found online at: https://www.frontiersin.org/articles/10.3389/fphys.2021.684569/full#supplementary-material

Supplementary Table 1 | Genes associated with CHAs investigated through a 43 genes-targeted Next Generation Sequencing panel.

REFERENCES

Agarwal, A. M., Nussenzveig, R. H., Reading, N. S., Patel, J. L., Sangle, N., Salama, M. E., et al. (2016). Clinical utility of next-generation sequencing in the diagnosis of hereditary haemolytic anaemias. *Br. J. Haematol.* 174, 806–814. doi: 10.1111/bjh.14131

Berge, K. E., Tian, H., Graf, G. A., Yu, L., Grishin, N. V., Schultz, J., et al. (2000). Accumulation of dietary cholesterol in sitosterolemia caused by mutations in adjacent ABC transporters. *Science* 290, 1771–1775.

Beutler, E., Blume, K. G., Kaplan, J. C., Lohr, G. W., Ramot, B., and Valentine, W. N. (1977). International Committee for Standardization in Haematology: recommended methods for red-cell enzyme analysis. *Br. J. Haematol.* 35, 331–340.

Bianchi, P., Fermo, E., Glader, B., Kanno, H., Agarwal, A., Barcellini, W., et al. (2019). Addressing the diagnostic gaps in pyruvate kinase deficiency: Consensus recommendations on the diagnosis of pyruvate kinase deficiency. *Am. J. Hematol.* 94, 149–161. doi: 10.1002/ajh.25325

Bianchi, P., Fermo, E., Vercellati, C., Marcello, A. P., Porretti, L., Cortelezzi, A., et al. (2012). Diagnostic power of laboratory tests for hereditary spherocytosis: a comparison study in 150 patients grouped according to molecular and clinical characteristics. *Haematologica* 97, 516–523. doi: 10.3324/haematol.2011.052845

Bianchi, P., Vercellati, C., and Fermo, E. (2020). How will next generation sequencing (NGS) improve the diagnosis of congenital hemolytic anemia?. *Ann. Transl. Med.* 8:268. doi: 10.21037/atm.2020.02.151

Choi, H. O., Choi, Q., Kim, J. A., Im, K. O., Park, S. N., Park, Y., et al. (2019). Molecular diagnosis of hereditary spherocytosis by multi-gene target sequencing in Korea: matching with osmotic fragility test and presence of spherocyte. *Orphanet. J. Rare Dis.* 14:114. doi: 10.1186/s13023-019-1070-0

Chonat, S., Risinger, M., Sakthivel, H., Niss, O., Rothman, J. A., Hsieh, L., et al. (2019). The Spectrum of SPTA1-Associated Hereditary Spherocytosis. *Front. Physiol.* 10:815. doi: 10.3389/fphys.2019.00815

Conway, A. J., Brown, F. C., Hortle, E. J., Burgio, G., Foote, S. J., Morton, C. J., et al. (2018). Bone marrow transplantation corrects haemolytic anaemia in a novel ENU mutagenesis mouse model of TPI deficiency. *Dis. Model Mech.* 11:dmm034678. doi: 10.1242/dmm.034678

Del Orbe Barreto, R., Arrizabalaga, B., De la Hoz, A. B., García-Orad, Á, Tejada, M. I, Garcia-Ruiz, J. C., et al. (2016). Detection of new pathogenic mutations in

patients with congenital haemolytic anaemia using next-generation sequencing. *Int. J. Lab. Hematol.* 38, 629–338. doi: 10.1111/ijlh.12551

Dessy-Rodriguez, M., Fañanas-Baquero, S. A., Venturi, V., Payán-Pernía, S., Tornador, C., Hernandez, G., et al. (2020). Quintana Bustamante, O. Modelling Congenital Dyserythropoietic Anemia Type II through Gene Editing in Hematopoietic Stem and Progenitor Cells. *Blood* 136(Suppl. 1):27.

Fairbanks, G., Steck, T. L., and Wallach, D. F. H. (1971). Electrophoretic analysis of the major polypeptides of the human erythrocyte membrane. *Biochemistry* 10, 2606–2617.

Fermo, E., Monedero-Alonso, D., Petkova-Kirova, P., Makhro, A., Pérès, L., Bouyer, G., et al. (2020). Gardos channelopathy: functional analysis of a novel KCNN4 variant. *Blood Adv.* 4, 6336–6341. doi: 10.1182/bloodadvances.2020003285

Fermo, E., Vercellati, C., and Bianchi, P. (2021). Screening tools for hereditary hemolytic anemia: new concepts and strategies. *Expert Rev. Hematol.* 1:11. doi: 10.1080/17474086.2021.1886919

Fermo, E., Vercellati, C., Marcello, A. P., Zaninoni, A., Aytac, S., Cetin, M., et al. (2019). Clinical and Molecular Spectrum of Glucose-6-Phosphate Isomerase Deficiency. Report of 12 New Cases. *Front. Physiol.* 10:467. doi: 10.3389/fphys.2019.00467

Fermo, E., Vercellati, C., Marcello, A. P., Zaninoni, A., van Wijk, R., Mirra, N., et al. (2017). Hereditary Xerocytosis due to Mutations in PIEZO1 Gene Associated with Heterozygous Pyruvate Kinase Deficiency and Beta-Thalassemia Trait in Two Unrelated Families. *Case Rep. Hematol.* 2017:2769570. doi: 10.1155/2017/2769570

Garcia-Gomez, M., Calabria, A., Garcia-Bravo, M., Benedicenti, F., Kosinski, P., López-Manzaneda, S., et al. (2016). Safe and Efficient Gene Therapy for Pyruvate Kinase Deficiency. *Mol. Ther.* 24, 1187–1198. doi: 10.1038/mt.2016.87

Grace, R. F., Rose, C., Layton, D. M., Galactéros, F., Barcellini, W., Morton, D. H., et al. (2019). Safety and Efficacy of Mitapivat in Pyruvate Kinase Deficiency. *N. Engl. J. Med.* 381, 933–944. doi: 10.1056/NEJMoa1902678

Hrizo, S. L., Eicher, S. L., Myers, T. D., McGrath, I., Wodrich, A. P. K., Venkatesh, H., et al. (2021). Identification of protein quality control regulators using a Drosophila model of TPI deficiency. *Neurobiol. Dis.* 15:105299. doi: 10.1016/j.nbd.2021.105299

Kedar, P. S., Gupta, V., Dongerdiye, R., Chiddarwar, A., Warang, P. P., and Madkaikar, M. R. (2019a). Molecular diagnosis of unexplained haemolytic anaemia using targeted next-generation sequencing panel revealed (p.Ala337Thr) novel mutation in GPI gene in two Indian patients. *J. Clin. Pathol.* 72, 81–85. doi: 10.1136/jclinpath-2018-205420

Kedar, P. S., Harigae, H., Ito, E., Muramatsu, H., Kojima, S., Okuno, Y., et al. (2019b). Study of pathophysiology and molecular characterization of congenital anemia in India using targeted next-generation sequencing approach. *Int. J. Hematol.* 110, 618–626. doi: 10.1007/s12185-019-02716-9

King, M. J., Garçon, L., Hoyer, J. D., Iolascon, A., Picard, V., Stewart, G., et al. (2015). International Council for Standardization in Haematology.ICSH guidelines for the laboratory diagnosis of nonimmune hereditary red cell membrane disorders. *Int. J. Lab. Hematol.* 37, 304–325. doi: 10.1111/ijlh.12335

Kopanos, C., Tsiolkas, V., Kouris, A., Chapple, C. E., Albarca Aguilera, M., Meyer, R., et al. (2019). VarSome: the human genomic variant search engine. *Bioinformatics* 35, 1978–1980. doi: 10.1093/bioinformatics/bty897

Laemmli, U. K. (1970). Cleavage of structural proteins during the assembly of the head of bacteriophage T4. *Nature* 227, 680–685.

Luzzatto, L., Ally, M., and Notaro, R. (2020). Glucose-6-phosphate dehydrogenase deficiency. *Blood* 136, 1225–1240. doi: 10.1182/blood.2019000944

Mansour-Hendili, L., Aissat, A., Badaoui, B., Sakka, M., Gameiro, C., Ortonne, V., et al. (2020). Exome sequencing for diagnosis of congenital hemolytic anemia. *Orphanet. J. Rare Dis.* 15:180. doi: 10.1186/s13023-020-01425-5

Mariani, M., Barcellini, W., Vercellati, C., Marcello, A. P., Fermo, E., Pedotti, P., et al. (2008). Clinical and hematologic features of 300 patients affected by hereditary spherocytosis grouped according to the type of the membrane protein defect. *Haematologica* 93, 1310–1317.

Niss, O., Chonat, S., Dagaonkar, N., Almansoori, M. O., Kerr, K., Rogers, Z. R., et al. (2016). Genotype-phenotype correlations in hereditary elliptocytosis and hereditary pyropoikilocytosis. *Blood Cells Mol. Dis.* 61, 4–9. doi: 10.1016/j.bcmd.2016.07.003

Pereira, J., Bento, C., Maco, L., Gonzalez, A., Vagace, J., and Ribeiro, M. L. (2016). Congenital dyserythropoietic anemia associated to a GATA1 mutation aggravated by pyruvate kinase deficiency. *Ann. Hematol.* 95, 1551–1553. doi: 10.1007/s00277-016-2720-0

Picard, V., Guitton, C., Mansour-Hendili, L., Jondeau, B., Bendélac, L., Denguir, M., et al. (2021). Rapid Gardos Hereditary Xerocytosis Diagnosis in 8 Families Using Reticulocyte Indices. *Front. Physiol.* 11:602109. doi: 10.3389/fphys.2020.602109

Picard, V., Guitton, C., Thuret, I., Rose, C., Bendelac, L., Ghazal, K., et al. (2019). Clinical and biological features in PIEZO1-hereditary xerocytosis and Gardos channelopathy: a retrospective series of 126 patients. *Haematologica* 104, 1554–1564. doi: 10.3324/haematol.2018.205328

Richards, S., Aziz, N., Bale, S., Bick, D., Das, S., Gastier-Foster, J., et al. (2015). ACMG Laboratory Quality Assurance Committee. Standards and guidelines for the interpretation of sequence variants: a joint consensus recommendation of the American College of Medical Genetics and Genomics and the Association for Molecular Pathology. *Genet. Med.* 17, 405–424. doi: 10.1038/gim.2015.30

Roy, N. B. A., Wilson, E. A., Henderson, S., Wray, K., Babbs, C., Okoli, S., et al. (2016). A novel 33-Gene targeted resequencing panel provides accurate, clinical-grade diagnosis and improves patient management for rare inherited anaemias. *Br. J. Haematol.* 175, 318–330. doi: 10.1111/bjh.14221

Russo, R., Andolfo, I., Manna, F., Gambale, A., Marra, R., Rosato, B. E., et al. (2018). Multi-gene panel testing improves diagnosis and management of patients with hereditary anemias. *Am. J. Hematol.* 93, 672–682. doi: 10.1002/ajh.25058

Russo, R., Marra, R., Rosato, B. E., Iolascon, A., and Andolfo, I. (2020). Genetics and Genomics Approaches for Diagnosis and Research Into Hereditary Anemias. *Front. Physiol.* 11:613559. doi: 10.3389/fphys.2020.613559

Shefer Averbuch, N., Steinberg-Shemer, O., Dgany, O., Krasnov, T., Noy-Lotan, S., Yacobovich, J., et al. (2018). Targeted next generation sequencing for the diagnosis of patients with rare congenital anemias. *Eur. J. Haematol.* 101, 297–304. doi: 10.1111/ejh.13097

Steinberg-Shemer, O., and Tamary, H. (2020). Impact of next-generation sequencing on the diagnosis and treatment of congenital anemias. *Mol. Diagn Ther.* 4, 397–407. doi: 10.1007/s40291-020-00478-3

Svidnicki, M. C. C. M., Zanetta, G. K., Congrains-Castillo, A., Costa, F. F., and Saad, S. T. O. (2020). Targeted next-generation sequencing identified novel mutations associated with hereditary anemias in Brazil. *Ann. Hematol.* 99, 955–962. doi: 10.1007/s00277-020-03986-8

Tzavella, E., Hatzimichael, E., Kostara, C., Bairaktari, E., Elisaf, M., and Tsimihodimos, V. (2017). Sitosterolemia: A multifaceted metabolic disorder with important clinical consequences. *J. Clin. Lipidol.* 11, 1095–1100. doi: 10.1016/j.jacl.2017.04.116

van Vuren, A., van der Zwaag, B., Huisjes, R., Lak, N., Bierings, M., Gerritsen, E., et al. (2019). The complexity of genotype-phenotype correlations in hereditary spherocytosis: a cohort of 95 patients. *HemaSphere* 3:4.

van Zwieten, R., van Oirschot, B. A., Veldthuis, M., Dobbe, J. G., Streekstra, G. J., van Solinge, W. W., et al. (2015). Partial pyruvate kinase deficiency aggravates the phenotypic expression of band 3 deficiency in a family with hereditary spherocytosis. *Am. J. Hematol.* 90, E35–E39. doi: 10.1002/ajh.23899

Vives-Corrons, J. L., Krishnevskaya, E., Rodriguez, I. H., and Ancochea, A. (2021). Characterization of hereditary red blood cell membranopathies using combined targeted next-generation sequencing and osmotic gradient ektacytometry. *Int. J. Hematol.* 113, 163–174. doi: 10.1007/s12185-020-03010-9

Wang, G., Cao, L., Wang, Z., Jiang, M., Sun, X., Bai, X., et al. (2012). Macrothrombocytopenia/stomatocytosis specially associated with phytosterolemia. *Clin. Appl. Thromb. Hemost.* 18, 582–587.

Wang, Z., Cao, L., Su, Y., Wang, G., Wang, R., Yu, Z., et al. (2014). Specific macrothrombocytopenia/hemolytic anemia associated with sitosterolemia. *Am. J. Hematol.* 89, 320–324.

Xue, J., He, Q., Xie, X., Su, A., and Cao, S. (2019). Clinical utility of targeted gene enrichment and sequencing technique in the diagnosis of adult hereditary spherocytosis. *Ann. Transl. Med.* 7:527.

Zaninoni, A., Fermo, E., Vercellati, C., Consonni, D., Marcello, A. P., et al. (2018). Use of Laser Assisted Optical Rotational Cell Analyzer (LoRRca MaxSis) in the Diagnosis of RBC Membrane Disorders, Enzyme Defects, and Congenital Dyserythropoietic Anemias: A Monocentric Study on 202 Patients. *Front. Physiol.* 9:451. doi: 10.3389/fphys.2018.00451

Zheng, J., Ma, J., Wu, R. H., Zhang, X., Su, Y., Zhang, R., et al. (2019). Unusual presentations of sitosterolemia limited to hematological abnormalities: A report of four cases presenting with stomatocytic anemia and thrombocytopenia with macrothrombocytes. *Am. J. Hematol.* 94, E124–E127.

Conflict of Interest: The authors declare that the research was conducted in the absence of any commercial or financial relationships that could be construed as a potential conflict of interest.

Advantages of publishing in Frontiers

OPEN ACCESS
Articles are free to read for greatest visibility and readership

FAST PUBLICATION
Around 90 days from submission to decision

HIGH QUALITY PEER-REVIEW
Rigorous, collaborative, and constructive peer-review

TRANSPARENT PEER-REVIEW
Editors and reviewers acknowledged by name on published articles

Frontiers
Avenue du Tribunal-Fédéral 34
1005 Lausanne | Switzerland

Visit us: www.frontiersin.org
Contact us: frontiersin.org/about/contact

REPRODUCIBILITY OF RESEARCH
Support open data and methods to enhance research reproducibility

DIGITAL PUBLISHING
Articles designed for optimal readership across devices

FOLLOW US
@frontiersin

IMPACT METRICS
Advanced article metrics track visibility across digital media

EXTENSIVE PROMOTION
Marketing and promotion of impactful research

LOOP RESEARCH NETWORK
Our network increases your article's readership